

PROCEEDINGS OF THE
14th INTERNATIONAL
CONFERENCE
ON NUCLEAR REACTION
MECHANISMS

Varenna (Italy), Villa Monastero
June 15 – 19, 2015

edited by
F. Cerutti, M. Chadwick, A. Ferrari, T. Kawano and P. Schoofs



CERN
Geneva
2015

**Proceedings of the
14th International Conference
on Nuclear Reaction Mechanisms**

Varenna (Italy), Villa Monastero,
June 15-19, 2015

edited by
F. Cerutti, M. Chadwick, A. Ferrari, T. Kawano and P. Schoofs

CERN-Proceedings-2015-001
ISBN 978-92-9083-418-2 (paperback)
ISBN 978-92-9083-419-9 (PDF)
Copyright ©the Authors, 2015. Published by CERN

This volume is indexed in: CERN Document Server (CDS), INSPIRE and Scopus
Available online at <https://cds.cern.ch>
This volume should be cited as:

Proceedings of the 14th International Conference on Nuclear Reaction Mechanisms, edited by F. Cerutti, M. Chadwick, A. Ferrari, T. Kawano and P. Schoofs, CERN-Proceedings-2015-001 (CERN, Geneva, 2015).

A contribution in this volume should be cited as:

[Author name(s)], in Proceedings of the 14th International Conference on Nuclear Reaction Mechanisms, edited by F. Cerutti, M. Chadwick, A. Ferrari, T. Kawano and P. Schoofs, CERN-Proceedings-2015-001 (CERN, Geneva, 2015), pp. [first page] – [last page].

FOREWORD

We would like to sincerely thank Professor Hans A. Weidenmüller, who was kindly available to come again to Varenna for his celebration, unanimously and enthusiastically endorsed by the International Advisory Committee, during this 14th Conference on Nuclear Reaction Mechanisms (NRM). It was a nice privilege to listen to his enlightening talk in the course of the special evening session and to benefit from his continuous presence throughout the week.

Remaining faithful to the specific identity and traditional structure of the NRM meetings, this year's program featured about 75 oral presentations, filling 17 regular sessions that, put together, compose a rich landscape including novel progresses in fundamental nuclear physics as well as forefront applications, especially focused on the medical field.

A special thought is dedicated to Prof. Giuseppe Viesti, who served in the past on the Organizing Committee, as an eminent exponent of the Padua's school, and passed away in January 2015. A vivid memory of him was offered by Prof. Laszlo Sajo Bohus last June.

In acknowledging the essential support we got from several institutions and colleagues and the motivating interest of all the participants, we renew the Varenna appointment for 2018.

A. Ferrari

F. Cerutti

M. Chadwick

T. Kawano

DEDICATION

It is an honor for us to dedicate this 14th edition of the Varenna's Conference to

Professor Hans A. Weidenmüller



- 1957** : PhD in Theoretical Physics, Heidelberg University
- 1957 - 1958** : Postdoctoral Fellow, Heidelberg University
- 1958 - 1959** : Research Associate, Department of Physics, University of Minnesota
- 1959 - 1960** : Research Assistant, Department of Physics and Astronomy, Caltech
- 1960 - 1962** : Visiting Assistant Professor, Department of Physics and Astronomy, Caltech
- 1962 - 1963** : Visiting Professor, Heidelberg University
- 1963 - 1972** : Full Professor (Ordinarius), Heidelberg University
- 1968 - 2001** : Scientific Member and Director, Max-Planck-Institut für Kernphysik, Heidelberg
- 1972 - 2001** : Full Professor ad personam, Heidelberg University
- 2001 - :** Professor Emeritus, Heidelberg University
- 2001 - :** Scientific Member, Max-Planck-Institut für Kernphysik, Heidelberg

RESEARCH AREAS

Theoretical Nuclear Physics

Beta Decay, Scattering Theory, Nuclear Reactions in the Shell Model, Doorway States and Isobaric Analogue Resonances, Effective Interaction, Direct and Compound Nucleus Reactions, Precompound Reactions, Heavy-Ion Reactions, Fission, Symmetries and Invariances in Nuclear Reactions, Statistical Theory of Nuclear Reactions, Random Matrices and Chaos in Nuclei.

Random Matrices

Supersymmetry (Susy), Universality, Susy in QCD, Chaotic Scattering in Nuclei and in Microwave Billiards, Embedded Random-Matrix Ensembles.

Condensed-Matter Physics

Quantum Hall Effect, Universal Conductance Fluctuations, Quantum Dots, Persistent Currents, Quantum Zeno Effect.

HONORS

1968 - 1969 : Visiting Professor, Yale University

1970 - : Fellow, American Physical Society

1971 : Visiting Professor, ETH Zurich

1973 - : Member, Heidelberg Academy of Sciences

1975 and 1988 : Fellow, Japan Society for the Promotion of Science

1977 - 1978 : Visiting Fellow, Balliol College, Oxford

1982 : Max-Planck-Medal of the German Physical Society

1984 : Visiting Scientist, Universite de Paris, Orsay

1985 : Fairchild Distinguished Scholar, Caltech

1991 : Honorary PhD, Weizmann Institute of Science, Rehovot, Israel

1991 - 1992 : Fellow, Wissenschaftskolleg zu Berlin

1993 : Order of Merit, Federal Republic of Germany

1993 : Festschrift Nuclear Physics A 560 (1993)

1995 : Humboldt South African Award

1997 - : Member, Leopoldina (German National Academy)

2000 : Dr. h. c. Rostock University

2000 : Capes Humboldt Prize, Brazil

2010 - : Life Member of the International Board, Weizmann Institute of Science

SELECT FUNCTIONS

1988 - 1992 : Chair, Chemisch-Physikalisch-Technische Sektion der Max-Planck-Gesellschaft

1992 - 1998 : Elected Member, Senat der Max-Planck-Gesellschaft

2001 - 2009 : Cochair, Scientific and Academic Advisory Committee, Weizmann Institute of Science

CHAIRMEN OF THE CONFERENCE

M.B. Chadwick	Los Alamos	A. Ferrari	CERN
----------------------	------------	-------------------	------

SCIENTIFIC SECRETARIES

F. Cerutti	CERN	T. Kawano	Los Alamos
-------------------	------	------------------	------------

ORGANIZING COMMITTEE

G. Battistoni	Milan	F. Camera	Milan
F. Cerutti	CERN, Geneva	M.B. Chadwick	Los Alamos
A. Ferrari	CERN, Geneva	T. Kawano	Los Alamos
A. Mairani	Pavia/Heidelberg	D. Pifferetti	Milan
P. Sala	Milan	E. Tomasi-Gustafson	CEA, Saclay

INTERNATIONAL ADVISORY COMMITTEE

F. Ballarini	Pavia	E. Bauge	Bruyères-le-Châtel
A. Bonaccorso	Pisa	T. Borello Lewin	São Paulo
B.A. Brown	Michigan State	Z. Buthelezi	iThemba Labs
L. Canton	Padua	R. Capote	IAEA, Vienna
F. Cappuzzello	LNS, Catania	S. Chiba	TITech, Tokyo
N. Colonna	Bari	L. Corradi	LNL, Legnaro
P. (Vivian) Demetriou	IAEA, Vienna	J. Escher	Livermore
S. Förtsch	iThemba Labs	E. Gadioli	Milan
A. Guglielmetti	Milan	M. Herman	Brookhaven
H. Horiuchi	Osaka	A. Koning	NRG, Petten
S. Leray	CEA, Saclay	T. Motobayashi	RIKEN, Tokyo
F.M. Nunes	Michigan State	K. Parodi	Munich
R.J. Peterson	Colorado	L. Pinsky	Houston
A. Plompen	EC-IRMM, Geel	L. Sajo Bohus	Caracas
L. Sihver	Gothenburg	K. Tanaka	KEK, Tsukuba
H. Toki	Osaka		

SECRETARY'S OFFICE

A. Fedynitch	CERN	C. Mancini Terracciano	CERN
F. Meneghini	Lecco	D. Pifferetti	Milan
P. Schoofs	CERN	N. Shetty	CERN

ACKNOWLEDGEMENTS

The conference was supported by:

- Los Alamos National Laboratory, USA
- CERN, European Organization for Nuclear Research, Switzerland
- Department of Physics, University of Milan, Italy
- National Institute of Nuclear Physics (INFN), Italy
- "Piero Caldirola" International Centre for the promotion of Science

The chairmen and the members of the organizing committee of the conference wish to express their deepest appreciation and thanks to all these institutions.

CONFERENCE PROGRAM

MONDAY, JUNE 15

9.30 – 11.00 *Chairman : M.B. Chadwick*

Fission

- F. Tovesson** Studies of fission fragment properties at LANSCE
F.J. Hambsch Prompt fission neutron emission of $^{235}\text{U}(n,f)$: thermal and resonance region
R. Léguillon Systematic behavior of fission fragment mass distribution for nuclei populated by multi-nucleon transfer reaction

11.30 – 13.00 *Chairman : E. Bauge*

Fission

- C.Y. Wu** Total prompt γ -ray emission in fission of ^{235}U , ^{239}Pu , ^{241}Pu , and ^{252}Cf
A. Tsinganis Measurement of the $^{240}\text{Pu}(n,f)$ cross-section at the CERN n_TOF facility: first results from Experimental Area II (EAR-2)
P. Talou Correlated prompt fission data
A. Chebboubi Determinations of fission fragment spin distributions after neutron evaporation at LOHENGRIN spectrometer

15.00 – 17.00 *Chairman : L. Canton*

Nuclear Structure

- Y. Alhassid** Microscopic nuclear level densities by the shell model Monte Carlo method
B.R. Barrett The No-Core Gamow Shell Model: Including the Continuum in the NCSM
W. Luo Study of nuclear collective states above neutron threshold using monochromatic γ -ray beams at ELI-NP
G. Gosselin Simplified configuration effects for Nuclear Excitation by Electronic Transition in plasma
G. Bocchi Study of Ca isotopes via neutron capture reactions

17.35 – 19.10 *Chairman : C.H. Dasso*

Nuclear Structure

- B.A. Brown** Related Aspects of the Pairing Interaction in Neutrinoless Double-Beta Decay, Nuclear Masses and Two-Nucleon Transfer
M. Lenske Bound States Embedded in the Continuum in Nuclear and Hadron Physics
G. Royer ^8Be , ^{12}C , ^{16}O , ^{20}Ne , ^{24}Mg , and ^{32}S nuclei and alpha clustering within a Generalized Liquid Drop Model
R. Neveling Characterization of cluster states in ^{16}O

TUESDAY, JUNE 16

9.30 – 11.00 *Chairman : H. Lenske*

Reactions: models

- | | |
|---------------------|---|
| A. Palffy | Laser-induced reactions in the quasiadiabatic regime |
| L. Canton | Alpha- ^6He scattering and the quest for microscopic guidance for orthogonalizing pseudopotentials |
| M. Toyokawa | Microscopic approach to nucleon-nucleus and nucleus-nucleus scattering in the framework of chiral effective field theory and BHF theory |
| P. Marini | Strengths and limitations of the surrogate reaction method to access neutron-induced cross sections of actinides |
| M. Avrigeanu | Role of the direct mechanisms in the deuteron-induced surrogate reactions |

11.30 – 13.00 *Chairman : A. Ferrari*

Reactions: measurements

- | | |
|-----------------------|--|
| D. Dell'Aquila | Investigation of ^{10}Be and ^{16}C structure with break-up reactions at intermediate energies |
| I. Lombardo | New direct measurements of the $^{19}\text{F}(p, \alpha_0)^{16}\text{O}$ reaction at very low energies |
| C. Mancini | Quasi-elastic break-up of ^{12}C in ^8Be and ^4He at an incident energy of 33 MeV/n |
| M. Labalme | ^{12}C fragmentation measurements for hadrontherapy |

15.00 – 17.00 *Chairman : R.A. Broglia*

Hadronic and EM probes

- | | |
|-----------------------------|--|
| F.M. Nunes | One-nucleon transfer reactions and the optical potential |
| R. Capote Noy | Nucleon scattering on major actinides using a dispersive optical model with extended couplings |
| S. Karataglidis | Comparison of coupled-channel studies of nucleon scattering from oxygen isotopes with the shell model |
| T. Borello Lewin | Coulomb-nuclear interference in the inelastic scattering of ^6Li to the first quadrupole state in the Ge isotopic chain |
| E. Tomasi-Gustafsson | Peculiar features of proton electromagnetic form factors |

17.30 – 18.40 *Chairman : E. Tomasi-Gustafsson*

Neutrino, hypertriton

- | | |
|---------------------|--|
| A.N. Antonov | Charge-current and Neutral Current Quasielastic Neutrino(Antineutrino) Scattering on ^{12}C with Realistic Spectral and Scaling Functions |
| M.V. Ivanov | Charged current inclusive neutrino cross sections: Superscaling extension to the pion production and realistic spectral function for quasielastic region |
| C. Hartnack | Hypertritons from intermediate energy heavy ion collisions: a marriage of fire and ice |

WEDNESDAY, JUNE 179.30 – 11.00 *Chairman : L. Pinsky**Codes*

- A. Fontana** Nuclear interaction model developments in FLUKA
A. Fedynitch PHOJET/DPMJET-III: status and recent developments
T. Ogawa Revision of JAERI quantum molecular dynamics model for analysis of peripheral nucleus-nucleus collisions
L. Sihver Improvements and developments of physics models in PHITS for radiotherapy and space applications
H. Duarte Deterministic approach compared to an Intranuclear Cascade model for particle production in nonelastic reactions induced by nucleon
N. Shetty Nuclear reactions in the context of LHC operation

11.30 – 13.00 *Chairman : R. Capote Noy**Facilities*

- G. La Rana** The new generation ISOL facility SPES at LNL
F. Gunsing The upgraded neutron time-of-flight facility n_TOF at CERN
P. Tanaka Present Status and Future Plans of J-PARC Hadron Experimental Facility

EVENING SESSION**in honor of Prof. Weidenmüller**21.00 – 23.00 *Chairman : A. Palfy*

- T. Kawano** Random matrix approach to the statistical compound nuclear reactions at low energies using the Monte Carlo technique
M. Herman
H. Weidenmüller

THURSDAY, JUNE 189.30 – 11.00 *Chairman : F.M. Nunes****Deuteron induced reactions, breakup***

- I.J. Thompson** Challenges for the description of one-nucleon transfers to resonance states
- G. Potel** Deuteron induced reactions, compound nucleus momentum distributions and the surrogate method
- B.V. Carlson** Systematics of Elastic and Inelastic Deuteron Breakup
- G. Arbanas** Coupled-channel computation of direct neutron capture and (d, p) reactions on non-spherical nuclei
- T. Matsumoto** Study on breakup mechanism of unstable nuclei with CDCC

11.30 – 13.00 *Chairman : F. Camera****Exotic Nuclei***

- R.A. Broglia** Testing two-nucleon transfer reaction mechanism with elementary modes of excitation in exotic nuclei
- R. Avigo** Investigation of Pygmy Dipole Resonance in neutron rich exotic nuclei
- S. Ceruti** Isospin mixing at finite temperature in proton rich 80 Zr nucleus
- A. Giaz** Thermal and Fast Neutron detection with two CLYC scintillators

15.00 – 17.00 *Chairman : L. Sihver****Hadrontherapy***

- P. Fossati** Clinical experience with carbon ion radiotherapy
- A. Mairani** Recent developments and applications of the FLUKA Monte Carlo code in ion beam therapy
- A. Embriaco** On the parametrization of lateral dose profiles in proton radiation therapy
- E.V. Bellinzona** An analytical solution to lateral dose prediction in Hadrontherapy
- A. Rucinski** Measurements of secondary particles emitted by ^{12}C , ^4He and ^{16}O ion beams in view of innovative dose profiling technique in Particle Therapy

17.35 – 19.10 *Chairman : A. Fontana****Radiobiology and Imaging***

- F. Ballarini** BIANCA, a model of radiation-induced cell death: biophysical mechanisms and possible applications for hadron therapy
- I. Dokic** Integrative Radiobiology of X-ray vs. Protons, Helium, Carbon and Oxygen Ions
- I. Rinaldi** Status and perspective of emission imaging techniques for ion beam therapy in Lyon
- L. Sajo Bohus** GDR (γ, n) Reaction in Radiotherapy Treatment-Fields with 18 MV Linear Accelerators

FRIDAY, JUNE 199.00 – 11.00 *Chairman : M. Herman**Data and Astrophysics*

- M.B. Chadwick** Measuring nuclear reaction cross sections on actinides at LANSCE
G. Henning Measurement of (n, xn gamma) reaction cross section in W isotopes
W.A. Richter Determination of the important $^{30}\text{P}(p,\gamma)^{31}\text{S}$ astrophysical rapid-proton capture reaction rate
A.C. Larsen Enhanced low-energy gamma-decay probability for nuclei in the Fe-Mo region – implications for r-process (n, γ) reaction rates
G. Tagliente Recent results in Nuclear Astrophysics of n_TOF facility at CERN

11.30 – 12.30 *Chairman : F. Gunsing**Data*

- P. Zugec** Integral cross section measurement of the $^{12}\text{C}(n,p)^{12}\text{B}$ reaction at n_TOF
T. Sanami Experimental data of light mass fragment production for intermediate energy nucleon and nucleus induced reactions
L. Pinsky Measurement of the Radiation Environment Inside NASA's New Orion Spacecraft On Its First Test-Flight

14.30 – 16.10 *Chairman : T. Kawano**Reactions*

- F.C.L. Crespi** Isospin Character of Low-Lying Pygmy Dipole States via Inelastic Scattering of ^{17}O
R. Linares Appearance of rainbow-like feature in the elastic scattering of ^{16}O on ^{27}Al at $E_{lab} = 280$ MeV
E. Betak Pre-equilibrium (exciton) model and the heavy-ion reactions with cluster emission
R.N. Sagaidak Formation, separation and detection of evaporation residues produced in complete fusion reactions
C. Agodi NUMEN Project@LNS: Heavy Ions Double Charge Exchange reactions towards the $0\nu\beta\beta$ Nuclear Matrix Element determination

Contents

F. Tovesson <i>et al.</i> Studies of fission fragment properties at LANSCE	1
F.-J. Hamsch <i>et al.</i> Prompt fission neutron emission from $^{235}\text{U}(\text{n},\text{f})$: thermal and resonance region	7
C.Y. Wu <i>et al.</i> Total prompt γ -ray emission in fission of ^{235}U , $^{239,241}\text{Pu}$, and ^{252}Cf	15
A. Tsinganis <i>et al.</i> Measurement of the $^{240}\text{Pu}(\text{n},\text{f})$ cross-section at the CERN n_TOF facility: first results from EAR-2	21
P. Talou <i>et al.</i> Correlated Prompt Fission Data	27
A. Chebboubi <i>et al.</i> Determination of neutron-induced fission fragment spin distribution after neutron evaporation	33
Y. Alhassid <i>et al.</i> Microscopic nuclear level densities by the shell model Monte Carlo method	41
B. R. Barrett, G. Papadimitriou, N. Michel and M. Płoszajczak The No-Core Gamow Shell Model: Including the continuum in the NCSM	49
G. Bocchi <i>et al.</i> Study of Ca isotopes via neutron capture reactions	57
H. Lenske, S.E.A. Orrigo and Xu Cao Bound States in the Continuum in Nuclear and Hadron Physics	61
G. Royer, G. Ramasamy and P. Eudes ^8Be , ^{12}C , ^{16}O , ^{20}Ne , ^{24}Mg , and ^{32}S nuclei and alpha clustering within a generalized liquid drop model	71
R. Neveling <i>et al.</i> Characterization of a potential 4- α cluster state	79
R.A. Broglia <i>et al.</i> Testing two-nucleon transfer reaction mechanism with elementary modes of excitation in exotic nuclei	85
R. Avigo <i>et al.</i> Investigation of Pygmy Dipole Resonance in neutron rich exotic nuclei	91

A. Giaz <i>et al.</i>	
Thermal and fast neutron detection with two CLYC scintillators	95
A. N. Antonov <i>et al.</i>	
Charge-current and neutral-current quasielastic neutrino(antineutrino) scattering on ^{12}C with realistic spectral and scaling functions	101
M.V. Ivanov <i>et al.</i>	
Charged-current inclusive neutrino cross sections: Superscaling extension to the pion production and realistic spectral function for quasielastic region	109
C. Hartnack <i>et al.</i>	
Production of hypertritons in heavy ion collisions around the threshold of strangeness production	115
F.M. Nunes <i>et al.</i>	
One-nucleon transfer reactions and the optical potential	123
S. Karataglidis <i>et al.</i>	
Comparison of coupled-channel studies of nucleon scattering from oxygen isotopes with the shell model	131
T. Borello-Lewin <i>et al.</i>	
Coulomb-nuclear interference in the inelastic scattering of ^6Li to the first quadrupole state in the Ge isotopic chain	137
E. Tomasi-Gustafsson <i>et al.</i>	
Peculiar features of proton electromagnetic form factors	141
I.J. Thompson <i>et al.</i>	
One-nucleon transfers to resonance states	147
G. Potel <i>et al.</i>	
Inclusive deuteron-induced reactions and final neutron states	155
B.V. Carlson <i>et al.</i>	
Elastic and inelastic breakup of deuterons with energy below 100 MeV	163
G. Arbanas <i>et al.</i>	
A model of neutron capture and deuteron stripping on deformed nuclei	171
T. Matsumoto	
Study on breakup mechanism of unstable nuclei with CDCC	177
L. Canton <i>et al.</i>	
Alpha- ^6He scattering and the quest for microscopic guidance for orthogonalizing pseudopotentials	181

M. Toyokawa <i>et al.</i> Microscopic approach to NA and AA scattering in the framework of chiral effective field theory and Brueckner-Hartree-Fock theory	189
P. Marini <i>et al.</i> Strengths and limitations of the surrogate reaction method to access neutron-induced cross sections of actinides	195
M. Avrigeanu and V. Avrigeanu Role of the direct mechanisms in the deuteron-induced surrogate reactions	203
D. Dell'Aquila <i>et al.</i> Investigation of ^{10}Be and ^{16}C structure with break-up reactions at intermediate energies	209
I. Lombardo <i>et al.</i> New direct measurement of the $^{19}\text{F}(p,\alpha_0)^{16}\text{O}$ reaction at very low energies	215
F.C.L Crespi Isospin Character of Low-Lying Pygmy Dipole States via Inelastic Scattering of ^{17}O	221
E. Běták and J. Cseh Pre-equilibrium (exciton) model and the heavy-ion reactions with cluster emission	225
R.N. Sagaidak Formation, separation and detection of evaporation residues produced in complete fusion reactions	231
C. Agodi <i>et al.</i> NUMEN Project : challenges in the investigation of double charge-exchange nuclear reactions, towards neutrino-less double beta decay	239
M. B. Chadwick The ^{12}C Hoyle State and the Multiverse	243
G. Henning <i>et al.</i> Measurement of $(n,xn\gamma)$ reaction cross sections in W isotopes	247
W. A. Richter <i>et al.</i> Determination of the important $^{30}\text{P}(p,\gamma)^{31}\text{S}$ astrophysical rapid-proton capture reaction rate	255
A.-C. Larsen <i>et al.</i> Enhanced low-energy γ -decay probability – Implications for r -process (n, γ) reaction rates	261
G. Tagliente <i>et al.</i> Nuclear Astrophysics at the n_TOF facility, CERN	267
P. Zugec <i>et al.</i>	

Integral cross section measurement of the $^{12}\text{C}(n,p)^{12}\text{B}$ reaction	275
A. Fontana Nuclear interaction model developments in FLUKA	283
A. Fedynitch, R. Engel Revision of the high energy hadronic interaction models PHOJET/DPMJET-III	291
T. Ogawa <i>et al.</i> Revision of JAERI-QMD for analysis of peripheral nucleus-nucleus collisions	301
H. Duarte Comparison of a deterministic reaction model with an INC model for the production of nucleon in nucleon induced reaction on light nuclei	307
N. Shetty <i>et al.</i> Nuclear reactions in the context of LHC operation	313
G. La Rana <i>et al.</i> The new generation ISOL facility SPES at LNL	319
F. Gunsing <i>et al.</i> Nuclear data measurements at the upgraded neutron time-of-flight facility n_TOF at CERN	323
K. Tanaka Present Status and Future Plans of J-PARC Hadron Experimental Facility	331
A. Embriaco On the parametrization of lateral dose profiles in proton radiation therapy	339
E. V. Bellinzona <i>et al.</i> An analytical solution to lateral dose prediction in Hadrontherapy	347
A. Rucinski <i>et al.</i> Measurements of secondary particles emitted by ^{12}C , ^4He and ^{16}O ion beams in view of innovative dose profiling technique in Particle Therapy	355
M.P. Carante and F. Ballarini Modelling the induction of cell death and chromosome damage by therapeutic protons	361
L. Sajo-Bohus <i>et al.</i> GDR in Radiotherapy Treatment Fields with 18 MV Accelerators	369
B.A. Brown, D.L. Fang and M. Horoi Nuclear Matrix Elements for the $\beta\beta$ Decay of ^{76}Ge	377

List of participants

Clementina Agodi	INFN-LNS, Catania, Italy
Yoram Alhassid	Yale University, New Haven CT, USA
Anton Antonov	Inst. of Nuclear Research and Nuclear Energy, Bulgarian Academy of Science, Sofia, Bulgaria
Goran Arbanas	Oak Ridge National Laboratory, Oak Ridge TN, USA
Riccardo Avigo	Univ. Milano - INFN Milano, Milan, Italy
Marilena Avrigeanu	Horia Hulubei National Inst. for Physics and Nuclear Engineering (IFIN-HH), Ilfov, Romania
Francesca Ballarini	Univ. Pavia - INFN Pavia, Pavia, Italy
Bruce Barrett	Univ. Arizona, Tucson AZ, USA
Erik Bauge	CEA, Arpajon, France
Valentina Bellinzona	Univ. Pavia - INFN Pavia, Pavia, Italy
	LM University, Munich, Germany
Emil Betak	Inst. of Physics SAS, Bratislava, Slovakia
Giovanni Bocchi	Univ. Milano - INFN Milano, Milan, Italy
Thereza Borello-Lewin	Inst. de Fisica, Univ. Sao Paulo, Sao Paulo, Brazil
Ricardo Broglia	Dept. Of Physics, Univ. Milano, Milan, Italy
Alex Brown	Michigan State Univ., East Lansing MI, USA
Franco Camera	Univ. Milano, Milan, Italy
Luciano Canton	INFN Padova, Padua, Italy
Roberto Capote Noy	Nuclear Data Section, IAEA, Vienna, Austria
Francesco Cappuzzello	INFN-LNS, Catania, Italy
Brett Carlson	Inst. Tecnológico de Aeronautica, Sao Jose dos Campos, Brazil
Simone Ceruti	Univ. Milano - INFN Milano, Milan, Italy
Francesco Cerutti	CERN, Geneva, Switzerland
Mark Chadwick	Los Alamos National Laboratory, Los Alamos NM, USA
Abdelaziz Chebboubi	LPSC, Grenoble, France
Fabio Crespi	Univ. Milano - INFN Milano, Milan, Italy
Carlos Dasso	Sevilla, Spain
Daniele Dell'Aquila	Univ. Naples "Federico II", Naples, Italy
Ivana Dokic	German Cancer Research Center (DKFZ) and University Hospital, Heidelberg, Germany
Helder Duarte	CEA-DAM-DIF, Arpajon, France
Alessia Embriaco	Univ. Pavia - INFN Pavia, Pavia, Italy
Anatoli Fedynitch	CERN, Geneva, Switzerland
	KIT, Karlsruhe, Germany
Alfredo Ferrari	CERN, Geneva, Switzerland
Andrea Fontana	INFN Pavia, Pavia, Italy
Piero Fossati	Fondazione CNAO, Pavia, Italy
Agnese Giaz	INFN Milano, Milan, Italy
Gilbert Gosselin	CEA, Arpajon, France
Frank Gunsing	CEA Saclay, Gif-sur-Yvette, France
Magne Sveen Guttormsen	Oslo, Norway
Franz-Josef Hamsch	EC-JRC Inst. for Reference Materials and Measurements (IRMM), Geel, Belgium
Christoph Hartnack	Laboratoire Subatech, Nantes, France
Greg Henning	IPHC, Strasbourg, France

Michal Herman	Brookhaven National Laboratory, Brookhaven NY, USA
Martin Ivanov	Institute for Nuclear Research and Nuclear Energy, Sofia, Bulgaria
Steven Karataglidis	Univ. Johannesburg, South Africa
Toshihiko Kawano	Los Alamos National Laboratory, Los Alamos NM, USA
Giovanni La Rana	Univ. Naples "Federico II" and INFN, Naples, Italy
Marc Labalme	LPC, Caen, France
Ann-Cecilie Larsen	Dept. of Physics, Univ. Oslo, Oslo, Norway
Romain Léguillon	Advanced Science Research Center, Japan Atomic Energy Agency, Japan
Horst Lenske	JLU Giessen, Giessen, Germany
Roberto Linares	Universidade Federal Fluminense, Gragoata, Brazil
Ivano Lombardo	Univ. Naples "Federico II", Naples, Italy
Wen Luo	ELI-NP, Bucharest, Romania
Andrea Mairani	Fondazione CNAO, Pavia, Italy
	HIT, Heidelberg, Germany
Carlo Mancini Terracciano	CERN, Geneva, Switzerland
Paola Marini	CENBG, Gradignan, France
Takuma Matsumoto	Kyushu University, Fukuoka, Japan
Retief Neveling	iThemba LABS, Somerset West, South Africa
Filomena Nunes	Michigan State Univ., East Lansing MI, USA
Tatsuhiko Ogawa	Japan Atomic Energy Agency, Tokai/Ibaraki, Japan
Adriana Palffy	Max Planck Institute for Nuclear Physics, Heidelberg, Germany
Vincenzo Patera	Rome, Italy
Lawrence Pinsky	University of Houston, Houston TX, USA
Gregory Potel	Michigan State Univ., East Lansing MI, USA
	Lawrence Livermore National Laboratory, Livermore CA, USA
José Manuel Quesada Molina	Sevilla, Spain
Werner Richter	iThemba LABS, Somerset West, South Africa
Ilaria Rinaldi	Université de Lyon, France
Guy Royer	Laboratoire Subatech, Nantes, France
Antoni Rucinski	INFN sezione di Roma, Rome, Italy
Roman Sagaidak	Joint Institute for Nuclear Research, Dubna, Russia
Laszlo Sajo Bohus	Universidad Simon Bolivar, Caracas, Venezuela
Toshiya Sanami	KEK, Ibaraki, Japan
Nikhil Vittal Shetty	CERN, Geneva, Switzerland
Lembit Sihver	Atominstytut - Technische Universität Wien, Vienna, Austria
Giuseppe Tagliente	INFN Bari, Italy
Patrick Talou	Los Alamos National Laboratory, Los Alamos NM, USA
Kazuhiro Tanaka	Inst. of particle and Nuclear Studies, KEK, Ibaraki, Japan
Ian Thompson	Lawrence Livermore National Laboratory, Livermore CA, USA
Egle Tomasi-Gustafsson	CEA, Saclay, France
Fredrik Tovesson	Los Alamos National Laboratory, Los Alamos NM, USA
Masakazu Toyokawa	Kyushu University, Fukuoka, Japan
Andrea Tsinganis	NTUA, Dept. Of Physics, Athens, Greece
Hans Weidenmüller	Heidelberg, Germany
Ching-Yen Wu	Lawrence Livermore National Laboratory, Livermore CA, USA
Petar Zugec	Dept. Of Physics, Univ. Zagreb, Croatia

Studies of fission fragment properties at LANSCE

F. Tovesson, D. L. Duke, B. Manning, R. Meharchand, K. Meierbachtol, S. Mosby and D. Shield
Los Alamos National Laboratory, Los Alamos, New Mexico, USA

Abstract

The fission processes is studied at the Los Alamos Neutron Science Center (LANSCE) in order to provide high accuracy nuclear data for applications and advance our understanding of this complex many-body process. Frisch-gridded ionization chambers have been used to study correlated kinetic energy release and masses in fission with 4-5 amu resolution for incident neutron energies from thermal to 30 MeV. A new instrument, SPIDER, was developed for higher resolution mass measurements and has been used to determine the fission product yields for thermal neutrons. Some preliminary results from these studies will be presented here together with plan for future research directions.

1 Introduction

Nuclear fission has been extensively studied since it was first discovered in 1938, and much has been learned about the properties of the fission fragments and other aspects of the fission process over the years. There are, however, certain types of experimental information that would be very useful for guiding and benchmarking advanced fission modelling that currently are in short supply. One limitation of the existing data relates to the excitation energy of the fission system: many experiments have been performed at various excitation energies, but there are very few studies that observe systematic trends in fission properties as a function of excitations energy. Another limitation is the lack of data that describes the correlations in fission, as most experiments only determine one observable at a time.

There has been a renaissance in fission research in recent years, mainly for two reasons. One is that nuclear data continues to be important for modelling and simulation in nuclear technology. As new advanced reactor designs are considered and current applications needs to be better modelled we rely on nuclear data to support that effort. The other reason is the advances that have been made in models describing the fission process. The macroscopic-microscopic approach to describing fission potential energy barriers has proven to be very successful, and models building on that work are showing promise for predicting fission fragment properties for systems where no data exists.

In order to provide accurate information about fission fragment properties for science and technology an experimental program has been developed at LANSCE. Here we will describe the status of two experimental efforts: high efficiency, low mass resolution measurements with a Frisch-gridded Ionization Chamber (FGIC) and low efficiency, high mass resolution studies with the SPIDER instrument. Preliminary results on the average total kinetic energy release ($\langle \text{TKE} \rangle$) as a function of incident neutron energy, correlations between $\langle \text{TKE} \rangle$ and fragment mass, and independent fission product yields will be presented for $^{235}\text{U}(n,f)$.

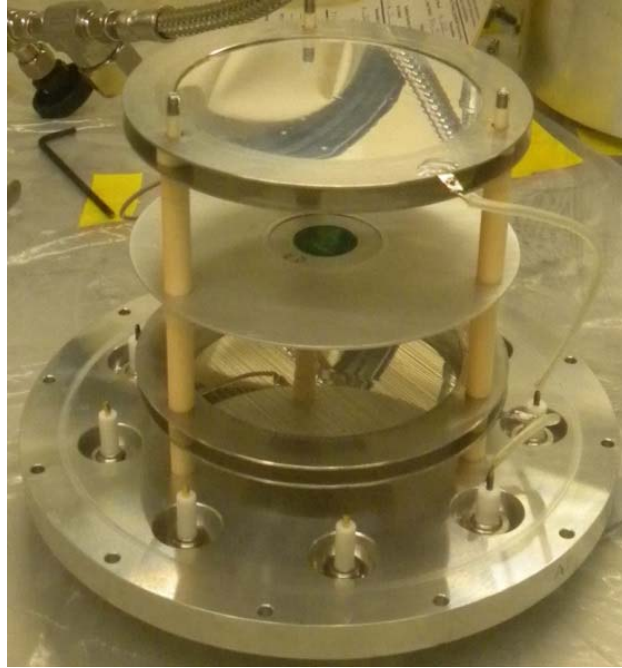


Fig. 1: Picture of the interior of the Frisch-Gridded Ionization Chamber used in this work. The actinide deposit can be seen as a green circle on the central cathode plate.

2 Experimental approach

The experiments were carried out at the Los Alamos Neutron Science Center (LANSCE), and made use of two different flight paths at the Lujan Center and the Weapons Neutron Research (WNR) facilities at LANSCE. The detector systems used were a Frisch-gridded Ionization Chamber (FGIC) and the SPectrometer for Ion DEtermination in fission Research (SPIDER).

2.1 Neutron Source

Neutrons are produced at LANSCE through spallation when an 800-MeV proton beam hit tungsten targets. The experiments were carried out at WNR where a bare tungsten target produces high-energy neutrons with energies of hundreds of keV up to hundreds of MeV, and at the Lujan Center where the tungsten target is surrounded by moderators and thus generate a thermalized neutron spectrum.

Incident neutron energy was determined using the time-of-flight (TOF) method. For the experiments at WNR a 10-meter flight path was used, and neutron time-of-flight was measured with 2 ns resolution over the 1.8 μ s that separated the proton micro-pulses. At the Lujan Center the flight path was approximately 25 meters, and the proton pulse repetition rate is 20 Hz. In this case the neutron time-of-flight is measured over 20 ms with a resolution of 25ns.

2.2 Targets

The targets were prepared by W. Loveland at Oregon State University, and consist of approximately 1 mg of actinide material deposited on thin carbon film. The actinide deposits are 2 cm in diameter, and the carbon films have areal densities of 100 μ g/cm², which allows both fragments to escape the target with energy loss in the 5-10% range.

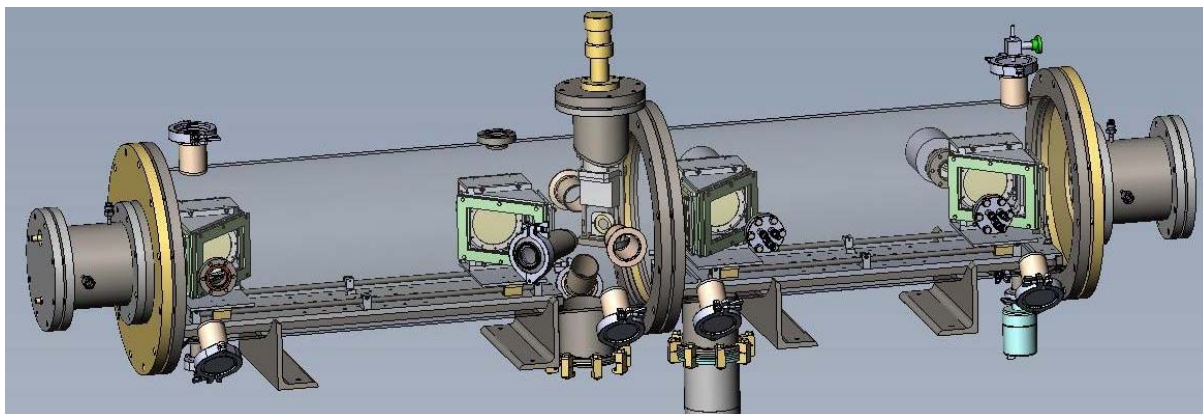


Fig. 2: Mechanical drawing of the SPIDER instrument.

2.3 Fission detectors

As previously mentioned two types of detectors were used to investigate the properties of fission fragments emitted in neutron-induced fission: the FGIC and SPIDER.

2.3.1 *Frisch-Gridded Ionization Chamber (FGIC)*

The Frisch-Gridded Ionization Chamber (FGIC) was used to measure the kinetic energy of the two fragments emitted in fission, which in turn is used to determine the total kinetic energy (TKE) as well as mass splits with 4-5 amu resolution using momentum and nucleon number conservation.

The FGIC is a gas ionization detector with a central cathode where the transparent target is placed, and two identical arrangements of a Frisch-grid and anode on either side of the cathode. As fission is induced in the actinide target the two fragments each ionizes the gas in the two sections of the chamber, and an electric fields applied between the electrodes causes the positive ions and electrons created to drift in opposite directions. The grid shields the anode from the positive ions, and thus electrons drifting between the grid and anode generate the anode signal. The anode signal is directly proportional to the amount of energy deposited by the fragments in the gas.

The FGIC experiments ran on the 4FP90L flight path at LANSCE-WNR, and the data collected for each fission event was the neutron time-of-flight, the anode signals that are proportional to the fragment energies, and the grid signals that are used to measure the polar emission angle. Detail of the setup can be found in Ref. [1].

2.3.2 *SPectrometer for Ion DEtermination in fission Research (SPIDER)*

The SPIDER instrument measures the velocity and kinetic energy of fission fragment in order to determine the mass. This method provides more precise measurements of the fragment mass than the FGIC, and has to date been able to provide about 1.5 amu resolution for light fragments. The goal is to reach 1 amu.

The current SPIDER instrument has two spectrometer arms, which allows for coincidence measurements of the fragments emitted in binary fission. Each arm consists of a time-of-flight section under vacuum, where the fragments pass through two fast timing detectors. After clearing the approximately 60 cm long TOF section the fragment enters into an ionization chamber through a thin silicon nitride window where the kinetic energy is measured. The SPIDER instrument is described in detail in Ref. [2].

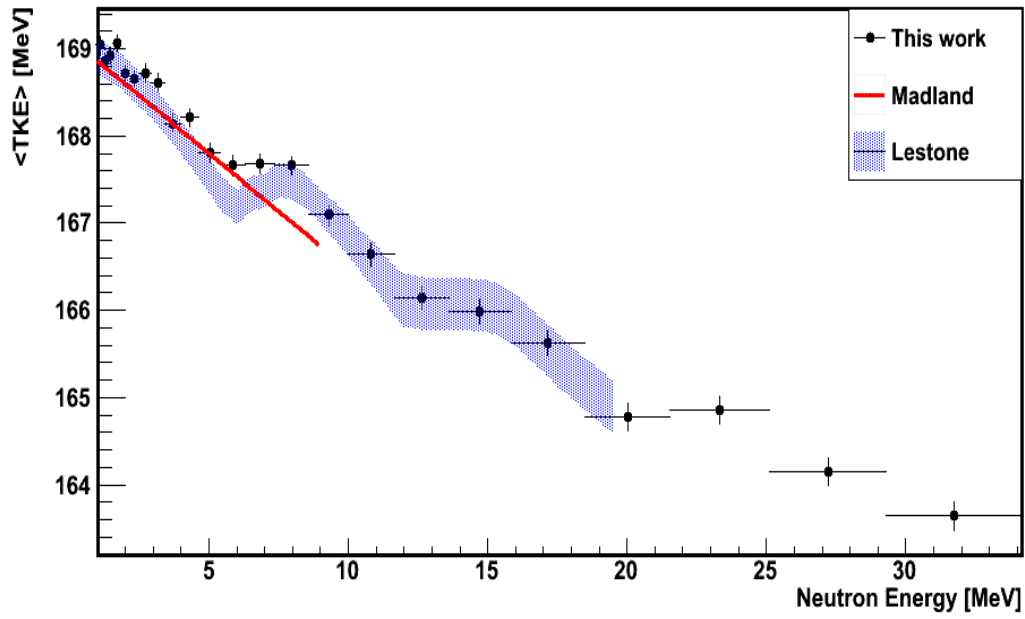


Fig. 3: Preliminary results for the average total kinetic energy release in fission of ^{235}U as a function of incident neutron energy. Also shown are calculations by D. Madland and J. Lestone.

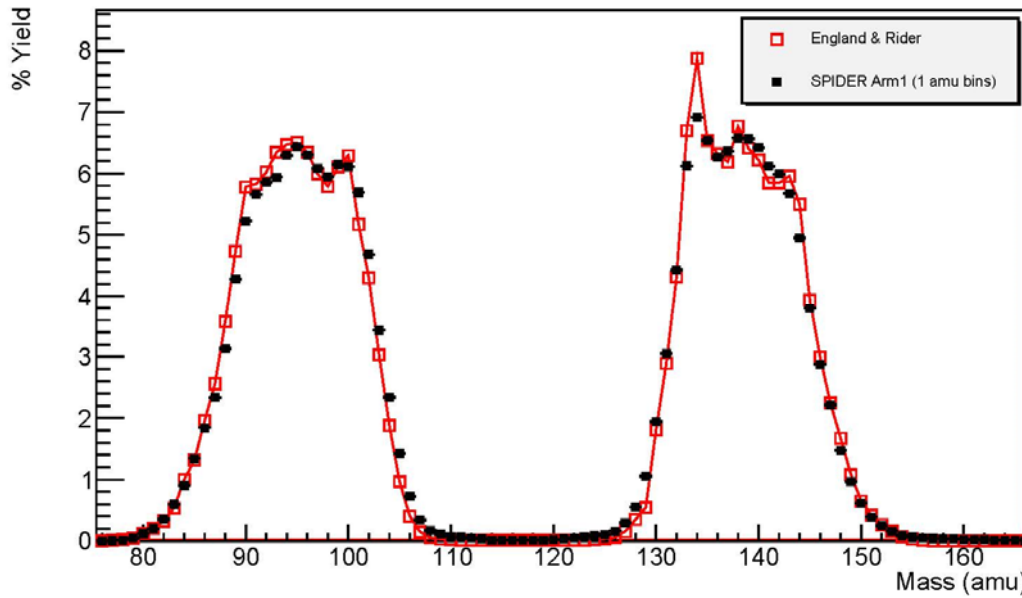


Fig 4: Preliminary results for fission product mass yield for thermal neutron-induced fission.

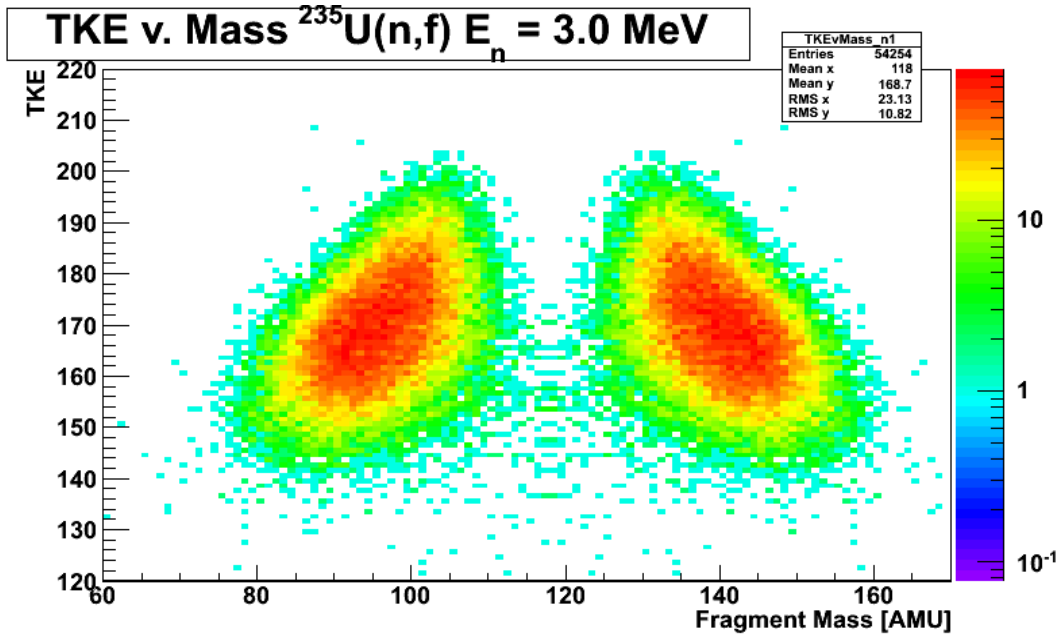


Fig. 5: Preliminary results for the correlation between fragment mass and total kinetic energy release in ^{235}U for 3 MeV of incident neutron energy.

3 Results and Conclusions

The average total kinetic energy (TKE) release as a function of incident neutron energy for ^{235}U is shown in Fig. 3. This is a preliminary experimental result, and is compared to a fit to previously measured data by D. Madland [3] as well as a semi-empirical prediction by J. Lestone [4]. Previous measurements only went up to 9 MeV, so this new data extends that energy range. The average TKE is observed to generally decrease with increasing incident neutron energy, with a local increase at the threshold for second- and third-chance fission.

The ^{238}U and ^{239}Pu $\langle\text{TKE}\rangle$ was studied as well, and show similar trends with increasing incident neutron energy. These results will be published elsewhere.

The preliminary result for mass yields in thermal neutron induced fission is shown in Fig. 4, and compared to the evaluation by England and Rider [5]. The estimated mass resolution is 1.5 amu for the light peak and 2 amu for the heavy peak, which explains the yield discrepancy between measurement and evaluation for $M=134$. The independent fission product yields are difficult to measure experimentally, and the evaluation is largely based on calculations using the cumulative yields. This new data set is therefore important for confirming the current evaluation. The next step will be to perform the same measurement at higher excitation energy in order to study the relative change in yield of individual masses as a function of incident neutron energy.

The correlation between fragment mass and TKE for ^{235}U at $E_n=3$ MeV is shown in Fig. 5. This clearly shows how the more asymmetric mass splits results in lower total kinetic energy release, while symmetric mass splits will result in significantly higher TKE values. This correlation will be studied at different excitation energies and different fission systems, in order better understand the underlying processes involved.

The study of fission fragment properties continues at the LANSCE facility, and the current focus is on building a larger detector array based on the SPIDER design. This will allow us to perform the high mass resolution studies for higher incident neutron energies, and thus provide higher fidelity data for mass yields and their correlation with TKE over a broad range of incident neutron energies.

Acknowledgements

We wish to thank W. Loveland for providing the targets used in this work. We are also grateful to F.-J. Hamsch for the use of a Frisch-gridded ionization chamber.

References

- [1] S. Mosby *et al.*, Nucl. Instr. and Meth. **A 757**, 75 (2014).
- [2] K. Meierbachtol *et al.*, Nucl. Instr. and Meth. **A 788**, 59 (2015).
- [3] D.G. Madland, , Nucl. Phys. **A 772**, 113 (2006).
- [4] J. Lestone, private communication.
- [5] T. R. England and B. F. Rider, LANL report LA-UR-94-3106, (1994).

Prompt fission neutron emission from $^{235}\text{U}(\text{n},\text{f})$: thermal and resonance region

F.-J. Hamsch¹, A. Göök¹, S. Oberstedt¹, M. Vidali¹, A. Al-Adili², D. Tarrio², A. Solders², K. Jansson², V. Rakopoulos², S. Pomp²

¹European Commission, Joint Research Centre, Institute for Reference Materials and Measurements, Retieseweg 111, B-2440 Geel, Belgium

²Department of Physics and Astronomy, Uppsala University, Box 516, 751 20 Uppsala, Sweden

Abstract

For nuclear modelling and improved evaluation of nuclear data, knowledge of fluctuations of the prompt neutron multiplicity as a function of incident neutron energy is requested for the major actinides ^{235}U and ^{239}Pu . Experimental investigations of the prompt fission neutron emission in resonance-neutron induced fission on ^{235}U are taking place at the GELINA facility of the IRMM. The experiment employs an array of scintillation detectors (SCINTIA) in conjunction with a newly designed 3D position-sensitive twin Frisch-grid ionization chamber.

In addition, the mass-dependent prompt neutron multiplicity, $\nu(\text{A})$, has attracted particular attention. Recent, sophisticated nuclear fission models predict that the additional excitation energy, brought into the fission system at higher incident neutron energies, leads to an increased neutron multiplicity only for heavy fragments, as observed in the $^{237}\text{Np}(\text{n},\text{f})$ reaction. A first feasibility study has been performed at the JRC-IRMM VdG accelerator to measure $\nu(\text{A})$ for $^{235}\text{U}(\text{n},\text{f})$.

1 Introduction

The energy spectrum as well as the multiplicity of prompt neutrons emitted in nuclear fission plays an important role in many applications. In particular, accurate predictions of nuclear criticality using neutron transport codes are dependent on the underlying nuclear data, especially the prompt neutron multiplicity and the prompt fission neutron spectrum. Both observables have received recently a lot of attention. On the one hand for the prompt fission neutron spectrum an IAEA Coordinated Research Project has been launched, and the final report is being published [1]. On the other hand recent OECD-Nuclear Energy Agency (NEA), Working Party of Evaluation Cooperation (WPEC) documents [2, 3] state the lack of inclusion of prompt neutron multiplicity fluctuations for the major isotopes ^{235}U and ^{239}Pu , in the resonance region relevant for fission cross section evaluations. In Ref. [2] it has been clearly stated that both reliable measurements and modelling of the shape of the prompt neutron multiplicity ($\bar{\nu}$) in the resonances are still lacking. In addition, at higher incident neutron energy, recent theoretical modelling [4, 5] has confirmed the increase of prompt neutron multiplicity mainly for heavy fragment masses, if the incident neutron energy is increased. This is so far not considered in the correction for the energy dependence of prompt neutron multiplicity as a function of mass (see e.g. Fig. 8 in Ref. [6]). For pre-neutron mass determination from 2E experiments this may have important consequences in the post-neutron yield distributions [7].

The nuclear data facilities at the JRC-IRMM are predestined to tackle the above mentioned problems. With the white neutron source GELINA and using the neutron time-of-flight technique the resonance region is accessible. The Van de Graaff (VdG) accelerator gives high neutron flux at

incident neutron energies in the MeV region to study the change of the prompt neutron multiplicity as a function of fragment mass.

The experimental technique used to study prompt neutron emission both in resonance-neutron induced fission at the GELINA facility and at higher incident neutron energy at the VdG accelerator is based on techniques pioneered by Bowman et al. [8]. The method involves extracting fission fragment masses by measuring either velocity ($2v$) or energy ($2E$) of the two fragments, and coincident measurements of fission neutron time-of-flight at known angles with respect to the fission axis. In an experiment on prompt fission neutrons in $^{252}\text{Cf}(\text{SF})$ Budtz-Jørgensen and Knitter exploited the combination of a twin Frisch-grid ionization chamber for fission fragment properties ($2E$ technique) and a liquid scintillator for neutron detection [9]. Their result serves as the basis for our experimental setup for studying prompt neutron emission. The ionization chamber has a large solid angle, which not only facilitates the fragment-neutron coincidence rate, but also introduces a less biased selection of coincident events. The ionization chamber allows determining the fission fragment emission angle relative to the chamber axis. By placing the neutron detector along the chamber axis this angle coincides with the angle relative to the momentum of detected neutrons.

In the following sections the different experiments will be highlighted and first results discussed.

2 Prompt fission neutron multiplicity

2.1 Introduction

The total prompt fission-neutron multiplicity is an important quantity for nuclear applications and needs to be known to very high accuracy in the 0.25% range [1, 10] for major actinides. For the analysis of fission yield data also the information about the prompt fission neutron multiplicity as a function of fission fragment mass, $\nu(A)$, is needed. In recent years the focus was put towards the behaviour of this quantity $\nu(A)$ as a function of incident neutron energy. Improved model calculations predict that the additional excitation energy, brought into the fission system at higher incident neutron energies, leads to an increased neutron multiplicity only for heavy fragments [4, 5], like observed in the $^{237}\text{Np}(n,f)$ reaction [11]. In Ref. [7] an analysis of the impact of the prompt fission neutron multiplicity correction on the fission fragment yield of $^{234}\text{U}(n,f)$ was performed. The result showed an effect in the order of up to 30% on the most abundant fission fragments whether the standard correction (e.g. as done in Ref. [6]) with an upscale of the neutron multiplicity as a function of mass or a solely higher heavy fragment neutron multiplicity was used.

An experiment campaign has been started to verify the theoretical predictions in collaboration with Uppsala University within the frame of the EUFRAT project [12].

2.2 Experiment

The data presented in this paper were measured at the 7 MV Van de Graaff accelerator of the IRMM in Geel, Belgium. Neutrons of 0.5 MeV were produced via the reaction $^7\text{Li}(p,n)$. A twin Frisch-Grid ionization chamber (FGIC) was used to detect the fission fragments. The chamber was operated with P-10 (90% Ar and 10%CH₄) as counting gas, and the gas pressure was set to 1.05×10^5 Pa with a gas flow of 0.1 l/min. A thin, transparent ^{235}U sample was mounted at the common cathode. The prompt fission neutrons from the $^{235}\text{U}(n,f)$ reaction were measured with two NE213 equivalent scintillation detectors. The experimental setup is shown in Fig. 1. The beam was thermalized with the help of a thick layer of paraffin. The thermal neutron induced fission of ^{235}U was studied in this experiment. In future experiments the energy range will be extended towards higher incident neutron energies.

MCNP and FLUKA simulations have been performed to see the influence of the direct beam and the moderated beam (using paraffin of 7.5 cm thickness) on the neutron detectors. Using a direct beam of only 0.5 MeV neutron energy helped in this experiment a lot as the sensitivity of the used scintillation neutron detectors is very low at this neutron energy. In addition the neutron detectors were shielded towards the direct beam by an additional 10 cm of paraffin, 3 cm of lead and 5 mm of copper.

The data from the ionisation chamber and the neutron detectors were acquired using waveform digitizers of 250 MHz and 12 bit pulse height resolution. Data analysis was done using the ROOT software package [13] and digital signal processing routines developed at JRC-IRMM.

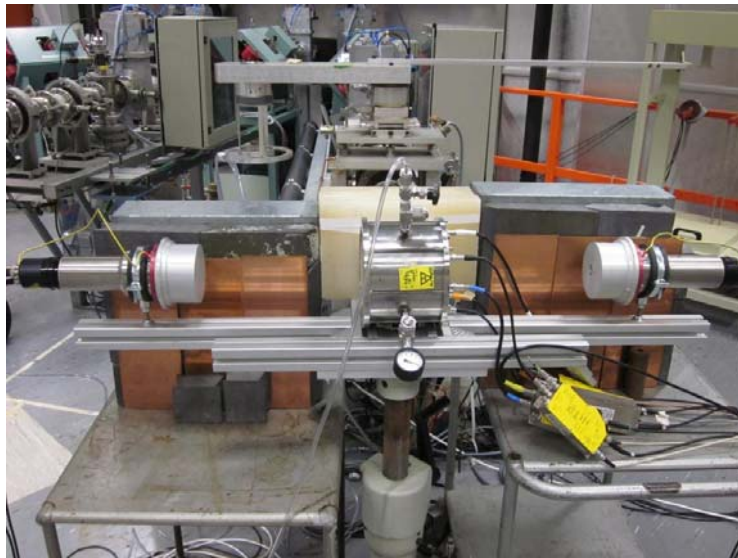


Fig. 1: Upstream view of the experimental setup for the neutron multiplicity measurement at the VdG. The FGIC is seen in the centre with the two NE213 on either side. The shielding arrangement is also visible.

2.3 Preliminary results

The analysis of the fission fragment signals taken without coincidences with the neutron detectors can be used as quality check of the set-up. In Fig. 2a the pulse height distributions for forward (red) and backward (blue) emission of the fragments are shown. Both distributions are in very good agreement showing that all the corrections needed to be applied to the raw signals are well under control. Fig. 2b shows the cosine of the angular distribution of the fission fragments again for forward (red) and backward (blue) direction of the fragment emission. Also the cosine of the angle from both emission directions of the fragments is in good agreement.

Fig. 3 shows the pulse shape information from the neutron scintillation detectors versus the time-of-flight information. Despite the large γ -ray background the neutrons of interest could be identified in the encircled region. Further analysis is still in progress.

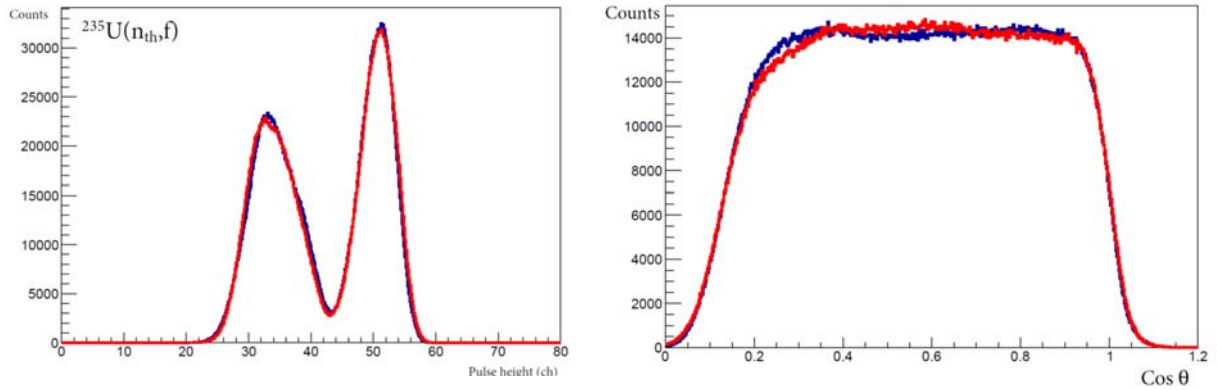


Fig. 2: a) Pulse height distributions for forward (red) and backward (blue) emission of the fragments. b) Cosine of the emission angle for forward (red) and backward (blue) emission of the fragments.

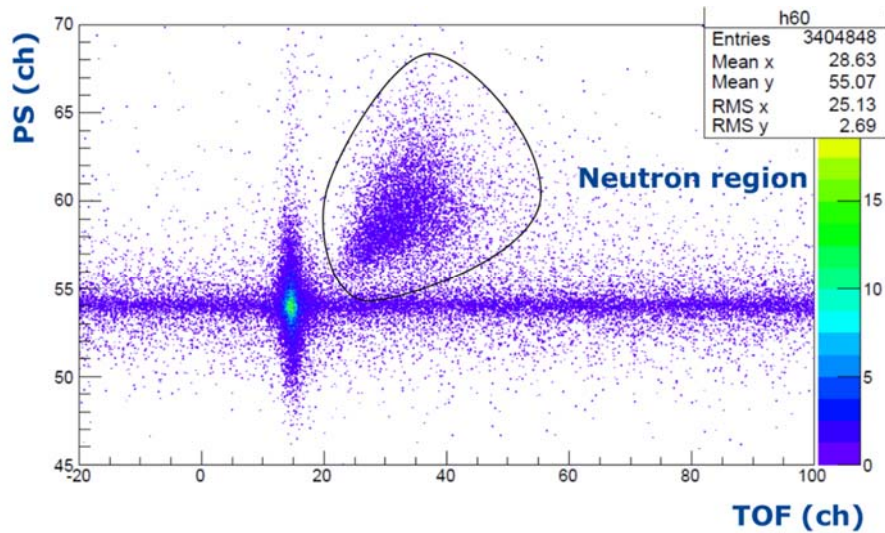


Fig. 3: Pulse shape information versus time-of-flight of the neutron detector signals. Among a large γ -ray background the neutrons of interest are found in the encircled area.

3 Neutron-fission fragment correlations in the resolved resonance region

3.1 Introduction

For nuclear modelling and improved evaluation of nuclear data the knowledge about fluctuations in the prompt neutron multiplicity as a function of incident neutron energy is requested for the major actinides ^{235}U and ^{239}Pu [2, 3]. Fluctuations in fission fragment mass and total kinetic energy (TKE) in both isotopes have been observed in resonance neutron induced fission [14, 15]. Independently, fluctuations in the number of emitted neutrons have also been observed [16]. In view of the fact that both neutron number and fission fragment properties have been found to vary it is necessary to study the correlations of prompt neutron multiplicity and fission fragments properties in the resonance region [17]. Furthermore, the knowledge of the prompt neutron multiplicity as a function of mass and TKE is needed when determining post-neutron emission fission fragment mass distributions experimentally via the double kinetic energy or double velocity techniques. Experimental investigations of correlations between the prompt fission neutron multiplicity with fragment properties

in resonance-neutron induced fission on ^{235}U and ^{239}Pu are taking place at the GELINA facility of the JRC-IRMM.

3.2 Experiment

The experimental setup for investigating correlations of prompt neutrons with fission fragments in resonance neutron induced fission on ^{235}U and ^{239}Pu is illustrated in Fig. 4. The fission target is placed inside the ionization chamber, about 9.2 m away from the neutron production target of the GELINA facility. An array of neutron detectors (SCINTIA) is employed in order to achieve a reasonable fission-neutron coincidence count rate. The SCINTIA array consists of 7 NE213 equivalent liquid scintillators (Scionix LS-301) and 5 para-therphenyl crystalline scintillation detectors.

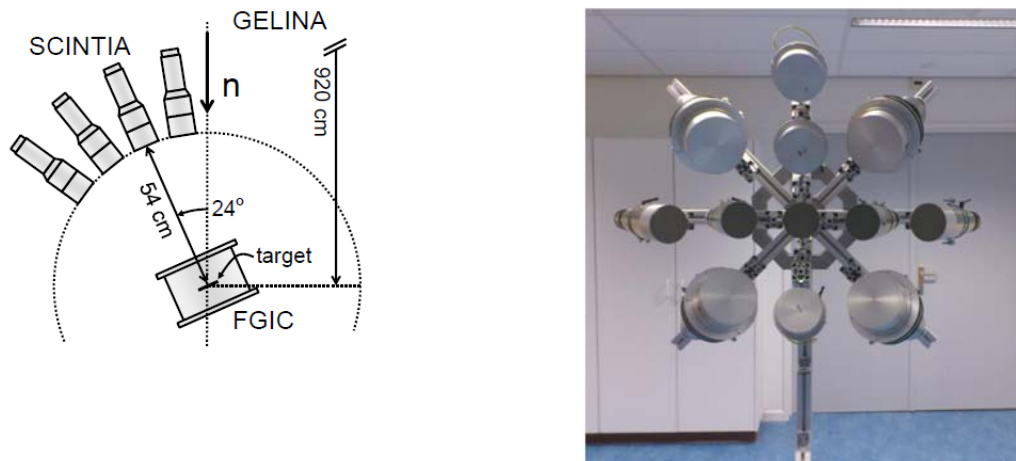


Fig. 4: Schematic drawing (left) and photograph (right) of the experimental arrangement at the GELINA facility.

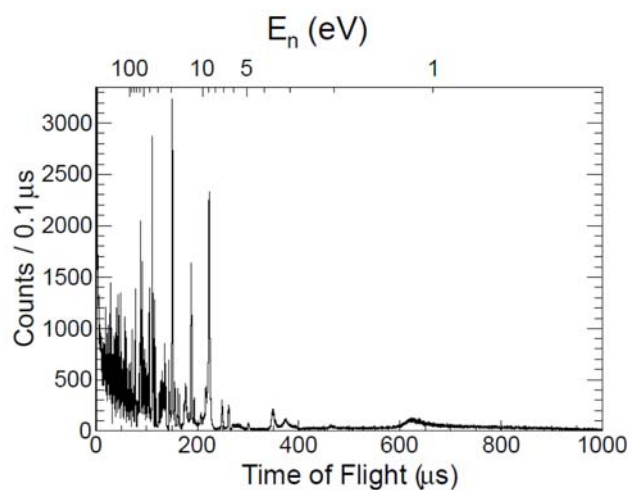


Fig. 5: Time-of-flight spectrum with resonance of $^{235}\text{U}(n,f)$.

When employing an array of neutron detectors, each detector forms an axis of symmetry around which the orientation of the fission axis needs to be known. Hence, the traditional ionization chamber is no longer sufficient to reconstruct the kinematics in the fragment rest frame. In order to solve this problem, the ionization chambers anode plate is replaced by a position sensitive readout structure.

This allows determination of all three space components of the fission fragments direction of travel. A 22 channel, fully digital data acquisition is used.

The acquisition is triggered by the current signal from the ionization chamber cathode, giving the instant of a fission event in time with a resolution better than 1 ns FWHM. For each fission event the digital waveforms of all channels, sampled at 400 MS/s with 14-bit resolution, are stored on disk for off-line treatment together with the incident neutron time-of-flight for each event. In Fig. 5 a time-of-flight spectrum of the on-going $^{235}\text{U}(n,f)$ experiment is shown.

3.3 Preliminary results

The top panel of Fig. 6 shows the average total kinetic energy (TKE) as a function of incident neutron

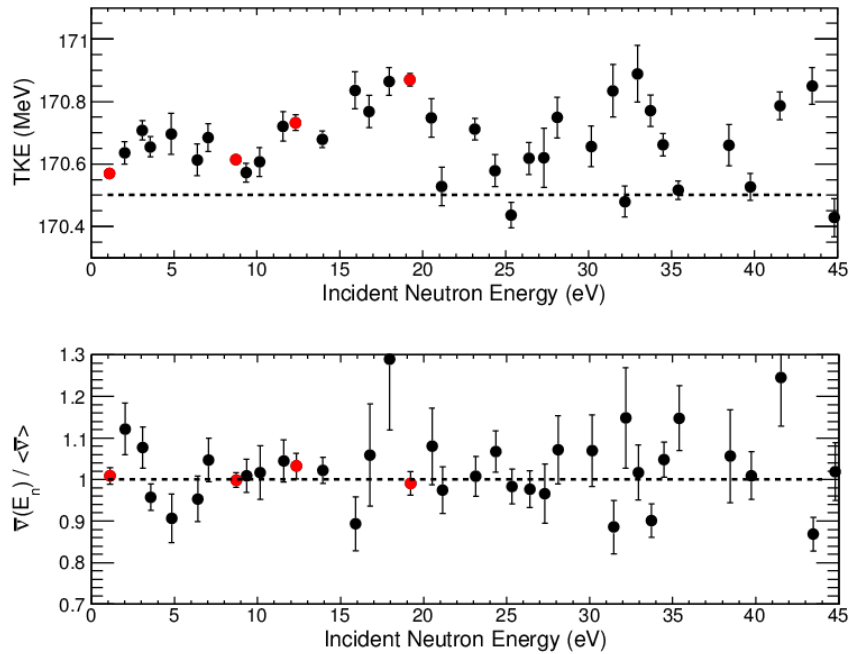


Fig. 6 Top panel: average total kinetic energy (TKE) as a function of incident neutron energy in the range up to 45 eV. Lower panel: ratio of the neutron multiplicity for a given resonance or resonance group relative to the mean neutron multiplicity. The red points highlight strong resonances in the fission cross section of ^{235}U . The dashed line refers to the thermal value.

energy in the range up to 45 eV. Each point corresponds to either a single resonance or resonance group. The red points highlight the strongest resonances in the fission cross section of ^{235}U . A clear fluctuation exceeding the experimental uncertainty is observed. This was already pointed out in Ref. [14]. However, the statistical significance has very much improved in the present work leading to a clearer picture of the energy dependent changes compared to the earlier work.

In the lower panel of Fig. 6 the ratio of the neutron multiplicity for a given resonance or resonance group relative to the mean neutron multiplicity is shown. Again, the strongest resonances are highlighted in red. At the current moment of data collection, an anti-correlation, i.e., high TKE corresponds to lower neutron multiplicity, is observed when all points in the given incident neutron energy interval are plotted. This is expected from energy conservation. Of course, also possible changes in the mass distribution need to be accounted for. Nevertheless, there seem to be no sizable fluctuations in the neutron multiplicity in the strong resonances.

Conclusions

In conclusion, new experiments have been started to measure prompt neutron multiplicity in neutron-induced fission of ^{235}U . Presently both the thermal and the resonance region are covered. Measurements at higher incident neutron energies are planned for the near future. We are confident that the new data will shed light in the understanding of the observed neutron multiplicity fluctuations in the resonance region and the behaviour of the neutron multiplicity as a function of mass and incident neutron energy.

Acknowledgement

The Uppsala group would like to thank the JRC-IRMM for the support given within the EUFRAT program. The authors are also indebted to the operational staff of the GELINA and VdG facilities for providing stable beams.

References

- [1] R. Capote-Noy *et al.*, <https://www-nds.iaea.org/pfns/public.html>
- [2] <https://www.oecd-nea.org/science/wpec/volume22/volume22.pdf>
- [3] <https://www.oecd-nea.org/science/wpec/sg34/>
- [4] K.-H. Schmidt and B. Jurado, *Phys. Rev.* **C83** (2011) 061601.
- [5] C. Morariu *et al.*, *J. Phys. G: Nucl. Part. Phys.* **39** (2012) 055103
- [6] J. P. Lestone, *Nuclear Data Sheets* **112** (2011) 3120.
- [7] A. Al-Adili, F.-J. Hamsch, S. Pomp, S. Oberstedt, *Phys. Rev.* **C86** (2012) 054601.
- [8] H.R. Bowman *et al.*, *Phys. Rev.* **129** (1963) 2133.
- [9] C. Budtz-Jørgensen, H.-H. Knitter, *Nucl. Phys.* **A490** (1988) 307.
- [10] A.D. Carlson *et al.*, *Nucl. Data Sheets* **110**, 3215 (2009).
- [11] A. Naqvi *et al.*, *Phys. Rev.* **C34**, 21 (1986).
- [12] EUFRAT project: <https://ec.europa.eu/jrc/en/eufrat>
- [13] Rene Brun and Fons Rademakers, *Nucl. Inst. Meth. A* **389** (1997) 81.
- [14] F.-J. Hamsch, H.-H., Knitter, C. Budtz-Jørgensen, J.P. Theobald, *Nucl. Phys. A* **491** (1989) 56.
- [15] F.-J. Hamsch *et al.*, in: Proc. Scientific Workshop on Nuclear Fission Dynamics and the Emission of Prompt Neutrons and Gamma Rays (Theory-1), EUR 24802, Sinaia, Romania. p. 41. 2011
- [16] R.E. Howe, T.W. Phillips, C.D. Bowman, *Phys. Rev.* **C13** (1976) 195.
- [17] R. Gwin, R.R. Spencer, R.W. Ingle, *Nucl. Sci. Eng.* **87** (1984) 381.

Total prompt γ -ray emission in fission of ^{235}U , $^{239,241}\text{Pu}$, and ^{252}Cf

C.Y. Wu¹, A. Chyzh¹, E. Kwan^{1,2}, R.A. Henderson¹, T.A. Bredeweg³, R.C. Haight³, A.C. Hayes-Sterbenz³, H.Y. Lee³, J.M. O'Donnell³, and J.L. Ullmann³

¹ Lawrence Livermore National Laboratory, Livermore, California 94550 USA

² National Superconducting Cyclotron Laboratory, East Lansing, Michigan, 48824, USA

³ Los Alamos National Laboratory, Los Alamos, New Mexico 87545 USA

Abstract

The total prompt γ -ray energy distributions for the neutron-induced fission of ^{235}U , $^{239,241}\text{Pu}$ at incident neutron energy of 0.025 eV – 100 keV, and the spontaneous fission of ^{252}Cf were measured using the Detector for Advanced Neutron Capture Experiments (DANCE) array in coincidence with the detection of fission fragments by a parallel-plate avalanche counter. DANCE is a highly segmented, highly efficient 4π γ -ray calorimeter. Corrections were made to the measured distribution by unfolding the two-dimension spectrum of total γ -ray energy vs multiplicity using a simulated DANCE response matrix. The mean values of the total prompt γ -ray energy, determined from the unfolded distributions, are $\sim 20\%$ higher than those derived from measurements using single γ -ray detector for all the fissile nuclei studied. This raises serious concern on the validity of the mean total prompt γ -ray energy obtained from the product of mean values for both prompt γ -ray energy and multiplicity.

1 Introduction

The total prompt γ -ray emission in fission accounts for about 40% of the total energy released by γ -ray emission that makes up about 10% of the total energy released in reactor core. The heating in nuclear reactors attributed to the total γ -ray emission in fission is underestimated up to 28% using the evaluated data for the main reaction channels, $^{235}\text{U}(n,f)$ and $^{239}\text{Pu}(n,f)$ [1]. This discrepancy is significantly greater than 7.5%, an upper bound of the uncertainty deemed necessary to adequately model the heat deposit in the fuel core [2,3]. Therefore, efforts are needed to improve the experimental data on the γ -ray emission in fission. As a matter of fact, the request for the new data on the prompt fission γ rays at thermal energy and above for those two isotopes has been categorized as the high-priority by the Nuclear Energy Agency under the Organization for Economic Co-operation and Development [4]. The majority of measurements made for the prompt γ -ray emission in fission always employed a single or a few γ -ray detectors. For example, a single NaI detector was used by Verbinski *et al.* [5] more than 40 years ago and the cerium-doped LaBr₃, CeBr₃, and LaBr₃ detectors were used recently by Billnert *et al.* [1] and Oberstedt *et al.* [6,7].

Below we describe results on the total γ -ray emission in fission measured by the DANCE array [8,9]. DANCE consists of 160 equal-volume, equal-solid-angle BaF₂ detectors, covering a 4π geometry space, and is located at the Los Alamos Neutron Science Center (LANSCE). Several unique features exhibited by DANCE are particularly attractive for those measurements, such as the nearly γ -ray energy independence for the detection efficiency, the multiplicity response, and the peak-to-total ratio, all of which are described in detail in Refs. [10-12]. For example, it enables one to measure the total γ -ray energy as a function of multiplicity. The only limitation is the energy resolution, which is about 14% for the measured total γ -ray energy. A series of measurements of the prompt γ rays in the neutron-induced fission of ^{235}U and $^{239,241}\text{Pu}$, and the spontaneous fission of ^{252}Cf has been carried out

recently using DANCE in coincidence with the detection of fission fragments by a compact parallel-plate avalanche counters (PPAC) [13]. The results on the measured and unfolded fission prompt γ -ray energy and multiplicity distributions for those isotopes have been published [12,14]. An independent analysis of the same data for ^{239}Pu , by assuming a general parameterized correlation between E_γ and M_γ , was presented in Ref. [15]. We also reported the total prompt γ -ray energy distributions for those isotopes, obtained by unfolding the measured two-dimensional spectrum of total γ -ray energy vs multiplicity [16]. This unfolding procedure and the implication on the γ heating in nuclear reactors are described.

2 Experiments and data analysis

The measurements of the prompt γ emission in the neutron-induced fission of ^{235}U and $^{239,241}\text{Pu}$ as well as the spontaneous fission in ^{252}Cf were performed at the Lujan Center of LANSCE. The experimental setup and the data analysis have been described in detail in our early publications [12,14-16]. A brief summary of the experiments is given here. For the neutron-induced fission experiment, neutrons with energies from thermal up to several hundred keV were produced first by bombarding an 800-MeV proton beam at a repetition rate of 20 Hz on a tungsten target then moderated by water. The prompt γ rays emitted in fission were detected by the DANCE array in coincidence with the detection of fission fragments by a compact PPAC [13]. More than 10^6 fission events with at least one γ ray detected by DANCE were collected for all isotopes studied. The hardware threshold for detecting γ -ray energy by DANCE was 150 keV. The summed energy of all γ rays detected by DANCE within a time window of 40 ns was defined as the total prompt γ -ray energy ($E_{\gamma,\text{tot}}$) in fission for a given event. With this time window extended to 100 ns, little change was observed for the $E_{\gamma,\text{tot}}$ spectrum [15]. The possible background contribution to $E_{\gamma,\text{tot}}$ is due to capture of thermalized prompt fission neutrons by Ba isotopes, which is on the order of μs and too long in the time scale for prompt γ rays. Additional suppression of neutron contribution is made by placing a gate on the pulse height spectrum of PPAC in addition to the 8-ns gate on the time spectrum between PPAC and DANCE, show in Fig. 1. All the offline data analysis was carried out using the code, FARE [17]. Note that both DANCE and PPAC have a similar intrinsic time resolution of ~ 1.2 ns [13]. The total γ -ray multiplicity (M_γ) in fission is established not according to the number of detectors observing the γ ray, but instead according to the number of clusters by grouping adjacent detectors catching the γ ray in the same time window. This counting method for M_γ is closer to the simulated results using the γ -ray calibration sources [10-12]. In addition, the nearly γ -ray energy independence of the DANCE response to M_γ , indicated by the numerical simulations, enables one to unfold approximately the measured M_γ distribution in fission for the first time [12,14].

Corrections have to be made to the measured $E_{\gamma,\text{tot}}$ distribution to obtain the physical one, which would be useful for the applications. This can be accomplished by unfolding the two-dimensional spectrum of $E_{\gamma,\text{tot}}$ vs M_γ . The two-dimensional unfolding is necessary because of the strong dependence of $E_{\gamma,\text{tot}}$ on M_γ . It is numerically implemented by adopting the iterative Bayesian method [18-20]. The DANCE response matrix for $E_{\gamma,\text{tot}}$ vs M_γ is simulated using the GEANT4 [21] geometrical model of both DANCE and PPAC [12,14,22]. To make sure this two-dimensional response matrix has a sufficient coverage of the phase space beyond the measured one, the value of M_γ up to 25 and $E_{\gamma,\text{tot}}$ up to 40 MeV are included. The $E_{\gamma,\text{tot}}$ has a bin size of 200 keV and an energy threshold of 150 keV. So the response matrix has a size of 200×25 .

For any given grid point ($E_{\gamma,\text{tot}}$, M_γ) in the response matrix, a two-dimensional DANCE response matrix of a size of 200×25 is generated using GEANT4 with a given assembly of no more than 20,000 samples. Note that the DANCE response to the total prompt γ -ray is relatively insensitive

to the content of γ rays for a given sample since the γ -ray detection efficiency (84 to 88%) and the peak-to-total ratio ($\sim 55\%$) remain nearly constant for the γ -ray energy ranging from 150 keV to 10 MeV [10-12]. Each sample has a matching number of γ rays to M_γ , selected randomly according to the unfolded γ -ray energy distributions [12,14] with the condition on the total γ -ray energy that is equal to $E_{\gamma,\text{tot}} \pm 100$ keV. This simulation is repeated for all the grid points within the lower and upper bound of $E_{\gamma,\text{tot}}$ for a given M_γ , established by this random sampling technique.

The resulting $(E_{\gamma,\text{tot}}, M_\gamma)$ DANCE response matrix consists of ~ 3300 two-dimensional matrices with a size of 200×25 each. This numerically simulated DANCE response matrix is unique for each isotope studied, and was used to unfold the measured two-dimensional spectrum of $E_{\gamma,\text{tot}}$ vs M_γ into a physical one using the iterative Bayesian method. During the iteration stage, a single factor was applied to and varied for the response matrix at any given grid point.

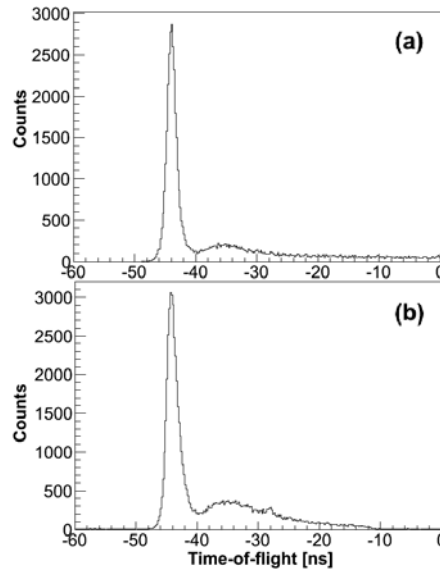


Fig. 1: Time difference between γ rays detected by DANCE and fission fragments detected by PPAC for (a) ^{235}U and (b) ^{241}Pu experiments with an achieved time resolution of ~ 1.7 ns. The bump next to the peak is related to events with ambiguous correlation between DANCE and PPAC.

3 Results and discussions

Typically it takes about 30 iterations to reach the convergence in the unfolding of the two-dimensional spectrum of $E_{\gamma,\text{tot}}$ vs M_γ using the Bayesian method. The results for the spontaneous fission in ^{252}Cf are shown in Fig. 2 where the unfolded $E_{\gamma,\text{tot}}$ vs M_γ spectrum together with the measured one are given. In addition, the comparisons of the projected $E_{\gamma,\text{tot}}$ and M_γ distributions between the unfolded and measured ones are also given. The general trend of the results is that the mean value and the width of projected $E_{\gamma,\text{tot}}$ and M_γ distributions increases noticeably after the unfolding.

Given in Table 1 is the comparison of $\langle M_\gamma \rangle$ derived from the unfolded M_γ distribution between the recent work (2-D) and the early one using the one-dimension unfolding technique [14] for all isotopes studied. For ^{235}U , the recent (2-D) mean value of 7.35 is 0.37 higher than 6.98 in the earlier 1-D work. However, the latter value is known to be underestimated by about 0.30. Since these values

were derived from the same data set, this consistence in the derived mean M_γ from both the one- and two-dimensional unfolding techniques gives us a certain confidence in the validity of our work. This trend is the same for $^{239,241}\text{Pu}$ and ^{252}Cf . The comparison with other measurements and evaluations also is given in Table 1. Our measured $\langle M_\gamma \rangle$'s for all isotopes studied are consistently higher than the weighted-average of earlier measurements [23] by $\sim 10\%$ except for the most recent measurements [1,6,7], where their measured $\langle M_\gamma \rangle$ is $\sim 11\%$ greater than ours for ^{235}U but near in agreement with ours for both ^{241}Pu and ^{252}Cf . Moreover, ours are consistent with the evaluated data listed in ENDF/B-VII.1 [24]. The uncertainty for our derived $\langle M_\gamma \rangle$ has an upper bound of about 0.3-0.4 or $\sim 5\%$.

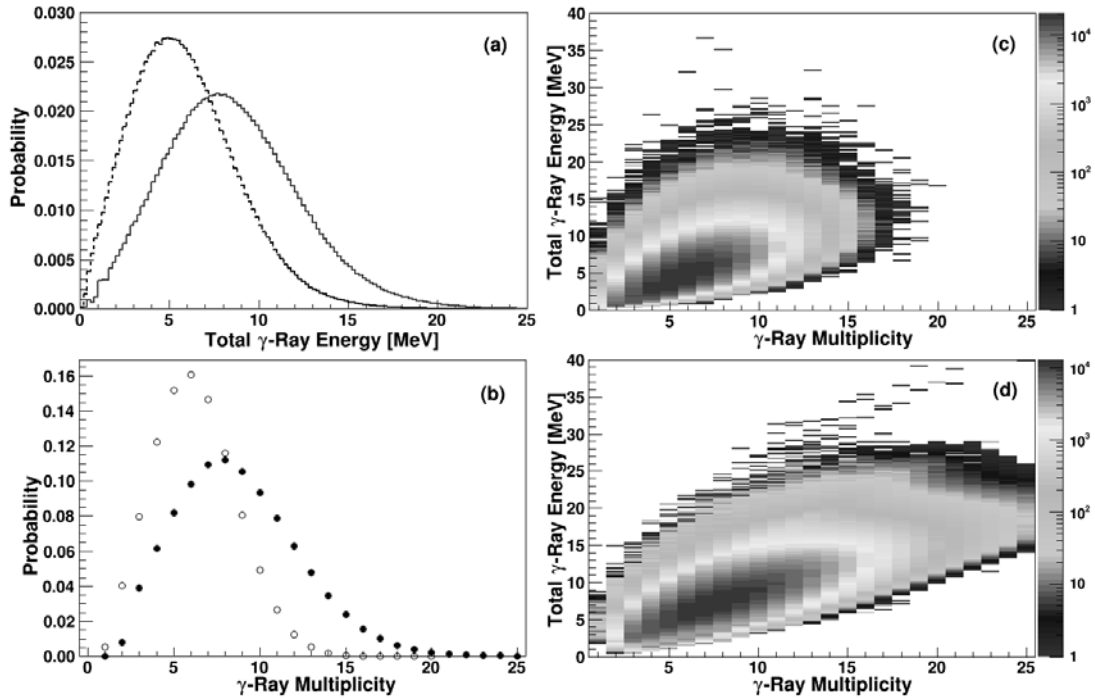


Fig. 2: Shown in panel (c) and (d), respectively, are the measured and unfolded total prompt γ -ray energy vs. multiplicity distribution for the spontaneous fission of ^{252}Cf . Comparison of the projected total γ -ray energy and multiplicity distributions between measured (dashed line, open circles) and unfolded one (solid line, filled circles) are given in panels (a) and (b), respectively.

The comparison of $\langle E_{\gamma,\text{tot}} \rangle$ between our measurements and previous ones is given in Table 2. For ^{235}U , the recent (2-D) derived mean $E_{\gamma,\text{tot}}$ of 8.35 MeV is higher than 6.53(20) MeV, the weighted average of previous measurements [23], and 6.60 MeV, the evaluated data listed in ENDF/B-VII.1. It also is higher than 6.92(9) MeV, the most recent measurement [6]. The same comparisons are also made for the neutron-induced fission in $^{239,241}\text{Pu}$ and the spontaneous fission in ^{252}Cf . Our measured $\langle E_{\gamma,\text{tot}} \rangle$ are consistently higher than the previous ones [1,6,7,23] by $\sim 20\%$ for all isotopes studied. The

Table 1: Comparison of the mean M_γ between our recent measurement and previous ones for the neutron-induced fission of ^{235}U and $^{239,241}\text{Pu}$ as well as the spontaneous fission of ^{252}Cf .

Isotope	2-D	1-D	Ref. 15	ENDF/B-VII.1	Ref. 23	Refs. 1, 6, 7
^{235}U	7.35	6.95		7.04	6.60(10)	8.19(11)
^{239}Pu	7.93	7.50	7.15	7.78	7.06(20)	
^{241}Pu	7.97	7.50		8.18		8.21(9)

^{252}Cf	8.75	8.16	7.98(40)	8.30(8)
-------------------	------	------	----------	---------

uncertainty for our derived $\langle E_{\gamma,\text{tot}} \rangle$ is dominated by the systematic error and roughly estimated to be better than 5%, assuming a similar uncertainty to that of the derived $\langle M_{\gamma} \rangle$.

An independent analysis of the same DANCE data for ^{239}Pu by assuming a very general parameterized correlation between E_{γ} and M_{γ} has been carried out by Ullmann et al. [15], which yields the $\langle E_{\gamma,\text{tot}} \rangle = 7.46$ MeV and $\langle M_{\gamma} \rangle = 7.15$. The $\langle E_{\gamma,\text{tot}} \rangle$, derived from the $E_{\gamma,\text{tot}}$ distribution, agrees within 6% of that obtained by using the 2-D unfolding technique. This agreement is significant and indicates the importance of the correlation between E_{γ} and M_{γ} to be considered in the determination of $\langle E_{\gamma,\text{tot}} \rangle$. It raises serious concern on the validity of the equation, $\langle E_{\gamma,\text{tot}} \rangle = \langle E_{\gamma} \rangle \times \langle M_{\gamma} \rangle$, which ignores the correlation between E_{γ} and M_{γ} exhibited in Fig. 2.

Table 2: Comparison of the mean $E_{\gamma,\text{tot}}$ (MeV) between our recent measurements and previous ones for the neutron-induced fission of ^{235}U and $^{239,241}\text{Pu}$ as well as the spontaneous fission of ^{252}Cf .

Isotope	2-D	Ref. 15	ENDF/B-VII.1	Ref. 23	Refs. 1, 6, 7
^{235}U	8.35		6.60	6.53(20)	6.92(9)
^{239}Pu	7.94	7.46	6.74	6.78(10)	
^{241}Pu	8.01		7.26		6.41(6)
^{252}Cf	8.52			6.95(30)	6.64(8)

4 Summary

A systematic study of the total prompt γ -ray emission in the neutron-induced fission of ^{235}U and $^{239,241}\text{Pu}$ as well as the spontaneous fission of ^{252}Cf has been carried out using the DANCE array together with a compact PPAC to select the fission event by detecting its fission fragments. The total γ -ray energy vs multiplicity spectrum for all fissile nuclei studied was constructed and unfolded using a two-dimensional unfolding technique, numerically implemented by adopting the iterative Bayesian method. The $\langle E_{\gamma,\text{tot}} \rangle$ derived from the projected $E_{\gamma,\text{tot}}$ distribution of the unfolded $E_{\gamma,\text{tot}}$ vs M_{γ} spectrum is about 20% higher than the previous measurements for all fissile nuclei studied. However, it agrees reasonably well with the result derived from the analysis by considering the correlation between E_{γ} and M_{γ} in a very general parameterization manner. In addition, the measured total prompt γ -ray energy vs multiplicity spectrum in fission enables one to evaluate the variance in addition to the average value of the energy deposited in a reactor core by the prompt fission γ rays. This may improve our understanding of the γ heating in many applications involving nuclear fission.

Acknowledgement

This work benefited from the use of the LANSCE accelerator facility as was performed under the auspices of the US Department of Energy by Lawrence Livermore National Security, LLC under contract DE-AC52-07NA27344 and by Los Alamos National Security, LLC under contract DE-AC52-06NA25396. Partial funding is gratefully acknowledged from the U.S. DOE/NNSA Office of Defense Nuclear Nonproliferation Research and Development. All isotopes used in the measurements were obtained from Oak Ridge National Laboratory.

References

- [1] R. Billnert, F.-J. Hamsch, A. Oberstedt, and S. Oberstedt, *Phys. Rev. C* **87** (2013) 024601.
- [2] G. Rimpault, in Nuclear Data Needs for Generation IV, edited by P. Rullhusen (World Scientific, Antwerp, 2006), p. 46.
- [3] G. Rimpault, A. Courcelle, and D. Blanchet, comment to HPRL: ID H.3 and H.4.
- [4] Nuclear Data High Priority Request List of the NEA (Req. ID: H.3, H4)
<http://www.oecd-nea.org/dbdata/hprl/hprlview.pl?ID=421>
<http://www.oecd-nea.org/dbdata/hprl/hprlview.pl?ID=422>.
- [5] V.V. Verbinski, H. Weber, and R.E. Sund, *Phys. Rev. C* **7** (1973) 1173.
- [6] A. Oberstedt *et al.*, *Phys. Rev. C* **87** (2013) 051602(R).
- [7] A. Oberstedt *et al.*, *Phys. Rev. C* **90** (2014) 024618.
- [8] M. Heil *et al.*, *NIM A* **459** (2001) 229.
- [9] R. Reifarh *et al.*, *IEEE Transactions on Nuclear Science* **53**, 880 (2006) 880.
- [10] R. Reifarh *et al.*, Los Alamos National Laboratory, LA-UR-01-4185 (2001).
- [11] R. Reifarh *et al.*, Los Alamos National Laboratory, LA-UR-03-5560 (2003).
- [12] A. Chyzh, C. Y. Wu *et al.*, *Phys. Rev. C* **85** (2012) 021601(R).
- [13] C.Y. Wu *et al.*, *NIM A* **694** (2012) 78.
- [14] A. Chyzh, C.Y. Wu *et al.*, *Phys. Rev. C* **87** (2013) 034620.
- [15] J.L. Ullmann *et al.*, *Phys. Rev. C* **87** (2013) 044607.
- [16] A. Chyzh, C. Y. Wu *et al.*, *Phys. Rev. C* **90** (2014) 014602.
- [17] M. Jandel, T.A. Bredeweg, A. Couture, J.M. O'Donnel, and J.L. Ullmann, Los Alamos National Laboratory, LA-UR-12-21171 (2012).
- [18] G. D'Agostini, *NIM A* **362** (1995) 487.
- [19] G. D'Agostini, arXiv:1010.0612 (2010).
- [20] T.J. Auye, arXiv:1105.1160 (2011).
- [21] S. Agostinelli *et al.*, *NIM A* **506** (2003) 550.
- [22] M. Jandel *et al.*, *NIM B* **261** (2007) 1117.
- [23] T.E. Valentine, *Ann. Nucl. Energy* **28** (2001) 191 and references therein.
- [24] M.B. Chadwick *et al.*, *Nucl. Data Sheets* **112** (2011) 2887.

Measurement of the $^{240}\text{Pu}(n,f)$ cross-section at the CERN n_TOF facility: first results from EAR-2

A. Tsinganis^{1,2}, A. Stamatopoulos², N. Colonna³, R. Vlastou², P. Schillebeeckx⁴, A. Plompen⁴, J. Heyse⁴, M. Kokkoris², M. Barbagallo³, E. Berthoumieux⁵, M. Calviani¹, E. Chiaveri¹, O. Aberle¹, J. Andrzejewski⁶, L. Audouin⁷, M. Bacak⁸, J. Balibrea-Corred⁹, S. Barros¹⁰, Bécaries⁹, F. Bečvář¹¹, C. Beinrucker¹², J. Billowes¹³, D. Bosnar¹⁴, M. Brugger¹, M. Caamaño¹⁵, F. Calviño¹⁶, D. Cano-Ott⁹, F. Cerutti¹, G. Cortés¹⁶, M.A. Cortés-Giraldo¹⁷, L. Cosentino¹⁸, L. Damone³, K. Deo¹⁹, M. Diakaki⁵, C. Domingo-Pardo²⁰, R. Dressler²¹, E. Dupont⁵, I. Durán¹⁵, B. Fernández-Domínguez¹⁵, A. Ferrari¹, I. Ferreira-Gonçalves¹⁰, P. Finocchiaro¹⁸, R. Frost¹³, W. Furman²², K. Göbel¹², S. Ganesan¹⁹, A. Gheorghe²³, T. Glodariu²³, E. González⁹, A. Goverdovski²⁴, E. Griesmayer⁸, C. Guerrero¹⁷, F. Gunsing¹, H. Harada²⁵, T. Hehrich¹², S. Heinitz²¹, A. Hernández-Prieto¹, D. Jenkins²⁶, E. Jericha⁸, F. Käppeler²⁷, Y. Kadi¹, T. Katabuchi²⁸, P. Kavrigin⁸, V. Ketlerov²⁴, V. Khryachkov²⁴, A. Kimura²⁵, N. Kivel²¹, M. Kričak¹¹, E. Leal-Cidoncha¹⁵, C. Lederer¹², H. Leeb⁸, J. Lerendegui¹⁷, M. Licata²⁹, S. Lo Meo³⁰, R. Losito¹, D. Macina¹, J. Marganec⁶, T. Martínez⁹, P. Mastinu³¹, C. Massimi²⁹, M. Mastromarco³, F. Matteucci³², E. Mendoza⁹, A. Mengoni³⁰, P. Milazzo³², F. Mingrone²⁹, M. Mirea²³, S. Montesano¹, A. Musumarra¹⁸, R. Nolte³³, F. Palomo-Pinto¹⁷, C. Paradela¹⁵, N. Patronis³⁴, A. Pavlik³⁵, J. Perkowski⁶, I. Porrás-Sánchez³⁶, J. Praena¹⁷, J.M. Quesada¹⁷, T. Rauscher³⁷, R. Reifarth¹², A. Riego-Perez¹⁶, M. Robles¹⁵, C. Rubbia¹, J. Ryan¹³, M. Sabaté-Gilarte^{1,17}, A. Saxena¹⁹, S. Schmidt¹², D. Schumann²¹, P. Sedyshev²², G. Smith¹³, P. Steinegger²¹, S.V. Suryanarayana¹⁹, G. Tagliente³, J.L. Tain²⁰, A. Tarifeo-Saldivia²⁰, L. Tassan-Got⁷, V. Valenta¹¹, G. Vannini²⁹, V. Variale³, P. Vaz¹⁰, A. Ventura²⁹, V. Vlachoudis¹, A. Wallner³⁸, S. Warren¹³, C. Weiss¹, M. Weigand¹², T. Wright¹³, P. Žugec¹⁴

¹ European Organisation for Nuclear Research (CERN), Geneva, Switzerland

² Department of Physics, National Technical University of Athens (NTUA), Greece

³ Istituto Nazionale di Fisica Nucleare, Bari, Italy

⁴ European Commission JRC, Institute for Reference Materials and Measurements, Geel, Belgium

⁵ Commissariat à l'Énergie Atomique (CEA) Saclay - Irfu, Gif-sur-Yvette, France

⁶ Uniwersytet Łódzki, Lodz, Poland

⁷ Centre National de la Recherche Scientifique/IN2P3 - IPN, Orsay, France

⁸ Technische Universität Wien, Austria

⁹ Centro de Investigaciones Energeticas Medioambientales y Tecnológicas (CIEMAT), Madrid, Spain

¹⁰ Inst. Tecnológico e Nuclear, Instituto Superior Técnico, Univ. Técnica de Lisboa, Portugal

¹¹ Charles University, Prague, Czech Republic

¹² Johann-Wolfgang-Goethe Universität, Frankfurt, Germany

¹³ University of Manchester, Oxford Road, Manchester, UK

¹⁴ Department of Physics, Faculty of Science, University of Zagreb, Croatia

¹⁵ Universidade de Santiago de Compostela, Spain

¹⁶ Universitat Politècnica de Catalunya, Barcelona, Spain

¹⁷ Universidad de Sevilla, Spain

¹⁸ Istituto Nazionale di Fisica Nucleare, Laboratori Nazionali del Sud, Catania, Italy

¹⁹ Bhabha Atomic Research Centre (BARC), Mumbai, India

²⁰ Instituto de Física Corpuscular, CSIC-Universidad de Valencia, Spain

²¹ Paul Scherrer Institut (PSI), Villigen, Switzerland

²² Joint Institute for Nuclear Research (JINR), Dubna, Russia

²³ Horia Hulubei National Institute of Physics and Nuclear Engineering Bucharest, Romania

²⁴ Institute of Physics and Power Engineering (IPPE), Obninsk, Russia

²⁵ Japan Atomic Energy Agency (JAEA), Tokyo, Japan

²⁶ University of York, Heslington, York, UK

²⁷ Karlsruhe Institute of Technology, Institut für Kernphysik, Karlsruhe, Germany

²⁸ Tokyo Institute of Technology, Tokyo, Japan

²⁹ Dipartimento di Fisica e Astronomia, Università di Bologna, and Sezione INFN di Bologna, Italy

³⁰ ENEA, Bologna, Italy

³¹ Istituto Nazionale di Fisica Nucleare, Laboratori Nazionali di Legnaro, Italy

³² Istituto Nazionale di Fisica Nucleare, Trieste, Italy

³³ Physikalisch Technische Bundesanstalt (PTB), Braunschweig, Germany

³⁴ University of Ioannina, Greece

³⁵ University of Vienna, Faculty of Physics, Austria

³⁶ University of Granada, Spain

³⁷ University of Hertfordshire, Hatfield, UK

³⁸ Australian National University, Canberra, Australia

Abstract

The accurate knowledge of neutron cross-sections of a variety of plutonium isotopes and other minor actinides, such as neptunium, americium and curium, is crucial for feasibility and performance studies of advanced nuclear systems (Generation-IV reactors, Accelerator Driven Systems). In this context, the $^{240}\text{Pu}(n,f)$ cross-section was measured with the time-of-flight technique at the CERN n_TOF facility at incident neutron energies ranging from thermal to several MeV. The present measurement is the first to have been performed at n_TOF's newly commissioned Experimental Area II (EAR-2), which is located at the end of an 18 m neutron beam-line and features a neutron fluence that is 25-30 times higher with respect to the existing 185 m flight-path (EAR-1), as well as stronger suppression of sample-induced backgrounds, due to the shorter times-of-flight involved. Preliminary results are presented.

1. Introduction

The accurate knowledge of neutron cross-sections of a variety of plutonium isotopes and other minor actinides is crucial for feasibility and performance studies of advanced nuclear systems [1, 2]. Such isotopes, that present a fission threshold at a few hundred keV, accumulate during the operation of a conventional thermal reactor, but could be effectively transmuted in reactors with a fast neutron spectrum. Improved knowledge of the neutron-induced fission cross-sections of these isotopes is not only important for the design of advanced systems, but also for the more efficient operation of existing reactors, since safety margins can be more accurately defined. In particular, the non-fissile and long-lived ^{240}Pu isotope contributes to the long-term residual activity of nuclear waste. It is included in the Nuclear Energy Agency (NEA) High Priority List [3] and the NEA WPEC Subgroup 26 Report on the accuracy of nuclear data for advanced reactor design [4]. In this context, an experiment to measure the $^{240}\text{Pu}(n,f)$ cross-section was executed at the CERN n_TOF (neutron time-of-flight) facility [5, 6, 7, 8]. Preliminary results are presented in this article.

2. Experimental setup

2.1 The n_TOF facility and Experimental Area II (EAR-2)

Neutrons at n_TOF are spallation products created by a bunched 20 GeV/c proton beam delivered by CERN's PS (Proton-Synchrotron) accelerator onto a lead target 40 cm in length and 60 cm in diameter. A 1 cm-thick layer of circulating water surrounds the target in order to cool it down and also act as a neutron moderator. Beyond the target and after an additional 4 cm-thick layer of (borated) water, a

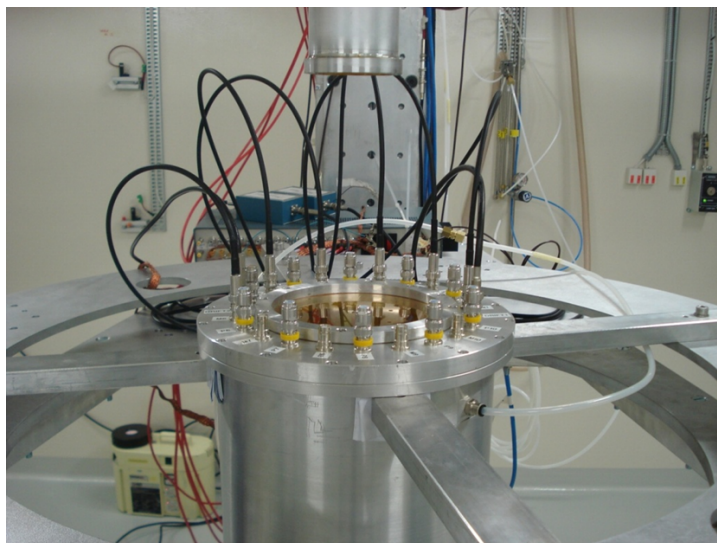


Fig. 1: A view of the chamber housing the samples and detectors, and the associated electronics placed in the neutron beam in EAR-2. The neutron beam arrives vertically from below and then continues in the vacuum tube above the chamber and onto the beam dump a few meters later. Approximately 15-20 cm of air are present before and after the chamber.

~185 m vacuum tube leads to the first measuring station (Experimental Area I, or EAR-1) which has been in operation since 1999.

A new experimental area (Experimental Area II or EAR-2) [9, 10] was commissioned in the second half of 2014. EAR-2 is located at the end of an 18 m neutron beam-line placed vertically above the spallation target. The proximity to the target yields a gain in flux of 25-30 times compared to the existing experimental area (EAR-1), while the neutrons are delivered in an approximately 10 times shorter time interval. The very high instantaneous flux and extended energy range (from thermal to over 100 MeV) allow to cover the region of interest in a single experiment and mitigate the adverse effects of the strong α -background produced by the samples and the low fission cross-section below and near the fission threshold.

Both experimental areas meet the requirements to operate as Type A Work Sectors [11], meaning unsealed radioactive samples can be handled.

2.2 Samples and detectors

Three plutonium oxide (PuO_2) samples were used [12], for a total mass of approximately 2.3 mg of ^{240}Pu ($\sim 0.10 \text{ mg/cm}^2$ per sample, 99.89% purity). The material was electro-deposited on an aluminium backing 0.25 mm thick and 5 cm in diameter, while the deposit itself had a diameter of 3 cm. Additionally, a ^{235}U sample with a mass of $\sim 0.6 \text{ mg}$ and a ^{238}U sample with a mass of $\sim 0.8 \text{ mg}$ were used as reference. All samples were manufactured at IRMM (Belgium). Contaminants present in the ^{240}Pu samples (most notably ^{239}Pu) have a non-negligible contribution to the fission yield in certain energy ranges (mainly below 1 keV) which was subtracted during the analysis.

The measurements were carried out with Micromegas (Micro-MESH Gaseous Structure) gas detectors [13, 14, 15]. The gas volume of the Micromegas is separated into a charge collection region (several mm, 5 mm in this case) and an amplification region (typically tens of μm , 50 μm in this case) by a thin “micromesh” with 35 μm diameter holes on its surface. A chamber capable of holding up to 10 sample-detector modules was used for the measurement. The detectors were operated with an

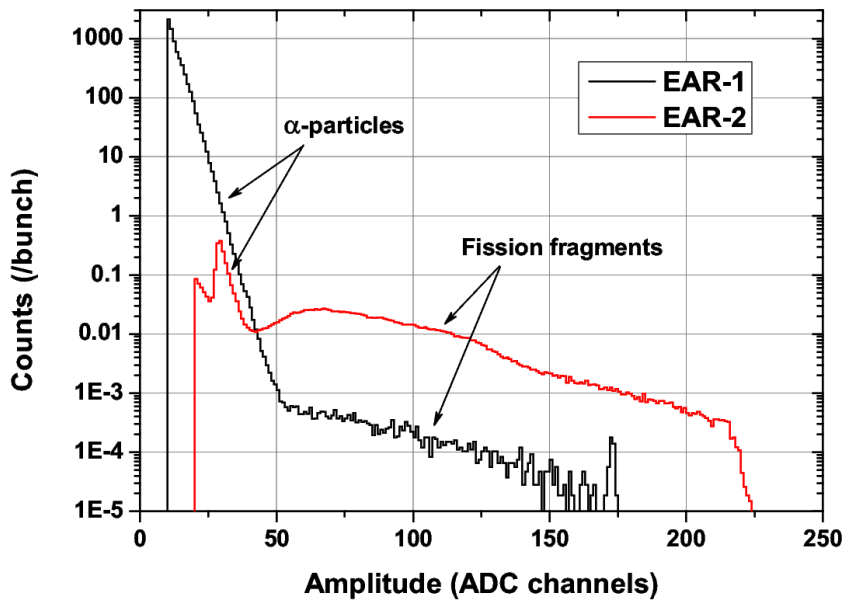


Fig. 2: Pulse-height spectra obtained from a ^{240}Pu sample during the measurements in EAR-1 (black) and EAR-2 (red). Counts are normalised per beam bunch for direct comparison. The significant suppression of the sample-induced α -background is evident, as is the much higher rate of fission events.

Ar:CF₄:isoC₄H₁₀ gas mixture (88:10:2) at a pressure of 1 bar. A picture of the chamber placed in the experimental area is shown in Figure 1.

The analogue detector signals were digitised with 8-bit flash-ADCs [16] with a 500 MHz sampling rate. In order to minimise the volume of data to be transferred and recorded, a zero-suppression algorithm was applied to avoid recording long sequences of noise where no useful signals are present.

3. The previous measurement in EAR-1

This measurement was originally attempted in EAR-1, in parallel with the measurement of the ^{242}Pu fission cross-section [17, 18]. Due to the lower neutron flux, it was necessary to measure over a period of several months to collect the necessary statistics. An unexpected effect of the high α -activity of the ^{240}Pu samples (>6 MBq per sample) was encountered in the course of the measurement [19], with a steady degradation of the fission fragment amplitude distribution. After the end of the measurement, a visual inspection of the detectors used with the ^{240}Pu samples revealed a circular discolouration of the mesh whose dimension and position exactly matched those of the samples. Upon closer inspection with a microscope, it became clear that the micromesh had suffered serious damage, particularly around the rims of the holes which were evidently deformed. This led to a degradation of the electrical field and therefore of the detector gain and overall performance. In time, this made the fission fragment and α -particle signals virtually indistinguishable in the obtained pulse-height spectra. It should be noted that, even when detectors were operating normally, the long α pile-up tail greatly reduced the quality of the separation, as can be seen in Figure 2 (black).

4. Data analysis and results

The digitised raw data from each detector are analysed off-line by means of a pulse recognition routine that determines the amplitude and position in time of the detected signals, as well as the signal baseline, among other quantities. Throughout the measurement, beam-off data were taken in order to record

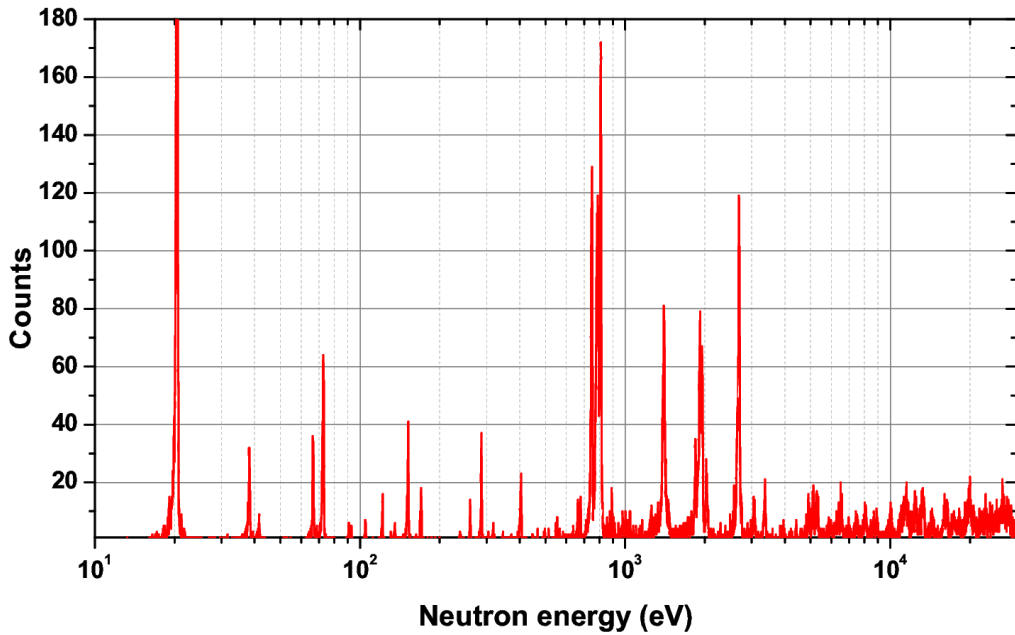


Fig. 3: Resonances observed in the measured fission yields from the three ^{240}Pu samples, after subtraction of contributions from contaminants. Several resonance clusters, attributable to the coupling between Class-I and Class-II states, are visible, while resonances can be observed up to a few tens of keV. Data are shown with a binning of 2000 bins per energy decade.

the α - and spontaneous fission background produced by the samples. The behaviour of the detectors is studied by means of Monte Carlo simulations performed with the FLUKA code [20, 2], focusing particularly on the reproduction of the pulse height spectra of α -particles and fission fragments for the evaluation of the detector efficiency and the correction associated to the signal amplitude threshold.

The interactions of the proton beam with the spallation target lead to a significant production of prompt γ -rays and other relativistic particles that reach the experimental area at (nearly) the speed of light and constitute what is commonly termed the “ γ -flash”. This causes an initial signal lasting a few hundred ns, followed by a baseline oscillation that lasts for several μs or, in terms of neutron energy, down to less than 1 MeV. In order to remove this oscillation, an average shape is obtained from at least several hundred signals and then subtracted from each raw data “movie” before processing the data.

In Figure 2, the pulse-height spectrum obtained from one of the ^{240}Pu samples (red) is compared to a spectrum recorded with the same sample during the measurement in EAR-1 (black). It can be clearly observed that the increased neutron flux leads to a considerably higher number of recorded fission events and that there is a much stronger suppression of the sample-induced α -particle background, resulting in a considerably clearer separation from the fission fragments.

Figure 3 shows the fission counts as a function of incident neutron energy recorded in all three ^{240}Pu samples between 10 eV and 30 keV, after applying an appropriate signal amplitude threshold to reject the background and subtracting the contribution of contaminants present in the sample. Several resonance clusters can be observed and resonances are visible up to a few tens of keV. Above 100 keV, data has been obtained up to at least several MeV, with statistical uncertainties below 2-3% and even below 1% in the range between 0.5-5 MeV.

5. Summary

The measurement of the ^{240}Pu fission cross-section is the first measurement to be performed at the newly commissioned Experimental Area II of the CERN n_TOF facility. Data were collected from thermal energies up to at least several MeV. Most notably, data showing clear resonant structures have been obtained even in the sub-threshold region (up to a few tens of keV) where the cross-section is lowest and where evaluations show a smooth behaviour of the cross-section. The success of this measurement is largely due to the favourable characteristics of EAR-2, in particular the increased neutron flux and stronger background suppression compared to EAR-1, where the measurement was not feasible. These features will allow n_TOF to expand its measurement capabilities to even more short-lived and rare isotopes, such as ^{230}Th , ^{232}U , $^{238,241}\text{Pu}$ and ^{244}Cm .

Acknowledgements

The authors would like to acknowledge the support of the European Commission under the ANDES, ERINDA and CHANDA projects (7th Framework Programme).

References

- [1] *Generation-IV International Forum*, www.gen-4.org
- [2] *International Framework for Nuclear Energy Cooperation (IFNEC)*, www.ifnec.org
- [3] *NEA Nuclear Data High Priority Request List*, www.nea.fr/html/dbdata/hprl
- [4] *OECD/NEA WPEC Subgroup 26 Final Report: Uncertainty and Target Accuracy Assessment for Innovative Systems Using Recent Covariance Data Evaluations*, www.nea.fr/html/science/wpec/volume26/volume26.pdf
- [5] U. Abbondanno, Tech. Rep. CERN-SL-2002-053 ECT, CERN, Geneva (2002)
- [6] C. Guerrero *et al.*, *Eur. Phys. J. A* **49**(2), (2013) pp. 1–15, DOI: 10.1140/epja/i2013-13027-6
- [7] E. Berthoumieux, cds.cern.ch/record/1514680
- [8] M. Barbagallo *et al.*, *Eur. Phys. J. A* **49**(12), (2013) pp. 1–11, DOI: 10.1140/epja/i2013-13156-x
- [9] E. Chiaveri and the n_TOF Collaboration, Tech. Rep. CERN-INTC-2012-029. INTC-O-015, CERN, Geneva (2012), cds.cern.ch/record/1411635
- [10] C. Weiss *et al.*, *NIM A* **799**, (2015) pp. 90 – 98, DOI: 10.1016/j.nima.2015.07.027
- [11] V. Vlachoudis *et al.*, edms.cern.ch/document/934369/0.13, CERN EDMS No. 934369
- [12] G. Sibbens *et al.*, *J. Radioanal. Nucl. Ch.* **299**, (2013) pp. 1–6, DOI: 10.1007/s10967-013-2668-7
- [13] Y. Giomataris *et al.*, *NIM A* **376**(1), (1996) pp. 29 – 35, DOI: 10.1016/0168-9002(96)00175-1
- [14] Y. Giomataris, *NIM A* **419**, (1998) pp. 239 – 250, DOI: 10.1016/S0168-9002(98)00865-1
- [15] I. Giomataris, ICFA Instrum. Bul. **19**, www.slac.stanford.edu/pubs/icfa/fall99/paper1/paper1a.html
- [16] U. Abbondanno *et al.*, *NIM A* **538**, (2005) pp. 692-702, DOI: 10.1016/j.nima.2004.09.002
- [17] A. Tsinganis, *Nucl. Data Sheets* **119**, (2014) pp. 58 – 60, DOI: 10.1016/j.nds.2014.08.018
- [18] A. Tsinganis, EPJ Web of Conf. **66**, (2014) p. 03088, DOI: 10.1051/epjconf/20146603088
- [19] Varii, *Fission cross section measurements for ^{240}Pu , ^{242}Pu : Deliverable 1.5 of the ANDES project*, Ch. 3, European Commission, Joint Research Centre, Belgium (2013), DOI: 10.2787/81004
- [20] A. Ferrari *et al.*, CERN, Geneva (2005), DOI: 10.5170/CERN-2005-010
- [21] G. Battistoni *et al.*, AIP, Fermilab, USA (2007), vol. 896, (pp. 31–49), DOI: 10.1063/1.2720455

Correlated Prompt Fission Data

Patrick Talou¹, Toshihiko Kawano¹, Ionel Stetcu¹ and Denise Neudecker²

¹Theoretical Division, Los Alamos National Laboratory, Los Alamos NM USA

²X-CP Computational Physics Division, Los Alamos National Laboratory, Los Alamos NM, USA

Abstract

Prompt fission neutrons and photons emitted in a fission event are studied through the lens of a Monte Carlo implementation of the Hauser-Feshbach statistical theory of nuclear reactions. Correlations in multiplicity, energy, angle, etc., are of particular interest, placing stringent constraints on fission physics models. Recent theoretical efforts are reviewed in light of new experimental data that probe more exclusive prompt fission quantities. The status of the integration of correlated fission physics codes into MCNP6 transport simulations is briefly described.

1. Introduction and Motivation

A nuclear fission event is characterized by a rich and vast data set, encompassing both pre- and post-scission data. While all those data are naturally correlated, limitations in our theoretical understanding and our predictive modeling tools lead to the segmentation of all fission data for the purpose of nuclear data evaluations. For instance, evaluated nuclear data libraries or/and transport code treating fission events do not include any correlation between the prompt fission neutrons, prompt fission photons, fission cross sections, fission fragment angular distributions, fission fragment yields in mass, charge and kinetic energy, etc. In recent times, significant efforts in both experiments and theory/modeling have been invested in trying to bridge this gap.

Current uncertainties in the evaluated prompt fission neutron spectra (PFNS) of several important actinides remain a major contributor to uncertainties in nuclear applications such as innovative energy production and stockpile stewardship activities [1]. Those uncertainties are especially difficult to reduce in the low- and high-energy tails of the spectrum. Experimentally, measurements of the low-energy part of the PFNS below about 500 keV are limited by the significant multiple down-scattering of surrounding neutrons in this energy range. On the other hand, above about 8-10 MeV, the very small number of emitted neutrons generally lead to very limited statistics. Figure 1 shows a recent evaluation [2] of the PFNS for fast neutron-induced fission of ²³⁹Pu, compared to existing experimental data with similar incident energies. The spread of experimental data in the low- and high-energy tails of the PFNS is quite significant.

However, many other data sets on prompt fission neutrons exist, such as the average prompt fission neutron multiplicity (PFNM), $\bar{\nu}$, the average PFNM as a function of the fragment mass, $\bar{\nu}(A)$, the same quantity as a function of the total kinetic energy (TKE) of the fragments, $\bar{\nu}(TKE)$, etc. All these quantities shed some light on a different aspect of the neutron emission mechanism(s) that can help constrain fission physics models that also happen to describe the PFNS. In addition to prompt fission neutrons, data on prompt fission γ rays, emitted somewhat in competition with the neutrons, can also reveal interesting characteristics of the de-excitation process of the fission fragments and on the configurations of the nascent fragments near the scission point.

By combining all these data sets, one can surely improve our understanding of the underlying physics processes, and thereby produce more reliable predictions even for the average PFNS and PFNM, which remain crucial for many nuclear applications. Studying those data and their correlations also

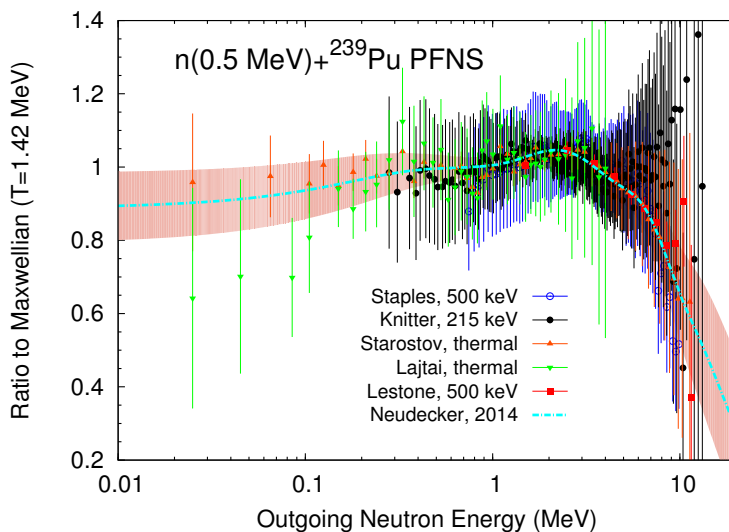


Fig. 1: Evaluated prompt fission neutron spectrum for 0.5 MeV neutron-induced fission reaction of ^{239}Pu in comparison with experimental data with similar incident neutron energies. The precise measurement of the low- and high-energy tails of this spectrum remains the object of intense experimental activities.

opens up new interesting applications, as in detector modeling and non-proliferation activities.

In this paper, we report on ongoing work and recent results obtained using our Monte Carlo Hauser-Feshbach code CGMF used to describe the decay of excited primary fission fragments. After a brief description of the theoretical framework used in CGMF, we discuss some results in the context of correlated fission data, and how they can help shed some light on various aspects of the nuclear fission process, including: evaporation of neutrons and γ rays, competition neutron- γ -ray emissions, excitation energy sorting mechanism(s) between the two fragments, nuclear structure of the fission fragments, etc. In this context, we present our numerical results in comparison with experimental correlated data. Finally, we mention our ongoing work in bringing the physics of CGMF into the MCNP6 transport code.

2. Theoretical and Computational Approach

This approach has been described already in several publications [3, 4, 5] and will only be briefly reviewed here for sake of completeness. Only *binary* fission is considered. The scission of the fissioning compound nucleus (A_c, Z_c) is then followed by the evaporation of prompt fission neutrons and γ rays from the excited fission fragments. In this work, we are not interested in the fission cross sections, and the probability of producing particular fission fragments is contained in the fission yields, $Y(A, Z, TKE)$, which are an input in the present calculations.

The CGMF code [3, 4] was developed to follow the decay of the primary fission fragments on an event-by-event basis. It is a Monte Carlo implementation of the Hauser-Feshbach theory of nuclear reactions applied to the fission fragment evaporation stage. The primary fission fragment yields in mass, charge, and kinetic energy are first sampled using the Monte Carlo technique. The initial conditions in energy U , spin J and parity π are then chosen according to calculated probabilities. The intrinsic excitation energies $U_{L,H}$ in the light and heavy fragments are chosen such that the total excitation energy (TXE) is equal to the difference between the Q value of the fission reaction and the total kinetic energy TKE of the fragments. The further partition of TXE between the two fragments is realized so that the experimental values for the average neutron multiplicity as a function of the fragment mass, $\bar{\nu}(A)$, are best reproduced by the calculations.

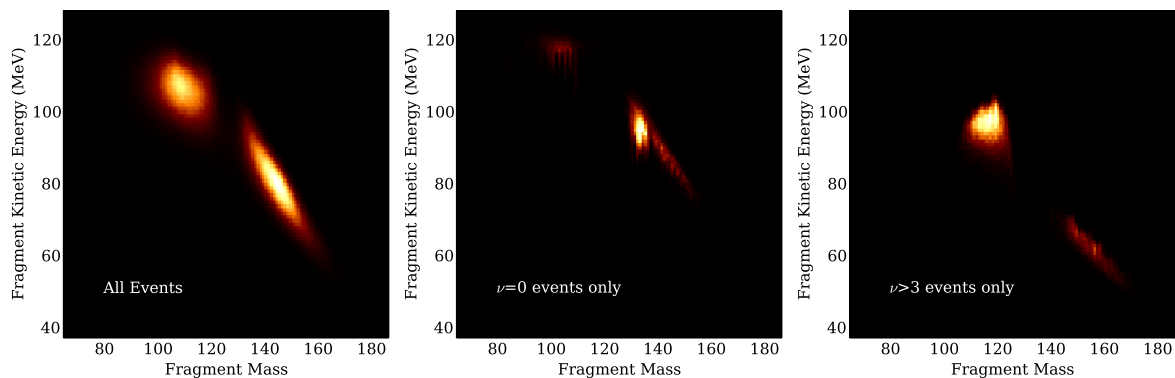


Fig. 2: Example of fission fragment yields, obtained in the case of ^{252}Cf spontaneous fission, filtered by the number of evaporated neutrons: (left) total yields; (center) $\nu = 0$, i.e., “cold fission”; (right) $\nu > 3$. Such results can be readily obtained with the application of simple filters to the CGMF code output.

The initial distribution of the angular momentum in the fragments is represented by a Gaussian whose mean value is a function of the temperature-dependent fragment moment of inertia. In this version of the code, we do not take into account any possible correlation between the angular momenta of the two fragments. Finally, the parity distribution is chosen to be equally positive and negative. Once the values for (A, Z, TKE) are chosen according to the input primary fragment yields, the initial conditions in (U, J, π) in each fragment are also sampled using the Monte Carlo technique.

Further assuming that the primary fragments can be represented as compound nuclei, the statistical Hauser-Feshbach theory [6] can be used to compute the emission of neutrons and γ rays at each stage of the decay. Again here, we use the Monte Carlo technique, thereby keeping track of the complete sequence of emissions and of the correlations between the different emitted particles. Energies and angles of emission are recorded, providing a rather complete picture of the evaporation process. Important in this type of calculations is the knowledge of the low-lying nuclear structure and level density of nuclei, i.e., fission fragments. In the present calculations, the Reference Input Parameter Library RIPL-3 [7] is used for all fragments. The probabilities for neutron emission are calculated using optical model calculations and the Koning-Delaroche global spherical optical potential [8]. The γ -ray emission probabilities are computed using the γ -ray strength function formalism for giant dipole resonances. At each stage of the decay, those probabilities are sampled, and the $n - \gamma$ competition is naturally accounted for.

The raw results of the CGMF code are a long suite of fission events characterized by a specific fragmentation, and the detailed characteristics of each neutron and γ -ray emitted. Inferring distributions and correlations (multiplicity, energy, angle) of the evaporated particles is a rather straightforward statistical game. As an example, Fig. 2 shows the the fission fragment yields in mass and kinetic energy distributions, in the case of ^{252}Cf spontaneous fission, filtered by the number of emitted neutrons, e.g., 0 (cold fission) and greater than 3, which can be readily obtained from CGMF output files.

3. Results and Discussion

Several examples of numerical results obtained with the CGMF code are shown here.

Figure 3 shows the calculated prompt fission neutron and γ -ray multiplicity distributions, compared to experimental data. To reproduce correctly the γ -ray multiplicity distribution, it is important to consider the threshold for the detection of the γ rays used in particular experiments. In addition, the time coincidence window used to define prompt fission particles is specific to each experiment,

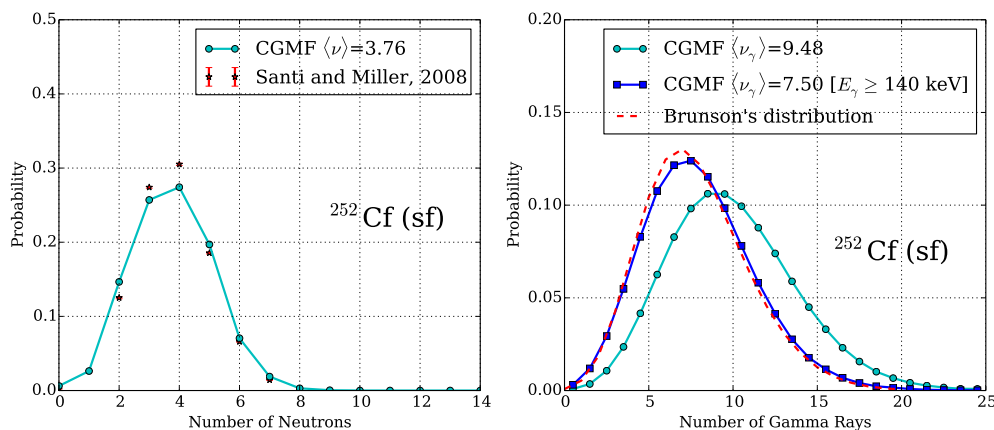


Fig. 3: Prompt fission neutron and γ -ray multiplicity distributions calculated with the CGMF code for ^{252}Cf spontaneous fission. Santi and Miller evaluated data [9] are the result of an evaluation of several experimental data sets, with very small error bars. The calculated γ -ray multiplicity distribution is compared to Brunson's distribution [10], fitted to available experimental data. The results are very sensitive to the threshold value for the γ -ray detector, here set at 140 keV.

making comparisons with just one calculated distribution delicate. The average prompt fission neutron multiplicity is very well reproduced, while discrepancies in $P(\nu)$ remain.

Calculated γ -ray spectra for specific fragments are shown in Fig. 4. The hardening of the γ -ray spectra for fission fragments near a shell closure, e.g., $A \sim 130$, is clearly visible in the top right figure. Gating even more specifically on fission fragment mass chains (here, $A = 144$) or even on a specific fragment (here, $A = 144$ and $Z = 56$) shows distinct γ lines corresponding to discrete transitions in the known low-lying spectrum of those particular fragments. Recent experimental results by Oberstedt *et al.* [11] will be used to test the present calculations.

Similarly, recent data on the fragment mass-dependent prompt fission neutron spectra by Gök *et al.* [12] can be compared directly to CGMF calculations, shining some light on the nuclear structure of neutron-rich fission fragments. This study is ongoing.

As a final example, the total prompt fission neutron spectrum calculated in the neutron-induced fission reaction on ^{239}Pu for 18 MeV incident neutron energy is shown in Fig. 5. At this energy, the correct treatment of multi-chance fission and pre-equilibrium neutron components is paramount to properly describe the PFNS.

4. Implementation in the MCNP6 Transport Simulation Code

A coding effort, sponsored by the U.S. Department of Energy for Nuclear Nonproliferation, is ongoing to incorporate the physics of correlated prompt data in fission events in the MCNP6 transport code. The CGMF as well as FREYA codes, both providing prompt fission neutron and γ -ray data on an event-by-event basis, are being incorporated to provide correlated neutron sources in transport simulations. Preliminary studies [13, 14] have shown that such correlations are important for neutron multiplicity counting studies where the appropriate neutron multiplicity distribution $P(\nu)$ has to be sampled to produce correct results. Detector development and characterization would also strongly benefit from the use of such capabilities in the MCNP6 code.

Similar earlier work led to the development of the MCNPX – PoLiMi code [15], which can sample

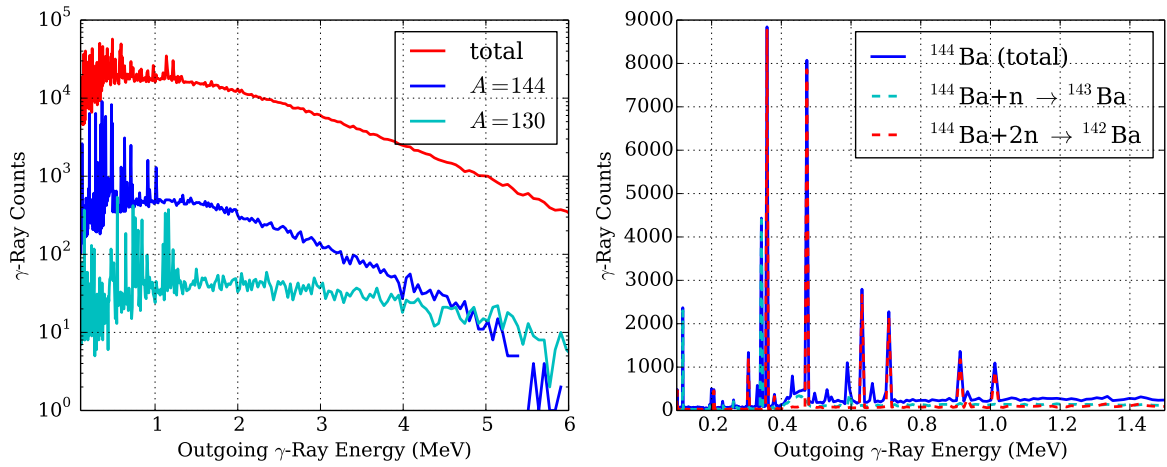


Fig. 4: Calculated γ -ray spectra in the case of Cf-252 spontaneous fission, with gates on specific mass chain (left) or even specific fission fragment (right- Te-144). The right plot shows that strong γ lines originate mostly from ^{143}Ba transitions in its ground-state rotational band ($0^+ \rightarrow 2^+$, $2^+ \rightarrow 4^+$, etc.).

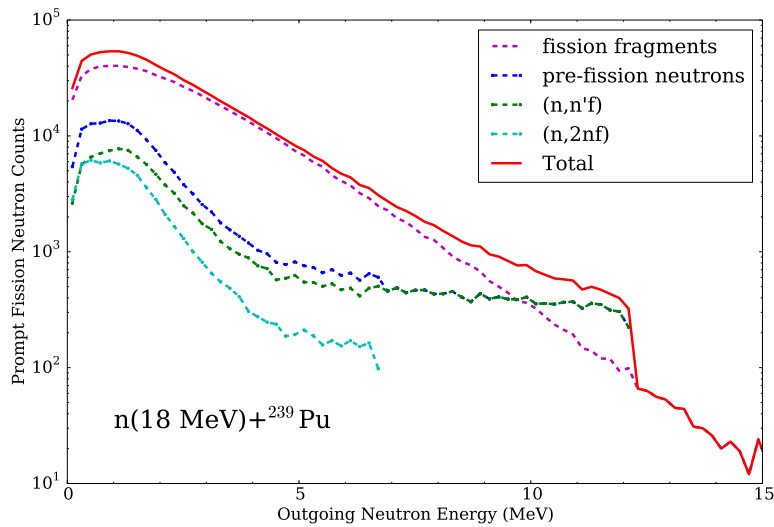


Fig. 5: The prompt fission neutron spectrum predicted by CGMF in the case of 18 MeV neutrons incident on ^{239}Pu is composed of several contributions: pre-fission neutron emissions in the multi-chance fission process, pre-equilibrium neutrons, and evaporation from excited fission fragments.

prompt neutron multiplicity distributions and multiplicity-dependent prompt neutron spectra for a limited set of isotopes and fission reactions. Our more recent efforts aim at extending the scope of those earlier calculations, as well as improving the physics of the fission process included in the transport simulations. A new release of the MCNP6 code that will include such features is expected for the end of 2016.

5. Conclusions

Monte Carlo simulations of the evaporation of prompt fission neutrons and γ rays from fission fragments on an event-by-event basis represent a powerful tool to address fundamental physics questions related to the nuclear fission process. Only by studying various fission observables in a coherent and consistent fission model can we hope to significantly improve the prediction and evaluation of nuclear fission data. In addition, these Monte Carlo simulators also provide unprecedented capabilities to model detector responses and study prompt fission data correlations for use in nuclear technologies, such as in safeguards and non-proliferation activities.

Acknowledgments

This work was performed at Los Alamos National Laboratory, under the auspices of the National Nuclear Security Administration of the U.S. Department of Energy at Los Alamos National Laboratory under Contract No. DE-AC52-06NA25396. It was supported by the Office of Defense Nuclear Non-proliferation Research & Development (DNN R&D), NNSA, DOE.

References

- [1] I. Kodeli *et al.*, *NIM A* **610**, 540 (2009).
- [2] D. Neudecker *et al.*, *NIM A* **791**, 80 (2015).
- [3] T. Kawano *et al.*, *J. Nucl. Sci. Tech.* **47**, No. 5, 462 (1010).
- [4] P. Talou *et al.*, *Phys. Rev. C* **83**, 064612 (2011).
- [5] I. Stetcu *et al.*, *Phys. Rev. C* **90**, 024617 (2014).
- [6] W. Hauser and H. Feshbach, *The inelastic scattering of neutrons*, *Phys. Rev.* **87**, 366 (1952).
- [7] R. Capote *et al.*, *Nucl. Data Sheets* **110**, 3107 (2009).
- [8] A. Koning and J. Delaroche, *Nucl. Phys.* **A713**, 231 (2003).
- [9] P. Santi and M. Miller, *Nucl. Sci. Eng.* **160**, 190 (2008).
- [10] G. S. Brunson, Jr., *Multiplicity and Correlated Energy of Gamma Rays Emitted in the Spontaneous Fission of Californium-252*, Ph.D. Thesis, University of Utah (1982).
- [11] S. Oberstedt, in *Proc. 2nd Int. Conf. on "Perspectives for Nuclear Data in the Next Decade," P(ND)²-2*, 2014, Bruyères-le-Châtel, France.
- [12] A. Göök, F.-J. Hamsch, and M. Vidali, *Phys. Rev. C* **90**, 064611 (2014).
- [13] J. M. Verbeke and O. Petit, in *Proc. 37th Meeting Eur. Safeguards R&D Association*, 2015, Manchester, UK.
- [14] M. E. Rising *et al.*, in *Proc. American Nuclear Society Winter Meeting*, Anaheim, USA, 2014.
- [15] S. A. Pozzi *et al.*, *NIM A* **694**, 119 (2012).

Determination of neutron-induced fission fragment spin distribution after neutron evaporation

A. Chebboubi¹, G. Kessedjian¹, O. Litaize², O. Serot², H. Faust³, D. Bernard², A. Blanc³, U. Köster³, O. Méplan¹, P. Mutti³, C. Sage¹

¹LPSC, Université Grenoble-Alpes, CNRS/IN2P3, F-38026 Grenoble Cedex, France

²CEA, DEN, DER, SPRC, Cadarache, Physics Studies Laboratory, F-13108 Saint-Paul-lès-Durance, France

³Institut Laue-Langevin, F-38042 Grenoble Cedex 9, France

Abstract

Nuclear fission consists of splitting a nucleus into smaller nuclei. Several observables are available to study the fission process such as fission yields or fission fragment angular momentum. Currently, fission models cannot predict all the observables with an acceptable accuracy for nuclear fuel cycle studies for instance. Improvement of fission models is an important issue for the knowledge of the process itself and for the applications. In this work, we take an interest in fission fragment angular momentum distribution. Isomeric ratios (IRs) are a common observable giving access to investigate these distributions. We measured accurate IRs for ⁸⁸Br, ¹³²Sn and ¹³²Te with the fission fragment separator LOHENGRIN and developed a new analysis method to assess the mean value and uncertainty of the IR. An evaluation of the angular momentum distribution of ¹³²Sn was also performed with the FIFFRELIN code.

1. Introduction

Although nuclear fission was discovered seven decades ago [1, 2], the fission process has still some characteristics barely understood such as the fission fragment angular momentum. However, this observable is critical for the determination of the prompt γ spectra, which are central in the calculation of γ heating and damage of nuclear reactor components [3]. A high accuracy of the prompt γ spectra is required in order to design the next generation of nuclear reactors with a higher level of confidence. In this work, the assessment of the fission fragment angular momentum through isomeric ratio measurements is presented [4, 5, 6]. In a first section, the experimental setup is exposed. Then the data analysis procedure to determine the isomeric ratio and its uncertainty is explained. The angular momentum distribution of ¹³²Sn is then derived. Finally a brief discussion and interpretation of our results are proposed.

2. Experimental set-up

The experiments were performed at the LOHENGRIN mass separator [7] located at the high flux reactor of Institut Laue-Langevin (ILL). Figure 1 (left) is a scheme of the LOHENGRIN spectrometer. The target of a fissile isotope is placed near the core of the reactor in a thermal neutron flux of $\approx 5 \times 10^{14}$ n.cm⁻².s⁻¹. In order to reduce the self-sputtering, the target may be covered by a sputtered Ta layer or a Ni foil (see Table 1) [8]. The produced fission fragments are then separated according to the ratios of their mass A over their ionic charge q and their kinetic energy E_k over their ionic charge by the combination of a magnetic and an electrostatic sector. The refocusing magnet [9] increases the particle density at the focal position 2.

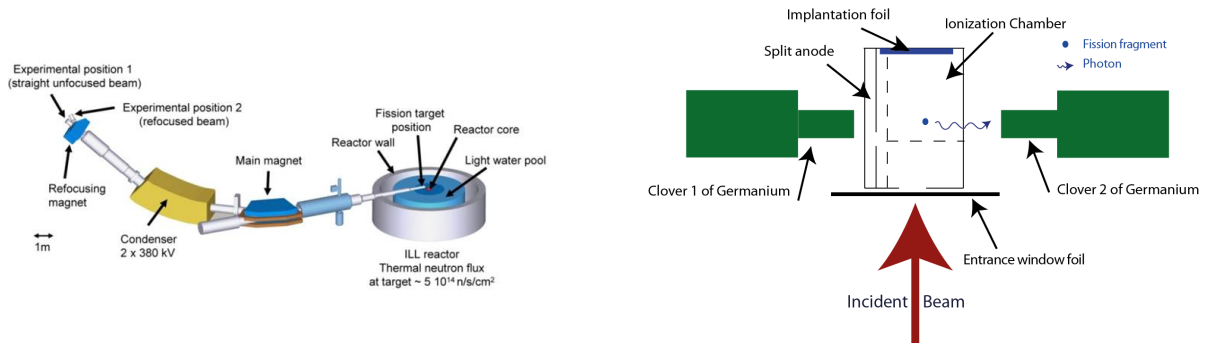


Fig. 1: Scheme of the LOHENGRIN spectrometer (left). Detection system placed at the focal position 2 (right).

Table 1: Characteristics of the two campaigns achieved at the LOHENGRIN spectrometer

Target	Thickness ($\mu\text{g}\cdot\text{cm}^{-2}$)	Cover	Measured nuclei
Target 1 (^{233}U)	323	Ni foil ($450 \mu\text{g}\cdot\text{cm}^{-2}$)	^{132}Te
Target 2 (^{235}U)	91	Sputtered Ta layers ($195 \mu\text{g}\cdot\text{cm}^{-2}$)	^{132}Sn , ^{132}Te
Target 3 (^{233}U)	113	None	^{88}Br

To identify the incoming fission fragments, an ionisation chamber (IC) surrounded by two clover detectors consisting of four high purity germanium (Ge) crystals were placed at the focal position 2 of the spectrometer [see Fig. 1 (right)]. Since signals from the IC and Ge detectors were recorded with a triggerless digital acquisition, the data were analysed off-line.

3. Analysis path

The required observable is the isomeric ratio IR :

$$IR = \frac{\eta(^mX)}{\eta(^mX) + \eta(^{gs}X)} \quad (1)$$

with $\eta(X)$ the fission rate of the isomeric state (m) or the ground state (gs) respectively. Several corrections are needed to assess this quantity from the raw data. In this section, the method developed to determine the IR mean value and uncertainty is presented. In this paper, only μs isomeric states are studied.

3.1 Count rate extractions from γ spectra

Since the time of flight within the LOHENGRIN spectrometer is about $1 - 2 \mu\text{s}$, the detection of μs isomeric states is possible. All of the isomeric states studied in this work decay through an isomeric transition whereas ground states disintegrate through β^- decay. The unique γ signature for each of both states allows to identify them unambiguously.

To measure the isomeric state population, a time coincidence of $\approx 10T_{1/2}^{isomer}$ was performed between IC and Ge signals. The ion-gated γ spectra were very clean and permitted to extract the isomeric state count rates with a high accuracy (see Fig. 1).

The measurement of the ground state was done by extracting its γ lines from the ungated spectra.

Because of the background coming from different separated nuclei and the ambient background, the uncertainty of the ground state count rate was larger than for the isomeric state.

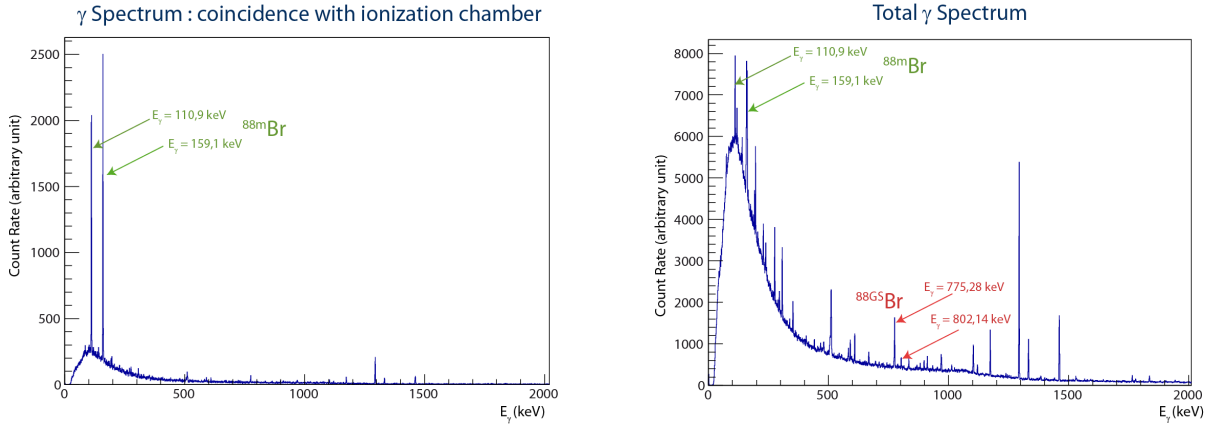


Fig. 2: Ion-gated spectra for ^{88}Br (left). The identification of the isomeric states is unambiguous. Ungated spectra for ^{88}Br (right). The extraction of the ground state is more complex because of the γ background.

3.2 Total Monte Carlo Method to extract the isomeric ratio

To obtain the isomeric and ground state fission rate $\eta(^mX)$ and $\eta(^sX)$ from the count rates extracted, different corrections are needed such as the γ lines intensity, detector efficiencies and the solution of the Bateman equation for the moment of fission taking into account the lifetimes and branching ratios.

Some parameters, like the lifetime of the isomeric and ground states, appear in different correction factors. The uncertainty propagation is then quite complex. In order to evaluate the uncertainty of the measurement without bias, a Monte Carlo method was developed. The principle is to draw every independent parameters according to a Gaussian distribution and calculate all the correction factors to evaluate the isomeric ratio. This procedure is then repeated (typically 10^6 times) and permits to obtain the probability density function (*pdf*) of the isomeric ratio. From this distribution the mean value and the uncertainty of the isomeric ratio is derived. The *pdf* is globally well reproduced by a Gaussian function, but for low number of counts with an important statistical uncertainty, the distribution is asymmetric. With a classical uncertainty propagation, this observation would not be possible.

3.3 Building of experimental correlation matrices

For a given experiment and nucleus, a set of IRs as function of kinetic energy E_i , was measured. Some parameters, γ intensity for instance, are common for all of the IR measurements. The experimental covariance matrix can then be built from the method described above. Since the common parameters are independent from one another, the covariance matrix is the product of the sensibility S_{ik} with a term linked to the independent parameters a_k for each measurement:

$$\begin{aligned}
 IR(E_i) &= f(\{a_k\}) \\
 S_{ik} &= \frac{\partial f_i}{\partial a_k} \frac{\bar{a}_k}{f(\{\bar{a}_k\})} \\
 \frac{\text{Cov}(IR(E_i), IR(E_j))}{IR(E_i)IR(E_j)} &= \sum_k S_{ik} S_{jk} \frac{\sigma_{a_k}^2}{\bar{a}_k^2}
 \end{aligned} \tag{2}$$

with f the function which relates the parameters and the isomeric ratio. The sensibilities are calculated from the Monte Carlo method. Indeed, for a given parameter, the other being fixed to their mean value,

a drawing was done according to a Gaussian distribution. A distribution of IRs was then obtained as a function of the parameter. The extracted slope around the mean value (the sensibility is a local parameter) permits to determine the sensibility.

4. Determination of the spin distribution for ^{132}Sn

Fission models can determine the fission fragment angular momentum distribution. To derive this value from the isomeric ratio a γ de-excitation code is required. In this work, we used FIFRELIN (FIssion FRagment Evaporation Leading to an Investigation of Nuclear data), which is a Monte Carlo code simulating the prompt fission neutron and γ -ray emission [10, 11]. Its particularity is to describe the fission fragment nuclear structure through the combination of the experimental level scheme and models of nuclear level density. The probability to decay from an initial state to a final state is related to models of γ strength function. In this article, CTM (Constant Temperature Model) [12] and EGLO (Enhanced Generalized Lorentzian model) [13] were used as nuclear level density and γ strength function models.

For a given excitation state and angular momentum (E^*, J^π), called an entry state, FIFRELIN is able to produce a γ de-excitation and then compute the probability to feed both isomeric and ground states. In other words, for each entry state, FIFRELIN calculates an isomeric ratio.

In this work, only the angular momentum distribution of ^{132}Sn was studied. Its entry states were divided by bins of 200 keV from the isomeric state energy, to the neutron binding energy. Indeed, since measurements were done after neutron evaporation, the angular momentum distribution after neutron emission is the more accurate. The binning in the J^π axis is $1 \hbar$ from 0^\pm to 30^\pm . Figure 3 presents the principle of the FIFRELIN calculation (left) and the IR as a function of the entry state (right).

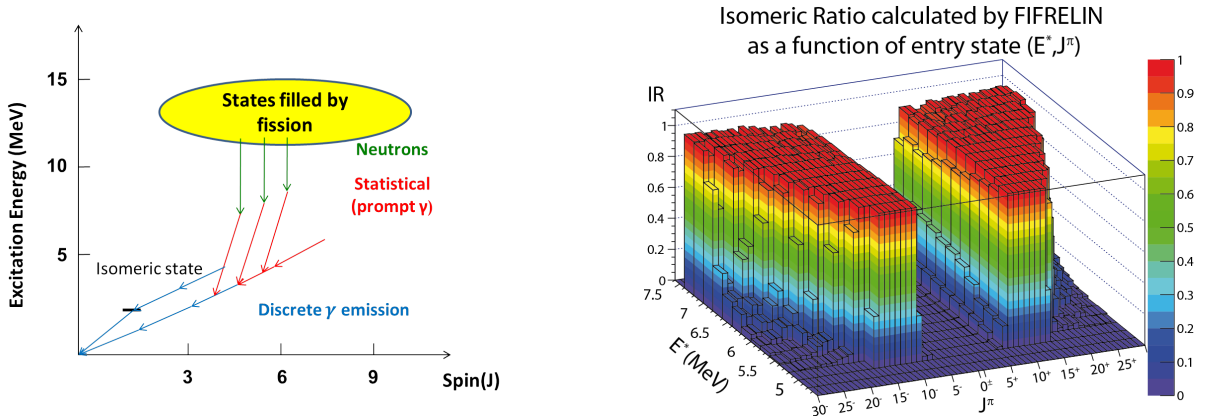


Fig. 3: Scheme of connection between initial fission entry state and isomeric ratio (left). In this work only the levels up to the binding energy were considered to be filled by the fission process. IR calculated with FIFRELIN as a function of the initial entry state (after neutron emission)(right).

The calculated IRs are then averaged :

$$IR_{calc}(E^*) = \sum_J \sum_{\pi} P(\pi) P(J) IR_{calc}(E^*, J^\pi) \quad (3)$$

with $P(\pi) = \frac{1}{2}$ and $P(J)$ following [14] :

$$P(J) \propto (2J + 1) \exp\left(-\frac{(J + 1/2)^2}{J_{rms}^2}\right) \quad (4)$$

with J_{rms} a free parameter also called spin cutoff. Its value is determined through a Bayesian comparison between experimental isomeric ratios and calculated ones. Figure 4 presents the probability to reproduce experimental results as a function of the excitation energy and the spin cutoff (left). The warmer the colors, the more probable the initial distributions are. In this example, an angular momentum distribution parametrized by a spin cutoff of $J_{rms} \approx 5 \hbar$ is more probable than with $J_{rms} \approx 10 \hbar$. This assessment is only valid if the calculated IRs (with the most probable spin cutoff value) are in agreement with the experimental results, which is the case as shown in Fig. 5.

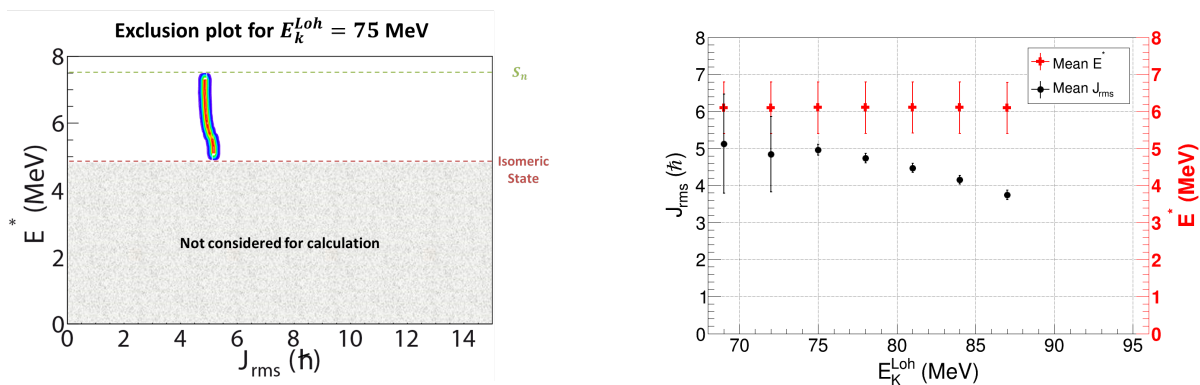


Fig. 4: Exclusion plot for ^{132}Sn at $E_k = 75$ MeV obtained from the comparison between experimental and calculated IRs (left). Spin cutoff as a function of the measured kinetic energy (right). A clear dependence is shown. The mean excitation energy is obtained without any prior in the analysis.

5. Results and discussion

An angular momentum distribution was extracted from our measurement of the isomeric ratio of ^{132}Sn . Figure 5 presents the experimental results, compared with the calculations performed by FIFRELIN (with the most probable spin cutoff determined through a comparison with experimental IRs) and the experimental correlation matrix. A clear dependence of the IRs and the spin cutoff [see Fig. 4 (right)] as a function of the kinetic energy is shown. This observation would lead to exclude the common mechanism of generation of fission fragment angular momentum, the so-called bending and wriggling modes [15]. Indeed in this model, a deformed pair of fission fragments is required. Otherwise the angular momentum is expected to be equal to zero [16, 17, 18]. Since the ^{132}Sn is supposed spherical at the scission point, our results are in contradiction with these modes. New theoretical calculations must be performed in order to interpret this result. It seems that ^{132}Sn is particularly appropriate to test the limits of angular momentum generation models. However, for deformed nuclei, the role of the deformation energy must be investigated in order to describe the mechanism of angular momentum generation.

In addition, results on ^{132}Te and ^{88}Br tend to show the significance of the covered target role in the kinetic energy dependence of IRs. A thick target washes out the correlation between these two quantities whereas the cover shifts the kinetic energy. Figure 6 illustrates this phenomenon by comparing IRs with differently covered targets.

6. Conclusion

The measurement of IRs as function of kinetic energy can provide useful information for theoretical works on the fission process and more exactly on the generation of the fission fragment angular mo-

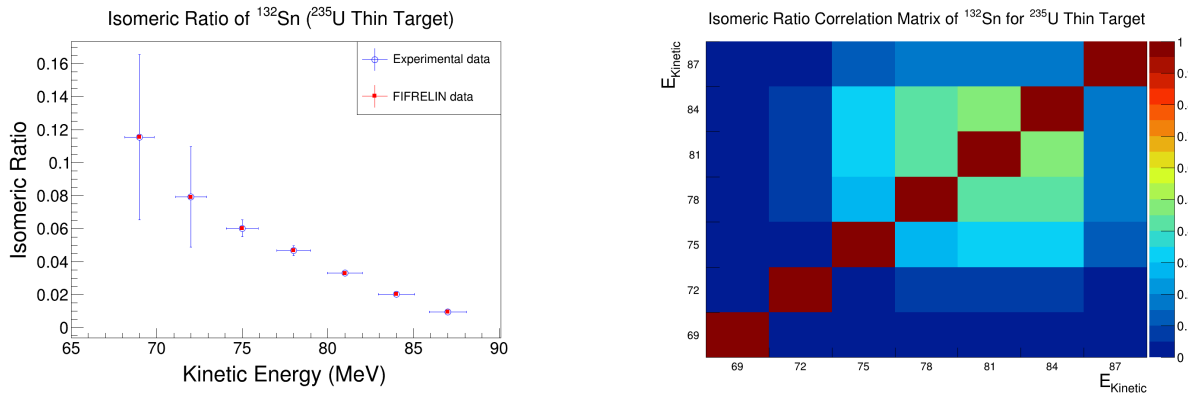


Fig. 5: Comparison between experimental and calculated IRs as a function of the measured kinetic energy for ^{132}Sn (left). The experimental correlation matrix shows the weight of the systematics to the total uncertainty (right).

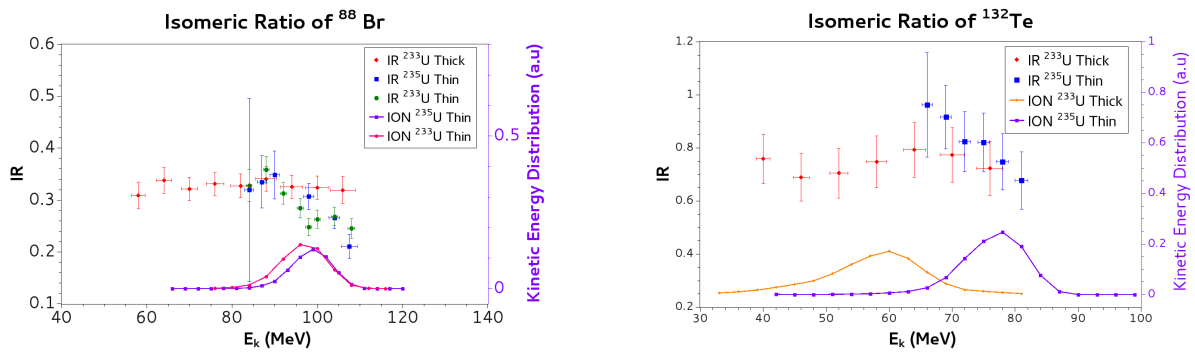


Fig. 6: IRs as a function of the measured kinetic energy. The slope depends drastically on the thickness of the target. Results are shown for ^{88}Br (left) and ^{132}Te (right).

mentum. The role of the covered target was emphasized. Thus the use of a thin target with a thin and regular cover is required to investigate properly the dependence of the IRs with kinetic energy. A new method of analysis was developed and permitted to obtain the probability function of IRs. Experimental correlation matrices were built and shed light on the leading role of systematics in the total uncertainty. To go further and reduce the uncertainties, an emphasis on the nuclear structure of the studied nuclei must be done.

A complete set of data, with different fissioning system and nuclei, will permit to validate the different models describing the fission fragment angular momentum. In this framework, ^{132}Sn is a cornerstone to test in depth the model robustness.

References

- [1] O. Hahn and F. Strassmann, *Naturwissenschaften* **27** (1939) 11.
- [2] L. Meitner and O.R. Frisch, *Nature* **143** (1939) 239.
- [3] G. Rimpault *et al.*, *Phys. Proc.* **31** (2012) 3.
- [4] H. Faust, *J. Korean Phys. Soc.* **59** (2011) 879.
- [5] R. Vandenbosch and J. Huizenga, *Nuclear Fission*, 1973 (Academic Press, New York and London)
- [6] F. Gönnerwein, I. Tsekhanovich and V. Rubchenya, *Int. J. Mod. Phys. E* **16** (2007) 410.
- [7] P. Armbruster *et al.*, *Nucl. Instrum. Methods* **139** (1976) 213.
- [8] U. Köster *et al.*, *Nucl. Instrum. Meth. A* **613** (2010) 363.

- [9] G. Fioni *et al.*, *Nucl. Instrum. Meth. A* **332** (1993) 175.
- [10] O. Litaize and O. Serot, *Phys. Rev. C* **82** (2010) 054616.
- [11] D. Regnier, O. Litaize and O. Serot, *Comput. Phys. Comm.*, to be published.
- [12] A. Gilbert and A. Cameron, *Can. J. Phys.* **43** (1965) 1446.
- [13] J. Kopecky and M. Uhl, *Phys. Rev. C* **41** (1990) 1941.
- [14] D.G. Madland and T.R. England, *Nucl. Sci. Eng.* **64** (1977) 859.
- [15] J.R. Nix and W.J. Swiatecki, *Nucl. Phys.* **71** (1965) 1.
- [16] J. Rasmussen, W. Nörenberg and H. Mang, *Nucl. Phys. A* **136** (1969) 465.
- [17] M. Zielinska-Pfabé and K. Dietrich, *Phys. Lett. B* **49** (1974) 123.
- [18] L. Bonneau, P. Quentin and I.N. Mokhailov, *Phys. Rev. C* **75** (2007) 064313.

Microscopic nuclear level densities by the shell model Monte Carlo method

Y. Alhassid¹, G.F. Bertsch², C.N. Gilbreth¹, H. Nakada³, and C. Özen⁴

¹ Center for Theoretical Physics, Sloane Physics Laboratory, Yale University, New Haven CT 06520, USA

² Dept. of Physics and Inst. for Nuclear Theory, Box 351560, University of Washington, Seattle WA 98195, USA

³ Dept. of Physics, Graduate School of Science, Chiba University, Inage, Chiba 263-8522, Japan

⁴ Faculty of Engineering and Natural Sciences, Kadir Has University, Istanbul 34083, Turkey

Abstract

The configuration-interaction shell model approach provides an attractive framework for the calculation of nuclear level densities in the presence of correlations, but the large dimensionality of the model space has hindered its application in mid-mass and heavy nuclei. The shell model Monte Carlo (SMMC) method permits calculations in model spaces that are many orders of magnitude larger than spaces that can be treated by conventional diagonalization methods. We discuss recent progress in the SMMC approach to level densities, and in particular the calculation of level densities in heavy nuclei. We calculate the distribution of the axial quadrupole operator in the laboratory frame at finite temperature and demonstrate that it is a model-independent signature of deformation in the rotational invariant framework of the shell model. We propose a method to use these distributions for calculating level densities as a function of intrinsic deformation.

1. Introduction

Nuclear level densities are an integral part of the calculation of transition rates through Fermi's Golden rule and of the Hauser-Feshbach theory [1] of statistical nuclear reactions. However, their microscopic calculation the presence of correlations is a challenging many-body problem. Theoretical models of level density are often based on mean-field and combinatorial methods [2] but they can miss important correlations.

The configuration-interaction (CI) shell model approach accounts for correlations and shell effects, but conventional diagonalization methods are limited to spaces of dimensionality $\sim 10^{11}$. The shell model Monte Carlo (SMMC) method [3, 4, 5, 6] permits calculations in model spaces that are many orders of magnitude larger than those that can be treated by conventional methods. Quantum Monte Carlo methods for fermions often have a sign problem that limits their applicability. However, the dominant collective components [7] of effective nuclear interactions have a good Monte Carlo sign in SMMC and are sufficient for realistic calculation of level densities and collective properties of nuclei. Small bad-sign components of the nuclear interaction can be treated in the method of Ref. [4].

As a finite-temperature method, SMMC is particularly suitable for the calculation of state densities [8]. It has been applied successfully to mid-mass nuclei [9] and to heavy nuclei [10, 11].

2. SMMC and the calculation of state densities

2.1 SMMC method

The Gibbs ensemble $e^{-\beta H}$ describing a nucleus with Hamiltonian H at inverse temperature β , can be decomposed as a superposition of ensembles U_σ of non-interacting nucleons in external auxiliary fields

$\sigma(\tau)$ that depend on imaginary time τ ($0 \leq \tau \leq \beta$)

$$e^{-\beta H} = \int D[\sigma] G_\sigma U_\sigma, \quad (1)$$

where G_σ is a Gaussian weight. This representation is known as the Hubbard-Stratonovich transformation [12]. The Hamiltonian H is taken to be a CI shell model Hamiltonian that is defined in a truncated single-particle space with N_s orbitals. The thermal expectation value of an observable O can be written as

$$\langle O \rangle = \frac{\text{Tr}(O e^{-\beta H})}{\text{Tr}(e^{-\beta H})} = \frac{\int D[\sigma] W_\sigma \Phi_\sigma \langle O \rangle_\sigma}{\int D[\sigma] W_\sigma \Phi_\sigma}, \quad (2)$$

where $W_\sigma = G_\sigma |\text{Tr} U_\sigma|$ is a positive-definite function, $\Phi_\sigma = \text{Tr} U_\sigma / |\text{Tr} U_\sigma|$ is the Monte Carlo sign, and $\langle O \rangle_\sigma = \text{Tr}(O U_\sigma) / \text{Tr} U_\sigma$.

Since U_σ is a one-body propagator, the quantities in the integrands of (2) can be calculated using matrix algebra in the single-particle space. For example, in the grand canonical ensemble

$$\text{Tr} U_\sigma = \det(\mathbf{1} + \mathbf{U}_\sigma), \quad (3)$$

where \mathbf{U}_σ is the $N_s \times N_s$ matrix that represents U_σ in the single-particle space. The grand canonical expectation value of a one-body observable $O = \sum_{i,j} O_{ij} a_i^\dagger a_j$ is calculated from

$$\langle a_i^\dagger a_j \rangle_\sigma = \left[\frac{1}{\mathbf{1} + \mathbf{U}_\sigma^{-1}} \right]_{ji}. \quad (4)$$

In SMMC we use the canonical ensemble of fixed numbers of protons and neutrons. This is accomplished by representing the particle-number projection as a discrete Fourier transform [13].

The number of auxiliary fields is very large and the integration is carried out by using Monte Carlo methods. Auxiliary-field samples σ_k are chosen according to the positive-definite weight W_σ and the expectation value of an observable O in (2) is estimated from

$$\langle O \rangle \approx \frac{\sum_k \langle O \rangle_{\sigma_k} \Phi_{\sigma_k}}{\sum_k \Phi_{\sigma_k}}. \quad (5)$$

2.2 State density

In SMMC, we calculate the thermal energy at inverse temperature β as the canonical expectation value of the Hamiltonian, $E(\beta) = \langle H \rangle$. The nuclear partition function $Z(\beta) \equiv \text{Tr} e^{-\beta H}$ is then calculated by integrating the thermodynamic relation $-\partial \ln Z / \partial \beta = E(\beta)$. We have

$$\ln Z(\beta) = \ln Z(0) - \int_0^\beta E(\beta) d\beta. \quad (6)$$

where $Z(0)$ is given by the total number of many-particle states in the model space. The state density is given by an inverse Laplace transform of $Z(\beta)$

$$\rho(E) = \frac{1}{2\pi i} \int_{-i\infty}^{i\infty} d\beta e^{\beta E} Z(\beta). \quad (7)$$

We evaluate the average state density in the saddle-point approximation to (7) [14]

$$\rho(E) \approx \left(-2\pi \frac{dE}{d\beta} \right)^{-1/2} e^{S(E)}, \quad (8)$$

where $S(E)$ is the canonical entropy given as a Legendre transform of $\ln Z(\beta)$

$$S(E) = \ln Z + \beta E. \quad (9)$$

In (8) and (9) we use the value of β which is determined by the saddle-point condition

$$E = -\frac{\partial \ln Z}{\partial \beta} = E(\beta). \quad (10)$$

The density calculated in SMMC is the *state* density, in which the magnetic degeneracy $2J + 1$ of each level with spin J is taken into account. However, the density measured in the experiments is often the *level* density, in which each level is counted once irrespective of its magnetic degeneracy. We introduced a method [15, 16] to calculate the level density $\tilde{\rho}$ directly in SMMC by using

$$\tilde{\rho} = \begin{cases} \rho_{M=0} & \text{even-mass nucleus} \\ \rho_{M=1/2} & \text{odd mass nucleus} \end{cases}, \quad (11)$$

where ρ_M is the density at a given value M of the spin component J_z . This M -projected density is calculated by implementing a spin-projection method in the Hubbard-Stratonovich transformation [17].

3. Application to heavy nuclei

We applied SMMC to nuclei as heavy as the lanthanides using a proton-neutron formalism that allows for different sets of single-particle orbitals for protons and for neutrons. In studies of rare-earth nuclei, we used the 50 – 82 shell plus the $1f_{7/2}$ orbital for protons, and the 82 – 126 shell plus the $0h_{11/2}$, $1g_{9/2}$ orbitals for neutrons. The single-particle energies and orbitals are determined by a Woods-Saxon potential plus spin-orbit interaction. The interaction includes an attractive monopole pairing interaction and attractive multipole-multipole interactions with quadrupole, octupole and hexadecupole components. The interaction strengths were determined empirically as discussed in Refs. [10, 11]. At large values of β the matrices \mathbf{U}_σ become ill-defined and require stabilization. Stabilization methods were developed for strongly correlated electron systems in the grand canonical ensemble [18] and we extended them to the canonical ensemble [10].

3.1 Collectivity in the CI shell model

Heavy nuclei are known to exhibit various types of collectivity that are well described by empirical models. An important question is whether these types of collectivity can be described within a spherical CI shell model framework, in which the single-particle model space is truncated. The large dimensionality of the many-particle model space in heavy nuclei necessitates the use of quantum Monte Carlo methods such as SMMC. The various types of collectivity are usually identified by their characteristic spectra. While SMMC is a powerful method that allows the accurate calculation of thermal observables, it is difficult to extract detailed spectroscopic information from the thermal expectation values (2).

To overcome this difficulty, we identified an observable whose low-temperature behavior is sensitive to the type of collectivity. This observable is $\langle \mathbf{J}^2 \rangle_T$, where \mathbf{J} is the total angular momentum of the nucleus. Assuming an even-even nucleus which is either vibrational or rotational, the low-temperature

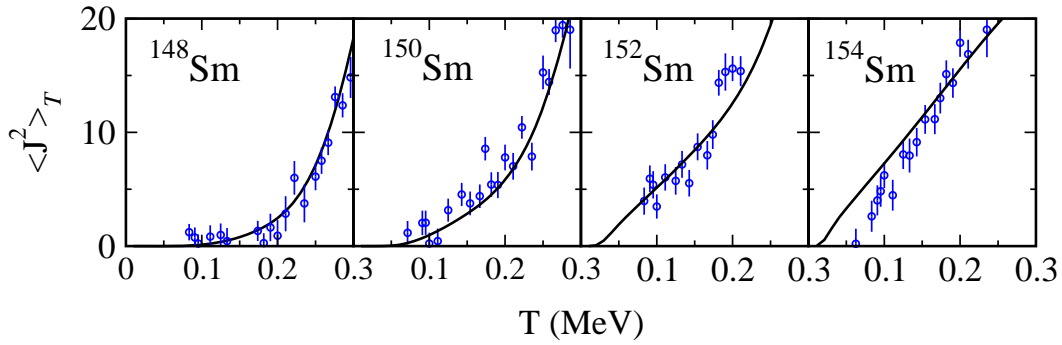


Fig. 1: $\langle \mathbf{J}^2 \rangle_T$ vs. temperature T in the even samarium isotopes $^{148-154}\text{Sm}$. The SMMC results (open circles) are compared with results deduced from experimental data (solid lines; see text). Adapted from Ref. [11].

behavior of $\langle \mathbf{J}^2 \rangle_T$ is given by

$$\langle \mathbf{J}^2 \rangle_T \approx \begin{cases} 30 \frac{e^{-E_{2^+}/T}}{(1 - e^{-E_{2^+}/T})^2} & \text{vibrational band} \\ \frac{6}{E_{2^+}} T & \text{rotational band} \end{cases}, \quad (12)$$

where E_{2^+} is the excitation energy of the lowest 2^+ level.

In Fig. 1, we show the SMMC results (open circles) for $\langle \mathbf{J}^2 \rangle_T$ as a function of temperature T for a family of even samarium isotopes $^{148-154}\text{Sm}$. This family of isotopes are known to describe a crossover from vibrational collectivity in the spherical ^{148}Sm nucleus to rotational collectivity in the deformed ^{154}Sm nucleus. We observe in the SMMC results for $\langle \mathbf{J}^2 \rangle_T$ a crossover from a “soft” response to temperature in ^{148}Sm to a rigid linear response in ^{154}Sm , in agreement with (12).

The solid lines in Fig. 1 are obtained from the experimental data by taking into account a complete set of measured energy levels up to certain excitation energy and by using a back-shifted Bethe formula (BBF) above that energy. This density is determined from level counting at low energies and neutron resonance data at the neutron separation energy.

3.2 State densities

We calculated the SMMC state densities in families of samarium and neodymium isotopes [11, 19]. To compare with experimental data, it is necessary to determine the excitation energy $E_x = E - E_0$, where E_0 is the ground-state energy. It is thus important to determine an accurate ground-state energy.

3.21 Even-even nuclei

The ground-state energy E_0 of even-even nuclei can be determine accurately from large β calculation of the thermal energy. Fig. 2 shows the SMMC state densities (open circles) in even-mass samarium and neodymium isotopes. The results are generally in good agreement with level counting data at low excitation energies (histograms) and with neutron resonance data (triangles) when available [20]. The solid lines describe BBF state densities determined empirically from the level counting and the neutron resonance data.

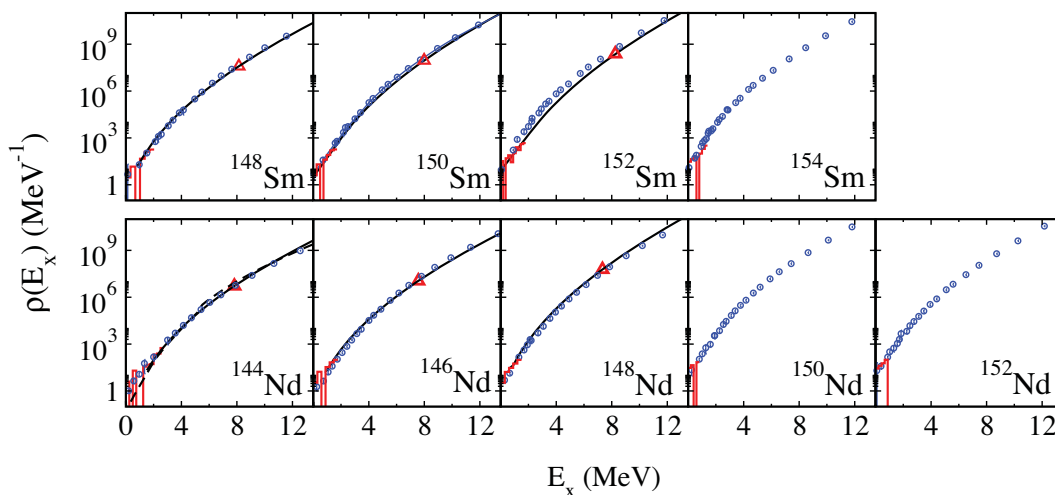


Fig. 2: State densities vs. excitation energy E_x in even-mass samarium (top panels) and neodymium (bottom panels) isotopes. The SMMC densities (open circles) are compared with level counting data (histograms) and neutron resonance data (triangles) when available [20]. The neutron resonance data was converted to a total state density assuming a spin cutoff model with rigid-body moment of inertia. The solid lines are empirical BBF densities (see text). Adapted from Refs. [11, 21].

3.22 Odd-even nuclei

SMMC calculations at low temperatures in odd-even nuclei have a sign problem that originates from the projection on odd number of particles, leading to large error bars in the thermal energy. Consequently, we can calculate the thermal energy only up to $\beta \sim 4 \text{ MeV}^{-1}$ and it is difficult to determine an accurate ground-state energy. A method to calculate an accurate ground-state energy for a system with odd number of particles despite the odd particle-number sign problem was introduced in Ref. [22] and applied to mid-mass nuclei. However, its application in heavy nuclei requires additional development. For the heavy nuclei we determine the ground-state energy E_0 from a one-parameter fit of the SMMC thermal energy to the thermal energy calculated from experimental data [19]. The corresponding state densities in odd-mass samarium and neodymium isotopes are shown in Fig. 3 and compared with experimental data.

4. Deformation in the CI shell model

Knowledge of state densities as a function of nuclear deformation is useful in the modeling of fission. Nuclear deformation is a key concept in our understanding of the physics of heavy nuclei. However, it is based on a mean-field approximation that breaks rotational invariance. The challenge is to study nuclear deformation in the framework of the CI shell model approach which preserves rotational symmetry.

4.1 Quadrupole distributions in the laboratory frame

We calculated the SMMC distribution $P_T(q)$ of the axial quadrupole operator \hat{Q}_{20} in the laboratory frame [23] at inverse temperature β by using its Fourier representation

$$P_T(q) = \frac{1}{\text{Tr} e^{-\beta H}} \int_{-\infty}^{\infty} \frac{d\varphi}{2\pi} e^{-i\varphi q} \text{Tr} \left(e^{i\varphi Q_{20}} e^{-\beta H} \right) \quad (13)$$

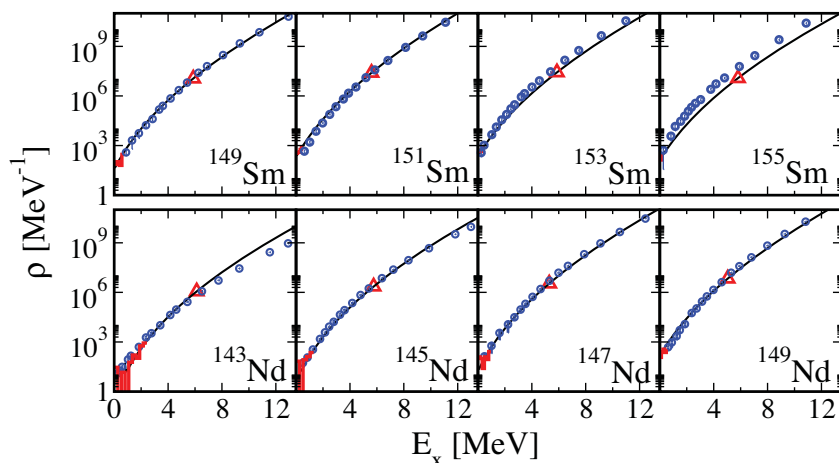


Fig. 3: State densities vs. excitation energy E_x in odd-mass samarium (top panels) and neodymium (bottom panels) isotopes. Symbols and lines are as in Fig. 2. Adapted from Ref. [19].

together with the Hubbard-Stratonovich representation (1) of $e^{-\beta H}$. We divide an interval $[-q_{\max}, q_{\max}]$ into $2M + 1$ intervals of length $\Delta q = 2q_{\max}/(2M + 1)$ and use a discrete Fourier representation

$$\text{Tr}(\delta(Q_{20} - q_m)U_\sigma) \approx \frac{1}{2q_{\max}} \sum_{k=-M}^M e^{-i\varphi_k q_m} \text{Tr}(e^{i\varphi_k Q_{20}} U_\sigma), \quad (14)$$

where $q_m = m\Delta q$ ($m = -M, \dots, M$) and $\varphi_k = \pi k/q_{\max}$ ($k = -M, \dots, M$).

The distributions $P_T(q)$ are shown for ^{154}Sm in Fig. 4 at three temperatures. At a low temperature ($T = 0.1$ MeV) we find a skewed distribution that is qualitatively similar to that of a prolate rigid rotor (dashed line) whose intrinsic axial quadrupole moment is taken from a finite-temperature Hartree-Fock-Bogoliubov (HFB) approximation. In the HFB approximation, we observe a shape transition from a deformed to a spherical shape around a temperature of $T = 1.2$ MeV. At this temperature the quadrupole distribution is still skewed. At high temperatures, e.g., $T = 4$ MeV, the distribution is close to a Gaussian. We also calculated the quadrupole distributions for ^{148}Sm which is spherical in its

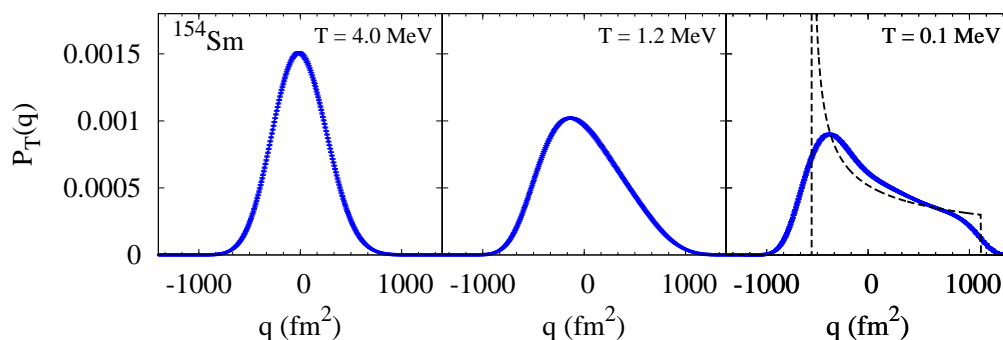


Fig. 4: The SMMC quadrupole distributions $P_T(q)$ in the laboratory frame for ^{154}Sm at a low temperature $T = 0.1$ MeV, an intermediate temperature $T = 1.2$ MeV (close to the HFB shape transition temperature) and a high temperature $T = 4$ MeV. Adapted from Ref. [23].

mean-field ground state and found that they are close to a Gaussian already at low temperatures. We conclude that the quadrupole distribution in the laboratory frame is a clear model-independent signature of nuclear deformation in the framework of the rotational-invariant CI shell model approach.

4.2 Quadrupole distributions in the intrinsic frame

For the formalism developed here to be useful for calculating level densities as a function of intrinsic deformation, it is necessary to determine the quadrupole distribution in the intrinsic frame. The intrinsic frame is usually defined within a mean-field approximation, so a direct calculation of this distribution in the CI shell model approach is not feasible. To overcome this difficulty, we consider the second rank quadrupole tensor $q_{2\mu}$ ($\mu = -2, \dots, 2$). In the intrinsic frame (characterized by a set of three Euler angles Ω), the quadrupole shape is characterized by two shape parameters β, γ . Note that we use the same symbol β to denote both the inverse temperature and the axial shape parameter, and the correct meaning should be clear from the context. The probability density $P_T(\beta, \gamma)$ in the intrinsic frame is a rotational invariant and therefore we can expand $-\ln P_T(\beta, \gamma)$ in rotational invariant combinations of $q_{2\mu}$. There are only three quadrupole invariants up to fourth order in $q_{2\mu}$ and they are given by $\beta^2, \beta^3 \cos 3\gamma$ and β^4 . Thus

$$-\ln P_T(\beta, \gamma) = N + A\beta^2 - B\beta^3 \cos 3\gamma + C\beta^4 + \dots, \quad (15)$$

where A, B, C are temperature-dependent parameters and N is a normalization constant. Eq. (15) is similar to the Landau expansion of the free energy in which the quadrupole tensor is considered as the order parameter of the shape transition [24, 25]. The parameters A, B, C in (15) can be determined from the expectation values of the above three quadrupole invariants. In calculating these expectation values from the density P_T it is necessary to take into account the volume element

$$\prod_{\mu} dq_{2\mu} \propto \beta^4 |\sin 3\gamma| d\beta d\gamma d\Omega. \quad (16)$$

In Ref. [23] we showed that the above three quadrupole invariants are related to moments of Q_{20} in the laboratory frame and thus can be directly calculated from the SMMC distribution $P_T(q)$ in the laboratory frame.

In Fig. 5 we show $-\ln P_T(\beta, \gamma = 0)$ as a function of the axial deformation parameter β for ^{154}Sm at three temperatures $T = 0.25, 1.19$ and 4 MeV. The curves in Fig. 5, derived in the CI shell model framework without the use of a mean-field approximation, seem to mimic the shape transition that is found in the HFB mean-field approximation. The minima of these curves describe a shape transition from a prolate minimum at low temperatures (e.g., $T = 0.25$ MeV) to a spherical minimum at high temperatures (e.g., $T = 4$ MeV).

By using the saddle-point approximation, the distributions $P_T(\beta, \gamma)$ at constant temperature can be converted to intrinsic shape distributions $P_{E_x}(\beta, \gamma)$ at constant excitation energy. The joint level density distribution as a function of excitation energy and intrinsic deformation can then be determined from $\rho(E_x, \beta, \gamma) = \rho(E_x)P_{E_x}(\beta, \gamma)$.

5. Conclusion

The SMMC method is a powerful method to calculate microscopically nuclear state densities in the presence of correlations, and was applied to nuclei as heavy as the lanthanides. We have also introduced a method to calculate the distribution of the quadrupole deformation in both the laboratory frame and in the intrinsic frame within the rotationally invariant CI shell model approach. We plan to use this method to calculate level densities as a function of intrinsic deformation.

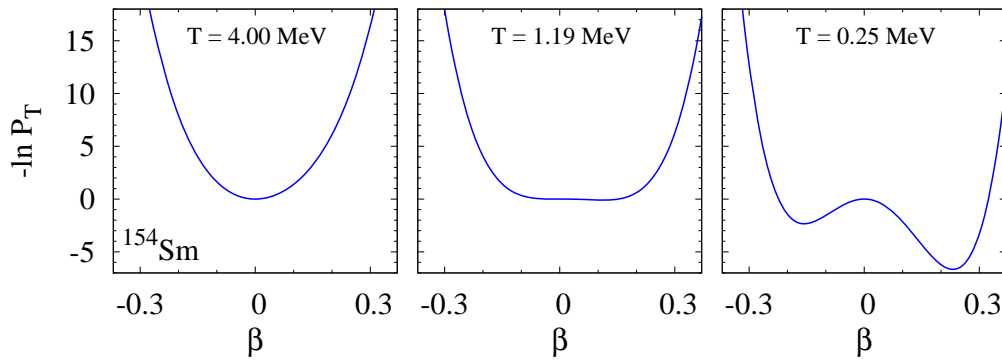


Fig. 5: $-\ln P_T(\beta, \gamma = 0)$ vs. axial deformation β for ^{154}Sm at three temperatures.

Acknowledgements

This work was supported in part by the DOE grant Nos. DE-FG-0291-ER-40608 and DE-FG02-00ER411132, by Grant-in-Aid for Scientific Research (C) No. 25400245 by the JSPS, Japan, and by the Turkish Science and Research Council (TÜBİTAK) grant No. ARDEB-1001-110R004 and ARDEB-1001-112T973. The research presented here used resources of the National Energy Research Scientific Computing Center, which is supported by the Office of Science of the U.S. Department of Energy under Contract No. DE-AC02-05CH11231. It also used resources provided by the facilities of the Yale University Faculty of Arts and Sciences High Performance Computing Center.

References

- [1] W. Hauser and H. Feshbach, *Phys. Rev.* **87** (1952) 366.
- [2] A.J. Koning, S. Hilaire and S. Goriely, *Nucl. Phys. A* **810** (2008) 13, and references therein
S. Hilaire, M. Girod, S. Goriely, and A.J. Koning, *Phys. Rev. C* **86** (2012) 064317.
- [3] G.H. Lang, C.W. Johnson, S.E. Koonin, and W.E. Ormand, *Phys. Rev. C* **48** (1993) 1518.
- [4] Y. Alhassid, D.J. Dean, S.E. Koonin, G.H. Lang, and W.E. Ormand, *Phys. Rev. Lett.* **72** (1994) 613.
- [5] S.E. Koonin, D.J. Dean, and K. Langanke, *Phys. Rep.* **278** (1997) 2.
- [6] Y. Alhassid, *Int. J. Mod. Phys. B* **15** (2001) 1447.
- [7] M. Dufour and A.P. Zuker, *Phys. Rev. C* **54** (1996) 1641.
- [8] H. Nakada and Y. Alhassid, *Phys. Rev. Lett.* **79** (1997) 2939.
- [9] Y. Alhassid, S. Liu and H. Nakada, *Phys. Rev. Lett.* **83** (1999) 4265.
- [10] Y. Alhassid, L. Fang and H. Nakada, *Phys. Rev. Lett.* **101** (2008) 082501.
- [11] C. Özen, Y. Alhassid and H. Nakada, *Phys. Rev. Lett.* **110** (2013) 042502.
- [12] J. Hubbard, *Phys. Rev. Lett.* **3** (1959) 77 and R.L. Stratonovich, *Dokl. Akad. Nauk. S.S.S.R.* **115** (1957) 1097.
- [13] W.E. Ormand, D.J. Dean, C.W. Johnson, and S.E. Koonin, *Phys. Rev. C* **49** (1994) 1422.
- [14] A. Bohr and B. Mottelson, *Nuclear Structure*, Vol. 1 (Benjamin, New York, 1969).
- [15] Y. Alhassid, M. Bonett-Matiz, S. Liu and H. Nakada, *Phys. Rev. C* **92** (2015) 024307.
- [16] M. Bonett-Matiz, A. Mukherjee and Y. Alhassid, *Phys. Rev. C* **88** (2013) 011302 (R).
- [17] Y. Alhassid, S. Liu and H. Nakada, *Phys. Rev. Lett.* **99** (2007) 162504.
- [18] E.Y. Loh Jr. and J.E. Gubernatis, in *Electronic Phase Transitions*, (North Holland, Amsterdam, 1992).
- [19] C. Özen, Y. Alhassid and H. Nakada, *Phys. Rev. C* **91** (2015) 034329.
- [20] R. Capote *et al.*, *Nuclear Data Sheets*, **110** (2009) 3107.
- [21] Y. Alhassid, C. Özen and H. Nakada, *Nuclear Data Sheets* **118** (2014) 233.
- [22] A. Mukherjee and Y. Alhassid, *Phys. Rev. Lett.* **109** (2012) 032503.
- [23] Y. Alhassid, C.N. Gilbreth, and G.F. Bertsch, *Phys. Rev. Lett.* **113** (2014) 262503.
- [24] S. Levit and Y. Alhassid, *Nucl. Phys. A* **413** (1984) 439.
- [25] Y. Alhassid, S. Levit and J. Zingman, *Phys. Rev. Lett.* **57** (1986) 539.

The No-Core Gamow Shell Model: Including the continuum in the NCSM

B. R. Barrett¹, G. Papadimitriou², N. Michel³, and M. Płoszajczak³

¹ Department of Physics, University of Arizona, Tucson, AZ, USA

² Department of Physics and Astronomy, Iowa State University, Ames, IA, USA

³ Grand Accélérateur National d'Ions Lourds (GANIL), Caen, France

Abstract

We are witnessing an era of intense experimental efforts that will provide information about the properties of nuclei far from the valley of β stability, regarding resonant and scattering states as well as (weakly) bound states. This talk describes our formalism for including these necessary ingredients into the No-Core Shell Model by using the Gamow Shell Model approach. Applications of this new approach, known as the No-Core Gamow Shell Model, both to benchmark cases as well as to unstable nuclei will be given.

1. Introduction

The atomic nucleus, which at energies in the range of mega-electron volts can be viewed as a quantum system of strongly interacting protons and neutrons [1, 2, 3], is a very fascinating object. One of the most intriguing challenges is the description of its time evolution. Indeed the nucleus can be naturally found in quantum states that decay by emitting photons, electrons or even nucleons and heavier particles. This endeavor becomes even more necessary in the rise of new experiments that probe new modes of radioactivity which will need theoretical justification [4]. One way is to solve the time-dependent Schrödinger equation by means of time discretization techniques [5, 6, 7]. A different approach lies in the solution of the time-independent Schrödinger equation in the complex energy or momentum space. The time dependence is then absorbed by the complex nature of the solution, whose imaginary part is associated with the decay time. Metastable nuclear states and resonances could then be described in a time-independent formalism [8, 9, 10, 11]. Formulating the structure and reaction problem in the complex energy plane [12, 13, 14, 15, 16, 17, 18, 19, 20, 21, 22], provides with an alternative step towards the unification of structure (bound states) and reaction (resonances) aspects in nuclear physics, which will lead in a more controlled and model independent evaluation of observables. Noted that there already exists vivid progress on the *ab-initio* description of structure and reactions on the real-axis by Lawrence Livermore and TRIUMF groups [23, 24, 25], by Los Alamos/Argonne groups [26] and also on the lattice by [27, 28].

2. The NC(GSM) formalism

One of the ways to obtain complex energy solutions of a physical system is by turning the Schrödinger equation into an eigenvalue problem and diagonalizing the complex Hamiltonian matrix. The basic code that has been employed for the description of resonances, by diagonalizing a very large non-Hermitian complex symmetric Hamiltonian matrix, is the Gamow Shell Model (GSM) code [29, 30, 31, 32, 33]. The orthonormal underlying basis, upon which the Hamiltonian matrix is diagonalized, is known as Berggren basis [9] which provides a symmetric description of bound states, resonances and scattering states. The Hamiltonian matrix is non-Hermitian and complex symmetric with complex eigenvalues. The matrix is sparse and a relatively small number of eigenvectors and eigenvalues is of interest. At this point there is no conceptual difference between GSM with a core and the NCGSM besides the underlying Hamiltonian. Indeed, in the GSM case the Hamiltonian consists of the one-body kinetic energy,

the one-body mean-field (either schematic or Hartree-Fock) and the residual NN interaction, whereas in the NCGSM case the one-body mean field is not present in the A-body Hamiltonian [32]. The nucleon-nucleon interaction is expressed in the Berggren basis using the potential separable expansion (PSE) [34] in a HO basis method [35, 36, 32]. In this way, matrix elements between scattering and/or resonant states never diverge, due to the Gaussian fall-off of the HO radial form factor, and in addition one can conveniently transform matrix elements from the relative frame to the lab frame. For matrix elements of other operators, such as electromagnetic transition operators, the renormalization of integrals relies on the method of external complex scaling (ECS). We note here though that the PSE method has also been employed for the calculation of the recoil matrix elements of the intrinsic Hamiltonian, since in this case the ECS technique does not provide converged results.

For the diagonalization of the large complex symmetric matrix we have used a complex extension of the Lanczos algorithm [31]. The largest matrix that has been diagonalized has a dimension of $\sim 10^6$. This number materializes to about $A=4,5$ for *ab-initio* no-core calculations in the Berggren basis and to 7-8 active valence particles when assuming a frozen configuration (also known as “core”) but allowing only a portion of the particles occupying the continuum (Berggren) orbitals (particle-hole truncations). The second alternative is the Davidson method [31] (see also a recent application on the description of tunneling for a two-body atomic system [37]). We would like to highlight a unique feature of the GSM diagonalization. Both the Lanczos and the Davidson methods calculate the ground state of the system as the lowest eigenvalue. In the GSM where the Hamiltonian matrix is non-Hermitian, the lowest eigenvalue is not guaranteed to coincide with the ground state and it may as well be a scattering state. A criterion is established which separates the state of interest from the wealth of scattering states; that is the overlap method [31]. In the overlap method a smaller diagonalization takes place first, in a space spanned by a few states (usually single particle bound states and resonances). This smaller

Table 1: Comparisons [38] between the NCGSM and the computer program MFDn. $N_{\text{shell}} = 2n + \ell$ and $\hbar\omega = 20$ MeV.

Nucleus	MFDn	NCGSM	Difference
${}^2\text{H } 1^+$ ($N_{\text{shell}} = 4$)	-1.6284	-1.6284	≤ 0.1 keV
${}^2\text{H } 1^+$ ($N_{\text{shell}} = 8$)	-2.1419	-2.1419	≤ 0.1 keV
${}^3\text{H } 1/2^+$ ($N_{\text{shell}} = 4$)	-7.6016	-7.6016	≤ 0.1 keV
${}^3\text{H } 1/2^+$ ($N_{\text{shell}} = 8$)	-8.3203	-8.3203	≤ 0.1 keV
${}^3\text{He } 1/2^+$ ($N_{\text{shell}} = 8$)	-7.6084	-7.6084	≤ 0.1 keV
${}^4\text{He } 0^+$ ($N_{\text{shell}} = 4$)	-27.3685	-27.3684	0.1 keV
${}^6\text{Li } 1^+$ ($N_{\text{shell}} = 4$)	-24.9778	-24.9776	0.2 keV
${}^6\text{Li } 3^+$ ($N_{\text{shell}} = 4$)	-22.4959	-22.4957	0.2 keV

space sometimes is also called the “pole approximation”. The solution is the reference eigenvector. At a second step a diagonalization in the full space (bound states+resonances+scattering states) takes place and the solution is the one that maximizes the overlap with the reference eigenvector.

Together with the GSM, another algorithm known as the Density Matrix Renormalization Group (DMRG) has also been used [39, 40, 41, 42, 32]. The method is a truncation algorithm which aims in reducing the sizes of the matrices to be diagonalized, while keeping the same accuracy as in the full calculation. DMRG is an iterative method for which at each step the space is increased by adding basis states one-by-one and the truncation is dictated by the density matrix which is constructed in each step. At each step a complex symmetric non-Hermitian matrix is diagonalized via the Lanczos method and

the matrix is smaller than the typical matrix of a full-fledged GSM calculation. Several diagonalizations of such smaller matrices are performed until a convergence criterion is reached. A recent variant of the DMRG method [43] has shown that very large model spaces can be reached and many “sweeps” can be performed in a timely manner, making it tempting to use such a variant also in Berggren basis DMRG based calculations.

3. Applications of the NCGSM approach

3.1 Benchmarks

Aiming at a predictive theory it becomes increasingly important to complete a quality control on the solvers which are employed for the solution of the many-body problem, a task that implies validation and cross-checks (benchmarks) of existing codes [44]. To test the NCGSM algorithm we have performed benchmark calculations, in which we compared the NCGSM results with results obtained using the NCSM [45] Many-Fermion Dynamics nuclear (MFDn) computer program [46, 47], and in Table (1) we present applications for systems up to ${}^6\text{Li}$. For this benchmark we employed a Harmonic Oscillator (HO) basis in a Full Configuration Interaction (FCI) truncation and the JISP16 realistic interaction [48]. Nevertheless, chiral interactions were also tested successfully [38]. This agreement reassures that the calculations are not contaminated with unintentional errors or flaws. It should be noted that there has also been two other successful works that benchmarked the GSM algorithm, using central interactions and a α -core, against the complex scaling technique [49, 50].

3.2 ANCs and widths

In its current implementation the NCGSM is not ready to provide scattering observables on the real-axis, such as cross-sections, even though such a goal is not far from reach after the combination of the GSM with the Resonating Group Method [51] using phenomenological interactions/optical potentials [52, 15]. We are able however to compute overlaps between nuclear states and access information asso-

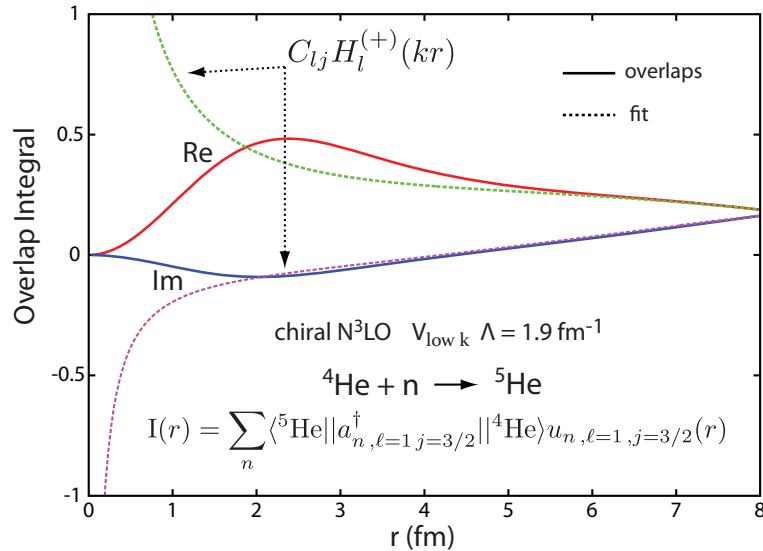


Fig. 1: (Color online) Overlap function and tail fit with a Hankel function. C_{lj} stands for the ANC. Figure is from [32].

ciated with the “tail” of the overlap. The relevant quantity in the study of asymptotic properties of the nuclear wavefunction or actually its projection onto cluster (sub-cluster) states [53] is the Asymptotic

Normalization Coefficient (ANC). Recently there is a collective effort in nuclear theory to compute asymptotic quantities and we are witnessing an abandonment of quantities such as spectroscopic factors in favor of ANCs and widths or partial widths. The basic argument behind this endeavor, besides the physics interest (e.g. relevance to astrophysical processes for both resonance widths and ANCs), is the fact that asymptotic quantities are less model dependent and closer to the notion of an observable quantity [54, 55]. At the same time ANCs can serve as an internal consistency test between many-body methods since calculations at distances far away from the nuclear interaction range always pose challenges and difficulties (see e.g. discussion at [56] for some of the *ab-initio* methods). The GSM or the NCGSM which are formulated on a basis that has a correct asymptotic behavior and captures the relevant long range physics, become appropriate for the calculation of asymptotic quantities. For a detailed review of the progress that has been made in the calculation of ANCs and also the experimental situation we refer the reader to [56] and also [57] for ANCs calculations within the GSM.

In this contribution we present calculations that were published in [32] of ANCs within the NCGSM using realistic interactions. The model space of the calculation, as it was described in [32], includes single particle (s.p.) partial waves with angular momentum up to $\ell = 4$ (g-waves). For ${}^5\text{He}$, being particle unstable in its ground state, we employed a complex GHF basis consisting of the s.p. $0p_{3/2}$ resonant state and non-resonant $p_{3/2}$ states along the complex contour which encloses the s.p. resonant state, a necessary condition for the s.p. Berggren completeness to be satisfied. In order to obtain the many-body solution and calculate the overlap for the reaction: ${}^4\text{He}_{0+} + n \rightarrow {}^5\text{He}_{3/2-}$ we used the Davidson diagonalization [31] method and limited our selves to continuum configurations that allowed up to four particles occupying continuum orbits (4p-4h truncation). In the future it will be important to assess the importance of the configurations involving many particles in continuum orbits and also try to accompany the results with a truncation error associated with the missing configurations. It should also be noted that the creation operator for the calculation of the overlap does not only create on a single state, but there is a sum over all continuum states; a fundamental difference between NC(GSM) and traditional configuration interaction calculations in a HO basis [58].

We present our results in Fig.1 which was taken from [32] for the effective V_{lowk} [59, 60, 61] $\Lambda = 1.9\text{fm}^{-1}$ chiral N^3LO NN interaction [62]. We see that the overlap exhibits both real and imaginary parts reflecting the complex nature of the Berggren basis. After fitting the asymptotic part of the overlap with a complex Hankel function we extract an ANC with a real part of $0.197\text{ fm}^{-1/2}$. Now knowing the ANC we are able to obtain the width of ${}^5\text{He}$ using the formula:

$$C = \sqrt{\frac{\Gamma\mu}{\hbar^2\Re(k)}} \quad (1)$$

that relates the width and the ANC [57], where μ is the reduced mass, k is the real part of the complex linear momentum that corresponds to the neutron-separation energy of ${}^5\text{He}$ and C stands for the ANC. The result for the width is $\Gamma = 311\text{ keV}$. Within the 4p-4h truncation, the complex Davidson diagonalization provided for the S_{1n} the value of -1.561 MeV and a width Γ of 370 keV . The small difference between the width obtained from the ANC formula and the one obtained from the diagonalization stems from an approximation that was made on the proof of formula (1). The approximation is that the real part of the linear momentum has to be considered. It has been shown in [32] that this approximation implies the condition $\frac{\Gamma}{2S_{1n}} \rightarrow 0$, namely, formula (1) will work for states that have widths much smaller as compared to two-times the separation energy. In our case $\frac{\Gamma}{2S_{1n}} = 11.8\%$, which explains the deviation from the exact diagonalization result.

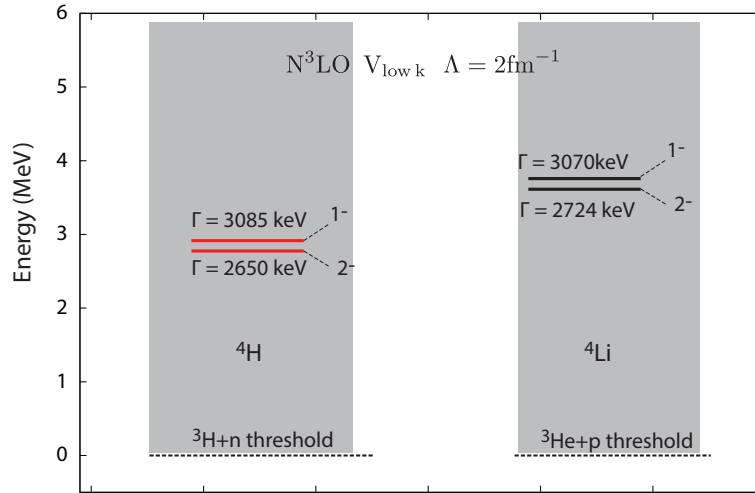


Fig. 2: (Color online) Ground state and first excited state spectra of ${}^4\text{H}$ and ${}^4\text{Li}$. Gray scale denotes the continuum/scattering regime which is described by adopting a complex Beggren basis.

3.3 NCGSM results for ${}^4\text{H}$ and ${}^4\text{Li}$

Next we are presenting calculations for ${}^4\text{H}$ and ${}^4\text{Li}$. These systems have also been computed in approaches with realistic interactions, in [63] for a scattering benchmark calculation within several few body methods and in [64] within the complex scaling method. Especially for hydrogen isotopes there exists a recent experimental interest since measurements claim to observe a relatively narrow ${}^7\text{H}$ resonance [65]. In addition, it is believed that the triplet of isotopes ${}^5,6,7\text{H}$ resemble the Helium isotopic chain (${}^6,7,8\text{He}$). Namely ${}^7\text{H}$ resembling ${}^8\text{He}$ is the most “bound” member of the triplet having a relatively small width, ${}^6\text{H}$ resembling ${}^7\text{He}$ is “unbound” reflecting its extremely large width while ${}^5\text{H}$ is just a broad resonance (broader than ${}^7\text{H}$), resembling in this case ${}^6\text{He}$ which is less bound than ${}^8\text{He}$. The theoretical investigation of the shell structure and the pairing correlations in the continuum will be a decisive factor in the understanding of the binding mechanism in this area of the chart and it will also be a challenging task.

In this work we are using a phenomenological WS potential for the generation of the basis. For ${}^4\text{H}$ and ${}^4\text{Li}$ the WS basis is created for the ${}^3\text{H} + \text{n}$ or ${}^3\text{He} + \text{p}$ systems respectively. Namely for ${}^4\text{H}$ a neutron $0p_{3/2}$ s.p. resonant state is considered whereas for ${}^4\text{Li}$ a proton $0p_{3/2}$ s.p. resonant state. The long-range Coulomb interaction in the case of ${}^4\text{Li}$ is treated in the same way as in [32, 66, 67]. Besides the complex neutron and proton resonances and the associated complex continua, we consider s.p. partial waves up to h-waves ($\ell=5$) as HO basis states characterized by a frequency of $\hbar\omega = 20$ MeV. In particular, for ${}^4\text{H}$ and for the neutron space we used a basis that consisted of $15p_{3/2}$ complex s.p. states and $7s_{1/2}$, $7p_{1/2}$, $2d$, $2f$, $2g$, $1h$ real HO s.p. states, while for the proton space all basis states are HO states with $7s_{1/2}$, $7p_{1/2}$, $2d$, $2f$, $2g$, $1h$. Noted that we are using a different truncation scheme that departs from the typical N_{max} or N_{shell} HO truncation. Here, and also in other NCGSM calculations, we choose to use more radial nodes for specific ℓ states. Here states with $\ell=0,1$ have been chosen to have more nodes since we noticed that they contribute more energy to the system. Further calculations that investigate this behavior are in progress. The same basis was used for ${}^4\text{Li}$ but instead of a neutron s.p. resonant state we considered a proton s.p. resonant state. Our results for the g.s. and first excited states of ${}^4\text{H}$ and ${}^4\text{Li}$ are shown on Fig.2. The energies are with respect to the one-neutron and one-proton particle thresholds. For the thresholds, the g.s. energies of ${}^3\text{H}$ and ${}^3\text{He}$ are found to be -7.92 MeV and -7.12 MeV respectively, for an effective V_{lowk} $\Lambda = 2.0\text{fm}^{-1}$ $N^3\text{LO}$ Chiral EFT interaction. Overall we observe a good agreement with experimental measurements [68] and especially the small gap between

the 1^- and 2^- states that has been observed is also predicted in our calculation. Even though the calculations for the widths show stability, the widths are very large, so we are not dealing with typical resonances that would have an appreciable impact on cross-sections. In the calculation presented here we restricted the occupation of continuum orbits to a maximum of three particles (3p-3h). In our future work we will provide results without truncations and also with investigations on the impact of missing excitations on energies and widths.

4. Conclusions and outlook

In conclusion, we presented applications of the NCGSM for the calculation of energies, widths and asymptotic quantities such as ANCs of unbound nuclei. At the same time we benchmarked our algorithm against another commonly used solver. Our immediate goals are to continue working on applications of the NCGSM for light unbound nuclear systems in the neutron and proton rich side of the nuclear chart. The success of the NCGSM is tied with advances in computer algorithms and the formulation of efficient complex symmetric diagonalization solvers. On the physics side, even when the most efficient solver will be at hand, a full calculation in the Berggren basis (no p-h truncations) for a system such as ^{11}Li will be very demanding. Hence, one of our goals is to quantify at first the impact of missing truncations (we already know that the weight of many particles in continuum orbits is small). Also we aim at a construction of a realistic effective interaction, i.e. an interaction in the NCGSM nuclear medium¹ that would stem from a realistic free-space interaction, which we will then utilize for NCGSM calculations (see e.g. [69] for a Lee-Suzuki transformation for interactions in the complex energy plane and a multireference perturbation theory approach). Finally, we would like to contribute to the effort of bridging the gap between Lattice-QCD and low energy physics and a possible way was shown in [70]. This could be achieved once NCGSM will be utilized to handle NNN interactions. Then we could naturally compute resonant features of finite nuclei at any pion mass that is available at that time.

5. Acknowledgments

This work was supported by the US DOE under grants No. DESC0008485 (SciDAC/NUCLEI). This work was also supported in part by the FUSTIPEN (French-U.S. Theory Institute for Physics with Exotic Nuclei) under U.S. DOE grant No. DE-FG02-10ER41700. We would like to thank H. M. Aktulga, W. Nazarewicz, J. P. Vary, C. Yang, E. G. Ng and G. I. Fann for fruitful discussions on complex energy diagonalization solvers and P. Maris for his help with the benchmark calculations of Table I.

References

- [1] Bertsch, G., Dean, D., and Nazarewicz, W. *Scidac Review* **6**, 42 (2007).
- [2] Furnstahl, R. *Nucl. Phys. News* **21**(2), 18–24 (2011).
- [3] <http://nuclei.mps.ohio-state.edu>, (-).
- [4] Z. Kohley *et al.* *Phys. Rev. Lett.* **110**, 152501 Apr (2013).
- [5] Bulgac, A., Luo, Y.-L., Magierski, P., Roche, K. J., and Yu, Y. *Science* **332**(6035), 1288–1291 (2011).
- [6] Volya, A. *Phys. Rev. C* **79**, 044308 Apr (2009).
- [7] Oishi, T., Hagino, K., and Sagawa, H. *Phys. Rev. C* **90**, 034303 Sep (2014).
- [8] Gamow, G. *Z. Phys.* **51**, 204 (1928).
- [9] Berggren, T. *Nucl. Phys. A* **109**(2), 265 – 287 (1968).
- [10] Romo, W. *Nucl. Phys. A* **191**(1), 65 – 87 (1972).

¹NCGSM medium here should be seen as the model space that the A-nucleons evolve, but in addition, scattering to continuum orbits will be allowed through the Berggren basis

- [11] Dobaczewski, J. and Nazarewicz, W. *Philos. T. Roy. Soc. A* **356**(1744), 2007–2031 (1998).
- [12] Papadimitriou, G. and Vary, J. P. *Phys. Rev. C* **91**, 021001 Feb (2015).
- [13] Papadimitriou, G. and Vary, J. *Phys. Lett. B* **746**(0), 121 – 126 (2015).
- [14] Hagen, G. and Michel, N. *Phys. Rev. C* **86**, 021602 Aug (2012).
- [15] Fosseuz, K., Michel, N., Płoszajczak, M., Jaganathen, Y., and Id Betan, R. M. *Phys. Rev. C* **91**, 034609 Mar (2015).
- [16] Lazauskas, R. *Phys. Rev. C* **91**, 041001 Apr (2015).
- [17] Lazauskas, R. and Carbonell, J. *Phys. Rev. C* **84**, 034002 Sep (2011).
- [18] Deltuva, A. and Fonseca, A. C. *Phys. Rev. C* **86**, 011001 Jul (2012).
- [19] Deltuva, A. and Fonseca, A. C. *Phys. Rev. C* **92**, 024001 Aug (2015).
- [20] Kruppa, A. T., Suzuki, R., and Katō, K. *Phys. Rev. C* **75**, 044602 Apr (2007).
- [21] Myo, T., Kikuchi, Y., Masui, H., and Katō, K. *Prog. Part. Nucl. Phys.* **79**(0), 1 – 56 (2014).
- [22] Kikuchi, Y., Myo, T., Katō, K., and Ikeda, K. *Phys. Rev. C* **87**, 034606 Mar (2013).
- [23] Quaglioni, S. and Navrátil, P. *Phys. Rev. C* **79**, 044606 Apr (2009).
- [24] Baroni, S., Navrátil, P., and Quaglioni, S. *Phys. Rev. C* **87**, 034326 Mar (2013).
- [25] Hupin, G., Quaglioni, S., and Navrátil, P. *Phys. Rev. Lett.* **114**, 212502 May (2015).
- [26] K. M. Nollett *et al.*, *Phys. Rev. Lett.* **99**, 022502 Jul (2007).
- [27] S. Elhatisari *et al.* *arXiv* (1506.03513) (2015).
- [28] Briceño, R. A., Davoudi, Z., and Luu, T. C. *J. Phys. G* **42**(2), 023101 (2015).
- [29] N. Michel *et al.* *Phys. Rev. Lett.* **89**, 042502 Jul (2002).
- [30] N. Michel *et al.* *Phys. Rev. C* **67**, 054311 May (2003).
- [31] N. Michel *et al.* *J. Phys. G* **36**, 013101 (2009).
- [32] G. Papadimitriou *et al.* *Phys. Rev. C* **88**, 044318 (2013).
- [33] Y. Jaganathen *et al.* *To be submitted* (2015).
- [34] Gyarmati, B. and Kruppa, A. T. *Phys. Rev. C* **34**, 95–102 Jul (1986).
- [35] Hagen, G., Hjorth-Jensen, M., and Michel, N. *Phys. Rev. C* **73**, 064307 Jun (2006).
- [36] Papadimitriou, G., Kruppa, A. T., Michel, N., Nazarewicz, W., Płoszajczak, M., and Rotureau, J. *Phys. Rev. C* **84**, 051304 Nov (2011).
- [37] Forssén, C., Lundmark, R., Rotureau, J., Larsson, J., and Lidberg, D. *Few-Body Systems* , 1–8 (2015).
- [38] G. Papadimitriou and P. Maris . *Unpublished* (2014).
- [39] White, S. R. *Phys. Rev. Lett.* **69**, 2863–2866 Nov (1992).
- [40] Papenbrock, T. and Dean, D. J. *J. Phys. G* **31**(8), S1377 (2005).
- [41] Pittel, S. and Sandulescu, N. *Phys. Rev. C* **73**, 014301 (2006).
- [42] Rotureau, J., Michel, N., Nazarewicz, W., Płoszajczak, M., and Dukelsky, J. *Phys. Rev. Lett.* **97**, 110603 Sep (2006).
- [43] Legeza, Ö. and Veis, L. and Poves, A. and Dukelsky, J. (2015).
- [44] Dobaczewski, J., Nazarewicz, W., and Reinhard, P.-G. *J. Phys. G* **41**(7), 074001 (2014).
- [45] Barrett, B. R., Navrátil, P., and Vary, J. P. *Progress in Particle and Nuclear Physics* **69**, 131 – 181 (2013).
- [46] P. Sternberg *et al.* In *Proceedings of the 2008 ACM/IEEE Conference on Supercomputing*, SC '08, 15:1–15:12 (IEEE Press, Piscataway, NJ, USA, 2008).
- [47] P. Maris *et al.* *Procedia Computer Science* **1**(1), 97 – 106 (2010). {ICCS} 2010.
- [48] Shirokov, A., Vary, J., Mazur, A., and Weber, T. *Phys. Lett. B* **644**(1), 33 – 37 (2007).
- [49] Kruppa, A. T., Papadimitriou, G., Nazarewicz, W., and Michel, N. *Phys. Rev. C* **89**, 014330 Jan (2014).
- [50] Masui, H., Katō, K., Michel, N., and Płoszajczak, M. *Phys. Rev. C* **89**, 044317 Apr (2014).
- [51] Wildermuth, K. and Tang, Y. C. *A Unified Theory of the Nucleus*. Vieweg Teubner Verlag, (1977).
- [52] Jaganathen, Y., Michel, N., and Płoszajczak, M. *Phys. Rev. C* **89**, 034624 Mar (2014).
- [53] Nollett, K. M. and Wiringa, R. B. *Phys. Rev. C* **83**, 041001 Apr (2011).
- [54] Mukhamedzhanov, A. M. and Kadyrov, A. S. *Phys. Rev. C* **82**, 051601 Nov (2010).
- [55] Furnstahl, R. J. and Schwenk, A. *J. Phys. G* **37**(6), 064005 (2010).
- [56] Nollett, K. M. *Phys. Rev. C* **86**, 044330 Oct (2012).
- [57] Okołowicz, J., Michel, N., Nazarewicz, W., and Płoszajczak, M. *Phys. Rev. C* **85**, 064320 Jun (2012).
- [58] Michel, N., Nazarewicz, W., and Płoszajczak, M. *Phys. Rev. C* **75**, 031301 Mar (2007).
- [59] Bogner, S., Furnstahl, R., and Schwenk, A. *Prog. Part. Nucl. Phys.* **65**(1), 94 – 147 (2010).
- [60] Hjorth-Jensen, M., Kuo, T. T., and Osnes, E. *Phys. Rep.* **261**(3–4), 125 – 270 (1995).

- [61] T. Engeland, M.-J. and Jansen, G. CENS, a Computational Environment for Nuclear Structure, in preparation., (2015).
- [62] Entem, D. R. and Machleidt, R. *Phys. Rev. C* **68**, 041001 Oct (2003).
- [63] M. Viviani *et al.* *Phys. Rev. C* **84**, 054010 Nov (2011).
- [64] Horiuchi, W. and Suzuki, Y. *Phys. Rev. C* **87**, 034001 Mar (2013).
- [65] M. Caamaño *et al.* *Phys. Rev. Lett.* **99**, 062502 Aug (2007).
- [66] Michel, N. *Phys. Rev. C* **83**, 034325 Mar (2011).
- [67] Michel, N., Nazarewicz, W., and Płoszajczak, M. *Phys. Rev. C* **82**, 044315 Oct (2010).
- [68] <http://www.tunl.duke.edu/nucldata/chain/04.shtml>, (2015).
- [69] Hagen, G., Hjorth-Jensen, M., and Vaagen, J. S. *Phys. Rev. C* **71**, 044314 Apr (2005).
- [70] Barnea, N., Contessi, L., Gazit, D., Pederiva, F., and van Kolck, U. *Phys. Rev. Lett.* **114**, 052501 Feb (2015).

Study of Ca isotopes via neutron capture reactions

G. Bocchi^{1,2}, *S. Leoni*^{1,2}, *G. Benzoni*^{1,2}, *S. Bottoni*^{1,2,3}, *A. Bracco*^{1,2}, *M. Jentschel*⁴, *U. Köster*⁴, *P. Mutti*⁴, *T. Söldner*⁴, *A. Blanc*⁴, *G. de France*⁵, *J.-M. Régis*⁶, *G. S. Simpson*⁷, *W. Urban*⁸, *C. A. Ur*⁹, *A. Türler*^{10,11}

¹ Università degli Studi di Milano, Milano, Italy

² INFN, sezione di Milano

³ KU Leuven, Belgium

⁴ ILL, Grenoble, France

⁵ GANIL, France

⁶ IKP, University of Cologne, Germany

⁷ University of Western Scotland, UK

⁸ Institute of Experimental Physics, University of Warsaw, Poland

⁹ INFN Sezione di Padova, Padova, Italy

¹⁰ Paul Scherrer Institute, 5232 Villigen, Switzerland

¹¹ Universität Bern, 3012 Bern, Switzerland

Abstract

Preliminary results are presented from a γ -spectroscopy study of low-spin states of several Ca isotopes, produced by neutron capture on a Ca target, at very high coincidence rates. The experiment was performed at the PF1B cold-neutron facility at ILL (Grenoble, France), using the array of HpGe detectors, named EXILL.

1. Introduction

Nuclei around doubly closed shells play a crucial role in determining both the nucleonic single-particle energy levels and the two-body matrix elements of the effective nuclear interactions. In addition, they offer an excellent tool to study the coupling between a particle/hole and collective excitation of the core. This is a key ingredient to explain important phenomena, such as the observed reduction of spectroscopic factors, the anharmonicity of vibrational spectra, the damping of Giant Resonances, etc. Experimentally, several indications have been found of discrete states of particle-phonon nature, mostly in medium-heavy nuclei, while only few examples are known in lighter mass regions.

The nuclei under examination in this work, $^{41,49}\text{Ca}$ isotopes, have 1 neutron outside the doubly magic ^{40}Ca and ^{48}Ca cores and they represent good systems in which particle-vibration coupled states can be investigated. This is because phonons such as the 3^- , have sizable collectivity.

In order to study the nature of the excited state in $^{41,49}\text{Ca}$ isotopes, their energy, spin, parity and lifetime have to be measured experimentally with a good precision. Of particular importance is the comparison of experimental data with calculations either based on a shell-model approach or taking into account couplings between core excitations (such as vibrations) and single particle.

In this work we present a detailed low spin γ -spectroscopy study of Ca isotopes, produced by a neutron capture reaction on a ^{48}Ca target. The experiment was performed at the PF1B cold-neutron facility at ILL (Grenoble, France), using the EXILL array, consisting of EXOGAM, GASP and ILL-Clover HpGe detectors.

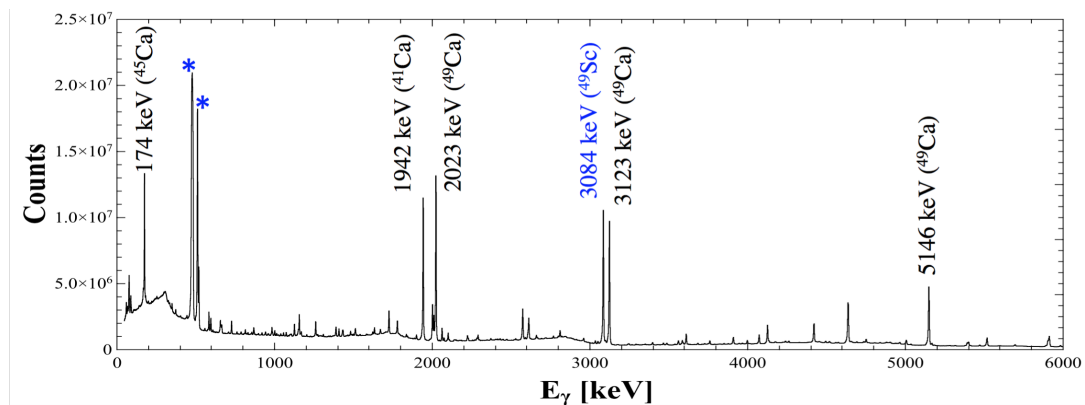


Fig. 1: Total γ spectrum measured in the n-capture reaction with the Ca target. The strongest transitions from $^{41,45,49}\text{Ca}$ and ^{49}Sc are given. Background lines are marked by stars.

2. The experiment

The experiment was performed at the PF1B cold-neutron facility at Institut Laue Langevin (Grenoble, France), where the world's brightest continuous neutron flux is delivered with a thermal-equivalent of $2 \times 10^{10} \text{ ns}^{-1} \text{ cm}^{-2}$. The HpGe array EXILL was used, consisting of 8 EXOGAM clovers, 6 large coaxial detectors from GASP and 2 ILL-Clovers, placed at 90° , 45° and 0° with respect to the beam direction (the latter at 180° with respect to the GASP detectors), respectively. The total photopeak efficiency was about 6%. A digital data acquisition allowed event rates up to 0.84 MHz to be handled.

The (n, γ) reaction was performed using a 620 mg CaCO_3 target with 69.2%, 27.9% and 2.5% isotopic abundances of ^{48}Ca , ^{40}Ca and ^{44}Ca , respectively. As a consequence, a large fraction of double and triple γ coincidences were coming from ^{41}Ca , ^{45}Ca and from ^{49}Sc , populated by β -decay of ^{49}Ca . In general, the populated nuclei of $^{41,45,49}\text{Ca}$ were found to decay from the capture level by primary (E1) transitions of several MeV and to populate in a statistical way, excited states within few units of spin. Figure 1 shows the total spectrum measured in the n-capture reaction, with strong lines coming from the de-excitation of $^{41,45,49}\text{Ca}$ and ^{49}Sc .

3. The analysis

The experimental analysis is devoted to investigate the possible levels that are good candidate to be member of the multiplet generated by coupling single particle states and the 3^- octupole vibration of the core nucleus. As a starting point, the neutron separation energies were calculated by using several cascades and values of 8363.10(42), 7414.34(35) and 5146.46(50) keV were found for ^{41}Ca , ^{45}Ca and ^{49}Ca , respectively. Such values agree, within the errors, with the ones reported in literature.

As a consequence of the low energy of the $1/2^+$ capture level in ^{49}Ca , only two-steps cascades were observed in ^{49}Ca , with intermediate states of negative parity. On the contrary, in ^{41}Ca and ^{45}Ca multisteps cascades were observed, populating intermediate states of both positive and negative parities. Figure 2 shows the preliminary level scheme of the ^{49}Ca nucleus. The characterization of the levels and of the γ -transitions is the key aspect of this work. This can be done by measuring the angular correlation between two γ -rays of the same cascade. The symmetry of the EXOGAM detectors allowed angular correlation measurements at three relative angles between the detectors, i.e. 0° , 45° and 90° degrees. The expression for the angular correlation function between two consecutive γ transitions, γ_1 and γ_2 (in a cascade emitted from an unoriented state with spin J_1 , through an intermediate level with spin J_2 to

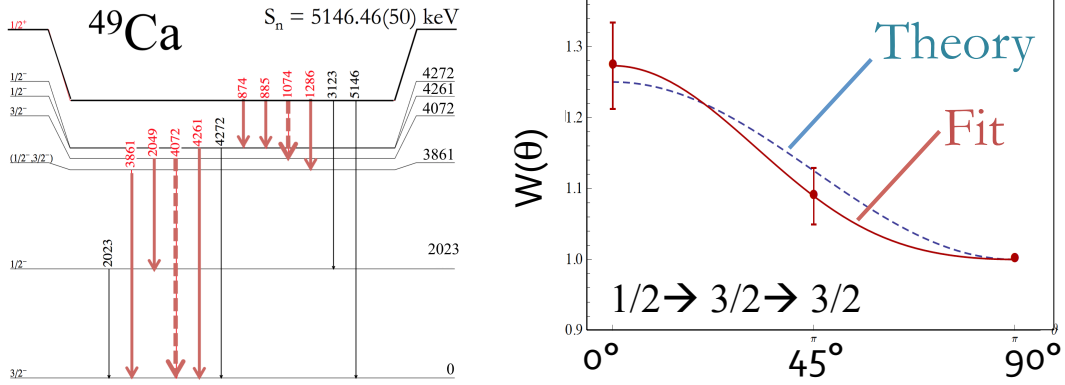


Fig. 2: Left panel): Preliminary level scheme of ^{49}Ca with newly found transitions given in red. Right panel: Angular correlation of the 1074 and 4072 keV transitions (dotted arrows in right panel. Solid and dashed lines are the experimental fit and the theoretical interpolation (obtained by fitting the δ mixing parameter), giving the spin assignment 1/2, 3/2 and 3/2, for the initial, middle and final states, respectively.

the final level with spin J_3) is well described by a linear combination of Legendre polynomials P_k

$$W(\vartheta) = \sum_{\text{even } k}^{k_{\max}} A_{kk} P_k(\cos \vartheta) Q_k(1) Q_k(2) \quad (1)$$

where ϑ is the angle between the directions of γ_1 and γ_2 and Q_k are the attenuation coefficients. By fitting the parameters A_{kk} it is possible to evaluate the spin of the initial, intermediate and final states, the multipolarity of the transitions and the possible mixing ratio. Right panel of Fig. 3 shows the results obtained considering the angular correlation between for the 1074 and 4072 keV transitions of ^{49}Ca . The spin of the initial, intermediate and final states are confirmed to be 1/2, 3/2 and 3/2, respectively, taking the 4073 keV line as a pure dipole and a mixing δ on the 1074 keV transition equal to $-1.87^{+0.19}_{-0.22}$, which indicates a strong dipole character.

4. Conclusions

Preliminary results were presented from a neutron capture experiment performed at ILL (Grenoble) on a Ca target. The setup consisted of the high-efficiency Ge array EXILL, which allowed to perform high-resolution γ - spectroscopy and angular correlation studies of $^{41,45,49}\text{Ca}$ nuclei. The work aims, in particular, at identifying states arising by coupling single particles to core excitations, such as the 3^- octupole phonon in the corresponding $^{40,44,48}\text{Ca}$ cores.

References

- [1] A. Bohr, B.R. Mottelson, Nuclear Structure, vols. I and II, W.A. Benjamin, 1975.
- [2] D. Montanari *et al.*, *Phys. Lett. B* **697**, 288 (2011).
- [3] D. Montanari *et al.*, *Phys. Rev. C* **85**, 044301 (2012).
- [4] H. Mach, R. L. Gill, M. Moszyński, *Nucl. Instr. and Meth. A* **280**, 49 (1989).
- [5] J.-M. Régis *et al.*, *Nucl. Instr. and Meth. A* **684**, 36 (2012).
- [6] G. Bocchi *et al.*, *Phys. Rev. C* **89**, 054302 (2014).
- [7] C.R. Nita *et al.*, *Phys. Rev. C* **89**, 064314 (2014).

Bound States in the Continuum in Nuclear and Hadron Physics

H. Lenske^{1,2}, *S.E.A. Orrigo*³, *Xu Cao*⁴

¹Institut für Theoretische Physik, U. Giessen, Giessen, Germany

²GSI Darmstadt, Darmstadt, Germany

³Instituto de Física Corpuscular, CSIC-Universidad de Valencia, E-46071 Valencia, Spain

⁴Institute of Modern Physics, Chinese Academy of Sciences, Lanzhou, China

Abstract

The population of bound states in the continuum and their spectral properties are studied on the nuclear and hadronic scale. The theoretical approach is presented and realizations in nuclear and charmonium spectroscopy are discussed. The universality of the underlying dynamical principles is pointed out. Applications to nuclear systems at the neutron dripline and for charmonium spectroscopy by $e^-e^+ \rightarrow D\bar{D}$ production are discussed.

1. Introduction

A general feature observed in quantum systems at all scales from atomic to hadron physics is the occurrence of long-lived states embedded into the spectral region of continuum states. The internal structure and dynamical properties of a discrete state coupled to a continuum are encoded in its line shape. Only in simple potential problems the line shapes of spectral distributions come close to the widely used Lorentz- or Breit-Wigner shapes. Under more realistic physical conditions the line shape of resonance is modified by the interaction between the discrete and continuum components of the spectra. This kind of interference among states of different configuration type is ubiquitous in quantum physics and leads to a plethora of interesting phenomena in nuclear, atomic, condensed matter and quantum optical physics. The foundations of quantum mechanical continuum spectroscopy were laid as early as 1961 by the pioneering work of Fano [1]. The relevance of that approach for nuclear physics was soon recognized and the concept of bound states in the continuum was formulated in a systematic manner by Mahaux and Weidenmüller in their book [2] published in the late 1960s. An exciting recent progress on continuum interactions in atomic physics was the control of line shapes by the direct manipulation of spectral distributions with intense laser light with different frequencies [3]. In that paper a representative list of other work in atomic, molecular, and laser physics is found. Obviously, this kind of immediate external influence is out of reach for nuclear and hadron physics. An early application of the Fano-approach to nuclear physics is found in [4] and in Ref. [5] the formalism was used to investigate pionic resonances. The basically different situation in nuclear and hadronic systems is their much shorter lifetime because of the strong interaction with neighbouring states. Hence, in sub-atomic systems the line shapes are often found to be convoluted by overlapping contributions and, additionally, are influenced by coupled-channels effects [6, 7, 8]. In section 2. we discuss continuum spectroscopy at the neutron dripline by the representative example of ^{10}Li . Configuration interactions in the $D\bar{D}$ continuum and their influence on charmonium line shapes are discussed in section 3.. A summary and an outlook is given in section 4..

2. Nuclear Bound States in the Continuum

Away from shell closures pairing and core polarization effects from particle-particle and particle-hole interactions, respectively, are playing an increasingly significant role. A full picture of the spectral properties in weakly bound nuclei should account for bound and continuum interactions on the same

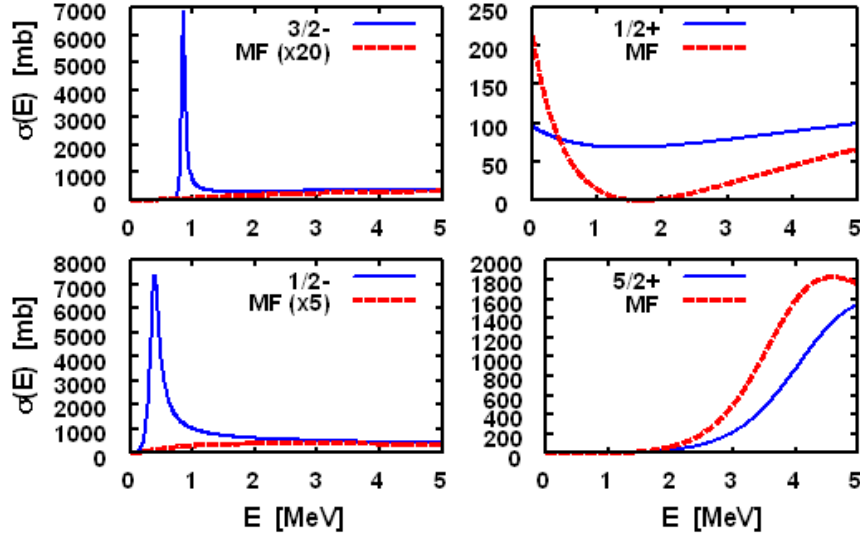


Fig. 1: Spectral distributions seen in elastic partial wave cross sections for the scattering of a neutron on ${}^9\text{Li}$ [7] by the HFB mean-field and Gorkov-coupling. Full HFB Gorkov-pairing and bare mean-field results are compared for partial waves up to d-waves. The attractive pairing self-energy produces resonances in the p-wave channels.

footing. In our previous work [6, 7] we have described interplay of closed and open channels in nuclear continuum spectra. In [7] it was pointed out that pairing interactions lead in weakly bound nuclei already on the mean-field level to a mixing of particle- and hole-type states. We denote their respective wave functions by $u_{\alpha q}$ and $v_{\alpha q}$ carrying quantum numbers $\alpha = (n\ell jm)$ and where $q = p, n$ denotes protons and neutrons. In addition to the overall single particle mean-field potential U_q , close to the particle threshold the pairing fields Δ_q are of special importance because they lead to coupled channels effects already on the mean-field level. The problem is properly described by the Gorkov equations [7]:

$$\begin{pmatrix} T_q + U_q - 2\lambda_q + e_\alpha & \Delta_q(r) \\ -\Delta_q^\dagger(r) & -(T_q + U_q - e_\alpha) \end{pmatrix} \begin{pmatrix} u_{\alpha q}(r) \\ v_{\alpha q}(r) \end{pmatrix} = 0 \quad (1)$$

derived from an underlying energy density functional [7]. T_q is the kinetic energy operator and the chemical potentials λ_q account for particle number conservation. The quasiparticle energy is expressed in terms of the quasi-hole energy $e_\alpha < \lambda_q$. For weakly bound exotic nuclei with separation energies well below 1 MeV the continuum gap is easily overcome by residual interactions. Thus, the dominance of the static nuclear mean-field is broken and is competing with induced interactions in the particle-particle, hole-hole and the particle-hole channels. As discussed in [6, 7] the increased polarizability of dripline nuclei leads to the dissolution of shell structures in the bound state region and initiates a rich spectrum of sharp particle resonances above the particle threshold. They are produced by complex many-body states containing interfering contributions from closed channels due to multi-particle-hole core excitations and open channels given by single particle scattering states. The closed channel states cannot decay by themselves but only through the coupling to the single particle continua. That mechanism is an universal feature of all open quantum systems. In Fig. 4 the dynamical principles are depicted schematically. Since close to the dripline, the usual BCS approach is no longer meaningful, we solve Eq.1 as a coupled

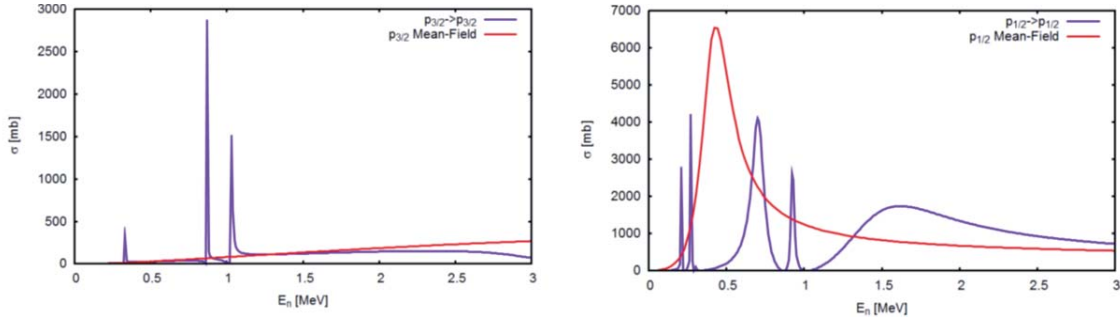


Fig. 2: Spectral distribution for the p-wave elastic scattering continua of $^{10}\text{Li} = ^9\text{Li} + n$. Pure mean-field and core polarization results are compared. The sharp resonances in the $3/2^-$ (left) and the $1/2^-$ partial wave are due to core polarization.

channels problem thus accounting properly for the asymptotics of bound and unbound states [7]. Core polarization is described by an extended system of coupled equation. Integrating out the core degrees of freedom we end up at a set of equations describing single particle motion under the influence of residual particle-hole interactions [6]:

$$\left(H_{MF}^{(\alpha)} - \varepsilon_{\alpha} \right) \phi_{\alpha k} + \sum_{\beta n} F_{\alpha\beta} \phi_{\beta n} = 0 \quad (2)$$

The mean-field (HFB) Hamiltonian for the core state α is denoted by $H_{MF}^{(\alpha)}$ and the effective single particle energy $\varepsilon_{\alpha} \equiv E - E_{\alpha}$ is given by subtracting the energy E_{α} of the core state $|\alpha\rangle$ from the total energy E . The transition form factors are given by matrix elements of the residual interaction, $F_{\alpha\beta} = \langle \alpha | V_{res} | \beta \rangle$. For further details we refer to ref. [7]. Both Eq.(1) and Eq.(2) can be recast formally into an effective single particle equation

$$\left(H_{MF}^{(\alpha)} + \Sigma_{\alpha k}(\omega) - \omega \right) \phi_{\alpha k} = 0 \quad (3)$$

with an energy dependent, non-local complex self-energy $\Sigma_{\alpha k}(\omega) U_{tr} G(\omega) U_{tr}$ and the transition potentials U_{tr} are given either by the pairing field or the core polarization form factors, respectively. The real and imaginary part of the self-energy modify the spectral distributions substantially by energy shifts and decay and damping widths, thus expressing the finite life time of single particle states in an interacting quantum many-body system.

The spectral distributions obtained by Eq. 1 for the $^{10}\text{Li} = ^9\text{Li} + n$ system are displayed in Fig. 1. Two distinct regions can be identified: 1) the region of discrete bound states for $2\lambda_q < \varepsilon_{\alpha} < \lambda_q$ with $2\lambda_q - \varepsilon_{\alpha} < 0$ (negative particle energies); 2) the continuum region $e_{\alpha} < 2\lambda_q$ with $2\lambda_q - e_{\alpha} > 0$ (positive particle energies) [7]. Although the hole wave functions are still bound states they obtain continuous spectral distributions with peak structures slightly shifted from the bare mean-field positions. These effects are much more enhanced when core polarization is taken into account. In Fig. 2 the p-wave single particle continuum spectral distributions for $^{10}\text{Li} = ^9\text{Li} + n$ are shown. In both the $3/2^-$ and the $1/2^-$ partial wave sharp resonances occur, mainly caused by the coupling to the $^9\text{Li}(2^+, 2.691)$ and a few other core states. The single particle and the core spectrum are obtained fully microscopically by HFB and QRPA calculations, respectively. The effect is especially pronounced in the $1/2^-$ channel where the mean-field resonance couples strongly to the core excitations and is fragmented considerably. The width and energy shifts are determined by the channel coupling, reflecting the real and imaginary parts

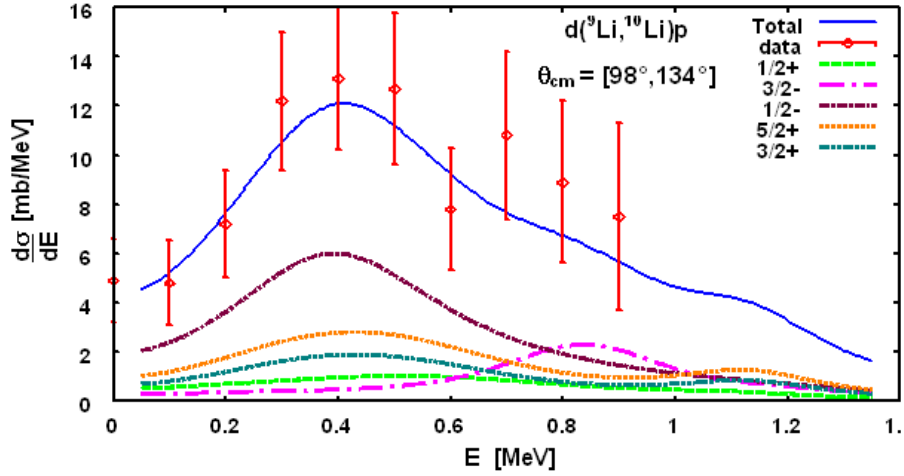


Fig. 3: Angle-integrated cross section for the $d(^9\text{Li}, ^{10}\text{Li})p$ reaction at 2.36 AMeV [7], including the experimental energy resolution and compared with data from Refs. [10]. Two resonances are seen in the $1/2^-$ and $3/2^-$ partial waves.

of the dynamical self-energies discussed above. These interaction effects lead to a suppression of the spectral strengths, given by the residues of the spectral distributions at the pole positions, to values well below unity. In [6] corresponding results for ^{15}C have been used to describe sharp resonances, experimentally observed well above the neutron threshold. Pairing spectral distributions corresponding to Fig. 1 were used in [7, 9] to analyse ^{10}Li data, observed the first time in a $d(^9\text{Li}, ^{10}\text{Li})p$ REX-ISOLDE experiment [10]. As seen in Fig. 3 the data are well described by the Gorkov spectral functions, Fig. 1 and DWBA transfer calculations, treating the transfer kernel by the Vincent-Fortune method. Recently, the same reaction has been remeasured at TRIUMF with a much better energy-resolution. The new data are presently being analysed and theoretical calculations including core polarization are in preparation.

3. Charmonium Line Shapes

Next we turn our attention to configuration mixing effects of the same kind as discussed in the previous section but with a quite different realization in charmonium spectroscopy. Following closely the Fano-formulation, we assume a pre-diagonalization of the confined $c\bar{c}$ states and of the continua given by the $D\bar{D}$ meson channels. As before, the two types of configurations are coupled by residual interactions, e.g. giving rise to a finite life time to the confined $c\bar{c}$ states. As in [8] we investigate specifically the $\psi(3770)$ state, considered as a bare 1^3D_1 $c\bar{c}$ charmonium state interacting with the $D\bar{D}$ continuum, as schematically depicted in Fig. 4. Of course, this *ansatz* is easily extended to higher lying states and other open charm channels, e.g. the $\psi(4040)$ state and $D^*\bar{D} + c.c.$ channel. The confined $c\bar{c}$ states define the set of closed channels with respect to $c\bar{c}$ motion. Because of confinement, the QCD-type $c\bar{c}$ channels remain closed channels at all energies while sub-threshold hadronic $D\bar{D}$ channels eventually change to open channels.

We assume that the bare $c\bar{c}$ states, their wave functions ϕ_c and mass m_c are known, as well as the hadronic $D\bar{D}$ scattering states and their relative motion wave functions ϕ_d . At total center-of-mass

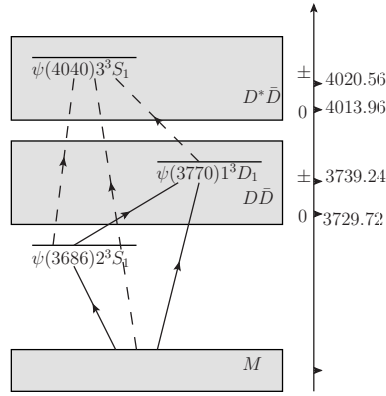


Fig. 4: Schematic representation of the transition from the non-resonant continuum built on the ground state M to 1^{--} charmonium states with two nearby continua $D^*\bar{D}$. The units of the charged (\pm) and neutral (0) thresholds are MeV.

energy $\omega = \sqrt{s}$ we expanded the wave function into the basis of these states,

$$\Psi_\omega = z_c(\omega)\phi_c(\omega) + \int d\omega' z_d(\omega')\phi_d(\omega') \quad . \quad (4)$$

For simplicity, we consider the simplest case given by a single closed channels c and a single open channel d . We separate intermediate propagators into pole and principle values parts and consider that the coupling to closed channels lead to dispersive, but not absorptive self-energies, as shown in the original Fano paper [1]. Interactions modify the closed channel wave functions by dressing by a cloud of virtual $D\bar{D}$ states

$$\chi_c(\omega) = \phi_c + P \int d\omega' \frac{V_{cd}}{\omega - \omega'} \phi_d(\omega') \quad (5)$$

and the correlated state vector is obtained as

$$\Psi_\omega = x_c(\omega)\chi_c(\omega) + x_d(\omega)\phi_d(\omega) \quad (6)$$

The channel interaction may lower one or a few eigenstates below the particle emission threshold, and one may speculate whether $\psi(3686)$ is of such a nature, see e.g. Ref. [11]. The amplitudes $x_{c,d}$ are obtained for the solution of a set of coupled equations and by the proper normalization of the state vector [1, 6, 8]. Their detailed forms are of no special interest here. A more important message of Eq. (4) is that the observed charmonium states like $\psi(3770)$ have to be considered as varying mixtures of $c\bar{c}$ and $D\bar{D}$ configurations. While the bare $c\bar{c}$ closed channel by itself lives indefinitely long, the configuration interactions V_{cd} induce a spectral distribution of a width $\Gamma_c(\omega) = 2\pi|V_{cd}(\omega)|^2$ and a related energy dependent mass shift $\Delta m_c(\omega)$. Here, $V_{cd}(\omega)$ denotes the matrix element of the configuration mixing interaction. The coupling to closed channels induces in the open channels an additional configuration mixing phase shift, derived in the present context as

$$\tan \delta_{cd}(\omega) = \frac{x_c(\omega)}{x_d(\omega)} = \frac{m_c \Gamma_c(\omega)}{m_c^2 - \omega^2} \quad (7)$$

where $m_c = m_c^0 + \Delta m_c$ includes the mass shift. However, because of the extremely small width, $\Gamma_c \ll m_c$, both m_c and Γ_c can be taken as constant in the resonance region. The phase shift δ_{cd} varies rapidly with energy on a scale set by $V_{cd} \sim \sqrt{\Gamma_c}$. δ_{cd} has to be added to bare $D\bar{D}$ channel phase shift varying on

a much larger energy scale, given by t - and u -channel interactions from the exchange of light mesons. Hence, in (hypothetical) $D\bar{D}$ scattering one would observe a sharp resonance around $\omega \sim m_c$, superimposed on and interfering with a slowly varying background.

In order to work out the role played by $c\bar{c}$ states in the resonances observed in e^+e^- -annihilation reactions we need to combine properly the reaction model on the one side and the configuration model on the other side. Starting from an initial reaction channel $|\tau\rangle$ at total energy ω , let be M_τ the transition operator for the production of the state Ψ_ω . In the following formulae we omit partial wave indices because we are studying the production and decay of 1^{--} charmonium vector states which couple to $D\bar{D}$ P -waves. Obviously, the formalism is easily extended to any other partial waves. The charmonium production amplitude out of the incident channel $|\tau\rangle$ is described by the matrix element of the corresponding operator M_τ

$$\langle\Psi_\omega|M_\tau|\tau\rangle = x_c(\omega)\langle\chi_c|M_\tau|\tau\rangle + x_s(\omega)\langle\phi_d|M_\tau|\tau\rangle \quad . \quad (8)$$

The reaction amplitude is given by a production form factor which we express as [1, 8]

$$|F_\tau|^2 = |\langle\phi_d|M_\tau|\tau\rangle|^2 \frac{|q_{c\tau} - \varepsilon|^2}{1 + \varepsilon^2} \quad , \quad (9)$$

where $\varepsilon = \cot\delta_{cd} = (-\omega^2 + m_c^2)/m_c\Gamma_c$ is due to configuration mixing. The parameter

$$q_{c\tau}(\omega) = \frac{\langle\chi_c|M_\tau|\tau\rangle}{\langle\phi_d|M_\tau|\tau\rangle} \quad (10)$$

plays a central role in our approach. Obviously, $|q_{c\tau}|^2$ is the a measure of the population probability of the (dressed) closed $c\bar{c}$ QCD-channel relative to the population probability of the purely hadronic $D\bar{D}$ channel. To a very good approximation we are allowed to use $q = q_{c\tau}(m_c) = \text{const.}$. Eq. (9) shows that q is controlling the line shape of the spectral distribution: a dip, eventually down to zero, will appear at an energy ω_0 where $q = \varepsilon(\omega_0)$. For $q = 0$ an inverted resonance line shape with a minimum at $\omega = m_c$ will occur. The widely used Breit-Wigner profile is recovered if $q \gg \varepsilon$ over the whole resonance region:

$$F_c(s) = \frac{A_c}{s - m_c^2 + im_c\Gamma_c} \quad . \quad (11)$$

The latter two cases correspond to the limiting scenarios of the reaction, namely for $q = 0$ exclusive annihilation into the hadronic $D\bar{D}$ channel and, as the other extreme, exclusive annihilation into the $c\bar{c}$ channel for $q \rightarrow \infty$. The latter case describes, by the way, sub-threshold charmonium production for which the form factor, Eq. (9) reduces to the $c\bar{c}$ amplitude. Thus, besides fixing the line shape, q provides information on the reaction mechanism. As such, it depends naturally on the type of reaction and we have to expect different line shapes when populating *the same final state* in different reactions. Thus, spectral distribution of different shapes have to be expected in charmonium production in leptonic $\ell\bar{\ell}$ and hadronic $h\bar{h}$ annihilation reactions. If many open channels are contributing, the interference minimum will be superimposed on a finite background. The structural properties of charmonium are imprinted in ε , given by the configuration mixing phase shift δ_{cd} . Hence, ε contains the full spectral information on the mass and the width of the resonance. In the specific case of $c = \psi'(3770)$ the width is given by the P -wave relation [16]

$$\Gamma_{\psi'}(s) = \frac{g_{\psi'D\bar{D}}^2}{6\pi s} (p_0^3(s) + p_\pm^3(s)) \quad (12)$$

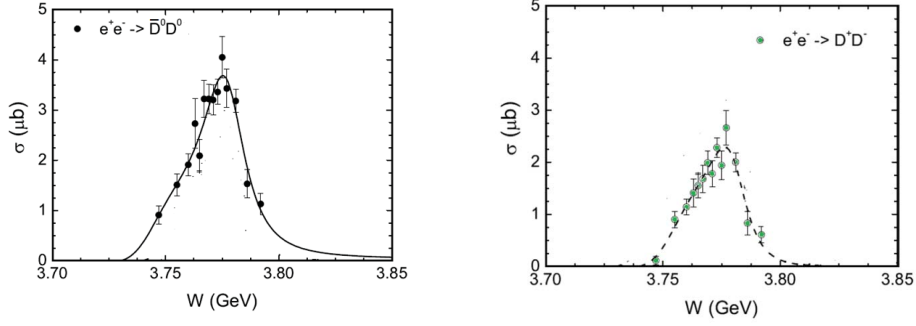


Fig. 5: Total cross section of $e^+e^- \rightarrow D^0\bar{D}^0$ (left) and $e^+e^- \rightarrow D^+D^-$ (right) charmonium production. The results are compared to data obtained by the BES collaboration [13].

where the c.m. momenta are $p_i(s) = \sqrt{s/4 - m_{D_i}^2}$ for neutral ($i = 0$) and charged ($i = \pm 1$) $D\bar{D}$ channels.

Finally, the yet missing population probability of the hadronic $D\bar{D}$ component in Eq. (9) is defined by the *ansatz*

$$|\langle \phi_d | M_\tau | \tau \rangle|^2 = |A_{\psi'} F_d|^2 \quad (13)$$

The energy dependence is described by the form factor

$$F_d(s) = \frac{1}{s - m_d^2 + im_d \Delta_d} \quad , \quad (14)$$

mimicking the weak energy dependence induced by the non-resonant $D\bar{D}$ interactions. The quantities m_d and Δ_d , which are purely numerical parameters, are determined by the data, as listed in Tab.1. The magnitude of the $e^+e^- \rightarrow D\bar{D}$ production amplitude is fixed by the residue $A_{\psi'} = m_{\psi'}^2 g_{\psi' D\bar{D}} / g_{\psi' \gamma}$, determined essentially by the $g_{\psi' D\bar{D}}$, dimensionless coupling constant of $\psi(3770)$ to $D\bar{D}$.

For the present investigations, we determine the photo-vector coupling constant $g_{\psi' \gamma}$ phenomenologically. The electronic width of vector charmonium states is given by $\Gamma_{\psi' e^+ e^-} = 4\pi\alpha^2 m_{\psi'} / 3g_{\psi' \gamma}^2$, see e.g. [17] where $\alpha \simeq 1/137$ denotes the electromagnetic fine structure constant. With $\Gamma_{\psi' e^+ e^-} = 0.265$ keV from the recent compilation of the Particle Data Group [12] the photo-vector coupling constant $g_{\psi' \gamma}$ at $m_{\psi'} = 3770$ MeV could be determined to be 56.35.

We define the hadronic $e^+e^- \rightarrow D\bar{D}$ cross section, including the appropriate two-body phase space factor,

$$\sigma_{D\bar{D}}(s) = \frac{8\pi\alpha^2 p_i^3}{3s^{5/2}} |\langle \phi_d | M_\tau | \tau \rangle|^2 \quad . \quad (15)$$

and obtain the full charmonium production cross section as

$$\sigma(s) = \frac{8\pi\alpha^2 p_i^3}{3s^{5/2}} |F_\tau|^2 = \sigma_{D\bar{D}}(s) \frac{|q - \varepsilon|^2}{1 + \varepsilon^2} \quad . \quad (16)$$

	$D^0\bar{D}^0$	D^+D^-
$m_{\psi'}$ (MeV)	3782.1 ± 1.6	3784.0 ± 2.0
$g_{\psi'D\bar{D}}$	11.8 ± 0.9	10.7 ± 1.3
q	-2.1 ± 0.3	-1.6 ± 0.3
m_d (MeV)	3743.0 ± 5.4	3753.3 ± 3.9
Δ_d (MeV)	34.1 ± 5.2	33.3 ± 5.6
$\chi^2/d.o.f$	0.83	0.90

Table 1: Charmonium production in the $e^+e^- \rightarrow D^0\bar{D}^0$ and $e^+e^- \rightarrow D^+D^-$ annihilation reactions: Fano-parameters according to Eq. (9) from the fit to the data shown in Fig.5.

Hence, the charmonium production cross section is separated into the annihilation cross section populating the hadronic $D\bar{D}$ component and a form factor containing the population and spectroscopy of the confined $c\bar{c}$ component of the full charmonium state vector.

Applying the approach to the BESIII data [13], the spectral distributions in the $D^0\bar{D}^0$ and the D^+D^- production cross sections are well described, as seen in Fig. 5. In order to illustrate possible applications to data analyses, the mass, width and line shape parameters, respectively, have been varied freely in a χ^2 minimization process. The resulting parameter sets are shown in Tab. 1. The bare mass and width of $\psi(3770)$ in the neutral and charged channels are consistent with each other. The different behaviour of the two production cross sections results almost totally from the difference in phase space factors of the $D^0\bar{D}^0$ and D^+D^- channels, namely the mass gap of neutral and charged D -meson. It should be mentioned that the dip at around 3.82 GeV could be reproduced with above prescription if the Belle data at high energies are included in the fit, as we have shown previously [8]. Finally, attempting a fit with a simple Breit-Wigner line shape (i.e. assuming $q \rightarrow \infty$) the description deteriorates as reflected by the increased values $\chi^2 = 2.72$ for the $D^0\bar{D}^0$ channel and $\chi^2 = 3.27$ for the fit to the D^+D^- data, respectively.

The results for q obtained from the $D^0\bar{D}^0$ and the D^+D^- data are agreeing within the error bars. The slight differences may be taken as an indication on the reaction-dependence of spectral line shapes observed in production reactions. Despite of the remaining uncertainties due to the relatively large experimental errors the two q -values are indicating differences in the reaction mechanism, probably mainly caused by differences in the final states interactions. More precise data from future experiments, either at e^-e^+ -facilities or from $p\bar{p}$ annihilation as planned at PANDA@FAIR are important for a more detailed analysis.

4. Summary

Universal aspects in nuclear and hadronic spectroscopy have been investigated by general methods, equally well applicable to various kinds of open quantum systems at any scale. The relation to atomic and molecular physics was pointed out. The scale-independent feature is configuration mixing of asymptotically open and closed channels. A theoretical scheme was developed which provides a microscopic approach to spectral distributions in nuclear and hadron spectroscopy. Frequently observed sharp resonances with non-standard, asymmetric line shapes and interference pattern have been explained dynamically in terms of configuration mixing effects. The theory was applied to continuum spectroscopy at the neutron dripline and charmonium production in e^-e^+ annihilation reactions.

Acknowledgements:

Supported in part by Helmholtz International Center for FAIR, GSI, BMBF, contract 05P12RGFTE, and

DFG, contracts Le439/7, Le439/8, and Le439/9. S.E.A Orrigo and Xu Cao acknowledge the support by Helmholtz International Center for FAIR for their research stay at Giessen.

References

- [1] U. Fano, Phys. Rev. **124** (1961) 1866.
- [2] C. Mahaux and H.A. Weidenmüller, *Shell Model Approach to Nuclear Reactions*, North-Holland, Amsterdam (1969).
- [3] C. Ott *et al.*, Science **340**, 716 (2013).
- [4] G. Baur, H. Lenske, Nucl. Phys. A 282 (1977) 201; H. Fuchs, J.A. Nolen, G.J. Wagner, H. Lenske, G. Baur, Nucl. Phys. A 343 (1980) 133.
- [5] N.E. Ligterink, PiN Newslett. 16 (2002) 400, nucl-th/0203054.
- [6] S.E.A. Orrigo, H. Lenske *et al.*, Phys. Lett. B **633** (2006) 469 [nucl-th/0603019].
- [7] S.E.A. Orrigo and H. Lenske, Phys. Lett. B **677** (2009) 214.
- [8] Xu Cao and H. Lenske, arXiv:1408.5600 [nucl-th].
- [9] S.E.A. Orrigo, H. Lenske, ISOLDE newsletter Spring 2010, CERN/Geneva, 2010, p.5.
- [10] H.B. Jeppesen *et al.*, Phys. Lett. B **642** (2006) 449 and private communications.
- [11] Yu. S. Kalashnikova, Phys. Rev. D **72**, 034010 (2005).
- [12] J. Beringer *et al.* (Particle Data Group), Phys. Rev. D **86**, 010001 (2012).
- [13] M. Ablikim *et al.* (BES Collaboration), Phys. Lett. **B668**, 263 (2008).
- [14] G. Pakhlova *et al.* (Belle Collaboration), Phys. Rev. D **77**, 011103(R) (2008).
- [15] Q. He *et al.* (CLEO Collaboration), Phys. Rev. Lett. **95**, 121801 (2005); S. Dobbs *et al.* (CLEO Collaboration), Phys. Rev. D **76**, 112001 (2007).
- [16] Y. J. Zhang and Q. Zhao, Phys. Rev. D **81**, 034011 (2010).
- [17] V. A. Novikov *et al.*, Phys. Rept. **41**,1 (1978).

^8Be , ^{12}C , ^{16}O , ^{20}Ne , ^{24}Mg , and ^{32}S nuclei and alpha clustering within a generalized liquid drop model

G. Royer, G. Ramasamy and P. Eudes

Laboratoire Subatech, UMR : IN2P3/CNRS-Université-Ecole des Mines, Nantes, France

Abstract

The potential energy governing the shape and the entrance and decay channels of the ^{12}C , ^{16}O , ^{20}Ne , ^{24}Mg , and ^{32}S 4n-nuclei has been determined within a generalized liquid drop model. Different three-dimensional and planar shapes have been investigated: linear chain, triangle, square, tetrahedron, pentagon, trigonal bipyramid, square pyramid, hexagon, octahedron, octagon and cube. The rms radii of the linear chains are higher than the experimental rms radii of the ground states. The binding energies of the planar shapes at the contact point are lower than the ones of the three-dimensional configurations. The α particle plus A-4 daughter configuration leads always to the lowest potential barrier relatively to the sphere configuration.

1. Introduction

Hydrogen burning in stars leads to a dense and hot core of helium and to the nucleosynthesis of other nuclei having a possible n- α structure: ^{16}O , ^{20}Ne , ^{24}Mg , ^{28}Si , ^{32}S ... In these 4n-nuclei the cluster-type states coexist with the mean-field-type states [1]. In ^{12}C the ground state wave function contains a large amount of 3α cluster wave function. Experimentally, a new high spin 5^- state has been observed recently. It fits well the ground state rotational band of an equilateral triangular spinning top [2]. In ^{16}O recent calculations lead for the ground state to a tetrahedral configuration of α particles in agreement with the energy spectrum and with the electromagnetic properties [3, 4] while some excited states are due to the mean-field-type excitation mode while other ones are due to the cluster structure of $\alpha+^{12}\text{C}$. In connection with the excited 0_2^+ Hoyle state of ^{12}C and possible excited Hoyle state of ^{16}O , the α condensate character of the α -linear chain has been proposed after comparing a large number of Brink functions with Tohsaki-Horiuchi-Schuck-Röpke wave functions [5, 6].

The generalized liquid drop model (GLDM) previously defined to describe the fission, fusion... processes [7, 8, 9] has been used to determine the L-dependent potential energy of the following planar or three-dimensional α clusters: aligned α chains, isosceles triangle, square, tetrahedron, pentagon, trigonal bipyramid, square pyramid, hexagon, octahedron, octagon and cube.

2. Generalized liquid drop model

The GLDM energy is the sum of the volume, surface, Coulomb and proximity energies.

For two separated spherical nuclei :

$$E_V = -15.494 [(1 - 1.8I_1^2)A_1 + (1 - 1.8I_2^2)A_2] \text{ MeV}, \quad (1)$$

$$E_S = 17.9439 [(1 - 2.6I_1^2)A_1^{2/3} + (1 - 2.6I_2^2)A_2^{2/3}] \text{ MeV}, \quad (2)$$

$$E_C = 0.6e^2Z_1^2/R_1 + 0.6e^2Z_2^2/R_2 + e^2Z_1Z_2/r, \quad (3)$$

where I_i is the relative neutron excess.

The proximity energy must be added to the surface energy to take into account the effects of the nuclear forces between the surfaces in regard in a gap or a neck between nuclei.

3. ^{12}C nucleus

Calculations using Antisymmetrized Molecular Dynamics and Fermionic Molecular Dynamics and without assuming α clustering led for the different states to triangular α -configurations with different angles allowing the reproduction of the low-lying spectrum [10, 11]. Using effective field theory and Monte Carlo lattice calculations it has been shown that the ^{12}C ground state and the first excited state have a compact triangular configuration while the Hoyle state and the second excited state have an obtuse triangular configuration of alpha clusters [12]. These predictions are strengthened by the observation of a new high spin 5^- state at 22.4 MeV compatible with a ground state rotational band of an equilateral triangular spinning top with a D_{3h} symmetry. Then the Hoyle state is interpreted as the band head of the stretching vibration or breathing mode of this triangular configuration [2].

These oblate ternary configurations have been studied within the GLDM in placing three α particles at the tops on an isosceles triangle characterized by the angle θ . At the contact point the energy of the linear chain of three α particles ($\theta=180$ deg.) is higher than the energy of the equilateral triangular shape, the energy difference reaching 7.4 MeV. This is also in favor of an equilateral triangular configuration of the ground state (the energy being almost constant between 120 and 180 degrees). The experimental rms charge radius of the ground state is $\langle r^2 \rangle^{1/2} = 2.47$ fm. Within the GLDM, at the contact point the rms radius is 2.43 fm for a triangular shape and 3.16 fm for a linear chain. Furthermore the empirical electric quadrupole moment is negative which disagrees with the configuration of three-aligned α particles for the ground state shape [9].

4. ^{16}O nucleus

For the ground state a tetrahedral molecule of alpha particles is predicted [3, 4] and for the first excited

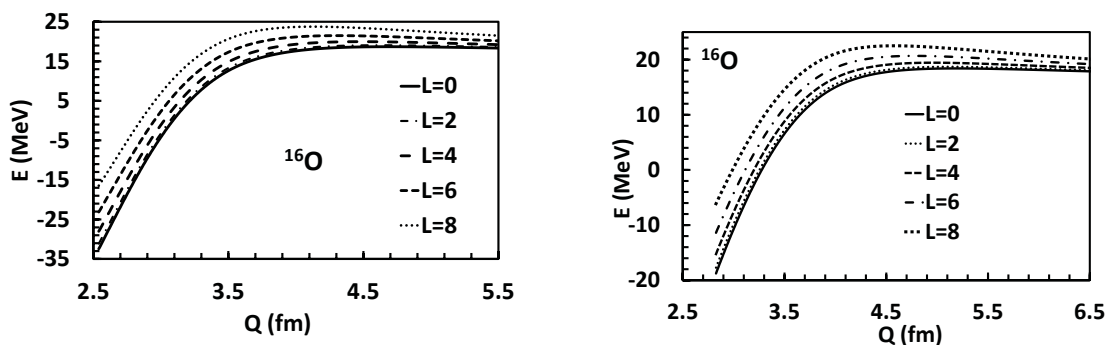


Fig. 1: Potential energy of the α -tetrahedron (left part) and of the α -square (right part) as functions of the angular momentum (in \hbar unit) and rms radius.

spin-0 state a square configuration [3]. In Fig. 1 the energies of these two configurations determined from the GLDM are shown. At the contact point between the four spherical α particles the rms radius is 2.54 fm for a tetrahedron, 2.83 fm for a square and 4.15 fm for a prolate linear chain. Experimentally the rms charge radius of the ground state is $\langle r^2 \rangle^{1/2} = 2.70$ fm. The ground state has probably not a linear chain configuration. The binding energy is higher for the tetrahedral molecule than for the

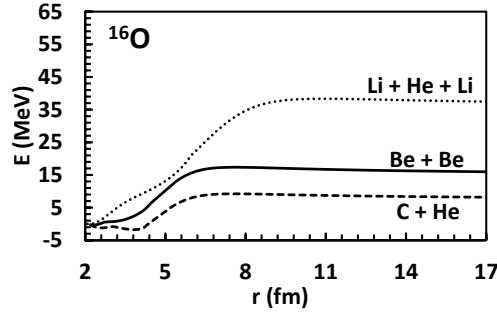


Fig. 2: Potential energy governing the ${}^{12}\text{C}+{}^4\text{He}$, ${}^8\text{Be}+{}^8\text{Be}$, and ${}^6\text{Li}+{}^4\text{He}+{}^6\text{Li}$ nuclear systems versus the distance between the mass centres (at $L = 0$).

square shape since for these configurations the proximity energy plays a very important role and the tetrahedron is linked by six bonds and the square by only four bonds. On the contrary, the Coulomb repulsion is lower for the square. The energy difference between the two shapes is 13.7 MeV which is close to $Q_{4\alpha}$ (14.4 MeV), the energy of the 0_6^+ state (15.1 MeV) and 14.0 MeV the energy of a 0^+ state. The relative energies at the contact point are respectively 0, 1.3, 4.4, 9.3 and 16 MeV for $L = 0, 2, 4, 6$ and $8 \hbar$ for the tetrahedral shape and 0, 1.1, 3.5, 7.4 and 12.6 MeV for $L = 0, 2, 4, 6$ and $8 \hbar$ for the square shape.

The ground state can also be described as double closed shell wave functions but several low-lying excited states are also described within the ${}^{12}\text{C}+{}^4\text{He}$ cluster. The potential energies of the ${}^{12}\text{C}+{}^4\text{He}$, ${}^8\text{Be}+{}^8\text{Be}$, and aligned ${}^6\text{Li}+{}^4\text{He}+{}^6\text{Li}$ systems have been calculated assuming a spherical shape for the compound nucleus and each nucleus (see Fig. 2). The threshold energies are : 7.2 MeV for $Q_{{}^4\text{He}+{}^{12}\text{C}}$, 14.4 for $Q_{4\alpha}$, 14.6 for $Q_{{}^8\text{Be}+{}^8\text{Be}}$, and 35.3 for $Q_{{}^6\text{Li}+{}^4\text{He}+{}^6\text{Li}}$. The top of the barriers corresponds to separated nuclei maintained in unstable equilibrium by the balance between the attractive nuclear proximity forces and the repulsive Coulomb forces. Quasimolecular ${}^{12}\text{C}+{}^4\text{He}$ one-body shapes have almost the same energy than the spherical compound nucleus.

5. ${}^{20}\text{Ne}$ nucleus

The trigonal bipyramid, square pyramid and pentagonal molecules have been studied. Their energies are compared in Fig. 3. The rms radius is 2.76 fm for a trigonal bipyramid, 2.79 fm for a square pyramid and 3.29 fm for a pentagon at the contact point. The experimental rms charge radius is $\langle r^2 \rangle^{1/2} = 3.01$ fm, lower than the rms radius of a prolate linear chain. The binding energy of the trigonal bipyramid is the highest. The number of bonds is five for the pentagon, eight for the square pyramid and nine for the trigonal bipyramid. At the contact point, the energy difference between the trigonal bipyramid and the square pyramid is 21.3 MeV and 15.3 between the square pyramid and the pentagon, while $Q_{5\alpha} = 19.2$ MeV. For the trigonal bipyramid the relative energies to the ground state at the contact point are respectively 0, 1.7, 5.6, 11.7 and 20.1 MeV for $L = 0, 2, 4, 6$ and $8 \hbar$. For the square pyramid the values are 0, 1.0, 3.2, 6.8 and 11.7 MeV for $L = 0, 2, 4, 6$ and $8 \hbar$. For the pentagon it is : 0, 0.6, 2.0, 4.3 and 7.3 MeV for $L = 0, 2, 4, 6$ and $8 \hbar$. Experimentally the energies of the 2_0^+ and 4_0^+ states are respectively 1.63 and 4.25 MeV.

The ground state band contains the ${}^{16}\text{O}+{}^4\text{He}$ cluster at most 70% and the potential energies of

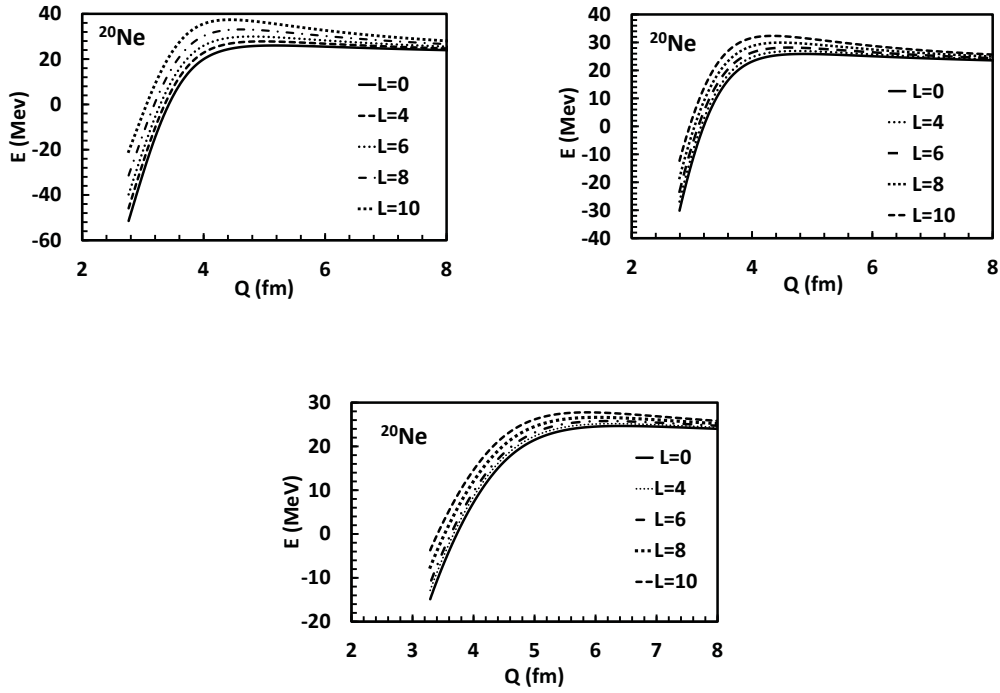


Fig. 3: Potential energy of the trigonal bipyramid (on the left), square pyramid (on the right) and the pentagon (on the bottom) as functions of the angular momentum (in \hbar unit) and rms radius.

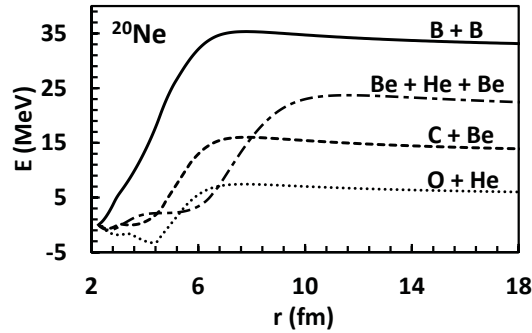


Fig. 4: Potential energy governing the $^{16}\text{O}+^4\text{He}$, $^{12}\text{C}+^8\text{Be}$, $^{10}\text{B}+^{10}\text{B}$, and linear $^8\text{Be}+^4\text{He}+^8\text{Be}$ systems versus the distance between the mass centres (at $L=0$).

the $^{16}\text{O}+^4\text{He}$, $^{12}\text{C}+^8\text{Be}$, $^{10}\text{B}+^{10}\text{B}$, and linear $^8\text{Be}+^4\text{He}+^8\text{Be}$ systems have been determined assuming spherical shapes for all the nuclei (see Fig. 4). The respective threshold energies are : 4.73 MeV for $Q_{^{16}\text{O}+^4\text{He}}$, 11.98 for $Q_{^8\text{Be}+^{12}\text{C}}$, 19.35 for $Q_{^8\text{Be}+^4\text{He}+^8\text{Be}}$, and 31.14 MeV for $Q_{^{10}\text{B}+^{10}\text{B}}$. In the $^{16}\text{O}+^4\text{He}$ channel quasimolecular one-body shapes have roughly the same energy than the spherical nucleus and

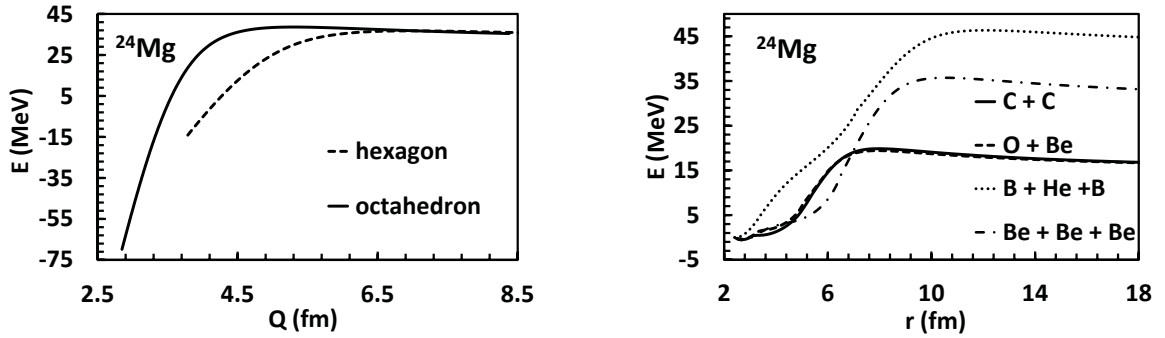


Fig. 5: Potential energies of an hexagon and an octahedron from the contact point as a function of the rms radius and potential barriers governing the $^{16}\text{O}+^8\text{Be}$, $^{12}\text{C}+^{12}\text{C}$, $^8\text{Be}+^8\text{Be}+^8\text{Be}$, and $^{10}\text{B}+^4\text{He}+^{10}\text{B}$ reactions versus the distance between the mass centres.

the minimum has a cluster structure corresponding to the two ^4He and ^{16}O nuclei in contact.

6. ^{24}Mg nucleus

The energies of the hexagonal and octahedral α -molecules are displayed in Fig. 5. The experimental rms charge radius of the ground state is only $\langle r^2 \rangle^{1/2} = 3.06$ fm. At the contact point the rms radius is 2.85 fm for an octahedron and 3.79 fm for an hexagon, which excludes the planar shape and the linear chain as possible ground state shapes. The binding energy is higher for the octahedral configuration since there are twelve bonds for the octahedron and only six for the hexagon.

The potential energies of the $^{16}\text{O}+^8\text{Be}$, $^{12}\text{C}+^{12}\text{C}$, $^8\text{Be}+^8\text{Be}+^8\text{Be}$, and $^{10}\text{B}+^4\text{He}+^{10}\text{B}$ systems are also shown in Fig. 5. The different Q values are : 9.32 MeV for $Q_{^4\text{He}+^{20}\text{Ne}}$, 13.93 for $Q_{^{12}\text{C}+^{12}\text{C}}$, 14.14 for $Q_{^8\text{Be}+^{16}\text{O}}$, 28.48 for $Q_{6\alpha}$, 28.76 for $Q_{^8\text{Be}+^8\text{Be}+^8\text{Be}}$, and 40.46 for $Q_{^{10}\text{B}+^4\text{He}+^{10}\text{B}}$.

7. ^{32}S nucleus

The octogonal and cubic α -molecules have been investigated. Their energies are compared in Fig. 6. The experimental rms charge radius is $\langle r^2 \rangle^{1/2} = 3.26$ fm. The rms radius is 4.85 fm for an octogon and 3.37 fm for a cube at the contact point which seems to exclude the planar and linear configurations. The binding energy is higher for the cubic configuration than for the octogonal shape, indeed there are twelve bonds for the cube and only eight for the octogon.

The potential energies of the $^{28}\text{Si}+^4\text{He}$, $^{24}\text{Mg}+^8\text{Be}$, $^{20}\text{Ne}+^{12}\text{C}$, and $^{16}\text{O}+^{16}\text{O}$ systems are also given in Fig. 6. The threshold energies are : 6.95 MeV for $Q_{^4\text{He}+^{28}\text{Si}}$, 16.54 for $Q_{^{16}\text{O}+^{16}\text{O}}$, 17.02 for $Q_{^8\text{Be}+^{24}\text{Mg}}$, 18.97 for $Q_{^{12}\text{C}+^{20}\text{Ne}}$, 30.96 for $Q_{^{12}\text{C}+^8\text{Be}+^{12}\text{C}}$, 34.17 for $Q_{^{14}\text{N}+^4\text{He}+^{14}\text{N}}$, and 45.42 for $Q_{8\alpha}$. The energy of the $^{28}\text{Si}+^4\text{He}$ one-body nucleus is relatively constant till the spherical nucleus allowing the cohabitation of different quasimolecular shapes. The superdeformed band contains the $^{16}\text{O}+^{16}\text{O}$ component by about 44 %.

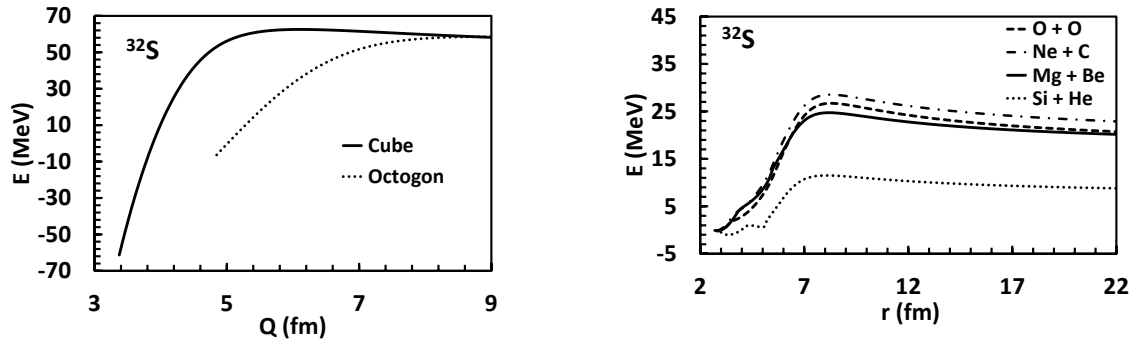


Fig. 6: Potential energies of octogonal and cubic molecules from the contact point as a function of the rms radius and potential barriers governing the $^{28}\text{Si}+^4\text{He}$, $^{24}\text{Mg}+^8\text{Be}$, $^{20}\text{Ne}+^{12}\text{C}$, and $^{16}\text{O}+^{16}\text{O}$ systems versus the distance between the mass centres.

8. Binding energy

The binding energy of these nuclei can be reproduced within the molecular structure picture by summing the binding energy of n alphas plus the number of bonds multiplied by around 2.4 MeV.

$$B(^{12}\text{C}) = 3 \times B(\alpha) + 3(\text{bonds}) \times 2.42 \text{ MeV}, \quad (4)$$

$$B(^{16}\text{O}) = 4 \times B(\alpha) + 6(\text{bonds}) \times 2.41 \text{ MeV}, \quad (5)$$

$$B(^{20}\text{Ne}) = 5 \times B(\alpha) + 8(\text{bonds}) \times 2.40 \text{ MeV}, \quad (6)$$

$$B(^{24}\text{Mg}) = 6 \times B(\alpha) + 12(\text{bonds}) \times 2.37 \text{ MeV}. \quad (7)$$

$$(8)$$

It is difficult to explain this value of 2.4 MeV per bond since it does not correspond to the sum of the mean Coulomb energy and proximity energy by bond.

The binding energy of these nuclei can also be obtained within a core+ α cluster model since this energy is the sum of the binding energies of one alpha and the one of the daughter nucleus plus roughly the Coulomb energy and the proximity energy between the two nuclei.

$$B(^{12}\text{C}) = B(^8\text{Be}) + B(\alpha) + 7.37 \text{ MeV}, \quad (9)$$

$$B(^{16}\text{O}) = B(^{12}\text{C}) + B(\alpha) + 7.16 \text{ MeV}, \quad (10)$$

$$B(^{20}\text{Ne}) = B(^{16}\text{O}) + B(\alpha) + 4.73 \text{ MeV}, \quad (11)$$

$$B(^{24}\text{Mg}) = B(^{20}\text{Ne}) + B(\alpha) + 9.32 \text{ MeV}. \quad (12)$$

9. Conclusion

Within an α -particle model the energy of the ^{12}C , ^{16}O , ^{20}Ne , ^{24}Mg and ^{32}S nuclei has been determined assuming different α -molecule configurations: linear chain, triangle, square, tetrahedron, pentagon, trigonal bipyramid, square pyramid, hexagon, octahedron, octogon, and cube. Within a macroscopic approach the potential barriers governing the entrance and decay channels of these $4n$ -nuclei via alpha emission or absorption have also been compared.

The rms radii of the prolate chains seem incompatible with the experimental rms radii of the ground states. The binding energies of the three-dimensional molecules are higher than the binding

energies of the planar shapes. The core+ α cluster system leads always to the lowest potential barrier. The binding energy can be obtained within the sum of the binding energy of n alphas plus 2.4 MeV multiplied by the number of bonds or by the sum of the binding energy of one alpha and the one of the daughter nucleus plus the Coulomb energy and the proximity energy between the two nuclei.

References

- [1] W. von Oertzen, M. Freer, and Y. Kanada-En'yo, *Phys. Rep.* **432** (2006) 43.
- [2] D.J. Marin-Lambarri *et al.*, *Phys. Rev. Lett.* **113** (2014) 012502.
- [3] E. Epelbaum *et al.*, *Phys. Rev. Lett.* **112** (2014) 102501.
- [4] R. Bijker and F. Iachello, *Phys. Rev. Lett.* **112** (2014) 152501.
- [5] Y. Funaki *et al.*, *Phys. Rev. C* **80** (2009) 064326.
- [6] T. Suhara, Y. Funaki, B. Zhou, H. Horiuchi, and A. Tohsaki, *Phys. Rev. Lett.* **112** (2014) 062501.
- [7] G. Royer, B. Remaud, *Nucl. Phys. A* **444** (1985) 477.
- [8] G. Royer, M. Jaffré, and D. Moreau, *Phys. Rev. C* **86** (2012) 044326.
- [9] G. Royer, A. Escudie, and B. Sublard, *Phys. Rev. C* **90** (2014) 024607.
- [10] Y. Kanada-En'yo, *Prog. Theor. Phys.* **117** (2007) 655.
- [11] M. Chernykh *et al.*, *Phys. Rev. Lett.* **98** (2007) 032501.
- [12] E. Epelbaum *et al.*, *Phys. Rev. Lett.* **109** (2012) 252501.

Characterization of a potential 4- α cluster state

R. Neveling¹, K.C.W. Li², P. Adsley^{1,2}, P. Papka^{1,2}, F.D. Smit¹, J.W. Brümmer², M. Freer³, Tz. Kokalova³, F. Nemulodi^{1,2}, L. Pellegrini^{1,4}, B. Rebeiro⁵, J.A. Swartz⁶, J.J. van Zyl², S. Triambak⁵, and C. Wheldon³

¹ iThemba Laboratory for Accelerator Based Sciences, Somerset West 7129, South Africa

² Stellenbosch University, Department of Physics, Stellenbosch 7600, South Africa

³ University of Birmingham, School of Physics and Astronomy, Birmingham, B15 2TT, United Kingdom

⁴ University of the Witwatersrand, School of Physics, Johannesburg 2050, South Africa

⁵ University of the Western Cape, Department of Physics, Bellville 7535, South Africa

⁶ KU Leuven, Instituut voor Kern- en Stralingsfysica, B-3001 Leuven, Belgium

Abstract

The reaction $^{16}\text{O}(\alpha, \alpha')$ was studied at 0° at an incident energy of $E_{lab} = 200$ MeV using the K600 magnetic spectrometer at iThemba LABS. Proton and α -decay from the natural parity states were observed in a large-acceptance silicon-strip detector array at backward angles. The coincident charged particle measurements were used to characterize the decay path of the 0_6^+ state in ^{16}O located at $E_x = 15.097$ MeV. This state is identified by several theoretical cluster calculations to be a good candidate for the 4- α cluster state. Preliminary results indicate the possibility that the 0_6^+ state in ^{16}O is contaminated by the presence of an unresolved state that does not have a 0^+ character.

1. Introduction

Clustering phenomena in light nuclei, in particular α -clustering, have recently attracted much interest [1]. Light nuclei are expected to exhibit cluster-like properties in excited states with a low density structure. Such states should exist at excitation energies near the separation energies to these clusters, as described by the Ikeda diagram [2]. Aside from the interest in the nuclear structure of such states, they have astrophysical relevance as they can enhance element production in stars [3, 4]. The Hoyle state, the 0_2^+ state at 7.654 MeV in ^{12}C , may be considered the prototype of a state that exhibits α -particle condensation [5], i.e. it is considered to have a 3α gas-like structure similar to a Bose-Einstein condensate consisting of three α particles all occupying the lowest $0S$ state.

It is expected that equivalent Hoyle-like states should also exist in heavier $N\alpha$ nuclei such as ^{16}O , ^{20}Ne , etc. [5]. Indeed a potential candidate in ^{16}O has been identified. Funaki *et al.* [6] solved a four-body equation of motion based on the Orthogonality Condition Model (OCM) that succeeded in reproducing the observed 0^+ spectrum in ^{16}O up to the 0_6^+ state. They showed that the 4α condensation state could be assigned to the 0_6^+ state located at 15.096 MeV. The 0_6^+ state obtained from the calculation is 2 MeV above the four α -particle breakup threshold ($S_{4\alpha}=14.437$ MeV) and has a large radius of 5 fm, indicating a dilute density structure. Ohkubo and Hirabayashi showed in a study of $\alpha+^{12}\text{C}$ elastic and inelastic scattering [7] that the moment of inertia of the 0_6^+ state is drastically reduced, which suggests that it is a good candidate for the 4α cluster condensate state. Calculations performed with the Tohsaki-Horiuchi-Schuck-Röpke (THSR) α -cluster wave function [8] also supports this notion, and yields a total width of 34 keV for the 0_6^+ state [9], much smaller than the experimentally determined value of 166 ± 30 keV [10].

The measurement of particle decay widths of the 0_6^+ state in ^{16}O is required for a characterization of its structure. Recent attempts at such measurements highlighted the need for an experiment that com-

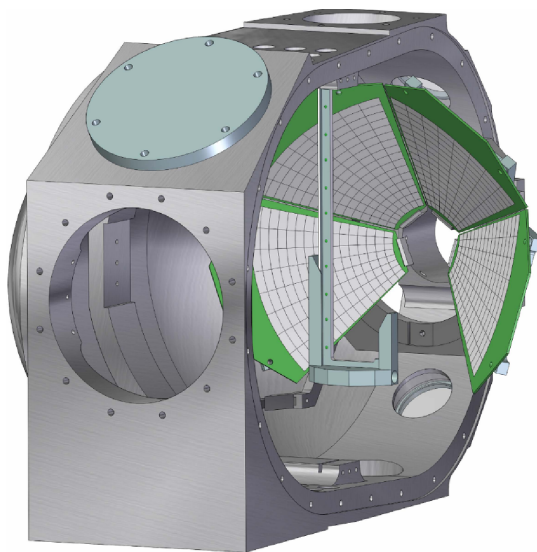


Fig. 1: The scattering chamber viewed from downstream with internal structure exposed, illustrating the target ladder and the lampshade configuration of the CAKE positioned at backward angles.

combines a high energy resolution experimental setup with a reaction capable of preferentially populating 0^+ states. Haigh *et al.* [11] used the $^{12}\text{C}(^{13}\text{C},^9\text{Be})^{16}\text{O}$ reaction at $E_{lab} = 141$ MeV to populate excited states in ^{16}O . The ^9Be ejectile was observed in a Q3D magnetic spectrometer in coincidence with ^{16}O decay products observed in an array of double-sided silicon strip detectors (DSSSD). An energy resolution of several hundred keV allowed only for the extraction of precise values for $\Gamma_{\alpha 0}/\Gamma_{tot}$ as well as limits for $\Gamma_{\alpha 1}/\Gamma_{tot}$ for the 5^- state at 14.66 MeV and the 6^+ state at 16.275 MeV. This was followed by a study of the $^{12}\text{C}(^6\text{Li},d)^{16}\text{O}$ reaction, using a similar experimental setup but with an improved excitation energy resolution of 60 keV [12]. However, 0^+ states were not prominently excited due to momentum matching conditions not being fulfilled.

Inelastic α -particle scattering at zero degrees has the advantage that it only excites natural parity states, and particularly the 0^+ states. A measurement of the $^{16}\text{O}(\alpha, \alpha')^{16}\text{O}$ reaction at zero degrees, coupled with coincident observations of the ^{16}O decay products, is therefore an ideal tool to measure particle decay widths of the 0_6^+ state in ^{16}O , provided the experimental energy resolution is adequate. The results of such a measurement performed at the iThemba Laboratory for Accelerator Based Sciences (iThemba LABS) in South Africa are reported.

2. Experimental method

A 200 MeV dispersion matched α -beam was provided by the separated sector cyclotron at iThemba LABS. Inelastically scattered α -particles from a $^{nat}\text{Li}_2\text{CO}_3$ target were momentum analyzed with the K600 magnetic spectrometer positioned at zero degrees [13]. The $510 \mu\text{g}\cdot\text{cm}^{-2}$ thick $^{nat}\text{Li}_2\text{CO}_3$ target was prepared on a $50 \mu\text{g}\cdot\text{cm}^{-2}$ thick ^{12}C backing [14]. The solid angle acceptance of the spectrometer (3.83 msr) was defined by a circular collimator with horizontal and vertical acceptance of $\pm 2^\circ$. The focal-plane detectors of the spectrometer consisted of two multiwire drift chambers, followed by a 6.35 mm thick plastic scintillator. The scintillator provided the master trigger signal for the VME-based MIDAS data acquisition (DAQ) system [15], and also aided with particle identification by providing energy loss and time-of-flight (TOF) information, measured as the time difference between scintillator signals and the RF signal for the pulsed beam.

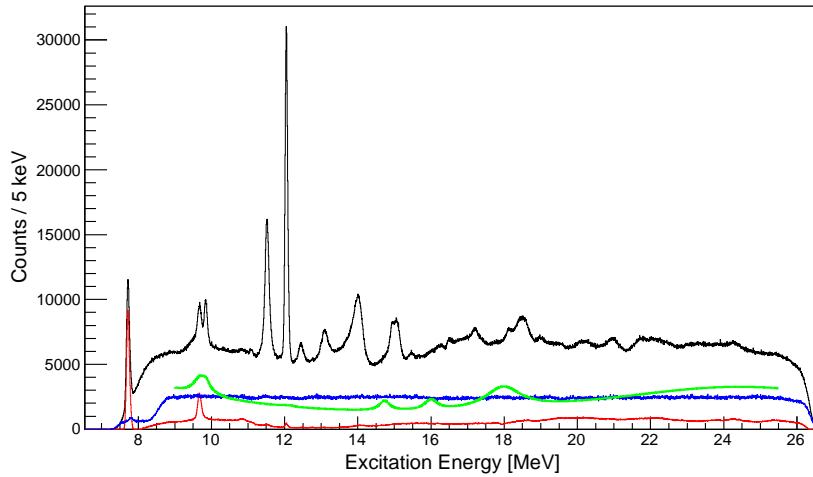


Fig. 2: The Li_2CO_3 excitation energy spectrum obtained from inelastic alpha particle scattering (black line), compared to the fitted contributions from ^{nat}Li (green line), the measured ^{12}C spectrum (red line) as well as the measured instrumental background (blue line).

The decay products were observed with the Coincidence Array for K600 Experiments (CAKE), consisting of four TIARA HYBALL MMM-400 double sided silicon strip detectors (DSSSDs) as shown in Fig. 1. Each of the $400\ \mu\text{m}$ thick wedge-shaped DSSSDs consists of 16 rings and 8 sectors, and were positioned at backward angles with the rings covering the polar angle range $114^\circ < \theta_{lab} < 166^\circ$, resulting in coverage of 21% of the decay particle solid angle. The target-detector separation was $\sim 100\ \text{mm}$ which is sufficient for identification of protons and α 's through TOF measurements. This was however not required due to the well separated kinematic loci of the different decay channels. For each focal-plane event all signals from CAKE within a time window of six μs were digitized, yielding both K600 singles as well as K600 + CAKE coincidence events. A beam pulse selector at the entrance of the cyclotron was employed to ensure a sufficient time window (273 ns) for coincidence measurements.

3. Results

The ^{16}O excitation energy spectrum obtained from inelastic alpha particle scattering is shown in Fig. 2. An energy resolution of $\sim 85\ \text{keV}$ (FWHM) was achieved, sufficient to allow for a deconvolution of the strength around 15 MeV into the 14.926 MeV 2^+ and 15.097 MeV 0^+ states. There are various background components to the spectrum due to the presence of ^{nat}Li and ^{12}C on the target. Fortunately these components have little influence on the data extracted for the ^{16}O states of interest due to the flat or slow varying nature of these background components. For the same reason, the unavoidable instrumental background contribution inherent to inelastic scattering measurements at zero degrees [13] is not a concern.

Good coincidence data were extracted by gating on the prompt peak in the coincidence time spectrum, which yielded a random-to-real coincidence ratio of $\frac{1}{50}$. The coincidence matrix for all events with the target excitation energy as measured by the K600 on the horizontal axis and the energy of the charged particle decay as measured in CAKE on the vertical axis is shown in Fig. 3. The resolution of CAKE is dependent on the MMM detector ring number due to target attenuation effects, and was found to vary between 60 keV and 90 keV at $\sim 5\ \text{MeV}$. Several ^{16}O decay modes (α_0, α_1 and p_0) were clearly observed. For each of these decay channels the region around the 0_6^+ state was found to be free from target or instrumental background. The excitation energy spectra for each of these decay channels,

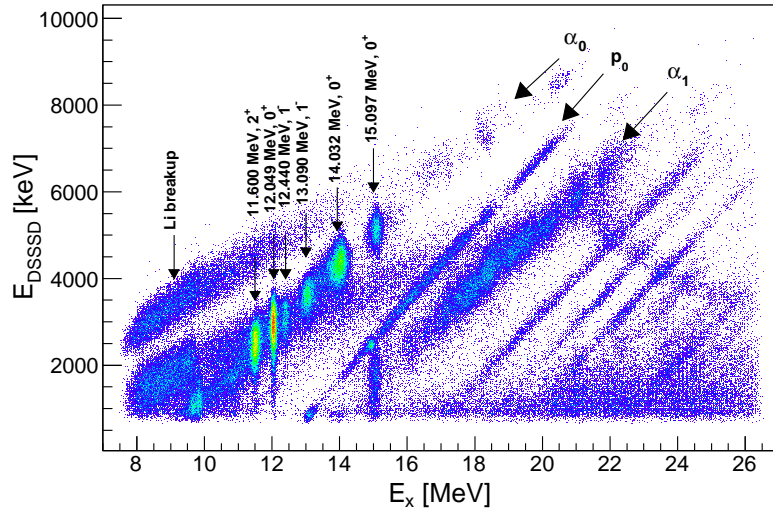


Fig. 3: Two-dimensional coincidence matrix for inelastically scattered α -particles from a $^{nat}\text{Li}_2\text{CO}_3$ target summed over all CAKE channels. Three ^{16}O decay channels (α_0 , α_1 , p_0) are indicated, as well as prominent low spin states in ^{16}O . A display threshold of >3 was used in plotting the data.

selected by applying appropriate software gates to the coincidence matrix, are shown in Figs. 4(b)-(d).

In order to determine the branching ratios of the different decay channels of a particular state/resonance it is necessary to reliably extract the state population in the singles and coincidence datasets. The different excitation energy spectra were fitted with R-matrix Voigt lineshapes for all the natural parity states in ^{12}C and ^{16}O as well as states allowed by angular selection rules in $^{6,7}\text{Li}$. The results of the fitting procedure, together with the experimental excitation spectra, are shown in Fig. 4 for the singles results and various decay channels. The spectra for the decay channels represent data summed over all CAKE channels. The resonance energies were constrained to be within 2σ of the value known from literature, where σ represents the error from literature [16]. The Wigner limit was imposed as the upper limit of the reduced width parameter. The reduced chi-squared values obtained for the fits are 0.9, 1.37, 1.10 and 1.30 for the singles, α_0 -, α_1 - and p_0 -decay channels, respectively. A complicated fit of this nature across a wide excitation energy range, while not absolutely essential in order to extract the strength of the 0_6^+ state at 15.097, does instill confidence in the treatment of the background under the state.

The angular distributions of decay modes from resonances in ^{16}O were extracted after a similar fitting procedure was applied to data from individual CAKE rings. The resonance widths and energies were fixed by the results of the fitting procedure to all CAKE channels. The angular distribution of the α_0 decay channel of the 11.520 MeV 2^+ and 12.049 MeV 0^+ states are shown in Fig. 5.

4. Discussion and summary

In order to assess the validity of the experimental method, the results of known states are considered first. From Fig. 5 it is clear that the angular distribution of the α_0 decay channel of the 11.520 MeV 2^+ and 12.049 MeV 0^+ states display the characteristic distributions associated with 2^+ and 0^+ states respectively. Also encouraging is the extracted branching ratio of $95.3 \pm 0.5\%$ for the α_0 decay channel of the 12.049 MeV 0^+ state, known from literature to be 100% [10]. The branching ratio for the 11.520 MeV 2^+ state will only be extracted at a later stage upon the completion of detailed angular correlation

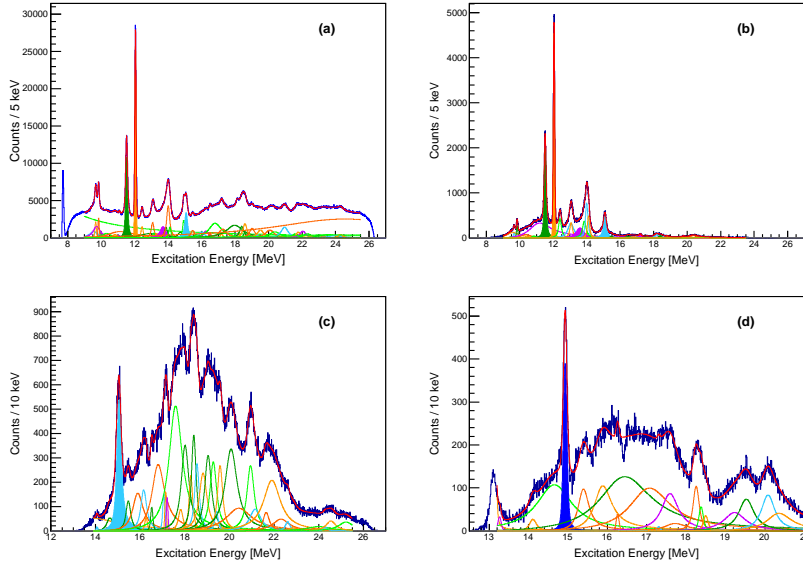


Fig. 4: Experimental and fitted excitation energy spectra for the singles dataset (panel a) as well as the various decay channels summed over all CAKE channels: α_0 (panel b), α_1 (panel c), and p_0 (panel d). Various prominent ^{16}O peaks are highlighted: 11.520 MeV (green), 12.049 MeV (orange), 14.926 MeV (dark blue) and 15.097 MeV (light blue). The red line represents the combined fit.

calculations for this particular experimental setup.

From literature the 15.097 MeV state in ^{16}O is known to have a width of 166 ± 30 keV [10]. The total width extracted in this study from the singles spectrum is 162 ± 4 keV. Assuming isotropic decay from the 0_6^+ state the branching ratios for the α_0 and α_1 decay channels were found to be $70 \pm 2\%$ and $64 \pm 1\%$ respectively. This problematic result follows from the seemingly incorrect assumption that the observed decays originate purely from a 0^+ state. Early indications are that while the angular distribution of the 15.097 MeV α_1 decay channel exhibits an isotropic nature, surprisingly the distribution for the 15.097 MeV α_0 decay channel does not.

It is therefore postulated that there are 2 unresolved states in the region of what is considered to be the 15.097 MeV state in ^{16}O . The angular distribution is indicative of the existence of a 0^+ state combined with a 2^+ state, although the exact nature can only be confirmed after the completion of angular correlation calculations for this experimental setup. The existence of two unresolved states could explain why the experimentally extracted width exceed that of theoretical calculations. Further analysis is underway to extract the angular distributions of the α_0 , α_1 , and p_0 decays in the region of the 15.097 MeV state, which will enable the extraction of accurate branching ratios and exact nature of the spin and parity of the resonances in the $E_x = 15.097$ MeV region.

Acknowledgements

The authors thank the accelerator staff of iThemba LABS for providing excellent beams. This work was supported by the South African National Research Foundation (NRF), and financial support through the NRF Research Infrastructure Support Programme (Grant 86052) is gratefully acknowledged.

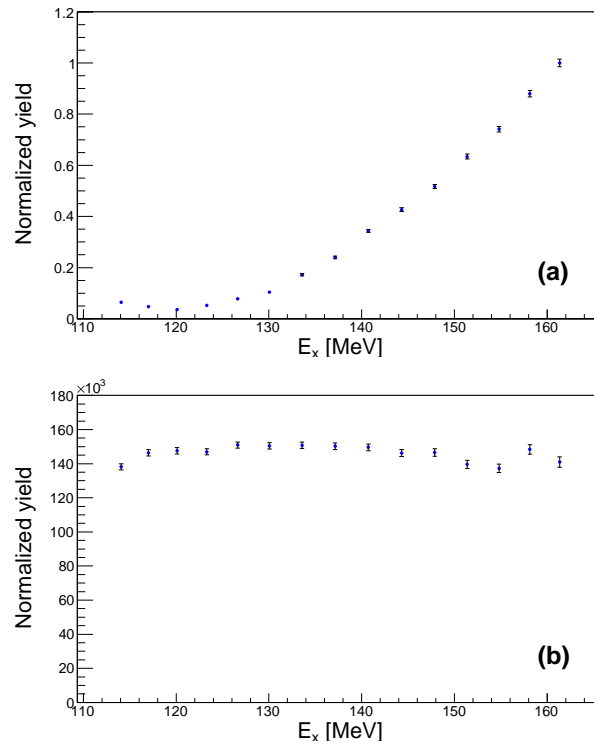


Fig. 5: The angular distribution of the α_0 decay channel of the 11.520 MeV 2^+ (panel a) and 12.049 MeV 0^+ (panel b) states.

References

- [1] M. Freer, Rep. Prog. Phys. 70 (2007) 2149.
- [2] K. Ikeda, N. Takigawa and H. Horiuchi, Japan. Suppl. Prog. Theor. Phys., Extra Number (1968) 464.
- [3] M. Freer, Nature 487 (2012) 309.
- [4] J.-P. Ebran *et al.*, Nature 487 (2012) 341.
- [5] P. Schuck *et al.*, J. Phys.: Conf. Ser. 413 (2013) 012009.
- [6] Y. Funaki *et al.*, Phys. Rev. Lett. 101 (2008) 082502.
- [7] S. Ohkubo and Y. Hirabayashi, Phys. Lett. B 684 (2010) 127.
- [8] Y. Funaki *et al.*, Phys. Rev. C 82 (2010) 024312.
- [9] Y. Funaki *et al.*, Phys. Rev. C 80 (2009) 064326.
- [10] J. H. Kelley *et al.*, Nucl. Phys. A 564 (1993) 1.
- [11] P. J. Haigh *et al.*, J. Phys. G: Nucl. Part. Phys. 37 (2010) 035103.
- [12] C. Wheldon *et al.*, Phys. Rev. C 83 (2011) 064324.
- [13] R. Neveling *et al.*, Nucl. Instr. and Meth. A 654 (2011) 29.
- [14] P. Papka *et al.*, Journal of Radioanalytical and Nuclear Chemistry 03 (2015) 305.
- [15] Maximum Integration Data Acquisition System (MIDAS), TRIUMF, <https://midas.triumf.ca>.
- [16] National Nuclear Data Center, information extracted from the Chart of Nuclides database, <http://www.nndc.bnl.gov/chart/>

Testing two-nucleon transfer reaction mechanism with elementary modes of excitation in exotic nuclei

R.A. Broglia^{1,2}, G.Potel^{3,4}, A. Idini⁵, F. Barranco⁶ and E. Vigezzi⁷

¹Dipartimento di Fisica, Università di Milano, Via Celoria 16, I-20133 Milano, Italy

²The Niels Bohr Institute, University of Copenhagen, DK-2100 Copenhagen, Denmark

³ National Superconducting Cyclotron Laboratory, Michigan State University, East Lansing, Michigan 48824, USA

⁴ Lawrence Livermore National Laboratory L-414, Livermore, CA 94551, USA

⁵ Department of Physics, University of Jyväskylä, FI-40014 Jyväskylä, Finland

⁶ Departamento de Física Aplicada III, Escuela Superior de Ingenieros, Universidad de Sevilla, Camino de los Descubrimientos, Sevilla, Spain

⁷ INFN Sezione di Milano, Via Celoria 16, I-20133 Milano, Italy

Abstract

Nuclear Field Theory of structure and reactions is confronted with observations made on neutron halo dripline nuclei, resulting in the prediction of a novel (symbiotic) mode of nuclear excitation, and on the observation of the virtual effect of the halo phenomenon in the apparently non-halo nucleus ${}^7\text{Li}$. This effect is forced to become real by intervening the virtual process with an external (t,p) field which, combined with accurate predictive abilities concerning the absolute differential cross section, reveals an increase of a factor 2 in the cross section due to the presence of halo ground state correlations, and is essential to reproduce the value of the observed $d\sigma({}^7\text{Li}(t,p){}^9\text{Li})/d\Omega$.

1. Foreword

At the basis of single-particle motion, fermionic elementary modes of nuclear excitation, one finds delocalization, measured by the quantality parameter ($q \ll 1$ localisation, $q \sim 1$ delocalization [1]), ratio of the kinetic energy (ZPF) of confinement, and of the strength of the NN-interaction ($V_0 = -100$ MeV, $a \approx 1$ fm),

$$q = \frac{\hbar^2}{ma^2} \frac{1}{|V_0|} \approx 0.4. \quad (1)$$

At the basis of BCS pairing one finds Cooper pairs and independent pair motion, in which the partner nucleons are correlated over distances of the order of

$$\xi = \frac{\hbar v_F}{2E_{corr}} \approx 20\text{fm} \quad (2)$$

in keeping with the value of $E_{corr} \approx 1 - 1.5$ MeV (see e.g. [2]) displayed by pair addition and pair subtraction modes [3, 6, 5] around closed shell nuclei ($E_{corr} \approx \Delta$ in superfluid systems (≈ 1.5 MeV in ${}^{120}\text{Sn}$) [6, 4]), and the fact that, for nuclei along the stability valley, $v_F/c \approx 0.3$. The (generalised) quantality parameter associated with Cooper pairs can be redefined as

$$q' = \frac{\hbar^2}{2m\xi^2} \frac{1}{2E_{corr}} \approx 0.02, \quad (3)$$

implying localization. In other words, in a Cooper pair, each nucleon is solidly anchored to its partner leading to an emergent property: rigidity in gauge space. In keeping with the fact that the Cooper pair

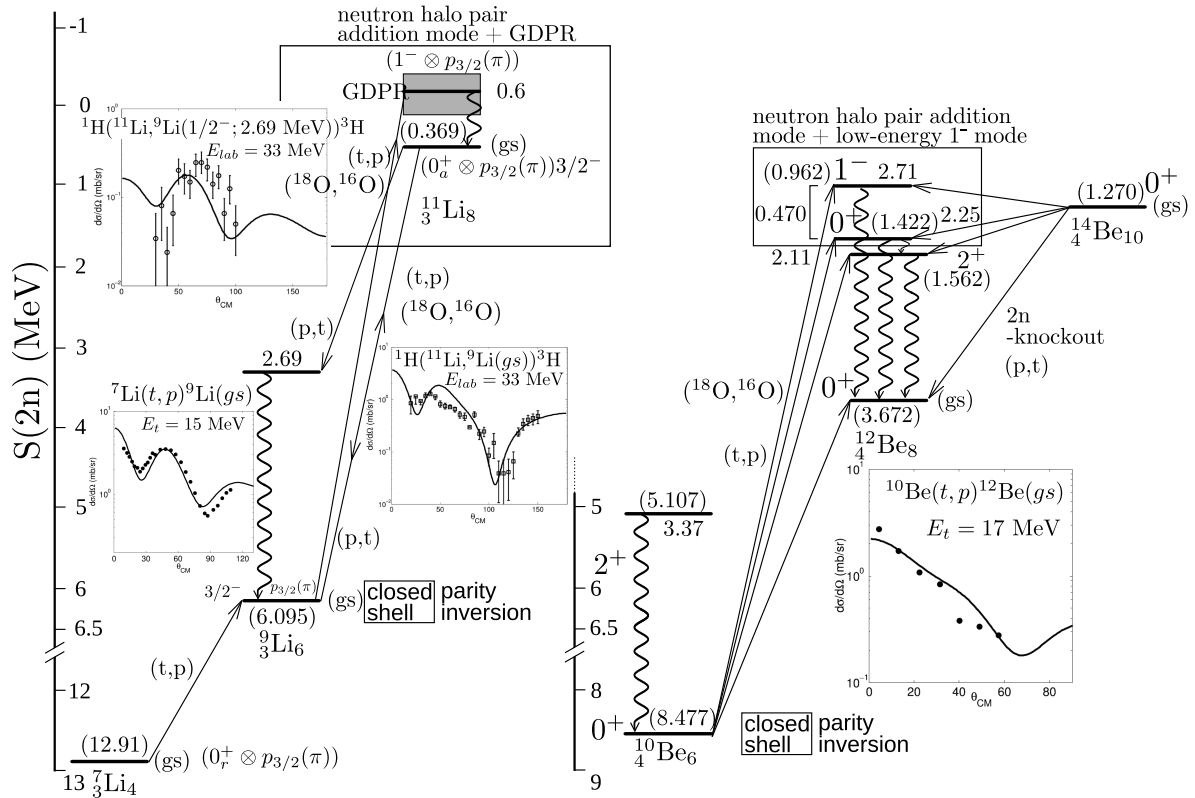


Fig. 1: Monopole pairing vibrational modes associated with $N = 6$ parity inverted closed shell isotopes, together with low-energy $E1$ -strength modes. The levels are displayed as a function of the two-neutron separation energies $S(2n)$. These quantities are shown in parenthesis on each level, the excitation energies with respect to the ground state are quoted in MeV. Absolute differential cross sections from selected (t,p) and (p,t) reactions calculated as described in the text (cf. [17, 18]), in comparison with the experimental data [23, 24].

transfer cross section $\sigma \sim \sum_{\nu>0} U_{\nu} V_{\nu} = (\Delta/G)^2 \sim (N(0))^2$ is proportional to the square of the density of levels $N(0)$, Cooper tunneling takes place essentially as successive transfer (without breaking the pair) as a particle of mass $2m$ which sets instantaneously into rotation (vibration) superfluid (normal) nuclei, in gauge space [5]. Adding to independent particle motion and pair addition and subtraction modes correlated particle-hole vibrations, complete the elementary modes of excitation count [3] around closed shell nuclei. This basis of states is able to provide a first overall picture of the low energy spectra as probed by nuclear reactions.

However, the basis is non-orthogonal and violates Pauli principle, in keeping with the fact that all the degrees of freedom of the nucleus are exhausted by the nucleonic degrees of freedom. Pauli exchanging and orthogonalizing it with the help of NFT rules [7]-[10], together with two-nucleon transfer reaction theory (second order DWBA describing simultaneous and successive transfer corrected for non-orthogonality, see refs. [11, 12, 13] and refs. therein), one can calculate the variety of absolute cross sections and transition probabilities which can be directly compared with the experimental data.

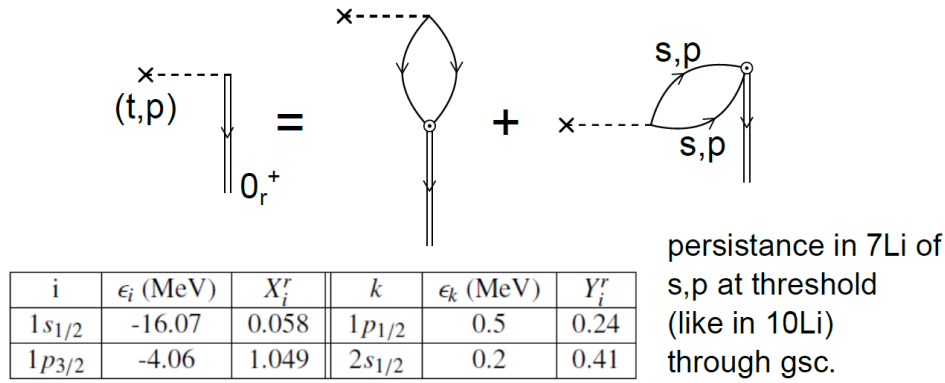


Fig. 2: RPA wavefunction of the pair removal mode ($|gs({}^7\text{Li})\rangle$) of the closed shell $N = 6$ parity inverted system ${}^9\text{Li}$ obtained solving the dispersion relation graphically displayed in the upper part of the figure.

2. Pairing vibrations of N=6 magic number isotopes

As a result of the (mainly quadrupole) dressing and Pauli exchange of the $2s_{1/2}$ and of the $1p_{1/2}$ orbitals respectively [15, 14], parity inversion takes place in an island of light nuclei at the drip line. As a result, the $N = 8$ closed shell dissolves, $N = 6$ becoming a novel magic number. This has profound effects in the associated (multipole) pairing vibrational spectrum. In particular for ${}^9\text{Li}_6$, in which case one is confronted with exotic monopole and dipole pair addition modes ($|{}^{11}\text{Li}(\text{gs})\rangle$, $|{}^{11}\text{Li}(1^-; 0.4\text{MeV})\rangle$) namely the Giant Dipole Pygmy Resonance (GDPR) and with an, apparently, normal pair removal mode ($|{}^7\text{Li}(\text{gs})\rangle$). At the basis of the almost degenerate 0^+ and 1^- pair addition modes one finds the fact that in ${}^{10}\text{Li}$ (not bound) the $s_{1/2}$ and $p_{1/2}$ orbitals are both at threshold lying close in energy ($\epsilon_{s_{1/2}} \approx 0.2$ MeV, $\epsilon_{p_{1/2}} \approx 0.5$ MeV). They are thus not available to contribute to standard nuclear Cooper pairing (1S_0 short range NN-potential). Induced pairing becomes overwhelming. In keeping with the heavily dressed inverted pairing s, p orbitals, the GDPR mode ($E_x \leq 1$ MeV, $\approx 8\%$ of TRK) exchanged between $s_{1/2}^2(0)$ and $p_{1/2}^2(0)$ configurations provides most of the glue binding the halo neutron Cooper pair to the core ${}^9\text{Li}$ [14], as testified by ${}^1\text{H}({}^{11}\text{Li}, {}^9\text{Li}(\text{gs})){}^3\text{H}$ absolute cross section. The population of the first excited state of ${}^9\text{Li}$ (${}^1\text{H}({}^{11}\text{Li}, {}^9\text{Li}(1/2^-)){}^3\text{H}$) provides information on phonon induced pairing mechanism [16, 17, 18]. This is the reason why the pair of symbiotic states under discussion are boxed in Fig. 1. They are expected to be a new (composite) elementary mode of excitation.

Turning back to the probing of this 1^- mode, it could be illuminating in shedding light into its actual structure (low energy E1-vortex-like mode, i.e. a Cooper pair with angular momentum and parity 1^-), to carry out the ${}^9\text{Li}(t,p){}^{11}\text{Li}$ reaction. Aside from weak Q -value effects and simple geometrical factors, one will be able to relate the "intrinsic" contribution to the absolute cross sections associated with the population of the ground state and of the 1^- state¹. One can then test the role ground state correlations (gsc) play in both states. To the extent that the 1^- state can be viewed as a particle-hole-like (2qp) excitation, gsc will decrease the cross section, the inverse being expected to be the case if this state is the dipole pair addition mode of ${}^9\text{Li}$ (vortex-like Cooper pair). These effects should be reversed concerning the intensity of the γ -decay, as discussed in [19]. How these relations get qualified in the case of the exotic system under discussion is an open question, which may benefit from the analogies to be drawn concerning the situation encountered in connection with the first 0^{+*} excited state of ${}^{12}\text{Be}$.

In fact, it is posited that the pair of $0^{+*}, 1^-$ (boxed) states of ${}^{12}\text{Be}$ displayed in Fig. 1, are (part

¹These two states paradigmatically represent the competition between paired and aligned coupling schemes, which play such an important role in defining e.g. quadrupole shape transitions (see ref. [4] and refs. therein).

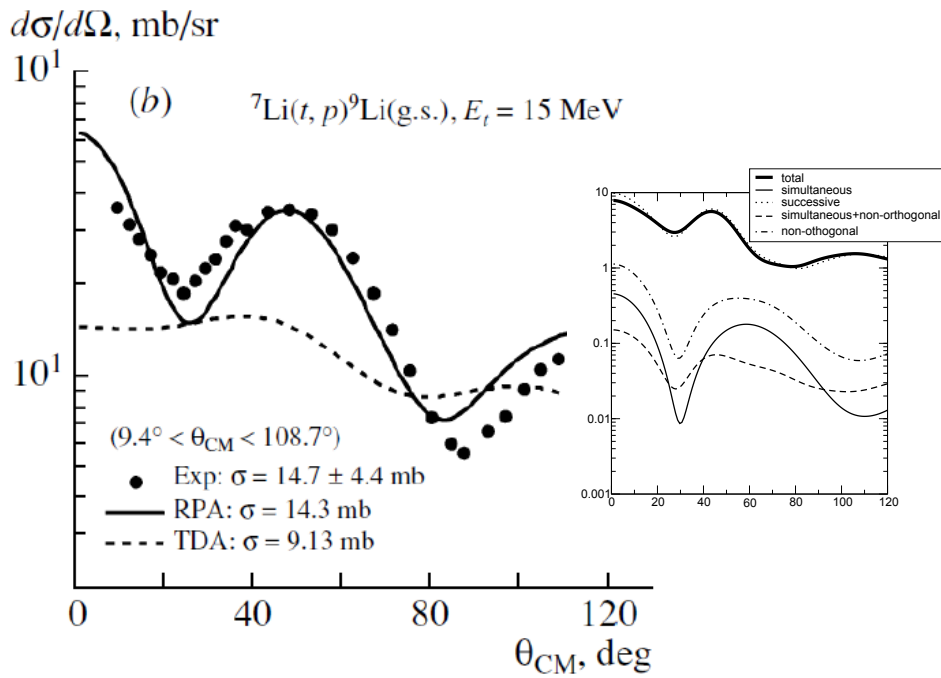


Fig. 3: Absolute differential cross section associated with the reaction ${}^7\text{Li}(t,p){}^9\text{Li}(\text{gs})$ calculated making use of the forwardgoing and backwards going amplitudes displayed in fig. 2. The dashed curve corresponds to the result obtained by neglecting the backwards going amplitudes, normalising the X's to 1 (TD approximation). In the inset the variety of contributions (successive, simultaneous, non-orthogonality) to the cross section are shown.

of ?) the corresponding symbiotic states of ${}^{11}\text{Li}$, modified by the extra binding energy provided by the fourth proton. In this case, the possibility of studying the new proposed elementary mode of excitation with a variety of probes is richer, due to the greater stability of the $|{}^{12}\text{Be}(0^{+*}, 2.24 \text{ MeV})\rangle$ state as compared to the $|{}^{11}\text{Li}(\text{gs})\rangle$.

It is quite suggestive the presence in ${}^{12}\text{Be}$, of a quadrupole pair addition mode almost degenerate with the halo monopole pair addition mode 0^{+*} . One can thus expect important quadrupole dynamic deformation effects resulting from this degeneracy. Within this context, parity inversion arises because of Pauli repulsion between the $p_{1/2}$ nucleon in ${}^{10}\text{Li}$ (${}^{11}\text{Be}$) and that participating in the quadrupole vibration of the core (${}^9\text{Li}$, ${}^{10}\text{Be}$). The polarization self energy processes make the $s_{1/2}$ particle heavier and thus closer to becoming bound [20, 21], see also [22].

The fact that one is now able to accurately calculate two-nucleon transfer absolute differential cross sections [13] opens a number of possibilities, in particular to find new elementary modes of excitation in exotic nuclei. A simple, but nonetheless instructive example of the consistency of the physics and associated accuracy of the results which is at the basis of clothed, physical elementary modes of excitation as building blocks of the nuclear spectrum, is provided by the ${}^7\text{Li}(t,p){}^9\text{Li}(\text{gs})$ absolute differential cross section. As seen from Figs. 1 and 3, theory provides an accurate account of the experimental findings [18, 23]. The two-nucleon spectroscopic amplitudes were calculated by solving the $\alpha = -2$ monopole dispersion relation [5, 18] in the RPA. The results are shown in Fig. 2. Eliminating ground state correlations theory underpredicts experiment by about 50% (cf. Fig. 3). In other words, even the ground state of an apparent "normal" nucleus like ${}^7\text{Li}$ ($S_{2n} = 12.91 \text{ MeV}$), resents of the properties displayed by the exotic nucleus ${}^{11}\text{Li}(\text{gs})$. In fact, the population of the pair removal

mode through ground state correlation proceeds by the pick-up of s, p parity-inverted orbits, typical of the neutron halo pair addition mode.

Within this context one expects that much insight on the interplay between the GPDR and the monopole neutron halo pair addition modes emerges from the systematic study of the reactions $^{10}\text{Be}(p,t)^8\text{Be}(\text{gs})$, $^8\text{Be}(t,p)^{10}\text{Be}$, $^{10}\text{Be}(t,p)^{12}\text{Be}$, $^{14}\text{Be}(p,t)^{12}\text{Be}$ as well as those associated with $(p,p2n)$ knockout reactions and eventually $2n$ -transfer induced by heavy ions (e.g. $^{18}\text{O}, ^{16}\text{O}$) (Fig. 1). An important example of such insight is provided by the fact that while the cross sections associated with the ground state and two-phonon (normal) monopole pairing vibrational states ($E_x \approx 4.8$ MeV in ^{10}Be), i.e. $d\sigma(^8\text{Be}(t,p)^{10}\text{Be}(\text{gs}))/d\Omega$ and $d\sigma(^8\text{Be}(t,p)^{10}\text{Be}(0^+; 4.8 \text{ MeV }))/d\Omega$ are expected to have the same order of magnitude (cf. Fig. 13 of [18]), that associated with the 0^{+*} state in ^{12}Be is predicted to be much smaller (observable?), reflecting the poor overlap between halo and core nucleons [24] (within this context see Table 3 of ref. [18] and associated discussion).

Arguably, one would be able to state that a real understanding of the neutron halo pair addition pattern displayed in Fig. 1 has been obtained, once the two-nucleon transfer predictions are tested, supplemented with one-particle and γ -decay data, worked out making use of microscopically calculated optical (polarization) potentials, with the help of the same physical modes to be probed.

References

- [1] B.R. Mottelson, , in *Trends in nuclear physics, 100 years later*, Proc. of Les Houches summer school, Session LXVI, Elsevier , p. 25 (1998)
- [2] R.A. Broglia, V. Paar and D.R. Bès, *Phys. Lett. B* **37** (1971) 159
- [3] A. Bohr, in *Comptes Rendus du Congrès International de Physique Nucléaire*, Vol. I, P. Gugenberger ed., Paris p. 487 (1964)
- [4] A. Bohr and B.R. Mottelson, *Nuclear structure*, Vol. II, Benjamin, New York (1975)
- [5] D. R. Bes and R.A. Broglia, *Nucl. Phys.* **80**, 289 (1966)
- [6] A. Bohr and B.R. Mottelson, *Nuclear structure*, Vol. I , Benjamin, New York (1969)
- [7] D. R. Bès *et al.*, *Nucl. Phys.* **A260**, 1 (1976)
- [8] D. R. Bès *et al.*, *Nucl. Phys.* **A260**, 27 (1976)
- [9] D. R. Bès *et al.*, *Nucl. Phys.* **A260**, 77 (1976)
- [10] P. F. Bortignon, R.A. Broglia, D. R. Bès and R. Liotta, *Phys. Rep.* **30C**, 305 (1977)
- [11] R.A. Broglia and A. Winther, *Heavy ion reactions*, Addison-Wesley, Menlo Park (1999)
- [12] R.A. Broglia, O. Hansen and C. Riedel, *Adv. Nucl. Phys.* **6** (1973) 287
- [13] G. Potel *et al.*, *Rep. Prog. Phys.* **76**, 106301 (2013)
- [14] F. Barranco *et al.*, *Eur. Phys. J. A* **11**, 385 (2001)
- [15] H. Sagawa, B.A. Brown and H. Esbensen, *Phys. Lett. B* **309** (1993) 1
- [16] I. Tanihata *et al.*, *Phys. Rev. Lett.* **100** (2008) 192502
- [17] G. Potel, F. Barranco, E. Vigezzi and R.A. Broglia, *Phys. Rev. Lett.* **105** (2010) 172502
- [18] G. Potel *et al.*, *Phys. At. Nucl.* **77** (2014) 941
- [19] R.A. Broglia, C. Riedel and T. Udagawa, *Nucl. Phys. A* **169** 225 (1971)
- [20] F. Barranco, P.F. Bortignon, R.A. Broglia, G. Colò and E. Vigezzi, *Eur. Phys. J. A* **11**, 305 (2001)
- [21] G. Gori, F. Barranco, E. Vigezzi and R.A. Broglia, *Phys. Rev. C* **69**, 041302(R) (2004)
- [22] I. Hamamoto and S. Shimoura, *J. Phys. G* **34**, 2715 (2007)
- [23] P.G. Young and R.H. Stokes, *Phys. Rev. C* **4** (1971) 1597
- [24] H. T. Fortune, G.B. Liu and D.E. Alburger, *Phys. Rev. C* **50** (1994) 1355

Investigation of Pygmy Dipole Resonance in neutron rich exotic nuclei

R.Avigo^{1,2}, O.Wieland¹, A.Bracco^{1,2}, F.Camera^{1,2} on behalf of the AGATA collaboration

¹ INFN, sezione di Milano

² Università degli Studi di Milano

Abstract

The electric dipole response of atomic nuclei is presently attracting large attention from the nuclear physics community. In particular the E1 strength, located around the particle separation energy (6-12 MeV), commonly called Pygmy Dipole Resonance (PDR), is the object of a large experimental and theoretical effort to investigate the properties and the correlations with nuclear structure. In spite of the large amount of data about E1 strength distribution in stable nuclei, very few data are available in neutron rich exotic nuclei. A measurement to search for the pygmy dipole resonance in ^{64}Fe and ^{62}Fe nuclei was performed in GSI in 2012 and concluded in 2014, during the PreSPEC – AGATA experimental campaign. The PDR excitation was obtained through relativistic Coulomb excitation in inverse kinematics. This reaction mechanism coupled with the detection of gamma rays emitted by excited nuclei is a well established experimental technique to investigate nuclear properties in the energy region of pygmy.

1 Introduction

The E1 response of atomic nuclei has provided in the past important information about nuclear structure. In particular Giant Dipole Resonance (GDR) has proved to be one of the building blocks for nuclear models. The GDR dominates the dipole response of nuclei in all region of mass; it was widely studied and used as a tool to investigate nuclear features.

In last decades, the so-called Pygmy Dipole Resonance (PDR) has attracted a lot of interest: in spite of the fact its nature has not been fixed yet, connections with both nuclear structure and astrophysics were demonstrated [1,2,3]. An amount of E1 strength, corresponding to few percentage of the total strength, was measured around one particle separation energy in wide regions of mass[4]. A systematic experimental investigation has been carried on about stable nuclei, while data available about exotic nuclei are still scarce.

2 The experiment and the data analysis

The measurement here discussed was performed at GSI laboratories, during PreSPEC-AGATA campaign[5], aiming to investigate the dipole response below the particle threshold of exotic Iron isotopes $^{62,64}\text{Fe}$. In particular this will provide the evolution of this dipole strength at varying the neutron number. Analogue measurements were already performed for stable nuclei [6]: this measurement will allow to add information in exotic medium mass region.

The experimental technique used in this experiment, consisted in relativistic coulomb excitation in inverse kinematics coupled with the gamma decay measurement. The advantage of coulomb interaction at relativistic beam energy consists in a selection of dipole excitation against higher multiplicities.

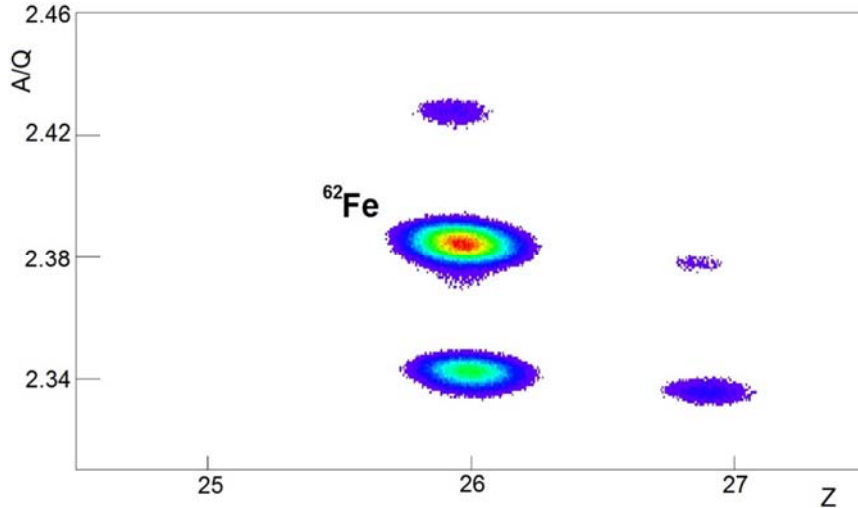


Fig. 1: Exemplum of identification of the beam impinging on secondary target.

The radioactive $^{62,64}\text{Fe}$ beams were produced by fragmentation of the primary ^{86}Kr beam delivered by the SIS synchrotron at 700 or 900 AMeV and focused on a Be target. The ions of interest were identified, selected and transported with the fragment separator FRS (Fig.1). The beam cocktail at 400-410 AMeV was then impinging on the Pb target (1 g/cm^2 thick) or Au target (2 g/cm^2 thick), which were surrounded by the γ -ray detectors. Coulomb excitation events were selected using LYCCA array [7]. E- ΔE telescopes provided identification of products from reactions on the secondary target, while ion tracking detectors were used to reconstruct the beam scattering angle. Selection of $^{62,64}\text{Fe}$ ions impinging and outgoing from the secondary target coupled with a required forward scattering angle, corresponding to a minimum impact parameter higher than 14 fm, guaranteed a pure coulomb interaction dataset.

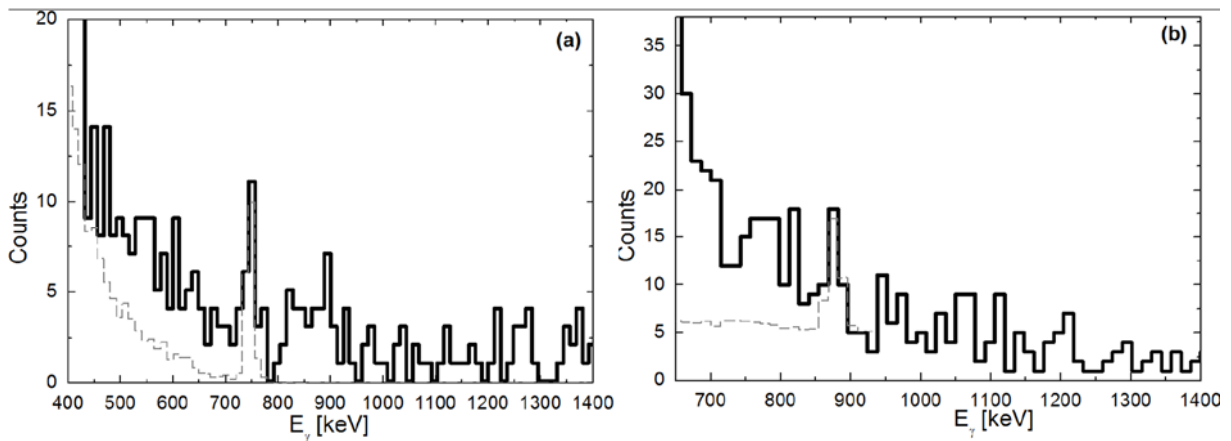


Fig. 2 : (a) AGATA energy spectrum for ^{64}Fe with a peak at first $2+$ state energy (746 keV); (b) AGATA energy spectrum for ^{62}Fe with a peak at first $2+$ state energy (877 keV). In both panels dashed line represents GEANT4 simulations

The gamma decay measurement was performed using AGATA array[8] combined with LaBr scintillators array (HECTOR⁺, [9]). AGATA array provided high energy resolution, thanks to the intrinsic properties of HPGe detectors and also the electrical segmentation that is exploited to reduce the Doppler broadening. In addition γ -ray tracking algorithms[10] were used for background suppression. LaBr scintillators, on the other hand, are characterized by high efficiency and good timing. AGATA γ -ray spectra at low energy, related to coulomb excitation dataset, show a peak at the energy

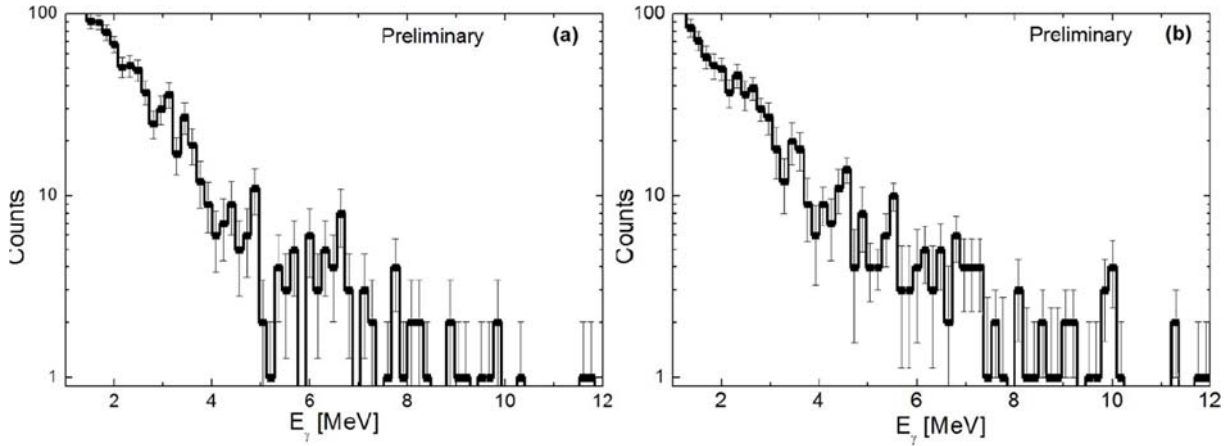


Fig. 3 : panel (a), Preliminary AGATA energy spectrum for ^{64}Fe in the range 1-12 MeV. Panel (b), Preliminary AGATA energy spectrum for ^{62}Fe in the range 1-12 MeV.

of the first 2^+ state decay for both the isotopes, 746 keV for ^{64}Fe and 877 keV for ^{62}Fe (Fig. 2a,b). The width of the measured peaks was also compared with the width expected by GEANT4[11] simulations for AGATA detectors. The comparison shows a good agreement between measurement and simulation. 2^+ state decay measurement is a key point because it provides a normalization for cross section, essential to deduce the $B(E1)$ values related to high energy γ -ray transitions.

Preliminary AGATA high energy γ -ray spectra, shows some structures in the energy range of 6-8 MeV (Fig. 3). The multipolarity character of this γ -ray data was investigated. We evaluated the ratio between the E2 and E1 emission at different summed angles, this ratio was compared with the ratio between the summed angular distribution of data from 2^+ decay and the data above 6 MeV. As shown in Fig. 4, though the width of error bars is quite large, the experimental data follows the expected trend. This comparison, coupled with reaction mechanism that select dipole excitation, shows that the high energy data are related to E1 transitions.

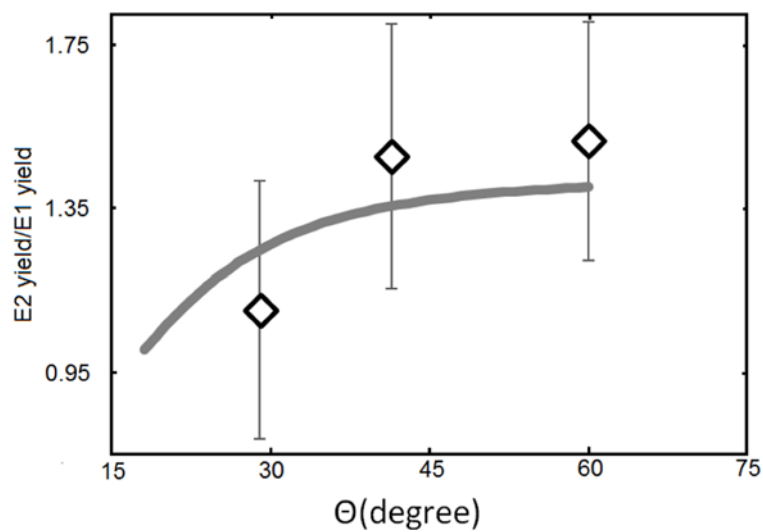


Fig. 4: Ratio of E2 yield with E1 yield at different summed angles. Grey line is the expected trend, considering the beam energy and the efficiency of gamma detectors; the squared points the experimental data.

3 Conclusion

A measurement of E1 response of $^{62,64}\text{Fe}$ below the one particle separation energy was performed in GSI laboratories during PreSPEC-AGATA experimental campaign. The experimental investigation consisted in relativistic coulomb excitation in inverse kinematics and measurement of the gamma decay. The data analysis is still on going. The results obtained at this point of the analysis show that the data collected will allow to evaluate the B(E1) values of high energy γ -ray transition for both of the nuclei.

References

- [1] A. Klimkiewicz, et al., Phys. Rev. C76, 051603 (2007).
- [2] A. Carbone et al. Phys. Rev. C 81 (2010) 041301(R).
- [3] J. Piekarewicz J. Phys.: Conf. Ser. 420 012143.
- [4] D. Savran, T. Aumann, A. Zilges PPNP 70(2013)210-245.
- [5] N. Pietralla et al., EPJ Web of Conferences 66, 02083 (2014).
- [6] R. Massarczyk et al. Phys. Rev. Lett. 112 (2014) 072501
- [7] P. Golubev et al., Nucl. Instrum. and Meth. In Phys. Res. A 723 (2013) 55-66.
- [8] S. Akkoyun et al., Nucl. Instrum. and Meth. In Phys. Res. A 668 (2012) 26.
- [9] A. Giaz et al., Nucl. Instrum. and Meth. In Phys. Res. A 729,913 (2013).
- [10] D. Bazzacco Nucl. Phys. A 746,248(2004).
- [11] E. Farnea et al., Nucl. Instrum. and Meth. In Phys. Res. A 621,331 (2010).

Thermal and fast neutron detection with two CLYC scintillators

A.Giaz¹, F.Camera¹⁻², N.Biasi¹, S.Brambilla¹, S.Ceruti¹⁻², B. Million¹, L.Pellegrini¹, S.Riboldi¹⁻²

¹INFN Sezione di Milano, Milano, Italy

²Università degli studi di Milano, Milano, Italy

Abstract

The CLYC scintillator has the capability to identify gamma rays and fast/thermal neutrons and it is characterized by a good properties for the gamma ray detection. In this work, the response to thermal and fast neutrons of two CLYC 1"x1" crystals (one enriched with ⁷Li and one with ⁶Li) was measured. The thermal neutrons were measured using both detectors. The measurements of fast neutrons were performed at Neutron Generator facility (Frascati, Italy) and at CN accelerator of LNL. At the neutron generator facility, neutrons at 2.5 and 14.1 MeV were measured. The response to fast neutrons was measured also from 1.9 MeV up to 3.8 MeV at LNL.

1 Introduction

The crystal Cs₂LiYCl₆:Ce (CLYC) it is a very interesting scintillator material because of its excellent energy resolution and its capability to identify gamma rays and fast/thermal neutrons. The crystal Cs₂LiYCl₆:Ce contains ⁶Li and ³⁵Cl isotopes, therefore, it is possible to detect thermal neutrons through the reaction ⁶Li(n,α)t (cross section of 940 barns). While ³⁵Cl ions allows to measure fast neutrons through the reactions ³⁵Cl(n, p)³⁵S and ³⁵Cl(n, α)³²P (the cross section is of the order of 0.1 barns) [1-6]. In this work, the response to thermal and fast neutrons of two CLYC 1"x1" crystals was measured: the first one, enriched with ⁶Li at 95%, is ideal for thermal neutron measurements (CLYC-6) while the second one, with an enrichment of ⁷Li higher than 99% (CLYC-7), is suitable for fast neutron measurements.

Thermal neutrons from an AmBe source were measured using both detectors, in the gamma spectroscopy laboratory of the University of Milano, Italy. The measurements of fast neutrons were performed at Frascati (Italy) Neutron Generator facility where a deuterium beam was accelerated on a deuterium or on a tritium target, providing neutrons of 2.5 MeV or 14.1 MeV, respectively. The response to fast neutrons was measured also at CN accelerator of Laboratori Nazionali di Legnaro (LNL), Italy. At LNL a proton beam was accelerated at 5.5, 5 and 4 MeV on a ⁷LiF target, to produce neutron with energy from 1.9 up to 3.8 MeV. The detector were placed at 0° or at 90° from the target to have for each beam energy two different neutrons energies.

The thermal neutron measurements are described in section 2. It is focuses on the differences between CLYC-6 and CLYC-7. Section 3 describes the fast neutron detection. In particular, section 3.1 is dedicated to the measurements performed at Neutron Generator of ENEA Laboratories in Frascati. Section 3.2, instead is dedicated to fast neutron detection exploiting both energy signal and the Time of Flight (TOF) technique at LNL. The conclusions of the work are in section 4.

2 Thermal Neutron Measurements

The thermal detection capability arises from ⁶Li ions, which have a 940 barns cross section for the reaction ⁶Li (n,α)³H [3]. Thermal neutrons were measured with both CLYC-6 and CLYC-7 crystals placed in the same position relative to the AmBe source.

The only difference between the two crystals is the Li isotope enrichment. In particular, as already mentioned, our CLYC-7 crystal has an enrichment of ${}^7\text{Li}$ higher than 99% while the CLYC-6 detector has an enrichment of $\sim 95\%$ of ${}^6\text{Li}$. These two different isotopes produce different sensitivity to thermal neutrons. In figure 1 the comparison between the energy spectra measured with the CLYC-6 and the CLYC-7 detectors are shown in left and right panel respectively. Both detectors were placed over a 40 cm box of paraffin with a source of AmBe in the centre. The spectra of figure 6 are normalized on the ${}^{137}\text{Cs}$ peak. The 3.2 MeV electron equivalent peak, induced by thermal neutrons, clearly visible in CLYC-6 spectrum, is absent in the CLYC-7 one. By estimating the counts in the thermal neutron peak, we can conclude that the CLYC-7 detector has an efficiency to thermal neutrons of $\sim 0.3\%$ with respect to the CLYC-6 one. Similar results were observed by D'Olympia *et al.*, as shown in Ref. [4].

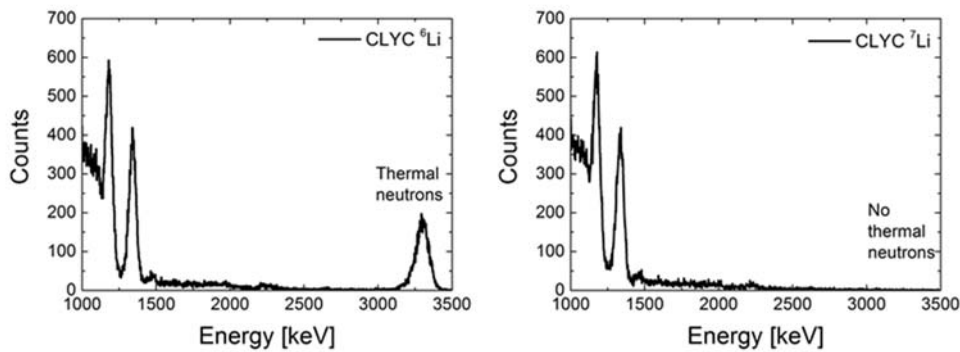


Fig. 1: the energy spectra measured with CLYC-6 (left panel) and CLYC-7 (right panel), respectively. An AmBe(Ni) source in a paraffin box and a ${}^{60}\text{Co}$ and a ${}^{137}\text{Cs}$ were present.

3 Fast Neutrons Measurements

Fast neutrons are detected exploiting the reactions ${}^{35}\text{Cl}(n, p){}^{35}\text{S}$ and ${}^{35}\text{Cl}(n, \alpha){}^{32}\text{P}$. The energy of the outgoing proton or α particle is linearly related to the neutron energy. For this reason, CLYC scintillators are neutron spectrometers. Furthermore, the neutron kinetic energy can also be measured via the Time of Flight technique (FWHM < 1 ns) [5-6].

3.1 Fast Neutron Measurements at Neutron Generator

A measurement was performed at the Neutron Generator at ENEA laboratories in Frascati (Italy), which provided a monochromatic beam of 14.1 MeV and ~ 2.5 MeV neutrons. The two CLYC scintillators were coupled with HAMAMATSU R6233-100Mod photomultiplier tubes (PMT) and with two standard HAMAMATSU E1198-26 and E1198-27 voltage dividers. The signal of both detectors were digitized using Le Croy waverunner HDO 6054 12 bit oscilloscope.

The 14.1 MeV neutron emission was obtained by bombarding a tritium doped titanium target with a 300 keV deuterium beam [7]. The neutron beam at 2.5 MeV was produced by the primary beam impinging on the beam dump, containing deuterium atoms. For this reason, the flux of the 2.5 MeV neutrons was weaker and less monochromatic than the flux of the 14.1 MeV neutrons. The two samples of CLYC scintillators were placed at 1.25 m from the neutron source. The neutron generator is at 4.5 m from the floor and walls, to reduce the thermal neutron background. Both CLYC detectors were used for the measurement of 14.1 MeV neutrons, whereas only CLYC-7 was used to detect neutrons at 2.5 MeV since the energy of the thermal-neutron peak is expected to overlap with the proton energy produced by the ${}^{35}\text{Cl}(n,p){}^{35}\text{S}$ reaction, because of the Q-value of the reaction, 0.6 MeV, to be added to the neutron energy.

The left and right panels of figure 2 show the PSD matrices obtained with 14.1 MeV neutrons measured in CLYC-6 and in CLYC-7 respectively. In both cases, the discrimination between gamma rays and neutrons is clearly visible. The thermal neutron peak is present only in the left panel of figure 2 at about 3.2 MeVee. In the figure, the neutron events show two components probably due to protons and α particles produced by the two reactions on ^{35}Cl as suggested in Ref [4]. The neutron contribution appears as a continuum without any distinct peak. This feature may be connected to the different two-body and three-body reaction mechanisms that may occur in these crystals with neutrons of 14.1 MeV.

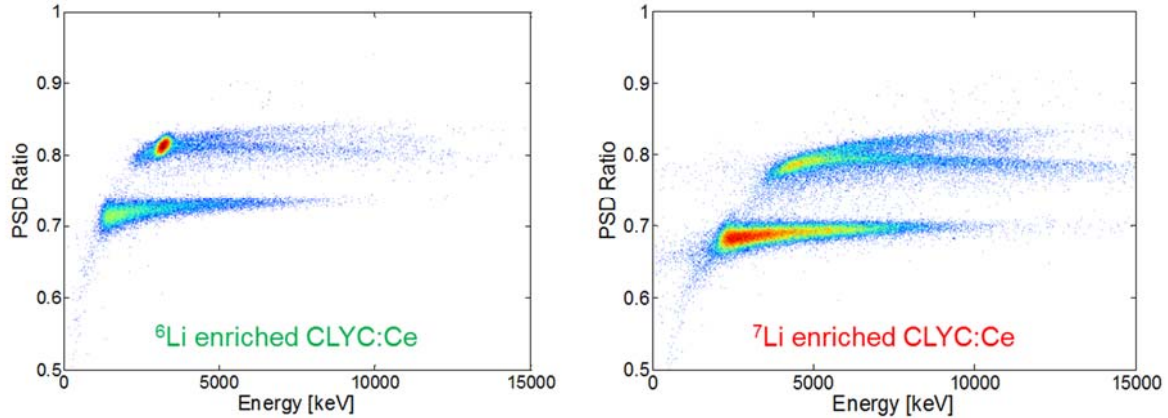


Fig. 2: the PDS matrixes obtained with fast neutrons of 14.1 MeV with CLYC-6 (left panel) and CLYC-7 (right panel), respectively. The matrix obtained with CLYC-6 shows thermal-neutron peak. The peak is located at $x \sim 3200$ and $y \sim 0.8$. The z axis is in log scale.

Figure 3 shows the resulting PSD matrix at 2.5 MeV measured with CLYC-7 scintillator. The fast neutron are highlighted by a red circle in the figure. The FWHM of the proton peak is dominated by the spread in the incident neutron energy. The additional time of flight measurement would allow the clean distinction between thermal and 2.5 MeV neutrons (see section 3.2).

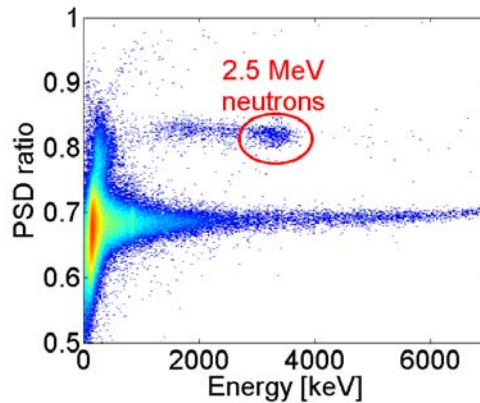


Fig. 3: The PDS matrix obtained with fast neutron of 2.5 MeV measured with CLYC-7 scintillator. The neutron peak, related to reaction $^{35}\text{Cl}(n, p)^{35}\text{S}$ is indicated by the circle. The z axis is in log scale.

3.2 Fast Neutron Measurements at LNL

The measurements were performed at LNL, on April 2015. The neutrons were produced making a proton beam impinging on a ^7LiF target. We selected different proton beam energies (4.5 – 5 – 5.5 MeV) to produce neutrons with energies from 1.9 MeV (detector at 90° – proton beam energy 4.5 MeV) up to 3.8 MeV (detector at 0° – proton beam energy 5.5 MeV). Exploiting the RF time signal, it was also possible to measure the neutron kinetic energy with the TOF technique.

The two cylindrical 1" x 1" CLYC scintillators were coupled with HAMAMATSU R6233-100Sel photomultiplier tubes (PMT) and with two standard HAMAMATSU E1198-26 and E1198-27 voltage dividers. The detectors were placed at 0.7 m from the target for the TOF measurements and at 0° and 90°, from the beam line, to measure of each proton beam energy two different neutrons energies. The anode signal was digitized with a 12 bit, 600 MHz LeCroy waverunner HRO 66Zi oscilloscope (digital acquisition system). The energy spectra were obtained by integrating the signal for 3 μ s. In the digital acquisition system, the neutron gamma discrimination was performed by integrating the signals within two different windows: the first one (W1) from the onset of the signal to 80 ns, the second one (W2) from 100 ns to 600 ns. The PSD ratio was defined as: $R=W2/(W2+W1)$ to be used to discriminate between gamma ray and neutrons. A digital CFD algorithm was used to provide the time spectra. The trigger of the experiment (for both the acquisition system) was the coincidence between the OR of the two CLYC detectors and the pulse beam.

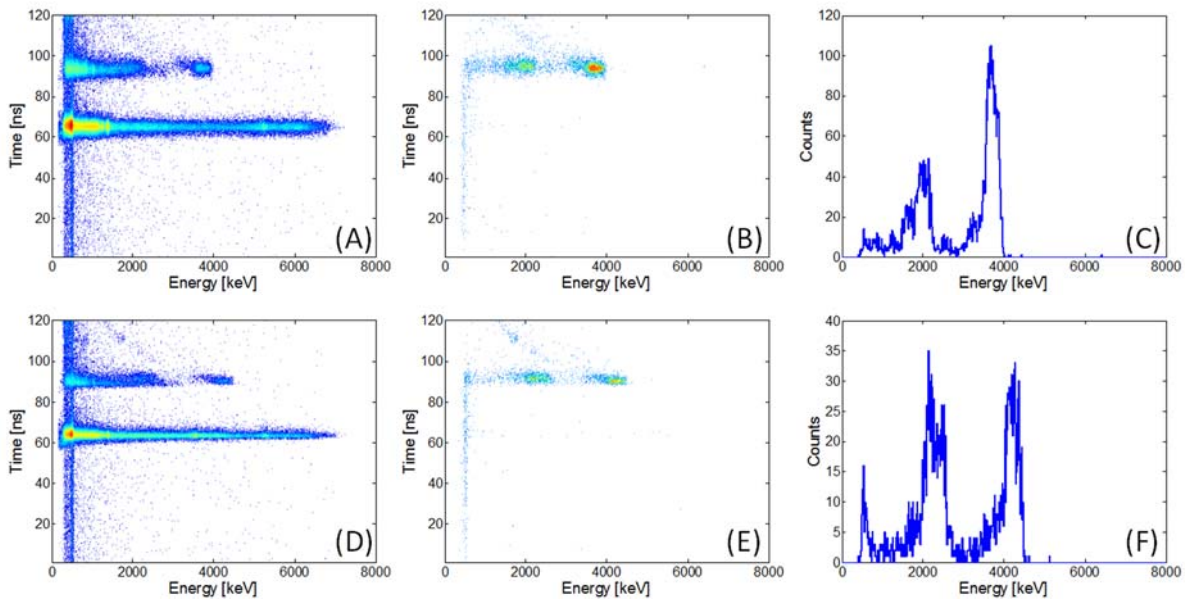


Fig. 4: Panel (A): The time vs energy matrix of the CLYC-7 scintillator. The proton beam energy was 5 MeV and the detector was placed at 0°. Panel (B): The same matrix of panel (A) with the condition that the events have to be discriminated as neutrons from the PSD. Panel (C): The measured energy spectrum of the neutrons. The neutron events were selected by the PSD and by the TOF. The two peaks of the reaction $^{35}\text{Cl}(n, p)^{35}\text{S}$ and $^{35}\text{Cl}(n, \alpha)^{32}\text{P}$ are visible. Panels (D), (E) and (F) are the same of panels (A), (B) and (C), the difference is the neutron energy. The z axis of the matrix is in log scale.

Figure 4 shows the preliminary results of the experiment, using the digital acquisition system. Only two of the six configuration (three proton energies and two detector angles) measured during the experiment are shown in figure 3. The results for CLYC-7 scintillator are reported. Panels (A) and (D) show the time vs energy matrix. The proton beam energy was 5 and 5.5 MeV for top panels ((A)-(B)-(C)) and for bottom panels ((D)-(E)-(F)), respectively. The detector was placed at 0°, therefore the neutrons are expected with an energy of 3.3 and 3.8 MeV for panels top panels ((A)-(B)-(C)) and for bottom panels ((D)-(E)-(F)), respectively. Panels (B) and (E) show the same matrix of panels (A) and (D) selecting neutrons using PSD. The TOF difference between panel (B) and panel (E) is about ~ 2 ns. Panels (C) and (F) show the measured energy spectra of the neutrons. The neutron events was selected by the PSD and by the TOF. The two peak of the reaction $^{35}\text{Cl}(n, p)^{35}\text{S}$ and $^{35}\text{Cl}(n, \alpha)^{32}\text{P}$ are visible. The peak of $^{35}\text{Cl}(n, p)^{35}\text{S}$ of panel (C) is at ~ 3.9 MeV (3.3 MeV plus the Q value of 0.6 MeV), while the same peak of panel (F) is at ~ 4.4 MeV (3.8 MeV plus the Q value of 0.6 MeV).

Similar results was found for the CLYC-6 detector. The CLYC-6 detects about 400 times more thermal neutrons than the CLYC-7. Therefore, the thermal neutrons are also detected, but they can be discriminated by the fast neutrons exploiting the TOF measurements.

Furthermore, the anode signal was formed with an amplifier (a modified BAFPRO unit [8]) with a shaping time of approximately 2 μ s (slow component, the integral of the anode signal) and then was sent to a CAEN VME-ADC. The time spectra were obtained from the modified BAFPRO unit (shaping delay of 8 ns) and a CAEN VME-TDC. The BAFPRO unit provides also a fast component, that is proportional to the maximum of the signal. The PSD, between gamma rays and neutrons, was performed producing a fast vs slow matrix. The data were acquires with a KMAX environment DAQ system [9] (analog acquisition system).

4 Conclusions

In this work, we presented the results from the response of two 1" x 1" samples of CLYC scintillators at fast and thermal neutrons: one enriched with 95% of ^6Li (CLYC-6) and the other with an enrichment of ^7Li higher than 99% (CLYC-7).

The thermal neutrons, produced by an AmBe source surrounded by paraffin, were measured with both detectors. It was observed that the thermal neutron detection efficiency for the CLYC-7 is 0.3% with respect to the CLYC-6 sample.

In order to test the capability of these crystals to detect fast neutrons, two experiments were performed one at the Frascati Neutron Generator facility (Italy) and the other one at LNL (Italy). At the neutron generator facility, a deuterium beam was used to provide neutrons of 2.5 MeV or 14.1 MeV, respectively. We found a clear peak related to 2.5 MeV neutrons while a continuum energy spectrum for 14.1 MeV neutrons owing to a superimposition of different reaction mechanisms. Fast neutrons, from 1.9 MeV up to 3.8 MeV, were measured also at the CN accelerator of LNL. In this case, fast neutrons were identified by both the energy signal and the TOF technique. Exploiting the TOF technique, it is possible to subtract the thermal neutrons, especially for CLYC-6 detector.

Acknowledgements

The project is co-financed by the European Union and the European Social Fund. This work was also supported by *NuPNET - ERA-NET* within the the NuPNET GANAS project, under grant agreement n° 202914 and from the European Union, within the "7th Framework Program" FP7/2007-2013, under grant agreement n° 262010 – ENSAR-INDESYS. This work was also supported by "Programmi di Ricerca Scientifica di Rilevante Interesse Nazionale" (PRIN) number 2001024324_01302.

References

- [1] J. Glodo et al. *Journal of Crystal Growth* **379**(2013)73–78.
- [2] N. D'Olympia et al. *Nucl. Instr. and Meth.* **A714**(2013)121.
- [3] Pointwise ENDF-VII library at 300 K: <http://atom.kaeri.re.kr/cgi-bin/endlplot.pl>
- [4] N. D'Olympia et al., *Nucl. Instr. and Meth.* **A763**, (2014), 433.
- [5] N. D'Olympia et al. *Nucl. Instr. and Meth.* **A694**(2012)140.
- [6] M.B. Smith et al. IEEE TRANSACTIONS ON NUCLEAR SCIENCE, 60(2013)855.
- [7] M. Martone, M. Angelone, M. Pillon., *Journal of Nuclear Materials* **212** (1994) 1661.
- [8] C. Boiano, et al, 2010 IEEE NSS and MIC Conference Record, 268.
- [9] S. Brambilla, et al., 2012 IEEE NNS and MIC Conference Record, 1087.

Charge-current and neutral-current quasielastic neutrino(antineutrino) scattering on ^{12}C with realistic spectral and scaling functions

A.N. Antonov¹, M.V. Ivanov^{1,2}, M.B. Barbaro³, J.A. Caballero⁴, G.D. Megias⁴, R. González-Jiménez⁵, C. Giusti⁶, A. Meucci⁶, E. Moya de Guerra², J.M. Udías²

¹ Institute for Nuclear Research and Nuclear Energy, Bulgarian Academy of Sciences, Sofia, Bulgaria

² Departamento de Física Atómica, Molecular y Nuclear, Universidad Complutense de Madrid, Spain

³ Dipartimento di Fisica, Università di Torino and INFN, Sezione di Torino, Italy

⁴ Departamento de Física Atómica, Molecular y Nuclear, Universidad de Sevilla, Spain

⁵ Department of Physics and Astronomy, Ghent University, Belgium

⁶ Dipartimento di Fisica, Università degli Studi di Pavia and INFN, Sezione di Pavia, Italy

Abstract

Charge-current (CC) and neutral-current (NC) quasielastic (anti)neutrino scattering cross sections on ^{12}C target are analyzed using a realistic spectral function $S(p, \mathcal{E})$ that gives a scaling function in accordance with the (e, e') scattering data. The spectral function accounts for the nucleon-nucleon correlations by using natural orbitals from the Jastrow correlation method and has a realistic energy dependence. The standard value of the axial mass $M_A = 1.032$ GeV is used in the calculations. The role of the final-state interaction on the spectral and scaling functions, as well as on the cross sections is accounted for. Our results in the CC case are compared with those from other theoretical approaches, such as the Superscaling Approach (SuSA) and the relativistic Fermi gas (RFG), as well as with those of the relativistic mean field (RMF) and the relativistic Green's function (RGF) in the NC case. Based on the impulse approximation our calculations for the CC scattering underpredict the MiniBooNE data but agree with the data from the NOMAD experiment. The NC results are compared with the empirical data of the MiniBooNE and BNL experiments. The possible missing ingredients in the considered theoretical methods are discussed.

1. Introduction

The observation of the y -scaling (*e.g.* [1, 2, 3]) and superscaling (*e.g.* [4, 5, 6, 7]) phenomena in the inclusive electron scattering on nuclei and their analyses within the relativistic Fermi gas (RFG) model [4, 5, 6] and beyond it, imposed the superscaling ideas to be exploited to describe the charge-current (CC) (anti)neutrino cross sections in nuclei for intermediate to high energies [8, 9]. Many theoretical models, such as the RFG, the RPA, the relativistic mean-field (RMF) model, the relativistic Greens function (RGF) model, the coherent density fluctuation model (CDFM), the phenomenological SuSA approach, the spectral function models and others (see, *e.g.*, [7, 10, 11, 12, 13, 14, 15, 16, 17, 18, 19, 20, 21]) have been devoted to analyses of the MiniBooNE [22, 23] data on quasielastic (CCQE) scattering of neutrino on nuclei. It turned out that the empirical cross sections are underestimated by most of the nuclear models. At the same time, the necessity to account for the multinucleon excitations has been proposed and a good agreement with the MiniBooNE data has been obtained in [24, 16, 25] using the standard value of the nuclear axial form factor $M_A = 1.032$ GeV/ c^2 . At the same time, it should be emphasized that the CCQE data for $\nu_\mu(\bar{\nu}_\mu)+^{12}\text{C}$ cross section measurements from 3 to 100 GeV of the NOMAD collaboration [26] do not impose an anomalously large value of M_A to be used (as in some analyses of MiniBooNE data) and have been described well by various approaches based on the

impulse approximation. The superscaling analyses have been carried a step further in Ref. [27] to include neutral current (NC) (anti)neutrino scattering cross sections from ^{12}C involving proton, as well as neutron knockout in the QE regime. The CDFM scaling function was applied in [28] to analyses of NC (anti)neutrino scattering on ^{12}C (“ u -channel” inclusive process). In our work [29] NCQE (anti)neutrino scattering on ^{12}C are analyzed using a realistic spectral function $S(p, \mathcal{E})$ that gives a scaling function in accordance with the (e, e') scattering data.

The main aims of our work are the following: i) To analyze CCQE (anti)neutrino cross sections on ^{12}C measured by MiniBooNE [22, 23] and NOMAD [26] by using a spectral function with realistic energy dependence and accounting for short-range NN correlations, and ii) To analyze by the above mentioned approach the NCQE neutrino cross sections on ^{12}C measured by MiniBooNE [30] and by BNL E734 experiment [31], as well as antineutrino-nucleus scattering by MiniBooNE collaboration [32, 33].

2. Charge-current QE (anti)neutrino scattering on ^{12}C

Within the PWIA (see, *e.g.*, [34, 35] and details therein) the differential cross section for the $(e, e'N)$ process factorizes in the form

$$\left[\frac{d\sigma}{d\mathcal{E}' d\Omega' dp_N d\Omega_N} \right]_{(e, e'N)}^{PWIA} = K \sigma^{eN}(q, \omega; p, \mathcal{E}, \phi_N) S(p, \mathcal{E}), \quad (1)$$

where σ^{eN} is the electron-nucleon cross section for a moving off-shell nucleon, K is a kinematical factor and $S(p, \mathcal{E})$ is the spectral function giving the probability to find a nucleon of certain momentum and energy in the nucleus. In Eq. (1) p is the missing momentum and \mathcal{E} is the excitation energy of the residual system. The scaling function can be represented in the form:

$$F(q, \omega) \cong \frac{[d\sigma/d\mathcal{E}' d\Omega']_{(e, e')}}{\bar{\sigma}^{eN}(q, \omega; p = |y|, \mathcal{E} = 0)}, \quad (2)$$

where the electron-single nucleon cross section $\bar{\sigma}^{eN}$ is taken at $p = |y|$, y being the smallest possible value of p in electron-nucleus scattering for the smallest possible value of the excitation energy ($\mathcal{E} = 0$). In the PWIA the scaling function Eq. (2) is simply given by the spectral function

$$F(q, \omega) = 2\pi \iint_{\Sigma(q, \omega)} p dp d\mathcal{E} S(p, \mathcal{E}), \quad (3)$$

where $\Sigma(q, \omega)$ represents the kinematically allowed region.

In the RFG model the scaling function $f_{\text{RFG}}(\psi') = k_F \cdot F$ has the form [6]:

$$f_{\text{RFG}}(\psi') \simeq \frac{3}{4} (1 - \psi'^2) \theta(1 - \psi'^2). \quad (4)$$

In Ref. [35] more information about the spectral function was extracted within PWIA from the experimentally known scaling function. It contains effects beyond the mean-field approximation leading to a realistic energy dependence and accounts for short-range NN correlations. It is written in the form:

$$S(p, \mathcal{E}) = \sum_i 2(2j_i + 1) n_i(p) L_{\Gamma_i}(\mathcal{E} - \mathcal{E}_i), \quad (5)$$

where the Lorentzian function is used:

$$L_{\Gamma_i}(\mathcal{E} - \mathcal{E}_i) = \frac{1}{\pi} \frac{\Gamma_i/2}{(\mathcal{E} - \mathcal{E}_i)^2 + (\Gamma_i/2)^2} \quad (6)$$

with Γ_i being the width for a given s.p. hole state. In the calculations we used the values $\Gamma_{1p} = 6$ MeV and $\Gamma_{1s} = 20$ MeV, which are fixed to the experimental widths of the 1p and 1s states in ^{12}C [36]. In Eq. (5) the s.p. momentum distributions $n_i(p)$ were taken firstly to correspond to harmonic-oscillator (HO) shell-model s.p. wave functions, and second, to natural orbitals (NOs) s.p. wave functions $\varphi_\alpha(\mathbf{r})$ defined in [37] as the complete orthonormal set of s.p. wave functions that diagonalize the one-body density matrix $\rho(\mathbf{r}, \mathbf{r}')$:

$$\rho(\mathbf{r}, \mathbf{r}') = \sum_{\alpha} N_{\alpha} \varphi_{\alpha}^*(\mathbf{r}) \varphi_{\alpha}(\mathbf{r}'), \quad (7)$$

where the eigenvalues N_{α} ($0 \leq N_{\alpha} \leq 1$, $\sum_{\alpha} N_{\alpha} = A$) are the natural occupation numbers. In [35] we used $\rho(\mathbf{r}, \mathbf{r}')$ obtained within the lowest-order approximation of the Jastrow correlation methods [38]. For accounting for the FSI we follow the approach given in Ref. [39] concerning two types of FSI effects, the Pauli blocking and the interaction of the struck nucleon with the spectator system by means of the time-independent optical potential (OP) $U = V - iW$. The latter can be accounted for [40] by the replacing in the PWIA expression for the inclusive electron-nucleus scattering cross section

$$\frac{d\sigma_i}{d\omega d|\mathbf{q}|} = 2\pi\alpha^2 \frac{|\mathbf{q}|}{E_{\mathbf{k}}^2} \int dE d^3p \frac{S_i(\mathbf{p}, E)}{E_{\mathbf{p}} E_{\mathbf{p}'}} \delta(\omega + M - E - E_{\mathbf{p}'}) L_{\mu\nu}^{\text{em}} H_{\text{em}, t}^{\mu\nu} \quad (8)$$

the energy-conserving delta-function by

$$\delta(\omega + M - E - E_{\mathbf{p}'}) \rightarrow \frac{W/\pi}{W^2 + [\omega + M - E - E_{\mathbf{p}'} - V]^2}. \quad (9)$$

In Eq. (8) the index t denotes the nucleon isospin, $L_{\mu\nu}^{\text{em}}$ and $H_{\text{em}, t}^{\mu\nu}$ are the leptonic and hadronic tensors, respectively, and $S_i(\mathbf{p}, E)$ is the proton (neutron) spectral function. The real (V) and imaginary (W) parts of the OP in (8) and (9) are obtained in Ref. [41] from the Dirac OP. The CC (anti)neutrino cross section in the target laboratory frame is given in the form (see for details [8, 10])

$$\left[\frac{d^2\sigma}{d\Omega dk'} \right]_{\chi} \equiv \sigma_0 \mathcal{F}_{\chi}^2, \quad (10)$$

where $\chi = +$ for neutrino-induced reaction (e.g., $\nu_{\ell} + n \rightarrow \ell^{-} + p$, where $\ell = e, \mu, \tau$) and $\chi = -$ for antineutrino-induced reactions (e.g., $\bar{\nu}_{\ell} + p \rightarrow \ell^{+} + n$). The quantity \mathcal{F}_{χ}^2 in (10) depends on the nuclear structure and is presented [8] as a generalized Rosenbluth decomposition containing leptonic factors and five nuclear response functions, namely charge-charge (CC), charge-longitudinal (CL), longitudinal-longitudinal (LL), vector-transverse (T) and axial-transverse (T') expressed by the nuclear tensor and the scaling function. To obtain the scaling function we use the spectral function $S(p, \mathcal{E})$ from (5) with $n_i(p)$ corresponding to HO or NOs s.p. wave functions, and the Lorentzian function (6). The scaling function $f(\psi')$ is presented in Fig. 1. As can be seen, the accounting for FSI leads to a small asymmetry in $f(\psi')$. The results for the total cross sections obtained in [21] within the RFG+FSI, HO+FSI and NO+FSI are given in Fig. 2 and compared with the SuSA results and the MiniBooNE [22, 23] and NOMAD [26] data (up to 100 GeV). All models give results that agree with the NOMAD data but underpredict the MiniBooNE ones, more seriously in the ν_{μ} than in $\bar{\nu}_{\mu}$. In Fig. 2(b) the results for T , L and T' contributions to the cross section of NO+FSI case are presented. In Fig. 2(c) the CCQE $\bar{\nu}_{\mu}$ - ^{12}C cross section is given. As can be seen in Fig. 2(b) the maximum of the T'

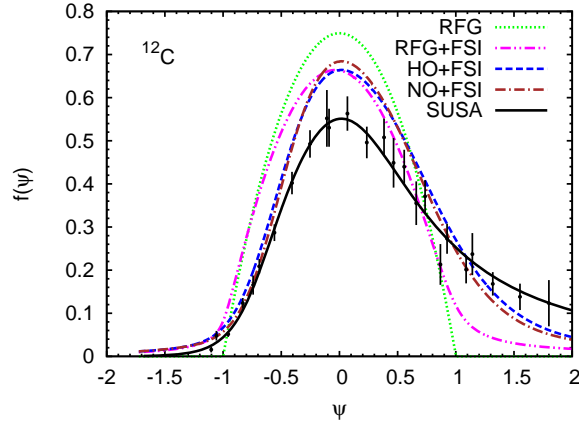


Fig. 1: Results for the scaling function $f(\psi)$ for ^{12}C obtained using RFG+FSI, HO+FSI, and NO+FSI approaches are compared with the RFG and SUSAs results, as well as with the longitudinal experimental data.

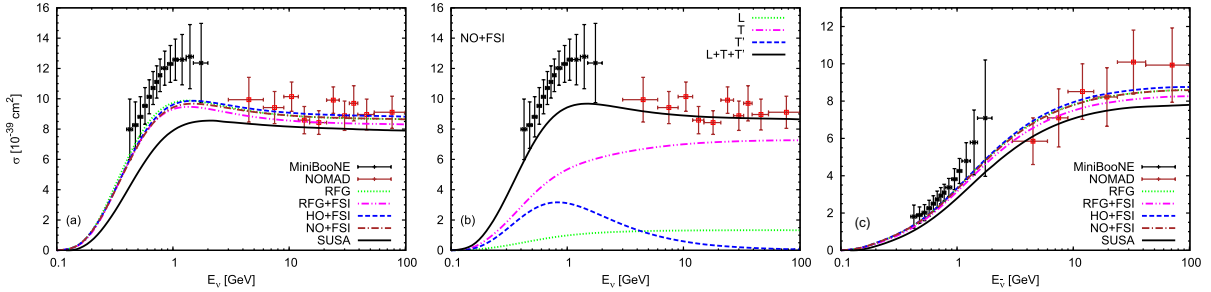


Fig. 2: (a) CCQE ν_μ - ^{12}C total cross sections as a function of E_ν compared with the MiniBooNE [22] and NOMAD [26] data; $M_A = 1.032 \text{ GeV}/c^2$; (b) separated contributions (L , T , T' , $L+T+T'$) in the NO+FSI approach; (c) CCQE $\bar{\nu}_\mu$ - ^{12}C total cross section. The MiniBooNE data are from [23].

contribution is around the maximum of the neutrino flux at MiniBooNE experiment. The effects of the T' contribution are negligible at $E_\nu > 10 \text{ GeV}$. For high ν_μ ($\bar{\nu}_\mu$) energies the total cross section for ν_μ and $\bar{\nu}_\mu$ are very similar, that is consistent with the negligible contribution of T' response in this region. Only L and T channels contribute for $E_\nu > 10 \text{ GeV}$ explored by NOMAD experiment (where the theory is in agreement with the data). The discrepancy with the MiniBooNE data (at energies $< 1 \text{ GeV}$) is most likely due to missing effects beyond the IA, *e.g.* those of the 2p-2h excitations that have contributions in the transverse responses. This concerns also the similar disagreement that appears when the phenomenological scaling function in SuSA is used.

3. Neutral-current QE neutrino scattering on ^{12}C

In the case of NC neutrino scattering only the outgoing nucleon (with momentum P_N^μ) is observed and the outgoing neutrino is integrated over. This is a “ u -channel” process, where the Mandelstam variable $u = (K^\mu - P_N^\mu)^2$ is fixed. In this case the transfer 4-momentum $Q^\mu = (\omega, q)$ is not specified. A new transfer 4-momentum $Q'^\mu = (K^\mu - P_N^\mu) = (\omega', q')$ is introduced and new scaling variables $y^{(u)}(q', \omega')$ and $\psi^{(u)}(q', \omega')$ are defined. The cross section for the $(l, l'N)$ process within the PWIA has the form [27]:

$$\frac{d\sigma}{d\Omega_N dp_N} \simeq \bar{\sigma}_{s.n.}^{(u)} F(y', q') \quad (11)$$

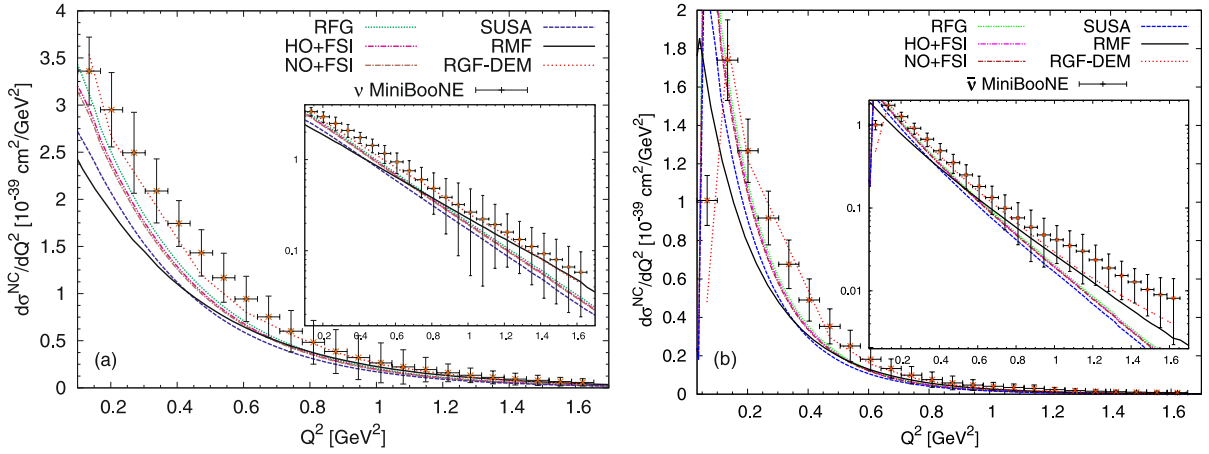


Fig. 3: NCQE neutrino [(a), $\nu N \rightarrow \nu N$] and antineutrino [(b), $\bar{\nu} N \rightarrow \bar{\nu} N$] flux-averaged differential cross section computed using the RFG, HO+FSI, NO+FSI, SUSA scaling functions, RGF and RMF models and compared with the MiniBooNE data [30, 33], $M_A = 1.032 \text{ GeV}/c^2$ and strangeness $\Delta s = 0$.

with

$$F(y', q') \equiv \int_{\mathcal{D}_u} p dp \int \frac{d\mathcal{E}}{E} \Sigma \simeq F(y'), \quad (12)$$

where $\bar{\sigma}_{s.n.}^{(u)}$ is the effective (s.n.) cross section (for details, see [27, 29]), \mathcal{D}_u being the domain of integration in the “u-channel” and Σ is the reduced cross section. Assuming that the domain \mathcal{D}_u and the “t-channel” domain \mathcal{D}_t are the same or very similar (they are different only at large \mathcal{E} and p), the results for the scaling function obtained in the (e, e') scattering can be used in the case of NC neutrino reactions. The NCQE process is sensitive to both isoscalar and isovector weak currents carried by the nucleon. Using the spectral function $S(p, \mathcal{E})$ [Eq. (5)], we calculated the NCQE flux-integrated cross sections with RFG, HO+FSI, NO+FSI and SuSA scaling functions and compare them with the MiniBooNE neutrino [30] and antineutrino [33] scattering on mineral oil (CH_2) target, as well as with the results of the RMF [42, 43] and RGF [44, 45, 46] methods. The calculations are performed using the values of $M_A = 1.032 \text{ GeV}/c^2$ and of strangeness $\Delta s = 0$. The results are presented in Fig. 3. As can be seen, the theoretical results of all models except the RGF-DEM underestimate the neutrino data in the region $0.1 < Q^2 < 0.7 \text{ GeV}^2$ ($Q^2 = 2M_N T_N$), while all theories are within the error bars for higher Q^2 . On the other hand, the same models underestimate the antineutrino data at high Q^2 . The results of our models are compared also with the BNL E734 data [31] in Fig. 4. It can be seen that a good agreement exists for neutrino and antineutrino NC cross sections for $Q^2 > 0.8 \text{ GeV}^2$.

4. Conclusions

The results of the present work can be summarized as follows: i) The use of different spectral functions (RFG, HO, NO) gives quite similar results (*e.g.*, within 5–7% for the CCQE cross sections), signaling that the CC and NC processes are not too sensitive to the specific treatment of the bound state; ii) The FSI leads to small changes of the cross sections for different approaches in both CCQE and NCQE cases; iii) In the CCQE neutrino case all approaches based on IA underestimate the MiniBooNE data for the flux-averaged differential and total cross sections, although the shape of the cross sections is represented by NO+FSI, HO+FSI and RGF+FSI approaches. For the antineutrino the agreement is much better. All models give a good agreement with the NOMAD data; iv) In both CCQE and NCQE scattering our calculations are based on IA. They do not include *e.g.*, 2p-2h contributions induced by

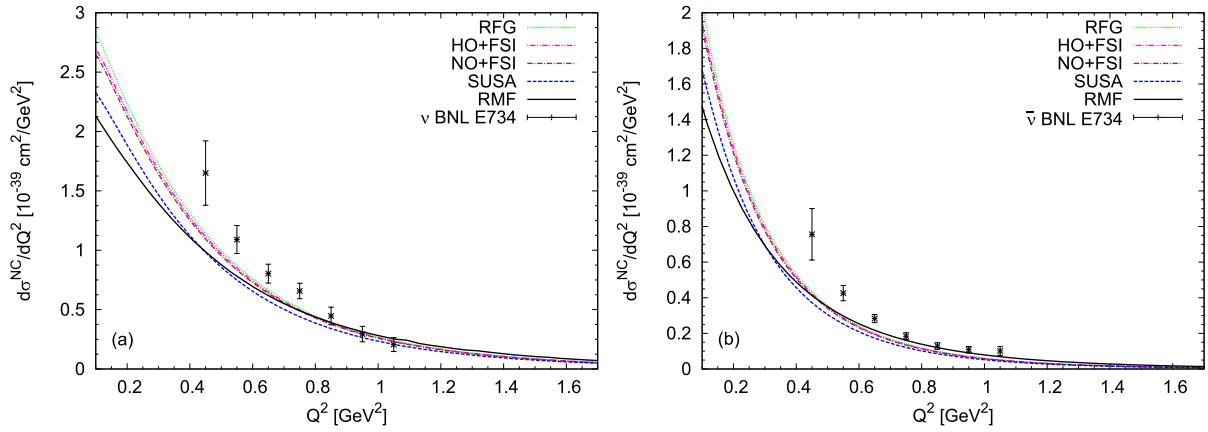


Fig. 4: NCQE flux-averaged cross section: (a) $\nu p \rightarrow \nu p$ and (b) $\bar{\nu} p \rightarrow \bar{\nu} p$ compared with the BNL E734 experimental data [31]. Our results are evaluated using the RFG, HO+FSI, NO+FSI, SUSA scaling functions, and RMF model with $M_A = 1.032 \text{ GeV}/c^2$ and strangeness $\Delta s = 0$.

MEC that are very important in the $\nu(\bar{\nu})$ -nuclei scattering processes.

Acknowledgements

This work was partially supported by INFN under project MANYBODY, by Spanish DGI and FEDER funds (FIS2011-28738-C02-01, FPA2013-41267), by the Junta de Andalucia, by the Spanish Consolider-Ingenio 2000 program CPAN (CSD2007-00042), by the Campus of Excellence International (CEI) of Moncloa project (Madrid) and Andalucia Tech, by the Bulgarian National Science Fund under contracts No. DFNI-T02/19 and DFNI-E02/6. R.G.J. acknowledges financial help from the Interuniversity Attraction Poles Programme initiated by the Belgian Science Policy Office.

References

- [1] G. B. West, *Phys. Rep.* **18** (1975) 263.
- [2] D. B. Day, J. S. McCarthy, T. W. Donnelly, and I. Sick, *Annu. Rev. Nucl. Part. Sci.* **40** (1990) 357.
- [3] C. Ciofi degli Atti, E. Pace, and G. Salmè, *Phys. Rev. C* **43** (1991) 1155.
- [4] W. M. Alberico, A. Molinari, T. W. Donnelly, E. L. Kronenberg, and J. W. Van Orden, *Phys. Rev. C* **38**, 1801 (1988).
- [5] M. B. Barbaro, R. Cenni, A. De Pace, T. W. Donnelly, and A. Molinari, *Nucl. Phys. A* **643**, 137 (1998).
- [6] T. W. Donnelly and I. Sick, *Phys. Rev. C* **60**, 065502 (1999).
- [7] A. N. Antonov *et al.*, *Phys. Rev. C* **69** (2004) 044321; *Phys. Rev. C* **71** (2005) 014317.
- [8] J. E. Amaro, M. B. Barbaro, J. A. Caballero, T. W. Donnelly, A. Molinari, and I. Sick, *Phys. Rev. C* **71** (2005) 015501.
- [9] J. E. Amaro, M. B. Barbaro, J. A. Caballero, T. W. Donnelly, and C. Maieron, *Phys. Rev. C* **71** (2005) 065501.
- [10] A. N. Antonov *et al.*, *Phys. Rev. C* **74**, 054603 (2006).
- [11] J. T. Sobczyk, *Phys. Rev. C* **86** (2012) 015504.
- [12] A. Meucci, M. B. Barbaro, J. A. Caballero, C. Giusti, and J. M. Udias, *Phys. Rev. Lett.* **107** (2011) 172501.
- [13] M. B. Barbaro, *J. Phys.: Conf. Ser.* **336** (2011) 012024.
- [14] G. Megias, J. Amaro, M. Barbaro, J. Caballero, and T. Donnelly, *Phys. Lett. B* **725** (2013) 170.
- [15] O. Benhar, P. Coletti, and D. Meloni, *Phys. Rev. Lett.* **105** (2010) 132301.
- [16] M. Martini and M. Ericson, *Phys. Rev. C* **87** (2013) 065501.
- [17] A. Meucci, C. Giusti, and F. D. Pacati, *Phys. Rev. D* **84** (2011) 113003.
- [18] J. Nieves, I. R. Simo, and M. V. Vacas, *Phys. Lett. B* **721** (2013) 90.
- [19] O. Lalakulich, K. Gallmeister, and U. Mosel, *Phys. Rev. C* **86** (2012) 014614.

- [20] A. M. Ankowski, Phys. Rev. C **86** (2012) 024616.
- [21] M. V. Ivanov, A. N. Antonov, J. A. Caballero, G. D. Megias, M. B. Barbaro, E. Moya de Guerra, and J. M. Udias, Phys. Rev. C **89** (2014) 014607.
- [22] A. A. Aguilar-Arevalo *et al.* (MiniBooNE Collaboration), Phys. Rev. D **81** (2010) 092005.
- [23] A. A. Aguilar-Arevalo *et al.* (MiniBooNE Collaboration), Phys. Rev. D **88** (2013) 032001.
- [24] M. Martini, M. Ericson, G. Chanfray, and J. Marteau, Phys. Rev. C **81** (2010) 045502.
- [25] J. Nieves, I. R. Simo, and M. V. Vacas, Phys. Lett. B **707** (2012) 72.
- [26] V. Lyubushkin *et al.*, Eur. Phys. J. C **63** (2009) 355.
- [27] J. E. Amaro, M. B. Barbaro, J. A. Caballero, and T. W. Donnelly, Phys. Rev. C **73**, 035503 (2006).
- [28] A. N. Antonov, M. V. Ivanov, M. B. Barbaro *et al.*, Phys. Rev. C **75**, 064617 (2007).
- [29] M. V. Ivanov *et al.*, Phys. Rev. C **91** (2015) 034607.
- [30] A. A. Aguilar-Arevalo *et al.* (MiniBooNE Collaboration), Phys. Rev. D **82** (2010) 092005.
- [31] K. Abe *et al.*, Phys. Rev. Lett. **56** (1986) 1107; **56** (1986) 1883(E); L. A. Ahrens *et al.*, Phys. Rev. D **35** (1987) 785.
- [32] A. A. Aguilar-Arevalo *et al.* (MiniBooNE Collaboration), Phys. Rev. D **88** (2013) 032001.
- [33] A. A. Aguilar-Arevalo *et al.* (MiniBooNE Collaboration), Phys. Rev. D **91** (2015) 012004.
- [34] J. A. Caballero *et al.*, Phys. Rev. C **81** (2010) 055502.
- [35] A. N. Antonov *et al.*, Phys. Rev. C **83** (2011) 045504.
- [36] D. Dutta, Ph.D. thesis, Northwestern University, (1999).
- [37] P.-O. Löwdin, Phys. Rev. **97** (1955) 1474.
- [38] M. V. Stoitsov, A. N. Antonov, and S. S. Dimitrova, Phys. Rev. C **48** (1993) 74.
- [39] A. M. Ankowski and J. T. Sobczyk, Phys. Rev. C **77** (2008) 044311.
- [40] Y. Horikawa, F. Lenz, and N. C. Mukhopadhyay, Phys. Rev. C **22** (1980) 1680.
- [41] E. D. Cooper, S. Hama, B. C. Clark, and R. L. Mercer, Phys. Rev. C **47** (1993) 297.
- [42] M. C. Martinez, J. A. Caballero, T. W. Donnelly and J. M. Udias, Phys. Rev. C **77** (2008) 064604.
- [43] M. C. Martinez, J. A. Caballero, T. W. Donnelly and J. M. Udias, Phys. Rev. Lett. **100** (2008) 052502.
- [44] F. Capuzzi, C. Giusti and F. D. Pacati, Nucl. Phys. A **524** (1991) 681.
- [45] A. Meucci, F. Capuzzi, C. Giusti and F. D. Pacati, Phys. Rev. C **67** (2003) 054601.
- [46] R. Gonzalez-Jimenez, J. A. Caballero, A. Meucci, C. Giusti, M. B. Barbaro, M. I. Ivanov and J. M. Udias, Phys. Rev. C **88** (2013) 025502.

Charged-current inclusive neutrino cross sections: Superscaling extension to the pion production and realistic spectral function for quasielastic region

M.V. Ivanov^{1,2}, A.N. Antonov¹, M.B. Barbaro³, J.A. Caballero⁴, G.D. Megias⁴, R. González-Jiménez⁵, E. Moya de Guerra², J.M. Udías²

¹ Institute for Nuclear Research and Nuclear Energy, Bulgarian Academy of Sciences, Sofia, Bulgaria

² Departamento de Física Atómica, Molecular y Nuclear, Universidad Complutense de Madrid, Spain

³ Dipartimento di Fisica, Università di Torino and INFN, Sezione di Torino, Italy

⁴ Departamento de Física Atómica, Molecular y Nuclear, Universidad de Sevilla, Spain

⁵ Department of Physics and Astronomy, Ghent University, Proeftuinstraat 86, Belgium

Abstract

Superscaling approximation (SuSA) predictions to neutrino-induced charged-current π^+ production in the Δ -resonance region are explored under MiniBooNE experimental conditions. The results obtained within SuSA for the flux-averaged double-differential cross sections of the pion production for the $\nu_\mu + \text{CH}_2$ reaction as a function of the muon kinetic energy and of the scattering angle are compared with the corresponding MiniBooNE experimental data. The SuSA charged-current π^+ predictions are in good agreement with data on neutrino flux average cross-sections. The SuSA extension to the pion production region and the realistic spectral function $S(p, \mathcal{E})$ for quasielastic scattering are used for predictions of charged-current inclusive neutrino-nucleus cross sections. The results are compared with the T2K experimental data.

1. Introduction

The properties of neutrinos, particularly the parameters of their oscillations, are being studied with increasing interest as these may carry important information about the limits of the Standard Model. In most neutrino experiments, the interactions of the neutrinos occur with nucleons bound in nuclei. Model predictions for these reactions involve many different effects such as nuclear correlations, interactions in the final state, possible modification of the nucleon properties inside the nuclear medium, that presently cannot be computed in an unambiguous and precise way. This is particularly true for the channels where neutrino interactions take place by means of excitation of a nucleon resonance and ulterior production of mesons. The data on neutrino-induced charged-current (CC) charged pion production cross sections on mineral oil recently released by the MiniBooNE collaboration [1] provides an unprecedented opportunity to carry out a systematic study of double differential cross section of the processes: $\nu_\mu p \rightarrow \mu^- p \pi^+$ and $\nu_\mu n \rightarrow \mu^- n \pi^+$ averaged over the neutrino flux. Also, new measurements of inclusive CC neutrino-nucleus scattering cross sections, where only the outgoing lepton is detected, have been recently performed by the T2K [2]. For neutrino energies around 1 GeV (T2K) the main contributions to the cross sections are associated with quasielastic (QE) scattering and one pion (1π) production.

The analyses of the world data on inclusive electron-nucleus scattering [3] confirmed the observation of superscaling and thus justified the extraction of a universal nuclear response to be also used for weak interacting probes. However, while there is a number of theoretical models that exhibit superscaling, such as for instance the relativistic Fermi gas (RFG) [4, 5], the nuclear response departs from the one derived from the experimental data. This showed the necessity to consider more complex dy-

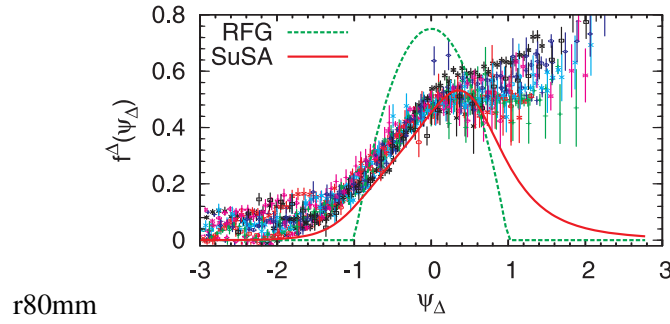


Fig. 1: The SuSA scaling function in the Δ -region $f^\Delta(\psi_\Delta)$ (solid line) extracted from the world data on electron scattering [7]. The dotted line shows the scaling functions $f^\Delta(\psi_\Delta)$ in the RFG model.

namical pictures of finite nuclear systems – beyond the RFG – in order to describe the nuclear response at intermediate energies. SuSA predictions are based on the phenomenological superscaling function extracted from the world data on quasielastic electron scattering [6]. The model has been extended to the Δ -resonance region [7] where the response of the nuclear system proceeds through excitation of internal nucleonic degrees of freedom. Indeed, a non-quasielastic cross section for the excitation region in which nucleon excitations, particularly the Δ , play a major role was obtained by subtracting from the data QE-equivalent cross sections given by SuSA [8, 9]. This procedure has been possible due to the large amount of available high-quality data of inelastic electron scattering cross sections on ^{12}C , including also separate information on the longitudinal and transverse responses, the latter containing important contributions introduced by effects beyond the impulse approximation (non-nucleonic).

Here we extend the analysis to CC pion production cross-section measured at MiniBooNe, that from the theoretical point of view can be seen as more challenging. For instance, Δ properties in the nuclear medium, as well as both coherent and incoherent pion production for the nucleus should be considered in any theoretical approach, while in the SuSA procedure they are included phenomenologically extracted from the electron scattering data. All what is assumed within SuSA approach is the nuclear response to be factorized into a single-nucleon part and a ‘nuclear function’ accounting for the overall interaction among nucleons. As mentioned before, the SuSA assumptions have been tested against a great deal of electron-nucleus scattering data with fair success (see Section 2.1). The factorization assumption allows to apply the same nuclear responses derived from electron scattering to neutrino-induced reactions, with a mere use of the adequate single-nucleon terms for this case. To show the importance of nuclear interaction effects as predicted within SuSA, as a reference, we also show results obtained within the RFG, with no interactions among nucleons, for which the scaling function in the Δ -domain is simply given as $f_{RFG}^\Delta(\psi_\Delta) = \frac{3}{4}(1 - \psi_\Delta^2)\theta(1 - \psi_\Delta^2)$ with ψ_Δ the dimensionless scaling variable extracted from the RFG analysis that incorporates the typical momentum scale for the selected nucleus [10, 7]. In Fig. 1 we compare the Δ -region SuSA [7] and RFG scaling functions, which we use in our study.

2. Theoretical scheme and results

2.1 Test versus electron scattering

In Fig. 1 we compare our theoretical predictions with inclusive electron scattering data on ^{12}C . In the QE region we use natural orbitals scaling function including final state interaction (NO+FSI), whereas for the Δ region we make use *e.g.* the scaling function presented in Fig. 1. Details in how the NO+FSI scaling function is obtained is given in Ref. [11] (see also A.N. Antonov in this Proceedings). Here we only show results for a few representative choices of kinematics, similar to those involved in the neutrino

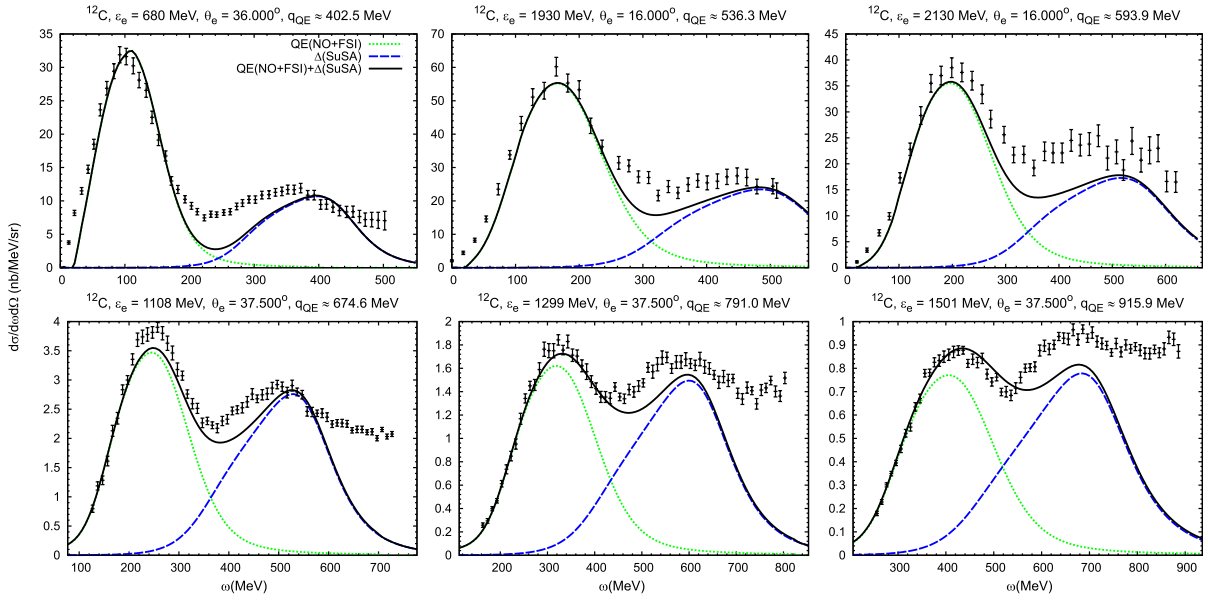


Fig. 2: Double-differential inclusive electron-carbon cross sections, $d\sigma/d\omega d\Omega$. The panels are labeled according to beam energy, scattering angle, and value of q_{QE} at the quasielastic peak. The results are compared with the experimental data from [12].

experiments that we address in the following sections. As observed, results are in good agreement with the data, while some disagreement remains in the comparison to the data in the “dip” region between the QE and Δ peaks. Meson-exchange current (MEC) contribution, that is not accounted for in this work, plays a major role in filling the “dip” region.

2.2 π^+ production in the MiniBooNE experiment

In what follows we present the results of applying the SuSA and RFG Δ -scaling function to neutrino-induced CC charged pion production. We follow the formalism given in [7]. The charged-current neutrino cross section in the target laboratory frame is given in the form

$$\frac{d^2\sigma}{d\Omega dk'} = \frac{(G \cos \theta_c k')^2}{2\pi^2} \left(1 - \frac{|Q^2|}{4E\varepsilon'}\right) \mathcal{F}^2, \quad (1)$$

where Ω , k' and ε' are the scattering angle, momentum and energy of the outgoing muon, G is the Fermi constant and θ_c is the Cabibbo angle. The function \mathcal{F}^2 depends on the nuclear structure through the R responses and can be written as [7, 13]:

$$\mathcal{F}^2 = \widehat{V}_{CC}R_{CC} + 2\widehat{V}_{CL}R_{CL} + \widehat{V}_{LL}R_{LL} + \widehat{V}_T R_T + 2\widehat{V}_{T'}R_{T'}$$

that is, as a generalized Rosenbluth decomposition having charge-charge (CC), charge-longitudinal (CL), longitudinal-longitudinal (LL) and two types of transverse (T, T') responses (R 's) with the corresponding leptonic kinematical factors (V 's). The nuclear response functions in Δ -region are expressed in terms of the nuclear tensor $W^{\mu\nu}$ in the corresponding region. The basic expressions used to calculate the single-nucleon cross sections are given in [7]. These involve the leptonic and hadronic tensors as well as the response and structure functions for single nucleons. A convenient parametrization of the single-nucleon $W^{+n} \rightarrow \Delta^+$ vertex is given in terms of eight form-factors: four vector ($C_{3,4,5,6}^V$) and four axial ($C_{3,4,5,6}^A$) ones. Vector form factors have been determined from the analysis of photo and

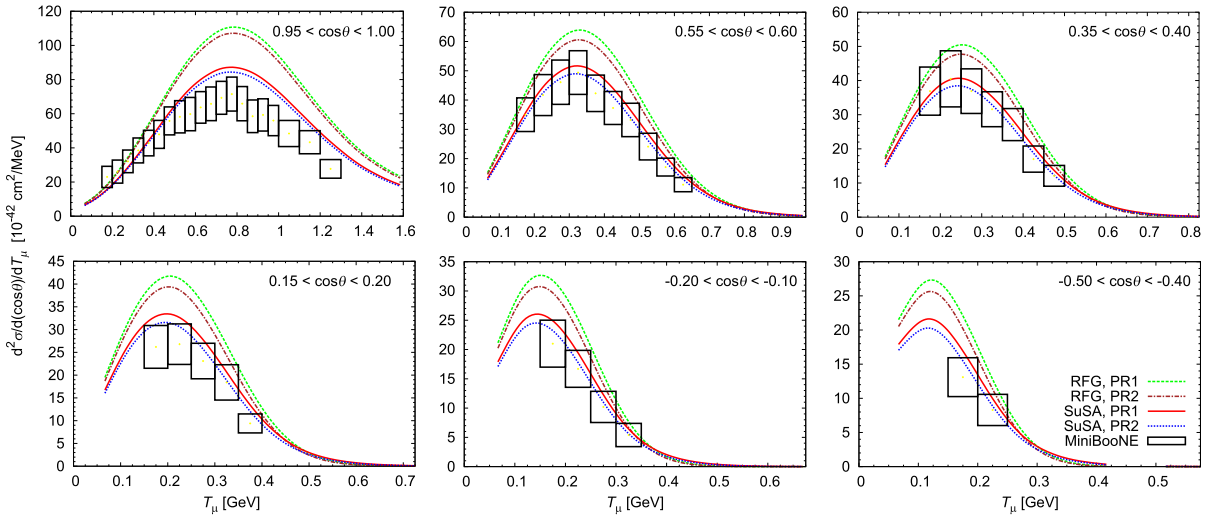


Fig. 3: (Color online) The double-differential cross section averaged over the neutrino energy flux as a function of the muon kinetic energy T_μ obtained by SuSA and RFG Δ -region scaling functions. In each subfigure the results have been averaged over the corresponding angular bin of $\cos\theta$. For vector and axial form-factors two parameterizations, “PR1” [14] and “PR2” [15], are used.

electro-production data, mostly on a deuteron target. Among the axial form factors, the most important contribution comes from C_5^A . The factor C_6^A , whose contribution to the differential cross section vanishes for massless leptons, can be related to C_5^A by PCAC. Since there are no other theoretical constraints for $C_{3,4,5}^A(q^2)$, they have to be fitted to data. We use two different parameterizations: the one given in [14] where deuteron effects were evaluated (authors estimated that the latter reduce the cross section by 10%), denoted as “PR1”, and the one from [15], called “PR2”.

With these ingredients, we evaluate the cross section for CC Δ^{++} and Δ^+ production on proton and neutron, respectively. Once produced, the Δ decays into πN pairs. For the amplitudes \mathcal{A} of pion production the following isospin decomposition applies: $\mathcal{A}(\nu_l p \rightarrow l^- p \pi^+) = \mathcal{A}_3$, $\mathcal{A}(\nu_l n \rightarrow l^- n \pi^+) = \frac{1}{3}\mathcal{A}_3 + \frac{2\sqrt{2}}{3}\mathcal{A}_1$, $\mathcal{A}(\nu_l n \rightarrow l^- p \pi^0) = -\frac{\sqrt{2}}{3}\mathcal{A}_3 + \frac{2}{3}\mathcal{A}_1$, with \mathcal{A}_3 being the amplitude for the isospin 3/2 state of the πN system, predominantly Δ , and \mathcal{A}_1 the amplitude for the isospin 1/2 state that is not considered here.

The double-differential cross section for CC neutrino-induced π^+ production averaged over the neutrino energy flux as a function of the muon kinetic energy T_μ is presented in Fig. 3. Each panel corresponds to a bin of $\cos\theta$. PR1 and PR2 parameterizations have been considered. Results with the PR1 parameterization are about 5% higher, that is a measure of the degree of uncertainty that we expect from the choice of the single-nucleon response for this reaction. We compare the predictions of SuSA and RFG with the MiniBooNE data [1]. The nuclear target has been considered as carbon and hydrogen in the mineral oil target. Here we show that SuSA predictions are in good agreement with the MiniBooNE experimental data for π^+ cross-section in the case of the flux averaged data.

2.3 Charged-current inclusive neutrino cross sections in the T2K experiment

In Fig. 4 we show the CC inclusive $\nu_\mu - {}^{12}\text{C}$ double-differential cross section per nucleon versus the muon momentum, p_μ , for different angular bins, folded with the T2K flux. The QE curve corresponds to the results obtained using NO+FSI scaling function [11] (see also A.N. Antonov in this Proceedings). The NO+FSI scaling function is obtained using realistic energy dependence of the spectral function $S(p, \mathcal{E})$ and an account for the effects of short-range nucleon-nucleon correlations when natural orbitals

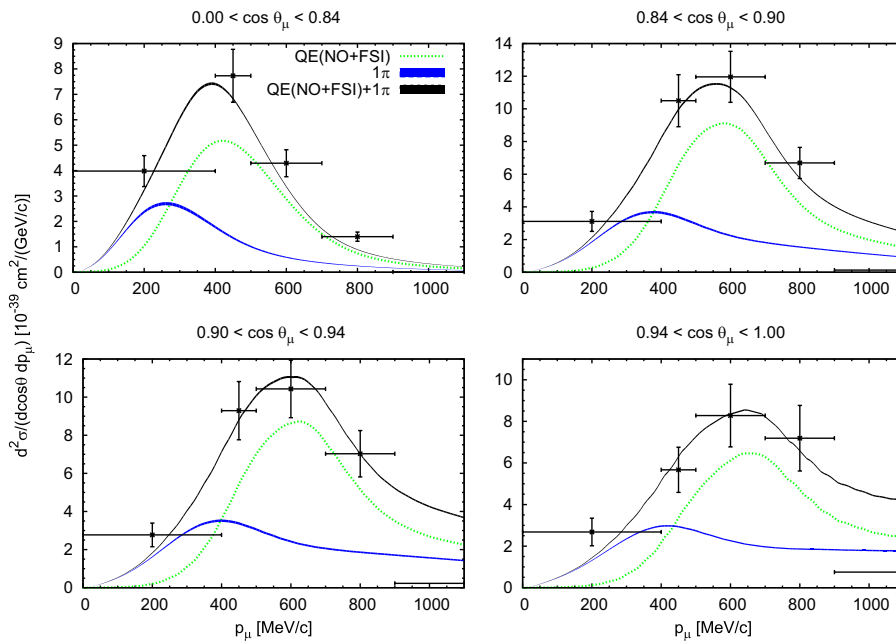


Fig. 4: The CC inclusive T2K flux-folded ν_μ - ^{12}C double-differential cross section per nucleon evaluated using NO+FSI scaling function in the QE region [QE(NO+FSI)] and SuSA scaling function in the Δ -region [1π] is displayed as a function of the muon momentum for different bins in the muon angle. The separate contributions of the QE and 1π are displayed. The data are from [2].

(NOs) from the Jastrow method are included. The NO+FSI scaling function is accounting also for the role of the final-state interactions (FSI). The resonant pion production curve (1π) is derived with the SuSA scaling function in the Δ -region $f^\Delta(\psi_\Delta)$ (Fig. 1). The band corresponds to the two different parametrizations, PR1 and PR2, described in Section 2.2. We observe that the model yields very good agreement with the T2K data.

3. Conclusions

We conclude that the idea of the SuSA approach for the Δ -region (extracted from electron scattering experiments) in addition with the use of natural orbitals scaling function and including final state interaction (NO+FSI) for the QE-region, when being extended to neutrino processes, proves to be very successful in describing ν_μ inclusive charged-current cross sections. Our model, after being tested against electron scattering data, has been proved to explain with success neutrino scattering data taken at different kinematics and explaining several regions of great interest, such as the QE and Δ ones.

Acknowledgements

This work was partially supported by INFN under project MANYBODY, by Spanish DGI and FEDER funds (FIS2011-28738-C02-01, FPA2013-41267), by the Junta de Andalucía, by the Spanish Consolider-Ingenuo 2000 program CPAN (CSD2007-00042), by the Campus of Excellence International (CEI) of Moncloa project (Madrid) and Andalucía Tech, by the Bulgarian National Science Fund under contracts No. DFNI-T02/19 and DFNI-E02/6. R.G.J. acknowledges financial help from the Interuniversity Attraction Poles Programme initiated by the Belgian Science Policy Office.

References

- [1] A.A. Aguilar-Arevalo *et al.* (MiniBooNE Collaboration), *Phys. Rev. D* **83** (2011) 052007.
- [2] K. Abe *et al.* [T2K Collaboration], *Phys. Rev. D* **87** (2013) 092003.
- [3] T. W. Donnelly and I. Sick, *Phys. Rev. Lett.* **82** (1999) 3212; *Phys. Rev. C* **60** (1999) 065502.
- [4] W. M. Alberico, A. Molinari, T. W. Donnelly, E. L. Kronenberg, and J. W. Van Orden, *Phys. Rev. C* **38** (1988) 1801.
- [5] M. B. Barbaro, R. Cenni, A. De Pace, T. W. Donnelly, and A. Molinari, *Nucl. Phys. A* **643** (1998) 137.
- [6] J. Jourdan, *Nucl. Phys. A* **603** (1996) 117.
- [7] J. E. Amaro, M. B. Barbaro, J. A. Caballero, T. W. Donnelly, A. Molinari and I. Sick, *Phys. Rev. C* **71** (2005) 015501.
- [8] M. B. Barbaro, J. A. Caballero, T. W. Donnelly, and C. Maieron, *Phys. Rev. C* **69** (2004) 035502.
- [9] C. Maieron, J. E. Amaro, M. B. Barbaro, J. A. Caballero, T. W. Donnelly, C. F. Williamson, *Phys. Rev. C* **80** (2009) 035504.
- [10] C. Maieron, T. W. Donnelly, and I. Sick, *Phys. Rev. C* **65** (2002) 025502.
- [11] M. V. Ivanov, A. N. Antonov, J. A. Caballero, G. D. Megias, M. B. Barbaro, E. Moya de Guerra, J. M. Udias, *Phys. Rev. C* **89** (2014) 014607; M. V. Ivanov, A. N. Antonov, M. B. Barbaro, C. Giusti, A. Meucci, J. A. Caballero, R. González-Jiménez, E. Moya de Guerra, and J. M. Udías, *Phys. Rev. C* **91** (2015) 034607.
- [12] O. Benhar, D. Day, I. Sick, *Rev. Mod. Phys.* **80** (2008) 189;
<http://faculty.virginia.edu/qes-archive/>.
- [13] Y. Umino and J. M. Udias, *Phys. Rev. C* **52** (1995) 3399.
- [14] L. Alvarez-Ruso, S. K. Singh and M. J. Vicente Vacas, *Phys. Rev. C* **59** (1999) 3386.
- [15] E. A. Paschos, J.-Y. Yu and M. Sakuda, *Phys. Rev. D* **69** (2004) 014013.

Production of hypertritons in heavy ion collisions around the threshold of strangeness production

C. Hartnack¹, A. Le Fèvre², Y. Leifels² and J. Aichelin¹

¹ SUBATECH, UMR 6457, Ecole des Mines de Nantes, IN2P3/CNRS, Université de Nantes, 44307 Nantes, France

² GSI Helmholtzzentrum für Schwerionenforschung GmbH, Planckstraße 1, 64291 Darmstadt, Germany

Abstract

We use the Isospin Quantum Molecular Dynamics approach supplemented with a phase space coalescence to study the properties of the production of hypertritons. We see strong influences of the hyperon rescattering on the yields. The hypertritons show up to be quite aligned to the properties of nuclear matter underlining the necessity of rescattering to transport the hyperons to the spectator matter.

1. Introduction

The production of hypernuclei as extension of the common periodic system or as important ingredient for understanding strong interaction (see e.g. [1, 2, 3]) has recently gained strong interest for understanding the properties of the hyperon interaction with nuclear matter, in particular since the publication of recent results of experimental collaborations [4, 5, 6, 7]. Several theoretical approaches have proposed the combination of transport and fragmentation models in order to understand the data [8, 9, 10]. Very recently a novel fragmentation approach, FRIGA [11], based on the maximization of the binding energy of the fragments, succeeded in explaining FOPI data on hypertritons as well as brandnew data of HypHI [12] concerning hypertritons and $^4_\Lambda\text{H}$.

In this contribution we use a transport model, IQMD [13], supplemented by a phase space coalescence to study the properties of hypertritons in collision of Ni+Ni at an incident energy of 1.93 AGeV. This model shows quite comparable results for the hypertriton yields as the much more sophisticated analysis presented in [11].

2. Production of hyperons in heavy ion collisions

In this section we want only to sketch the production of hyperons in nuclear matter and refer for a detailed discussion to [14]. At energies around the threshold kaons are dominantly produced in multistep processes using resonances (especially the Δ) as intermediate energy storage. The energetically most favorable channel is the production of a kaon together with a hyperon, this channel being also the major channel for the hyperon production. This common production channel links the effects acting on the kaon production to that of the hyperon. Thus the hyperon yields are also depending on the nuclear equation of state and on the kaon optical potential: a soft EOS reaches higher densities than a hard one and thus causes a smaller mean free path of the nucleons which enhances the collision rate. This allows more deltas to undergo a second high energetic collision (and thus to produce a kaon-hyperon pair) before decaying again into a nucleon and a pion. However at these high densities the kaon optical potential causes a penalty on the strangeness production by enhancing the thresholds and thus lowering the production cross section for a given energy. This causes a reduction of the production of kaon-hyperon pairs with respect to calculations with a kaon optical potential.

This effect can be seen in Fig. 1 where we compare the spectra of K^0 and Λ measured by FOPI in collisions of Ni+Ni at 1.93 AGeV incident energy and IQMD calculations performed with (full line)

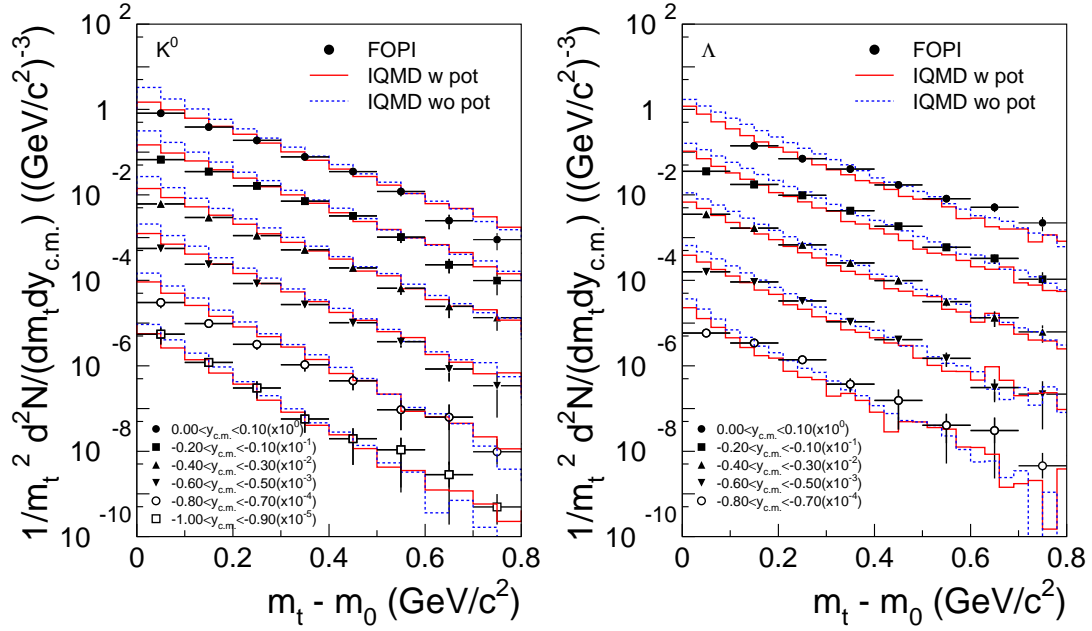


Fig. 1: Comparison of K^0 and hyperon spectra of Ni+Ni collisions between FOPI data and IQMD calculations

and without (dotted line) kaon optical potential. We see that the potential penalizes as well kaons as hyperons. The spectra are in good agreement, however it should be noted that the calculated temperatures for hyperons are somehow lower than the experimental values. It should also be noted that the rapidity distributions of the kaons measured by FOPI and KaoS can be well described.

Let us now compare the rapidity distributions of nucleons, hyperons and hypertritons. Fig.2 shows on the l.h.s the absolute yields as function of the rapidity. The ordinate is presented in logarithmic scale due to the large differences in absolute yields. This nicely demonstrates that the production of hypertritons is really a rare event. The r.h.s. shows the same distribution in linear scale but normalized to the particle yields. We see clearly that nucleons and hyperons are peaked in completely different regions in phase space. While the nucleon (dashed lines) peak around projectile and target rapidity, which means that the nuclear matter is not at all stopped, the hyperons (full line) peak around midrapidity. This is due to the effect that their production points are distributed around the cm of the colliding system which is typically the centre-of-mass of a NN system. It should be noted, that the production follows the kinematics of a 3 body phase space decay, where the hyperon has the highest mass - and thus the lowest velocity - of the 3 outgoing particles. Thus the hyperons show relatively low momenta at production in the NN centre of mass. The hypertritons (dotted line) have to combine Lambdas with nuclear spectator matter: their production peak lies in between the distributions of nucleons and hyperons but with a strong dominance of the nuclear matter.

3. The role of hyperon rescattering

The final rapidity distribution of the hyperons reflects not only the kinematics of the production process but also the rescattering with nuclear matter as it can be depicted from the l.h.s. of fig 3, where we

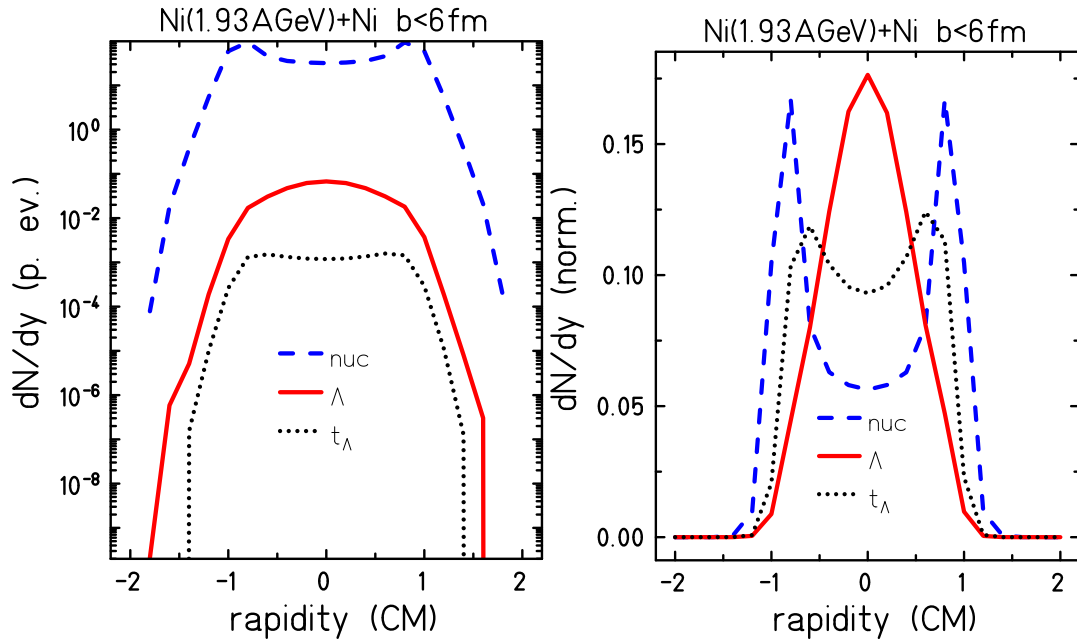


Fig. 2: Rapidity distributions of nucleons, hyperons and hypertritons in an absolute yield (left) and normalised to the total yield.

plot the normalized rapidity distributions of hyperons (full lines) and hypertritons (dotted lines). The rapidity distribution of hyperons with rescattering disabled (blue lines) correspond to the distribution at production and is therefore quite narrow. It is the rescattering (green thick lines) that enhances the momenta of the hyperons and thus leads to higher temperatures and broader rapidity distributions. This also influences the rapidity distributions of the hypertritons which need as well hyperons and nucleons for being created. The rapidity distribution of hypertritons is thus also broader if rescattering is allowed.

Besides the shape of the rapidity distributions of hypertritons, the rescattering influences also the yield of hypertritons significantly. This can be seen on the r.h.s. where the ratio hypertriton/hyperon is shown as function of the impact parameters using different options for the rescattering. The calculations using full rescattering (full lines) yield nearly 3 times more hypertritons than calculations disabling the rescattering (dash-dotted lines). If we set the rescattering cross sections to the half of its value (dotted lines) we still obtain nearly the double yield as in the calculations without rescattering. This can be easily understood from the rapidity distribution on the l.h.s. of fig 3: without rescattering the distribution of hyperons becomes this kind of narrow that only few hyperons can reach the region of spectator matter. However it is that region which is fertile for the production of fragments since it is there where clusters may remain undestroyed.

We can thus conclude that the main processus for creating hypertritons is to transport hyperons via rescattering to the region of the spectator matter where it may insert into a nucleon cluster. When having joined a cluster the hyperon-nucleon potentials help to keep the fragment stable. In this context we want to indicate that in IQMD the nucleons propagate by 2 and 3 body interactions of Skyrme, Yukawa, and Coulomb type, supplemented by momentum dependent interactions and asymetry potentials. Hyperons only interact by Skyrme interactions assuming a factor of two third in the strength of the potential. For details see [14].

The ratio of hypertritons/hyperons has the advantage to compensate other effects on the hypertriton yield stemming from the absolute hyperon yield. Effects acting on the kaon numbers like the equation

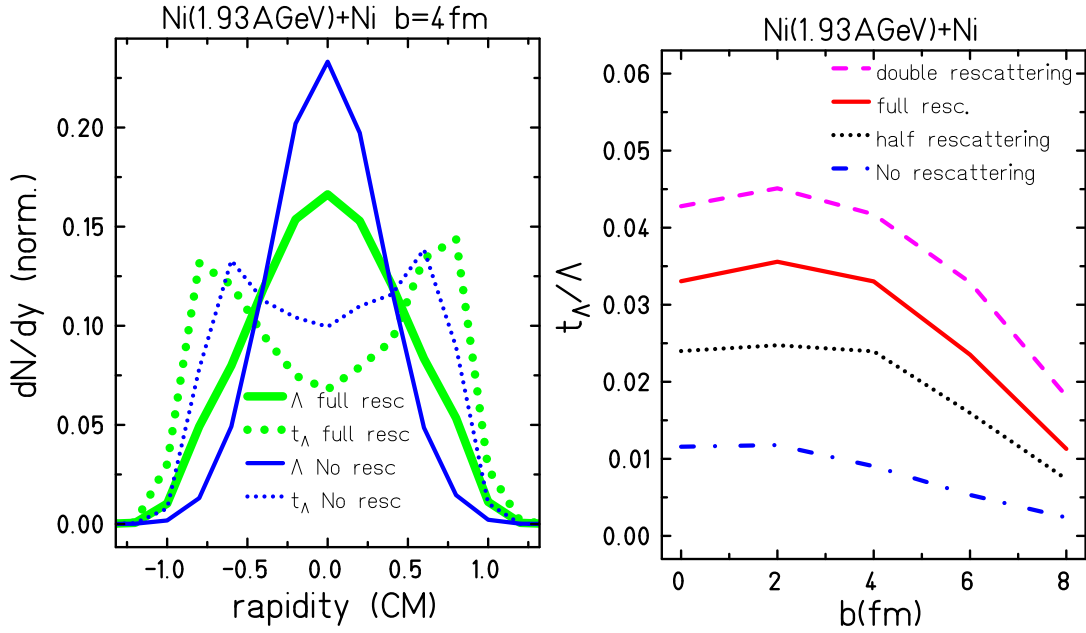


Fig. 3: Normalised rapidity distributions of hyperons and hypertritons with and without rescattering (left) and the ratio hypertritons/hyperons as a function of the impact parameter for different assumptions on the rescattering cross sections (right)

of state or kaon optical potentials of course influence the absolute yield of hypertritons.

Taking into account that the calculated hyperon spectra get lower temperatures than the experimental values we investigated the use of a novel cross section parametrisation inspired by ANKE data [15]. Fig.4 presents on the l.h.s. the “old” parametrisation (dashed line) and the new fit (full line) and on the r.h.s. its effect on the hypertriton to hyperon ratios as function of rapidity. We see that the enhanced cross sections also raise the ratios. For comparison we included results of a more sophisticated analysis [11] but which was still using the old parametrisation. That sophisticated analysis uses a minimum binding energies approach and applies the acceptance cuts of FOPI. We see a good agreement of our simplified model with these calculations which comforts us in using that simplified model for analysing the properties of hypertritons in detail.

4. Properties of hypernuclei

In order to show the correlation of hypertritons to nuclear matter let us compare the transverse flow of Lambdas (full line), nucleons (dashed line) and hypertritons (dotted line), shown on the l.h.s. of Fig. 5. We see that Lambdas show already a significant flow, which is dominantly due to the rescattering of the hyperons with the nuclear matter. That nuclear matter itself shows an even higher flow. Hypertritons show a flow compatible with the rest of the nuclear matter, which underlines the alignment of hypernuclei to the nuclear matter. It is due to a large number of collisions that the hyperons enters into the cluster.

This mechanism is supported by the observation of the freeze-out densities in the mid of Fig. 5: while the maximum density that a hyperon experienced (dashed line), typically the density of its production, is around twice time nuclear density, the freeze-out density (dotted line), i.e. the density of the last collisional contact, is quite lower. This indicates that the collisions persist up to a late phase of the expansion of the nuclear matter. If we regard the hyperons bound in a hypertriton (full line), they

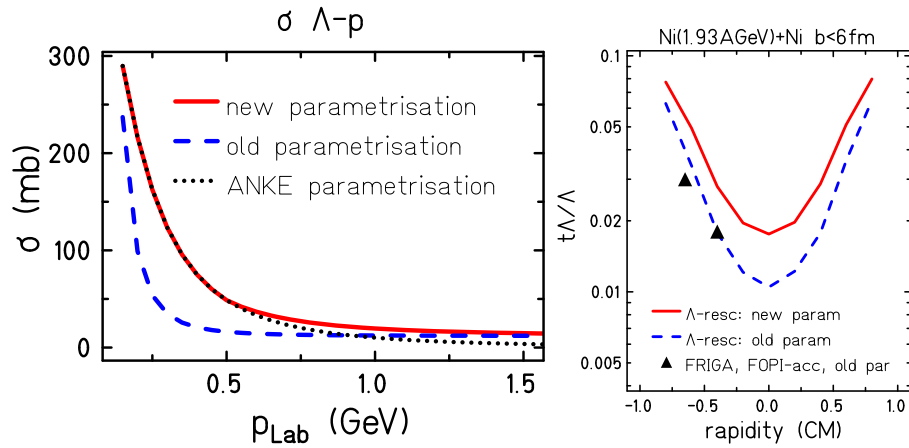


Fig. 4: Description of two parametrizations of rescattering and the hypertriton to hyperon ratio as function of rapidity.

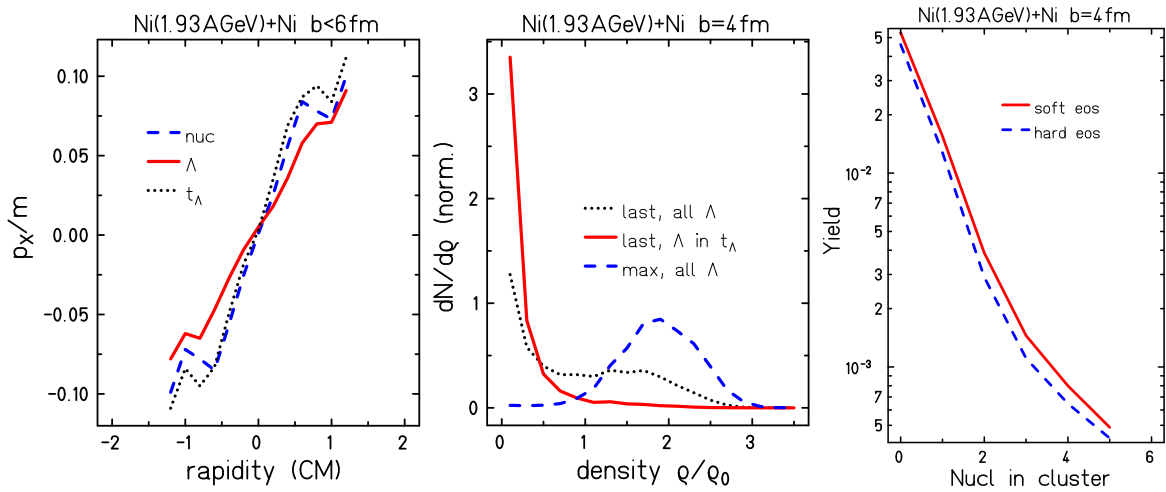


Fig. 5: Left: Transverse flow divided by the mass as function of the rapidity for Lambdas, nucleons and hypertritons. Mid: Maximum densities experienced by the Lambdas and densities at last contact for all Lambdas and Lambdas in hypertritons. Right: Yield of the clusters as a function of the numbers of nucleons in the cluster.

practically all freezed out at densities well below normal matter density.

Let us now look on the properties of hypernuclei at different cluster size. In the following we will describe the hypernuclei by the number of accompanying nucleons in the cluster. Zero means a single unclustered hyperon and serves to underline the difference between unclustered hyperons and hyperons in a cluster. As already indicated, the Lambda has to join the region of spectator matter in order to integrate a cluster. Since these regions are quite far away from the distributions of hyperons (see fig 2), their production is of course extremely suppressed. This finding is confirmed on the r.h.s. of fig 5, which describes the yield of the clusters as a function of the cluster size. The slight dependence of hypercluster yield on the nuclear equation of state is due to the effect of the EOS on the hyperon production. As already mentioned a soft EOS (full line) yields a higher hyperon yield than a hard EOS (dashed line) and thus more hyperclusters can be formed.

Let us first look on the dynamical observables of the clusters. Fig 6 shows on the l.h.s. the directed flow (normalised to the total mass) of the hyperclusters. As already seen on the l.h.s. of

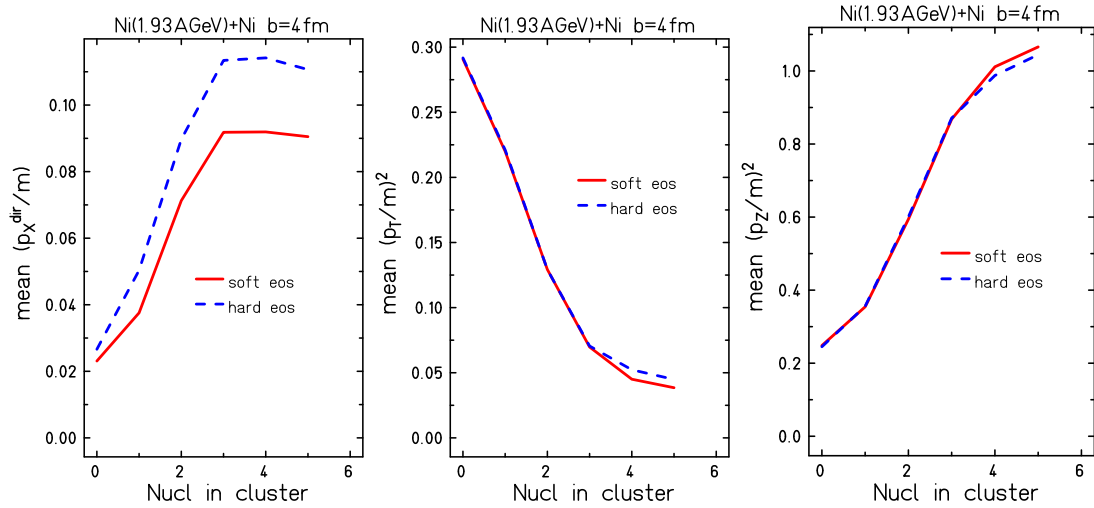


Fig. 6: Directed flow, mean quadratic transverse momentum and mean transverse longitudinal momentum of the hyperon as function of the cluster size

Fig. 5 even unclustered hyperons show a directed flow due to rescattering. Clustered hyperons show an enhanced flow, which increases with fragment size, an effect which is already known from the behaviour of normal nuclear fragments (“The fragments go with the flow”). At higher cluster sizes the flow value seems to saturate. It should also be noted that this observable shows a dependence on the nuclear equation of state, similar to the behaviour known for normal nuclear matter: a hard equation of state causes a higher directed flow.

The mid part and r.h.s. of Fig. 6 show respectively the squared transverse and longitudinal momenta, again normalised by the mass. The transverse momentum decreases with fragment size while the longitudinal momentum increases. This reflects the effect that large clusters can only be found at the projectile/target remnants which remain practically at projectile/target rapidities. This supports the previous statement that the production of large hyperclusters is strongly suppressed by the effect that only few hyperons enter the region of spectator matter.

5. Freeze-out of hypernuclei

As we have demonstrated in the previous section, the hyperons have to undergo rescattering in order to integrate a fragment. This effect is even more pronounced when going to larger hyperclusters. As already seen in the mid of fig 5 practically all hyperons found in a hypertriton show a very low freeze-out density. This feature remains for other hyperclusters as it can be depicted from the l.h.s. of fig 7, which presents the density (in units of the ground state density) at which the last collisional contact between the hyperon and the nuclear matter takes place. While unclustered hyperons freeze out at a density visibly higher than ground state density, while clustered hyperons freeze out at about on third of normal matter density.

The mid part of Fig. 7 presents the total number of collisions the hyperon has undergone in the reaction. Even if unclustered hyperons have already undergone almost 3 collisions with nucleons, the number of collisions increases strongly with the size of the cluster. In hypertritons the hyperons have already collided more than 7 times in the average. This means that many collisions are necessary in order to arrange the hyperon that way in nuclear matter that way that they can be bound into isotopes by the potentials.

The r.h.s. finally gives the “freeze-out time” of the hyperons, i.e the time when the last collision

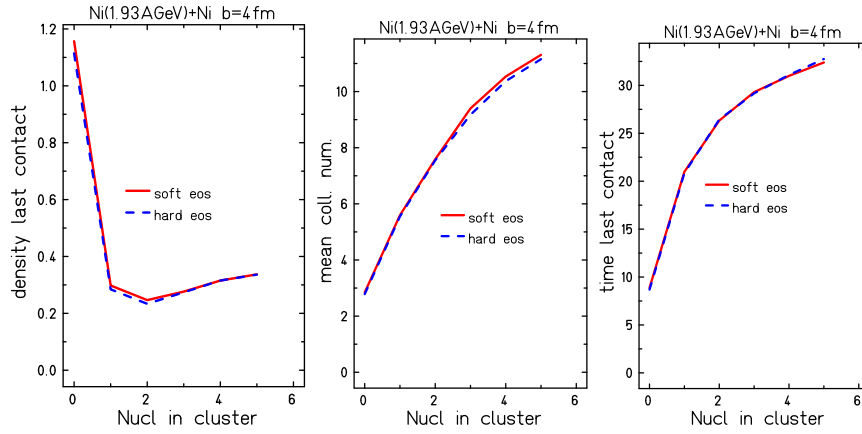


Fig. 7: Freeze-out density, mean collision number of the hyperon and freeze-out time of the hyperon as function of the cluster size

of a hyperon with a nucleon has happened. To give a reference point, the maximum density is reached after about 4-5 fm/c and the passing time (time which would be needed by the projectile to pass the target) is roughly 9 fm/c. This time corresponds exactly to the mean freeze-out time of unclustered nucleons. However, the formation of a hypertriton needs about 2-3 times the passing time and larger hyperclusters still stay in contact for more than 40 fm/c. This demonstrates again that a significant time of "rearrangement" is needed in order to allow a hyperon to take place in a cluster.

6. FRIGA results

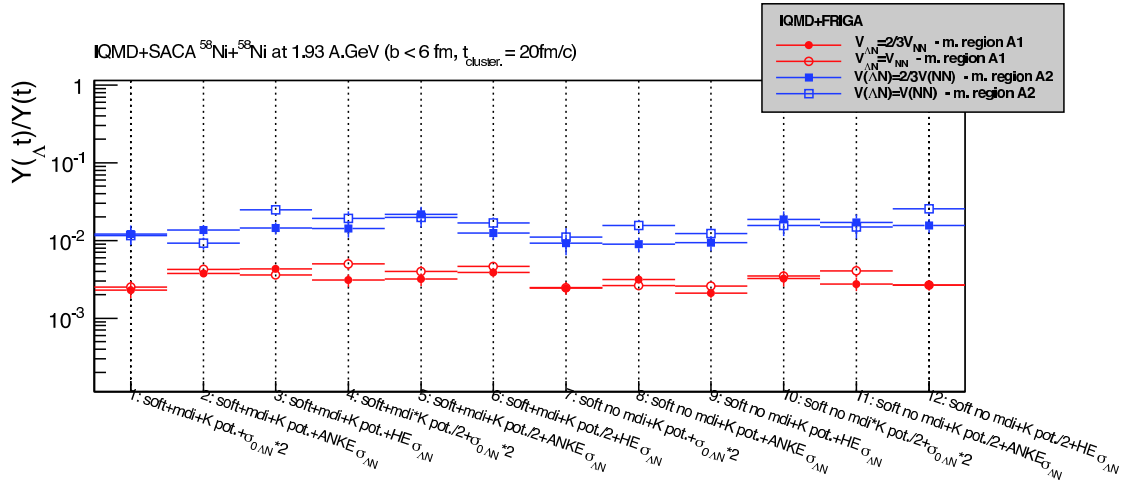


Fig. 8: FRIGA results on the ratio hypertriton/triton applying FOPI acceptance cuts

At the end of this article we want to summarize briefly several effects which can influence the absolute hypertriton yields. For this purpose we present on the r.h.s. of Fig. 8 the results of the FRIGA model on the ratio of hypertritons to tritons obtained in two different phase space regions accessible to FOPI. These phase space regions correspond to the rapidity marked by the triangles in Fig. 4. It should be note that experiment detects the hypernuclei by analysis of the vertex of the decay products ${}^3\text{He}$ and π^- (which have to be detected in a sufficiently large phase space region), by determination of

the invariant mass and by subtraction of combinatorical background. These constraints diminish the accessible region to two rather small areas.

FRIGA is a novel fragmentation approach described more in detail in [11]. It is working similarly to the SACA model [16] applying a Metropolis algorithm in order to find the configuration of maximum binding energy of the clusters. Like SACA it includes Skyrme type interactions and momentum dependent interactions but also surface and asymmetry energies. There is the additional possibility to include pairing energy and shell effects. In order to treat hypernuclei correctly FRIGA also includes hyperon-nucleons interactions, which are normally assumed to correspond to two third of the Skyrme potentials of nucleons. These results are presented in Fig. 8 by full symbols. Additionally calculations assuming the hyperon-nucleon interactions to be identical to the nucleon Skyrme interactions are presented by open symbols. We see that the second option changes the hypertriton yield slightly, since the binding of hyperons in nuclear matter is changed with the forces.

We see additionally the influence of the rescattering cross sections and the kaon optical potential. These results confirm the previous indications about the influence of these quantities: enhancing the cross sections enhances the hypertriton yields. Diminishing the kaon optical potential enhances also the hyperon yield and thus the number of hypertritons again. The preselection of parameters was restrained to calculations using a soft equation of state since the analysis of kaon data clearly indicates that the experimental data can only be explained by the use of a soft EOS [17, 18]. Preliminary results of the FOPI collaboration on this ratio exist, but still under reanalysis, thus an official release has not been published yet.

7. Conclusion

In conclusion we have demonstrated that the formation of hypertritons is strongly affected by the hyperon-nucleon rescattering, which allows the hyperons to enter the phase space of the clusters remaining from the spectator remnants. For that purpose a high number of rescattering is necessary. Hypernuclei show thus a low freeze-out density and a late freeze-out time. Their kinematical properties are strongly aligned to the behaviour of the spectator matter. Further analysis has to be done in order to allow for detailed comparison to nuclear data.

References

- [1] J. Schaffner, C.B. Dover, A. Gal, C. Greiner and H. Stöcker, *Phys. Rev. Lett.* **71**, 1328 (1993)
- [2] P. Papazoglou *et al.*, *Phys. Rev. C* **57**, 2576 (1998)
- [3] O. Hashimoto and H. Tamura, *Prog. Part. Nucl. Phys.* **57**, 564 (2006)
- [4] Y-G Ma (Star collaboration), EPJ Web Conf 66, 04020 (2014)
- [5] T.R. Saito *et al.* (HypHI collaboration), *Nucl. Phys. A* **881** (2012) 218
- [6] R. Lea, (Alice collaboration), *Nucl. Phys. A* **914**, 415 (2013)
- [7] Ch. Rappold *et al.* *Nucl. Phys. A* **913** (2013) 170
- [8] Th. Gaitanos, H. Lenske, U. Mosel, *Phys. Lett B* **675** (2009) 297
- [9] J. Steinheimer *et al.*, *Phys. Lett. B* **714** (2012) 85
- [10] A. Botvina, J. Steinheimer, E. Bratkovskaja, M. Bleicher, J. Pochodzalla, *Phys. Lett. B* **742** (2015) 7
- [11] A. Le Fèvre *et al.*, arXiv:1509.06648v1, to be published in J. Phys. G
- [12] Ch. Rappold *et al.*, *Phys. Lett. B* **747** (2015) 129.
- [13] C. Hartnack *et al.*, *Eur. Phys. J. A* **1**, 151 (1998)
- [14] C. Hartnack, H. Oeschler, Y. Leifels, E. L. Bratkovskaya and J. Aichelin, *Phys. Rep.* **510** (2012) 119
- [15] M. Büscher *et al.*, *Phys. Rev. C* **65**, 014603 (2002) [arXiv:nucl-ex/0107011].
- [16] P.B. Gossiaux, R. Puri, Ch. Hartnack, J. Aichelin, *Nucl. Phys. A* **619** (1997) 379-390.
- [17] C. Fuchs, A. Faessler, E. Zabrodin and Y. M. Zheng, *Phys. Rev. Lett.* **86**, 1974 (2001)
- [18] C. Hartnack, H. Oeschler and J. Aichelin, *Phys. Rev. Lett.* **96**, 012302 (2006) [arXiv:nucl-th/0506087].

One-nucleon transfer reactions and the optical potential

F.M. Nunes^{1,2}, A. Lovell^{1,2}, A. Ross^{1,2}, L.J. Titus^{1,2}, R.J. Charity³, W.H. Dickhoff⁴, M.H. Mahzoon⁴, J. Sarich⁵, S. M. Wild⁵

¹National Superconducting Cyclotron Laboratory, Michigan State University, MI, USA

²Department of Physics and Astronomy, Michigan State University, MI, USA

³Department of Chemistry, Washington University, Saint Louis, MO, USA

⁴Department of Physics, Washington University, Saint Louis, MO, USA

⁵Mathematics and Computer Science Division, Argonne National Laboratory, IL, USA

Abstract

We provide a summary of new developments in the area of direct reaction theory with a particular focus on one-nucleon transfer reactions. We provide a status of the methods available for describing (d,p) reactions. We discuss the effects of nonlocality in the optical potential in transfer reactions. The results of a purely phenomenological potential and the optical potential obtained from the dispersive optical model are compared; both point toward the importance of including nonlocality in transfer reactions explicitly. Given the large ambiguities associated with optical potentials, we discuss some new developments toward the quantification of this uncertainty. We conclude with some general comments and a brief account of new advances that are in the pipeline.

1. Introduction

Nuclear reactions are an important and versatile tool to study nuclei, particularly those nuclei away from stability. One-nucleon transfer reactions can provide information about the single-particle structure of the nucleus of interest (see e.g., [1, 2]). Deuterons are often used as a probe. However, due to its loosely bound nature, it is understood that deuteron breakup effects need to be considered carefully.

A number of experimental programs in rare-isotope facilities worldwide are also using (d,p) and (d,n) reactions as a tool to extract capture rates of astrophysical relevance (e.g., [3, 4]). Given the many ongoing and planned experimental efforts in this direction, it is critical that the reaction theory used to interpret those results be reliable and that the uncertainties in the reaction theory be well understood.

2. Status of the treatment of reaction dynamics

The treatment of deuteron induced reactions involving intermediate and heavy nuclei pose severe challenges to microscopic theory. For most reactions involving these systems, the problem is cast as a three-body scattering problem with effective nucleon-nucleus interactions. We first briefly review the current status of reaction theories for describing deuteron-induced one-nucleon transfer reactions.

The continuum discretized coupled channel method (CDCC) [5] developed in the eighties has now been benchmarked against the exact Faddeev method [6]. The results of this benchmark [7] demonstrate that while the reduction to one Jacobi component is adequate for transfer reaction at low energies, the convergence rate for the low-energy breakup distributions is extremely slow and does not allow for reliable extrapolations. Reaction calculations at higher energies introduce the issue of the energy dependence in the optical potentials. While in coordinate-based methods there is typically a fixed choice of the energy at which the optical potentials are evaluated, in the current implementation of the Faddeev

method [6], calculations are performed in momentum space and can take into account the explicit energy dependence of the interaction in the reaction dynamics. This poses an ambiguity in the comparison that is discussed in detail in [7].

While both the CDCC and Faddeev methods are computationally intensive, the adiabatic distorted wave approximation (ADWA) [8], which is essentially a simplification of CDCC to make all the channels in the continuum degenerate with the ground state (adiabatic approximation), provides a very efficient tool to analyze transfer reactions and explicitly includes deuteron breakup to all orders. A benchmark of this approach with the exact Faddeev has also been performed [9] and the results show that the adiabatic method, while only valid for deuteron-induced transfer reactions, provides as good an agreement as the CDCC method.

Understanding the regions of validity of these reaction theories is very important. However, the current implementation of the Faddeev method [6] also has its limitations, a fact that became clear during the benchmarking process [10]. As the effects of the Coulomb force increase, namely as the energy decreases and/or the charge increases, the method of Coulomb screening used by [6] begins to fail. For example, currently we are not able to produce exact cross sections for $^{10}\text{Be}(d,p)$ below ≈ 5 MeV, $^{48}\text{Ca}(d,p)$ below ≈ 15 MeV, or any reaction cross section of interest for isotopes heavier than Ni. One way to overcome this problem is to cast the Faddeev equations in the Coulomb basis instead of the traditional plane wave basis [11]. By doing this, one avoids Coulomb screening completely. The TORUS collaboration [12], a topical collaboration in nuclear theory with the goal of advancing methods of (d,p) reactions, has put in place many pieces of the puzzle necessary to solve the Faddeev equations in the Coulomb momentum space basis [13, 14, 15]. We expect in the next couple of years to have a completely new and fully developed code that can address the three-body problem of $A(d,p)B$ for nuclei with large Z .

3. Nonlocality in optical potentials and transfer reactions

One of the most important ingredients in predictions of reaction cross sections are the optical potentials. From a microscopic point of view, it is clear that the nucleon-nucleus optical potential should be non local due to many-body effects, including antisymmetrization and excitations. However, phenomenological potentials have traditionally been assumed local, for convenience. The consequence of this simplification is that it becomes strongly energy dependent. As many-body methods improve, including more and more correlations and a careful treatment of the continuum, one can expect the optical potential to be fully extracted from these many-body theories in the near future. It is therefore timely for reaction theory to be prepared to handle nonlocality in the effective interactions and to understand the magnitude of the effects.

It is clear that for any non-local potential, one can construct local phase-equivalent potentials, i.e., reproducing the exact same elastic scattering. Even when the elastic scattering is exactly reproduced, nonlocality can imprint itself in other channels. In [16, 17] the problem is addressed for one-nucleon transfer reactions. In the first of these works [16], a large number of reactions at different beam energies and for different targets are considered. The Perey and Buck non-local optical potential was used [18] and local phase-equivalent potentials were constructed. Finally, the inclusion of nonlocality in one-nucleon transfer reactions populating single-particle states was studied. The study was performed in DWBA and nonlocality was included only in the exit channel, namely in the neutron-bound state and the proton-distorted wave. A similar study was performed using the dispersive optical model [19]. Generally, the nonlocality in the scattering state reduced the cross section, while the nonlocality in the bound state increased it, with the net effect being an increase as large as 30%. In [17] we consider hole states in ^{40}Ca , again using DWBA and nonlocality only in the exit channel. The dispersive optical model and the Perey and Buck potentials provide similar results. The effect of nonlocality on transfer

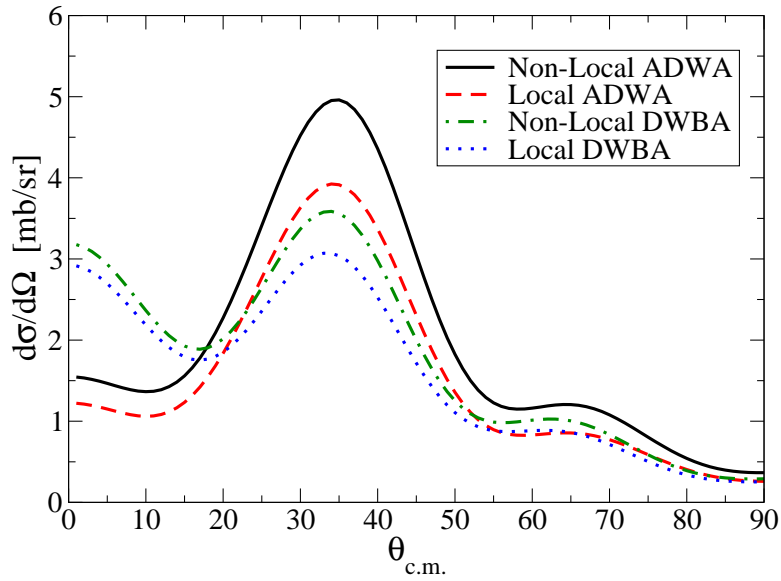


Fig. 1: Angular distributions for $^{126}\text{Sn}(d,p)^{127}\text{Sn}$ at $E_d = 20$ MeV: comparing the inclusions of nonlocality in the exit channel for ADWA and for DWBA.

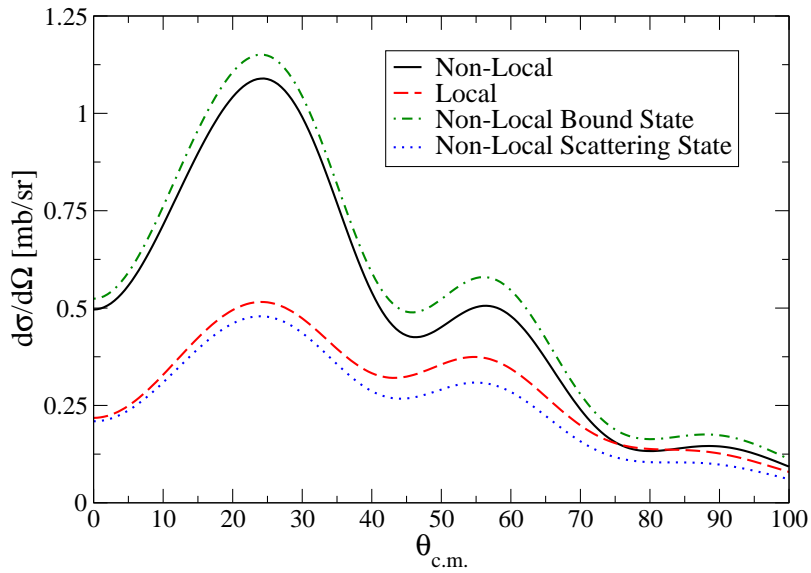


Fig. 2: Angular distributions for $^{126}\text{Sn}(d,n)^{127}\text{Sb}$ at $E_d = 20$ MeV: comparing the inclusions of nonlocality in the exit channel for ADWA and for DWBA.

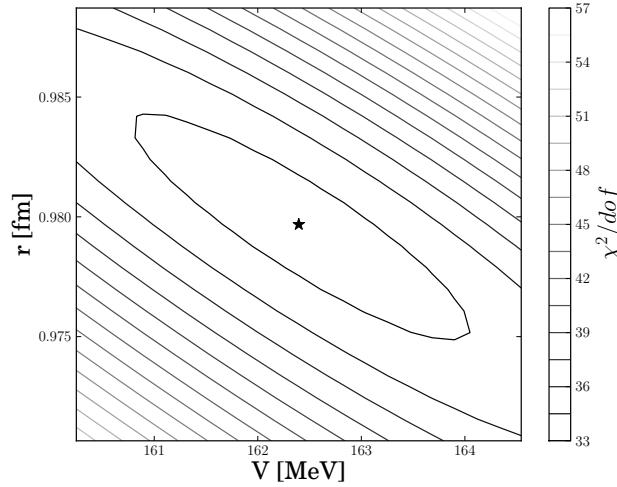


Fig. 3: Contour plot for the residuals resulting for the fit of neutron elastic scattering on ^{48}Ca at 23 MeV, when varying the radius parameter r of the real part of the optical potential and the corresponding depth V .

is very large for these hole states (up to 50%).

In Fig. 1 we show the predicted transfer cross sections for $^{126}\text{Sn}(d,p)^{127}\text{Sn}$ at $E_d = 20$ MeV. Comparing the local DWBA predictions (blue dotted line) with the corresponding non local (green dot-dashed line), we see an effect of up to 20% in magnitude. Also shown, for completeness, are the same results within ADWA (red dashed for the local and black solid for the non local). While ADWA and DWBA show noticeably different angular distributions (a difference coming from the different treatment of deuteron breakup), the relative effect of nonlocality is magnified in ADWA. Note that in these ADWA calculations, the nonlocality in the deuteron channel is not yet included. Nonlocality in the deuteron channel will be discussed elsewhere [20].

Because nonlocality is introduced in the nuclear interaction only, one would expect to find similar effects in the study of (d,n) reactions. In Fig. 2 we show the angular distributions for $^{126}\text{Sn}(d,n)^{127}\text{Sb}$ at $E_d = 20$ MeV. All lines in Fig. 2 correspond to DWBA calculations. The result when using the local interactions is shown by the red dashed line and that including the non-local interactions is the black solid line. Note that the ground state of ^{127}Sb is different than that of ^{127}Sn , given the different proton and neutron numbers of the target. While the ground state of ^{127}Sn is a $1h_{11/2}$ state, in ^{127}Sb the ground state is $1g_{7/2}$ with a significant difference in the binding energy. In addition, the proton state is subject to Coulomb repulsion. All these differences compound to produce a very different effect of nonlocality for the (d,p) and (d,n) reactions on heavy nuclei. For $^{126}\text{Sn}(d,n)^{127}\text{Sb}$, the effect of nonlocality is very large, doubling the cross section at the peak. We also show in Fig. 2 the separate effects of introducing nonlocality in the neutron bound state (green dot-dashed line) and the proton scattering state (blue dotted line). Nonlocality in the proton scattering state reduces the cross section but only by a little. The larger effect is in the nonlocality in the bound state.

These studies all call for the need to include nonlocality explicitly in reactions for a reliable description of the process.

4. Optical potential uncertainties

The study in [1] demonstrates that the optical potential uncertainties are reduced in ADWA when compared to DWBA, the main reason being that ADWA relies only on nucleon optical potentials, whereas

DWBA requires a deuteron optical potential that is less well constrained. Knowing that these effective interactions carry ambiguities, it is important to quantify the uncertainties in the predicted reaction observables. So far estimates of these uncertainties have been performed by comparing the results when two arbitrary optical potentials are chosen (e.g., [2]). Then the results of the estimated error bars depend on the choice of the two representative potentials. Alternatively, one can make use of modern techniques in the field of uncertainty quantification and explore these tools in the domain of reaction theory.

Our plan is to use modern statistical tools to quantify uncertainties in nuclear reactions (see e.g., [21]). This is largely an untapped field and therefore we start with a simple case. We look at the case of $^{48}\text{Ca}(d,p)^{49}\text{Ca}$ in DWBA and examine the effect of the uncertainty from constraining the deuteron optical potential on the predicted transfer cross section. We use elastic scattering data at 23.2 MeV from [23] and perform a χ^2 minimization to find the best fit. We take a typical Woods-Saxon shape and the parametrization of [24] as a starting point for the minimization routine. We allow all three parameters in the central volume real and the central surface imaginary terms (depth, radius, and diffuseness) to vary simultaneously (the spin-orbit interaction is kept fixed). Parameters are only allowed to vary within physical limits. The minimum found is summarized in Table I, with initial parameters shown in parentheses. We then verify that the distribution of the total χ^2 in the elastic channel, around the minimum, is Gaussian. This can be seen by the elliptical behavior of the $||\chi^2||$ contour plots. In Fig. 3 we show an example of such a plot, where the vertical axis is the potential depth and the horizontal axis is the radius of the volume term.

We then pull 200 sets randomly from the Gaussian distribution based on the elliptical behaviour surrounding the minimum, throw out the largest 5 and lowest 5 predicted cross sections per angle, to obtain the 95% confidence band. Using the same 200 sets, we define the 95% confidence bands independently for elastic and transfer. The results are depicted in Figs. 4 and 5.

The error bars considered in quantifying the χ^2 for these calculations were the experimental error bars. However, often the difference between data and theory is larger than the experimental error bars. One can then repeat the procedure including the theoretical error. Also noteworthy, there are cases in which the distribution around the minimum is not Gaussian. Then one may need to pull the random sets from the regions of constant χ^2 directly and/or appeal to Bayesian techniques [25, 26].

A refinement of the fitting can be done by including a larger set of data, with perhaps a variety of observables. As an example, we have started to look at simultaneously fitting elastic and inelastic cross sections, including target excitation in the reaction model. While a larger number of parameters are available for fitting, the actual procedure for extracting confidence bands is the same. A more challenging problem is that of the uncertainty in the theoretical model itself. More work will be needed to determine the best approach.

	Depth [MeV]	Radius [fm]	Diffuseness [fm]
Volume Term (real)	162.4 (103.2)	0.98 (1.05)	0.69 (0.86)
Surface Term (imaginary)	48.7 (16.5)	1.1 (1.43)	0.30 (0.67)
Spin-Orbit Term	3.33	1.07	0.66

Table 1: Best fit parameters for the elastic scattering of $^{48}\text{Ca}(d,d)^{48}\text{Ca}$. The spin-orbit term was not fit. All optical model potential parameters not listed here were zero. The optimization was initialized at the value in parentheses.

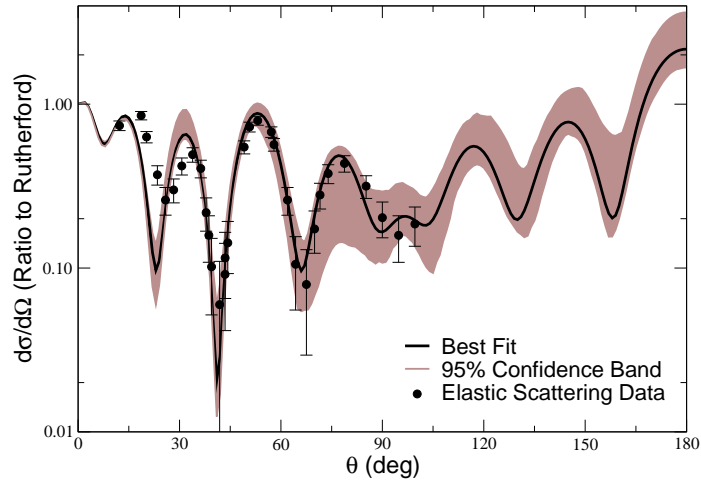


Fig. 4: Elastic scattering angular distribution for neutrons on ^{48}Ca at 23.2 MeV: solid black line is the best fit, the brown corresponds to the 95% confidence band and in black are the data points [23].

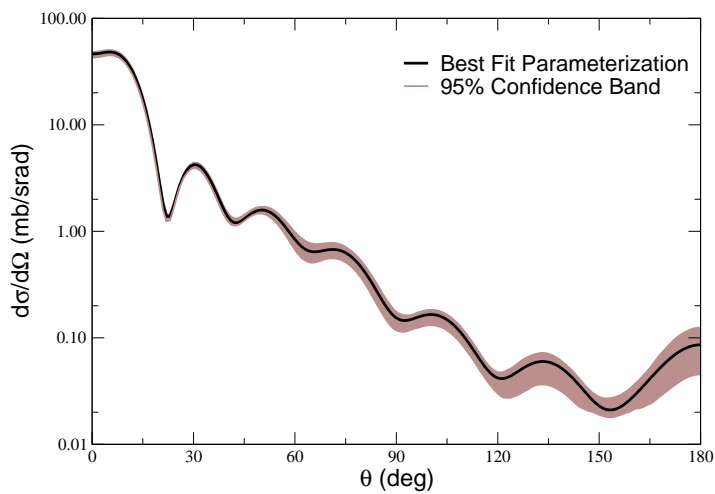


Fig. 5: Angular distribution for $^{48}\text{Ca}(d,p)^{49}\text{Ca}$ at 23.2 MeV: solid black line is the best fit, the brown corresponds to the 95% confidence band.

5. Outlook

As described here, there are a number of exciting developments in reaction theory. The implementation of the Faddeev equations in the Coulomb basis is progressing and will provide reliable predictions for (d,p) reactions for a wide range of nuclei and energies. The studies performed on non-local interactions demonstrate the need to include these interactions explicitly in describing transfer processes. While these are critical studies for the future of the field, they still rely on the knowledge of the effective interactions between nucleons and the target.

Although traditionally these effective interactions have been extracted phenomenologically, we are currently beginning an era where the level of nuclear many-body methods may enable the extraction of these potentials directly from the NN interaction. A new collaboration between our group and the ORNL theory group aims at extracting these potentials from coupled-cluster theory. While one might still expect a deficiency in the absorptive component, the inclusion of a variety of correlations and the continuum basis hold promise for using this method versus other many-body methods.

Last but not least, we are starting to develop techniques to quantify uncertainties in reaction theory. This work is still in its infancy. As described in this proceedings, we are still exploring the best way to characterize the uncertainties for the limited problem of the effect of the errors in a given data set in constraining the interaction and the propagation to reaction observables. There are many other sources of uncertainties in reaction theory, which may be equally or even more important. These need to be considered case by case and then accounted for jointly so that we can provide a reliable and useful procedure for uncertainty quantification in this field.

This work was supported by the National Science Foundation under Grant No. PHY-1403906 and PHY-1304242 and the Department of Energy, Office of Science, Office of Nuclear Physics under award No. DE-FG52-08NA28552, DE-SC0004087, DE-87ER-40316. This work was also supported by the U.S. Department of Energy, Office of Science, Advanced Scientific Computing Research program under contract number DE-AC02-06CH11357.

References

- [1] K. Schmitt, K. Jones, A. Bey, S. Ahn, D. Bardayan, et al., *Phys.Rev.Lett.* 108, 192701 (2012).
- [2] K. L. Jones, F. M. Nunes, A. S. Adekola, D. W. Bar7 dayan, J. C. Blackmon, K. Y. Chae, K. A. Chipps, J. A. Cizewski, L. Erikson, C. Harlin, et al., *Phys. Rev. C* 84, 034601 (2011).
- [3] R. Kozub, *et al.*, *Phys.Rev.Lett.* 109, 172501 (2012).
- [4] C. Langer, *et al.*, *Phys. Rev. Lett.* 113, 032502 (2014).
- [5] N. Austern, Y. Iseri, M. Kamimura, M. Kawai, G. Rawitscher, and M. Yahiro, *Physics Reports* 154, 125 (1987).
- [6] A. Deltuva and A. Fonseca, *Phys.Rev.* C79, 014606 (2009).
- [7] N. Upadhyay, A. Deltuva, and F. Nunes, *Phys.Rev.* C85, 054621 (2012), 1112.5338.
- [8] R. C. Johnson and P. C. Tandy, *Nucl. Phys. A* 235, 56 (1974).
- [9] F. M. Nunes and A. Deltuva, *Phys.Rev.* C84, 034607 (2011).
- [10] F. M. Nunes and N. J. Upadhyay, *J. Phys: Conf. Series*, 403 (2012) 012029.
- [11] C. Elster, L. Hlophe, V. Eremenko, F. M. Nunes, G. Arbanas, J. E. Escher, and I. J. Thompson, *Proceedings of the International Conference on Nuclear Theory in the Supercomputing Era*, (2014).
- [12] TORUS collaboration reactiontheory.org
- [13] N. Upadhyay *et al.*, *Phys. Rev. C* 90 (2014) 014615.
- [14] L. Hlophe, *et al.*, *Phys. Rev. C*, 88 (2013) 064608; *Phys. Rev. C*, 90 (2014) 061602.
- [15] V. Eremenko, *et al.*, *Comp. Phys. Comm.* 187, 195 (2015).
- [16] L. J. Titus and F. M. Nunes, *Phys. Rev. C* 89, 034609 (2014).
- [17] A. Ross, *et al.*, *Phys. Rev. C* *submitted*.
- [18] F. Perey and B. Buck, *Nuclear Physics* 32, 353 (1962).

- [19] M. H. Mahzoon, R. J. Charity, W. H. Dickhoff, H. Dussan, and S. J. Waldecker, *Phys. Rev. Lett.* 112, 162503 (2014).
- [20] L.J. Titus and F.M. Nunes, *in preparation*.
- [21] S.M. Wild, J. Sarich, and N. Schunck, *J. Phys. G: Nucl. Part. Phys.* 42, 034031 (2015) [arXiv:1406.5464].
- [22] A. Lovell and F. Nunes, *J. Phys. G* 42, 034014 (2015).
- [23] A. Marinov, L.L. Lee, and J.P. Schiffer, *Phys. Rev.* 145, 852 (1966).
- [24] J.M. Lohr and W. Haeberli, *Nucl. Phys. A* 232 381 (1974).
- [25] D. Higdon, J.D. McDonnell, N. Schunck, J. Sarich, and S.M. Wild, *J. Phys. G: Nucl. Part. Phys.* 42, 034009 (2015) [arXiv:1407.3017].
- [26] J. D. McDonnell *et al.*, *Phys. Rev. Lett.* 114, 122501 (2015).

Comparison of coupled-channel studies of nucleon scattering from oxygen isotopes with the shell model

S. Karataglidis^{1,2}, J. P. Svenne³, K. Amos^{2,1}, L. Canton⁴, P. R. Fraser⁵, and D. van der Knijff²

¹ Dpt. of Physics, University of Johannesburg, South Africa

² School of Physics, University of Melbourne, Australia

³ Dpt. of Physics and Astronomy, University of Manitoba and Winnipeg Institute for Theoretical Physics, Winnipeg, Canada

⁴ Istituto Nazionale di Fisica Nucleare, Sezione di Padova, Italia

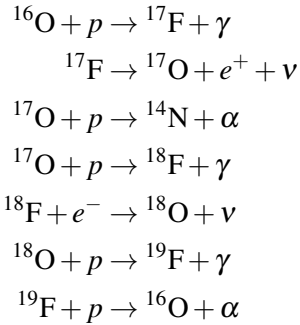
⁵ Dpt. of Physics, Astronomy, and Medical Radiation Sciences, Curtin University, Perth, Australia

Abstract

The structures of ^{17}O and ^{17}F are studied via the Multi-Channel Algebraic Scattering (MCAS) method, which describes low-energy nucleon-nucleus scattering with a collective model specification for the target states. The model allows for the incorporation of the Pauli Principle in the interactions describing the scattering and the formation of the compound states. The collective model in the current version of MCAS can be either rotational or vibrational, and we utilise a vibrational model specification of the spectrum of ^{16}O to obtain the states in the mass-17 systems. Comparison is made with results from large-scale multi- $\hbar\omega$ shell model calculations for the mass-17 nuclei. Results for the spectra of mass-19 nuclei, formed by the coupling of a nucleon from ^{18}O , from both the shell model and MCAS are also presented.

1. Introduction

The mass-17 nuclei are important in the synthesis of the elements beyond carbon. After carbon burning begins, elements up to fluorine are created by successive proton capture reactions [1] and β -decays. If one considers the NO and OF parts of the CNO cycle [2], one finds,



illustrating that both ^{17}O and ^{17}F play a vital role in the cycle, and lead to the breakout from the cycle to those creating the heavier elements. In the first reaction, proton capture on ^{16}O will preferably proceed via capture to the $1s_{1/2}$ state, which has a Q value of only 105 keV. The $1/2^+$ state in ^{17}F is a proton halo [3].

As the two nuclei are formed by a single nucleon coupling to an ^{16}O core, they are of interest for their own sake. They are mirror nuclei, with the first three-positive parity states reflecting the single particle energies of the $0d_{5/2}$, $1s_{1/2}$, and $0d_{3/2}$ levels in the sd -shell model. However, there is significant mixing of $2\hbar\omega$ components in the wave functions: $\sim 25\%$ in the ground states, coming from $2p$ - $2h$

components giving rise to additional particles in the sd shell. It is instructive, then, to compare the shell models available with the collective model structures that a Multi-Channel Algebraic Scattering (MCAS) theory [4] provides for the compound nuclei formed in the scattering of a nucleon from ^{16}O . It is not a trivial exercise: the spectrum of ^{16}O requires a minimum of a $4\hbar\omega$ model [5, 6, 7].

2. MCAS in summary

MCAS has been extensively described elsewhere [4], and so only a brief summary is presented herein, for the purposes of highlighting the aspects of the method of relevance to the present results. The method is a means of solving the coupled-channel Lippmann-Schwinger (LS) equations for the scattering of low-energy (spin-1/2) projectiles from target (spin-0) nuclei, in momentum space. More generally, it is the description of a two-cluster system, which is formed by the coupling of the projectile to the target. For the present set of calculations the projectile is a nucleon. It is assumed that the core (target) is described by the collective model, with the spectrum of the target suggesting a rotational or vibrational model. That allows for the specification of the matrix of interaction potentials defining the coupled-channel problem. The matrix of potentials is expanded in terms of sturmian functions, and a finite set of ~ 30 sturmians is used to ensure convergence. The Pauli Principle is handled by the use of orthogonalising pseudo-potentials (OPP), with weights of 10^6 MeV to guarantee that the sturmians are orthogonal to any states corresponding to a nucleon coupling to a filled orbit in the target [8, 9].

Once the sturmians and OPPs are set, the matrix of potentials is expressed as a sum of separable potentials in momentum space, which are input to the coupled LS equations. Solutions of the equations are obtained in momentum space, allowing for the evaluation of both bound (negative energy solutions) and scattering (positive energy solutions) states. Those are found as poles in the S matrix, by which both the centroid energies and (partial) widths corresponding to the specific nucleon-nucleus channel (where appropriate) of the states are found. It is important to note that by this means there is no requirement for the specification of any spectroscopic factor linking the A to the $A + 1$ system.

3. Shell model aspects

While the spectrum of ^{16}O requires a full $4\hbar\omega$ shell model for description [5], the ground state found by Brown and Green is dominated by $0\hbar\omega$ and $2\hbar\omega$ components which correspond approximately to those found from a pure $(0 + 2)\hbar\omega$ shell model [7]. In that respect, we may calculate the spectra of ^{17}O and ^{17}F in a $(0 + 2)\hbar\omega$ model space, for the positive parity states, and a $(1 + 3)\hbar\omega$ model space for the negative parity states. In both sets of calculations all shells from the $0s$ to the $0f1p$ are used, with all particles active. We calculate the spectrum using OXBASH [10] with the WBP interaction of Warburton and Brown [11]. Any calculations of transition rates between states in ^{16}O to indicate the strength of the couplings, however, will require a full $4\hbar\omega$ model space calculation to ensure a proper description of the ^{16}O spectrum; that is work in progress. The resultant spectrum, together with the known spectra for ^{17}O and ^{17}F [12], is shown in Fig. 1.

It is clear that the spectrum obtained from the shell model compares well with both spectra. Discrepancies between the calculated and observed spectra may result from both restrictions placed upon the model space and the underlying limitation on the ^{16}O ground state. Nevertheless, this result illustrates that a single-particle picture of the mass-17 system is inadequate, and that a coupled-channel approach with many excited states of ^{16}O is warranted. The spectrum of ^{19}O , below the neutron scattering threshold, is shown in Fig. 2. Both the shell model and MCAS reproduce the spectrum, although the first excited state appears a little higher from the shell model. An additional $3/2^+$ state appears in the spectrum obtained from MCAS, however; that may be due to the potential parameter set used.

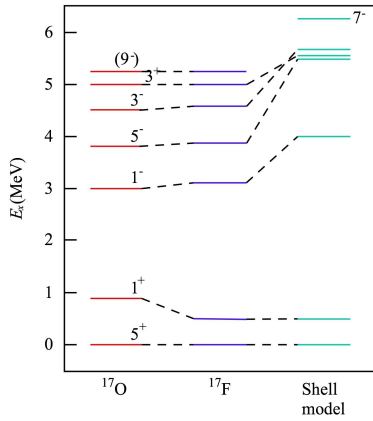


Fig. 1: Spectra for ^{17}O and ^{17}F [12], with zero energy corresponding to the ground states of each. The state labels denote $2J^\pi$.

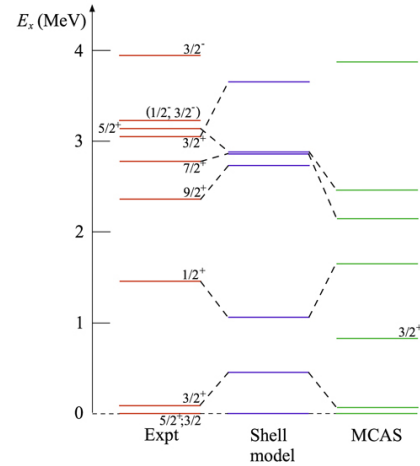


Fig. 2: Spectrum of ^{19}O , below the $n + ^{18}\text{O}$ threshold.

4. MCAS aspects

The MCAS has been applied to $n + ^{16}\text{O}$, leading to compound states in ^{17}O , using the vibrational model and 5 target states in ^{16}O , namely the ground state, the 0_2^+ state (6.049 MeV), the 3_1^- state (6.130 MeV), the 2_1^+ state (6.917 MeV), and the 1_1^- state (7.117 MeV). The parameters for the Woods-Saxon functions used in the calculation are $R_0 = 3.15$ fm, and $a = 0.65$ fm. The potential parameters (positive and negative parity) are, in units of MeV,

$$\begin{aligned} V_0^- &= -47.15; V_0^+ = -50.60 \\ V_{ll}^- &= 2.55; V_{ll}^+ = 0.00 \\ V_{ls}^- &= 6.90; V_{ls}^+ = 7.20 \\ V_{ss}^- &= 2.50; V_{ss}^+ = -2.0, \end{aligned} \quad (1)$$

with two deformation parameters, $\beta_2 = 0.21$ and $\beta_3 = 0.42$. To obtain the spectrum of ^{17}F , we add a Coulomb potential. Also, while Pauli blocking of the $0s_{\frac{1}{2}}$ and $0p_{\frac{3}{2}}$ orbits have been incorporated by the addition of the OPP, Paul hindrance [9] has also been included for the higher orbits. In particular, this includes the $0p_{\frac{1}{2}}$ orbit, to account for the ground state of ^{16}O being $4\hbar\omega$ in character.

Fig. 3 shows the spectra of ^{17}O and ^{17}F as compared to the result obtained from MCAS. Agreement with the known spectra is quite good, with the low-lying states well-reproduced. Comparison to Fig 1 shows the results from MCAS agree well also with the results from the shell model. Above the nucleon thresholds, the density of states make identification of states difficult, though the trends in the groupings of states in the known spectra are reproduced. Changes to the Coulomb potential parameters have little influence on the spectrum of ^{17}F .

The low-energy neutron scattering cross section from ^{16}O is shown in Fig. 4. It is clear from Fig. 4 that the cross section obtained from MCAS is in agreement with the data. The resonance structure is reproduced, and there is some indication for more resonances around 1 MeV which are not present in the available data.

The spectrum of ^{19}O from both the shell and MCAS, with the scattering states, is shown in Fig. 5. Only the positive parity states from the shell model are shown. As with Fig. 2, there is generally good agreement. But above the scattering threshold there is indication of more states predicted by MCAS that

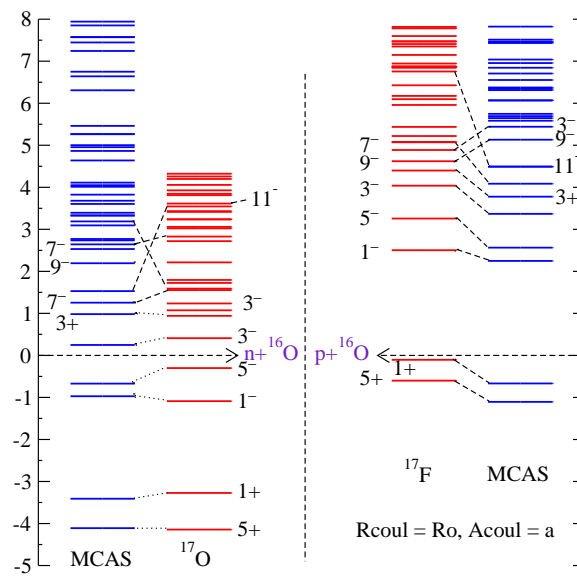


Fig. 3: Spectra of ^{17}O and ^{17}F obtained from MCAS, as compared to the known spectra. Notation is as for Fig. 1, and the zero energy corresponds to the nucleon scattering threshold.

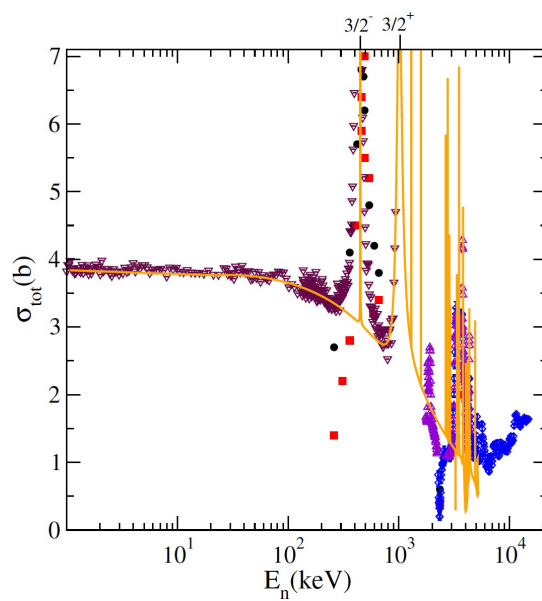


Fig. 4: Low-energy neutron scattering cross section from ^{16}O , showing states in ^{17}O . Note that the energy is on a log-scale.

- and W. D. M. Rae, and N. S. Godwin (MSU version by B. A. Brown, 1986); B. A. Brown, A. Etchegoyen, and W. D. M. Rae, MSUCL Report Number 524 (1986).
[11] E. K. Warburton and B. A. Brown, *Phys. Rev. C* **46** (1992) 923.

Coulomb-nuclear interference in the inelastic scattering of ${}^6\text{Li}$ to the first quadrupole state in the Ge isotopic chain

T. Borello-Lewin¹, M. R. D. Rodrigues¹, X. X. Zhang¹, C. L. Rodrigues¹, G. M. Ukita², J. L. M. Duarte¹, L. B. Horodynski-Matsushigue¹

¹Instituto de Física, Universidade de São Paulo, São Paulo, Brasil

²Faculdade de Psicologia, Universidade de Santo Amaro, São Paulo, Brasil

Abstract

Angular distribution for the inelastic scattering of 28 MeV ${}^6\text{Li}$ on ${}^{76}\text{Ge}$ was measured using the São Paulo Pelletron-Enge-Spectrograph facility. The Coulomb-nuclear interference (CNI) analysis was applied to the first quadrupole state transition. The value of $C_2 = \delta_2^C / \delta_2^N$, the ratio of charge to isoscalar deformation lengths, and of δ_2^N were extracted through the comparison of experimental and DWBA-DOMP predicted cross sections. The ratio of reduced charge to isoscalar transition probabilities, B(E2) to B(IS2) respectively, is related to the square of the parameter C_2 and was thus obtained due to the advantage of scale uncertainty cancellation with a relative accuracy of less than 4%. The value of $C_2 = 1.101(20)$ obtained indicates a slight predominance of the protons relative to the neutrons in the transition for ${}^{76}\text{Ge}$. In this context the present result composed with previous results of CNI measurements obtained in ${}^{70,72,74}\text{Ge}$ suggests for ${}^{74}\text{Ge}$ a strong ground state configuration mixing.

1 Introduction

The characteristics of excited states 2_1^+ are widely used as indicators of nuclear structure, particularly the electric reduced transition probability B (E2) is used as a measure of the collective characteristic of these transitions. The B (E2) is in principle sensitive, if polarization effects may be disregarded, only to the contribution of the charge and to quantify the contributions of neutrons is also an important ingredient to characterize the collective behaviour. The Ge (Z=32) isotopic chain, in the transitional mass region around A=70, is particularly well suited to study the role of the neutrons. In fact, the evolution of B (E2) values indicate around N=40 a transition and furthermore the nucleus ${}^{72}\text{Ge}$ presents a 0^+ first state, possible consequence of the correspondent subshell closure [1,2]. In this context it to be stressed that direct access to reduced isoscalar transition probability B (IS2) is also required. Particularly suitable to reach this aim are inelastic scattering measurements of isoscalar interacting projectiles in an incident energy that enhance coulomb-nuclear interference (CNI). These measurements allow simultaneous extractions of B(IS2) and the ratio between electric and isoscalar reduced transition probabilities B(E2)/B(IS2) [3-5]. The values of $C_2 = \delta_2^C / \delta_2^N$, the ratio of charge to isoscalar deformation lengths, and of $(\delta_2^N)^2$ are extracted through the comparison of experimental and DWBA-DOMP predicted angular distributions. The ratio of reduced charge to isoscalar transition probabilities, B(EL) to B(ISL) respectively, are related to the square of the parameter C_2 and were thus obtained with the advantage of scale uncertainties cancellation. This paper refers to the CNI study of 28 MeV ${}^6\text{Li}$ inelastic scattering on ${}^{76}\text{Ge}$ recently measured using the São Paulo Pelletron-Enge-Spectrograph facility in comparison with the results of the previous work on ${}^{70,72,74}\text{Ge}$ [5]. The C_2 values obtained for ${}^{70,72}\text{Ge}$ are slightly higher than 1.0, indicating a homogeneous excitation with a small predominant contribution of protons in the transition to the first quadrupole state 2_1^+ . On the other hand an abrupt change with $C_2 = 0.775(8)$ was obtained for ${}^{74}\text{Ge}$.

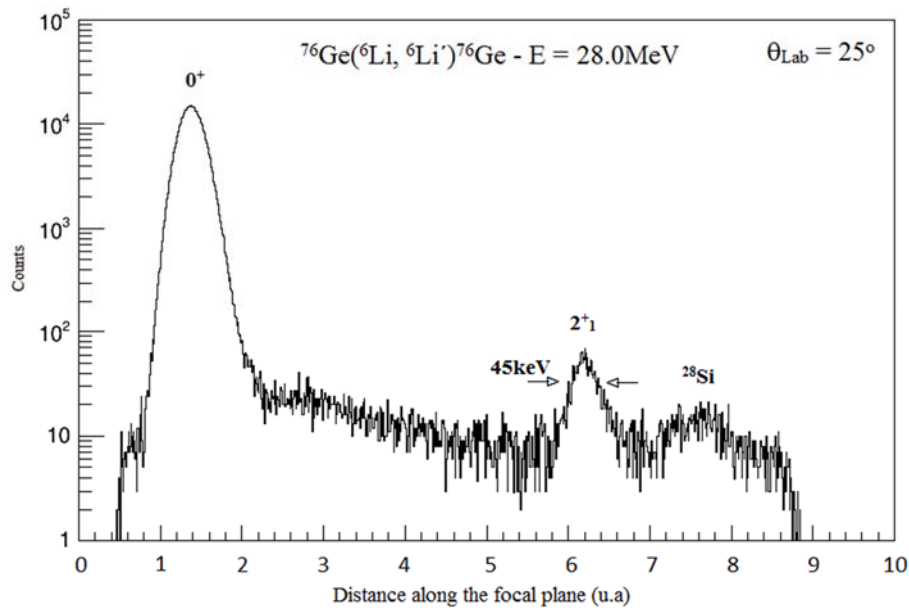


Fig. 1: Position spectrum at the scattering angles $\theta_{\text{Lab}} = 25^\circ$.

2 Experimental setup

Inelastic scattering of ${}^6\text{Li}$ on ${}^{76}\text{Ge}$ data were obtained using the Pelletron-Spectrograph-Magnet-Enge facility. A solid-state position sensitive detector (PSD) of $500\ \mu\text{m}$ thickness, area $47 \times 8\ \text{mm}^2$ was positioned on the focal plane. The ${}^6\text{Li}$ is the lightest isoscalar projectile appropriate for CNI measurements in the region around $A=70$, at bombarding energies suitable for stable operation of the São Paulo Pelletron accelerator. The 28.0 MeV energy ${}^6\text{Li}$ beam was focused after passing defining slits of $1.0 \times 2.0\ \text{mm}^2$ on an enriched self-supported target of ${}^{76}\text{Ge}$ with $510.5 \cdot 10^{15}$ atoms/ cm^2 thickness. An entrance solid angle of 0.65 msr was used, the emerging ions of the reaction admitted and momentum analysed by the field of the spectrograph were detected in the PSD. Twenty-six spectra were measured at carefully chosen scattering angles in a range of $10^\circ \leq \theta_{\text{Lab}} \leq 55^\circ$, in order to characterize CNI in the angular distribution corresponding to the first quadrupole excitation. Relative normalization of the data for the various scattering angles was obtained through the total charges collected by the Faraday cup. The absolute normalization was obtained from the target thickness and the solid angle values. The scale uncertainty was estimated to be around 20%.

The digital pulse processing (DPP) acquisition system used in the measurement was composed by the board PCI-6133 from National Instrument, setting 2.5 MS/s as the maximum rate sample of analogic inputs for the digitalization. The analysis of the pulse shape and the use of electronic noise filters provide an important resolution improvement. Figure 1 shows the position spectrum along the focal plane at the scattering angle $\theta_{\text{Lab}} = 25^\circ$. The three peaks observed on figure are associated with the elastic scattering, the inelastic scattering to the 2_1^+ state and the elastic scattering on silicon contaminant. The energy resolution achieved was about 45 keV.

3 Data analysis and Results

The distorted wave Born approximation (DWBA) prediction using the deformed optical potential model (DOMP) approach with global optical parameters was applied.

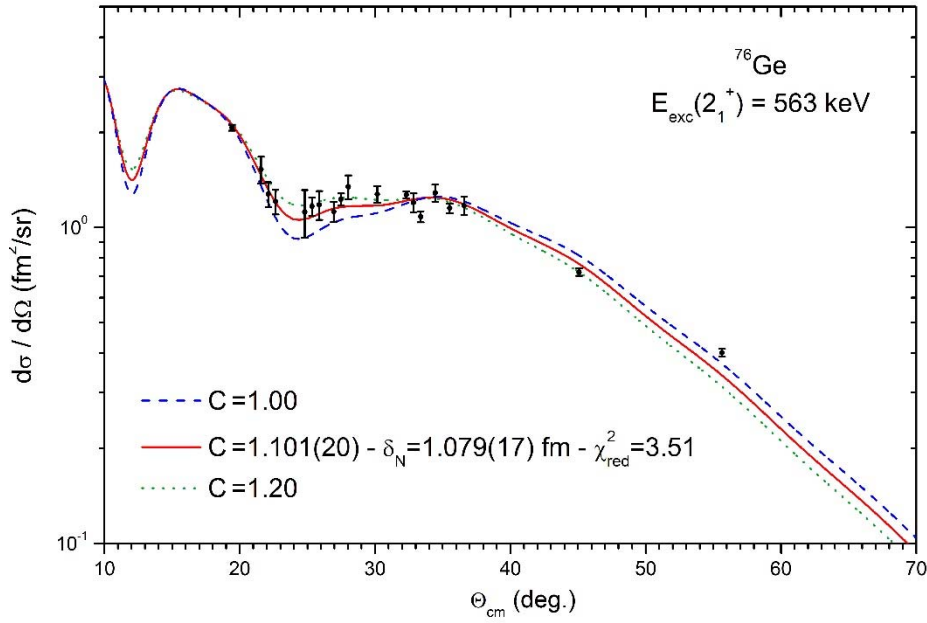


Fig. 2: Experimental angular distribution in comparison with DWBA-DOMP predictions.

The value of the ratio between charge (δ_2^C) and mass (δ_2^N) deformation lengths C_2 was obtained from the angular distribution shape. The square of mass deformation length, $(\delta_2^N)^2$, is also extracted, as a scale factor. The procedure applied for the χ^2 minimization was the iterative method of Gauss [6], extracting the correlated parameters δ_2^N and C_2 .

Figure 2 illustrates the results obtained in the fit from the experimental angular distribution of ${}^{76}\text{Ge}({}^6\text{Li}, {}^6\text{Li}){}^{76}\text{Ge}$ to the first quadrupole excited state in comparison with the DWBA-DOMP prediction. The error bars shown represent only the relative uncertainties. These ones are composed by the statistical uncertainties and the contribution from the background and contaminant subtraction. The prediction was calculated using the global optical model parameters of Cook [7] and considering the reduced Coulomb radius $r_C = 1.22$ fm (red curve). The results for the two correlated parameters in the data analysis are $C_2 = 1.101(20)$ and $\delta_2^N = 1.079(17)$ fm. In order to illustrate the sensibility of the method and that the experimental angular distribution does not admit a fit that could result in a C_2 value much smaller than one, as obtained for the neighbor ${}^{74}\text{Ge}$ [5], two predictions corresponding to $C_2 = 1.00$ (interrupted blue curve) and $C_2 = 1.20$ (dotted green curve) are also shown.

The C_2 value extracted is slightly higher than 1.0, indicating a homogeneous excitation with a slight predominant contribution of protons in the first quadrupole excited state 2_1^+ of ${}^{76}\text{Ge}$. Due to the uncertainty scale cancellation, the experimental ratio $B(E2)/B(1S2) e^2$, proportional to the square of C_2 , was obtained with a relative accuracy of less than 4%.

The present CNI study composed with the results of the previous work [5], using the same technique, indicates that although the protons relative to the neutrons reveal a small predominant contribution in ${}^{70,72,76}\text{Ge}$ to the first quadrupole excitation, the neutron role is strongly enhanced in ${}^{74}\text{Ge}$. In fact a C_2 abrupt change is shown comparing the ${}^{74}\text{Ge}$ value with those observed for neighbor isotopes ${}^{72,76}\text{Ge}$.

Discontinuities of some experimental indicators in even-A germanium chain from ${}^{70}\text{Ge}$ to ${}^{76}\text{Ge}$ were associated with shape transition or shape coexistence and described in the literature by a two-state coexistence model of some kind [8,9]. The investigation by means of large-scale shell model calculation suggested that a rapid increase in the number of $g_{9/2}$ protons and neutrons could explain the structure change near $N=40$ [2], associated with the strong neutron-proton interaction. The basic idea of the two-

state model is the existence of different configurations which may coexist and mix in different proportions to form the physical states observed. The experimental results obtained by Coulomb excitation and two neutron transfer measurements [10-13] indicate that the ground state configuration transition should occur between ^{72}Ge and ^{74}Ge . The analyses of the $L=0$ transfers in both (t,p) and (p,t) reactions, had shown transition strengths indicating similar nature between the ground states of ^{74}Ge and ^{76}Ge . On the other hand, the CNI results reveal a C_2 value strongly depressed in the first quadrupole excitation for ^{74}Ge , in comparison with the almost homogeneous excitation in ^{76}Ge . It is to be noted that the inelastic scattering, even if there is configuration mixing in the ground state, would excite only the configuration that connects the ground and the 2_1^+ states of each isotope which are rather pure [8,14]. In this context, the ^{74}Ge C_2 value suggests a strong ground state configuration mixing involving not only the neutron degree of freedom, but also probably other configurations. One possibility could be an alpha plus ^{70}Zn ($Z=30$, $N=40$) isomeric state configuration involving a subshell closure.

Acknowledgements

This work was partially supported by the Brazilian Agencies CNEN and FAPESP.

References

- [1] G. Gurdal et al., *Phys. Rev. C* **88** (2013) 014301.
- [2] M. Hasegawa et al., *Nucl. Phys. A* **789** (2007) 46.
- [3] G. M. Ukita et al., *Phys. Rev. C* **64** (2001) 014316.
- [4] J. L. M. Duarte et al., *Phys. Rev. C* **56** (1997) 1855.
- [5] M. D. L. Barbosa et al., *Phys. Rev. C* **71** (2005) 024303.
- [6] W. H. Press, B. P. Flannery, S. A. Teukolsky, and W. T. Vetterling, *Numerical Recipes* Cambridge, New York (1990).
- [7] J. Cook, *Nucl. Phys. A* **388** (1982) 153.
- [8] H. T. Fortune and M. Carchidi, *Phys. Rev. C* **36** (1987) 2584.
- [9] M. Carchidi et al., *Phys. Rev. C* **30** (1984) 1293.
- [10] R. Lecomte, M. Irshad, S. Landsberger, G. Kajrys, P. Paradis, S. Monaro, *Phys. Rev. C* **22** (1980) 2420.
- [11] R. Lecomte, G. Kajrys, S. Landsberger, P. Paradis, S. Monaro, *Phys. Rev. C* **25** (1982) 2812.
- [12] F. Guilbault et al., *Phys. Rev. C* **16** (1977) 1840.
- [13] A. C. Rester, J. B. Ball, R. L. Auble, *Nucl. Phys. A* **346** (1980) 371.
- [14] M. Sugarawa et al., *Eur. Phys. J. A* **16** (2003) 409.

Peculiar features of proton electromagnetic form factors

*E. Tomasi-Gustafsson*¹, *A. Bianconi*² and *Y. Wang*³

¹ CEA,IRFU,SPhN, Saclay, 91191 Gif-sur-Yvette Cedex, France

² Università degli Studi di Brescia and INFN, 25133 Brescia, Italy

³ CNRS/IN2P3, Institut de Physique Nucléaire, UMR 8608, 91405 Orsay, France

Abstract

Electromagnetic hadron form factors are fundamental quantities which describe the internal structure of the hadron. Experimental programs are ongoing or foreseen at the world facilities to increase the precision and/or to extend the kinematical range of the measurements. The collected data call for a unified interpretation of form factors in the scattering (space-like) and annihilation regions (time-like). In the time-like region form factors are complex functions and their meaning is not so obvious. The imaginary part, driven by unitarity, possibly contains information on the early process of the hadron formation. We focus here on a peculiar oscillatory behavior recently observed in the data on electron-positron annihilation from the BABAR collaboration, in the near threshold region, carrying information on the early stages of the hadron formation.

1. Introduction

Electromagnetic hadron form factors (FFs) are fundamental quantities which describe the internal structure of the hadron (for a recent review see Ref. [1]). Since decades the knowledge of electromagnetic form factors (EMFFs) of hadrons, their measurement and their description has been considered essential to access the internal structure of hadrons and to understand their dynamical properties as the charge and magnetic distributions. Surprising features have been observed during the last years, renewing the interest in the field. New observations in polarization experiments, have been possible due to experimental developments: high intensity polarized electron beams, high luminosity colliders, large solid angle, high resolution spectrometers and detectors, and in particular, proton and neutron polarimeters in the GeV region. FFs are generally measured through electron-proton elastic scattering, assuming that the interaction occurs through the exchange of one photon that carries a space-like (SL) four-momentum q^2 and are functions of one variable, only. The crossing symmetry related annihilation reactions, $e^+ + e^- \leftrightarrow \bar{p} + p$, access the time-like (TL) region of momentum transfer. Being FFs analytical functions, the scattering and annihilation regions are strongly related and nucleon models are required to incorporate the necessary analytical properties to describe FFs in all the kinematical region. Due to unitarity, FFs are real functions in the scattering and complex functions in the annihilation region. The Phragmén-Lindelöf theorem for analytical functions requires them to coincide at the limit for $|q^2| \rightarrow \infty$ and then the imaginary part has to vanish.

Theoretically, FFs enter explicitly in the coupling of a virtual photon with the hadron electromagnetic current, and can be directly compared to hadron models which describe dynamical properties of hadrons. They are experimentally accessible through the knowledge of the differential cross section and the polarization observables. Efforts are presently directed, on one side, to increase the precision and, on the other side, to extend the kinematic range of the measurements.

The electromagnetic vertex $\gamma^* \rightarrow hh$ (h is any hadron) is defined by two structure functions, which, in turn, are expressed in terms of $(2S + 1)$ FFs, S being the hadron spin. Assuming parity and time-invariance, Protons (and neutrons) have two FFs, electric G_E , and magnetic G_M , which are

normalized at $q^2 = 0$ to the static values of the charge $G_E(0) = 1$ and of the magnetic moment, $G_M(0) = \mu$.

In the TL region where a hadron pair is formed by or annihilated into a virtual photon, the unpolarized cross section contains the squared moduli of the two FFs. The angular distribution allows, in principle, for the individual determination of FFs, but until now the luminosity has not been sufficient and the experimental results assume $|G_E| = |G_M|$ or $G_E = 0$. The recent data by the BABAR collaboration [2, 3] cover a region from the $\bar{p}p$ threshold to $q^2 \approx 36 \text{ GeV}^2$. Thirty data points have been extracted in the region $q^2 < 10 \text{ GeV}^2$, with a relative error lower than 10 %. Regular structures have been found in these data [4]. These results are illustrated below and are interpreted in terms of an interplay between two steps in the annihilation process: the hadron formation from three bare quarks, taking place on a time scale $1/\sqrt{q^2}$, and a relatively small perturbation associated to rescattering processes taking place on a larger time scale.

Different theoretical models have been developed to describe the electromagnetic structure of the hadrons and applied to the calculation of SL FFs. Some of them can be applied in all kinematical region, as vector meson dominance [5] or dispersion relations [6], where the complex nature of TL FFs arises naturally.

Recently a model was suggested to interpret nucleon electromagnetic FFs both in SL and TL regions [7] that gives a qualitative explanation for the observed oscillations. It assumes that in ep elastic scattering or in the $e^+ + e^- \leftrightarrow \bar{p} + p$ annihilation a large quantity of energy (mass) and momentum is concentrated in a small volume creating a strong gluonic field, i.e., a gluonic condensate of clusters with a randomly oriented chromo-magnetic field. Applied to the scalar part of the field, it explains the observed additional suppression of the electric FF, and leaves unchanged the predictions from quark counting rules for the magnetic FF. Similarly, in TL region, above the physical threshold, $q^2 \geq 4M^2$ (M is the proton mass), the vacuum state created at the collision, transfers all the energy to a S-wave state with total spin 1, consisting in at least six massless valence quarks, a set of gluons and a sea of current $q\bar{q}$ quarks. The quarks as partons have no structure ($|G_E| = |G_M| = 1$), which may explain the observed point-like behavior of FFs at threshold. Then, the current quarks (antiquarks) absorb gluons and transform into constituent quarks (antiquarks). This model has one free parameter, in principle calculable, and it is expected to apply starting from moderate values of the momentum transfer. It gives a qualitative understanding of the experimental data, suggesting a generalization of the FF definition, where the meaning of FF in e^+e^- annihilation is the time evolution of the charge distribution of the newly formed hadron system.

2. Proton form factors: experimental status

An overview of selected data and models on proton form factors (FFs) is given in Fig. 1. For a complete review of data and references, see [1]. The physics content is highlighted below, following the q^2 axis.

2.1 The space-like region: $q^2 \leq 0$

Traditionally ep elastic scattering is considered as the preferred way to investigate the internal structure of the proton. Assuming one-photon exchange and due to the $J^{PC} = 1^{--}$ nature of the virtual photon, the unpolarized cross section for electron hadron elastic interaction has a characteristic dependence on $\cot^2 \theta$ (θ is the electron scattering angle in the laboratory (Lab) system).

The measurement of the differential cross section at fixed Q^2 , for different angles allows to extract the electric and magnetic FFs as the slope and the intercept, respectively, of this linear distribution. This is called the Rosenbluth method [8]. Backward eN -scattering is determined by the magnetic FF only, that is weighted by a factor $\tau = Q^2/(4M^2)$ (M is the proton mass) which makes the determination of

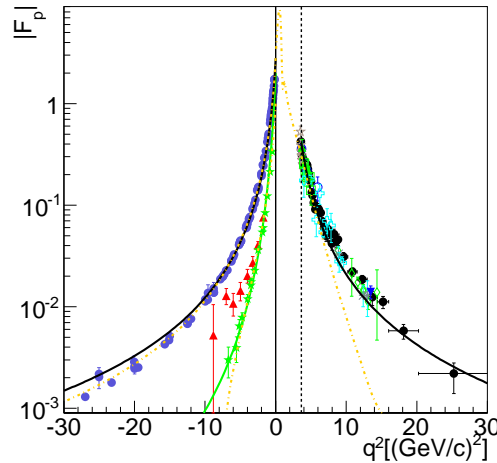


Fig. 1: World data on proton FFs as a function of q^2 . SL region: G_M data (blue circles), G_E data (red triangles) from unpolarized measurements [10] and from polarization measurements (green stars) [14]. Prediction of Ref. [7] for G_E (G_M) solid, green (black) line). TL region: $|G_E| = |G_M|$ world data for $q^2 > 4M^2$ and prediction for G_M from Ref. [7] (black, solid line). The prediction from Ref. [5] is the orange, dash-dotted line.

G_E more imprecise when Q^2 increases.

Since the pioneering experiments of Hofstadter [9] several measurements of the unpolarized cross section for ep elastic scattering have been performed. Radiative corrections, which depend on ϵ and Q^2 too, become larger with Q^2 , reaching up to 50%. They have been generally applied at first order in the electromagnetic fine constant α , beyond the Born approximation (α^3).

From unpolarized cross section measurements the determination of G_E and G_M has been done up to $Q^2 \simeq 8.8 \text{ GeV}^2$ [10] and G_M has been extracted up to $Q^2 \simeq 31 \text{ GeV}^2$ [11] under the assumption that the electric FF vanishes ($G_E = 0$) or that it equals the magnetic FF, G_M , scaled by the proton magnetic moment $G_E = G_M/\mu$ (full circles in In Fig. 1).

Polarization phenomena were studied and developed by the Kharkov school since the mid of last century. In Refs. [12, 13] it was first pointed out that the polarized cross section contains the interference of the amplitudes, giving access to the sign of FFs (while the unpolarized cross section contains FFs squared) and being more sensitive to a small G_E contribution. It was applied by the JLab GEp collaboration in a series of experiments, measuring precisely the ratio of the electric to magnetic FFs up to $Q^2 = 8.9 \text{ GeV}^2$ [14] (green triangles-down in In Fig. 1) which is directly related to the ratio of the transverse over longitudinal polarization in the scattering plane of the recoil proton.

The Akhiezer-Rekalo method for the measurement of the FFs ratio gave very precise results, as it was expected, because, at first order, the beam helicity as well as the analyzing power of the proton polarimeter cancel, reducing the systematic errors. But the experiment showed also a surprising behavior: a monotone decreasing of the FFs ratio when Q^2 increases. An extrapolation of this tendency at large Q^2 may lead to the ratio passing through zero and even becoming negative. As G_M is supposed to be well known from the unpolarized cross section, the present understanding is that G_M follows a dipole (Q^{-4}) behavior and that G_E follows a steeper decreasing. Recent unpolarized experiments confirm that unpolarized experiments give a FFs ratio consistent with unity (with a larger error as Q^2 increases) whereas polarized experiments deviate from unity as Q^2 increases. The reason has likely to be attributed to the contribution of higher order radiative corrections (for a recent discussion see Ref. [15]). Note that unpolarized data, selected in experiments where radiative corrections did not exceed

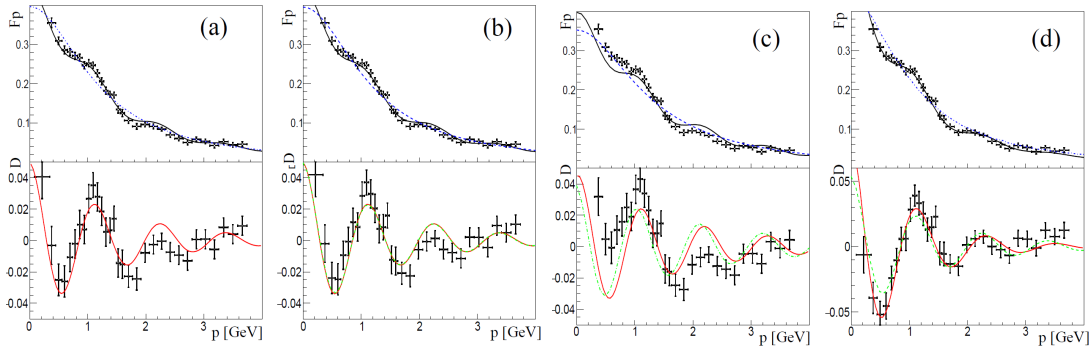


Fig. 2: Fits of Babar data, according to the four parametrizations a) F_R , b) F_S , c) F_{SC} , d) F_{TP} (see text). For each insert: (top) the data of Babar are plotted, together with the parametrization (blue, dashed line) and the global fit (solid line); (bottom) the difference of the data and the parametrization are shown, together with the corresponding damped oscillation fit (solid red line). In Figs. b), c), and d), F_R is shown for comparison (green dashed line).

20%, also show a deviation of the ratio from unity (see Fig. 9 of Ref. [1]).

It is expected that data on individual FFs in the TL region will help to clarify this issue.

2.2 The time-like region: $q^2 \geq 0$

The near threshold region is particularly intriguing. Several experiments have been performed. The Coulomb factor, plays a specific role at threshold, compensating the phase-space relative velocity. It turns out that the extrapolation of the cross section to threshold is consistent with $|G_E^p(4M^2)| = |G_M^p(4M^2)| = 1$, as in the case of a pointlike fermion [16].

The recent data on the generalized FF obtained by the BABAR collaboration [2, 3] from the initial state radiation reaction $e^+ + e^- \rightarrow \bar{p} + p + \gamma$ are very precise and extend with continuity from the threshold to $q^2 \simeq 37 \text{ GeV}^2$.

These data are well reproduced by the function F_R proposed in [17] that we will use as reference, see Table 1. Other parametrizations have been proposed in the literature: - following scaling pQCD rules, F_S , [18], - introducing a correction for α_s [19, 20] F_{SC} , and - a two-pole function F_{TP} in frame of ADS/CFT [21]. Their forms and parameters are reported in Table 1.

In the following, instead of q^2 , the relevant variable is taken as the 3-momentum p of one of the two hadrons in the frame where the other one is at rest: $p = \sqrt{E^2 - M^2}$ with $E = q^2/(2M) - M$. In this case, the structures shown by the data, become regularly spaced, indicating that a simple rescattering mechanism takes place. Therefore, we suggest that the annihilation process occurs in two steps, formation and rescattering, corresponding to different time scales. A consequence of this assumption is that the measured FFs can be fitted by a function: $F(p) = F_0(p) + F_{osc}(p)$ that is the sum of a regular "background" F_0 and an oscillating function $F_{osc}(p)$.

Since the rescattering mechanism is not known, we cannot identify the sources of rescattered waves, but we may gain some clue on their space distribution. Let r be the space variable that is conjugated to p via three-dimensional Fourier transform. We may identify r as the distance between the centers of the two forming or formed hadrons, in the frame where one is at rest. Let $M_0(r)$ and $M(r)$ be the Fourier transforms of the regular background fit and of the complete fit, Fig. 3. The most relevant feature is that $M_0(r)$ decreases by 7 orders of magnitude for r ranging from 0 and to 2 fm. The decrease is regular and almost constant on a semilog scale. $M_0(r)$ is steep near the origin, too. It can

Table 1: Fit functions and parameters

Ref.	Model	$A \pm \Delta A$ [GeV] ⁻¹	$B \pm \Delta B$ [GeV] ⁻¹	$C \pm \Delta C$	$D \pm \Delta D$
[17]	$ F_R = \frac{\mathcal{A}}{(1 + q^2/m_a^2)[1 - q^2/0.71]^2}$ $\mathcal{A} = 7.7 \text{ GeV}^{-4}, m_a^2 = 14.8 \text{ GeV}^2$	0.05±0.01	0.7±0.2	5.5±0.2	0.0±0.3
[18]	$ F_S = \frac{\mathcal{A}}{(q^2)^2 \log^2(q^2/\Lambda^2)}$ $\mathcal{A} = 40 \text{ GeV}^{-4}, \Lambda = 0.45 \text{ GeV}^2$	0.05±0.01	0.7±0.2	5.5±0.2	0.1±0.3
[19, 20]	$ F_{SC} = \frac{\mathcal{A}}{(q^2)^2 [\log^2(q^2/\Lambda^2) + \pi^2]}$ $\mathcal{A} = 72 \text{ GeV}^{-4}, \Lambda = 0.52 \text{ GeV}^2$	0.05±0.01	0.6±0.2	5.8±0.2	0.1±0.3
[21]	$ F_{TP} = \frac{\mathcal{A}}{(1 - q^2/m_1^2)(2 - q^2/m_2^2)}$ $\mathcal{A} = 1.56, m_{1,2}^2 = 1.5, 0.77 \text{ GeV}^2$	0.1±0.01	1.0±0.2	5.3±0.2	0.2±0.3

be interpreted by the fact that both $F_0(p)$ and its transform $M_0(r)$ are expression of that short distance quark-level dynamics [22, 23] that permits exclusive $\bar{p}p$ production at the condition that the final quarks and antiquarks are formed within a small region. Near threshold, the size of this region is ≤ 0.1 fm, much smaller than the standard hadron size.

In the right panel of Fig. 3 $M(r)$ is superimposed to $M_0(r)$. These two functions coincide for $r < 0.7$ fm, indicating that the physical reason of the data oscillation is related to processes occurring at a scale: $r \simeq 0.7$ -1.5 fm, corresponding to the largest annihilation probability in the phenomenological $\bar{p}p$ interactions in the near-threshold region [24]. At a distance of 1 fm, the relevant part of rescattering must involve physical or almost physical hadrons that annihilate into groups of 2-10 mesons.

3. Conclusions

After giving a fast review on the world data on proton FFs, in SL and TL regions, we have illustrated a systematic modulation pattern in the TLFF measured by the BABAR collaboration in the range $q^2 < 10 \text{ GeV}^2$. This modulation presents periodical features with respect to the momentum p associated with the relative motion of the final hadrons. It suggests an interference effect involving rescattering processes at moderate kinetic energies of the outgoing hadrons. Such processes take place when the centers of mass of the produced hadrons are separated by $\simeq 1$ fm. For this reason at least a relevant part of rescattering must consist of interactions between phenomenological or almost phenomenological protons and antiprotons.

Precise measurements in the near threshold region are ongoing at BESIII (BEPCII), on the proton as well as on the neutron, bringing a new piece of information. The measurement of TL FFs in a large q^2 range will be possible at PANDA (FAIR). In the SL region, programs at MAMI (Mainz) and at Jefferson Lab are planned to increase the precision and/or the kinematical range of the data. These experimental efforts will motivate the development of those models that apply to the whole kinematical region, for a unified vision of TL and SL form factors bringing to a better understanding of the internal dynamics of the hadron electromagnetic structure.

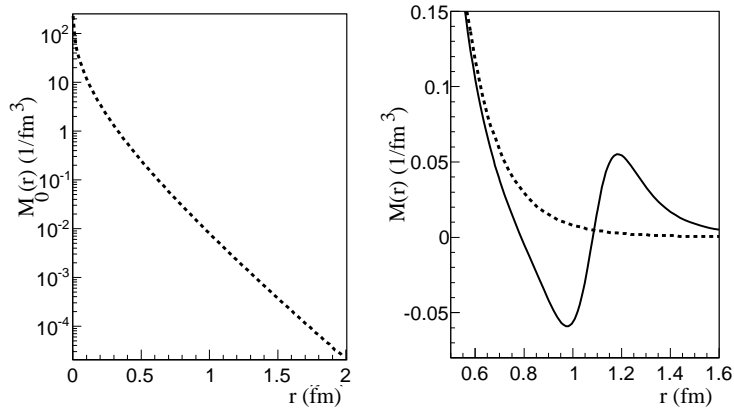


Fig. 3: (Left) Fourier transform of the background $M_0(r)$ (Right): total $M(r)$ (solid line) and $M_0(r)$ (dashed line) for comparison (linear vertical scale).

References

- [1] S. Pacetti, R. Baldini Ferroli and E. Tomasi-Gustafsson, *Phys. Rept.* **550-551** (2014) 1.
- [2] J. P. Lees *et al.* [BaBar Collaboration], *Phys. Rev. D* **87** (2013) 9, 092005.
- [3] J. P. Lees *et al.* [BaBar Collaboration], *Phys. Rev. D* **88** (2013) 7, 072009.
- [4] A. Bianconi and E. Tomasi-Gustafsson, *Phys. Rev. Lett.* **114** (2015) 232301.
- [5] F. Iachello and Q. Wan, *Phys. Rev. C* **69** (2004) 055204.
- [6] E. L. Lomon and S. Pacetti, *Phys. Rev. D* **85** (2012) 113004 [*Phys. Rev. D* **86** (2012) 039901].
- [7] E. A. Kuraev, E. Tomasi-Gustafsson and A. Dbeyssi, *Phys. Lett. B* **712** (2012) 240.
- [8] M. Rosenbluth, *Phys. Rev.* **79** (1950) 615–619.
- [9] R. Hofstadter, F. Bumiller, M. Croissiaux, *Phys. Rev. Lett.* **5** (1960) 263–265.
- [10] L. Andivahis *et al.*, *Phys. Rev. D* **50** (1994) 5491.
- [11] R. G. Arnold, *et al.*, *Phys. Rev. Lett.* **57** (1986) 174.
- [12] A. I. Akhiezer and M. P. Rekalov, *Sov. Phys. Dokl.* **13** (1968) 572 [*Dokl. Akad. Nauk Ser. Fiz.* **180** (1968) 1081].
- [13] A. I. Akhiezer and M. P. Rekalov, *Sov. J. Part. Nucl.* **4** (1974) 277 [*Fiz. Elem. Chast. Atom. Yadra* **4** (1973) 662].
- [14] A. J. R. Puckett *et al.*, *Phys. Rev. Lett.* **104** (2010) 242301.
- [15] E. A. Kuraev, A. I. Ahmadov, Y. M. Bystritskiy and E. Tomasi-Gustafsson, *Phys. Rev. C* **89** (2014) 065207.
- [16] R. Baldini, S. Pacetti, A. Zallo and A. Zichichi, *Eur. Phys. J. A* **39** (2009) 315.
- [17] E. Tomasi-Gustafsson and M. P. Rekalov, *Phys. Lett. B* **504** (2001) 291.
- [18] M. Ambrogiani *et al.* [E835 Collaboration], *Phys. Rev. D* **60** (1999) 032002.
- [19] D. V. Shirkov and I. L. Solovtsov, *Phys. Rev. Lett.* **79** (1997) 1209.
- [20] E. A. Kuraev, Private Communication.
- [21] S. J. Brodsky and G. F. de Teramond, *Phys. Rev. D* **77** (2008) 056007.
- [22] V. Matveev, R. Muradyan, A. Tavkhelidze, *Teor. Mat. Fiz.* **15** (1973) 332–339.
- [23] S. J. Brodsky and G. R. Farrar, *Phys. Rev. Lett.* **31** (1973) 1153.
- [24] A. Bianconi *et al.*, *Phys. Lett. B* **483** (2000) 353.

One-nucleon transfers to resonance states

I.J. Thompson¹, J.E. Escher¹, G. Arbanas², Ch. Elster³, V. Eremenko^{3,4}, L. Hlophe³, and F.M. Nunes⁵, TORUS Collaboration

¹ Lawrence Livermore National Laboratory L-414, Livermore, CA 94551, USA,

² Oak Ridge National Laboratory, Oak Ridge, TN 37831, USA,

³ Ohio University, Athens, OH 45701, USA,

⁴ M.V. Lomonosov Moscow State University, Moscow, 119991, Russia

⁵ Michigan State University, East Lansing, MI 48824, USA

Abstract

We examine the contributions from interior, surface and exterior parts of the matrix elements for (d,p) neutron-transfer matrix elements, and show how their sum may be written as interior-post, exterior-prior terms along with a surface term. If we locate our surface according to the distance of the transferred neutron to the target, then the three terms depend on the neutron wave function at specific radii, and the surface and exterior terms depend only on that part of the neutron wave function determined by R-matrix parameters for neutron-target scattering.

1. Deuteron stripping

Deuteron-induced reactions, in particular (d,p) one-neutron transfer reactions, have been used for decades to investigate the neutron single-particle structure of bound states of nuclei. The reaction typically involves a large momentum transfer of the neutron from a high-energy beam to a bound state, so the shape of the exit proton angular distribution depend on the transferred angular momentum ℓ . The analyzing powers for polarized deuterons depends on the neutron j value, and the magnitude of that cross sections is used to extract a spectroscopic factor $S_{\ell j}$ for each discrete bound state. In first order the cross section scales exactly with the spectroscopic factor, while for some cases higher-order corrections introduce non-linearities. These high-order corrections arise from collective excitations in the entrance or exit channels, leading to Coupled-Channels Born Approximation (CCBA) methods. They may also arise for weakly-bound neutron bound states, when multi-step transfers become significant, leading to Coupled-Reaction Channels (CRC) methods.

At excitation energies above the weakly-bound states, we see of course resonances. Specific resonances are very often of importance in astrophysics and other applications because their existence may change low-energy cross sections by many orders of magnitude. It is therefore of great importance to measure their structure by whatever means are possible. Resonances with open neutron channels, therefore, can and should be probed by (d,p) transfer reactions. Resonances, however, are not characterized by spectroscopic factors, but by their resonance energies E_r and widths Γ . For a resonance which can be populated (and hence decay) by multiple channels c , each channel has a partial width Γ_c such that the total width of the resonance is the sum $\Gamma = \sum_c \Gamma_c$. These channels, for example, could be inelastic excitations of the target, (n, γ) capture, or proton or α -particle emissions. Ideally each partial width Γ_c should be measured. These energies and widths are directly related to the parameters (pole energies and reduced-width amplitudes) of R-matrix theory [1, 2], either by fitting to observed cross sections, or by derivation from some microscopic model. It is therefore very desirable to have predictions of (d,p) cross sections that are based on R-matrix parameters for the neutron-target interaction. These are exactly the parameters that would describe neutron scattering on the target, so, in ideal cases, observables from (d,p) experiments could be used to predict neutron scattering and the multichannel cross sections for γ , proton or α exit channels. If the target is radioactive and therefore unable to be a target, then

results from inverse kinematic experiments with deuteron targets may be used to predict neutron cross sections.

But is it *possible* to formulate of (d,p) resonant cross sections in terms of R-matrix parameters for the neutron? These parameters describe surface and external properties of the wave function of neutron-target scattering, so we have to determine the dependence of (d,p) cross sections also on the neutron wave function *inside* the surface of the target.

One possible obstacle is that the ℓ -dependence of the (d,p) cross section involving resonances is much less than for reactions to bound states, because the momentum transfer is reduced. Since resonant (d,p) reactions involve the continuum, they represent one form of deuteron breakup. In the limit of ‘transfer’ to neutron states at the energies of about half the beam energy, the energy and momentum transfers pass through a minimum, and we must then expect almost *no* dependence on the transferred angular momentum ℓ . This means that (d,p) transfers to resonances may well require higher beam energies for the deuteron, even though this leads to lower cross sections.

2. Post-prior transformations

To examine the dependence of (d,p) cross sections on the interior, surface and exterior regions of the final neutron state, we use the new formalism [3] devised by Akram Mukhamedzhanov of our TORUS collaboration. This is to define a *surface operator* by means of transforming from post to prior matrix elements not over all space as usual, but at a specific surface radius ρ measured for the neutron-target distance r_n . Let us see how this comes about.

In first-order DWBA for A(d,p)B reactions, the post and prior matrix elements for transfer from the bound state $\Phi_d(r)$ in a deuteron to a final state $\Phi_n(r_n)$ around a target are

$$M_{dp}^{\text{post}} = \langle \Phi_n(r_n) u_p(r_p) | \mathcal{Y}_{\text{post}} | \Phi_d(r) u_d(R) \rangle \quad (1)$$

$$\text{and } M_{dp}^{\text{prior}} = \langle \Phi_n(r_n) u_p(r_p) | \mathcal{Y}_{\text{prior}} | \Phi_d(r) u_d(R) \rangle, \quad (2)$$

where $u_d(R)$ and $u_p(r_p)$ are the incoming deuteron and outgoing proton optical-model wave functions with potentials U_{dA} and U_{pB} respectively. The transfer operators are $\mathcal{Y}_{\text{post}} = V_{np} + V_{pA} - U_{pB}$ and $\mathcal{Y}_{\text{prior}} = V_{nA} + V_{pA} - U_{dA}$.

It can be proven in this first-order case that the post and prior expressions are exactly equivalent. This proof uses the Hermiticity of the total kinetic energy operator T , which has equivalent representations for post $\overleftarrow{T} = T_{nA} + T_{pB}$ and prior $\overrightarrow{T} = T_{np} + T_{dA}$ based on the two equivalent sets of Jacobi coordinates $\{r_n, r_p\}$ and $\{r, R\}$ for this three-body problem consisting of the proton, neutron and target A.

The kinetic energy operator is Hermitian in this case because at least one of the bound states $\Phi_d(r)$ and $\Phi_n(r_n)$ goes to zero at large distances. Since the deuteron bound state wave function $\Phi_d(r)$ decays to zero for large r , the post-prior equivalence of the DWBA matrix element holds not only for bound final states, but also for unbound scattering states of the neutron on the target.

We can also choose to interchange the two forms of the kinetic energy, \overleftarrow{T} and \overrightarrow{T} for *limited* regions of the integral over the neutron coordinate r_n . Let us define $M_{dp}^{\text{post}}(a, b)$ and $M_{dp}^{\text{prior}}(a, b)$ as the respective integrals over the range $a < r_n < b$ (the integral over the full range of the r_p coordinate is implied). These two matrix element differ by

$$M_{dp}^{\text{post}}(a, b) = M_{\text{surf}}(a) + M_{dp}^{\text{prior}}(a, b) - M_{\text{surf}}(b), \quad (3)$$

$$\text{where we define } M_{\text{surf}}(\rho) = \langle \Phi_n(r_n) u_p(r_p) | \overleftarrow{T} - \overrightarrow{T} | \Phi_d(r) u_d(R) \rangle_{r_n > \rho}. \quad (4)$$

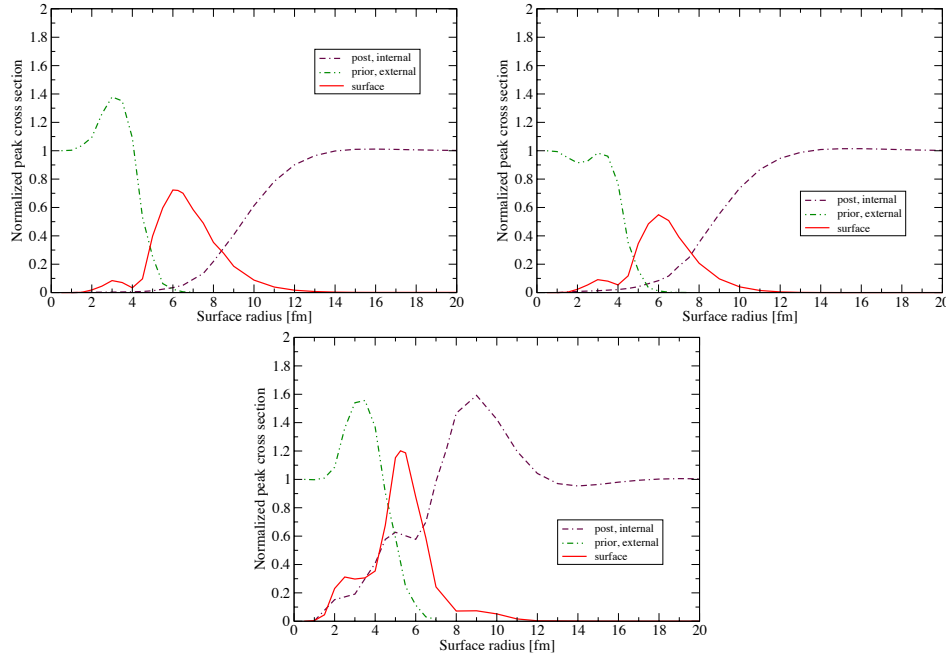


Fig. 1: Interior, surface, and exterior contributions for $^{48}\text{Ca}(d,p)^{49}\text{Ca}$ stripping to the $3/2^-$ ground state, at $E_d = 13$ (top left), 19.3 (top right), and 56 MeV (bottom). Shown are the peak cross sections of the individual contributions (which are proportional to $|M_{\text{int}}^{(\text{post})}(0, \rho)|^2$, $|M_{\text{surf}}(\rho)|^2$, $|M_{\text{ext}}^{(\text{prior})}(\rho, \infty)|^2$, respectively), as a function of surface radius selected. The results are normalized to the peak cross section of the full calculation.

The result in the previous paragraphs follows from $M_{\text{surf}}(0) = M_{\text{surf}}(\infty) = 0$.

If M_{dp} is the matrix element over the whole space (prior or post, since they are equal), then [3]

$$M_{dp} = M_{dp}^{\text{prior}}(0, \rho) + M_{dp}^{\text{prior}}(\rho, \infty), \quad (5)$$

$$\text{hence } M_{dp} = M_{dp}^{\text{post}}(0, \rho) + M_{\text{surf}}(\rho) + M_{dp}^{\text{prior}}(\rho, \infty). \quad (6)$$

This final equation (6) is of considerable practical value, as it shows a way to separate interior, surface and exterior contributions of different kinds. The split can be examined for a range of surface radii ρ . The interior post (first) term is model-dependent, while the exterior prior and surface (second and third) terms are related to the asymptotic properties of the wave function.

The term $M_{\text{surf}}(\rho)$ is called a *surface* term, although given in equation (4) as a volume integral, because the Green's theorem allows us to convert a volume integral into the surface integral

$$\begin{aligned} \int_{r \geq \rho} d\mathbf{r} f(\mathbf{r}) \left[\overleftarrow{T} - \overrightarrow{T} \right] g(\mathbf{r}) &= \frac{\hbar^2}{2\mu} \oint_{r=\rho} d\mathbf{S} [g(\mathbf{r}) \nabla_{\mathbf{r}} f(\mathbf{r}) - f(\mathbf{r}) \nabla_{\mathbf{r}} g(\mathbf{r})] \\ &= \frac{\hbar^2}{2\mu} \rho^2 \int d\Omega_{\mathbf{r}} \left[g(\mathbf{r}) \frac{\partial f(\mathbf{r})}{\partial r} - f(\mathbf{r}) \frac{\partial g(\mathbf{r})}{\partial r} \right]_{r=\rho}. \end{aligned} \quad (7)$$

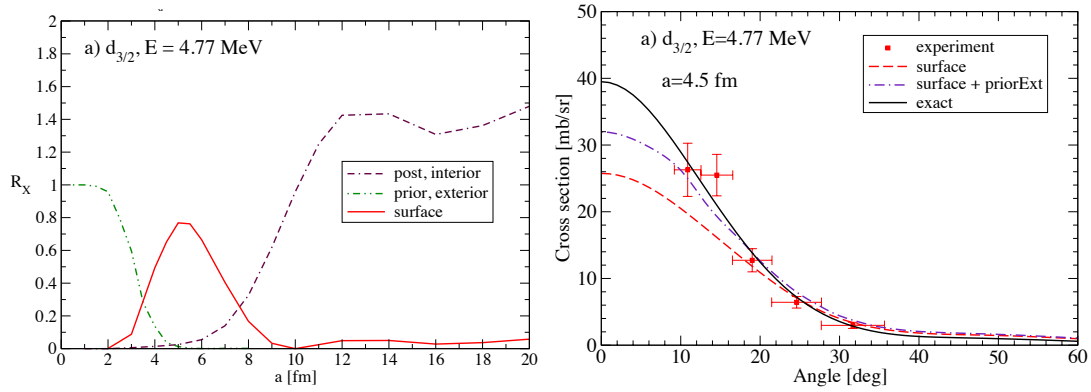


Fig. 2: Examination of interior, surface, and exterior contributions for transfers to resonance states in ^{21}O , for the $3/2^+$ resonance at 4.77 MeV. The left panel shows the interior (post) term, the surface term, and the exterior (prior) term, as a function of the surface radius. The right panel shows that improvements to the surface-term-only approximation can be achieved by including contributions from the prior-exterior term and selecting a small surface radius. The potential V_{nA} , which binds the neutron to the ^{20}O nucleus, has a radius of 3.39 fm and a diffuseness of 0.65 fm.

3. Surface transfer operator in first-order models

The matrix elements of a surface transfer operator $M_{\text{surf}}(\rho)$ can be very simply calculated in first-order DWBA. We may simply take the difference of equations (5) and (6) above, giving

$$M_{\text{surf}}(\rho) = M_{dp}^{\text{post}}(0, \rho) - M_{dp}^{\text{prior}}(0, \rho). \quad (8)$$

This can be easily accomplished using any code for first-order finite-range transfer calculations, such as FRESKO [4]. Using this equation we first examined [5, 6] the sizes of the three terms in equation (6) for a range of bound and resonant states for the final neutron in a (d,p) reaction.

Fig. 1 shows, within the DWBA formalism, that the surface contribution is dominant for bound states at around 5-7 fm for the $^{48}\text{Ca}(d,p)$ at three different beam energies. But still there are non-negligible contributions from both the interior (post) and exterior (prior) terms.

We have also carried out calculations that test the dominance of the surface term for transfer reactions that populate resonances, such as the $3/2^+$ resonance in ^{21}O at 4.77 MeV measured recently in a $^{20}\text{O}(d,p)$ experiment [7]. We see in the left panel of Fig. 2 that at around $\rho = 5$ fm the surface term appears to largely dominate. However, the other terms contribute not incoherently as cross sections, but coherently as amplitudes. The red-dashed curve in the right panel shows the angular distribution arising solely from the surface term, and this is clearly short of the exact result. Adding in an exterior-prior contribution does improve the accuracy considerably, but still not entirely.

4. Surface transfer operator in coupled-channel models

The surface contributions extracted in the previous section are within the context of first-order theory, as then post and prior matrix elements give identical results and differences can be taken. If breakup in the entrance channel, say, is important, then it is necessary to go beyond first order. In that case, only the post matrix element uses the coupled-channels wave function in the entrance channel from the CDCC methods discussed earlier. This means that the surface operator has to be calculated explicitly in terms of the multi-channel CDCC wave functions $\psi_{\text{CDCC}}(\mathbf{R}, \mathbf{r})$. In coupled-channel models for transfers, we use a source term $S_{\beta}(R')$ that depends on $\psi_{\text{CDCC}}(\mathbf{R}, \mathbf{r})$ to calculate the matrix elements M_{β} as the

asymptotic amplitude of the outgoing wave solutions of $[E_\beta - H_\beta]u_\beta(R') = S_\beta(R')$, where $R' \equiv r_p$ is the coordinate of the exiting proton.

In order to calculate transfer cross sections with the surface operator at some final neutron radius $r' = \rho$, we now have to implement the general surface operator of eq. (7), not just its value from the ‘prior–post’ difference as used in eq. (8) above.

The source term $S_\beta(R')$ for the transfer channel using the surface operator at radius $r' = \rho$ is

$$S_\beta^{\text{surf}}(R') = \langle Y_\beta(\hat{R}', \hat{r}') \Phi_\beta(r') | \overleftarrow{T} - \overrightarrow{T} | \psi_{\text{CDCC}}(\mathbf{R}, \mathbf{r}) \rangle_{r' > \rho} \quad (9)$$

$$= \langle Y_\beta(\hat{R}', \hat{r}') \Phi_\beta(r') | \overleftarrow{T}_{\text{vA}} - \overrightarrow{T}_{\text{vA}} | \psi_{\text{CDCC}}(\mathbf{R}, \mathbf{r}) \rangle_{r' > \rho} \quad (10)$$

where $r' \equiv r_n$ is the coordinate of the neutron in the final state. Transforming this matrix element into a surface integral with Green’s theorem, we have

$$\begin{aligned} S_\beta^{\text{surf}}(R') &= \frac{\hbar^2}{2\mu_n} \int_0^\infty dr' \left\langle Y_\beta(\hat{R}', \hat{r}') | \delta(r' - \rho) \left[\psi_{\text{CDCC}}(\mathbf{R}, \mathbf{r}) \frac{\partial \Phi_\beta(r')}{\partial r'} - \Phi_\beta(r') \frac{\partial \psi_{\text{CDCC}}(\mathbf{R}, \mathbf{r})}{\partial r'} \right] \right\rangle \\ &= \frac{\hbar^2}{2\mu_n} \int_0^\infty dr' \left\langle Y_\beta(\hat{R}', \hat{r}') | \delta(r' - \rho) \left[\frac{\partial \Phi_\beta(r')}{\partial r'} - \Phi_\beta(r') \frac{\partial}{\partial r'} \right] | \psi_{\text{CDCC}}(\mathbf{R}, \mathbf{r}) \right\rangle \end{aligned} \quad (11)$$

Since the derivative operator $\partial/\partial r'$ acts on both the radial and angular components of the vectors (\mathbf{R}, \mathbf{r}) in the entrance channel, a large number of terms and derivatives need to be evaluated:

We will need the following derivatives for the linear combination $\mathbf{r} = p\mathbf{r}' + q\mathbf{R}'$:

$$\begin{aligned} \frac{\partial}{\partial r'} Y_\ell^m(\hat{\mathbf{r}}) \frac{\varphi_\alpha(r)}{r} &= \frac{\varphi_\alpha(r)}{r} \frac{\partial}{\partial r'} Y_\ell^m(\hat{\mathbf{r}}) + Y_\ell^m(\hat{\mathbf{r}}) \frac{\partial}{\partial r'} \frac{\varphi_\alpha(r)}{r} \\ &= \frac{p}{r} \left\{ \sqrt{\frac{4\pi\ell(2\ell+1)}{3}} \frac{\varphi_\alpha(r)}{r} \sum_{\lambda=-1}^1 \langle \ell-1 \ m-\lambda, 1\lambda | \ell m \rangle Y_{\ell-1}^{m-\lambda}(\hat{\mathbf{r}}) Y_1^\lambda(\hat{\mathbf{r}}) + Y_\ell^m(\hat{\mathbf{r}}) \hat{\mathbf{r}} \cdot \hat{\mathbf{r}}' \left[\varphi'_\alpha(r) - \frac{\ell+1}{r} \varphi_\alpha(r) \right] \right\} \end{aligned} \quad (12)$$

The needed source term $S_{\beta\alpha}^{\text{surf}}(R')$ in a final (proton) channel β from the initial (deuteron) channel α is, with the surface operator,

$$\begin{aligned} S_{\beta\alpha}^{\text{surf}}(R') &= \langle Y_\beta(\hat{R}', \hat{r}') \Phi_\beta(r') | \overleftarrow{T}_{nA} - \overrightarrow{T}_{nA} | \Phi_\alpha(r) Y_L(\hat{R}) u_\alpha(R) \rangle_{r' > \rho} \\ &= \frac{-\hbar^2}{2\mu_n} \int_0^\infty dr' \left\langle Y_\beta(\hat{R}', \hat{r}') | \delta(r' - \rho) \left[\frac{\partial \Phi_\beta(r')}{\partial r'} - \Phi_\beta(r') \frac{\partial}{\partial r'} \right] | \Phi_\alpha(r) Y_L(\hat{R}) \right\rangle u_\alpha(R), \end{aligned} \quad (13)$$

where Φ_β is the final state of the neutron, whether bound or unbound. This coupling is non-local as $R' \neq R$, and depends on the derivatives of the deuteron incoming wave function $u_\alpha(R)$, so we need to calculate the two non-local kernel functions $X_{\beta\alpha}(R', R)$ and $Y_{\beta\alpha}(R', R)$ to give the source term as

$$S_{\beta\alpha}^{\text{surf}}(R') = \int_0^\infty dR X_{\beta\alpha}(R', R) u_\alpha(R) + \int_0^\infty dR Y_{\beta\alpha}(R', R) \left[u'_\alpha(R) - \frac{L_\alpha+1}{R} u_\alpha(R) \right]. \quad (14)$$

The derivative operators in Eq. (13) operate on all of the radii r, R and their angles \hat{r}, \hat{R} , so X has four terms. Using the $\Phi_\alpha(r)$ and $\hat{\Phi}_\alpha(r) = \frac{1}{r}(\varphi'_\alpha(r) - \frac{\ell+1}{r}\varphi_\alpha(r))$ variables for both entrance and exit

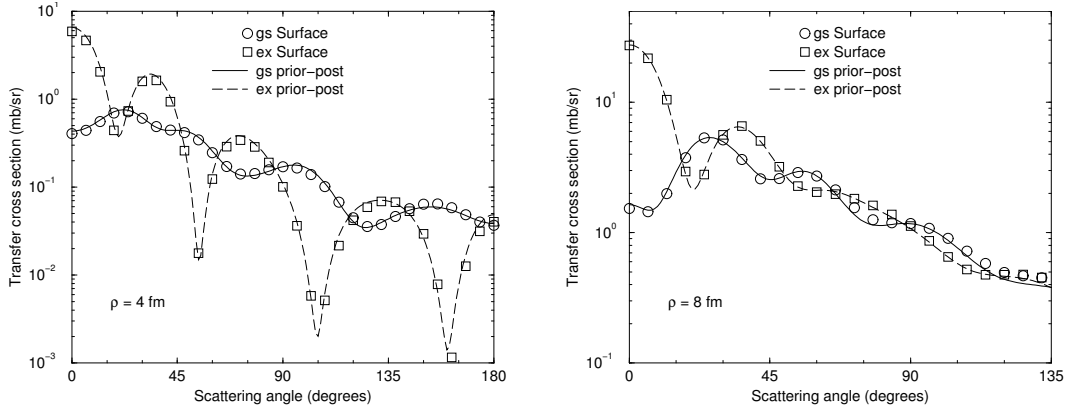


Fig. 3: Comparison of methods to calculate the surface transfer contribution, for the $^{90}\text{Zr}(d,p)$ reaction at deuteron energy of 11 MeV. On the left the surface radius is $a = 4$ fm, and on the right 8 fm. The gs is a $d_{5/2}$ neutron state, and the excited state is a $s_{1/2}$ state.

channels, kinematical coefficients a', b', p, P, J , and Clebsch-Gordan products $G_{m'_\ell M_L m_\ell}^{\alpha' \alpha}$, we have derived

$$\begin{aligned}
 X_{\alpha' \alpha}(R', R) = & J \frac{\hbar^2}{2\mu_n} \frac{\rho}{a' b'} \sum_{m'_\ell m_\ell} \sum_{M_L = -1}^1 G_{m'_\ell M_L m_\ell}^{\alpha' \alpha} P_{\ell'}^{|m'_\ell|}(\cos \theta_{R'}) P_{L'}^{|M_L + m_\ell - m'_\ell|}(\cos \theta_{R'}) \\
 & \left[\Phi'_\beta(\rho) Y_L^{M_L}(\hat{\mathbf{R}}) Y_\ell^{m_\ell}(\hat{\mathbf{r}}) \Phi_\alpha(r) \right. \\
 & - \Phi_\beta(\rho) Y_L^{M_L}(\hat{\mathbf{R}}) \frac{p}{r} \sqrt{\frac{4\pi\ell(2\ell+1)}{3}} \sum_{\lambda=-1}^1 \langle \ell-1 \ m_\ell - \lambda, 1\lambda | \ell m_\ell \rangle Y_{\ell-1}^{m_\ell - \lambda}(\hat{\mathbf{r}}) Y_1^\lambda(\hat{\mathbf{r}}) \Phi_\alpha(r) \\
 & - \Phi_\beta(\rho) Y_L^{M_L}(\hat{\mathbf{R}}) p \hat{\mathbf{r}} \cdot \hat{\mathbf{r}}' Y_\ell^{m_\ell}(\hat{\mathbf{r}}) \hat{\Phi}_\alpha(r) \\
 & \left. - \Phi_\beta(\rho) Y_\ell^{m_\ell}(\hat{\mathbf{r}}) \Phi_\alpha(r) \frac{P}{R} \sqrt{\frac{4\pi L(2L+1)}{3}} \sum_{\Lambda=-1}^1 \langle L-1 \ M_L - \Lambda, 1\Lambda | L M_L \rangle Y_{L-1}^{M_L - \Lambda}(\hat{\mathbf{R}}) Y_1^\Lambda(\hat{\mathbf{r}}) \right], \quad (15)
 \end{aligned}$$

and the derivative term (with $M_L = 0$):

$$\begin{aligned}
 Y_{\alpha' \alpha}(R', R) = & -J \frac{\hbar^2}{2\mu_n} \frac{\rho}{a' b'} P \Phi_\beta(\rho) \Phi_\alpha(r) \hat{\mathbf{R}} \cdot \hat{\mathbf{r}}' \\
 & \times \sum_{m'_\ell m_\ell} G_{m'_\ell 0 m_\ell}^{\alpha' \alpha} P_{\ell'}^{|m'_\ell|}(\cos \theta_{R'}) P_{L'}^{|m_\ell - m'_\ell|}(\cos \theta_{R'}) Y_\ell^{m_\ell}(\hat{\mathbf{r}}) Y_L^0(\hat{\mathbf{R}}). \quad (16)
 \end{aligned}$$

We use the rotated coordinate frame that has the z-axis parallel to \mathbf{R} and the x-axis in the plane of \mathbf{R} and \mathbf{R}' . The resulting operator is still non-local like other finite-range transfer operators, but does not require any internal quadrature over angles. The integral operators, when $\mathbf{r} = a\mathbf{R} + b\mathbf{R}'$, are now

$$\int d\hat{\mathbf{R}}' \int d\hat{\mathbf{R}} \delta(r' - \rho) = \frac{8\pi^2 \rho}{a' b' R R'} \Big|_{u=(\rho^2 - a^2 R^2 + b^2 R'^2)/(2a' b' R R')}. \quad (17)$$

These expressions (15) and (16) have been directly implemented in a LLNL version of our coupled-channels code FRESKO [4]. In this way we can go beyond first order for neutron transfers both to bound

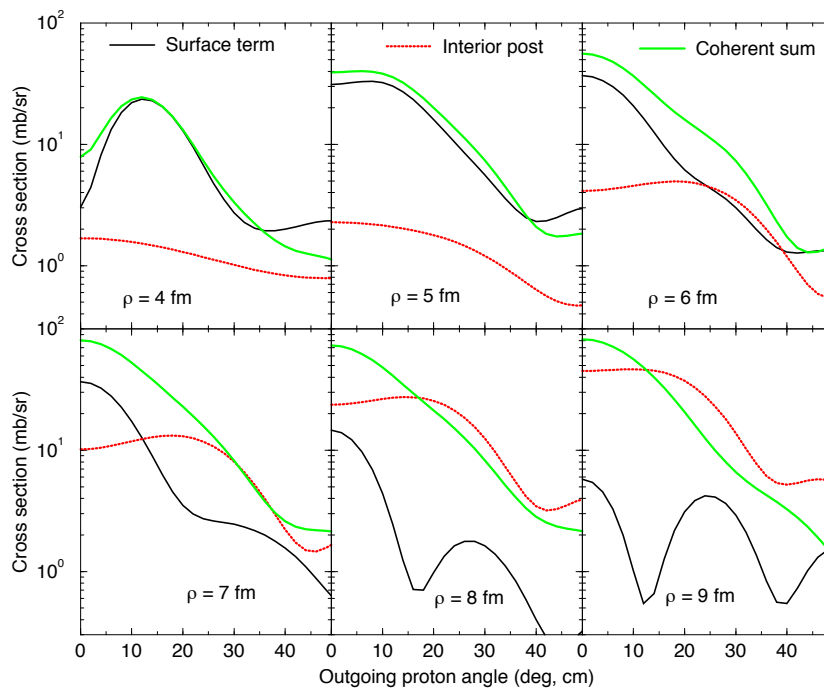


Fig. 4: The cross sections from separate surface and interior-post terms (black and red respectively) along with their coherent sum (green line). The different panels show the variations from using different radii ρ of the surface.

and resonance states. The new calculations for the surface term have been validated by comparison with the angular cross sections obtained in the work described in the previous section 3.. The comparisons are shown in Figure 3.

Furthermore, their values depends only on the wave function $\Phi_\beta(\rho)$ and derivative $\Phi'_\beta(\rho)$ of the final neutron wave function at the surface, and these are precisely the numbers that can be uniquely obtained from standard R-matrix fits of pole positions and reduced-width amplitudes.

When using the surface term derived from CDCC wave functions, the exterior-prior term in eq. (6) does not appear. That is because the prior term is the coupling derived from $\mathcal{V}_{\text{prior}} = V_{nA} + V_{pA} - U_{dA}$, and this interaction potential is expected to be that which is diagonalized by the CDCC solution.

5. Results

Nevertheless, as shown in the previous section, the interior-post terms are still significant and need to be added coherently to the surface contributions. The exterior-prior term is not expected to be present if we use sufficiently accurate CDCC wave functions in the source term.

Figure 4 shows the relative sizes of these terms for a $^{20}\text{O}(d,p)^{21}\text{O}$ reaction that populates a d -wave neutron resonance at 0.9 MeV. The different panels show the effects of different radii of the surface, where the black curve shows the surface term, the red line the interior post by itself, and the green curve shows their coherent sum. Except for the smallest surface radius, the coherent sums are nearly constant, but there are large variations in the relative sizes of the surface and interior-post terms. This will provide an essential tool for probing how much these transfer cross sections measure the surface properties described by R-matrix theory, compared with measuring in part the interior part of the resonance wave functions.

6. Discussion

Our aim is to fit neutron pole energies and partial widths to (d,p) cross sections across a resonance. There have been experiments with many wide and narrow resonances, often overlapping, such as the early $^{15}\text{N}(d,p)^{16}\text{N}^*$ experiments of [8, 9]. Our results can be generalized to multichannel exit wave functions, so that, for example, if experiments measure $^{12}\text{N}(d,p)^{16}\text{N}^* \rightarrow \alpha + ^{12}\text{B}$, then the results of our analyses can be used to predict the (n, α) cross section for a ^{12}N target.

Experimentally, resonance structures are most often studied in elastic and inelastic scattering reactions. For those reactions, the phenomenological R-matrix approach has been extremely useful for the interpretation of experiments and for extracting resonance energies and widths from measured cross sections. The surface integral formalism [3] is essentially an extension of the R-matrix approach to (d,p) transfer reactions. It holds the potential to overcome present difficulties in describing transfers to resonance states and to become a practical and sound way for extracting structure information from transfer experiments, since: a) It reduces the dependence of the cross section calculations on the model used for the nuclear interior; b) it reduce (in DWBA) or eliminates (in CDCC) the impact of the slow convergence of calculations of the exterior term when resonances are considered; and c) it establishes a useful link between resonance properties and transfer observables, since the surface term $M_{\text{surf}}(\rho)$ can be parameterized in terms of quantities that are familiar from traditional R-matrix approaches. When resonance studies were carried out in the DBWA formalism, convergence was found to be difficult to achieve, but the results obtained so far show trends similar to what was found for bound states, with reduced contributions from the nuclear interior.

In conclusion, we note that the surface formalism for studying resonances with (d,p) uses successful R-matrix ideas to emphasize asymptotic properties of the wave function. It is based on a separation into interior and exterior, and leads to a surface term which can be expressed in terms of familiar R-matrix parameters, thus providing spectroscopic information. Our DWBA and CDCC studies show that the surface term is dominant both in first-order and higher-order calculations, and that the dependence on a model for nuclear interior is reduced. The surface term alone is not sufficient, however, to entirely describe the cross sections for transfer reactions, since we find that corrections are required. We expect that an accurate CDCC implementation (which includes breakup effects) should already include copings in the exterior, so that there will be no need to include the exterior-prior term when using the formalism laid out here.

Acknowledgements

This work is supported through the US DOE's Topical Collaboration TORUS (www.reactiontheory.org). It is performed under the auspices of the DOE by LLNL under Contract No. DE-AC52-07NA27344, by Ohio University under Contract No. DE-SC0004087, under the U.T. Battelle LLC Contract No. DE-AC05000R22725 and by MSU Contract No. DE-SC0004084.

References

- [1] A. M. Lane, R. G. Thomas *Rev. Mod. Phys.* **30**, 257 (1958).
- [2] P. Descouvemont, D. Baye *Reports on Progress in Physics* **73**(3), 036301 (2010).
- [3] A. M. Mukhamedzhanov *Phys. Rev. C* **84**, 044616 Oct (2011).
- [4] I.J. Thompson *Computer Physics Reports* **7**(4), 167 – 212 (1988).
- [5] J. E. Escher, A. M. Mukhamedzhanov, I. J. Thompson, *J. Phys.: Conf. Series* **403**(1), 012026 (2012).
- [6] J. E. Escher, *et al.* *Phys. Rev. C* **89**, 054605 May (2014).
- [7] B. Fernández-Domínguez *et al.* *Phys. Rev. C* **84**, 011301 Jul (2011).
- [8] P. Hewka, C. Holbrow and R. Middleton, *Nucl. Phys.* **88**(3), 561 – 575 (1966).
- [9] H. Fuchs *et al.*, *Nucl. Phys. A* **196**(2), 286 – 302 (1972).
- [10] Carlson, B. V., Escher, J. E., and Hussein, M. S. *J.Phys.* **G41**, 094003 (2014).

Inclusive deuteron-induced reactions and final neutron states

G. Potel^{1,2}, *F. Nunes*¹, *I. J. Thompson*²

¹National Superconducting Cyclotron Laboratory, Michigan State University, East Lansing, MI 48824, USA

²Lawrence Livermore National Laboratory L-414, Livermore, CA 94551, USA

Abstract

We present in this paper a formalism for deuteron-induced inclusive reactions. We disentangle direct elastic breakup contributions from other processes (which we generically call non-elastic breakup) implying a capture of the neutron both above and below the neutron emission threshold. The reaction is described as a two step process, namely the breakup of the deuteron followed by the propagation of the neutron-target system driven by an optical potential. The final state interaction between the neutron and the target can eventually form an excited compound nucleus. Within this context, the direct neutron transfer to a sharp bound state is a limiting case of the present formalism.

1. Introduction

The population of discrete neutron states with (d, p) transfer reactions is a well established experimental method. It has proven to be the tool of choice for the study of the single-particle nature of states close to the Fermi energy, providing information about the energy, spin, parity, and spectroscopic factors, of those states. As a result of the coupling with more complex nuclear degrees of freedom, some of them get fragmented and spread over a finite energy region, and, as we move away from the Fermi energy, they acquire larger energy widths. As we go towards the neutron drip line, the Fermi energy gets closer to the neutron-emission threshold, and, eventually, slides into the continuum. Standard direct transfer reaction theory, such as the Distorted Wave Born Approximation (DWBA) and coupled channels approaches, deal, as a rule, with the population of sharp discrete states. They are thus not well adapted for the description of the transfer to wide states, let alone to states in the continuum region of the spectrum. Early works to provide a more suitable formalism were initiated in the late 70's, but the activity in this field ended quite abruptly in the early 90's, leaving behind an unresolved controversy regarding different approaches ([1, 2, 3, 4, 5, 6, 7, 8, 9]). Recently, a few groups have revived the subject, producing different computer codes to implement the reaction formalism ([10, 11, 12]). Though their approaches are slightly different, they are all based on a two-step description of the reaction mechanism. The two steps considered to describe the deuteron-target reaction are the breakup of the deuteron followed by a propagation of the loose neutron in the target field. This field is modeled with an optical potential, and can account for the absorption of the neutron both in finite-width bound states and in the above neutron-emission threshold continuum states.

Aside from providing valuable spectroscopic information about the nature of single-particle states in nuclei, the absorption of the neutron can be used at profit to study neutron-induced reactions in radio active isotopes with the surrogate reaction method in inverse kinematics. A considerable theoretical and experimental effort is being devoted to the study of neutron capture (n, γ) and neutron induced fission (n, f) reactions in exotic nuclei making use of the surrogate method ([13, 14, 15, 16, 17, 18]). In these experiments, an exotic beam impinging on a deuteron target absorbs the neutron of the deuteron, forming an (as a rule) excited compound nucleus that later decays emitting principally γ radiation and neutrons. The theoretical prediction of the cross section for the formation of the compound nucleus in a state of given excitation energy, angular momentum and parity (see [10]) is key for the extraction of

the (n, γ) cross sections from the analysis of the experiment ([18]). In section (1.) we briefly introduce the formalism, (we refer to [10] for a detailed derivation), and provide specific expressions for the numerical calculation of non-elastic breakup cross sections. In section (1) we show examples of final neutron states, and we discuss the relationship between the population of states below neutron-emission threshold and the direct neutron transfer in the DWBA approximation.

2. Theoretical formulation

2.1 General formalism in the *prior* representation

Let us consider the reaction $A(d,p)B^*$ which includes elastic breakup and any other inelastic processes. The three-body Hamiltonian for the problem is

$$H = K_n + K_p + h_A(\xi_A) + V_{pn}(r_{pn}) + V_{An}(r_{An}, \xi_A) + U_{Ap}(r_{Ap}), \quad (1)$$

where K_n and K_p are the kinetic energy operators acting on the neutron and proton coordinates respectively. We have adopted a spectator approximation for the outgoing proton, we thus model its interaction with the target by means of an optical potential U_{Ap} . The coordinates used throughout are defined in Fig. 1. Starting from neutron-target (U_{An}) and deuteron-target (U_{Ad}) optical potentials, we can define the optical model Green's function in the breakup channel,

$$G_B^{opt} = \frac{1}{E - E_p - \epsilon_A - K_n - U_{An}(r_{An}) + i\epsilon}, \quad (2)$$

and the source term

$$S_{\text{prior}} = \left(\chi_f^{(-)} \left| U_{Ap} - U_{Ad} + U_{An} \right| \phi_d \chi_i \right), \quad (3)$$

where round bracket indicates integration over the proton coordinate only, and the proton distorted wave $\chi_f^{(-)}$ satisfies the equation

$$\left(E_f - K_p - U_{Ap}^\dagger \right) \chi_f^{(-)} = 0, \quad (4)$$

where E_f is the final channel energy. We can then define the neutron final wavefunction in the *prior* representation,

$$\Psi_n^{\text{prior}} = G_B^{opt} S_{\text{prior}}, \quad (5)$$

and the non-orthogonality function

$$\Psi_n^{HM} = \left(\chi_f^{(-)} \left| \phi_d \chi_i \right. \right). \quad (6)$$

It can be shown (see [10]) that the non-elastic breakup cross section in the *prior* representation can then be written in term of (5) and (6) as

$$\begin{aligned} \left. \frac{d^2\sigma}{d\Omega_p dE_p} \right]^{NEB} &= -\frac{2}{\hbar v_d} \rho_p(E_p) \left[\Im \langle \Psi_n^{\text{prior}} | W_{An} | \Psi_n^{\text{prior}} \rangle \right. \\ &\left. + 2\Re \langle \Psi_n^{HM} | W_{An} | \Psi_n^{\text{prior}} \rangle + \langle \Psi_n^{HM} | W_{An} | \Psi_n^{HM} \rangle \right], \end{aligned} \quad (7)$$

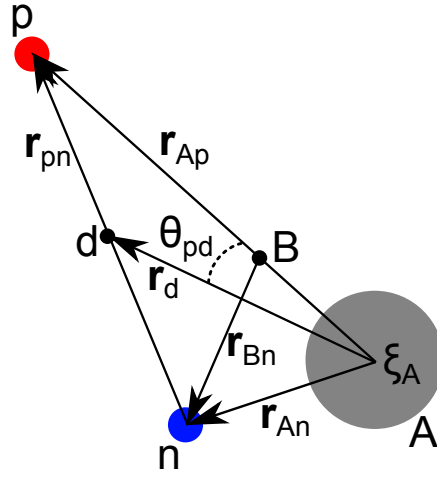


Fig. 1: Schematic representation of the system under consideration with the coordinates used in its description.

where

$$\rho_p(E_p) = \frac{m_p k_p}{8\pi^3 \hbar^2} \quad (8)$$

is the proton level density, and E_p is the kinetic energy of the detected proton.

2.2 Partial wave expansion

The implementation of the formalism relies on the numerical evaluation of the source term

$$\begin{aligned} S_{\text{prior}}(\mathbf{r}_{Bn}; \mathbf{k}_p) &= \langle \chi_p | V | \phi_d \chi_d \rangle \\ &= \int d\mathbf{r}_{Ap} \chi_p^{(-)*}(\mathbf{r}_{Ap}; \mathbf{k}_p) V(r_{An}, r_{Bn}, r_{pn}) \phi_d(\mathbf{r}_{pn}) \chi_d^{(+)}(\mathbf{r}_d). \end{aligned} \quad (9)$$

It is convenient to express the quantities of interest in terms of a partial wave expansion

$$S_{\text{prior}}(\mathbf{r}_{Bn}; \mathbf{k}_p) = \frac{2m_n}{\hbar^2} \sum_{lml_p} \mathcal{F}_{lml_p}(r_{Bn}; \mathbf{k}_p) Y_m^l(\theta_{Bn}) Y_{-m}^{l_p}(\hat{k}_p). \quad (10)$$

Let's first extract the dependence of the neutron final angular momentum l by defining the F coefficients,

$$F_{lm}(r_{Bn}; \mathbf{k}_p) = \int d\Omega_{Bn} S_{\text{prior}}(\mathbf{r}_{Bn}; \mathbf{k}_p) Y_m^{l*}(\theta_{Bn}), \quad (11)$$

and $d\Omega_{Bn} \equiv \sin(\theta_{Bn}) d\theta_{Bn} d\phi_{Bn}$. The distorted waves of the proton and the deuteron can be expanded in partial waves in a standard way,

$$\chi_p^{(-)*}(\mathbf{r}_{Ap}; \mathbf{k}_p) = \frac{4\pi}{k_p r_{Ap}} \sum_{l_p} i^{-l_p} e^{i\sigma_p^{l_p}} f_{l_p}(r_{Ap}) \sqrt{2l_p + 1} \left[Y^{l_p}(\hat{r}_{Ap}) Y^{l_p}(\hat{k}_p) \right]_0^0, \quad (12)$$

where $f_l(r_{Ap})$ is the solution, for each partial wave, of the radial part of the Schrödinger equation with an optical potential $U_{Ap}(r_{Ap})$.

$$\chi_d(+)(\mathbf{r}_d) = \frac{4\pi}{k_d r_d} \sum_{l_d} i^{l_d} e^{i\sigma_d^{l_d}} g_{l_d}(r_d) \sqrt{2l_d + 1} \left[Y^{l_d}(\hat{r}_d) Y^{l_d}(\hat{k}_d) \right]_0^0. \quad (13)$$

In this last expression, $g_l(r_d)$ is the solution, for each partial wave, of the radial part of the Schrödinger equation with the optical potential $U_{Ad}(r_d)$ describing the relative motion between the deuteron and A in the initial channel. If we only take into account the S -wave component of the deuteron wavefunction, we can write

$$\phi_d(\mathbf{r}_{pn}) = \frac{1}{\sqrt{4\pi}} u_d(r_{pn}). \quad (14)$$

Then

$$\begin{aligned} F_{lm}(r_{Bn}; \mathbf{k}_p) &= \frac{8\pi^{3/2}}{k_d k_p} \sum_{l_p l_d} i^{l_d - l_p} e^{i(\sigma_p^{l_p} + \sigma_d^{l_d})} \sqrt{(2l_p + 1)(2l_d + 1)} \\ &\times \int dr_{Ap} d\Omega_{Ap} d\Omega_{Bn} r_{Ap} \frac{f_{l_p}(r_{Ap}) g_{l_d}(r_d)}{r_d} u_d(r_{pn}) V(r_{An}, r_{Bn}, r_{pn}) \\ &\times \left[Y^{l_p}(\hat{r}_{Ap}) Y^{l_p}(\hat{k}_p) \right]_0^0 \left[Y^{l_d}(\hat{r}_d) Y^{l_d}(\hat{k}_d) \right]_0^0 Y_m^{l*}(\boldsymbol{\theta}_{Bn}). \end{aligned} \quad (15)$$

After some Racah algebra, we get

$$\begin{aligned} F_{lm}(r_{Bn}; \mathbf{k}_p) &= \frac{8\pi^{3/2}}{k_d k_p} \sum_{l_d - l_p} i^{l_d - l_p} e^{i(\sigma_p^{l_p} + \sigma_d^{l_d})} \sum_{KM} (-1)^{K-M} \left[Y^{l_p}(\hat{k}_p) Y^{l_d}(\hat{k}_d) \right]_{-M}^K \\ &\times \int dr_{Ap} d\Omega_{Ap} d\Omega_{Bn} r_{Ap} \frac{f_{l_p}(r_{Ap}) g_{l_d}(r_d)}{r_d} u_d(r_{pn}) V(r_{An}, r_{Bn}, r_{pn}) \\ &\times \left[Y^{l_p}(\hat{r}_{Ap}) Y^{l_d}(\hat{r}_d) \right]_M^K (-1)^{l-m} Y_{-m}^l(\boldsymbol{\theta}_{Bn}). \end{aligned} \quad (16)$$

We can then make the replacement

$$\begin{aligned} \left[Y^{l_p}(\hat{r}_{Ap}) Y^{l_d}(\hat{r}_d) \right]_M^K Y_{-m}^l(\boldsymbol{\theta}_{Bn}) &\rightarrow \langle l l m - m | 0 0 \rangle \left\{ \left[Y^{l_p}(\hat{r}_{Ap}) Y^{l_d}(\hat{r}_d) \right]^l Y^l(\boldsymbol{\theta}_{Bn}) \right\}_0^0 \\ &= \frac{(-1)^{l-m}}{\sqrt{2l+1}} \left\{ \left[Y^{l_p}(\hat{r}_{Ap}) Y^{l_d}(\hat{r}_d) \right]^l Y^l(\boldsymbol{\theta}_{Bn}) \right\}_0^0, \end{aligned} \quad (17)$$

as all other possible angular momentum couplings integrate to zero. Note that this is required for angular momentum conservation. The integrand being rotationally invariant, we can evaluate it for a particular configuration (say, the z -axis along $\mathbf{r}_{Bn}, \mathbf{k}_p$ and \mathbf{r}_{Ap} lying in the xy plane) and multiply the result by a factor of $8\pi^2$ (resulting from the integration over $\varphi_{Ap}, \varphi_{Bn}$ and θ_{Bn}). Then one can then write the l, m, l_p

coefficient defined in eq. (10) as the 2-D integral that is numerically evaluated in our code,

$$\begin{aligned} \mathcal{F}_{lm_l p}(r_{Bn}; \mathbf{k}_p) &= (-1)^m \frac{16\pi^{5/2}}{k_d k_p} \sum_{l_d} i^{l_d - l_p} e^{i(\sigma_p^{l_p} + \sigma_d^{l_d})} \langle l_p l_d - m 0 | l - m \rangle \\ &\times \sqrt{\frac{2l_d + 1}{2l + 1}} \int r_{Ap} dr_{Ap} \sin(\theta) d\theta \frac{f_{l_p}(r_{Ap}) g_{l_d}(r_d)}{r_d} \\ &\times u_d(r_{pn}) V(r_{An}, r_{Bn}, r_{pn}) \left[Y^{l_p}(\theta) Y^{l_d}(\theta_d) \right]_0^l, \end{aligned} \quad (18)$$

where θ_d, r_{pn}, r_d are obtained as functions of $r_{Ap}, r_{Bn}, \theta, \theta_{Bn}$ according to the definitions found in Fig. 1, and are to be evaluated for $\theta_{Bn} = 0$.

The non orthogonality term defined in eq. (6) can also be expanded in partial waves in a very similar way,

$$\psi_n^{HM}(\mathbf{r}_{Bn}; \mathbf{k}_p) = \sum_{l, m, l_p} \phi_{lm_l p}^{HM}(r_{Bn}; \mathbf{k}_p) Y_m^l(\theta_{Bn}) Y_{-m}^{l_p}(\hat{\mathbf{k}}_p) / r_{Bn}, \quad (19)$$

with

$$\begin{aligned} \phi_{lm_l p}^{HM}(r_{Bn}; \mathbf{k}_p) &= (-1)^m \frac{16\pi^{5/2}}{k_d k_p} \sum_{l_d} i^{l_d - l_p} e^{i(\sigma_p^{l_p} + \sigma_d^{l_d})} \langle l_p l_d - m 0 | l - m \rangle \\ &\times \sqrt{\frac{2l_d + 1}{2l + 1}} \int r_{Ap} dr_{Ap} \sin(\theta) d\theta \frac{f_{l_p}(r_{Ap}) g_{l_d}(r_d)}{r_d} u_d(r_{pn}) \left[Y^{l_p}(\theta) Y^{l_d}(\theta_d) \right]_0^l. \end{aligned} \quad (20)$$

2.3 Neutron wavefunction

The partial wave expansion of the Green's function (2) for a given neutron energy ε can be written as

$$G_l(r_{Bn}, r'_{Bn}) = \frac{f_l(k_n, r_{Bn <}) g_l(k_n, r_{Bn >})}{k_n r_{Bn} r'_{Bn}}, \quad (21)$$

where $k_n = \sqrt{2m_n \varepsilon} / \hbar$, and $f_l(k_n, r_{Bn})$ ($g_l(k_n, r_{Bn})$) is the regular (irregular) solution of the homogeneous equation

$$\left(-\frac{\hbar^2}{2m_n} \frac{\partial^2}{\partial r_{Bn}^2} + U_{Bn}(r_{Bn}) + \frac{\hbar^2 l(l+1)}{2m_n r_{Bn}^2} - \varepsilon \right) \{f_l(k_n, r_{Bn}), g_l(k_n, r_{Bn})\} = 0. \quad (22)$$

The neutron wavefunction

$$\psi_n(\mathbf{r}_{Bn}; \mathbf{k}_p) = \sum_{l, m, l_p} \phi_{lm_l p}(r_{Bn}; \mathbf{k}_p) Y_m^l(\theta_{Bn}) Y_{-m}^{l_p}(\hat{\mathbf{k}}_p) / r_{Bn}, \quad (23)$$

can then be obtained with according to eq. (5),

$$\begin{aligned} \phi_{lm_l p}(r_{Bn}, k_p) &= \int G_l(r_{Bn}, r'_{Bn}) \mathcal{F}_{lm_l p}(r'_{Bn}; k_p) r_{Bn}'^2 dr'_{Bn} \\ &= \frac{1}{k_n} \left(g_l(k_n, r_{Bn}) \int_0^{r_{Bn}} f_l(k_n, r'_{Bn}) \mathcal{F}_{lm_l p}(r'_{Bn}; k_p) r_{Bn}' dr'_{Bn} \right. \\ &\quad \left. + f_l(k_n, r_{Bn}) \int_{r_{Bn}}^\infty g_l(k_n, r'_{Bn}) \mathcal{F}_{lm_l p}(r'_{Bn}; k_p) r_{Bn}' dr'_{Bn} \right). \end{aligned} \quad (24)$$

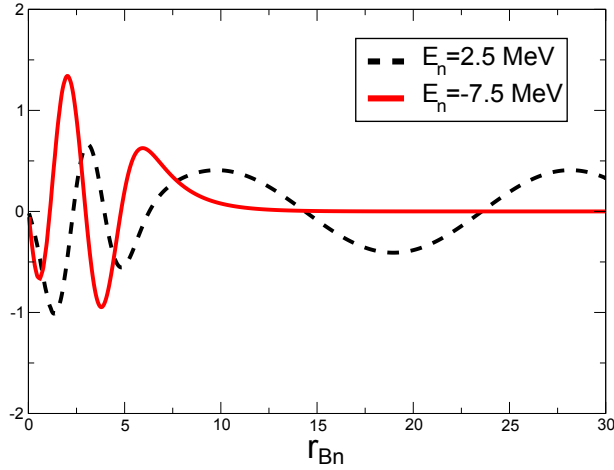


Fig. 2: Neutron partial wave coefficient $\phi_{000}(r_{Bn})$ for $\varepsilon = 2.5$ MeV (dashed black line) and $\varepsilon = -7.5$ MeV (red line).

3. Results

It is important to note that the neutron wavefunctions (23) are not eigenfunctions of a hermitian Hamiltonian, and can be associated with *any* arbitrary energy ε , both positive and negative. In order to get the physical wavefunctions, the corresponding boundary conditions have to be enforced by implementing them in the Green's function (21). In order to do that, we impose $\lim_{r_{An} \rightarrow 0} f_l(k_n, r_{An}) = 0$ for the regular solution. At large distances the boundary condition of course depends on whether the energy ε is positive or negative. For scattering neutron states (positive ε),

$$\lim_{r_{An} \rightarrow \infty} g_l(k_n, r_{An}) \rightarrow e^{i(k_n r_{An} - \frac{l\pi}{2})}, \quad (25)$$

while for final neutron bound states (negative ε),

$$\lim_{r_{An} \rightarrow \infty} g_l(k_n, r_{An}) \rightarrow e^{-\kappa_n r_{An}}, \quad (26)$$

with $\kappa_n = \sqrt{-2m_n \varepsilon} / \hbar$. This last, somewhat less standard, condition can be implemented by integrating inwards numerically a function with the boundary condition

$$g_l(k_n, R_\infty - h) = \frac{g_l(k_n, R_\infty)}{(1 - \kappa_n h)}, \quad (27)$$

where R_∞ is a large value of the radius and h is the numerical integration step, chosen such that $\kappa_n h \ll 1$. We can thus use eq. (24) to obtain the neutron wavefunction for arbitrary positive and negative energies. As an example, we show in Fig. 2 the wavefunction ϕ_{000} for $\varepsilon = 2.5$ MeV and $\varepsilon = -7.5$ MeV. The neutron wavefunction (23) and the non-orthogonality term (19) can then be used in (7) to obtain the non-elastic breakup cross section. If the final neutron energy is negative, the capture of the neutron in a region in which the imaginary part W_{An} of the optical is small is related to the direct transfer to a sharp bound state. Actually, it can be shown (see [10]) that, in first order of $\langle W_{An} \rangle \equiv \langle \phi_n | W_{An} | \phi_n \rangle$, there is a simple relationship between the cross section for the capture of a neutron in a bound state of finite width and the cross section for the direct transfer to the corresponding zero-width bound state. Assuming that

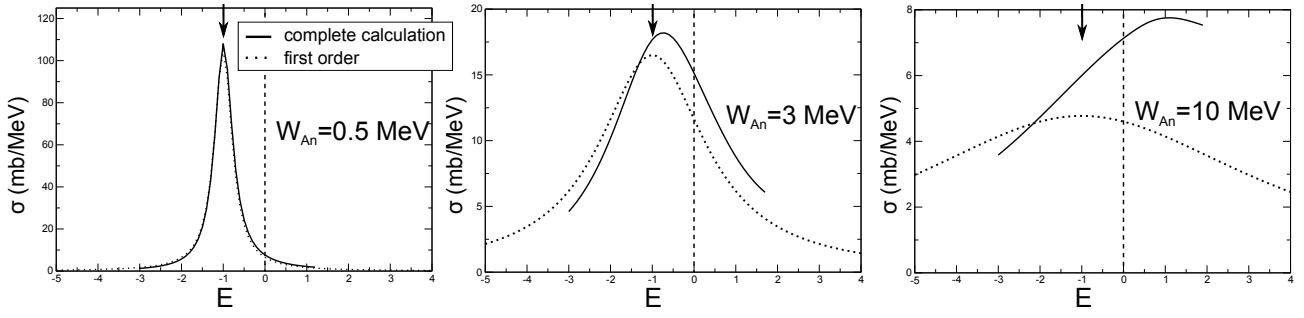


Fig. 3: Non-elastic breakup cross section computed at neutron energies E around a resonance $E_n = -1$ MeV. We compare the complete calculation (left side of eq. (29)) with the isolated-resonance, first-order approximation (right side of eq. (29)), for $W_{An} = 0.5$ MeV, $W_{An} = 3$ MeV and $W_{An} = 10$ MeV. The arrow indicates the value of the eigenstate E_n corresponding to the real part of the optical potential U_{An} , and the vertical dashed line is drawn at the neutron-emission threshold.

the one-neutron transfer DWBA amplitude

$$T_n^{(1NT)} = \int \phi_n^* \left(\chi_f^{(-)} |V_{prior} | \phi_d \chi_i \right) d\mathbf{r}'_{An} \quad (28)$$

to the single-particle state ϕ_n of the target-neutron residual nucleus is constant in an energy range of the order of $\Gamma_n = 2\langle W_{An} \rangle$, we have

$$\left. \frac{d^2\sigma}{d\Omega_p dE_p}(E, \Omega) \right]^{NEB} \approx \frac{1}{2\pi} \frac{\Gamma_n}{(E_n - E)^2 + \Gamma_n^2/4} \frac{d\sigma_n}{d\Omega}(\Omega), \quad (29)$$

where $\frac{d\sigma_n}{d\Omega}$ is the direct transfer differential cross section to the n th eigenstate of the real potential. For the above approximation to be valid, $\langle W_{An} \rangle$ needs to be small, and the distance ΔE between the resonance E_n and the closest one has to be big enough ($\Delta E \gg \Gamma_n$). In particular, the latter condition is hardly verified if the resonance is too close (i.e., within a distance of the order or smaller than Γ_n) to the continuum (neutron emission threshold). In Fig. 3 we compare the first order approximation with the exact calculation for energies close to a resonance 1 MeV away from the neutron emission threshold, for three different values of W_{An} .

4. Conclusions

We have presented a formalism for inclusive deuteron-induced reactions, in which the final neutron-target system is left in an arbitrary state characterized by its energy, angular momentum and parity. The general derivation of the expression of the non-elastic breakup eq. (7) is given elsewhere ([10]), as well as the comparison with experimental results. In this paper we have focused our attention in the final neutron wavefunction, presenting an explicit expression that can be computed numerically (see eqs. (23) and (24)). If the target-neutron interaction is modeled with an optical potential U_{An} with a non-zero imaginary part W_{An} , the negative-energy part of the neutron spectrum is no longer discrete. Instead of being composed by sharp single-particle states, the neutron can have any continuous value of the energy above the Fermi energy. This continuous spectrum exhibit a resonant behavior around a discrete set of energies, with widths naturally related with the value of W_{An} . We show that, in the limit in which W_{An} is small compared to the real part of U_{An} and to the distance between resonances, the set of discrete resonances can be related to the discrete single-particle spectrum, i.e., the set of eigenvalues corresponding to the real part of U_{An} . Moreover, the energy-integrated cross section around a resonance

gives the direct DWBA transfer cross section to that particular state.

Acknowledgements

This work was supported by the National Science Foundation under Grant No. PHY-1403906, and the Department of Energy, Office of Science, Office of Nuclear Physics under award No. DE-FG52-08NA28552, and by Lawrence Livermore National Laboratory under Contract DE-AC52-07NA27344.

References

- [1] A. Kerman and K. McVoy, *Annals of Physics*, vol. 122, no. 1, p. 197, 1979.
- [2] T. Udagawa and T. Tamura, *Phys. Rev. Lett.*, vol. 45, p. 1311, 1980.
- [3] N. Austern and C. M. Vincent, *Phys. Rev. C*, vol. 23, p. 1847, 1981.
- [4] X. H. Li, T. Udagawa, and T. Tamura, *Phys. Rev. C*, vol. 30, p. 1895, 1984.
- [5] T. Udagawa and T. Tamura, *Phys. Rev. C*, vol. 33, p. 494, 1986.
- [6] M. Ichimura, N. Austern, and C. M. Vincent, *Phys. Rev. C*, vol. 32, p. 431, 1985.
- [7] M. Ichimura, *Phys. Rev. C*, vol. 41, p. 834, 1990.
- [8] M. Hussein and K. McVoy, *Nuclear Physics A*, vol. 445, p. 124, 1985.
- [9] M. S. Hussein and R. Mastroleo, *Nuclear physics A*, vol. 491, p. 468, 1989.
- [10] G. Potel, F. M. Nunes, and I. J. Thompson, *Phys. Rev. C*, vol. 92, p. 034611, 2015.
- [11] J. Lei and A. Moro, *Physical Review C*, 2015. To be published.
- [12] B. V. Carlson, R. Capote, M. Sin, *arXiv:1508.01466 [nucl-th]*, 2015.
- [13] J. Escher and F. Dietrich, *Phys. Rev. C*, vol. 81, p. 024612, 2010.
- [14] N. D. Scielzo *et al.* *Phys. Rev. C*, vol. 81, p. 034608, 2010.
- [15] J. Escher *et al.* *Rev. Mod. Phys.*, vol. 84, p. 353, 2012.
- [16] R. O. Hughes *et al.* *Phys. Rev. C*, vol. 85, p. 024613, 2012.
- [17] T. J. Ross *et al.* *Phys. Rev. C*, vol. 85, p. 051304, 2012.
- [18] B. Carlson, J. Escher, and M. Hussein, *J. Phys. G*, vol. 41, p. 094003, 2014.

Elastic and inelastic breakup of deuterons with energy below 100 MeV

*B. V. Carlson*¹, *R. Capote*², *M. Sin*³

¹Instituto Tecnológico de Aeronáutica, São José dos Campos SP, Brazil

²NAPC-Nuclear Data Section, International Atomic Energy Agency, 1400 Vienna, Austria

³University of Bucharest, P.O. Box MG-11, 70709 Bucharest-Magurele, Romania

Abstract

We present calculations of deuteron elastic and inelastic breakup cross sections and angular distributions at deuteron energies below 100 MeV obtained using the post-form DWBA approximation. Although the elastic breakup cross section was extensively studied in the past, until recently, very few calculations of inelastic breakup have been performed. We also analyze the angular momentum - energy distributions of the cross section for formation of the compound nucleus after inelastic breakup.

1. Introduction

Deuteron-induced reactions are being used to produce medical radioisotopes [1], to study the shell structure of exotic nuclei through stripping and as surrogates to neutron-induced reactions (see review [2] and references therein), among recent applications. Although they have been studied for decades [3, 4], the complexity of these reactions continues to make their theoretical description challenging.

The direct reaction mechanism is a major contributor to the deuteron reaction cross section due to the particle's low binding energy. Competition between elastic breakup, absorption of only a neutron or a proton (stripping and inelastic breakup) and absorption of the deuteron must be taken into account to determine the formation or not of a compound nucleus and its subsequent decay. The inelastic breakup reactions - those in which either only a neutron or a proton is absorbed - are particularly complex, as they form compound nuclei with a wide range of excitation energies and angular momenta. These reactions were discussed at great length in the 80's but few calculations were performed. Interest in them has resurged recently within the context of reactions with exotic nuclei, of which the deuteron may be considered the simplest [5, 6].

We present the results of a theoretical study of elastic and inelastic deuteron breakup for selected targets at incident deuteron energies below 100 MeV. We use the zero-range post-form DWBA approximation to calculate the elastic breakup cross section [3] and its extension to absorption channels to calculate the inelastic breakup cross sections [4]. We discuss the regularities and ambiguities in our results, as well as the irregularities in the inelastic breakup energy and angular momentum distributions that complicate their substitution by a smooth distribution obtained from systematics.

2. Theory

A reasonable theoretical description of elastic deuteron breakup was developed and applied to a multitude of experimental data almost forty years ago by G. Baur and collaborators [3]. The double-differential inelastic breakup cross section can be written in terms of its T-matrix element as

$$\frac{d^6\sigma^{bu}}{dk_p^3 dk_n^3} = \frac{2\pi}{\hbar v_d} \frac{1}{(2\pi)^6} |T(\mathbf{k}_p, \mathbf{k}_n; \mathbf{k}_d)|^2 \delta(E_d + \epsilon_d - E_p - E_n) \quad (1)$$

where \mathbf{k}_n and \mathbf{k}_p are the final neutron and proton momenta, respectively, \mathbf{k}_d is the initial deuteron momentum and the sum of neutron and proton final kinetic energies is constrained to the sum of the initial deuteron kinetic energy and its binding energy by the δ -function. The T-matrix element can be well approximated by the post-form of the DWBA matrix element,

$$T(\mathbf{k}_p, \mathbf{k}_n; \mathbf{k}_d) = \left\langle \tilde{\psi}_p^{(-)}(\mathbf{k}_p, \mathbf{r}_p) \tilde{\psi}_n^{(-)}(\mathbf{k}_n, \mathbf{r}_n) | v_{pn}(\mathbf{r}) | \psi_d^{(+)}(\mathbf{k}_d, \mathbf{R}) \phi_d(\mathbf{r}) \right\rangle, \quad (2)$$

which, in turn, can be well-approximated within the zero-range DWBA approximation

$$T(\mathbf{k}_p, \mathbf{k}_n; \mathbf{k}_d) \rightarrow D_0 \left\langle \tilde{\psi}_p^{(-)}(\mathbf{k}_p, a\mathbf{R}) \tilde{\psi}_n^{(-)}(\mathbf{k}_n, \mathbf{R}) \Lambda(R) | \psi_d^{(+)}(\mathbf{k}_d, \mathbf{R}) \right\rangle \quad (3)$$

by including a correction for finite-range effects $\Lambda(R)$ [7] and taking $D_0 = -125 \text{ Mev}\cdot\text{fm}^{3/2}$.

To calculate the inelastic breakup cross section, one first analyzes the inclusive double differential breakup cross section, here given for the proton, again in the post-form of the DWBA. The initial state of the target is its ground state, Φ_A , but the final neutron-target state, ψ_{nA}^c , can be any composite state allowed by energy and angular momentum conservation,

$$\frac{d^3\sigma}{dk_p^3} = \frac{2\pi}{\hbar v_d} \frac{1}{(2\pi)^3} \sum_c \left| \left\langle \tilde{\psi}_p^{(-)}(\mathbf{k}_p, \mathbf{r}_p) \psi_{nA}^c | v_{pn}(\mathbf{r}) | \psi_d^{(+)}(\mathbf{k}_d, \mathbf{R}) \phi_d(\mathbf{r}) \Phi_A \right\rangle \right|^2 \delta(E_d + \varepsilon_d - E_p - E_{nA}^c). \quad (4)$$

Following Kasano and Ichimura [4], we write the δ -function as the imaginary part of an energy denominator,

$$\begin{aligned} \frac{d^3\sigma}{dk_p^3} = & -\frac{2}{\hbar v_d} \frac{1}{(2\pi)^3} \text{Im} \sum_c \left\langle \psi_d^{(+)} \phi_d \Phi_A | v_{pn} | \tilde{\psi}_p^{(-)} \psi_{nA}^c \right\rangle \\ & \times (E_d^+ + \varepsilon_d - E_p - E_{nA}^c)^{-1} \left\langle \tilde{\psi}_p^{(-)} \psi_{nA}^c | v_{pn} | \psi_d^{(+)} \phi_d \Phi_A \right\rangle, \end{aligned} \quad (5)$$

the target ground-state matrix element of which we interpret as a neutron optical propagator,

$$G_n^{(+)}(E_d + \varepsilon_d - E_p) = \sum_c (\Phi_A | \psi_{nA}^c) \frac{1}{E_d^+ + \varepsilon_d - E_p - E_{nA}^c} \langle \psi_{nA}^c | \Phi_A \rangle.$$

This furnishes a cross section of the form

$$\frac{d^3\sigma}{dk_p^3} = -\frac{2}{\hbar v_d} \frac{1}{(2\pi)^3} \text{Im} \left\langle \chi_n(\mathbf{r}_n) \left| G_n^{(+)}(E_d + \varepsilon_d - E_p) \right| \chi_n(\mathbf{r}_n) \right\rangle, \quad (6)$$

where the effective neutron wave function is given by

$$\chi_n(\mathbf{r}_n) = \left(\tilde{\psi}_p^{(-)}(\mathbf{r}_p) | v_{pn}(\mathbf{r}) | \psi_d^{(+)}(\mathbf{R}) \phi_d(\mathbf{r}) \right). \quad (7)$$

To reduce this further, the imaginary part of the optical propagator is decomposed as

$$\text{Im}G_n = (1 + G_n^\dagger U_n^\dagger) \text{Im}G_0 (1 + U_n G_n) + G_n^\dagger W_n G_n. \quad (8)$$

The inclusive proton emission cross section from breakup can then be separated into an elastic and inelastic part, denoted here by *bu* for elastic breakup and *bf* for inelastic breakup or breakup-fusion,

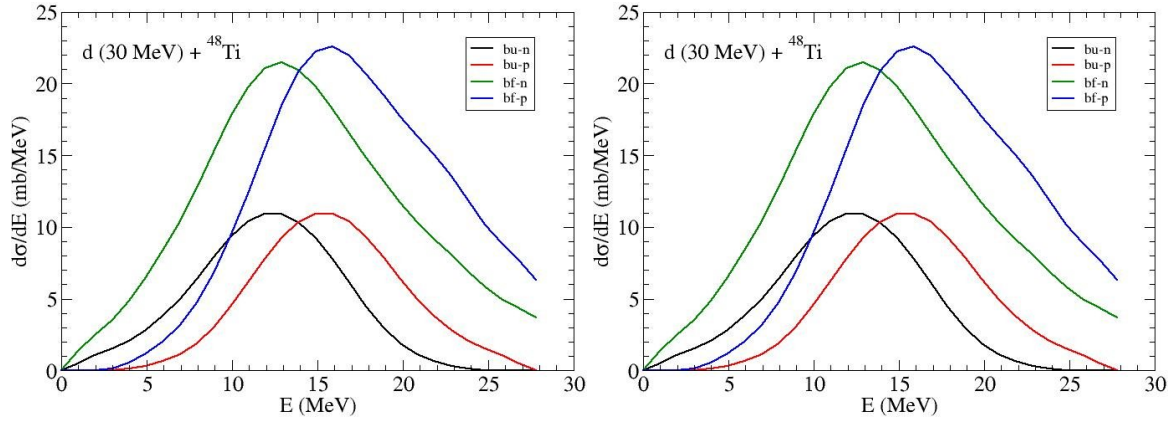


Fig. 1: (a) Proton and neutron emission spectra from elastic and inelastic breakup spectra of 30 MeV deuterons incident on ^{48}Ti . (b) Proton and neutron emission spectra from elastic and inelastic breakup spectra of 30 MeV deuterons incident on ^{181}Ta .

corresponding to the first and second terms of the decomposition of the propagator, respectively,

$$\frac{d^3\sigma}{dk_p^3} = \frac{d^3\sigma^{bu}}{dk_p^3} + \frac{d^3\sigma^{bf}}{dk_p^3}. \quad (9)$$

The contribution due to elastic breakup

$$\frac{d^3\sigma^{bu}}{dk_p^3} = \frac{2\pi}{\hbar v_d} \frac{1}{(2\pi)^3} \int \frac{d^3k_n}{(2\pi)^3} |T(\mathbf{k}_p, \mathbf{k}_n; \mathbf{k}_d)|^2 \delta(E_d + \varepsilon_d - E_p - E_n), \quad (10)$$

is just the double differential cross section of Eq. (1) integrated over the neutron momentum. The inelastic breakup cross section takes the form of an expectation value of the imaginary part of the optical potential,

$$\frac{d^3\sigma^{bf}}{dk_p^3} = -\frac{2}{\hbar v_d} \frac{1}{(2\pi)^3} \langle \Psi_n(\mathbf{k}_p, \mathbf{r}_n; \mathbf{k}_d) | W_n(\mathbf{r}_n) | \Psi_n(\mathbf{k}_p, \mathbf{r}_n; \mathbf{k}_d) \rangle, \quad (11)$$

where the effective neutron wave function is given by

$$|\Psi_n(\mathbf{k}_p, \mathbf{r}_n; \mathbf{k}_d)\rangle = \left(\tilde{\psi}_p^{(-)}(\mathbf{k}_p, \mathbf{r}_p) G_n^{(+)}(\mathbf{r}_n, \mathbf{r}'_n) |v_{pn}(\mathbf{r})| \psi_d^{(+)}(\mathbf{k}_d, \mathbf{R}) \phi_d(\mathbf{r}) \right). \quad (12)$$

The physical interpretation of this cross section is simple: the deuteron first breaks up and, after propagating further, the neutron is absorbed while the proton is emitted. This wave function can be well-approximated in the zero-range approximation, again including the finite range correction $\Lambda(R)$ of Ref. [7], as

$$|\Psi_n(\mathbf{k}_p, \mathbf{r}_n; \mathbf{k}_d)\rangle \rightarrow D_0 \left(\tilde{\psi}_p^{(-)}(\mathbf{k}_p, a\mathbf{R}) G_n^{(+)}(\mathbf{r}_n, \mathbf{R}) \Lambda(R) | \psi_d^{(+)}(\mathbf{k}_d, \mathbf{R}) \right). \quad (13)$$

To perform numerical calculations, the wave functions and matrix elements are expanded in partial waves of the orbital angular momentum alone. We thus neglect the effects of spin-orbit coupling but thereby reduce the number of matrix elements by a factor of almost 12.

To calculate the distorted wave functions, the Koning-Delaroche global optical potentials [8]

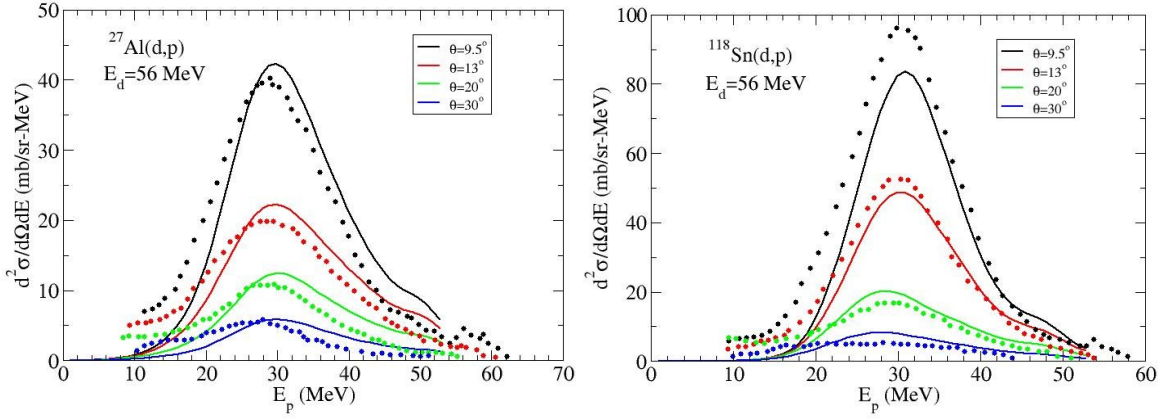


Fig. 2: (a) Inclusive double differential proton spectra for 56 MeV deuterons incident on ^{27}Al . (b) Inclusive double differential proton spectra for 56 MeV deuterons incident on ^{118}Si .

were used in the proton and neutron channels while the potentials of Refs. [9] or [10] were used to describe the deuteron scattering. Both deuteron optical potentials yield very similar results. We used the potential of Ref. [9] in the calculations presented here.

The elastic breakup matrix elements of Eq. (3) are only conditionally convergent. A simple brute force application of standard integration methods requires integrating to radii of the order of a nanometer. The numerical integration can be reduced to radii of the order of picometers by using asymptotic expansions of the Coulomb wave functions to approximate the integral in the external region analytically. However, we have found the most efficient means of performing the integrals to be their extension to the complex plane as proposed by Vincent and Fortune [11]. In this case, we can usually limit the numerical integration to several hundreds of fm and could probably limit it even more, were we to invest more effort in the evaluation of the Coulomb wave functions in the complex plane.

3. Calculations

We begin by presenting calculations of neutron and proton spectra from the elastic and inelastic breakup of 30 MeV deuterons incident on ^{48}Ti and ^{181}Ta , shown in Fig. 1. In both cases, the inelastic breakup spectra are larger than the elastic ones. The elastic and inelastic spectra for neutron or proton both peak at about the same energy in both reactions with the proton spectra peaking at higher energy than the neutron ones.

The difference in the the maxima of the neutron and proton spectra in Fig. 1 can be interpreted in terms of the Coulomb deceleration of the deuteron and posterior Coulomb acceleration of the outgoing proton. At the radius at which breakup occurs, R_{bu} , we would expect the deuteron to have lost a kinetic energy of Ze^2/R_{bu} , which is later recovered by the outgoing proton. On the average, we would thus expect to find for the outgoing neutron and proton kinetic energies

$$\begin{aligned} E_n &\approx \frac{1}{2} \left(E_d - \frac{Ze^2}{R_{bu}} - \varepsilon_d \right) \\ E_p &\approx \frac{1}{2} \left(E_d + \frac{Ze^2}{R_{bu}} - \varepsilon_d \right). \end{aligned} \quad (14)$$

Interpreting the difference in the peaks as the energy difference at the most probable radius, we find the breakup radius R_{bu} to be 10.6 fm for ^{48}Ti and 14.6 fm for ^{181}Ta . We compare these values to strong

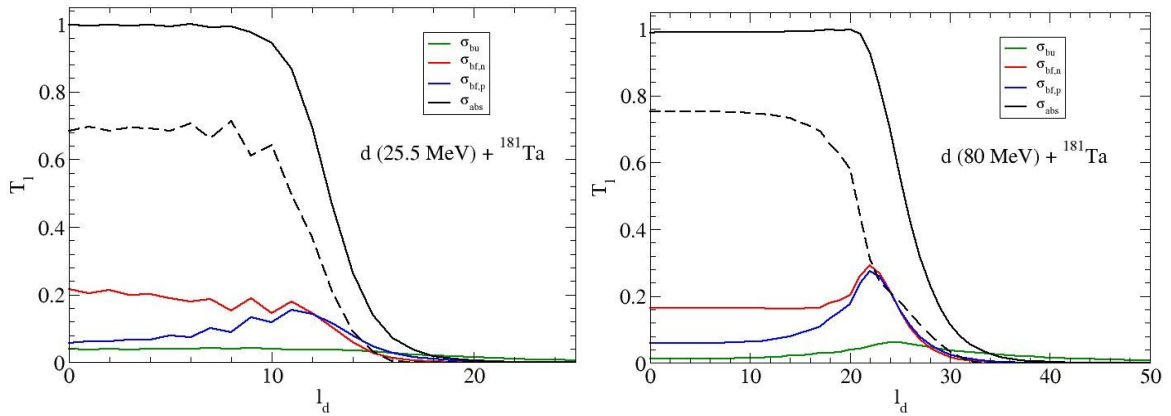


Fig. 3: (a) Reaction probabilities as a function of the deuteron angular momentum for 25.5 MeV deuterons incident on ^{48}Ti . (b) Reaction probabilities as a function of the deuteron angular momentum for 80 MeV deuterons incident on ^{181}Ta .

interaction radii of 6.0 fm for ^{48}Ti and 8.6 fm for ^{181}Ta , obtained by taking $R_{int} \approx 1.25(A^{1/3} + 2^{1/3})$ fm, with A the target mass number. We conclude that the breakup occurs predominantly in the Coulomb field of the target.

In Fig. 2, we compare our calculations with the experimental inclusive double differential proton cross sections for 56 MeV deuterons incident on ^{27}Al and ^{118}Sn [12]. The cross sections include protons from both elastic and inelastic breakup. The calculations agree well with the experimental data for the case of ^{27}Al although the calculations are shifted to slightly higher energies, probably due to the fact that their center-of-mass motion is not extracted correctly. This shift is much smaller in the case of ^{118}Sn . However, here the spectrum is underpredicted by about 20% at an angle of 9.5° and by a few percent at 13° . As the breakup at small scattering angles (corresponding to large impact parameters) is principally elastic, we suspect that more partial waves should be included in our elastic breakup calculation.

A standard optical model calculation of deuteron scattering furnishes a deuteron absorption probability (transmission coefficient) close to 1 below the grazing value of the angular momentum, corresponding to the solid black lines shown in Fig. 3 for deuterons incident at 25.5 and 80 MeV on ^{181}Ta .

The flux lost due to elastic and inelastic breakup reduces this probability to about 75% for low partial waves in the nuclear interior and eliminates it in the surface region, as shown by the dashed lines in Fig. 3. Also shown are the neutron and proton absorption probabilities from inelastic breakup, which dominate in the surface region and extend into the nuclear interior with probabilities of about 10% and 20%, respectively. Only elastic breakup extends to higher angular momenta outside the range of the nuclear interaction.

A complete calculation of a deuteron-induced reaction must also take into account the formation and decay of the compound nucleus (CN) formed by absorption of the deuteron, as well as those formed by absorption of the neutrons or protons of inelastic breakup. The deuteron absorption cross section is determined by the subtracted transmission coefficients, shown as dashed lines in Fig. 3. The excitation energy of the CN that results is determined by the kinetic energy of the incident deuteron. Inelastic breakup reactions produce protons and neutrons over the entire kinematically allowed range of energy. The corresponding differential formation cross sections are thus distributions in energy and angular momentum. An example, for neutron and proton absorption due to inelastic breakup in deuteron-induced reactions at an incident energy of 25.5 MeV is shown in Fig. 4.

In the reaction at 25.5 MeV, we observe in Fig. 4 that the neutron + target CN formation is

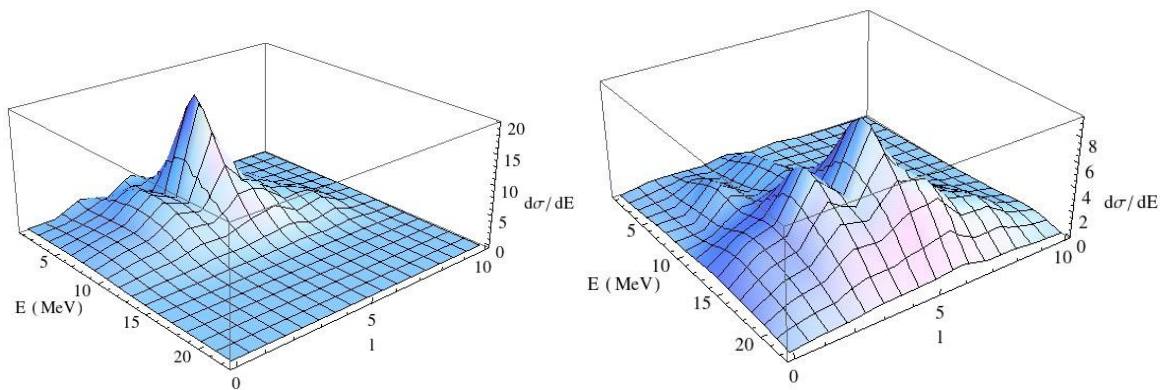


Fig. 4: (a) Energy - angular momentum distribution of neutron + target differential CN formation cross section for 25.5 MeV deuterons incident on ^{181}Ta . (b) Energy - angular momentum distribution of proton + target differential CN cross section formation for 25.5 MeV deuterons incident on ^{181}Ta .

well concentrated at lower energies while the proton + target CN formation is concentrated for the most part at higher energies, due to the importance of the Coulomb repulsion at this energy. The separation in energy of the neutron and proton distributions is still visible but becomes less distinct at higher energies. At low incident energies, the proton + target distribution extends to larger values of the angular momentum, mainly due to the higher average energies of the protons that are absorbed.

Well-defined structures in energy and angular momentum appear in the differential cross sections at the incident deuteron energy of 25 MeV and, to a lesser extent, at higher energies. These reactions should thus be used with care as surrogates to other reactions [2]. The compound nucleus formed could have an initial energy-angular momentum distribution very different from the one expected of a neutron- or proton-induced reaction.

4. Summary

We have used the post-form DWBA to calculate elastic and inelastic deuteron breakup cross sections in the zero-range limit. The breakup occurs for the most part outside the range of the nuclear interaction. However, the inelastic breakup cross sections, in which either the proton or neutron is absorbed by the target, are larger than the elastic one, in which the neutron and proton are simultaneously emitted.

The breakup reactions reduce deuteron absorption at small impact parameters by about 25% and dominate the surface region completely. The neutron + target absorption of inelastic breakup tends to occur at lower energy than the proton + target one, due to Coulomb repulsion, which inhibits low-energy protons from entering the range of the nuclear interaction. The low-energy inelastic breakup CN formation cross sections are found to have well-defined structures in energy and angular momentum, which could have important consequences in reactions in which they are intended to serve as surrogates.

Acknowledgements

BVC acknowledges partial support from FAPESP (Project 2009/00069-5), the CNPq (Project 306692/2013-9) and the International Atomic Energy Agency (Research Contract 17740).

References

- [1] E. Betak *et al.*, Technical Reports Series 473, IAEA, Vienna, Austria, 2011, ISBN 978-92-0-115010-3.
- [2] J.E. Escher *et al.*, *Rev. Mod. Phys.* **84**, 353 (2012).

- [3] G. Baur and D. Trautmann, *Phys. Rep.* **25**, 293 (1976);
G. Baur, F. Rösler, D. Trautmann and R. Shyam, *Phys. Rep.* **111**, 333 (1984).
- [4] A. Kasano *et al.*, *Phys. Rep.* **154**, 125 (1987).
- [5] Jin Lei, A.M. Moro, arXiv:1510.02602; accepted *Phys. Rev. C*.
- [6] G. Potel, F. Nunes, I.J. Thompson, *Phys. Rev. C* **92**, 034611 (2015); arXiv:1510.02727.
- [7] P.J.A. Buttle and L.J.B. Goldfarb, *Proc. Phys. Soc.* **83**, 701 (1964).
- [8] A.J. Koning and J.P. Delaroche, *Nucl. Phys. A* **713** 231, (2003).
- [9] Y. Han, Y. Shi and Q. Shen, *Phys. Rev. C* **74**, 044615 (2006).
- [10] Haixia An and Chonghai Cai, *Phys. Rev. C* **73**, 054605 (2006).
- [11] C.M. Vincent and H.T. Fortune, *Phys. Rev. C* **2**, 782 (1970).
- [12] N. Matsuoka *et al.*, *Nucl. Phys.* **A345**, 1 (1980).

A model of neutron capture and deuteron stripping on deformed nuclei

G. Arbanas¹, I. J. Thompson², J. E. Escher², Ch. Elster³, F. M. Nunes⁴ (TORUS Collaboration), and S.-S. Zhang^{5,1,6}

¹ Oak Ridge National Laboratory, Oak Ridge, TN 37831, USA

² Lawrence Livermore National Laboratory L-414, Livermore, CA 94551, USA

³ Ohio University, Athens, OH 45701, USA

⁴ Michigan State University, East Lansing, MI 48824, USA

⁵ Beihang University, Beijing 100191, China

⁶ University of Tennessee, Knoxville, Tennessee 37996, USA

This manuscript has been authored by UT-Battelle, LLC under Contract No. DE-AC05-00OR22725 and Lawrence Livermore National Laboratory under Contract No. DE-AC52-07NA27344 with the U.S. Department of Energy. The US government retains and the publisher, by accepting the article for publication, acknowledges that the US government retains a nonexclusive, paid-up, irrevocable, worldwide license to publish or reproduce the published form of this manuscript, or allow others to do so, for US government purposes. The Department of Energy will provide public access to these results of federally sponsored research in accordance with the DOE Public Access Plan (<http://energy.gov/downloads/doe-public-access-plan>).

Abstract

A coupled channel model of direct neutron capture and deuteron stripping reactions, which consistently accounts for effects of nuclear deformations in both reactions, is constructed by coupling all incoming and outgoing partitions of both reactions to the same set of collective states. This model is demonstrated using the FRESCO coupled-channels code [1], and it is applied to capture and stripping reactions on even-mass calcium isotopes ^{40,42,44,46,48}Ca. All incoming and outgoing partitions in capture and stripping reactions were coupled to 2⁺, 4⁺, and 3⁻ collective states using a consistent set of deformation lengths. Coupling to these collective states significantly decreases the direct capture cross section relative to the capture in a spherical model for the nuclides considered. Similarly, deuteron stripping is approximately cut in half for the same nuclides. These results suggest that single-particle spectroscopic factors used in this model of direct capture ought to be refitted by computing deuteron stripping with coupling to the same collective states.

1. Introduction

The neutron radiative capture cross section can be computed as a sum of interfering amplitudes of direct, semi-direct, and compound-resonant capture processes. Direct capture take place by a single electromagnetic transition of the neutron from its incoming state in the continuum to its final bound state. Semidirect capture is a two step process that occurs via excitation of a giant dipole nuclear resonance, for example, that subsequently decays via a γ -ray emission. Compound nuclear resonant capture occurs via narrow compound nuclear resonances conventionally described by R-matrix formalism [2], and it constitutes the dominant component of the total low-energy neutron capture on heavy stable nuclides.

Direct capture cross sections can contribute a significant fraction of the total capture on light nuclides or on neutron-rich doubly closed shell nuclei like Ca⁴⁸ and Sn¹³² [3]. Nucleosynthesis models of nuclear astrophysics have been found to be sensitive to direct capture cross sections [4]. Furthermore, direct capture is combined with compound resonant capture in evaluations of neutron capture data on light and medium mass nuclei [5].

Direct neutron capture cross sections are conventionally computed using single particle potential models where the incoming neutron wave function is computed in a complex optical potential and

the final bound state is computed in a real potential.¹ A matrix element of electromagnetic operators between the initial and the final state is then computed to yield a direct capture cross section. Semidirect capture could be modeled by adding a Lorentzian term to the electromagnetic operator [6] or by a coupled-channel formalism [7, 8].

Previous models of direct neutron capture have accounted for the effects of nonspherical nuclei either in the incoming wave functions only (via nonspherical optical model potentials), or in the final bound states only (via nonspherical real potential wells). Since it is known that spherical optical potentials do not yield good agreement with low energy neutron-scattering observables of deformed nuclei, calculations have been performed in which initial and final states are consistently treated in a nonspherical-nucleus picture. This was accomplished by introducing coupling to the 2+, 4+, and 3- collective states into incoming and outgoing partitions. A spherically symmetric model of direct capture is restored in the limit of removing all couplings to collective states.

This work focuses on direct capture of thermal neutrons (incident energy 25.3 meV) into even mass calcium isotopes ^{40,42,44,46,48}Ca for which good data exist [9, 11]. Collective strengths and excitation energies for this set of isotopes span a wide range of magnitudes between the two closed shells, as shown in Fig. 1. This leads to a corresponding variety of effects computed by coupling to those collective states.

Thermal neutron capture cross sections are often measured to a relatively high accuracy, including measurements of prompt γ -ray energies and corresponding branching ratios, all of which could be used to test models of neutron capture. Furthermore, relatively large spectroscopic factors of bound states with orbital angular momentum $l = 1$ found in ^{40,42,44,46,48}Ca allow electric dipole (E1) capture of low-energy s-wave neutrons into those bound states. This feature makes E1 capture a large and dominant component of total thermal neutron capture. Specifically, the E1 components of the thermal neutron capture components has been reported to be 82%, 93%, 98%, 96%, and 100% for ^{40,42,44,46,48}Ca, respectively [9]. The compound resonant component of the thermal neutron capture was computed from the resonance parameters [12] fitted to neutron capture data via the R-matrix formalism in [5]. Compound resonant contribution to thermal neutron capture is practically negligible under the assumption that there are no subthreshold resonances.

Single particle models of direct capture and deuteron stripping are related by spectroscopic factors. A spectroscopic factor of a given bound state quantifies the overlap between it and an idealized single-particle wave function. Spectroscopic factors are conventionally inferred by fitting angular distributions computed by a (d, p) model to measured data [10]. A spectroscopic factor of a given bound state is then used to multiply the direct capture cross section into that state, as shown in Sec. 2.. This connection between direct capture and deuteron stripping suggests that a consistent treatment of both reactions should be pursued.

2. Direct capture with couplings to collective states

The expression for direct capture cross section of a neutron in the incoming channel α_i into a bound state b via the electromagnetic transition of multipolarity (LM) coupled to total angular momentum J_{tot} is computed by FRESKO using the partial-wave T -matrix

$$\mathbf{T}_{LM;b\alpha_i}^{J_{tot}} = -i^{L+1} \sqrt{4\pi} \sqrt{2L+1} \sqrt{\frac{8\pi\hbar c(L+1)}{kL}} \frac{q}{k} \frac{k^L}{(2L+1)!!} \sum_{\alpha} \langle \phi_{b\alpha} | r^L Y_L^M | \psi_{\alpha\alpha_i} \rangle \quad (1)$$

¹Potential depth is fitted to the binding energy of the final neutron state.

used in the usual expression for cross sections

$$\sigma_{\gamma;b\alpha_i}^L = S_b \frac{4\pi}{k_i^2} \frac{1}{(2I_p + 1)(2I_t + 1)} \frac{c}{v_i} \sum_{MJ_{tot}} (2J_{tot} + 1) |\mathbf{T}_{LM;b\alpha_i}^{J_{tot}}|^2, \quad (2)$$

where the neutron's incoming velocity is v_i , γ -ray exit velocity is c , and I_p (I_t) is the intrinsic spin of the neutron (target). S_b is the single-particle spectroscopic factor of the bound state obtained by analysis of (d, p) reaction addressed in Sec. 3.. Here the label α indicates a partial wave component of the initial or the bound neutron wave-functions, with the core Φ_α being either in its ground state ($\alpha = 0^+$) or in any one of the excited collective states to which these wave functions may couple, namely $\alpha = 2^+, 4^+, 3^-$, so $\phi_{b\alpha} = [\Phi_\alpha u_{l_\alpha j_\alpha}(r_n)]_{J_b}$ for neutron wave function $u_{l_\alpha j_\alpha}(r_n)$ [13]. At this stage transitions are considered for which the core remains in the same fractional state α as it was prior to the EM transition. This is indicated by the same superscript α labeling for both the initial and the final states in Eq. (1), as is also shown schematically in Fig. 1(a). In future work, electromagnetic transitions between different components of the initial and final states (i.e., $\sum_{\alpha\alpha'} \langle \phi_{b\alpha'} | r^J Y_J^M | \psi_{\alpha\alpha_i} \rangle$) will be accounted for. The energies and deformation strengths of $2^+, 4^+, 3^-$ collective states were taken from RIPL [14] and are plotted in Fig. 1(b) and (c). All computations in this work use Koning-Delaroché optical potential [15] for neutron in the continuum, and its real part is used for single-particle neutron bound states.

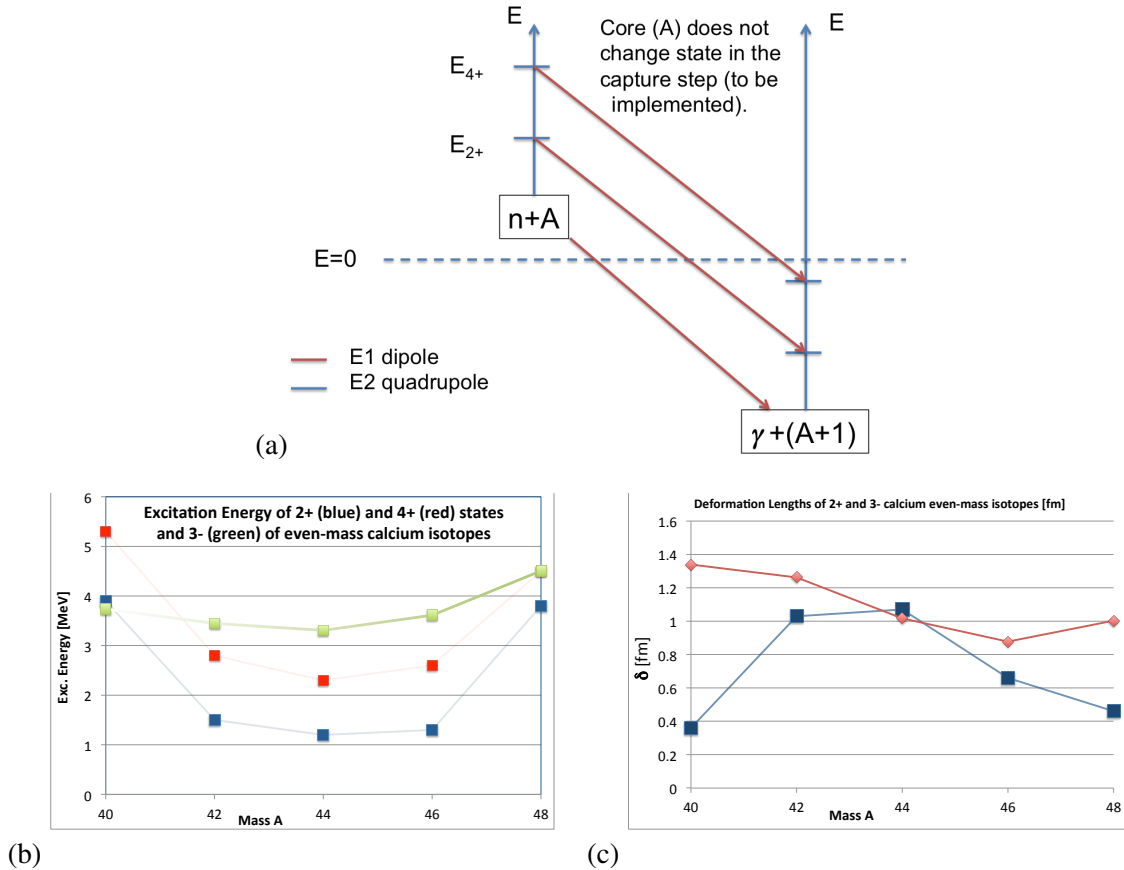


Fig. 1: Couplings between the ground state, 2^+ , and 4^+ quadrupole states in the coupled-channel model of neutron capture and deuteron stripping (a), and the energies (b) and deformation lengths (c) of those states for $^{40,42,44,46,48}\text{Ca}$ isotopes used in the coupled-channel computations.

In Eqs. (1) and (2), Siegert's theorem [16] was employed because it conveniently expresses electromagnetic transition matrix elements in terms of effective charge density. Since Siegert's theorem is strictly valid for many-body nuclear wave functions, it should be used with caution in single-particle capture models where its validity cannot be guaranteed. However, it can be shown that Siegert's theorem remains valid when the binding potential for the neutron in the final state is approximately equal to the real part of the optical potential for the incoming neutron. It has been empirically verified that this condition is reasonably satisfied for the calcium isotopes considered.

A comparison of direct capture computed using the deformed and spherically symmetric models for even-mass calcium isotopes $^{40,42,44,46,48}\text{Ca}$ shows that the deformed method yields a substantially smaller direct capture cross section than the spherically symmetric method in between the two closed shells with a minimum at ^{44}Ca , as seen in Fig. 2(a).

3. Deuteron stripping (d, p) with couplings to collective states

To examine the connection between (d, p) and (n, γ) cross sections in a model that consistently accounts for nuclear deformations in both reactions, coupling is introduced to the same collective states for computation of the (d, p) reactions. The deformation lengths of collective states used for deuteron stripping are the same as those used for direct capture. Daehnick global potential for elastic deuteron scattering [17] is used for the incoming deuteron partition.

We find again a decrease in the magnitude of the deuteron stripping cross section shown in Fig. 2(b), suggesting that spectroscopic factors should be refitted (to experimental data) by using this deformed-potential model of (d, p) reactions. This is suggested because the direct capture cross section computed in Eq. (2) is multiplied by a corresponding single particle spectroscopic factor of the capturing final state. Extant spectroscopic factors are extracted by fitting the computed deuteron stripping cross section to measured (d, p) data. With few notable exceptions [18], spectroscopic factors have generally been extracted using spherically symmetric models of deuteron stripping [19, 20].

If a direct neutron capture model accounts for coupling to collective states, it should use spectroscopic factors that were extracted with an analogous model of deuteron stripping, i.e., a model that accounts for the effects of deformed nuclei by coupling to the same set of collective states. The computation of total deuteron stripping cross section shown in Fig. 2 suggests that a proposed refit of the spectroscopic factor would increase the spectroscopic factors by approximately a factor of 2, and this increase would in turn increase the computed direct neutron capture by the same factor. Such a rescaling process may restore a magnitude of neutron capture that is more consistent with the data.

4. Conclusions

A coupled channel model of direct capture and deuteron stripping that consistently takes nuclear deformation into account in both reactions by coupling to the same set of collective states in both reactions is presented. The results indicate that coupling to collective states decreases direct capture and deuteron stripping by a factor of approximately two for $^{40,42,44,46,48}\text{Ca}$.

These results suggest that a more thorough application of this model should use spectroscopic factors refitted by using the model of deuteron stripping with coupling to collective states. Such spectroscopic factors could then be consistently used in the model of neutron capture with coupling to the same collective states. Considerations such as these should lead to a more intricate understanding of the spectroscopic factors. Since the core is considered to be inert during the capture step, further improvements of the presented model should allow for core (de-)excitations in the capture step.

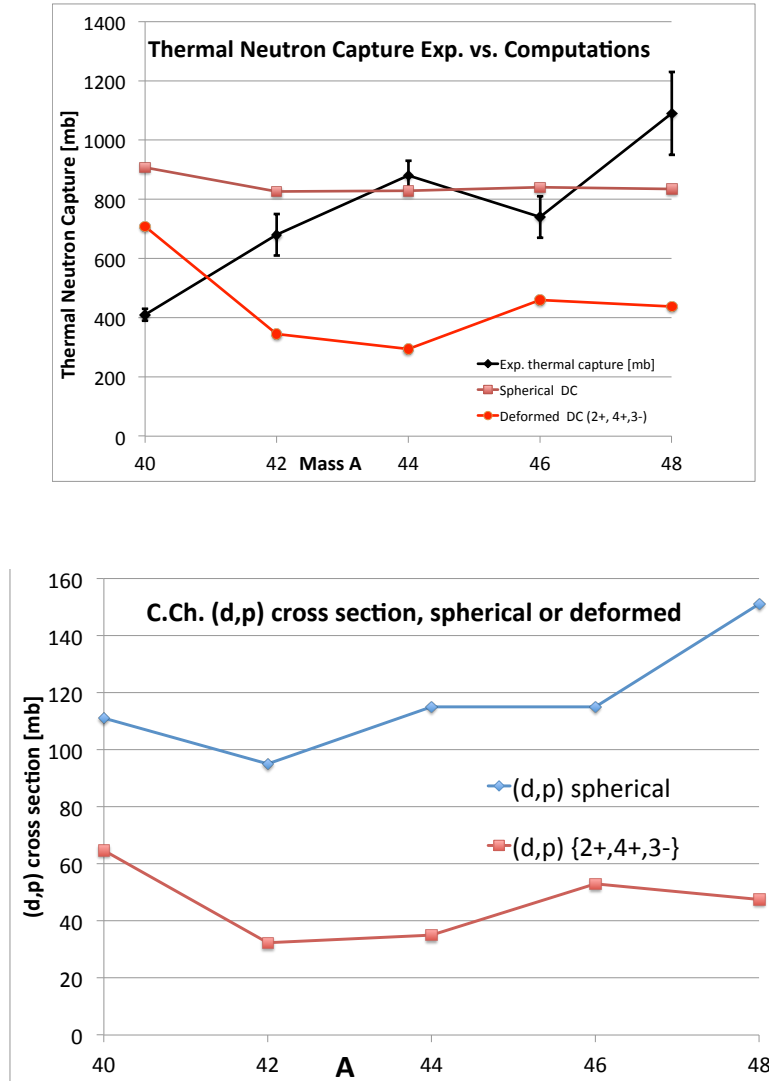


Fig. 2: FRESKO computations of thermal neutron capture (a, upper) and deuteron stripping (b, lower) with coupling to 2^+ , 4^+ , and 3^- collective states in the coupled-channel model on $^{40,42,44,46,48}\text{Ca}$ isotopes. These results suggest that refitting of spectroscopic factors to the (d, p) data would make (n, γ) computations more consistent with the capture data. The decrease observed for deformed (d, p) calculations suggests that an off-setting increase in spectroscopic factors would increase the computed capture cross section for better agreement with the data.

5. Acknowledgments

This work is supported through the US Department of Energy Topical Collaboration TORUS (website www.reactiontheory.org). It is performed under the auspices of DOE by Lawrence Livermore National Laboratory under Contract No. DE-AC52-07NA27344, by Ohio University under Contract No. DE-SC0004087, under the UT Battelle LLC Contract No. DE-AC05-00OR22725, and by Michigan State University under Contract No. DE-SC0004084.

References

- [1] I. J. Thompson, *Computer Physics Reports* **7**, 167 (1988).
- [2] A. M. Lane and R. G. Thomas, *Rev. Mod. Phys.* **30** 257 (1958).
- [3] S.-S. Zhang, M. S. Smith, G. Arbanas, and R. L. Kozub, *Phys. Rev.* **C86**, 032802 (2012).
- [4] R. Surman, J. Beun, G. C. McLaughlin, and W. R. Hix, *Phys. Rev.* **C79**, 045809 (2009).
- [5] N. M. Larson, *Updated Users' Guide for SAMMY: Multilevel R-Matrix Fits to Neutron Data Using Bayes' Equations*, ORNL/TM-9179/R8 (2008).
- [6] W. E. Parker, et al., *Phys. Rev.* **C52**, 252 (1995).
- [7] I. J. Thompson, J. E. Escher, G. Arbanas, *Nuclear Data Sheets* **118**, 292 (2014).
- [8] J. P. Boisson and S. Jang, *Nuclear Physics* **A189**, 334 (1972).
- [9] S. Kahane, et al., *Phys. Rev.* **C36**, 533 (1987).
- [10] A. M. Mukhamedzhanov and F. M. Nunes em *Phys. Rev.* **C72**, 017602 (2005).
- [11] S. Raman, et al., *Phys. Rev.* **C39**, 1297 (1989).
- [12] M. B. Chadwick, et al., *Nuclear Data Sheets* **112**, 2887-2996 (2011); <http://ndc.bnl.gov>.
- [13] I. J. Thompson, F. M. Nunes, *Nuclear Reactions for Astrophysics*, (Cambridge Univ. Press, 2009).
- [14] R. Capote *et al.*, *Nuclear Data Sheets* **110**, 3107 (2009); *Reference Input Parameter Library (RIPL)* <https://www-nds.iaea.org/>.
- [15] A. J. Koning and J. P. Delaroche, *Nucl. Phys.* **A713**, 231 (2003).
- [16] A. J. F. Siegert, *Phys. Rev.* **52**, 787 (1937).
- [17] W. W. Daehnick, J. D. Childs, and Z. Vrcelj, *Phys. Rev.* **C21**, 2253 (1980).
- [18] P. Capel, P. Danielewicz, and F. M. Nunes, *Phys. Rev.* **C82**, 054612 (2010).
- [19] K. L. Jones, et al., *Nature (London)* **465**, 454 (2010); *Phys. Rev.* **C84**, 034601 (2011).
- [20] R. L. Kozub, et al. *Phys. Rev. Lett.* **109**, 172501 (2012).

Study on breakup mechanism of unstable nuclei with CDCC

T. Matsumoto

Department of Physics, Kyushu University, Fukuoka 812-8581, Japan

Abstract

The continuum-discretized coupled-channels method (CDCC) has been successful in describing breakup reactions involving unstable nuclei. Moreover, CDCC is a useful method for evaluation of nuclear data, which are important for nuclear engineering. In this article, we present the theoretical foundation of CDCC and some results of CDCC analyses.

1. Introduction

Breakup reactions have played a key role in investigating the exotic properties of unstable nuclei. The observables such as breakup and neutron removal cross sections reflect information of the ground and resonance continuum states. Therefore to understand the exotic properties from the observables, an accurate analysis of breakup processes is significant.

As one of the most reliable methods for treating breakup processes, the continuum-discretized coupled-channels method (CDCC) [1, 2, 3] has been proposed. At first, CDCC has been applied to analyses of three-body scattering problems, in which a projectile breaks up into two constituents. Recently, we have developed CDCC as a method of treating four-body scattering with a three-body projectile. This new version of CDCC is called four-body CDCC [4, 5, 6, 7]. As another development of CDCC, the eikonal reaction theory (ERT) [8] has been proposed. In ERT, we can calculate inclusive breakup cross sections such as neutron removal cross sections, in which Coulomb breakup processes are consistently described by CDCC without making the adiabatic approximation used in the Glauber model.

In this workshop, we reviewed recent studies of CDCC for analyses of various reactions involving unstable nuclei and application to nuclear engineering. This presentation is based on the review paper of CDCC [3].

2. Theoretical foundation of CDCC

We consider a reaction of a weakly bound projectile (a) and a target nucleus (A). The reaction is described by a model Hamiltonian

$$H = T_R + U_{aA} + h_a, \quad (1)$$

where T_R is a kinetic energy for the relative coordinate R between a and A , and h_a is a internal model Hamiltonian of a . If the projectile a consists of two particles, a_1 and a_2 , the potential U_{aA} is described by

$$U_{aA} = U_{a_1A}(R_{a_1}) + U_{a_2A}(R_{a_2}), \quad (2)$$

where R_{xA} is the coordinate between a particle x and A . In the case of a three-body projectile with a_1 , a_2 , and a_3 , U_{aA} becomes

$$U_{aA} = U_{a_1A}(R_{a_1}) + U_{a_2A}(R_{a_2}) + U_{a_3A}(R_{a_3}). \quad (3)$$

In CDCC, the total wave function of the reaction system is expanded in terms of bound and

discretized continuum states of the projectile

$$\Psi_{\text{CDCC}}^{(+)}(\xi, R) = \Phi_0(\xi)\chi_0^{(+)}(R) + \sum_{\nu} \Phi_{\nu}(\xi)\chi_{\nu}^{(+)}(R). \quad (4)$$

Here Φ_0 and Φ_{ν} represent bound and discretized continuum wave functions with the internal coordinate ξ of the projectile. To obtain the discretized continuum wave functions, the pseudo-state discretization method [9, 10, 11, 12] is applied in this paper. In the pseudo-state discretization, the internal Hamiltonian h_a is diagonalized with the L^2 -type basis functions, such as the Gaussian basis functions [13].

Inserting Eq. (4) into the Schrödinger equation of the scattering system, $(H - E)\Psi_{\text{CDCC}}^{(+)} = 0$, leads to a set of coupled differential equations of the relative wave functions between a and A , $\chi_0^{(+)}$ and $\chi_{\nu}^{(+)}$:

$$[T_R + V_{\nu\nu}(R) - E_{\nu}] \chi_{\nu}^{(+)}(R) = - \sum_{\nu' \neq \nu} V_{\nu\nu'}(R) \chi_{\nu'}^{(+)}(R), \quad (5)$$

where the coupling potentials $V_{\nu'\nu}$ are defined by

$$V_{\nu'\nu}(R) = \langle \Phi_{\nu'} | U_{aA} | \Phi_{\nu} \rangle_{\xi}. \quad (6)$$

This coupled-channel equations are solved under the outgoing boundary condition. The details of CDCC are shown in Refs. [1, 2, 3].

3. Analysis of ${}^6\text{He}$ breakup reaction

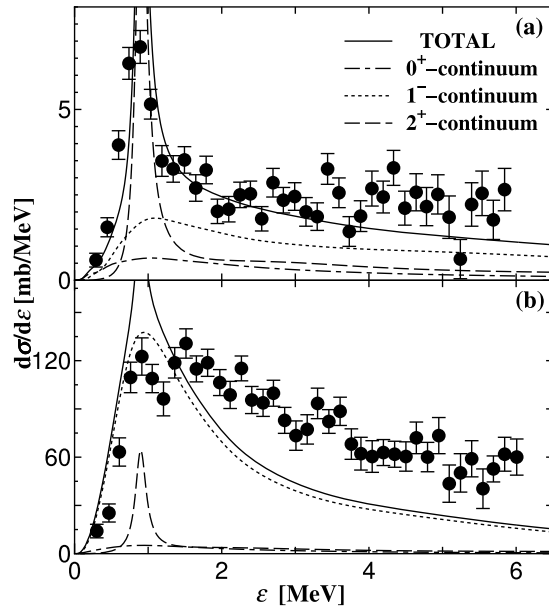


Fig. 1: Comparison of the breakup cross section calculated by CDCC (solid line) with experimental data for (a) ${}^6\text{He} + {}^{12}\text{C}$ scattering at 240 MeV/nucleon and (b) ${}^6\text{He} + {}^{208}\text{Pb}$ scattering at 240 MeV/nucleon. This figure is taken from Ref. [14]. The dot-dashed, dotted, and dashed lines correspond to contributions of 0^+ , 1^- , and 2^+ breakup, respectively. The experimental data are taken from Ref. [15].

In this section, we show results for CDCC analyses of ${}^6\text{He}$ breakup reactions [14]. ${}^6\text{He}$ is a typical example of two-neutron halo nuclei, and can be described by $n + n + {}^4\text{He}$ three-body model well. Therefore the scattering of ${}^6\text{He}$ is treated as a four-body reaction system including a target nucleus.

Figure 1 shows the calculated breakup cross sections as a function of the excitation energy of ${}^6\text{He}$. In the case of ${}^6\text{He} + {}^{12}\text{C}$ scattering at 240 MeV/nucleon shown in panel (a), we can see the clear peak around $\varepsilon = 1$ MeV corresponding to the 2^+ -resonance of ${}^6\text{He}$ because nuclear breakup processes are dominant. Meanwhile Coulomb breakup to 1^- continuum is dominant for ${}^6\text{He} + {}^{208}\text{Pb}$ scattering at 240 MeV/nucleon shown in panel (b). For ${}^{208}\text{Pb}$ target, the present analysis overestimates around $\varepsilon \sim 1$ MeV but underestimates in $\varepsilon \gtrsim 2$ MeV. These disagreements are also seen in the results of the previous works [16, 17]. A possible origin of the disagreements is that the inelastic breakup reactions are not included in the present calculation. As mentioned in the previous work [16], the inelastic breakup effect is not negligible.

4. Application of CDCC to nuclear engineering

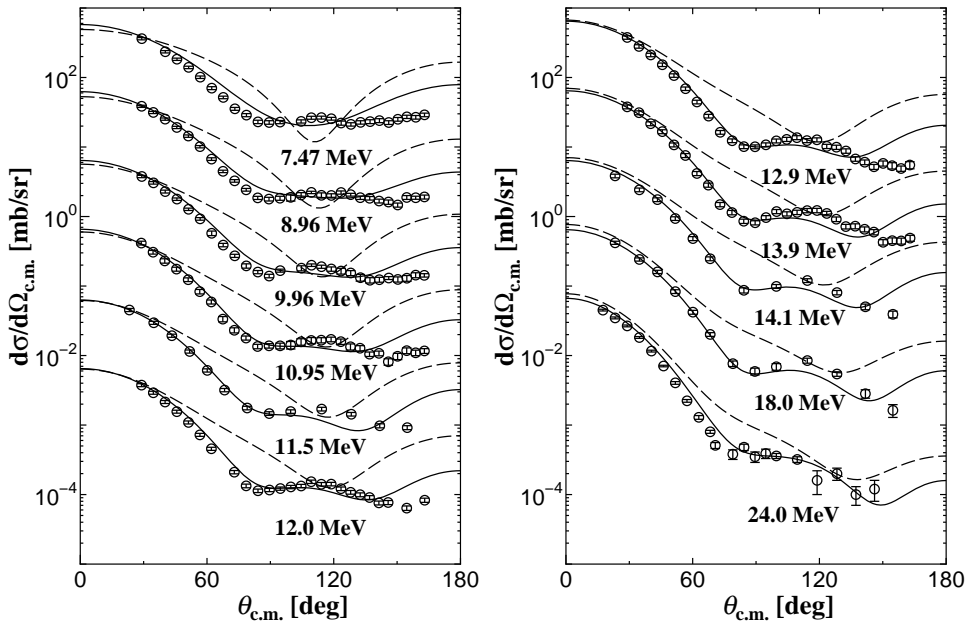


Fig. 2: Angular distribution of the elastic differential cross section of $n + {}^6\text{Li}$ scattering for incident energies between 7.47 and 24.0 MeV. This figure is taken from Ref. [18]. Experimental data are taken from Refs. [20, 21, 22].

Next we show results of an application of CDCC to evaluating of nuclear data. Since CDCC is a fully quantum-mechanical method, it is applicable to reactions at low incident energies, which are important for nuclear engineering. Recently, accurate nuclear data of nucleon induced reactions on ${}^6,7\text{Li}$ that is important material for DT fusion reactor are highly required. In Ref. [18], we analyzed $n + {}^6\text{Li}$ scattering by the three-body CDCC method, in which ${}^6\text{Li}$ is described as a $d + \alpha$ system. In this analysis, we calculate diagonal and coupling potentials between n and ${}^6\text{Li}$ by using the folding model with the JLM effective interaction [19] with the normalization factor of the imaginary part (λ_w) that is optimized to reproduce the elastic cross sections. Details of the calculation are shown in Ref. [18].

Figure 2 shows the differential elastic cross sections of $n + {}^6\text{Li}$ for incident energies between 7.47 and 24.0 MeV. One sees that the results calculated by CDCC (the solid lines) are in good agreement with

the experimental data. The dashed lines represent the results of a single-channel calculation without couplings to the breakup states of ${}^6\text{Li}$. For all incident energies, we take $\lambda_w = 0.1$ to reproduce the data. It should be noted that the single-channel calculation cannot reproduce the experimental data with any values of λ_w . Thus breakup effects are significant to reproduce the angular distributions of the elastic scattering.

5. Summary

CDCC is one of the most reliable methods for not only studying on unstable nuclei but also evaluation of nuclear data. Recently, we have proposed the four-body CDCC method to describe breakup reaction of a three-body projectile, in which the projectile breaks up into three constituents. For analyses of ${}^6\text{He}$ reactions, the four-body CDCC well reproduces the breakup cross sections. Thus the four-body CDCC is indispensable for investigating of properties of unstable nuclei.

CDCC with the JLM interaction is expected to be a powerful framework for the data evaluation of the ${}^6\text{Li}(n, n')$ reactions. Once the JLM parameter is determined by an analysis of elastic scattering, evaluation of the inelastic cross sections and neutron breakup spectra can be done with no free adjustable parameters. This is a very important feature of the present framework that enables a quantitative calculation of the cross sections for nuclear engineering studies.

Acknowledgements

The author is grateful to M. Yahiro, K. Ogata, and K. Minomo for helpful discussion. Furthermore I wish to thank to members of JCPRG in Hokkaido University and Y. Watanabe and H. Guo for the discussion of nuclear data evaluation.

References

- [1] M. Kamimura *et al.*, *Prog. Theor. Phys. Suppl.* **89** (1986), 1.
- [2] N. Austern *et al.*, *Phys. Rep.* **154** (1987), 125.
- [3] M. Yahiro, K. Ogata, T. Matsumoto and K. Minomo, *Prog. Theor. Exp. Phys.* **01A206** (2012).
- [4] T. Matsumoto *et al.*, *Phys. Rev. C* **70** (2004), 061601(R).
- [5] M. Rodríguez-Gallardo *et al.*, *Phys. Rev. C* **72** (2005), 024007.
- [6] T. Matsumoto *et al.*, *Phys. Rev. C* **73** (2006), 051602(R).
- [7] M. Rodríguez-Gallardo, *et al.*, *Phys. Rev. C* **80** (2009), 051601(R).
- [8] M. Yahiro, K. Ogata, and K. Minomo, *Prog. Theor. Phys.* **126** (2011), 167.
- [9] A. M. Moro *et al.*, *Phys. Rev. C* **65** (2001), 011602(R).
- [10] T. Matsumoto *et al.*, *Phys. Rev. C* **68** (2003), 064607.
- [11] T. Egami *et al.*, *Phys. Rev. C* **70** (2004), 047604.
- [12] A. M. Moro, F. Perez-Bernal, J. M. Arias, J. Gomez-Camacho, *Phys. Rev. C* **73** (2006), 044612.
- [13] E. Hiyama, Y. Kino and M. Kamimura, *Prog. Part. Nucl. Phys.* **51** (2003), 223.
- [14] T. Matsumoto, K. Katō, and M. Yahiro, *Phys. Rev. C* **82** (2010), 051602.
- [15] T. Aumann *et al.*, *Phys. Rev. C* **59** (1999), 1252.
- [16] S. N. Ershov *et al.*, *Phys. Rev. C* **62**, 041001(R) (2000).
- [17] D. Baye *et al.*, *Phys. Rev. C* **79**, 024607 (2009).
- [18] T. Matsumoto, D. Ichinkhorloo, Y. Hirabayashi, K. Katō, and S. Chiba, *Phys. Rev. C* **83** (2011), 064611.
- [19] J.-P. Jeukenne, A. Lejeune, and C. Mahaux, *Phys. Rev. C* **16**, 80 (1977); *ibid.* *Phys. Rep.* **25** (1976), 83.
- [20] S. Chiba *et al.*, *Phys. Rev. C* **58**, 2205 (1998).
- [21] H. Hogue *et al.*, *Nucl. Sci. Eng.* **69**, 22 (1979).
- [22] L. Hansen *et al.*, *Phys. Rev. C* **38**, 525 (1988).

Alpha-⁶He scattering and the quest for microscopic guidance for orthogonalizing pseudopotentials

*L. Canton*¹, *Yu. A. Lashko*², *K. Amos*³, *P.R. Fraser*⁴, *S. Karataglidis*⁵, *J.P. Svenne*⁶, *D. van der Knijff*³

¹ Istituto Nazionale di Fisica Nucleare, Sezione di Padova, Italy

² Bogoliubov Institute for Theoretical Physics, Nat. Acad. of Sci. of Ukraine

³ School of Physics, University of Melbourne, Victoria, Australia

⁴ Department of Physics, Astronomy and Medical Radiation Sciences, Curtin University, Western Australia, Australia

⁵ Department of Physics, University of Johannesburg, South Africa

⁶ Department of Physics and Astronomy, University of Manitoba, Canada

Abstract

The multi-channel algebraic scattering (MCAS) method, mainly used for nucleon-nucleus processes, has been upgraded to solve coupled sets of Lippmann-Schwinger equations for the $\alpha+^6\text{He}$ cluster system. A phenomenological Hamiltonian has been found that gives good agreement with the known bound states and the first few low-lying resonances for ^{10}Be . We have also calculated low-energy α - ^6He -scattering cross sections finding reasonable reproduction of low-energy differential cross sections. This MCAS model Hamiltonian contains some free parameters for the Orthogonalizing Pseudo Potential (OPP) that are difficult to guess and interpret. We have used an algebraic version of the resonating-group method to analyze microscopically the $\alpha+^6\text{He}$ system and to derive the eigenvalues of the anti-symmetrization kernel in the Schroedinger equation. The deviation from unity of the Pauli-allowed eigenvalues introduces an effective inter-cluster interaction, genuinely generated by the Pauli/exchange effects, which can be used to qualitatively interpret the structure of the corresponding OPP.

1. Introduction

In this paper we consider the ^{10}Be nucleus, which has recently become the object of numerous experimental and theoretical investigations [1, 2, 3, 4, 5]. The threshold of ^{10}Be decaying into α -particle and ^6He is located only 1.2 MeV above the second 0^+ state of ^{10}Be , and in the vicinity of this threshold we treat ^{10}Be as $^6\text{He}+^4\text{He}$ cluster system. As ^6He is known to have two excited states (resonances) at reasonably low energies in its spectrum, we treat the low-energy $\alpha+^6\text{He}$ problem as a coupled-channel one, within the multi-channel algebraic scattering (MCAS) formalism.

To date MCAS has been used to solve bound and scattering equations for nucleon-nucleus systems. We have developed a version of MCAS to deal with α -nucleus systems and we report results of calculation for the ^{10}Be spectrum, as well as low-energy cross sections that can be compared with the measured data sets [3] taken for a range of energies and scattering angles.

The Pauli exclusion principle affects the motion between clusters, and in MCAS it is simulated with orthogonalizing pseudopotentials (OPP), containing the operators of projection onto the forbidden states. The elimination of the Pauli-forbidden states with the OPP technique is achieved by infinite strength of the pseudopotential. As is evident from the microscopic approaches to cluster studies, the elimination of the Pauli-forbidden states does not exhaust all exchange effects. Whereas eigenvalues of the antisymmetrization operator in nucleon-nucleon systems can take only the value 0 or 1, eigenvalues of Pauli-allowed states in two-cluster systems tend to unity only in the limit of large inter-cluster

distance. Because of the exchange of nucleons belonging to different clusters, at small intra-cluster distance the eigenvalues of the antisymmetrization operator are not equal to unity. The eigenvalues, which are less than unity, correspond to the partly forbidden (or Pauli hindered) states and result in effective repulsion of clusters. But there are also eigenvalues which exceed unity, and these correspond to the superallowed states which generate an effective Pauli attraction between clusters [6].

In dealing with macroscopic-type MCAS calculations in nucleon-nucleus systems, we have found several situations where we had to consider, in addition to strictly forbidden states, also partly-forbidden states, with the strength of the pseudopotential to be taken as a finite parameter. Since the same situation occurs also in the present MCAS study of α -nucleus dynamics, we consider in the second part of this contribution a microscopic-type RGM cluster model to seek for microscopic guidance in the possible selection of these parametric pseudopotentials.

2. The model for the α -nucleus matrix of potentials

The α - ${}^6\text{He}$ matrix of potentials has been defined using a collective model for the interaction. In that, the α particle is assumed to be structureless and the states of ${}^6\text{He}$ used are assumed to be members of a rotational band. The intercluster potential is phenomenologically structured with a central term (V_0), an orbit-orbit term ($V_{\ell\ell}$), and an orbit-nuclear spin ($V_{\ell I}$) component.

First, we define the channel basis according to the coupling

$$|c\rangle = |\ell I J^\pi\rangle = \left[|\ell\rangle \otimes |\psi_I\rangle \right]_J^{M,\pi}, \quad (1)$$

where ℓ is the orbital angular momentum of relative motion of a spin-0 projectile on the target whose states are $|\psi_I^{(N)}\rangle$. With each J^π hereafter understood, the (α -nucleus) potential has the following structure

$$V_{cc'}(r) = \langle \ell I | W(r) | \ell' I' \rangle = \left[V_0 \delta_{c'c} f(r) + V_{\ell\ell} f(r) [\ell \cdot \ell] + V_{II} f(r) [\mathbf{I} \cdot \mathbf{I}] + V_{\ell I} g(r) [\ell \cdot \mathbf{I}] \right]_{cc'} \quad (2)$$

in which local form factors have been assumed. We take Woods-Saxon functions and derivatives

$$f(r) = \left[1 + e^{\left(\frac{r-R}{a}\right)} \right]^{-1} ; \quad g(r) = \frac{1}{r} \frac{df(r)}{dr}. \quad (3)$$

Nuclear deformation is introduced via the operator ε measuring the deviation from sphericity

$$\varepsilon = \sum_L \sqrt{\frac{4\pi}{(2L+1)}} \beta_L [\mathbf{Y}_L(\Omega) \cdot \mathbf{Y}_L(\zeta)]; \quad (4)$$

β_L are deformation parameters and ζ are the Euler angles for the transformation from the body fixed frame and $\Omega = (\theta\phi)$ are the angles defining the surface in the space fixed frame. Expanding the nuclear shape to order ε^2 gives

$$f(r) \rightarrow f_0(r) - R_0 \frac{df_0(r)}{dr} \varepsilon + \frac{1}{2} R_0^2 \frac{d^2 f_0(r)}{dr^2} \varepsilon^2, \quad (5)$$

and similarly for $g(r)$.

In the MCAS method the effects of the Pauli principle are taken into account introducing pseudopotentials, or OPPs [7, 8], which have to be embedded in a coupled-channel context. The matrix of

pseudopotentials (in coordinate space) that adds on the regular interactions has the form

$$\mathcal{V}_{cc'} = \lambda_c A_c(r) A_{c'}(r') \delta_{cc'}. \quad (6)$$

The $A_c(r)$ are bound state wave functions (of the α in this application) associated with the diagonal nuclear interactions $V_{cc}(r)$ for the relevant orbital angular momentum in each channel c . The strengths λ_c are used for Pauli blocking which, for a specific orbit in a particular channel c , is obtained with a very large λ_c value. It should be infinite but 10^6 MeV suffices. Pauli allowed states have $\lambda_c = 0$.

In previous MCAS applications, we have already used the OPP formalism in a situation with partially forbidden orbits, a condition we termed as Pauli hindrance [9, 10] and that leads to λ_c values of few MeVs.

There is an additional interaction we considered in the Hamiltonian to account for pair correlation effects in the ground state of ¹⁰Be. In the simplest form we take this additional monopole-type interaction to be

$$H = V_{mono} \delta_{c'c} \delta_{I0^+_{g.s.}} f(r).$$

This "pairing" interaction of monopole type leads to additional binding in nuclear (ground) states of even mass nuclei, and leads to a large energy gap between the ground 0^+ and the first excited state (usually a 2^+). In MCAS we allow for the effects of pairing making the ground state of even-even nuclei more bound by including an extra strength in the central interaction between the α and ⁶He in its ground (0^+) state; a monopole interaction. Alternatively, with a rationale given later, the required extra binding of the ground state of ¹⁰Be can be achieved by including an extra term in the orthogonalising pseudo-potential, which enhances the $2s$ -relative motion orbit. Thus we use here for the first time the OPP to get a Pauli enhancement (attraction) instead of a more common repulsion.

3. Results for the coupled α +⁶He system

We have used the coupled-channel Hamiltonian described above to find as good a representation of the spectrum of ¹⁰Be as possible, up to the n +⁹Be threshold of 6.812 MeV and just beyond.

In Fig. 1 the low-excitation spectrum of ¹⁰Be is displayed. The positive and negative parity states are shown separately to aid visualisation. Known states are compared with the results from our MCAS calculations; calculations made under the constraint that the sub-threshold (bound) states in the known spectrum be best reproduced. The lines labelled 'A' and 'B' indicate the n +⁹Be and the α +⁶He thresholds respectively. The latter lies at 7.413 MeV above the ground state. Below those there are six known states, of which four have positive, and two negative, parity. Two more states (one of each parity) lie at excitations close to these thresholds. Thus all low-excitation resonances in ¹⁰Be, save for the 7.31 3_1^- , may decay by particle emission of a neutron and/or an α .

Three states were considered in the spectrum of ⁶He in the MCAS evaluations. They are the ground (0^+) that β decays and the two excited 2^+ resonance states that decay by two neutron break-up. The properties are shown in Tab. 1.

The coupled-channel matrix of potentials defining the Hamiltonian was specified by a collective rotational model with the parameter set listed in Table 2.

Using MCAS for the α +⁶He cluster gave the spectrum for ¹⁰Be identified with the label 'MCAS' in Fig. 1. Of note is that, save for the uncertain assigned spin-parity of (4^-) every known state has a matching partner in the calculated spectrum with excitation energies in quite good agreement.

Next we consider results for elastic scattering α -⁶He cross section. In Fig. 2, angular distribution data [3] taken at six energies are compared with MCAS results. We have used data uncertainties as listed in the tabulations of the experimental results [11]. The energies at which each of the data sets

Table 1: The states of ${}^6\text{He}$ used in the coupled-channel evaluations. With all states the α -cluster $1s$ -orbit was presumed blocked using $\lambda_{1s} = 10^6$ MeV in the OPP. The two columns in the right contain the OPP λ values (in MeV) used for the specified $1p$ and $2s$ orbitals. Of note is a $1p$ -wave hindrance and a suggestion for a $2s$ -wave enhancement.

state	Centroid	Width	λ_{1p}	λ_{2s}
$0_{\text{g.s.}}^+$	0.000	0.00	10.2	(-1.0)
2_1^+	1.797	0.113	10.0	0
2_2^+	5.60	10.0	8.0	0

Table 2: The potential parameters used for the interactions in the $\alpha+{}^6\text{He}$ system. All strengths are in MeV and lengths are in fermi. For simplicity the charge distribution has a fermi shape with the same geometric parameters shown in the table.

Pot. strengths	Neg.	Pos.	Geometry
V_0	-41.4	-41.4	$R_0 = 2.58$
V_{II}	1.5	1.0	$a_0 = 0.7$
V_{II}	-0.3	-1.5	$\beta_2 = 0.7$
V_{II}	1.7	1.6	
V_{mono}		-4.5	

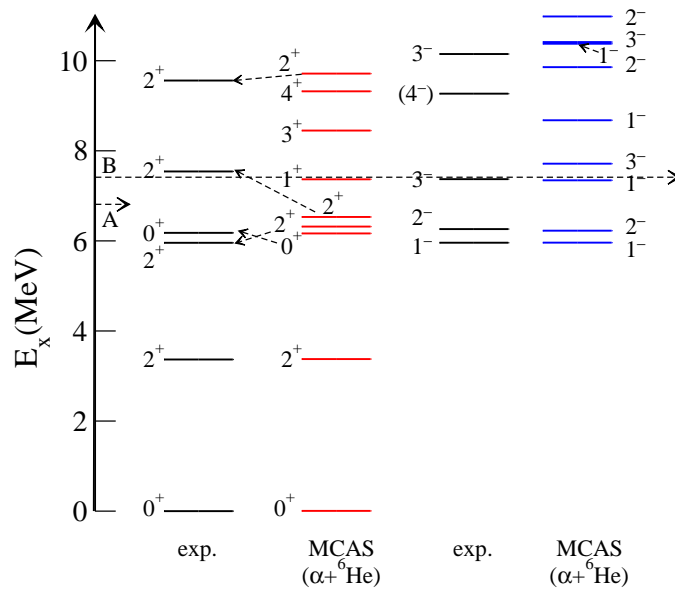


Fig. 1: The spectrum of low-excitation states in ${}^{10}\text{Be}$. To aid distinction the positive and negative parity states are shown on the left and right separately. The lines labelled ‘A’ and ‘B’ indicate the $n+{}^9\text{Be}$ and the $\alpha+{}^6\text{He}$ thresholds respectively.

have been taken and at which each of the MCAS evaluations were made are indicated in the figure. With the exception of the 2.7 MeV result, the calculated cross sections are in reasonable agreement with the data, having appropriate magnitudes and tracking the shape evolution quite well. The 2.7 MeV data are distinctly different to the other energy data sets (and of the MCAS expectation) and clearly the known 2_4^+ resonance in ${}^{10}\text{Be}$ (2.12 MeV) has a marked effect. MCAS finds such a resonance near to the observed energy but that partner is very broad. The 2.7 MeV cross section result is then simply like the others, a prediction of the background scattering. The results found using the monopole interaction give better forward angle comparisons with data while those from $2s$ -orbit enhancement are better at large scattering angles. The minima in the data are better described by the monopole evaluations.

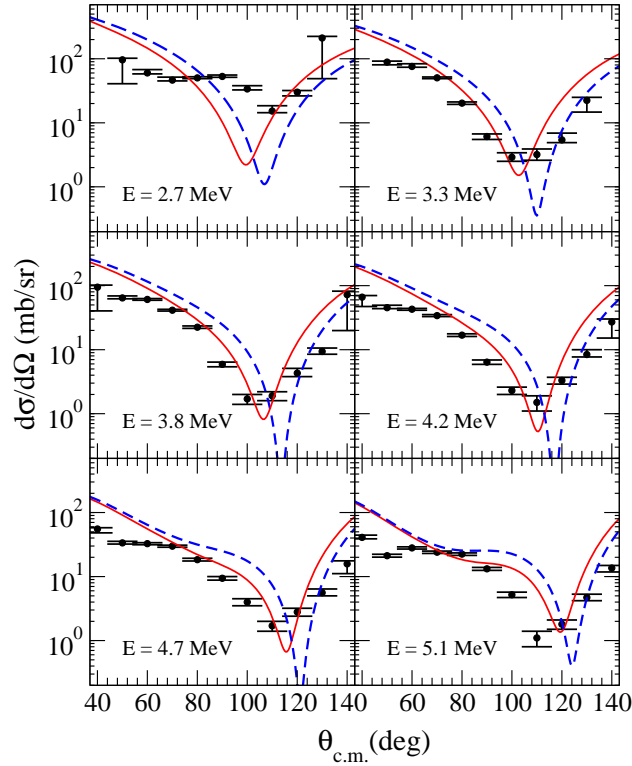


Fig. 2: Angular distributions at various fixed energies as listed compared with data [3]. The solid curves are the results when a monopole interaction is used, the dashed ones when 2*s*-orbit enhancement is applied.

4. Study of α -⁶He from a microscopic cluster model

Within a microscopic two-cluster model, the Schrödinger equation in the discrete representation is reduced to a set of linear equations for expansion coefficients of wave functions of discrete states with the energy $E_\kappa = -\kappa^2/2 < 0$, and of continuum states with the energy $E > 0$:

$$\Psi_{\kappa(E)}(\mathbf{r}) = \sum_n C_n^{\kappa(E)} \Psi_n(\mathbf{r}),$$

$$\sum_{\tilde{n}} \frac{\langle n | \hat{H} | \tilde{n} \rangle}{\sqrt{\Lambda_n \Lambda_{\tilde{n}}}} C_{\tilde{n}} - EC_n = 0.$$

To understand the results of the action of the antisymmetrization operator, first, let us discuss a set of the algebraic equations where only the operator of the kinetic energy of the relative motion of clusters (in the c.m. frame) is retained:

$$\sum_{\tilde{n}} \frac{\langle n | \hat{T} | \tilde{n} \rangle}{\sqrt{\Lambda_n \Lambda_{\tilde{n}}}} C_{\tilde{n}} - EC_n = 0.$$

In this simplest case, the collision of two (0*s*)-shell clusters in the state with angular momentum

ℓ , the equation for \hat{T} can be written in the form of the finite-difference equations

$$\begin{aligned}
& -\frac{1}{8} \left\{ \left(1 + \frac{\Lambda_{n-2}}{\Lambda_n} \right) \left(n + \frac{3}{2} - \frac{(2l+1)^2}{8n} \right) + 1 - \frac{\Lambda_{n-2}}{\Lambda_n} \right\} (C_{n+2} - 2C_n + C_{n-2}) + \\
& -\frac{1}{8} \left\{ 1 + \frac{\Lambda_{n-2}}{\Lambda_n} + \left(1 - \frac{\Lambda_{n-2}}{\Lambda_n} \right) \left(n + \frac{3}{2} - \frac{(2l+1)^2}{8n} \right) \right\} (C_{n+2} - C_{n-2}) + \\
& + \left\{ \left(1 + \frac{\Lambda_{n-2}}{\Lambda_n} \right) \frac{(2l+1)^2}{32n} + \frac{1}{4} \left(1 - \frac{\Lambda_{n-2}}{\Lambda_n} \right) \left(n + \frac{1}{2} \right) \right\} C_n = \frac{mr_0^2}{\hbar^2} EC_n. \quad (7)
\end{aligned}$$

The term evidenced by the boxed rectangle in the last equation represents the m.e. of an effective cluster-cluster interaction operator generated by the Pauli exclusion in the kinetic energy operator. Of note is that the character of this effective interaction is attractive if $\Lambda_n - \Lambda_{n-2} < 0$ and repulsive in the opposite case. More specifically, the absolute value of its intensity decreases if the difference $\Lambda_{n-2} - \Lambda_n$ tends to zero. If the latter remains negative as n increases (the eigenvalues monotonically tend to unity from above), then the effective antisymmetrization/Pauli potential is attractive. If, by increasing n , the difference of the eigenvalues remains positive (the eigenvalues monotonically tend to unity from below), then the effective antisymmetrization/Pauli potential is repulsive. In addition, the radius of this interaction can be related to the rapidity with which these eigenvalues tend to unity with increasing n . For a more detailed discussion over the properties of such effective potentials see Refs.[12, 13].

In Ref.[13] the eigenvalues for the norm kernel of the ${}^6\text{He} + \alpha$ system were considered. According to a calculation scheme discussed also in Ref.[14], to evaluate these eigenvalues the intrinsic wave functions of both clusters are described by the lowest functions of a translation-invariant shell model: the α -cluster has closed shell and can be only in its 0^+ ground state, while the ${}^6\text{He}$ has two neutrons in the p -shell and can be either in the 0^+ ground state or in 2^+ excited state, namely the narrow resonance state located at $E = 1.8$ MeV above the threshold for ${}^6\text{He}$ breakup into $\alpha + n + n$.

The eigenvalues of the norm kernel are reported in Table 3. The states with zero values are the strictly forbidden states, the states with value 1 denote the allowed states. It can be observed that two SU(3)-branches of positive parity and one SU(3)-branch of negative parity are characterized by the eigenvalues which exceed unity. Hence, the states belonging to $(2k+2,0)$, $(2k-2,2)$ and $(2k+1,1)$ SU(3) branches can be assigned to the superallowed states, while states $(2k,1)$, $(2k+3,0)$ and $(2k-1,2)$ have values significantly less than 1 and correspond to partly forbidden states. As follows from the effective interaction term (the boxed expression in Eq.7) we should expect an effective attraction of ${}^6\text{He}$ and α -particle in the former case and effective repulsion in the latter case.

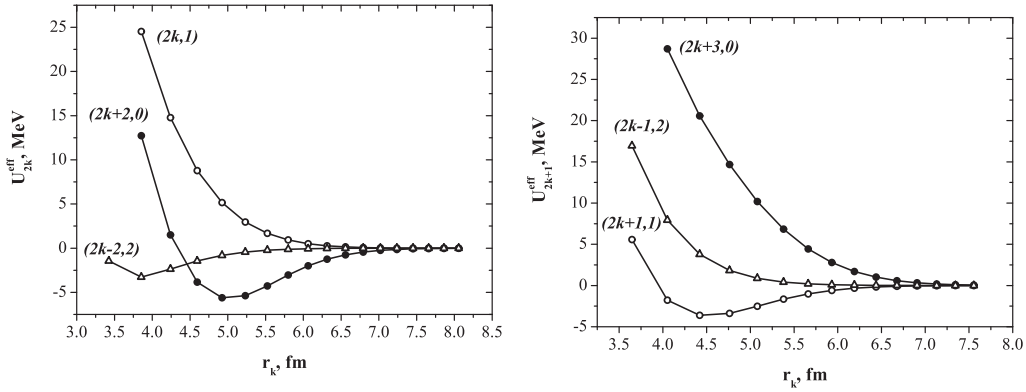
In the ${}^6\text{He} + \alpha$ system, derivation of the effective Pauli interaction is not so easy because the dynamics of the α -cluster is influenced by the presence of neutrons in the p -shell of ${}^6\text{He}$. Due to this fact, the problem becomes multi-channel and different SU(3)-branches are coupled by the kinetic-energy operator. Nevertheless, we have made an estimate of the effective Pauli potential, by analyzing its diagonal part (with respect to SU(3)-indices), with details discussed in Ref.[13]. In the same reference we have substantiated the study of this Pauli potential by considering also the impact of these interaction effects in the scattering phase shifts.

On Figure 3 the dependence of Pauli potential (generated by the boxed term in Eq.7) on the distance r_n between the centers of mass of the ${}^6\text{He}$ and α clusters is shown both for the states of positive and negative parity.

As evident from the left panel of Fig.3, the branch $(2k,1)$ is repulsive, the branch $(2k-2,2)$ is attractive, while the branch $(2k+2,0)$ has the mixture of repulsion and attraction. The right panel of Fig.3 suggests that for negative parity states two branches $(2k+3,0)$ and $(2k-1,2)$ are repulsive, while

Table 3: Eigenvalues $\Lambda_{(\lambda,\mu)}$ of the norm kernel of ${}^6\text{He}+\alpha$

k	States with $n = 2k$			States with $n = 2k + 1$		
	$(n + 2, 0)$	$(n, 1)$	$(n - 2, 2)$	$(n + 2, 0)$	$(n, 1)$	$(n - 2, 2)$
0	0	0	0	0	0	0
1	0	0	0	0	0	0
2	0	0	1.2056	0	1.0549	0.4521
3	0.9419	0.2721	1.1587	0.1831	1.2192	0.7650
4	1.2922	0.5698	1.0834	0.4045	1.1795	0.9011
5	1.3264	0.7645	1.0408	0.5983	1.1160	0.9581
6	1.2566	0.8760	1.0194	0.7448	1.0676	0.9821
7	1.1743	0.9363	1.0090	0.8454	1.0371	0.9923
8	1.1090	0.9678	1.0046	0.9097	1.0196	0.9967
9	1.0645	0.9840	1.0019	0.9489	1.0101	0.9985
10	1.0367	0.9921	1.0009	0.9718	1.0051	0.9994


Fig. 3: Effective ${}^6\text{He}+\alpha$ interaction generated by the kinetic energy exchange terms. Indices of SU(3) symmetry are indicated on the curves.

some attraction is present only in $(2k + 1, 1)$ branch.

All the Pauli-allowed states, except $(2k, 1)$ state, are the superpositions of the angular-momentum coupled basis functions. Hence, we can make definite conclusions only about repulsion in d -wave of relative motion of α -particle scattered on ${}^6\text{He}$ in the first 2^+ state. In other cases we should take into account also weights of different partial momenta in the SU(3)-basis functions.

5. Final Remarks

The MCAS method has been used to solve coupled sets of Lippmann-Schwinger equations for the $\alpha+{}^6\text{He}$ two-cluster system, finding a model spectrum for ${}^{10}\text{Be}$ in reasonable agreement with the known one to more than 10 MeV excitation. A good reproduction of elastic differential cross section at low energy was also achieved. However, one must note that these calculations are still preliminary and better consideration of the charge distribution of the two clusters is required, in order to seek for improvements. Work is already in progress in this direction [15].

We use the orthogonalizing pseudopotentials to offset the deep forbidden states. We have also

considered, in the OPP, partially forbidden states in $1p$ -waves. In addition to this, we have also added a phenomenological monopole-type interaction acting only on the 0^+ ground state to account for additional attraction possibly due to pairing effects. Alternative to this monopole-type interaction, we have speculated about a possible attractive interaction generated by antisymmetrization/Pauli effects. This attraction effect has been accommodated in the OPP formalism by using a negative strength that leads to an increase of attraction in the $2s$ orbit. These two alternative treatments lead to very similar ^{10}Be spectra, but differences show up in the cross sections, with the data somewhat favouring the phenomenological monopole term.

In the second part of this contribution, we have considered an algebraic version of a RGM description of the $\alpha+^6\text{He}$ two-cluster system. Following Ref.[13], we have constructed an effective inter-cluster interaction generated by antisymmetrization/Pauli effects due to the nucleon exchanges between the two clusters. It is found that this effective interaction has indeed components of attraction and repulsion in the various branches of the $\text{SU}(3)$ representation, with the attraction mainly concentrated on the positive parity states and the repulsion on the negative parity ones. However, since the $\text{SU}(3)$ representation correspond to a complicated superimposition of various angular momentum components it is difficult to pin down precisely the repulsion/attraction in each orbital state. In the present stage, comparison with this microscopic RGM approach suggests a possible use of OPP with finite strengths, with possibly positive values in the negative parity states, to account for finite repulsion effects for odd-type orbitals in connection to partially forbidden (or Pauli hindered) states. The same study suggests a possible use of OPP strengths with negative values for selected even orbital states, to account for effective antisymmetrization attraction effects in connection to superallowed (or Pauli enhanced) states. While this bridge between microscopic RGM-type approach and the more macroscopic and collective-type MCAS model is quite promising from the qualitative point of view, at the quantitative level it was not possible to find (yet) a sensible relation between the strengths of the MCAS pseudopotentials and the behavior of the eigenvalues of the norm kernels of the underlying microscopic theory.

6. Acknowledgments

YL acknowledges the hospitality of the Padova Section of INFN. SK acknowledges support from the National Research Foundation of South Africa. JPS acknowledges support from the Natural Sciences and Engineering Research Council of Canada (NSERC). PRF and LC acknowledge funds from the Dipartimento di Fisica e Astronomia dell'Università di Padova where a part of this work has been initiated.

References

- [1] M. Freer *et al.*, Phys. Rev. Lett. **96**, 042501 (2006).
- [2] M. Ito, K. Kato, and K. Ikeda, Phys. Lett. B **588**, 43 (2004).
- [3] D. Suzuki *et al.*, Phys. Rev. C **87**, 054301 (2013).
- [4] K. Arai, Phys. Rev. C **69**, 014309 (2004).
- [5] P. Descouvemont, Nucl. Phys. A **699**, 463 (2002).
- [6] G. Filippov, Yu. Lashko, Phys. Rev. C **70**, 064001 (2004).
- [7] L. Canton *et al.*, Phys. Rev. Lett **94**, 122503 (2005).
- [8] K. Amos *et al.*, Nucl. Phys. A **728**, 65 (2003).
- [9] L. Canton *et al.*, Phys. Rev. Lett **96**, 072502 (2006).
- [10] K. Amos *et al.*, Nucl. Phys. A **912**, 7 (2013).
- [11] www.nndc.bnl.gov/exfor.
- [12] G. F. Filippov and Yu. A. Lashko, Phys. Part. Nucl. **36**, 714 (2005).
- [13] Y. A. Lashko, G. F. Filippov and L. Canton, Ukr. J. Phys. **60**, 406 (2015).
- [14] G. F. Filippov, Yu. A. Lashko, S. V. Korennov, and K. Katō, Few-Body Syst. **33**, 173 (2003).
- [15] K. Amos *et al.*, Work in preparation, (2015).

Microscopic approach to NA and AA scattering in the framework of chiral effective field theory and Brueckner-Hartree-Fock theory

M. Toyokawa, M. Yahiro, T. Matsumoto, ^AK. Minomo, ^AK. Ogata, and ^AM. Kohno

Department of Physics, Kyushu University, Fukuoka, Japan

^AResearch Center for Nuclear Physics, Osaka University, Ibaraki, Japan

Abstract

We describe nucleon-nucleus (NA) and nucleus-nucleus (AA) elastic scattering based on the chiral two-nucleon forces (2NFs) and chiral three-nucleon forces (3NFs), using the standard microscopic framework composed of the Brueckner-Hartree-Fock method (BHF) and the g -matrix folding model. The g -matrix for symmetric nuclear matter is calculated from chiral 2NFs of $N^3\text{LO}$ and chiral 3NF of $N^2\text{LO}$ by using the BHF method. For elastic scattering, the optical potentials are calculated by folding chiral g -matrix with projectile and target density. This microscopic framework reproduces the experimental data with no adjustable parameter. Chiral-3NF effects are small for NA scattering, but sizable for AA scattering. Chiral 3NF, mainly originated from the 2π -exchange diagram, makes the folding potentials less attractive and more absorptive.

1. Introduction

One of the important issue in nuclear physics is to clarify the effects of three-nucleon force (3NF) on finite nuclei, nuclear matter, and nuclear reactions. Recently, a theoretical breakthrough on this issue was made with chiral effective field theory (Ch-EFT); see Refs. [1, 2] and references therein. Ch-EFT is a theory based on chiral perturbation theory and enables to determine two-nucleon force (2NF), 3NF, and many-nucleon forces systematically. The effects of chiral 3NF were analyzed in many papers, see Refs. [3, 4, 5] for some examples.

Another important issue in nuclear physics is microscopic understanding of the nucleon-nucleus (NA) and nucleus-nucleus (AA) scattering. Elastic scattering is the simplest process of the nuclear reaction, and it can be described with the optical potentials between two nuclei. Moreover the optical potentials are essential in describing not only elastic scattering but also inelastic scattering and transfer and breakup reactions.

The g -matrix folding model is the standard method for obtaining the optical potential microscopically. In this model, the potential is obtained by folding the g -matrix effective interaction with target density for NA scattering and with projectile and target densities for AA scattering. The g -matrix effective interaction is usually evaluated by Brückner-Hartree-Fock (BHF) method for positive energy with realistic 2NF and is obtained as density- and energy-dependent complex interaction [6, 7, 8].

In present work, we calculate the g matrix based on chiral 2NF and 3NF by the BHF method for positive energy, and apply the g matrix for NA and AA elastic scattering by using g -matrix folding model. The folding model with chiral g matrix well reproduce the experimental data for NA and AA scattering with no adjustable parameter. Therefore we can investigate chiral-3NF effects quantitatively on NA and AA elastic scattering with present framework. This work is summarized in Ref. [9].

2. Theoretical framework

2.1 g matrix calculation for 3NF

The g matrix for symmetric nuclear matter is evaluated from BHF method. The 3NF v_{123} is hard to treat in nuclear matter. We then derive an effective 2NF $v_{12(3)}$ from v_{123} by using mean field approximation [5], that is, v_{123} is averaged over the third nucleon in the Fermi sea:

$$\langle \mathbf{k}'_1, \mathbf{k}'_2 | v_{12(3)} | \mathbf{k}_1, \mathbf{k}_2 \rangle_A = \sum_{\mathbf{k}_3} \langle \mathbf{k}'_1, \mathbf{k}'_2, \mathbf{k}_3 | v_{12(3)} | \mathbf{k}_1, \mathbf{k}_2, \mathbf{k}_3 \rangle_A, \quad (1)$$

where the subscript A represents the antisymmetrization and the symbol \mathbf{k}_i stands for quantum numbers, momentum and z component of spin and isospin, of the i -th nucleon. By using this approximation, the potential energy is evaluated as

$$\begin{aligned} & \frac{1}{2} \sum_{\mathbf{k}_1, \mathbf{k}_2} \langle \mathbf{k}_1, \mathbf{k}_2 | v_{12} | \mathbf{k}_1, \mathbf{k}_2 \rangle_A + \frac{1}{3!} \sum_{\mathbf{k}_1, \mathbf{k}_2, \mathbf{k}_3} \langle \mathbf{k}_1, \mathbf{k}_2, \mathbf{k}_3 | v_{123} | \mathbf{k}_1, \mathbf{k}_2, \mathbf{k}_3 \rangle_A \\ &= \frac{1}{2} \sum_{\mathbf{k}_1, \mathbf{k}_2} \langle \mathbf{k}_1, \mathbf{k}_2 | v_{12} + \frac{1}{3} v_{12(3)} | \mathbf{k}_1, \mathbf{k}_2 \rangle_A. \end{aligned} \quad (2)$$

This means that the g matrix g_{12} should be calculated by

$$g_{12} = v_{12} + \frac{1}{3} v_{12(3)} + (v_{12} + \frac{1}{3} v_{12(3)}) G_0 g_{12} \quad (3)$$

with the nucleon propagator G_0 including the Q represents the Pauli exclusion operator. Here the single-particle energy $e_{\mathbf{k}}$ for a nucleon with momentum \mathbf{k} in the denominator of G_0 is obtained by

$$e_{\mathbf{k}} = \langle \mathbf{k} | T | \mathbf{k} \rangle + \text{Re}[\mathcal{U}(\mathbf{k})], \quad (4)$$

with the single-particle potential,

$$\mathcal{U}(\mathbf{k}) = \sum_{\mathbf{k}'}^{k_F} \langle \mathbf{k}, \mathbf{k}' | g_{12} + \frac{1}{6} v_{12(3)} (1 + G_0 g_{12}) | \mathbf{k}, \mathbf{k}' \rangle_A, \quad (5)$$

where T is a kinetic-energy operator. See the ref [5] for detail of BHF calculation. In the present BHF calculation, the cutoff energy $\Lambda = 550$ MeV is used both for N³LO 2NF and N²LO 3NF. The low-energy constants of chiral nuclear forces are taken from Ref. [10] as $(c_1, c_3, c_4) = (-0.81, -3.4, 3.4)$ in units of GeV^{-1} , and the other constants $(c_D, c_E) = (-4.381, -1.126)$ are from Ref. [11].

Because the original chiral g matrix obtained from BHF calculation is numerical and nonlocal, it is inconvenient for many applications such as g -matrix folding model. The original chiral g matrix is localized by following the Melbourne group procedure [12, 13]. The localized g matrix is equivalent with the on-shell and near-on-shell matrix elements of the original g matrix. In the present work, we adopt three-range Gaussian form as the local g matrix for each of central, spin-orbit, and tensor components and for each spin-isospin channel

$$g^{ST}(s, \rho, E) = \sum_{i=1}^3 g_0^{ST}(\rho, E) e^{s^2/\lambda_i^2}, \quad (6)$$

where λ_i is the range parameter and $g_0^{ST}(\rho, E)$ is the complex strength parameter. Here ρ is the density of the nuclear matter and E is the incident energy of the nucleon. The range parameters and strength

parameters are determined so as to reproduce the on-shell and near-on-shell matrix elements of the original chiral g matrix. We obtain the range parameters as (0.4, 0.9, 2.5) for central component and (0.5, 0.9, 1.8) for spin-orbit and tensor components to minimize the χ^2 -values of the matrix elements.

2.2 folding model

The NA and AA elastic scattering can be described by the one-body Schrödinger equation,

$$[T_{\mathbf{R}} + U - E]\chi = 0, \quad (7)$$

with the optical potential $U(\mathbf{R})$, where E is the incident energy of the projectile and $T_{\mathbf{R}}$ is the kinetic-energy operator concerning the relative coordinate \mathbf{R} between the projectile and the target. The optical potential U is composed of the central (CE) and spin-orbit (LS), and the Coulomb (Coul) component,

$$U = U_{\text{CE}} + U_{\text{LS}}\mathbf{L} \cdot \boldsymbol{\sigma} + V_{\text{Coul}} \quad (8)$$

The central and spin-orbit components of optical potential are calculated by single folding model for NA scattering and double folding model for AA scattering. The folding potentials contain the direct and knock-on exchange term U^{DR} and U^{EX} . The knock-on exchange term is nonlocal, but the term can be localized with high accuracy by the Brieva-Rook approximation [6]. The validity of this approximation is shown in Refs. [14, 15]. The central component of the localized folding potential for NA scattering is written as

$$U_{\text{CE}}^{\text{DR}}(\mathbf{R}) = \sum_{\mu'} \int d\mathbf{r}_{\text{T}} \rho_{\text{T}}^{\mu'}(r_{\text{T}}) g_{\mu\mu'}^{\text{DR}}(s, \rho), \quad (9)$$

$$U_{\text{CE}}^{\text{EX}}(\mathbf{R}) = \sum_{\mu'} \int d\mathbf{r}_{\text{T}} \rho_{\text{T}}^{\mu'}(|\mathbf{r}_{\text{T}} - \mathbf{s}/2|) \frac{3j_1(k_{\text{FS}})}{k_{\text{FS}}} g_{\mu\mu'}^{\text{EX}}(s, \rho) j_0(K(\mathbf{R})s), \quad (10)$$

where μ is the z component of the isospin, \mathbf{r}_{T} stands for the coordinate of the interacting nucleon from the center of mass of target, $\mathbf{s} = \mathbf{R} - \mathbf{r}_{\text{T}}$. $\rho_{\text{T}}^{\mu'}$ is the proton and neutron density of the target nucleus. $g_{\mu\mu'}^{\text{DR}(\text{EX})}$ is the direct (knock-on exchange) component of the effective interaction between two nucleons which is described by the combination of g^{ST} . Here, $K(\mathbf{R})$ is the local momentum defined as $\hbar K(\mathbf{R}) \equiv \sqrt{2\mu(E - U_{\text{CE}} - V_{\text{Coul}})}$, and $K(\mathbf{R})$ is obtained self-consistently. For spin-orbit component of the folding potential and detail of the single folding model, see Ref. [16].

For AA scattering, the central component of the localized folding potential is written as

$$U_{\text{CE}}^{\text{DR}}(\mathbf{R}) = \sum_{\mu\mu'} \int d\mathbf{r}_{\text{P}} d\mathbf{r}_{\text{T}} \rho_{\text{P}}^{\mu}(r_{\text{P}}) \rho_{\text{T}}^{\mu'}(r_{\text{T}}) g_{\mu\mu'}^{\text{DR}}(s', \rho), \quad (11)$$

$$U_{\text{CE}}^{\text{EX}}(\mathbf{R}) = \sum_{\mu\mu'} \int d\mathbf{r}_{\text{P}} d\mathbf{r}_{\text{T}} \rho_{\text{P}}^{\mu}(|\mathbf{r}_{\text{P}} - \mathbf{s}'/2|) \frac{3j_1(k_{\text{F}}^{\text{P}}s')}{k_{\text{F}}^{\text{P}}s'} \rho_{\text{T}}^{\mu'}(|\mathbf{r}_{\text{T}} + \mathbf{s}'/2|) \frac{3j_1(k_{\text{F}}^{\text{T}}s')}{k_{\text{F}}^{\text{T}}s'} \\ \times g_{\mu\mu'}^{\text{EX}}(s', \rho) j_0(K(\mathbf{R})s'/M), \quad (12)$$

where \mathbf{r}_{P} stands for the coordinate of the interacting nucleon from the center of mass of projectile, $\mathbf{s}' = \mathbf{r}_{\text{P}} - \mathbf{r}_{\text{T}} + \mathbf{R}$, and M is defined by the mass number of projectile and target nuclei A_{P} and A_{T} as $M = A_{\text{P}}A_{\text{T}}/(A_{\text{P}} + A_{\text{T}})$. See Refs. [17, 18] for the detail of the double folding model and the treatment of the local density ρ .

For the ^4He density, we use the phenomenological proton-density determined from electron scattering [19] in which the finite-size effect due to the proton charge is unfolded in the standard manner

[20]. The neutron density is assumed to have the same geometry as the proton one. For the target density, we take the matter densities calculated by the spherical Hartree-Fock method with the Gogny-D1S interaction [21] in which the spurious center-of-mass motion is removed in the standard manner [22].

3. Results

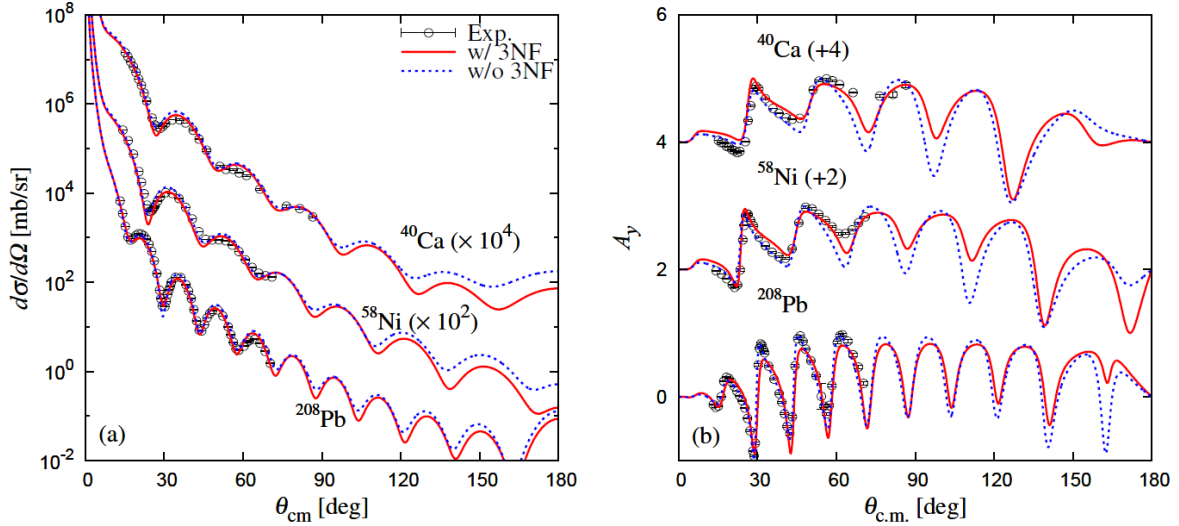


Fig. 1: The angular distribution of (a) differential cross sections and (b) vector analyzing powers for proton elastic scattering at $E = 65$ MeV. The solid and dashed lines represent to the results of chiral g matrix with and without 3NF effects, respectively. Each cross section is multiplied by the factor shown in the figure, while each vector analyzing power is shifted up by the number shown in the figure. Experimental data are taken from Ref. [23].

First, we consider proton elastic scattering at $E = 65$ MeV from ^{40}Ca , ^{58}Ni , and ^{208}Pb targets. Figure 1 shows the differential cross sections $d\sigma/d\Omega$ and vector analyzing power A_y as a function of scattering angle $\theta_{\text{c.m.}}$. The solid and dashed lines represent the results of chiral g matrix with and without 3NF effects. One can see that the chiral g matrix well reproduce the experimental data [23] without any adjustable parameters. Chiral-3NF effects are small for $d\sigma/d\Omega$ at forward and middle angles where the data are available, because the scattering is governed by the potentials in the surface region where 3NF effects are small. However chiral-3NF effects for A_y are seen at middle angles $\theta_{\text{c.m.}} \simeq 60^\circ$, because A_y is more sensitive for the difference of the potential than $d\sigma/d\Omega$.

Next, we show the results of ^4He elastic scattering at $E/A = 72$ MeV from ^{58}Ni and ^{208}Pb targets. Figure 2 show $d\sigma/d\Omega$ as a function of scattering angle $\theta_{\text{c.m.}}$. The solid and dashed lines represent the results of chiral g matrix with and without 3NF effects. For both targets, chiral g matrix reproduce the experimental data [24] and chiral-3NF effects are sizable at middle angles $\theta_{\text{c.m.}} > 20^\circ$. The reason why chiral-3NF effects are sizable for ^4He scattering can be explained by near-far decomposition [25]. When a detector is set on the right-hand side of the target, the outgoing wave going through the right-hand (left-hand) side of the target is called the near-side (far-side) scattering. The near-side (far-side) component is mainly induced by repulsive Coulomb (attractive nuclear) force, and in general the near-side (far-side) component dominates forward-angle (middle-angle) scattering. The oscillations of $d\sigma/d\Omega$, which are shown at $\theta_{\text{c.m.}} = 5\text{--}20^\circ$ in Fig.2, are appeared because of the interference between the near- and far-side component. When the scattering is dominated by the far-side component, $d\sigma/d\Omega$ has no oscillation and is sensitive to the change of nuclear force. For ^4He scattering, the middle angle $\theta_{\text{c.m.}} < 20^\circ$ is dominated by the far-side component and chiral 3NF effects appear in this region.

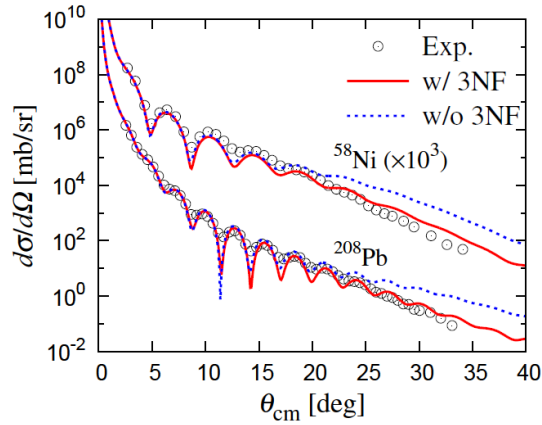


Fig. 2: The angular distribution of differential cross sections for ${}^4\text{He}$ elastic scattering at $E = 72$ MeV/nucleon from ${}^{58}\text{Ni}$ and ${}^{208}\text{Pb}$ targets. The solid and dashed lines represent the results of the chiral g matrix with and without 3NF effects, respectively. Each cross section is multiplied by the factor shown in the figure. Experimental data are taken from Ref. [24]

Figure 3 shows the central part $U_{\text{CE}}(R)$ of the folding potential for ${}^4\text{He}+{}^{208}\text{Pb}$ scattering at 72 MeV/nucleon. The solid and dashed lines represent the results of the chiral g matrix with and without 3NF effects. Chiral 3NF, mainly in its the 2π -exchange diagram, makes the potential less attractive and more absorptive. The repulsive effect mainly comes from the repulsion in the ${}^1\text{E}$ channel of g^{ST} because of the Pauli suppression of isobar Δ excitation in the nuclear-matter medium, and the absorptive effect mainly originated in the enhancement of the tensor correlations. The repulsive effect of chiral 3NF reduces $d\sigma/d\Omega$ at $\theta_{\text{c.m.}} > 20^\circ$ for ${}^4\text{He}$ scattering, whereas stronger absorption from chiral 3NF better separates the far-side amplitude from the near-side one.

4. Summary

We described nucleon-nucleus (NA) scattering at 65 MeV and nucleus-nucleus (AA) scattering at 72 MeV/nucleon based on chiral two-nucleon forces (2NFs) and three-nucleon forces (3NFs), using the standard BHF method and the g -matrix folding model. We calculated the g matrix for the symmetric nuclear matter from N^3LO 2NF and N^2LO 3NF for positive energy by BHF method. Chiral-3NF effects are mainly come from the 2π -exchange diagram. Chiral 3NF in the ${}^3\text{E}$ channel enhances the tensor correlations and makes the optical potential more absorptive. In the ${}^1\text{E}$ channel, chiral-3NF effect make the optical potential less attractive because of the Pauli suppression of isobar Δ excitation in the nuclear-matter medium in the conventional picture.

We provided the chiral g matrix with a three-range Gaussian form by following the Melbourne-group procedure [12, 13]. The localization of the g matrix was performed by making a χ^2 fitting to the on-shell and near-on-shell matrix elements of the original chiral g matrix. This localized Gaussian g matrix makes the folding procedure much easier. The g -matrix folding model with the chiral g matrix well reproduced the experimental data with no adjustable parameter for proton and ${}^4\text{He}$ scattering from various target. We found that chiral-3NF effects are small for proton scattering but sizable for ${}^4\text{He}$ scattering at the middle angle $\theta_{\text{c.m.}} > 20^\circ$. Chiral 3NF reduced the differential cross section at the middle angle because of its repulsive nature.

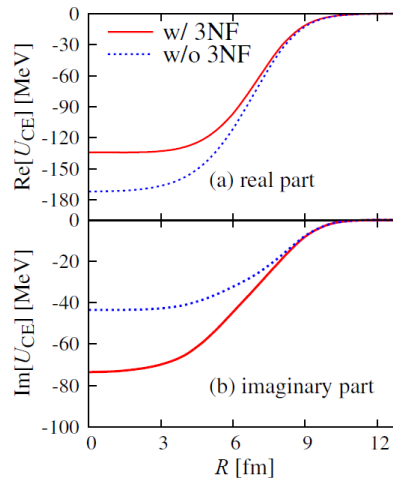


Fig. 3: R dependence of the central part of the folding potential for ${}^4\text{He}+{}^{208}\text{Pb}$ elastic scattering at $E = 72$ MeV/nucleon. The solid and dashed lines represent the results of chiral g matrix with and without 3NF effects. Panels (a) and (b) correspond to the real and imaginary parts of U_{CE} .

References

- [1] E. Epelbaum, H. -W. Hammer, and Ulf-G. Meißner, *Rev. Mod. Phys.* **81**, 1773 (2009).
- [2] R. Machleidt and D. R. Entem, *Phys. Rep.* **503**, 1 (2011).
- [3] N. Kalantar-Nayestanaki, E. Epelbaum, J. G. Messchendorp, and A. Nogga, *Rep. Prog. Phys.* **75**,016301 (2012).
- [4] J. D. Holt, J. Menéndez, J. Simonis, and A. Schwenk, *Phys. Rev. C* **90**, 024312 (2014).
- [5] M. Kohno, *Phys. Rev. C* **88**, 064005 (2013).
- [6] F. A. Brieva and J. R. Rook, *Nucl. Phys. A* **291**, 299 (1977); **291**, 317 (1977); **297**, 206 (1978).
- [7] K. Amos, P. J. Dortmans, H. V. von Geramb, S. Karataglidis, and J. Raynal, in *Advances in Nuclear Physics*, (Plenum, New York, 2000), Vol. 25, p. 275.
- [8] T. Furumoto, Y. Sakuragi, and Y. Yamamoto, *Phys. Rev. C* **78**, 044610 (2008).
- [9] M. Toyokawa, M. Yahiro, T. Matsumoto, K. Minomo, K. Ogata, and M. Kohno, *Phys. Rev. C* **92**, 024618 (2015).
- [10] E. Epelbaum, W. Glöckle, and Ulf-G. Meißner, *Nucl. Phys. A* **747**, 362 (2005).
- [11] K. Hebeler, S. K. Bogner, R. J. Furnstahl, A. Nogga, and A. Schwenk, *Phys. Rev. C* **83**, 031301(R) (2011).
- [12] H. V. von Geramb, K. Amos, L. Berge, S. Bräutigam, H. Kohlhoff, and A. Ingemarsson, *Phys. Rev. C* **44**, 73 (1991).
- [13] P. J. Dortmans and K. Amos, *Phys. Rev. C* **49**, 1309 (1994).
- [14] K. Hagino, T. Takehi, and N. Takigawa, *Phys. Rev. C* **74**, 037601 (2006).
- [15] K. Minomo, K. Ogata, M. Kohno, Y. R. Shimizu, and M. Yahiro, *J. Phys. G* **37**, 085011 (2010).
- [16] M. Toyokawa, K. Minomo, and M. Yahiro, *Phys. Rev. C* **88**, 054602 (2013).
- [17] K. Egashira, K. Minomo, M. Toyokawa, T. Matsumoto, and M. Yahiro, *Phys. Rev. C* **89**, 064611 (2014).
- [18] M. Toyokawa, T. Matsumoto, K. Minomo, and M. Yahiro, *Phys. Rev. C* **91**, 064610 (2015).
- [19] H. de Vries, C. W. de Jager, and C. de Vries, *At. Data Nucl. Data Tables* **36**, 495 (1987).
- [20] R. P. Singhal, M. W. S. Macauley, and P. K. A. De Witt Huberts, *Nucl. Instrum. Methods* **148**, 113 (1978).
- [21] J. F. Berger, M. Girod, and D. Gogny, *Comput. Phys. Commun.* **63**, 365 (1991).
- [22] T. Sumi *et al.*, *Phys. Rev. C* **85**, 064613 (2012).
- [23] H. Sakaguchi *et al.*, *Phys. Lett. B* **89**, 40 (1979); **99**, 92 (1981).
- [24] B. Bonin *et al.*, *Nucl. Phys. A* **445**, 381 (1985).
- [25] R. C. Fuller, *Phys. Rev. C* **12**, 1561 (1975).

Strengths and limitations of the surrogate reaction method to access neutron-induced cross sections of actinides

P. Marini¹, Q. Ducasse^{1,2}, B. Jurado¹, M. Aiche¹, L. Mathieu¹, G. Barreau¹, S. Czajkowski¹, I. Tsekhanovich¹, T. Tornyi³, A. Gorgen³, J. N. Wilson⁴, F. Giacoppo³, F. Gunsing⁵, M. Guttormsen³, A. C. Larsen³, M. Lebois⁴, T. Renstrom³, S. Rose³, S. Siem³, G. M. Tveten³, M. Wiedeking⁶, O. Serot², G. Boutoux⁷, V. Méot⁷, O. Roig⁷

¹ CENBG, Chemin du Solarium B.P. 120, 33175 Gradignan, France

² CEA-Cadarache, DEN/DER/SPRC/LEPh, 13108 Saint Paul lez Durance, France

³ University of Oslo, Department of Physics, P.O. Box 1048, Blindern 0316 Oslo, Norway

⁴ IPN Orsay, 15 rue G. Clémenceau, 91406 Orsay cedex, France

⁵ CEA Saclay, DSM/Irfu, 91191 Gif-sur-Yvette cedex, France

⁶ iThemba LABS, P.O. Box 722, 7129 Somerset West, South Africa

⁷ CEA DAM DIF, 91297 Arpajon, France

Abstract

Gamma decay and fission probabilities of $^{237,239}\text{U}$ and $^{238,239}\text{Np}$ have been measured, for the first time simultaneously, via the surrogate reactions $^{238}\text{U}(^3\text{He}, ^4\text{He})$, $^{238}\text{U}(\text{d}, \text{p})$, $^{238}\text{U}(^3\text{He}, \text{t})$ and $^{238}\text{U}(^3\text{He}, \text{d})$, respectively. While a good agreement between our data and neutron-induced data is found for fission probabilities, gamma decay probabilities are several times higher than the corresponding neutron-induced data for each studied nucleus. We study the role of the different spin distributions populated in the surrogate and neutron-induced reactions. The compound nucleus spin distribution populated in the surrogate reaction is extracted from the measured gamma-decay probabilities, and used as input parameter in the statistical model to predict fission probabilities to be compared to our data. A strong disagreement between our data and the prediction is obtained. Preliminary results from an additional dedicated experiment confirm the observed discrepancies, indicating the need of a better understanding of the formation and decay processes of the compound nucleus.

1. Introduction

Neutron-induced reaction cross sections of short-lived nuclei are crucial for fundamental nuclear physics, as well as for astrophysics and nuclear energy applications. In particular these data are important for understanding the nucleosynthesis r- and s- processes, and for nuclear waste transmutation via fast neutrons. However many of the key isotopes have often lives-time too short for producing and handling a target, making the direct measurement of these cross sections very difficult.

The surrogate reaction method, proposed for the first time in the 70's [3], is an indirect method which aims at determining compound nucleus reaction cross sections involving short lived and/or difficult-to-produce targets. The method is based on the assumption of the independence of the compound nucleus decay probability in a given channel on the formation channel (Bohr hypothesis): the same compound nucleus A^* formed in a neutron-induced reaction ($n+(A-1)\rightarrow A^*$) is now formed in a transfer reaction on a slightly different (but more accessible) target nucleus ($b+Y\rightarrow A^*+c$). In this case the identification of the ejectile c allows one to determine the charge and mass (Z, A) of the decaying nucleus A , and the ejectile kinetic energy and emission angle provide its excitation energy E^* . The nucleus A can decay through different exit channels: fission, gamma emission, neutron emission, etc.

Therefore the measurement of the number of coincidences between the ejectile and the decay products of interest, normalized to the total number of detected ejectiles (i.e. to the total number of nuclei A produced) allows one to extract the decay probability P_{decay}^A for the corresponding decay channel. The neutron-induced cross section for the nucleus A-1 can then be obtained as

$$\sigma_{decay}^{A-1} \simeq \sigma_{CN}^A(E_n) P_{decay}^A(E^*) \quad (1)$$

where $\sigma_{CN}^A(E_n)$ is the compound nucleus formation cross section via the (A-1)+n reaction and it is typically obtained by optical model calculations.

The main advantages of this method are that it allows to access short-living nuclei, not otherwise accessible via direct measurements, and that several transfer channels can be simultaneously investigated on a broad excitation energy range. In addition this kind of measurements is performed with charged particles, whose beam intensity can be few orders of magnitude higher than the nowadays available neutron beams, and that the measurement is performed in a neutron-free environment, eliminating the issues related to neutron scattering typically associated to direct measurements. However, the equivalence of neutron-induced and surrogate reaction measurements relies on two hypothesis, which need to be tested. First, the formation of a compound nucleus must take place both in the neutron-induced and in the transfer reactions. This means that the formed nucleus loses memory of the entrance channel (except for the conserved quantities, i.e. energy and J^π) and its decay is independent of its formation. This assumption is reasonable in the excitation energy region close to and above the neutron separation energy, where the nuclear level density is high. The second one is that the decay probabilities of the compound nucleus are independent of its angular momentum and parity distributions - J^π - (the so-called Weisskopf-Ewing limit, see Ref. [4]), or that the J^π distributions populated in neutron-induced and transfer reactions are the same. Further details on the method and on the underlying assumptions can be found in Ref.[5].

Several measurements (e.g. Ref.[6]) showed a very good agreement of the fission cross sections obtained with the surrogate and direct methods for actinides. However, in recent experiments [7, 8] radiative capture cross sections on rare earths obtained in surrogate reactions were found to be higher up to a factor of 10 than the corresponding neutron-induced reaction data. These important discrepancies were attributed to the large differences in the angular momentum between the mother and the daughter nuclei around the neutron separation energy, which results in the suppression of the neutron emission channel and therefore in the increase of the gamma emission probability [8]. This effect is expected to be reduced when studying actinides, whose level density is much higher than the rare earth one even at low excitation energies. However, a simultaneous measurement of fission and gamma emission probabilities of actinides was not performed up to now. In this work we report the results of this first-time experiment with the aim of further investigate the validity of the assumption of the surrogate reaction method and therefore to pin down to which extent it can be applied to infer neutron-induced cross sections.

2. Experiment

The measurement was performed at the Oslo cyclotron. A deuteron and a ^3He beams at 15 and 24MeV energy, respectively, were impinged on a 99.5% isotopically pure ^{238}U target of $260\mu\text{g}/\text{cm}^2$ thickness. The target, deposited on a $40\mu\text{g}/\text{cm}^2$ C layer, was produced at GSI and extreme attention was payed to reduce its oxidation.

The experimental setup coupled the CACTUS [9] NaI(Tl) array for gamma detection, the NIFF PPAC [10] for fission fragment detection and the SiRi silicon telescope array [11] for the ejectile detection and identification. The CACTUS array is constituted by 27 NaI(Tl) scintillators located 22 cm around the target. Its efficiency was determined with the Extrapolated Efficiency Method [12] and the

Pulse Height Weighting function Technique [13], which give results in good agreement up to several hundred of keV above the neutron separation energy. For more details see Ref. [14]. The NIFF array is constituted by 4 PPAC, filled with 5 mbar C₄H₁₀ gas, covering from 12° to 63° polar angle around the target, with a geometrical detection efficiency of 40% of 2π [14]. Finally, the SiRi telescope array is constituted by two segmented ΔE(130μm)-E(1500μm) silicon detectors, covering from 126° to 140° polar angle around the beam direction. The silicon telescopes allow one to unambiguously identify the ejectile and measure its angle and kinetic energy. This information, combined to the reaction Q-value of the studied reaction, allows one to determine the excitation energy of the formed compound nucleus. The experimental decay probability of the nucleus A* in the channel *j* (fission or gamma emission) can be obtained as:

$$P_j(E^*) = \frac{N_{coinc}^j(E^*)}{N_{singles}(E^*)\epsilon^j(E^*)} \quad (2)$$

where $N_{coinc}^j(E^*)$ is the number of ejectiles detected in coincidence with each decay channel product and $N_{singles}(E^*)$ is the total number of detected ejectiles, $\epsilon^j(E^*)$ is the detection efficiency of the decay product.

3. Results

As mentioned, several nuclei can be accessed simultaneously during surrogate reaction measurements. In particular, in this experiment we measured the gamma decay and fission probabilities of ²³⁹U via the ²³⁸U(d,p) transfer reaction and of ²³⁹Np, ²³⁷U and ²³⁸Np via the ²³⁸U(³He,d), ²³⁸U(³He,⁴He) and ²³⁸U(³He,t) reactions, respectively. In a first moment we will focus on the (d,p) reaction channel (i.e. the decay of the excited ²³⁹U), for which we have the highest statistics. However, the study of this reaction requires to account for the deuteron breakup, which is known since the 70's to modify the values of the measured fission cross section of about 50% [15]. Despite the difficulties associated to this correction, the (d,p) reaction channel is very relevant for the surrogate reaction method because it is the closest reaction to a neutron induced reaction.

In Fig. 1a we present the fission probability obtained for this nucleus. The experimental data (full squares) are corrected for the deuteron breakup (empty square) [16] and compared to the evaluated neutron-induced data (full line) given by JENDL 4.0. For more details on elastic and inelastic deuteron breakup correction see Ref.[14]. The shown error bars account for both statistical and systematic uncertainties. The fission threshold is located around 6.2 MeV ²³⁹U excitation energy. An agreement between the corrected data and the neutron-induced data is observed for the fission threshold and the cross section values above the threshold. Similar agreements were found when analysing the other transfer reactions, although with less statistics, for which the deuteron breakup correction was not necessary. In Fig. 1b the experimental gamma emission probability P_γ (full circles) of ²³⁹U is shown. As expected the P_γ is equal to 1 below the neutron emission threshold of 4.8MeV (we remind that the gamma emission is the only open channel below S_n since the nucleus is not fissile, and the proton separation energy is bigger than the neutron separation energy) and it significantly drops above this energy due to the competition with the neutron emission. Our data are then compared to neutron-induced data (JENDL 4.0 - full line) and discrepancies up to a factor 10 are observed. In Fig. 1c we plot both the fission and gamma emission probabilities shown in Figs. 1a and 1b in the region where both decay channels are open simultaneously, and we compare the experimental data to the evaluated neutron induced data. Also in this excitation energy region we observe a good agreement with the neutron-induced data for the fission probability and a discrepancy of up to a factor 3 for the gamma emission probability. This seems to indicate that, while the fission process is independent of the neutron emission hindering, and therefore independent of the compound nucleus populated J^π distribution, it is not the case for the gamma emission, which is strongly enhanced by the neutron emission hindering. However, calculations based on the statistical

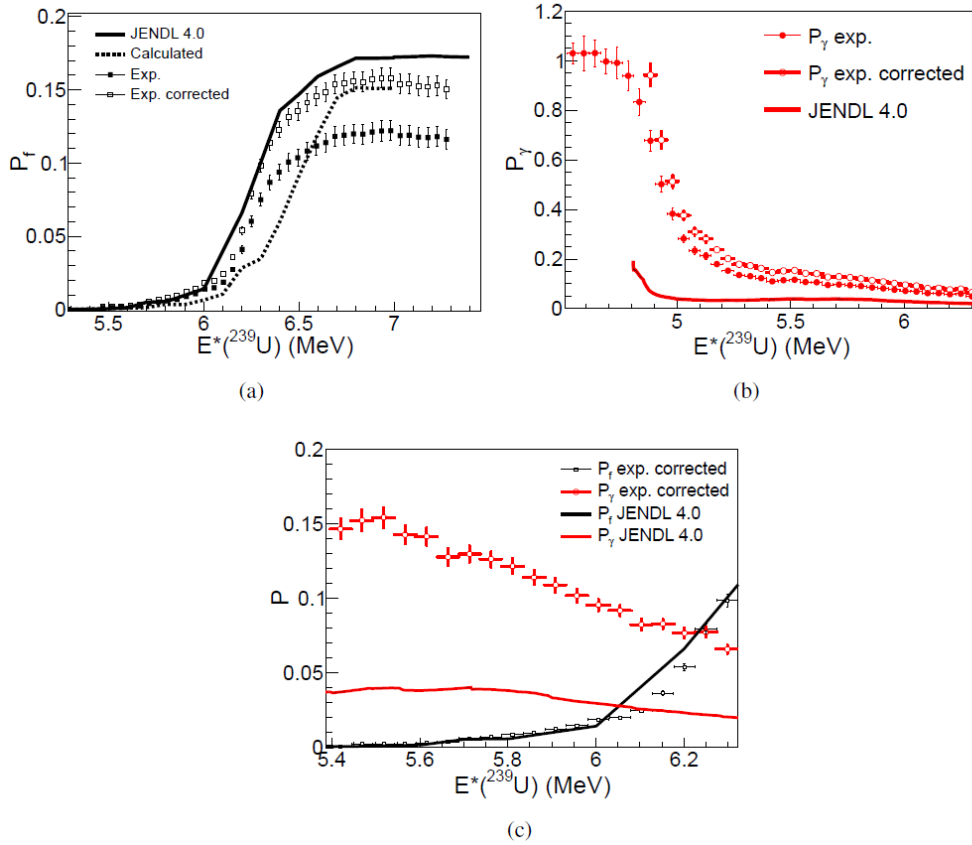


Fig. 1: ^{239}U fission P_f (a) and gamma emission P_γ (b) probabilities as a function of the compound nucleus excitation energy (E^*) obtained in the $^{238}\text{U}(d,p)$ reaction. Fig.c is a zoom of Figs. a and b, in the E^* region where the fission and gamma emission channels are both open.

model with standard ingredients show a strong dependence of the fission probability on the spin.

To further investigate it, we compare the measured fission probability to the one calculated by the statistical model. Following the procedure described in [8] we extracted direct information on the populated J^π distribution from the experimental gamma decay probabilities, using the TALYS code [17]. Assuming a Gaussian angular momentum distribution, with no dependence on the excitation energy, the experimental gamma emission probability can be written as:

$$P_\gamma(E^*) = \sum_{J^\pi} \left[\frac{1}{2\sigma\sqrt{2\pi}} e^{-\frac{(J-\bar{J})^2}{2\sigma^2}} \right] G_\gamma(E^*, J^\pi) \quad (3)$$

where $G_\gamma(E^*, J^\pi)$ are the TALYS gamma decay probability. The unknown \bar{J} and σ parameters, which correspond to the average and width of the spin distribution, are obtained by fitting the experimental data with Eq.3 in the compound-nucleus excitation energy region around 6MeV. The mean value of the surrogate spin distribution is around $5\hbar$ and the width is $2\hbar$. These values are higher than those obtained for the neutron-induced spin distribution, which is centered around $1\hbar$ with a width of about $0.5\hbar$. The surrogate spin distribution is now used as input parameter to the statistical model TALYS to determine the fission probability. The so-calculated fission probability is plotted in Fig.1a as dashed line and compared to the experimental data. The calculated fission probability does reproduce neither the values nor the fission threshold obtained experimentally. In particular, we observe that the statistical model

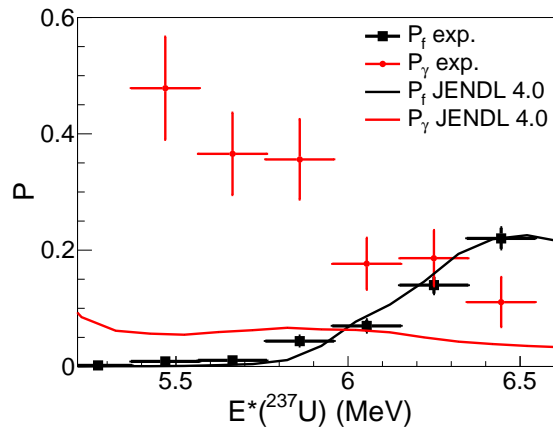


Fig. 2: ^{237}U fission P_f probability as a function of the compound nucleus excitation energy (E^*) obtained in the $^{238}\text{U}(^3\text{He}, ^4\text{He})$ reaction. (Oslo experiment)

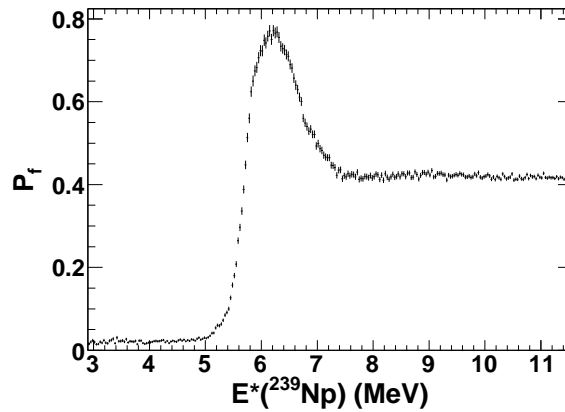


Fig. 3: ^{239}Np fission P_f probability as a function of the compound nucleus excitation energy (E^*) obtained in the $^{238}\text{U}(^3\text{He}, d)$ reaction. (IPN Orsay experiment)

predicts a dependence of the fission threshold on the mean angular momentum of the compound nucleus, which increases as we increase the input mean spin of the compound nucleus. On the contrary, the agreement between the fission thresholds measured in surrogate and neutron-induced reactions observed experimentally indicates an independence of the fission probability of the compound nucleus angular momentum. Therefore, our experimental observations are not currently explained within a statistical model.

Similar results are obtained when studying the other transfer channels. Although the statistics in these channels is lower (and therefore the fission threshold can be determined with less precision), they are not affected by the projectile break-up and therefore a direct comparison between the surrogate and neutron-induced data is possible, free of theoretical corrections. The $^{238}\text{U}(^3\text{He}, ^4\text{He})$ reaction is of particular interest and the results obtained for this transfer channel are shown in Fig. 2. A new dedicated experiment was performed in April 2015 at the Orsay TANDEM accelerator, with the aim of studying this reaction (among others) with an increased statistics, an increased precision in the excitation energy and in the fission and gamma emission probabilities. The latter is obtained by segmenting the fission fragment detectors to have a measurement of the fission fragments anisotropy, which affects both the fission and gamma probability measurements (indeed fission gamma rays need to be subtracted from

the gamma emission probability). The data analysis is currently ongoing. In fig.3 we present the fission probability of ^{239}Np compound nucleus, obtained in the $^{238}\text{U}(^3\text{He},d)$ transfer reaction. Although the results are very preliminary, a good agreement between the results obtained in the two experiments below S_n and between surrogate and neutron-induced fission threshold value is found.

4. Conclusions

In summary, we have performed an experiment to study the validity of the surrogate reaction method to extract neutron-induced reaction cross sections. It is the first time that transfer-induced gamma emission and fission probabilities of actinides are simultaneously measured. The comparison of our experimental data to those obtained in neutron-induced reactions shows a good agreement for the fission probability and a strong disagreement for the gamma emission probability for the same compound nucleus and excitation energy. This indicates a strong sensitivity of the gamma emission to the compound nucleus populated spin distribution at excitation energies slightly above the neutron separation energy. Indeed it was previously shown that the spin distribution populated in surrogate reaction is centered at higher values and it is broader than the one populated in neutron-induced reactions [8]. On the contrary we do not observe a dependence of the fission probability on the populated angular momentum distribution of the compound nucleus. We have compared these observations to the statistical model predictions. We have determined the spin distribution from a fit to the measured gamma emission probabilities via a statistical model calculation performed with the TALYS code. The so-obtained spin distribution is used as input parameter to deduce the fission probability. Statistical model calculations predict an influence of the angular momentum on the fission threshold. Such a dependence is not observed in the experimental data. Preliminary results of a more dedicated experiment confirm the presented results. Therefore our observations are nowadays not explained within a statistical model picture. It is then crucial to better understand the formation and decay mechanisms of the compound nucleus in transfer reactions. Indeed, the surrogate reaction method allows one to access cross sections of short-lived nuclei, that cannot be directly measured.

5. Acknowledgment

We would like to thank the staff of the Oslo Cyclotron and the Orsay tandem for the support during the experiments and the GSI Target Laboratory for the production of high-quality ^{238}U targets. We would also like to express our gratitude to A. Moro and J. Lei, and B. Morillon for performing deuteron break-up, and optical model and TALYS calculations, respectively, and for fruitful discussions. This work was supported by the University of Bordeaux, the European Commission within the 7th Framework Programme through Fission-2010-ERINDA (Project No 269499) and CHANDA (Project No 605203), by the European Atomic Energy Community's 7th Framework Programme under grant agreement number FP7- 249671 (ANDES) and by the French national research programs GEDEPEON and NEEDS.

References

- [1] C. Forssen *et al.* *Phys. Rev. C*, 75:055807.
- [2] M. Caamano *et al.* *Phys. Rev. C*, 88:024605, 2013.
- [3] H. C. Cramer, J. D. Britt. *Nucl. Sci. En.*, 41:177, 1970.
- [4] V. F. Weisskopf *et al.* *Phys. Rev.*, 57:472 and 935, 1940.
- [5] J. E. Escher *et al.* *Rev. Mod. Phys.*, 84:353, 2012. and refs. therein.
- [6] G. Kessedjian *et al.* *Phys. Lett. B*, 692:297, 2010.
- [7] N. D. Scielzo *et al.* *Phys. Rev. C*, 81:034608, 2010.
- [8] G. Boutoux *et al.* *Phys. Lett. B*, 712:319, 2012.
- [9] M. Guttormsen *et al.* *Phys. Scr.*, T32:54, 1990.
- [10] T. G. Tornyi *et al.* *Nucl. Instr. and Meth. in Phys. Res. Sec. A*, 738:6 – 12, 2014.

- [11] M. Guttormsen *et al.* *Nucl. Instr. and Meth. in Phys. Res. Sec. A*, 648(1):168, 2011.
- [12] G. Boutoux *et al.* *Nucl. Instr. and Meth. in Phys. Res. Sec. A*, 700:59 – 64, 2013.
- [13] R. L. Macklin and J. H. Gibbons. *Phys. Rev.*, 159:1007, 1967.
- [14] Q. Ducasse. PhD thesis, University of Bordeaux, 2015.
- [15] H. C. Britt and J. D. Cramer. *Phys. Rev. C*, 2:1758, 1970.
- [16] A. Moro. Priv. comm.
- [17] A. J. Koning *et al.* *User Manual TALYS*.

Role of the direct mechanisms in the deuteron-induced surrogate reactions

M. Avrigeanu, V. Avrigeanu

Horia Hulubei National Institute for Physics and Nuclear Engineering, P.O. Box MG-6, 077125 Bucharest-Magurele, Romania

Abstract

An extended analysis of the key role of direct interactions, i.e., breakup, stripping and pick-up processes, for the deuteron-induced surrogate reactions is presented. Particular comments concern the deuteron breakup which is dominant in the case of the $(d, p\gamma)$ surrogate reactions on actinides target nuclei, around the Coulomb barrier.

1. Introduction

The surrogate reaction method is an indirect measurement technique proposed by Cramer and Brit [1] to overcome the difficult problems of preparing and handling the highly radioactive targets required for cross-section measurements. Therefore, the outgoing channel of interest is studied via an alternative "surrogate" reaction that involves a projectile-target combination more accessible experimentally. The use of surrogate reaction method (e.g., [2, 3, 4, 5, 6, 7, 8, 9]) to provide indirect informations on cross sections that can not be measured directly or calculated accurately is steadily increasing. Since last decade this method has been involved mainly in the investigation of the neutron-induced (n, γ) , and (n, f) reaction cross sections, by means of an appropriate stable beam and target combination ([2, 3] and Refs. therein).

2. Deuteron surrogate reactions for neutron capture

The "desired" (n, γ) cross section for a target nucleus A is given in the Hauser-Feshbach formalism, in terms of compound nucleus (CN) formation cross section $\sigma_n^{CN}(E_{ex}, J, \pi)$ and the branching ratio $G_\gamma^{CN}(E_{ex}, J, \pi)$ toward the desired outgoing channel of γ -ray decay, by [4]:

$$\sigma_{n\gamma}(E_n) = \sum_{J, \pi} \sigma_n^{CN}(E_{ex}, J, \pi) G_\gamma^{CN}(E_{ex}, J, \pi), \quad (1)$$

where J, π are the spin and parity of the excited state E_{ex} of the decaying compound nucleus:

$$E_{ex} = \frac{A}{A+1} E_n + S_n, \quad (2)$$

E_n being the neutron incident energy, and S_n the binding energy of the neutron in the compound nucleus.

Usually the compound nucleus formation cross section is obtained from a neutron optical model potential, while the G_γ^{CN} branching ratio requires accurate information on the Hauser-Feshbach model ingredients of the all competing decay channels, e.g., optical potentials, level densities, strengths functions, etc. Such difficulties should be avoided by using alternative surrogate reactions. Among them, the deuteron surrogate reaction $(d, p\gamma)$ produces the same excited nucleus $(A+1)$, decaying through the desired γ channel.

The probability for the compound nucleus formed in the (d, p) surrogate reaction, with the same specific excitation energy, spin, and parity values as in the desired reaction, to decay through γ channel is [4]:

$$P_{d,p\gamma}(E_{ex}) = \sum_{J, \pi} F_{d,p}^{CN}(E_{ex}, J, \pi) G_\gamma^{CN}(E_{ex}, J, \pi), \quad (3)$$

where $F_{d,p}^{CN}(E_{ex}, J, \pi)$ is the probability for the formation of this excited surrogate compound nucleus.

The specific feature of the surrogate method is the experimental determination of $P_{d,p\gamma}(E_{ex})$, by measuring the total number of the surrogate events, e.g. number of (d, p) processes, and the number of coincidences surrogate ejectile–CN decay channel, e.g. number of $p - \gamma$ coincidences:

$$P_{d,p\gamma}^{exp}(E_{ex}) = \frac{N_{p,\gamma}^{coincidences}(E_{ex})}{N_{d,p}^{surrogate\ events}(E_{ex})} \quad (4)$$

corrected for the detector efficiency.

Further, the use of measured $P_{d,p\gamma}(E_{ex})$, together with the calculated $F_{d,p}^{CN}(E_{ex}, J, \pi)$, to determine the branching ratios $G_{\gamma}^{CN}(E_{ex}, J, \pi)$, leads to the determination of the desired cross section, Eq. (1). This is the theoretical frame of the surrogate reactions, before approximations which simplify the analysis.

A first approximation of the surrogate method considers similar $J - \pi$ distributions in both desired and surrogate reactions [2, 3]:

$$F_{d,p}^{CN}(E_{ex}, J, \pi) \approx F_n^{CN}(E_{ex}, J, \pi) \equiv \frac{\sigma_n^{CN}(E_{ex}, J, \pi)}{\sum_{J', \pi'} \sigma_n^{CN}(E_{ex}, J', \pi')}, \quad (5)$$

where $F_n^{CN}(E_{ex}, J, \pi)$ is the the probability for the formation of this excited compound nucleus in the desired reaction.

Next approximation, within the Weisskopf-Ewing (WE) limit of the Hauser-Feshbach formalism, considers the decay probabilities $G_{\gamma}(E_{ex}, J, \pi)$ to be independent of $J - \pi$:

$$G_{\gamma}(E_{ex}, J, \pi) = G_{\gamma}(E_{ex}), \quad (6)$$

the desired cross section becoming finally:

$$\sigma_{n\gamma}^{WE}(E_n) = \sigma_n^{CN}(E_n) P_{d,p\gamma}^{exp}(E_{ex}). \quad (7)$$

3. Tests of deuteron surrogate reaction approximations

Given the importance of (n, γ) reaction for basic and applied nuclear physics and the possibility of using $(d, p\gamma)$ as a surrogate reaction for neutron capture, the validation of the deuteron surrogate method has got a great importance. The validation test comparing already well known (n, γ) cross sections with those provided by deuteron surrogate reaction $(d, p\gamma)$ stressed out large discrepancies [5, 6, 7, 8, 9] which rise a strong question mark concerning the suitability of the associated theoretical frame.

Thus, Allmond *et al.* [7] reported a 23% deviation between the known ratio $^{235}\text{U}(n, \gamma)/^{235}\text{U}(n, f)$ [11] and the measured surrogate ratio $^{235}\text{U}(d, p\gamma)/^{235}\text{U}(d, pf)$. Such large discrepancy reveals "break-down of the Bohr compound nucleus and Weisskopf-Ewing approximation" [7], requesting an improved reaction model for the (d, p) surrogate reaction. The same request of an improved reaction model for the (d, p) surrogate process results from Hatarik *et al.* [8] validation test for the $^{171,173}\text{Yb}(d, p\gamma)$ surrogate reactions by comparison with known neutron capture cross sections [10]. The large discrepancy between ENDF/B-VII.0 [11] evaluated $^{92}\text{Mo}(n, \gamma)$ reaction cross sections and the corresponding $^{92}\text{Mo}(d, p\gamma)$ surrogate cross sections found by Goldblum *et al.* [9] points out the failure of the modeling the deuteron surrogate reactions through the Weisskopf-Ewing approximation. Wilson *et al.* [5] directed a "stringent test of the applicability" of the deuteron surrogate method in the actinides region, for the ^{232}Th target nucleus, for well known neutron-capture cross sections [12]. Large overestimation of the (n, γ) reaction cross sections by the $(d, p\gamma)$ surrogate reaction results for the low neutron energy

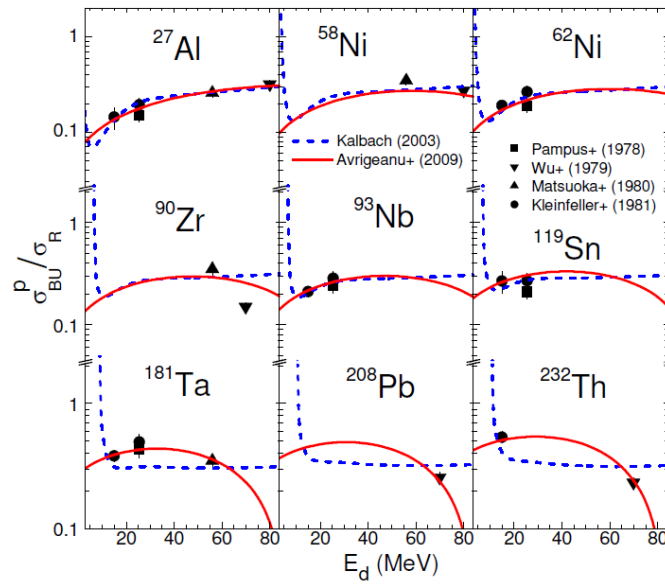


Fig. 1: Comparison of experimental [17] total proton-emission breakup fraction and the corresponding parametrization of Refs. [15, 19, 20] (solid curves), and [18] (dashed curves) for deuteron interactions with target nuclei from ^{27}Al to ^{232}Th .

range $E_n < 1$ MeV has thus been reported. Supplementary to the criticism of the Weisskopf-Ewing approximation used in the surrogate formalism, the effect of the breakup process is mentioned by Ducasse *et al.* [6] as another source of validation failure in the case of deuteron surrogate reaction $^{238}\text{U}(d, p\gamma)$.

It is obvious that the apparent discrepancies evidenced by validation tests [5, 6, 7, 8, 9] are the results of weak points, actually the approximations of the (d, p) interaction process analysis in the theoretical frame of surrogate method.

One approximation, appearing even as a contradiction in the terms of the surrogate reaction method is that the direct nucleon-transfer (d, p) reaction forms an excited compound nucleus [5, 6, 7, 8, 9]. Therefore, a reconsideration of the reaction mechanisms involved in deuteron surrogate reactions, populating a highly excited nucleus, should include the direct reactions (DR, e.g., stripping), statistical processes, e.g., pre-equilibrium emission (PE), and CN processes, as well as the deuteron breakup (BU) particularly for deuteron interaction processes [13, 14, 15]. Actually, in the case of the deuteron surrogate reactions at low incident energies, for heavy targets nuclei (actinides) the deuteron breakup has the strongest effects, as it has been pointed out for the low-energy deuteron interaction with ^{231}Pa target nucleus [16].

The physical picture of the deuteron breakup in the Coulomb and nuclear fields of the target nucleus considers two distinct processes, namely the elastic breakup (EB) in which the target nucleus remains in its ground state and none of the deuteron constituents interacts with it, and the inelastic breakup or breakup fusion (BF), where one of these deuteron constituents interacts with the target nucleus while the remaining one is detected. Overall, there are actually two opposite effects of the deuteron breakup on the deuteron activation cross sections that should be considered. Firstly, the total-reaction cross section, that is shared among different outgoing channels, is reduced by the value of the total breakup cross section σ_{BU} . On the other hand, the BF component, where one of deuteron constituents interacts with the target nucleus leading to a secondary composite nucleus, brings contributions to different reaction channels [13, 14, 15, 16]. Thus, the absorbed proton or neutron following the deuteron breakup, contributes to the enhancement of the corresponding (d, xn) or (d, xp) reaction cross sections, respec-

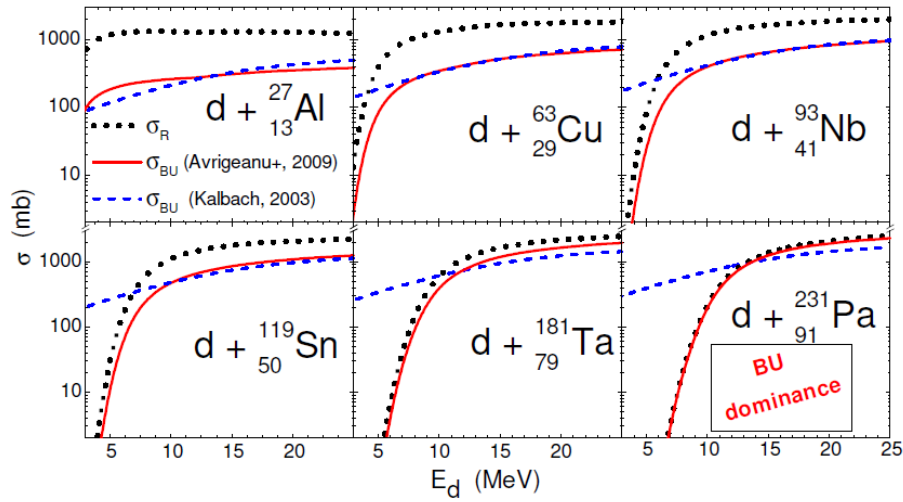


Fig. 2: The energy dependence of the total breakup cross sections given by Avrigeanu *et al.* [15, 19, 20] (solid curves) and Kalbach [18] (dashed curves) parametrizations for deuteron interactions with ^{27}Al , ^{63}Cu , ^{93}Nb , ^{119}Sn , ^{181}Ta , and ^{231}Pa , while σ_R is shown by dotted curves.

tively. The breakup effects which are present in the deuteron surrogate experiments will be stressed out in the following through a detailed examination of the work of Wilson *et al.* [5] using the surrogate reaction $^{232}\text{Th}(d, p\gamma)^{233}\text{Th}$ for an indirect measurement of the well-known $^{232}\text{Th}(n, \gamma)^{233}\text{Th}$ reaction cross sections [11, 12] for incident-neutron energies between 0 and around 1 MeV. A good agreement between indirect and direct (n, γ) cross-section measurements was found only in the range 500 keV–1 MeV while large discrepancies have been present outside this range.

First, the measurement of Wilson *et al.* [5] has involved 12 MeV deuterons incident on ^{232}Th target nucleus, while the decay probabilities $P_{d,p\gamma}(E_{ex})$ of the excited nucleus ^{233}Th have been measured at excitation energies between the corresponding neutron binding energy $S_n=4.786$ MeV and 1 MeV above it. The protons from the ($d, p\gamma$) reaction corresponding to this excitation have had energies between ~ 8.7 and 9.7 MeV while their maximum energy has been around 14.5 MeV. On the other hand, the BF protons have had a maximum energy of 9.673 MeV in the center-of-mass system, with a twofold outcome for these BF protons: they match the proton emission involved in the surrogate-reaction analysis, but have energies lower than the protons which populate the excited nucleus ^{233}Th below S_n and were considered to prove the lack of any BU effect (Fig. 6 of Ref. [5]).

Second, the BF protons with energies between ~ 8.7 and 9.7 MeV correspond to BF neutrons with energies between around 1 MeV and 0, respectively, i.e. very much alike to the desired neutron capture process. Furthermore, these BF neutrons interact with ^{232}Th target nucleus, populating the same analyzed ^{233}Th compound nucleus, at the same excitation energies of interest. The γ -ray decay of ^{233}Th compound nuclei populated through the BF enhancement contribute thus, together with the companion BF protons, to the measured $p - \gamma$ coincidence events.

Third, in addition to the BF, stripping, and PE contributions to the population of the excited nucleus ^{233}Th , one has to take into account the considerable amount of incident deuterons leakage through the above mentioned processes [13, 14, 15, 16], strongly diminishing the probability $F_{d,p}^{CN}(E_{ex}, J, \pi)$ for forming the compound nucleus ^{233}Th , Eq. (3).

The importance of the total (EB+BF) *proton*-emission breakup fractions σ_{BU}^p/σ_R , where σ_R is

the deuteron reaction cross section, is given in Fig. 1 by means of the comparison with the experimental systematics [17], measured for target nuclei from Al to Th. The calculated curves represent the predictions of the empirical Kalbach's [18] and Avrigeanu *et al.* [15, 19, 20] parametrizations.

A comparison of the *total* breakup cross sections predicted by Kalbach [18], and Avrigeanu *et al.* [15, 19, 20] for deuterons interaction with target nuclei from Al to Pa and the total deuteron cross section is presented in Fig. 2. Regardless of the differences for incident energy lower than ~ 10 MeV, where Kalbach's parametrization [18] predicts too high values for the breakup cross sections, both parametrizations predict an increasing role of deuteron breakup with increased target-nucleus mass/charge, pointing out the dominance of the breakup mechanism at the deuteron incident energies below and around the Coulomb barrier of ^{231}Pa [16]. Actually, this conclusion is in line with the experimental total proton-emission BU fraction data for deuterons on ^{232}Th [17], Fig. 1. Particularly, the dominance of the breakup mechanism for the actinides nuclei at energy around Coulomb barrier should be considered in the case of (d,x) surrogate reactions analysis.

From Figs. 1 and 2 it is obvious that the neglect of the breakup mechanism strongly affects the validation test, being the main reason of its failure.

The other assumption concerning the equality of the branching ratios for the deuteron surrogate and the neutron-induced reactions should be considered with increased caution in the analysis due to the population and decay differences between the excited and compound nuclei, respectively, formed in surrogate and desired reactions [21, 6].

Finally, one should be more careful in assuming that the failure of the surrogate-method validation tests follows the use of the too weak Weisskopf-Ewing approximation [5, 6, 7, 8, 9]. Even the use of the Hauser-Feshbach formalism alone within deuteron-induced reactions analysis can not lead to expected good results in the absence of the unitary account of BU+DR+PE+CN reaction mechanisms involvement.

4. Conclusions

The present work has concerned a deeper analysis of the key role of the direct interaction, particularly the breakup mechanism in the deuteron surrogate reactions. The opposite effects of the breakup mechanism, namely the enhancement of the counted *protons* – γ coincidences as well as the decrease of the compound nucleus cross section due to initial deuteron flux leakage through breakup but also stripping and pre-equilibrium processes should explain the failure of the validation tests of the deuteron surrogate method particularly at low incident energies around the Coulomb barrier and on actinides target nuclei.

Acknowledgments

This work was partly supported by Fusion for Energy (F4E-GRT-168-02), and by a grant of Unitatea Executiva pentru Finantarea Invatamantului Superior, a Cercetarii, Dezvoltarii si Inovarii (PN-II-ID-PCE-2011-3-0450).

References

- [1] J.D. Cramer and H.C. Britt, Nucl. Sci. Eng. **41** (1970) 177.
- [2] J. Escher *et al.*, Rev. Mod. Phys. **84** (2012) 353.
- [3] Jutta E. Escher and Frank S. Dietrich, Phys. Rev. C **81** (2010) 024612.
- [4] N.D. Scielzo *et al.*, Phys. Rev. C **81** (2010) 034608.
- [5] J.N. Wilson *et al.*, EPJ Web of Conferences **21** (2012) 01003; J.N. Wilson *et al.*, Phys. Rev. C **85** (2012) 034607.

- [6] Q. Ducasse *et al.*, Nuclear Data Sheets **119** (2014) 233; Q. Ducasse *et al.*, in 5th Workshop on Nuclear Level Density and Gamma Strength, 18–22 May 2015, Oslo, Norway, http://tid.uio.no/workshop2015/talks/Oslo2015_Ducasse.pdf.
- [7] J. M. Allmond *et al.*, *Phys. Rev. C* **79** (2009) 054610.
- [8] R. Hatarik *et al.*, *Phys. Rev. C* **81** (2010) 011602.
- [9] B.L. Goldblum *et al.*, *Phys. Rev. C* **85** (2012) 054616.
- [10] K. Wisshak *et al.*, *Phys. Rev. C* **61** (2000) 065801.
- [11] M.B. Chadwick *et al.*, Nuclear Data Sheets **107** (2006) 2931.
- [12] *Experimental Nuclear Reaction Data (EXFOR)*; www-nds.iaea.org/exfor.
- [13] P. Bém *et al.*, *Phys. Rev. C* **79** (2009) 044610; E. Šimečková *et al.*; *Phys. Rev. C* **84** (2011) 014605; M. Avrigeanu *et al.*, *Phys. Rev. C* **88** (2013) 014612; *Phys. Rev. C* **89** (2014) 044613.
- [14] M. Avrigeanu, V. Avrigeanu, Nucl. Data Sheets **118** (2014) 301; *Phys. Rev. C* **92** (2015) 021601.
- [15] M. Avrigeanu, V. Avrigeanu, AIP Conference Proceedings **1645** (2015) 139.
- [16] M. Avrigeanu, V. Avrigeanu, and A.J. Koning, *Phys. Rev. C* **85** (2012) 034603.
- [17] J. Pampus *et al.*, *Nucl. Phys. A* **311** (1978) 141;
J. R. Wu *et al.*, *Phys. Rev. C* **19** (1979) 370 ; N. Matsuoka *et al.*, *Nucl. Phys. A* **345** (1980) 1;
J. Kleinfeller *et al.*, *Nucl. Phys. A* **370** (1981) 205; M. G. Mustafa *et al.*, *Phys. Rev. C* **35** (1987) 2077.
- [18] C. Kalbach Walker, in *Triangle University Nuclear Laboratory Progress Report XLII (2002-2003)*; www.tunl.duke.edu/publications/tunlprogress/2003/.
- [19] M. Avrigeanu *et al.*, *Fusion Eng. Design* **84** (2009) 418.
- [20] M. Avrigeanu V. Avrigeanu, *EPJ Web of Conferences* **2** (2010) 01004; **21** (2012) 07003; *J. Phys.: Conf. Ser.* **205** (2010) 012014; **533** (2014) 012004; *J. Korean Phys.Soc.* **59** (2011) 903; in 5th Workshop on Nuclear Level Density and Gamma Strength, 18–22 May 2015, Oslo, Norway, http://tid.uio.no/workshop2015/talks/Oslo2015_MAvrigeanu.pdf
- [21] S. Chiba and O. Iwamoto, *Phys. Rev. C* **81** (2010) 044604.

Investigation of ^{10}Be and ^{16}C structure with break-up reactions at intermediate energies

D. Dell'Aquila⁴, L. Acosta¹¹, F. Amorini², R. Andolina³, L. Auditore⁵, I. Berceanu⁸, G. Cardella¹, M.B. Chatterjee⁹, E. De Filippo¹, L. Francalanza⁴, B. Gnoffo¹, A. Grzeszczuk¹⁰, G. Lanzalone^{2,6}, I. Lombardo⁴, N. Martorana², T. Minniti⁵, A. Pagano¹, E.V. Pagano^{2,3}, M. Papa¹, S. Pirrone¹, G. Politi^{1,3}, A. Pop⁸, F. Porto², L. Quattrocchi⁵, F. Rizzo^{2,3}, E. Rosato^{4,†}, P. Russotto¹, A. Trifirò⁵, M. Trimarchi⁵, G. Verde^{1,7} and M. Vigilante⁴.

¹ INFN-Sezione di Catania, Catania, Italy

² INFN-Laboratori Nazionali del Sud, Catania, Italy

³ Dipartimento di Fisica e Astronomia, Università di Catania, Catania, Italy

⁴ Dipartimento di Fisica, Università di Napoli Federico II and INFN Sezione di Napoli, Italy

⁵ INFN Gruppo Collegato di Messina and Dipartimento di Fisica e Scienze della Terra, Università di Messina, Italy

⁶ Facoltà di Ingegneria e Architettura, Università Kore, Enna, Italy

⁷ Institute de Physique Nucléaire d'Orsay, Orsay, France

⁸ Institute for Physics and Nuclear Engineering, Bucharest, Romania

⁹ Saha Institute for Nuclear Physics, Kolkata, India

¹⁰ Institute of Physics, University of Silesia, Katowice, Poland

¹¹ National Autonomous University of Mexico, Mexico City, Mexico

Abstract

The spectroscopy of ^{10}Be and ^{16}C isotopes is studied via projectile break-up reactions induced on polyethylene (CH_2) target, by using a 55 MeV/u ^{10}Be and a 49 MeV/u ^{16}C beams provided by the FRIBs facility at INFN-LNS. We reconstruct the ^{10}Be and ^{16}C relative energy spectra to evince the presence of excited states characterized by cluster structure. By inspecting the $^4\text{He}+^6\text{He}$ relative energy spectrum we find evidence of a new possible state of ^{10}Be at 13.5 MeV for which the corresponding angular correlation indicates a hypothetical 6^+ assignment. Finally, from binary ($^6\text{He}+^{10}\text{Be}$) cluster decomposition of ^{16}C we show the indication of a possible new state at about 20.6 MeV.

1. Introduction

The study of cluster structures in light nuclei is considered an important tool to understand the properties of nuclear forces in few body systems [1]. In fact, *clustering* in nuclei reflects the correlations between nucleons inside the nuclear volume, due to the quantum nature of nuclear systems. The simplest example is offered by the case of *self-conjugated* nuclei (such as ^8Be , ^{12}C , ^{16}O , ^{20}Ne), in which the nucleon-nucleon correlations, given the great stability of the α particle, could determine a spatial reorganization of nucleons into α -cluster structures [2]. These cluster structures could be characterized by very large deformations and peculiar shapes [3]. An important example is the Hoyle state in ^{12}C (0^+ , 7.654 MeV), whose cluster structure is of fundamental importance also in Nuclear Astrophysics [4, 5, 6, 7].

An increasing interest on the study of clusters in nuclei has been triggered by the evidence (in the last decades) that clustering effects could also be observed in non-self conjugated nuclei. In this case clustering phenomena could show very different features. Important examples are the *neutron-rich* nuclei, where the extra-neutrons can provide sort of covalent bonds between α -like centers with

the subsequent increasing of the nuclear stability (look for example at the ^9Be and ^{10}Be isotopes that are weakly bound while the ^8Be is unbound) eventually leading to the possible formation of the so called nuclear molecules [1, 8]. The neutron-rich beryllium isotopes, together with the carbon ones, represent a very important case also because of their possible, respectively, dimeric and linear chain configurations, discussed in several recent papers [3, 8].

In the study of the beryllium isotopic chain a special attention must be paid to the ^{10}Be isotope. This nucleus is characterized by a highly-deformed ground state [9] on which a positive parity rotational excitation is built. For this rotational band, the 2^+ member is well known (3.37 MeV excitation energy), while its continuation has been object of recent publications because of the uncertainties of the 4^+ member assignment [11, 10, 12, 13], predicted at about 11–12 MeV. A negative parity rotational band with a 1^- state at 5.96 MeV as band-head is also reported in [1]. The presence, close to the $^4\text{He}+^6\text{He}$ emission threshold, of a molecular 0^+ state (≈ 6.18 MeV), predicted in the AMD calculation [9], has been experimentally confirmed. This state can be well described in terms of molecular dimeric $\alpha : 2n : \alpha$ structure. The existence of a 2^+ state at 7.54 MeV, characterized by a strong molecular structure, is the indication of the rotational excitation of the 6.18 MeV state. The subsequent 4^+ member of this molecular rotational band is predicted to be located at about 10.5 MeV excitation energy. A 10.2 MeV state was found via the $^7\text{Li}(^7\text{Li}, ^4\text{He}+^6\text{He})^4\text{He}$ reaction [14]. Curtis et al assigned $J^\pi=3^-$ to this state via angular correlation measurements [15]. This assignment was subsequently contradicted in Ref. [16] and in recent $^6\text{He}+^4\text{He}$ inverse kinematic resonant elastic scattering experiments. This state could therefore be the 4^+ member of the molecular rotational band. A very recent resonant elastic scattering $^6\text{He}+^4\text{He}$ experiment at the ANASEN facility [17] has also shown, as a preliminary result, the existence of a 6^+ excited state in ^{10}Be at about 13.6 MeV. This state is compatible, on the energetic point of view, with the 6^+ member of the cluster state band in ^{10}Be [18], of which could represent the continuation.

Another interesting isotopic chain is the carbon one. In particular, the neutron-rich carbon isotopes represent an important case for the Nuclear Physics of clusters, because of the various theoretical predictions of possible linear chain and triangular configurations of these nuclei. Interesting studies have been done recently on ^{13}C [19, 20, 21] and ^{14}C [22] structure via resonant elastic scattering in direct and inverse kinematics. The ^{16}C , for which the spectroscopy is absolutely not well known, especially above the helium disintegration threshold, has recently attracted a large interest [23, 24]. For this isotope, a recent theoretical calculation [25] indicated the possible existence of various molecular states, constituted by three α centers bounded by two couple of valence neutrons, with triangular and linear shapes. These states could give rise to molecular bands, but unfortunately an experimental confirmation of these predictions is still missing because of the poor statistics of the experiments reported in literature.

In the present paper we report new results on the spectroscopy of ^{10}Be and ^{16}C excited states above the cluster emission thresholds, investigated via sequential projectile break-up reactions. Break-up fragments have been detected by the Chimera array. A relative energy analysis of correlated break-up fragments has allowed us to point out the possible existence of new states of these nuclei. In particular, we found indications of a possible state at about 13.5 MeV in ^{10}Be , as seen from the $^4\text{He}+^6\text{He}$ coincidence data. The corresponding angular correlation analysis shows an high spin value (possibly 6^+) for this state, confirming the findings of [17]. For the ^{16}C nucleus, the $^6\text{He}+^{10}\text{Be}$ correlations suggest the presence of a new state at about 20.6 MeV, in agreement with calculations of [25].

2. Experimental details

Break-up reactions have been induced on a polyethylene CH_2 target. For the present experiment we have selected reaction products from the $^1\text{H}(^{10}\text{Be}, ^4\text{He}+^6\text{He})$, $^2\text{H}(^{10}\text{Be}, ^4\text{He}+^6\text{He})$, $^{12}\text{C}(^{10}\text{Be}, ^4\text{He}+^6\text{He})$ and $^1\text{H}(^{16}\text{C}, ^6\text{He}+^{10}\text{Be})$, $^2\text{H}(^{16}\text{C}, ^6\text{He}+^{10}\text{Be})$ reactions. To obtain spectroscopic information on ^{10}Be and ^{16}C

nuclei we measured masses, energies and flight directions of the corresponding break-up fragments with the CHIMERA 4π multi-detector [27, 28, 29, 30]. It is constituted by 1192 Si-CsI(Tl) telescopes, covering $\simeq 94\%$ of the whole solid angle. The first stage of the telescope is constituted by a $300\ \mu\text{m}$ thick silicon detector and it is followed by a CsI(Tl) crystal, having a thickness of 12 cm and read-out by a photodiode. In the present experiment we used the first three forward rings of the Chimera array, covering the polar angle range $2.2^\circ \leq \theta \leq 6.4^\circ$. Thanks, on one hand, to the forward peaked cross section of inelastic excitation on carbon [31], and, on the other hand, to the small limiting angle of inverse kinematics excitation on hydrogen, we expect to detect a large amount of fragments coming from projectile break-up in this present angular domain.

2.1 The ^{10}Be case

The ^{10}Be spectroscopy has been studied via the $^4\text{He}+^6\text{He}$ correlation with the above described technique. The corresponding relative energy ($E_{rel} + E_{thr}$) spectrum is reported in Fig. 2 with the green line. Despite the low statistics and the limited resolution some peaks are visible. They are in agreement with suggestions given in the literature, as pointed out by the arrows indicating the energy position of known states. It is very interesting to observe that the presence of another bump at $E_x \simeq 13.5$ MeV suggests the possible fingerprint of a new, unreported, state in ^{10}Be . To check if the observed peak can be really ascribed to the existence of an excited state in ^{10}Be we evaluated the detection efficiency. This contribution was calculated via a Monte Carlo simulation with the same prescriptions than for the ^8Be case. Because of the different kinematics between inelastic scattering on Hydrogen or Carbon, the two components of the composite target, we performed two different simulation taking into account the different possible target nuclei.

Spin and parity of the suggested 13.5 MeV state can be tentatively estimated via an angular correlation analysis. Fig. 1 shows the $|\cos(\Psi')|$ distribution of the events falling into the 13.5 MeV peak, where we have indicated with Ψ' the angle formed by the relative velocity vector of the two fragments with the beam axis (Ψ) taking into account the phase shift term ($\Delta\Psi$), as suggested for example in [35, 36, 37]. This correction is useful to make direct comparisons with the corresponding Legendre polynomial squared, being $|\cos(\Psi')| \propto |P_J(\cos(\Psi'))|^2$, where P_J is the J -order Legendre polynomial and J is the spin of the resonance. As a first approximation, the phase shift term $\Delta\Psi$ can be calculated, following the suggestions of Refs. [35], by the relation $\Delta\Psi = \frac{\ell_i - J}{J} \theta_{cm}$, where ℓ_i is the angular momentum of the dominant partial wave in the entrance channel. Considering that, in a semi-classical picture, at intermediate energies inelastic scattering processes have essentially a direct and peripheral nature, only a narrow window of angular momenta centred around the grazing value ℓ_g would contribute to the scattering amplitude [37]. For this reason, we can assume $\ell_i \simeq \ell_g$. The ℓ_g has been calculated with the Wilcke model [38]. For example, in the present case we have $\ell_g \simeq 10\hbar$ for proton target. For clarity reasons we have presented in Fig.1 the behaviour of the experimental data (black points) corrected considering a $J = 6$ resonance and compared with the corresponding theoretical prediction (red line), for which we have obtained a better agreement. The last one has also been corrected for the estimated detection efficiency (represented by the dotted line). As clearly visible from the figure, the $J = 6$ theoretical prediction is in satisfactory agreement with the experimental data, possibly confirming the preliminary results reported in Ref. [17].

2.2 The ^{16}C case

Finally, we have studied the $^{10}\text{Be}+^6\text{He}$ correlations to investigate the spectroscopy of ^{16}C . The corresponding relative energy ($E_{rel} + E_{thr}$) is shown in Fig. 2. The red and black dashed lines are, re-

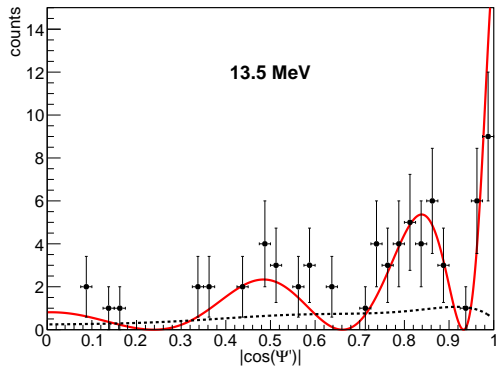


Fig. 1: (color online) ${}^6\text{He}-{}^4\text{He}$ angular correlations for the 13.5 MeV state of ${}^{10}\text{Be}$ corrected for the phase shift term considering a $J = 6$ resonance. The red line is the corresponding theoretical prediction $|P_6(\cos(\Psi'))|^2$ corrected for the efficiency (dashed line).

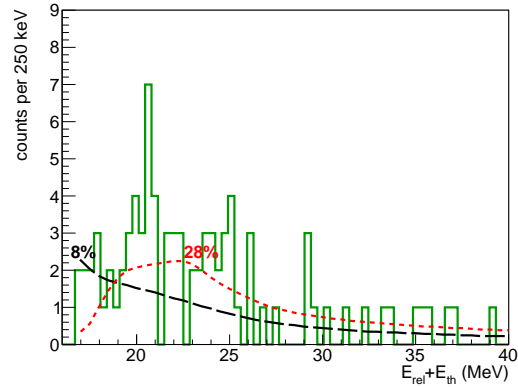


Fig. 2: (color online) ${}^{16}\text{C}$ relative energy spectrum ($E_{rel} + E_{thr}$) for the ${}^{10}\text{Be}+{}^6\text{He}$ break-up channel. The red and the black dashed lines represent, respectively, the simulated detection efficiency for inelastic scattering on proton, peaking at 28%, or carbon, peaking at 8%.

spectively, the efficiency for inelastic scattering on hydrogen or carbon, in analogy with the previous discussion. In this case the statistics is very low, but anyway an yield enhancement corresponding to an excitation energy of about 20.6 MeV is visible. As in the case of ${}^{10}\text{Be}$, the efficiency curves exhibit a flat behaviour, indicating that the 20.6 MeV bump should not be attributed to efficiency effects. It is very interesting to note that also previous experiments [24, 23] show, with lower statistics, the same yield enhancement. For these reasons, we could attribute this bump to a new state; furthermore, in these energy region, some linear chain states and triangular states have been pointed out in the theoretical paper [25].

3. Conclusions and perspectives

In conclusion, we studied the structure of ${}^{10}\text{Be}$ and ${}^{16}\text{C}$ via break-up reactions induced on CH_2 target and using a radioactive cocktail beam produced at the FRIBs facility (LNS).

From the analysis of ${}^6\text{He}-{}^4\text{He}$ coincidences we investigate the spectroscopy of ${}^{10}\text{Be}$, observing some excited state reported in literature and the evidence of a new state. For this new state, possibly observed also in the preliminary analysis [17], we studied the corresponding angular correlation, pointing out a tentative 6^+ spin and parity assignment in agreement with [17].

The structure of ${}^{16}\text{C}$ is investigated via the ${}^{10}\text{Be}+{}^6\text{He}$ break-up channel. In this case we find an yield enhancement at about 20.6 MeV excitation energy that could be the fingerprint of the possible existence of a new molecular state in ${}^{16}\text{C}$, possibly seen also in the previous experiments [24, 23], but with lower statistics.

References

- [1] W. Von Oertzen, M. Freer, and Y. Kanada-En'yo, *Phys. Rep.* **432** (2006) 43.
- [2] K. Ikeda, N. Tagikawa, and H. Horiuchi., *Prog. Theo. Phys. Suppl.* (1968) 464.
- [3] C. Beck, *Clusters in Nuclei* (Springer, Heidelberg, 2013), Vol. 1,2,3.
- [4] M. Livio *et al.*, *Nature* **340** (1989) 281.
- [5] M. Freer and H.O.U. Fynbo, *Prog. Part. Nucl. Phys.* **78** (2014) 1.
- [6] D.J. Marin-Lambarri *et al.*, *Phys. Rev. Lett.* **113** (2014) 012502.

- [7] W.R. Zimmermann *et al.*, *Phys. Rev. Lett.* **110** (2013) 152502.
- [8] W. Von Oertzen, *Zeit. Phys.* **A 357** (1997) 355.
- [9] Y. Kanada-En'yo, *J. Phys. G* **24** (1998) 1499.
- [10] H.T. Fortune and R. Sherr, *Phys. Rev.* **C 84** (2011) 024304.
- [11] N.I. Ashwood *et al.*, *Phys. Rev.* **C 68** (2003) 017603.
- [12] H.G. Bohlen *et al.*, *Phys. Rev.* **C 75** (2007) 054604.
- [13] D. Suzuki *et al.*, *Phys. Rev.* **C 87** (2013) 054301.
- [14] N. Soic *et al.*, *Europhys. Lett.* **34** (1996) 7.
- [15] N. Curtis *et al.*, *Phys. Rev.* **C 64** (2001) 044604.
- [16] M. Freer *et al.*, *Phys. Rev. Lett.* **96** (2006) 042501.
- [17] G.V. Rogachev *et al.*, *J. Phys.: Conf. Ser.* **569** (2014) 012004.
- [18] R. Wolski *et al.*, *Phys. At. Nucl.* **73** (2010) 1405.
- [19] M. Milin and W. von Oertzen, *Eur. Phys. J. A* **14** (2002) 295.
- [20] M. Freer *et al.*, *Phys. Rev.* **C 84** (2011) 034317.
- [21] I. Lombardo *et al.*, *Nucl. Instrum. Meth. Phys. Res.* **B 302** (2013) 19.
- [22] M. Freer *et al.*, *Phys. Rev.* **C 90** (2014) 054324.
- [23] P.J. Leask, *Jour. Phys. G: Nucl. Part. Phys.* **27** (2001) B9.
- [24] N. I. Ashwood *et al.*, *Phys. Rev.* **C 70** (2004) 0644607.
- [25] T. Baba, Y. Chiba and M. Kimura, *Phys. Rev.* **C 90** (2014) 064319.
- [26] I. Lombardo *et al.*, *Nuc. Phys.* **B 215** (2011) 272.
- [27] E. De Filippo and A. Pagano, *Eur. Phys. J. A* **50** (2014) 32.
- [28] A. Pagano *et al.*, *Nucl. Phys. News* **22** (2012) 25.
- [29] A. Pagano *et al.*, *Nucl. Phys.* **A 734** (2004) 504.
- [30] F. Porto *et al.*, *Acta Phys. Pol.* **B 31** (2000) 1489.
- [31] M. Freer *et al.*, *Phys. Rev.* **C 63** (2001) 034301.
- [32] A.G. Artyukh *et al.*, *Nucl. Exp. Tech.* **1** (2009) 19.
- [33] N. I. Ashwood *et al.*, *Phys. Rev.* **C 70** (2004) 024608.
- [34] S. Ahmed *et al.*, *Phys. Rev.* **C 69** (2004) 024303.
- [35] M. Freer *et al.*, *Phys. Rev. Lett.* **82** (1999) 1383.
- [36] A. Cunsolo *et al.*, *Phys. Rev.* **C 21** (1980) 2345.
- [37] G. R. Satchler, *Direct Nuclear Reactions* (Oxford University Press, New York, 1983), p. 553.
- [38] W.W. Wilcke *et al.*, *At. Data Nucl. Data Tab.* **25** (1980) 389.

New direct measurement of the $^{19}\text{F}(\text{p},\alpha_0)^{16}\text{O}$ reaction at very low energies

I. Lombardo^{1,2}, D. Dell'Aquila^{1,2}, A. Di Leva^{1,2}, I. Indelicato^{3,4}, M. La Cognata⁴, M. La Commara^{1,2}, A. Ordine², V. Rigato⁵, M. Romoli², E. Rosato^{1,2†}, G. Spadaccini^{1,2}, C. Spitaleri^{3,4}, A. Tumino^{4,6} and M. Vigilante^{1,2}

¹ Department of Physics, Federico II University of Naples, Naples, Italy

² INFN – Sezione di Napoli, Naples, Italy

³ Department of Physics and Astronomy, University of Catania, Catania, Italy

⁴ INFN – Laboratori Nazionali del Sud, Catania, Italy

⁵ INFN – Laboratori Nazionali di Legnaro, Legnaro (Padua), Italy

⁶ Faculty of Engineering and Architecture, Kore University of Enna, Enna, Italy

† *deceased*

Abstract

The $^{19}\text{F}(\text{p},\alpha_0)^{16}\text{O}$ reaction has been studied with two different experiments in Naples (0.6–1.0 MeV) and Legnaro (0.2–0.6 MeV). In this way a comprehensive view of the S -factor at low energy has been obtained. This reaction is relevant in Nuclear Structure, to study the ^{20}Ne compound nucleus, and in Nuclear Astrophysics, because is an important fluorine destruction channel in hydrogen rich stellar environments. Our works points out the role played by several low-energy resonances and confirms the presence of direct components in the S -factor. The R -matrix fit of experimental data allows us to perform the spectroscopy of ^{20}Ne excited states and to extrapolate the reaction rate at temperatures typical of the basis of the convective envelope of AGB stars.

1 Introduction

The first, pioneering, studies of α -particle emission in proton induced nuclear reactions on ^{19}F can be found in very old papers in Nuclear Physics [1-5]. These reactions can be distinguished in $^{19}\text{F}(\text{p},\alpha_0)^{16}\text{O}$ ($Q=8.114$ MeV), $^{19}\text{F}(\text{p},\alpha\pi)^{16}\text{O}_{6,05}$ ($Q=2.06$ MeV) and $^{19}\text{F}(\text{p},\alpha\gamma)^{16}\text{O}$ ($E_\gamma = 6.13, 6.92, 7.13$ MeV) [6]. The low energy ($E_p=0.5$ -2.0 MeV region) cross sections for all these three reaction branches show the presence of several resonances, testifying a quite large level density in the 13-15 MeV excitation energy region of the compound nucleus [5,6]. Typically, a state observed in the α_0 channel is also seen in the $\alpha\pi$ one, with some exceptions [6]. Despite the experimental efforts made in past times, the present knowledge of these reactions is still lacking in several parts. It is mainly based on the experimental works of Isoya et al [7], Clarke and Paul [5], Breuer [8], Ranken et al [9], Caracciolo et al [10], De Rosa et al [11], Cuzzocrea et al [12], Ouichaoui et al [13], Spyrou et al [14] A review on the spectroscopy of ^{20}Ne based on these and other works can be found in Tilley et al [6]. As pointed out by [6], ambiguities are still present in the spectroscopy of some natural parity states (for example the 13.522, 13.645 and 14.85 MeV states have uncertain J^π assignments).

Furthermore, the NACRE collaboration [15] has discussed the presence of discrepancies between the various data sets reported in the literature concerning the absolute cross section data of this reaction [16]. At low energies ($E_p \approx 0.5 - 0.7$ MeV), the data by Isoya *et al* and Breuer show discrepancies at 30% level or more; these discrepancies heavily influence the uncertainty level of low energy S -factor extrapolations and the consequent reaction rate determination, that is of the order of 50%, as discussed in Ref. [15]. Indeed, the accurate knowledge of this reaction cross section is important for Nuclear Astrophysics purposes. The nucleosynthesis of fluorine is an open problem in Astrophysics [17], and

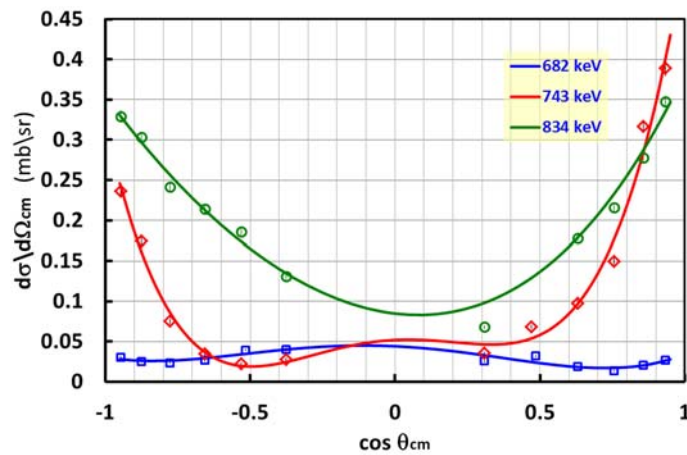


Fig. 1: Examples of three angular distributions obtained for the $^{19}\text{F}(p,\alpha)^{16}\text{O}$ reaction at $E_p = 0.682$, 0.743 and 0.834 MeV. Lines represent the results of Legendre Polynomial fits of data.

recent papers suggested that, in hydrogen-rich environments at the basis of the convective envelope of AGB stars, the $^{19}\text{F}(p,\alpha)^{16}\text{O}$ reaction can play a role in the destruction of fluorine by means of deep mixing processes [18-21].

In recent times, the need of new data has driven different groups to perform new experiments, by using both direct and indirect techniques. For example, a new measurement performed by using the Trojan Horse method [21,22] has suggested the presence of various low energy resonances. In particular, the $E_{\text{cm}}=113$ keV one is believed to highly influence the reaction rate value at temperatures near 0.6 GK, typical of AGB environments.

Considering all these discrepancies and the lack of low energy data, we performed two new direct measurements of the $^{19}\text{F}(p,\alpha)^{16}\text{O}$ reactions in the bombarding energy regions $E_p \approx 0.6-1.0$ MeV (experiment performed at the TTT3 tandem in Naples, Italy) and $E_p \approx 0.2-0.6$ MeV (experiment performed at the AN2000 Van de Graaf accelerator in Legnaro, Italy). In these proceedings we report some results of both experiments. The reader is referred to the more extended Refs. [23] and [24] for further details.

2 The $E_p \approx 0.6-1.0$ MeV experiment in Naples

The first of the two $^{19}\text{F}(p,\alpha)^{16}\text{O}$ cross section measurement was performed in Naples by using the TTT3 tandem [23,25,26]. The beam energy was varied from about 1.0 MeV down to 0.6 MeV in 10 keV steps. The accuracy in the beam energy determination was better than 0.2%, and the diameter of the beam spot on the target was less than 3 mm. The beam energy calibration was checked by investigating resonances in the elastic scattering of proton and α particles on ^{12}C and ^{16}O nuclei. A LiF layer ($94 \mu\text{g}/\text{cm}^2$ thick) evaporated on a thin carbon backing ($18 \mu\text{g}/\text{cm}^2$ thick) was used as target. The beam intensity was measured by means of a Faraday cup and the collected charge was determined with a digital current integrator. The detection system was made by an array of 12 silicon detectors, placed at 10-15 cm from the target centre. The detection system covered a broad range of polar angles in the laboratory frame, both in the forward and backward hemisphere ($20^\circ-70^\circ$ and $110^\circ-160^\circ$ in 10° steps). To suppress the high flux of elastically scattered protons we used thin Al absorbers ($14.5 \mu\text{m}$ thick) in front of detectors. Because of the high reaction Q -value (8.114 MeV), α particles emitted in the $^{19}\text{F}(p,\alpha)^{16}\text{O}$ reaction punch through the Al foils and are detected with 100% efficiency. The measured yields is transformed into absolute cross sections using standard equations. Examples of angular distributions obtained at various angles are reported in Figure 1.

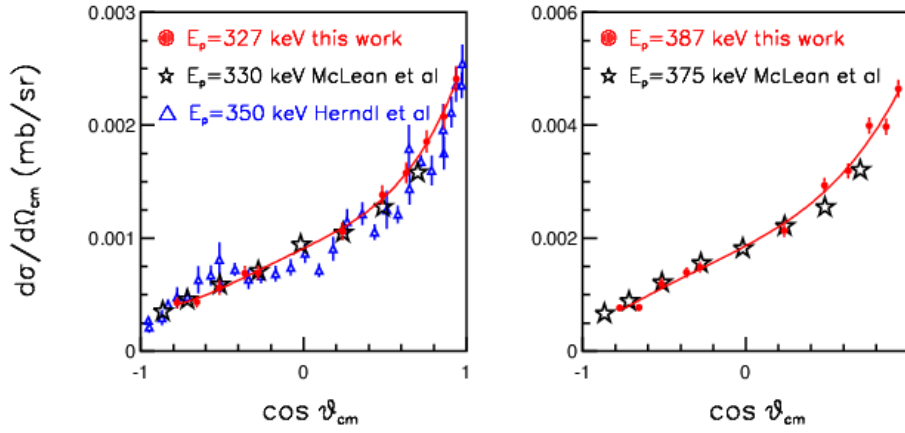


Fig. 2: Examples of angular distributions obtained for the $^{19}\text{F}(p,\alpha_0)^{16}\text{O}$ reaction at $E_p \approx 0.330, 0.380$ MeV. Full dots: results of the LNL experiment [24]. Triangles: data reported in [27]. Stars: data reported in Ref. [4]. Lines represents results of Legendre Polynomial fits of our data.

Examples of angular distributions are shown in Figure 1, where the continuous shape evolution as a function of energy testifies the contributions of different excited states in the compound nucleus. In particular, in the energy region here explored, large contributions are due to the $E_p = 842, 778, 733$ keV resonances (corresponding to ^{20}Ne states at $E_x = 13.642, 13.586, 13.544$ MeV, respectively). The analysis of angular distributions in terms of Legendre polynomials confirms the 2^+ assignment for the 778 and 733 keV resonances [6,7] and indicates $J^\pi = 0^+$ assignment for the 842 keV resonance, for which two different J^π assignments (0^+ and 2^+) have been reported in the literature [6,7,10]. Furthermore, the shape of angular distributions in the 820-850 keV region can be well reproduced by considering the overlap between the 842 keV state and a newly reported state (with tentative $J^\pi = 1^-$ assignment) at about 825 keV [23]. The integration of angular distributions allows us to derive the S -factor. Its behaviour as a function of energy is reported in Figure 3 as red triangles. The presence of resonant structures at energies corresponding to the previously mentioned excited states in ^{20}Ne can be recognized. In the $E_{\text{cm}} = 0.8$ MeV region ($E_x = 13.642$) our data are in good agreement with Caracciolo et al data [10] and Isoya et al data [7] as reported by NACRE [15]. In the $E_{\text{cm}} \approx 0.6-0.74$ MeV region our data are $\approx 30\%$ larger than the Isoya et al ones but matches well the absolute data by Breuer [8]. This last (and very old) data set pointed out (very tentatively) the possible existence of broad states at low energy ($E_{\text{cm}} \approx 0.4$ MeV), which can have some influence in the reaction rate determination at 0.5-0.7 GK. Furthermore, recent results based on the use of the Trojan Horse indirect technique [21,22] pointed out the important contribution of other low energy states at 380 and 113 keV ($E_x = 13.226$ and 12.957 MeV). Considering these suggestions, we decided to perform a new experiment aimed at exploring the low energy domain of this reaction, where very few results have been reported to date. The results of this experiment are discussed in the following section.

3 The $E_p \approx 0.2-0.6$ MeV experiment at LNL

The second experiment on the $^{19}\text{F}(p,\alpha_0)^{16}\text{O}$ reaction was performed at Laboratori Nazionali di Legnaro (LNL) by using the AN2000 single-ended van de Graaf accelerator [24]. The beam energy was varied from about 0.6 MeV down to 0.2 MeV in ≈ 20 keV steps. The maximum beam energy spread was ± 2.5 keV. The beam energy calibration was determined by scanning the 340 keV resonance in the $^{19}\text{F}(p,\alpha\gamma)$ reaction and the 992 keV resonance in the $^{27}\text{Al}(p,\gamma)$ reaction. CaF_2 layers ($30 \mu\text{g}/\text{cm}^2$ thick) evaporated on a thin carbon backing ($20 \mu\text{g}/\text{cm}^2$ thick) were used as reaction targets; they were frequently replaced to prevent degradation. Target thickness was estimated by means of the resonating quartz method; it

was subsequently cross-checked with dedicated elastic backscattering analysis. These analyses also pointed out a natural stoichiometry of the CaF₂ layer, as seen in [28].

The detection system was an array of 12 silicon detectors (covering the 20°-160° polar angular range) and placed 10 – 12 cm far from the centre of the target. The detectors thickness was 300 μm. 8 μm thick aluminium absorbers were used to stop scattered protons. The detection system was operated in high vacuum (better than 10⁻⁶ mbar). Absolute cross section measurements were obtained by using a Faraday Cup equipped with an electrostatic suppressor ring (-300V bias). Absolute normalizations were checked by means of an unshielded silicon detector placed at 160° monitoring the p+Ca elastic scattering whose cross section follows the Rutherford prediction in this low energy domain. Examples of α energy spectra obtained with the present array are reported in Figure 1 of Ref. [24]. The large *Q*-value of this reaction allowed us to unambiguously identify the peak due to the ¹⁹F(p,α₀)¹⁶O reaction.

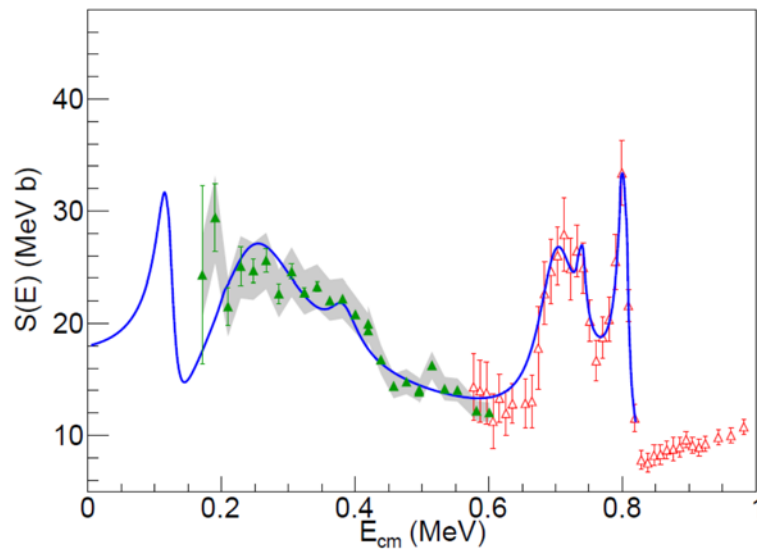


Fig. 3: ¹⁹F(p,α₀)¹⁶O *S*-factor obtained in the first experiment in Naples (red open triangles) and in the second one in Legnaro (green filled triangles). For the LNL data, the grey band indicates non statistical errors. The blue line is the result of the *R*-matrix fit of the whole data set. Further details can be found in Refs. [23,24].

Examples of angular distributions obtained at $E_p = 0.387$ and 0.327 MeV are reported as red dots in Figure 2. They have been compared with the (very few) data available in the literature at similar energies. Stars represent the data reported by Mc Lean, Ellett and Jacobs [5], while triangles are the data reported by Herndl et al [27]. Both the data sets have been normalized to match our absolute cross section scale. A very good agreement between the various data sets can be observed. The shape of angular distributions in this energy domain is quite peculiar, showing a strong forward-peaked anisotropy. This finding can be attributed both to the presence of direct processes at sub-Coulomb energies (possibly triggered by the $t+^{16}\text{O}$ or the $\alpha+^{15}\text{N}$ cluster structure in ¹⁹F) [27,29,30] or to the interference between close-lying states with opposite parities [7,8,10]. In Ref. [25] we analysed the energy evolution of the shapes of angular distributions and we find that both the effects can be simultaneously present in the energy region here explored.

Starting from the experimental angular distributions, we can estimate the integrated cross section and the *S*-factor. The results are shown in Figure 3 as green stars with bars (statistical errors) and grey band (non-statistical error), together with the results of the previous experiment discussed in Section 2. The two measurements matches quite well in their overlap region. To obtain information about the spectroscopy of ²⁰Ne states involved in this energy region, we performed an *R*-matrix fit of the whole

data set, shown as solid blue line in Figure 3. A non-resonant background of the same functional form as reported by NACRE has been included in the fit. We can observe important contributions given by the $E_x = 13.642, 13.586, 13.544$ MeV states, as pointed out in the previous section, together with the contributions of the lower excited states at $E_x = 13.226, 13.095$ MeV. At very low energy, we included also the $E_x = 12.957$ MeV state, as pointed out by recent analyses performed with the Trojan Horse Method [21,22]. The fit reproduces reasonably well the data in the whole domain; the only free parameters of the fit were the scaling factor of the direct contribution and the strength of the 250 keV resonance. The other resonance parameters have been fixed to the values reported in Refs. [21,22]. A strong contribution, due to the broad ($I^\pi=162$ keV, $J^\pi=2^+$) 13.095 MeV state can be observed. This state interferes with the 12.957 MeV 2^+ state at low energy, resulting in a typical interference pattern that enhance the cross section of the high energy tail of the 13.095 MeV resonance, in agreement with the experimental data.

Starting from the R -matrix fit here discussed, we calculated the reaction rate and we compared it to the extrapolations reported by NACRE. We observed an important enhancement of the reaction rate in the 0.4 and 0.08 GK regions, respectively due to the contributions of the 13.095 and 12.957 MeV states. In these temperature regions, the resulting reaction rate is a factor 1.5-2 larger than the NACRE extrapolation. This finding can indicate a more efficient destruction way of fluorine in hydrogen rich stellar environment, in the same direction of some recent stellar observation of abundance of fluorine in metal poor AGB stars.

4 Conclusions

In this paper we briefly report results obtained in two different experiments aimed at exploring the behavior of the $^{19}\text{F}(p,\alpha_0)^{16}\text{O}$ reaction in the 0.2-1.0 MeV energy domain, a region where very few data are present in the literature. The first experiment was performed in Naples and explored the 0.6-1.0 MeV bombarding energy region. We obtained improved spectroscopic information for excited states in ^{20}Ne in the 13.55-13.65 MeV excitation energy domain, pointing out the possible evidence of a new 1^- state at $E_x=13.628$ MeV. The second experiment was performed at Laboratori Nazionali di Legnaro and covered the 0.2-0.6 MeV range. In this case we observed contributions due to states at 13.095 and 13.226 MeV, together with a hint on the contribution given by the low energy 12.957 MeV state, seen also with the Trojan Horse Method. A R -matrix fit of the whole data set allowed us to determine the S -factor in a broad energy domain; starting from this fit it was possible to obtain an improved estimate of the reaction rate at temperatures typical of AGB stars, with a result 1.5-2 times larger than the NACRE predictions.

Acknowledgements

We wish to thank E. Perillo and G. Imbriani (Univ. Napoli) for enlightening discussions on the subjects of this work. We acknowledge gratefully L. Campajola (Univ. Napoli) and L. La Torre (INFN-LNL) for delivering good quality proton beams, and M. Borriello, M. Avellino, L. Roscilli, R. Rocco (INFN-Napoli) for their support during the mounting phase of the experiments.

References

- [1] J.D. Cockroft and E.T.S. Walton, *Proc. Roy. Soc. A* **137** (1932) 229.
- [2] W.E. Burcham and S. Devons, *Proc. Roy. Soc. A* **137** (1939) 555.
- [3] J.F. Streib, W.A. Fowler, and C.C. Lauritsen, *Phys. Rev.* **59** (1941) 253.
- [4] W.B. McLean, A. Ellett, and J.A. Jacobs, *Phys. Rev.* **58** (1940) 500.
- [5] R.L. Clarke and E.B. Paul, *Can. J. Phys.* **35** (1957) 155.
- [6] D.R. Tilley et al, *Nucl. Phys.* **A 636** (1998) 249.
- [7] A. Isoya, H. Ohmura, and T. Momota, *Nucl. Phys.* **7** (1958) 116.

- [8] G. Breuer, *Zeit. Phys.* **154** (1959) 339.
- [9] W.A. Ranken, T.W. Bonner and J.H. McCrary, *Phys. Rev.* **109** (1958) 1646.
- [10] R. Caracciolo *et al*, *Lett. Nuovo Cim.* **11** (1974) 33.
- [11] A. De Rosa, E. Perillo *et al*, *Nuovo Cim. A* **44** (1978) 433.
- [12] P. Cuzzocrea *et al*, *Lett. Nuovo Cim.* **28** (1980) 515.
- [13] S. Ouichaoui *et al*, *Nuovo Cim. A* **86** (1985) 170.
- [14] K. Spyrou *et al*, *Eur. Phys. Jour. A* **7** (2000) 79.
- [15] C. Angulo *et al*, *Nucl. Phys. A* **656** (1999) 3.
- [16] M. Wiescher, J. Gorres, and H. Schatz, *J. Phys. G* **25** (1999) R133.
- [17] S. Cristallo *et al*, *Astr. Astr. A* **46** (2014)570.
- [18] S. Lucatello *et al*, *Astr. Jour.* **729** (2011) 40.
- [19] V.V. Smith *et al*, *Astr. Jour.* **633** (2005) 392.
- [20] C. Abia *et al*, *Astr. Jour. Lett.* **737** (2011) L8.
- [21] M. La Cognata *et al*, *Astr. Jour. Lett.* **739** (2011) L54.
- [22] M. La Cognata *et al*, *Astr. Jour.* **805** (2015) 128.
- [23] I. Lombardo *et al*, *J. Phys. G* **40** (2013) 125102.
- [24] I. Lombardo *et al*, *Phys. Lett. B* **748** (2015) 178.
- [25] I. Lombardo *et al*, *Nucl. Instrum. Meth. Phys. Res. B* **302** (2013) 19.
- [26] I. Lombardo *et al*, *J. Phys. Conf. Ser.* **569** (2014) 012068.
- [27] H. Herndl *et al*, *Phys. Rev. C* **44** (1991) R952.
- [28] A. Couture *et al*, *Phys. Rev. C* **77** (2008) 015802.
- [29] Y. Yamashita and Y. Kudo, *Prog. Theor. Phys.* **90** (1993) 1303.
- [30] G. Raimann *et al*, *Phys. Lett. B* **249** (1990) 191.

Isospin Character of Low-Lying Pygmy Dipole States via Inelastic Scattering of ^{17}O

F.C.L. Crespi

Università degli Studi di Milano and INFN, I-20133 Milano, Italy

Abstract

The γ decay from the pygmy states was measured in ^{208}Pb , ^{124}Sn and ^{90}Zr nuclei using the inelastic scattering of ^{17}O at 340 MeV. The emitted γ rays were detected with high resolution with the AGATA demonstrator array and the scattered ions were detected in two segmented ΔE -E silicon telescopes. The multipolarity of the observed gamma transitions was determined with remarkable sensitivity thanks to angular distribution measurements. Cross sections and angular distributions of the γ rays and of the scattered particles were measured. The results are compared with (γ, γ') and (p, p') data. The data analysis with the distorted wave Born approximation approach gives a good description of the elastic scattering and of the inelastic excitation of the 2^+ and 3^- states. For the dipole transitions, a form factor obtained by folding a microscopically calculated transition density was used for the first time. This has allowed us to extract the isoscalar component of the 1^- excited states.

1 Introduction

The electric dipole (E1) strength in atomic nuclei is dominated by the extensively studied isovector giant dipole resonance (IVGDR). For neutron rich nuclei the E1 response is characterized by concentrations of strength, denoted as pygmy dipole resonance (PDR) or pygmy states, around and below the particle separation energy [1]. One important open problem for pygmy states is the cross section sensitivity to transition densities containing the nuclear structure information. To explore this one needs high-resolution measurements and comparison of data obtained with different probes. In particular, nuclei with sizable neutron skin, such as the doubly magic ^{208}Pb , are very interesting. The PDR is also expected to reflect the properties of the neutron skin [2–8] and in turn, this is relevant information to constrain the equation of state of neutron rich matter.

2 Experimental Technique

We performed inelastic scattering experiments using a ^{17}O beam at the energy of 20 MeV/u provided by Tadem-ALPI accelerator complex at the LNL-INFN laboratory. Different target nuclei were studied [9–15]: ^{208}Pb , ^{124}Sn and ^{90}Zr and ^{140}Ce . The scattered ^{17}O ions were detected using two segmented silicon ΔE -E telescopes [16,17] that were placed symmetrically with respect to the beam direction. These detectors have an energy resolution of about 0.3% at 340 MeV allowing a good separation of the oxygen isotopes. The gamma decay of the pygmy dipole states was measured with high resolution in coincidence using the AGATA demonstrator [17,18] (our experimental setup is schematically displayed in the lower right panel of Fig. 1). In the upper-left panel of Fig. 1 AGATA gamma spectra, for the case of the ^{208}Pb target, are shown in the 4.5–8 MeV range. These spectra are obtained requesting the ^{17}O inelastic scattering channel and that the energy detected in AGATA be equal to the Total Kinetic Energy Loss (TKEL) in the silicon detectors, this latter condition allows selecting transitions to the ground state. Furthermore the spectra were Doppler corrected for the recoil velocity. Furthermore, an unfolding

procedure [19] was applied to both spectra to suppress the escape peaks and most of the Compton background. The difference among the red “E1” and the blue “E2” spectrum is in the additional gating condition on the angle between the direction of the recoil and of the emitted gamma ray. In the red line spectrum the angular range 65° - 115° is selected (corresponding to a region in which the E1 multipolarity is maximized), while in the blue spectrum the angular range 15° - 65° is selected (corresponding to a region in which the E2 multipolarity is maximized). For comparison in the lower-left panel the $B(E1)\uparrow$ (red bars) and $B(E2)\uparrow$ (blue bars) strength distributions, obtained in (γ,γ') experiments are shown [20,21]. The measured angular distribution of the most intense E1 γ -ray transition in the pygmy region of ^{208}Pb is shown in the upper right panel.

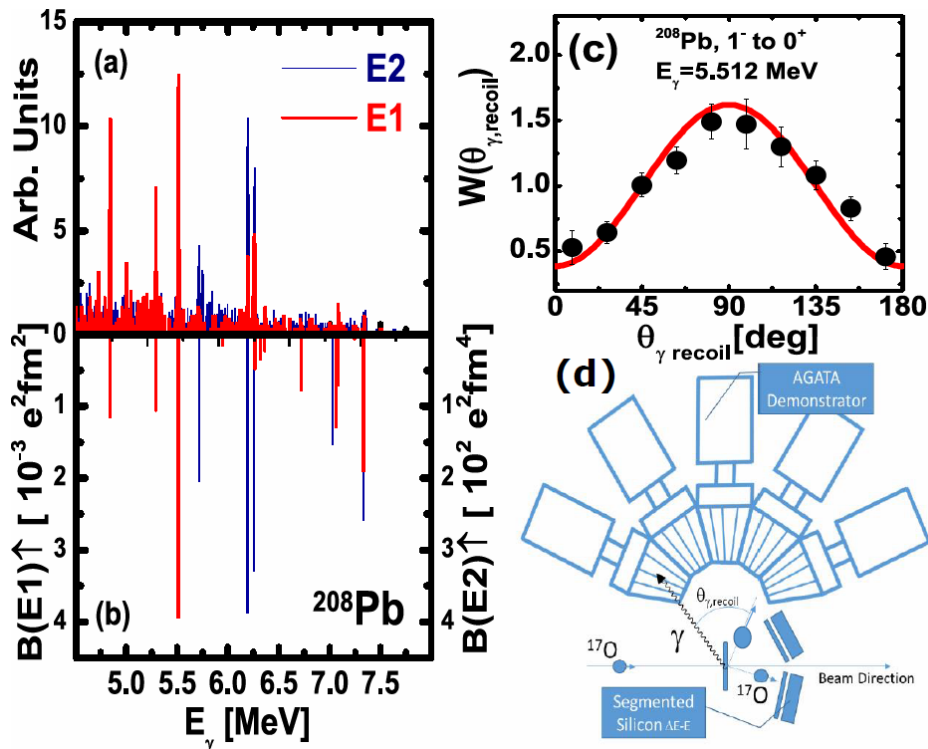


Fig. 1: (Color online) Panel (a): Gamma-ray spectra for ^{208}Pb displayed in the 4.5–8 MeV region, with a condition on the angle between the emitted γ -ray and the recoil direction which enhances the E1 decays (red line) and E2 decays (blue line). Panel (b): The $B(E1)\uparrow$ (red bars) and $B(E2)\uparrow$ (blue bars) strength distributions, obtained in (γ,γ') experiments [20,21]. Panel (c): The angular distribution of 5.512 MeV E1 γ -ray transitions of ^{208}Pb . Panel (d): Schematic representation of the experimental setup including segmented silicon detectors placed at forward angles and the AGATA HPGe detectors. The angle $\theta_{\gamma, \text{recoil}}$ between the direction of the recoiling ^{208}Pb ions (dashed line) and of the gamma-ray (when a scattered ^{17}O is detected in the right silicon telescope) is displayed. Figures adapted from [9].

3 Data Analysis

The measured angular distributions of the scattered ^{17}O ions were analysed performing DWBA calculations using the code FRESKO [22]. The first step was to calculate the elastic scattering cross section, this optical model calculations permitted to determine the absolute normalization of the data. We describe here the case of the $^{17}\text{O}+^{90}\text{Zr}$ reaction since these are the more recent results: the optical model parameters of Saxon-Woods potentials providing the best fit to the data used correspond to

$V=40.0$ MeV, $W=26$ MeV (with V and W the depth of the real and imaginary potentials), $rv=rW=1.15$ fm, $aV=aW=0.671$ fm (the radii and diffuseness of the real and imaginary parts) and $rC = 1.20$ fm (the Coulomb radius parameter). These are consistent with previous measurements at similar energy [23,24].

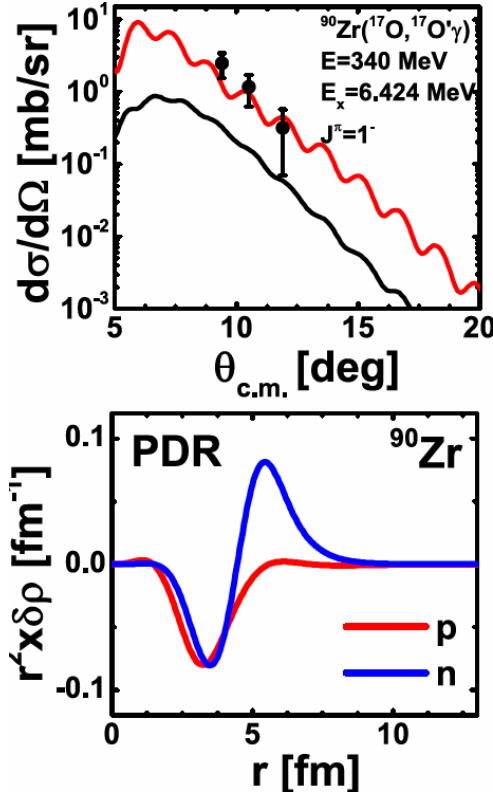


Fig. 2: (Top) Inelastic scattering cross section $^{90}\text{Zr}(^{17}\text{O},^{17}\text{O}'\gamma)^{90}\text{Zr}^*$ at 340 MeV for the 1^- state 6.424 MeV. The error bars are the statistical errors. The lines show DWBA calculations. The black solid curve represents the calculations with the standard phenomenological form factor. The red solid line includes the nuclear contribution calculated with the microscopic form factor derived with the transition density shown in the bottom panel. Figure adapted from [9,12].

The DWBA calculations for the differential cross section of the pygmy dipole states obtained using the standard collective model form factor for the nuclear part and the $B(E1)\uparrow$ value from (γ,γ') measurements are in a strong disagreement with the experimental data. The result of this calculation is shown with the black line in the upper panel of Fig. 2. In particular, in the figure it can be seen from the comparison with the experimental data that only for a fraction of the measured yield is accounted for. In order to make a more realistic calculation for the pygmy dipole states a microscopic form factor was obtained for $^{17}\text{O}+^{90}\text{Zr}$, by using a double folding procedure with an M3Y nucleon-nucleon interaction [25-28]. This form factor is derived from the transition density [25-28] that is shown in the lower panel of Fig. 2. The DWBA calculation performed using this form factor for the nuclear part allows to reproduce well the data. Using this procedure it was also possible also to extract the value of isoscalar dipole (ISD) EWSR associated to the pygmy states. The same kind of DWBA analysis has been applied to the data acquired also with ^{208}Pb and ^{124}Sn target [9-15]. In all the studied nuclei the observed behaviour is similar to what was found using the (α,α') reaction [29,30]: a number of states concentrated in the lower energy part of the spectrum are better populated via $(^{17}\text{O},^{17}\text{O}')$, while the higher lying group of states of isovector nature are suppressed in the isoscalar channel.

This form factor is derived from the transition density [25-28] that is shown in the lower panel of Fig. 2. The DWBA calculation performed using this form factor for the nuclear part allows to reproduce well the data. Using this procedure it was also possible also to extract the value of isoscalar dipole (ISD) EWSR associated to the pygmy states. The same kind of DWBA analysis has been applied to the data acquired also with ^{208}Pb and ^{124}Sn target [9-15]. In all the studied nuclei the observed behaviour is similar to what was found using the (α,α') reaction [29,30]: a number of states concentrated in the lower energy part of the spectrum are better populated via $(^{17}\text{O},^{17}\text{O}')$, while the higher lying group of states of isovector nature are suppressed in the isoscalar channel.

4 Summary and Conclusions

The inelastic scattering of the ^{17}O ions at 20 MeV/u was used to populate the pygmy states in ^{90}Zr , ^{208}Pb and ^{124}Sn nuclei. The differential cross section for the dipole transition was reproduced using a form factor obtained by folding a microscopically calculated transition density associated to the pygmy states. This allowed extracting the isoscalar component of the 1^- excited states.

References

- [1] D. Savran, T. Aumann, and A. Zilges, Prog. Part. Nucl. Phys. 70, 210 (2013)
- [2] A. Klimkiewicz et al., Phys. Rev. C 76, 051603 (2007)

- [3] A. Carbone, G. Col, A. Bracco, L.-G. Cao, P. F. Bortignon, F. Camera, and O. Wieland, Phys. Rev. C 81, 041301(R) (2010).
- [4] O. Wieland et al., Phys. Rev. Lett. 102, 092502 (2009)
- [5] A. Tamii et al., Phys. Rev. Lett. 107, 062502 (2011)
- [6] X. Roca-Maza, G. Pozzi, M. Brenna, K. Mizuyama, and G. Colò, Phys. Rev.C 85, 024601 (2012)
- [7] X. Viñnas, M. Centelles, X. Roca-Maza, and M. Warda, Eur. Phys. J. A 50, 27(2014)
- [8] N. Paar, D. Vretenar, E. Khan, and G. Col'ò, Rep. Prog. Phys. 70, 691 (2007)
- [9] A. Bracco, F.C.L. Crespi and E. Lanza Eur. Phys. J. A 51, 99(2015)
- [10] F.C.L. Crespi, et al., Phys. Rev. Lett. 113 (2014) 012501
- [11] L. Pellegri, et al. Phys. Lett. B 738, 519 (2014).
- [12] F.C.L. Crespi et al., Phys. Rev. C 91, 024323 (2015)
- [13] M. Krzysiek et al., Phys. Scr. 89, 054016 (2014)
- [14] L. Pellegri et al., Phys. Rev. C 92, 014330 (2015)
- [15] A. Bracco, F.C.L. Crespi, EPJ Web of Conferences 38, 03001 (2012)
- [16] D. Mengoni et al., Nucl. Instrum. Methods Phys. Res., Sect. A 764, 241 (2014)
- [17] A. Gadea et al., Nucl. Instrum. Methods Phys. Res., Sect. A 654, 88 (2011)
- [18] S. Akkoyun et al., Nucl. Instrum. Methods Phys. Res., Sect. A 668, 26, (2012)
- [19] D. C. Radford, I. Ahmad, R. Holzmann, R. V. F. Janssens, and T. L. Khoo, Nucl. Instrum. Methods Phys. Res., Sect. A 258, 111 (1987).
- [20] N. Ryezayeva et al., Phys. Rev. Lett. 89, 272502 (2002).
- [21] T. Shizuma et al., Phys. Rev. C 78, 061303 (2008).
- [22] I. J. Thompson, Comput. Phys. Rep. 7, 167 (1988)
- [23] J. R. Beene, F. Bertrand, M. Halbert, R. Auble, D. Hensley, D. Horen, R. Robinson, R. Sayer, and T. Sjoreen., Phys. Rev. C 39, 1307 (1989)
- [24] D. J. Horen et al., Phys. Rev. C 44, 128 (1991)
- [25] E.G. Lanza et al., Phys. Rev. C 79, 054615 (2009)
- [26] E. Lanza et al., Phys. Rev. C 84, 064602 (2011)
- [27] E.G. Lanza et al., Phys. Rev. C , 054607 (2015)
- [28] E.G. Lanza et al., Phys. Rev. C 89, 041601 (2014)
- [29] D. Savran et al., Phys. Rev. Lett. 100, 232501 (2008)
- [30] J. Endres et al., Phys. Rev. Lett. 105, 212503 (2010)

Pre-equilibrium (exciton) model and the heavy-ion reactions with cluster emission

E. Běták^a, J. Cseh^b

^a Institute of Physics SAS, Dúbravská cesta 9, 84511 Bratislava, Slovakia

^b MTA ATOMKI, Bem tér 18/c, P.O.B. 51, 4001 Debrecen, Hungary

Abstract

We bring the possibility to include the cluster emission into the statistical pre-equilibrium (exciton) model enlarged for considering also the heavy ion collisions. At this moment, the calculations have been done without treatment of angular momentum variables, but all the approach can be straightforwardly applied to heavy-ion reactions with cluster emission including the angular momentum variables. The direct motivation of this paper is a possibility of producing the superdeformed nuclei, which are easier to be detected in heavy-ion reactions than in those induced by light projectiles (nucleons, deuterons, α -particles).

1. Introduction

Original pre-equilibrium exciton model was formulated for reactions induced by light projectiles (nucleons to α 's) and the nucleon emission only (see, e.g., [1]). Emission of complex particles (light clusters) [3, 2, 4], γ 's [5, 6] and of the calculation of the initial stage of heavy-ion induced reaction (using the ideas of [7]) enabled also the inclusion of this class of reactions [8, 9].

Cluster emission, however, has been relatively intact by this effort. A way out uses the so-called Iwamoto-Harada(-Bisplinghoff) coalescence model [10, 11], which is of general nature suitable for different sorts of emitted clusters. The application of spin-dependent formulation has shown an improvement both of the form of energy spectra and of their absolute value in nucleon- and α -induced reactions [12]. To apply such approach to heavy-ion reactions, the initial configuration should be expressed not only specifying the exciton number(s), but also the distribution over allowed spins of the composite nonequilibrium system [13]. With this extension, we are able to calculate (at least some types of) the heavy-ion collisions with cluster emission. Doing that, anyway, one should keep in mind that the model is very crude and it does not enable to catch all detailed features of the process.

Apart from purely theoretical arguments to see, how the idea of pre-equilibrium model in its exciton version works for heavy-ion induced reactions, there is a pragmatic call from the side of nuclear structure, namely the superdeformed and/or hyperdeformed (and — possibly — also other) nuclei of exotic shapes. There are some indications of possible existence of superdeformed nuclei of mass $A \leq 40$ in reactions induced by heavy ions (light heavy ions).

The study of exotic nuclear shapes, in particular extreme deformation, is an interesting chapter of the present-day research. Superdeformed (SD) states (with approximate ratio of the major axes of 2:1:1) have been observed in several nuclei, while the appearance of hyperdeformation (HD), i.e. ellipsoidal shape of 3:1:1 is a hot topic for a discussion. Especially interesting is their existence in the $N = Z$ nuclei, in which the role of pairing, quartering, isospin, etc. can be studied.

As for the appearance of these shape isomers, usually different structure calculations give the same, or very similar results, thus providing us with a reliable prediction. Typically applied methods are those of the large-scale shell model, Nilsson-model, mean-field theories, cluster models, antisymmetrized molecular dynamics, etc.

Concerning the question of which reaction channels can populate these shape isomers, the answer is much less available. Not only reaction studies are missing, but also the connection between the structure and reaction channels is hardly known. In this respect a new symmetry-based method seems to be promising.

This method applies Nilsson-model in combination with quasi-dynamical SU(3) symmetry considerations. The shape isomers are obtained from a selfconsistency calculation concerning the quadrupole shape, or SU(3) symmetry [14, 15]. The results are usually in very good agreement with the results of the traditional energy-minimum calculations. The main advantage of this approach is that the SU(3) selection rule connects the shape isomers to binary clusterizations, i.e. to reaction channels [16]. In this way the likely reactions to populate the SD, HD, etc. states can be determined from the structure viewpoint.

The reason why this surprisingly simple method works is twofold [17]: *i*) On the one hand the SU(3) symmetry, which is known to be a good approximate symmetry in the ground-state region, but it breaks down with increasing excitation, rebuild again for the SD, HD, etc, shapes (sometimes even better than for the ground states); *ii*) Furthermore, the relation of the shell and cluster structure, which is usually very simple in the ground state, but becomes complicated with increasing excitation energy, simplifies again for those shapes which have comensurate axes.

2. Pre-equilibrium models and the Iwamoto-Harada coalescence model

We benefit from the fact that the pre-equilibrium exciton model, especially in its master-equation version, has very high level of generalization irrespective of changing the reaction mechanism, as both the (equilibrated) compound nucleus and the fast direct reactions may be considered as limit cases of the model. Obviously, one has to pay for this consistency by losing many details, as it is the case in all statistical approaches.

As for the cluster emission, two diametrically different models were proposed within pre-equilibrium formalisms in early 70ths, namely the idea of preformed α -particles [3] and different versions of coalescence models; the first really applicable of them was the one by C.K. Cline [2]. The main difference between the two approaches stems from the fact that the α -particle is a very compact entity, and it can be considered as one exciton (with specific mass, spin, etc.), whereas nucleons in coalescence models are all equal, and creating of a cluster by nucleon coalescence is a specific process which is essential for this group of approaches.

As the nucleons within α -particles are much stronger coupled together than in any other near-by nucleus, the idea cannot be generalized to different types of clusters. On the other hand, the coalescence model can be adapted to any light cluster from weakly-bound deuterons to strongly coupled α 's, and with some problems even to heavier clusters. We shall use the so-called Iwamoto-Harada (IH) coalescence model below, as it is probably the most justified one of the group of coalescence approaches.

2.1 Iwamoto-Harada-(Bisplinghoff) coalescence model

The basic idea of the IH model (and similar ones) is that not only excited nucleons can group together to form clusters, but both the excited ones as well as those from unexcited Fermi sea [11, 10], i.e., the model includes a kind of statistical description of pickup.

In the following, we follow the notation of [10], which is fully consistent with the density-of-states concept inherent to the exciton model. Within the old coalescence model [4], the cluster emission

rates of a cluster of type x are proportional to

$$\gamma_x \frac{\omega(p - p_x, h, U)}{\omega(p, h, E)} \frac{\omega(p_x, 0, \varepsilon_x + B_x)}{g_x}, \quad (1)$$

where p_x and g_x are the number of nucleons composing the cluster and the single-cluster density, respectively, γ_x is the probability to form the cluster from given excitons and $\omega(p, h, E)$ is the density of states of p particles and h holes at excitation energy E . Further-on, U is the residual energy, ε_x the energy of the emitted cluster and B_x its binding energy in the composite system.

In the IH model, the density product $\omega(p - p_x, h, U)\omega(p_x, 0, \varepsilon_x + B_x)$ is replaced by the folding expression

$$\sum_{p^*=1}^{p_x} \int_{\varepsilon_x + B_x} \omega(p - p^*, h, E - \varepsilon_1) \omega(p^*, 0, \varepsilon_1) \omega(0, p_x - p^*, \varepsilon_2) d\varepsilon_1, \quad (2)$$

where p^* is the number of excitons contributing to the forming of the cluster, and the remaining ($p_x - p^*$) nucleons are picked up from the Fermi sea. The cluster density g_x is proportional to the cluster formation probability γ_x [10], what makes the formulation of the problem — as far as complex particles (clusters) concerns — **parameterless** (!!).

Further improvements or generalizations of the model included the Bisplinghoff's suggestion [18] that not all nucleons are available for the cluster formation, but only those close to the Fermi energy, and the energy width of the "band of availability" is determined by the binding energy of nucleons within the cluster [18]. As the binding energy of nucleons in a deuteron is small, the pickup possibility of nucleon coalescence to form a deuteron is of minor effect. Thus, strongly bound entities like α 's, have large energy space available for pickup (which makes the approach close to the original ideas [10, 11]), whereas the loosely coupled objects (e.g. deuterons) get rather close to the standard coalescence model (see [19]).

Updates of the model include the modification to keep the consistency between the compound nucleus (Weisskopf-Ewing) formulae and the exciton model [20] not only for nucleons, but also for the cluster emission [19, 21], statistical "equivalent" of knockout [21] and some others [21, 22].

3. Heavy-ion induced reactions and the exciton model

The main problem of being able to calculate the pre-equilibrium emission from heavy ion reactions using the exciton model is to find a feasible way to get the initial exciton configuration. Essentially, this can be done by calculating the overlap of the colliding nuclei in their momenta space [7, 8]. For practical use, however, a simple empirical formula is preferred instead of trajectory and overlap calculations.

For not too high energies, the suitable one for the initial exciton number is

$$\frac{n_0}{A_P} = 0.09 + \left(0.38 - 0.08 \cdot \frac{A_T - A_P}{A_T + A_P} \right) \cdot \sqrt{\frac{E_{cm} - V_C}{A_P}}, \quad (3)$$

where V_C is the Coulomb barrier and the subscripts T and P denote the target and projectile, respectively [23]¹.

One important step was introduced later, namely the phenomenological way to account for the projectile breakup [24]. The formulae presented therein are surprisingly stable and practically independent of the binding energy of nucleons within the cluster, reaction energy etc. Therefore we dared

¹The formula assumes that $A_P \leq A_T$.

to introduce projectile breakup in our calculations using this suggestion, even though the breakup part should be taken with high care.

3.1 Heavy-ion reactions calculations using the exciton model with angular momentum

The inclusion of angular momentum is essential mainly for proper treatment of γ de-excitation and in the heavy-ion collisions. It was introduced into the pre-equilibrium calculations by Obložinský and Chadwick [25] and applied in the PEGAS computer code [26]. However, only the nucleon- and/or α -particle-induced reactions were considered at that time.

The idea on how to express appeared in [13], namely that one has to subtract the double nuclear system rotational energy from the available energy in the calculation of the initial exciton configuration n_0 ,

$$E'_{\text{cm}}(l) = E_{\text{cm}} - E_{\text{rot}}(l), \quad (4)$$

and it was soon implemented in the updated versions of computer codes (see, e.g., [27]).

However, all this was only for the nucleon and γ emission only. Here we report on the first attempts to consider pre-equilibrium (exciton model) cluster emission in heavy-ion collisions.

4. Super- and hyperdeformed nuclei and the choice of reaction

We take ^{36}Ar , where the calculations predict its existence also in super- and hyperdeformed state [14]. We sketch here, how the superdeformed and the hyperdeformed states of the ^{36}Ar nucleus can be populated in a single-alpha-emitting reaction, namely $^{20}\text{Ne}+^{20}\text{Ne} \rightarrow ^{36}\text{Ar}(\text{SD}) + \alpha$ and $^{20}\text{Ne}+^{20}\text{Ne} \rightarrow ^{36}\text{Ar}(\text{HD}) + \alpha$.

The U(3) selection rule has to be applied, and the relevant quantum numbers are [14]: ^{20}Ne : [12,4,4], $^{36}\text{Ar}(\text{SD})$: [32,16,8], $^{36}\text{Ar}(\text{HD})$: [48,8,8], ^4He : [0,0,0]. The following sets of equations express the matching of the structural and reaction symmetries [28]:

$$[12, 4, 4] \otimes [12, 4, 4] \otimes [16 + i, 0, 0] = [32, 16, 8] \otimes [0, 0, 0] \otimes [i, 0, 0] \oplus \dots \quad (5)$$

for the SD state, and

$$[12, 4, 4] \otimes [12, 4, 4] \otimes [24 + j, 0, 0] = [48, 8, 8] \otimes [0, 0, 0] \otimes [j, 0, 0] \oplus \dots \quad (6)$$

for the hyperdeformed state, where the minimum of the relative motion quantum numbers of $[n,0,0]$ is determined by the Pauli-principle: $i, j = 8, 9, 10, \dots$

5. Results of reaction calculations

As suggested above, we have taken $^{20}\text{Ne}+^{20}\text{Ne}$ collision leading to the ^{40}Ca composite system (composite system = system generally not in equilibrium), which after the emission of α particle (or two deuterons, or a deuteron plus neutron plus proton, or two neutrons and two protons in arbitrary order) transforms into ^{36}Ar , which is assumed to exist also in a superdeformed and also in hyperdeformed shape. For the very beginning, we have taken more simple (and faster) calculation without considering the angular momentum variables, just to see, how the yields vary with choosing different emission sequence and how the competition of channels depends on energy. This is to enable to estimate the best region for population of ^{36}Ar .

Fig. 1 brings the energy dependence of the ^{36}Ar production cross section from the $^{20}\text{Ne}+^{20}\text{Ne}$ reaction, together with contributions of different reaction chains, at this time not yet considering angular

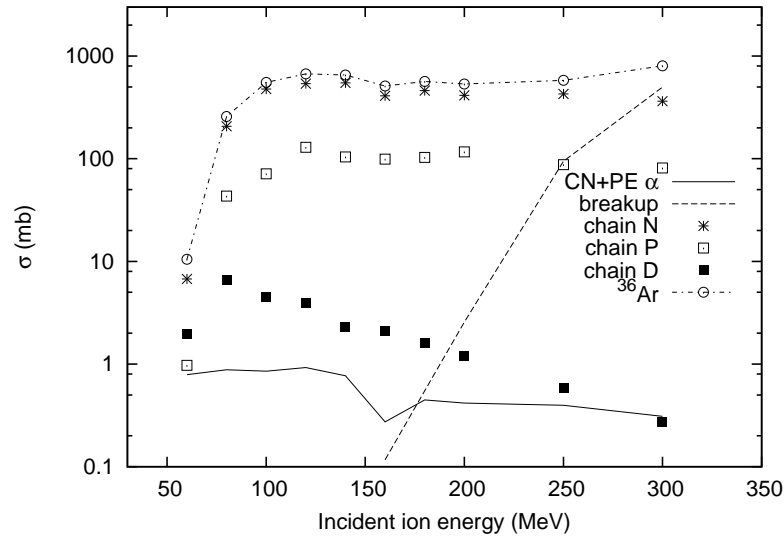


Fig. 1: Calculated cross section of ^{36}Ar production in $^{20}\text{Ne}+^{20}\text{Ne}$ reaction between 50 and 300 MeV energy (lab.). Together with the total cross section (dotted-and-dashed line with open circles), the individual components are shown as well: statistical (pre-equilibrium plus compound nucleus) α emission and the projectile breakup (calculated according to Kalbach Walker [24]), as well as different reaction chains with the indication of the last particle (only nucleons and deuterons are considered in addition to the α 's), whose emission leads to ^{36}Ar .

momentum variables, but calculated using more simple code PEQAG [29] (updated and enlarged for the possibility of heavy-ion collisions).

6. Conclusions

For the nearest future, we see two steps to be done: First, one should switch from the spin-independent version of the code to the one with included angular momentum variables. Second, it is obvious that not all ^{36}Ar coming from the reaction are in superdeformed state. An easy way to determine the portion of superdeformed nuclei from the total argon production is the use of master equation in the same way as was suggested for production of different isotopes by Moretto and Schmitt [30]².

7. Acknowledgments

The work has been supported in part by the VEGA and APVV grants Nos 2/0029/20 and 0177-11, and by OTKA Grant No K106035, respectively.

References

- [1] E. Gadioli, P.E. Hodgson, *Pre-Equilibrium Nuclear Reactions*, (Clarendon Press, Oxford, 1992).
- [2] C.K. Cline, *Nucl. Phys.* **A193**, 417 (1972).
- [3] L. Milazzo-Colli, G.M. Braga-Marcazzan, *Phys. Lett.* **B36**, 447 (1971); L. Colli-Milazzo, G.M. Marcazzan-Braga, *ibid.* **B38**, 155 (1972).
- [4] I. Ribanský, P. Obložinský, *Phys. Letts.* **B45**, 318 (1973).
- [5] E. Běták and J. Dobeš, *Phys. Lett.* **B45**, 368 (1979).
- [6] J.M. Akkermans and H. Gruppelaar, *Phys. Lett.* **B157**, 95 (1985).

²See also [31]).

- [7] E. Fabrici *et al.* *Phys. Rev.* **C40**, 2548 (1989);
- [8] N. Cindro *et al.* *Phys. Rev. Lett.* **66**, 868 (1991).
- [9] Ma Yugang *et al.* *Phys. Rev. Lett.* **70**, 2972 (1993).
- [10] J. Dobeš, E. Běták, in *Int. Conf. Reaction Models 77, Balatonfüred 1977*, Ed. L.P. Csernai, p. 195 (Budapest, 1977).
- [11] A. Iwamoto, K. Harada, *Phys. Rev.* **C26**, 1821 (1982).
- [12] E. Běták, *Nucl. Data Sheets* **118**, 284 (2014); E. Běták, *EPJ Web. Conf.* **69**, 00019 (2014).
- [13] E. Běták, *Fizika* **B12**, 11 (2003).
- [14] J. Cseh *et al.*, *Phys. Rev.* **C80**, 034320 (2009).
- [15] J. Darai *et al.* *Phys. Rev.* **C84**, 024302 (2011).
- [16] J. Cseh, A. Algora, J. Darai, P.O. Hess, *Phys. Rev.* **C70**, 034311 (2004).
- [17] J. Darai, J. Cseh, G. Adamian, N. Antonenko, *EPJ Web of Conferences*, **38**, 16001 (2012);
- [18] J. Bisplinghoff, *Phys. Rev.* **C50**, 1611 (1994).
- [19] E. Běták, *Int. J. Mod. Phys.* **E13**, 63 (2004).
- [20] I. Ribanský, P. Obložinský, E. Běták, *Nucl. Phys.* **A205**, 545 (1973).
- [21] E. Běták, *AIP Conf. Proc.* **769**, 1168 (2005).
- [22] C. Kalbach, *Phys. Rev.* **C71**, 034606 (2005); C. Kalbach Walker, *AIP Conf. Proc.* **769**, 1180 (2005).
- [23] N. Cindro, E. Běták, M. Korolija, J.J. Griffin, *Fizika* **B1**, 51 (1992).
- [24] C. Kalbach Walker, in *FENDL-3 Library. Final Report of the CRP on Nuclear Data Libraries for Advanced Systems: Fusion Devices*, Report INDC(NDS)-0645, p. 11, (IAEA, Vienna, 2013).
- [25] P. Obložinský, *Phys. Rev.* **C35**, 417 (1987); P. Obložinský and M.B. Chadwick, *ibid.* **42**, 1652 (1990).
- [26] E. Běták and P. Obložinský, *PEGAS: Pre-Equilibrium–Equilibrium Gamma-And-Spin Code (PC Version)*. Report INDC(SLK)-001, (IAEA, Vienna, 1993).
- [27] E. Běták, *AIP Conf. Proc.* **1491**, 342 (2012).
- [28] J. Darai, J. Cseh, A. Algora, *Int. J. Mod. Phys.*, **E20**, 815 (2011).
- [29] E. Běták, *PEQAG: A PC version of fully pre-equilibrium computer code with gamma emission*. Report INDC(CSR)-016/LJ. (IAEA, Vienna, 1989).
- [30] L.G. Moretto and R. Schmitt, *J. Phys. Coll.* **C5**, 109 (1976); *ibid.*, p. 140.
- [31] E. Běták and V.D. Toneev, *J. Phys.* **G9**, L47 (1983).

Formation, separation and detection of evaporation residues produced in complete fusion reactions

R.N. Sagaidak

Flerov Laboratory of Nuclear Reactions, Joint Institute for Nuclear Research, Dubna, Russia

Abstract

Some aspects of formation, separation and detection of evaporation residues (ERs) produced in complete fusion reactions induced by accelerated heavy ions are considered. These reactions allow to obtain heavy neutron-deficient nuclei and to study their properties. The statistical model analysis of the production cross sections for these nuclei obtained in a wide range of their neutron numbers allows to trace the changes in their macroscopic properties such as fission barriers. The fusion probability of massive projectile and target nuclei is of interest. Empirical estimates of this value allow to verify the predictions of theoretical models for the optimal ways of synthesis of unknown nuclei. Some peculiarities in the separation and detection of ERs in experiments are briefly considered by the example of the Ra ERs produced in the $^{12}\text{C}+\text{Pb}$ reactions. The reliable cross sections for ERs produced in very asymmetric projectile-target combination, such as $^{12}\text{C}+\text{Pb}$, are important for the empirical estimates of the fusion probability in more symmetric combinations leading to the same compound nuclei.

1. Introduction

Complete fusion of projectile and heavy target nuclei is defined as their amalgamation into a compound system inside the fission barrier. This process is unambiguously identified by the direct observation of evaporation residues (ERs) produced after cooling an excited compound nucleus (CN) by the evaporation of light particles (neutrons). The fusion-evaporation reactions have been successfully used in synthesis of the heaviest elements at the border of nuclear stability in experiments performed during the last 25 years [1, 2]. Such experiments are extremely challenging since the formation of heavy and superheavy ERs is strongly suppressed by the CN-fission. In addition, a non-equilibrium process called quasi-fission (QF) arises, when a system produced after the capture of massive projectile and heavy target nuclei may re-separate prematurely, not forming a true CN. Such events represent the transition between deep-inelastic collisions and complete fusion [3].

A number of models were developed to describe complete fusion of massive nuclei leading to the production of heavy ERs. In calculations, the resulting ER cross section can be parameterized as follows:

$$\sigma_{\text{ER}} = \sum_{L=0}^{L_{\text{max}}} \sigma_{\text{cap}}(E, L) P_{\text{fus}}(E, L) W_{\text{sur}}(E_{\text{CN}}^*, L), \quad (1)$$

where σ_{cap} is a capture cross section as a function of the c.m. energy E and angular momentum L , P_{fus} is the fusion probability and W_{sur} is the survivability of nuclei in the evaporation-fission process of the CN de-excitation at the excitation energy E_{CN}^* and angular momentum L . Various theoretical models demonstrate rather good agreement of the ER cross sections calculated according to Eq. (1) with experimental ones. This agreement is shown, for example, in the case of the analysis [4] of the production cross sections of the heaviest ERs formed in ‘cold fusion’ reactions [1]. At the same time, this analysis shows a large spread in the calculated P_{fus} values given by these models (the difference exceeds two orders of the value). It means that the same difference is inherent in the calculated survivability ob-

tained with these models. Such inherent inconsistency of models rises the question of the independent estimate of σ_{cap} , P_{fus} and W_{sur} determining the resulting ER production cross sections in Eq. (1).

2. Fusion probability

One of the ways to determine P_{fus} in the case of strongly fissile nuclei is to measure the capture (total fission) cross section and to extract the CN-fission component with the decomposition of the measured angular distributions for fission-like fragments. Such procedure is not completely model-independent one as it implies some constraints on the angular momenta and moments of inertia assumed in the consideration of the CN-fission and QF processes [5].

In the study of the $^{48}\text{Ca}+^{154}\text{Sm}$ reaction leading to the less-fissile $^{202}\text{Pb}^*$ CN the CN-fission component was extracted from the measured mass-angular distributions with taking into account the total kinetic energy of fission fragments (FF) [6]. This approach is distinct from the study [4], in which the decomposition of the angular distributions integrated over the mass and energy of fission-like fragments was used. With the constraints used in [6], FF corresponding to the mass region of $A_{\text{CN}}/2 \pm 20$ alone had a symmetric angular distribution in the c.m. system. These FF may correspond to the ‘true’ CN-fission. Therefore, the P_{fus} values could be estimated via the corresponding cross sections as $P_{\text{fus}} = (\sigma_{\text{ER}} + \sigma_{\text{CN-fis}}) / (\sigma_{\text{ER}} + \sigma_{\text{CN-fis}} + \sigma_{\text{QF}})$, where the denominator refers to the capture cross section.

At the same time, the comparison of the ER cross sections measured in the $^{48}\text{Ca}+^{154}\text{Sm}$ reaction with those obtained in $^{16}\text{O}+^{186}\text{W}$ (see Fig. 1a, [7] and Refs. therein) leading to the same $^{202}\text{Pb}^*$ CN shows distinctly lower P_{fus} values than those obtained in the fission experiment [6], as shown in Fig. 1b. For the very asymmetric $^{16}\text{O}+^{186}\text{W}$ reaction the lack of fusion suppression at energies above the Coulomb barrier is confirmed by the reproduction of the measured ER and fission cross sections with the statistical model (SM) calculations [8]. Such results of the SM analysis are shared by very asymmetric combinations of projectile-target nuclei [9], for which it is believed that $P_{\text{fus}}=1$.

In the framework of a barrier passing model, e.g., in [8], the capture cross section is written as

$$\sigma_{\text{cap}} = \pi/k^2 \sum_{L=0}^{L_{\text{max}}} (2L+1) T_L(E, L), \quad (2)$$

where k is a wave number and T_L is the transmission probability for the L partial wave passing the potential barrier between projectile and target nuclei. T_L is about unity at energies well above the barrier. Assuming that the survivability is independent of the way of the same CN production, one can write a simple relation for the estimate of P_{fus} for a massive projectile-target system (MS), which is expressed via ER cross sections obtained in this combination and in a very asymmetric (asym) one, as

$$P_{\text{fus}} = \sigma_{\text{ER}}^{\text{MS}}(E_{\text{CN}}^*) k_{\text{asym}}^2 / [\sigma_{\text{ER}}^{\text{asym}}(E_{\text{CN}}^*) k_{\text{MS}}^2]. \quad (3)$$

The comparison of both values obtained with the fission and ER data as well as with the P_{fus} calculations obtained in the framework of di-nuclear system concept [10] is shown in Fig. 1b. The difference in the P_{fus} estimates obtained in the fission and ER experiments [6, 7] could be explained by the conditions of the fission data processing procedure. Namely, one could underestimate the quantity of the QF events (using simple cutting and Gaussian fits) due to the interference of these events with the deep-inelastic ones and overestimate the quantity of the CN-fission events corresponding to a ‘right’ variance of the mass distribution in the symmetric mass-angular distribution. The latter implies some equilibration and compactness of a composite system formed near the saddle point without passing inside the fission barrier, i.e., without ‘true’ CN formation. So, fission data may not give us adequate values of P_{fus} , whereas the detection of ERs is the unambiguous signature of the CN formation, as mentioned above.

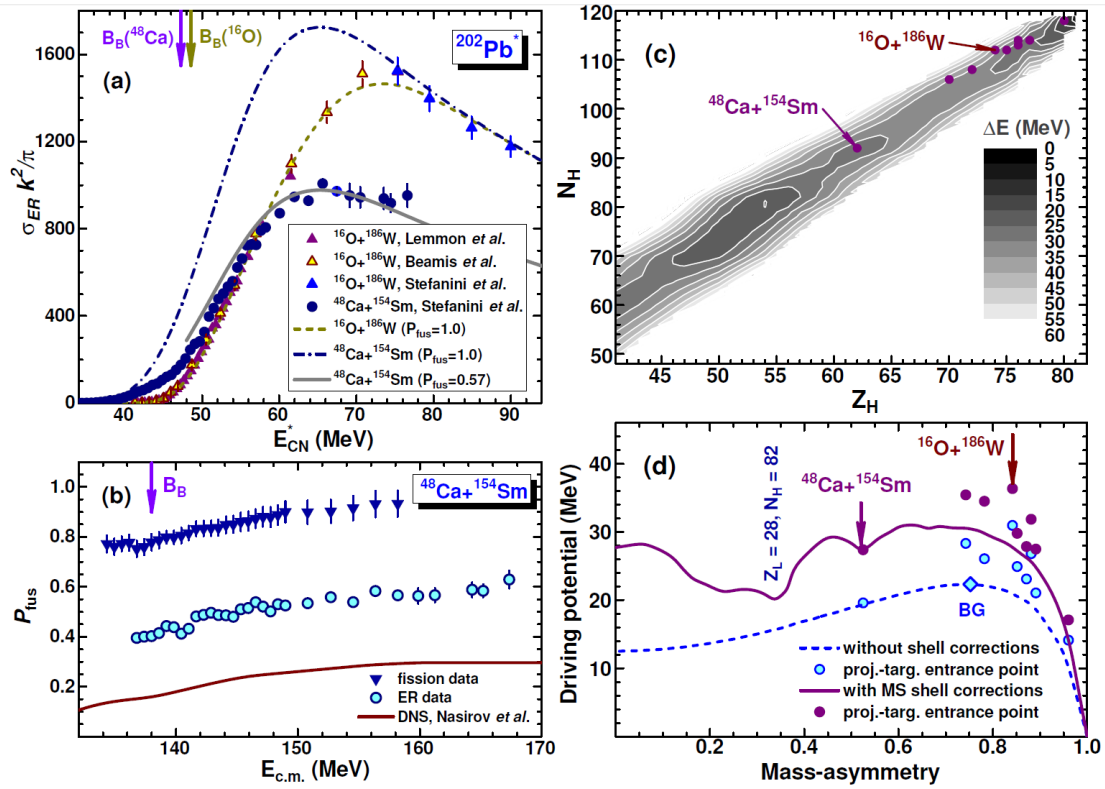


Fig. 1: (a) Reduced cross sections $\sigma_{ER}k^2/\pi$ for ERs produced in the $^{16}\text{O}+^{186}\text{W}$ and $^{48}\text{Ca}+^{154}\text{Sm}$ reactions [7] leading to the $^{202}\text{Pb}^*$ CN (symbols) in comparison with the statistical model [8] calculations for $P_{fus}=1.0$ and 0.57 [9] (lines). (b) The fusion probability values P_{fus} for the $^{48}\text{Ca}+^{154}\text{Sm}$ reaction as obtained with the analysis of fission data [6] (triangles), with the comparison of ER production cross sections obtained in this reaction and in $^{16}\text{O}+^{186}\text{W}$ (circles) [9] and with the calculations [10] (line). (c) The potential-energy surface (PES) map calculated in the (Z_H, N_H) -coordinates in the framework of GLDM [14] with and without shell corrections [16] for the contact configuration of light (L) and heavy (H) spherical fragments composing ^{202}Pb . (d) The minimal values of PES as a function of the mass-asymmetry $(A_H - A_L)/(A_H + A_L)$. Some entrance (projectile-target) point positions, the Businaro-Gallone (BG) point [13], as well as Z and N of nuclear shells are indicated in the panels of (c) and (d).

A qualitative explanation of the fusion suppression effect due to QF was proposed in the framework of the liquid drop (LD) model [11]. It is suggested that the transition from the contact configuration to the CN one is determined by the presence of the conditional barrier along the mass-asymmetry coordinate [12] and the entrance-point position with respect to the top of the barrier, i.e., relatively to the Businaro-Gallone point [13]. The Generalized Liquid-Drop Model (GLDM) [14] calculations of the potential energy surface (PES) in the (Z, N) -plane for the contact configuration of spherical nuclei, with taking into account the proximity energy [15] and shell corrections [16], allow one to examine the approach [11] for the $^{202}\text{Pb}^*$ CN. The calculations show that the entrance points for asymmetric combinations (with Ar and lighter projectiles) lay well above the PES valley (the minima of PES) on its ‘mountainsides’ (see Fig. 1c). Shell corrections strongly modulate the landscape of PES. Thus, in the framework of this consideration, fusion with ^{48}Ca and ^{136}Xe could be considered as the suppressed one. Corresponding entrance points lay in the minima of PES. In front of these points the conditional barriers in the driving potential arise during the evolution of the initial systems along the mass-asymmetry coordinate either to the mono-nucleus (CN) or to the symmetric fragmentation (see Fig. 1d).

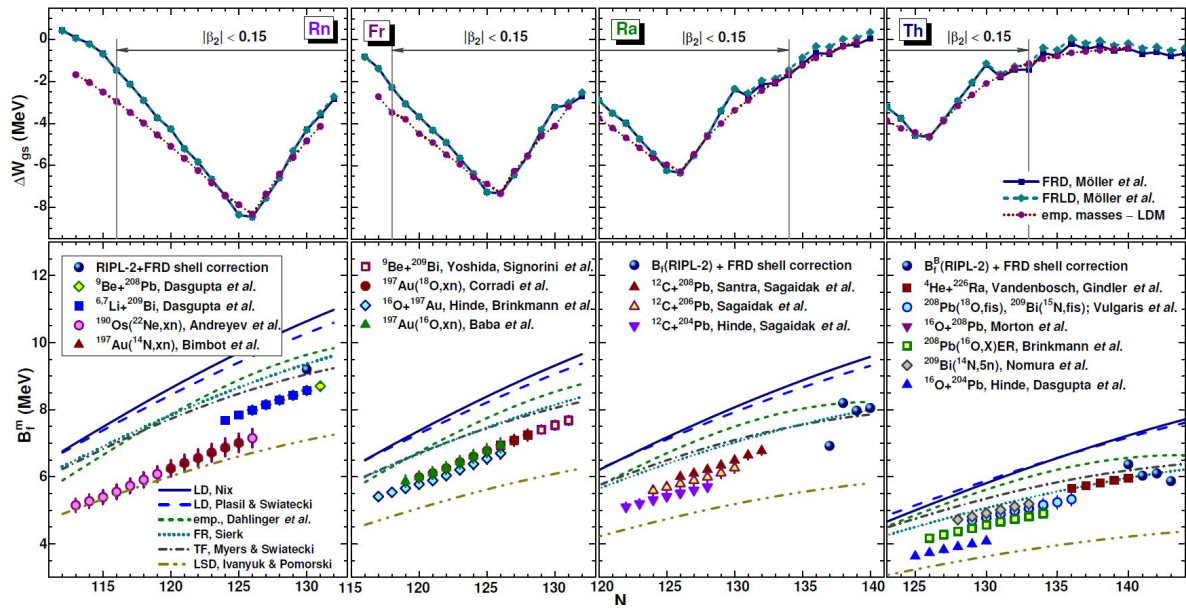


Fig. 2: Bottom panels: the macroscopic fission barriers B_f^m for Rn, Fr, Ra and Th nuclei as a function of the neutron number N , which were derived with the SM [8] analysis of ER and fission excitation functions obtained in very asymmetric projectile-target fusion reactions (symbols), in comparison to the different model predictions [17, 20, 21, 22, 23] (lines) and tabulated values [24] (spheres). **Upper panels:** the ground-state shell corrections ΔW_{gs} for the same nuclei and the regions of nearly spherical nuclei around $N=126$, corresponding to $|\beta_2| < 0.15$ [25].

3. Survivability and fission barriers

The survivability of heavy nuclei produced in the fusion-evaporation reactions can be estimated in the framework of SM approximations [8]. Within these approximations, one can use Reisdorf's expressions [8] for the calculations of the macroscopic level-density parameters \tilde{a}_f and \tilde{a}_v in fission and evaporation channel, respectively. With such admission on the level-density parameters, the survivability of nuclei against fission depends only on the fission barrier heights B_f for nuclei of the CN decay chain. B_f can be parameterized with the scaling factor k_f at the rotating LD fission barriers B_f^{LD} [17] as $B_f = k_f B_f^{LD} - \Delta W_{gs}$, where the shell corrections ΔW_{gs} are calculated as the difference between the empirical and LD masses [18, 19]. The empirical masses [18] are also used to calculate excitation and separation energies at the CN decay. The influence of shell effects on the level density is included assuming their exponential damping with increasing excitation energy (the damping constant is 18.5 MeV). So, within the data analysis, k_f becomes the only parameter determining the survivability of nuclei.

The macroscopic components of the fission barriers $B_f^m = k_f B_f^{LD}$ for heavy nuclei from Rn to Th were estimated with the SM analysis of the ER and fission cross sections measured in very asymmetric projectile-target combinations. These data together with the predictions of different models [17, 20, 21, 22, 23] and tabulated values [24] for the macroscopic barriers (bottom panels) are shown in Fig. 2. The ground-state shell corrections calculated in [25] and those obtained in the framework of the present analysis (see also [9]) are also shown (upper panels). As we see, the extracted macroscopic fission barriers for neutron-deficient nuclei are lower than any model calculations, with the exception of the predictions given by the LSD model [23]. At the same time, the values for relatively neutron-rich Th nuclei approach the tabulated ones [24], as earlier observed for Po nuclei [26] within similar data analysis.

One might remind that the macro-microscopic calculations [17, 21, 22, 23] give us a smooth

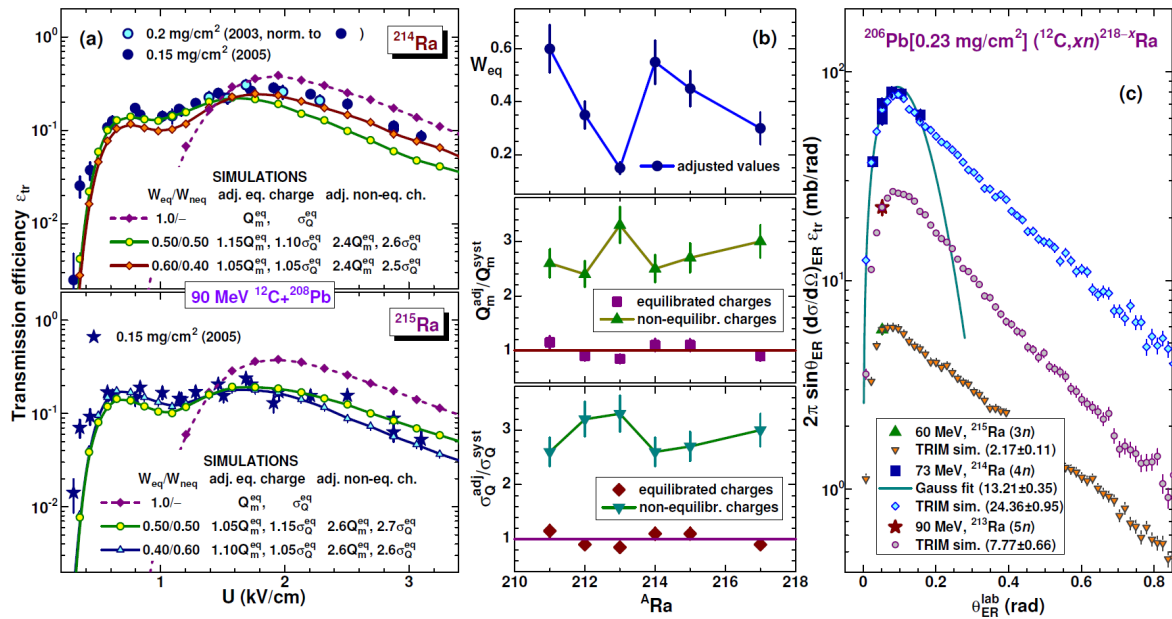


Fig. 3: (a) Transmission efficiencies versus the electric field strength U for $^{214,215}\text{Ra}$ produced in the $^{208}\text{Pb}(^{12}\text{C}; 5n,6n)$ reactions at $E_{lab}=90$ MeV, as measured with the electrostatic deflector [29, 33] (large symbols) and some examples of MC simulations obtained with the variations of charge parameter values (expressed via the equilibrated charge parameters [32]) for the equilibrated and non-equilibrated components of the distributions [34] (small symbols connected with lines). (b) Fractions of the equilibrated component W_{eq} , relative values of mean charges Q_m^{adj}/Q_m^{syst} and widths $\sigma_Q^{adj}/\sigma_Q^{syst}$ (Q_m^{syst} and σ_Q^{syst} are taken from systematics [32]) adjusted for the equilibrated and non-equilibrated charge distributions observed for Ra isotopes (symbols) [36]. (c) Differential production cross sections obtained in the $^{12}\text{C}+^{206}\text{Pb}$ experiments for ^{215}Ra , ^{214}Ra and ^{213}Ra at $E_{lab}=60, 73$ and 90 MeV, respectively [29] (large full symbols) and the results of the MC TRIM simulations (see details in [34]) normalized to the data obtained at 3° (small open symbols); integrated cross section values (in mb) are indicated in brackets.

behavior of B_f^m , as derived for Fr with the SM analysis. It is not the case for Rn, Th and, seemingly for Ra. Living aside possible ‘physical reasons’ for these inconsistencies, one may pay attention to the consistency of experimental cross section data. For example, the most representative ER data for the $^{197}\text{Au}(^{12}\text{C},xn)^{209-x}\text{At}$ reactions (see Refs in the last works [27]) show a difference in the cross section values corresponding to the factor of 5–8. Such difference leads to the ‘adjusted’ k_f values in the range of 0.5 to 1.0, in attempts to analyze data with SM. To overcome these difficulties the analysis of the ER and fission excitation functions obtained in the reactions induced by ^3He on the Pb and Bi target nuclei was performed. An acceptable mutual data agreement allowed to estimate B_f^m for Po and At [28]. Rather good agreement was obtained for Po nuclei comparing the B_f^m values derived in [28] and those obtained with the similar analysis of ER and fission cross section data for very asymmetric reactions [26].

4. Separation and detection of Ra ERs

Bearing in mind dealing with reliable ER cross section data for the derivation of B_f^m , some re-estimate of our previous data on Ra production cross sections obtained in the $^{12}\text{C}+^{204,206,208}\text{Pb}$ fusion reactions [29] has to be performed. These data are in satisfactory agreement with the similar ones [11, 30], however, they were affected by normalization problems which were understood and solved in later experiments and data analysis. In the previous experiments [29] the LNL electrostatic deflector (ED) coupled with a

semiconductor detector [31] was used for the separation and detection of Ra ERs produced in the reactions. Transmission of ERs was optimized by adjusting the electric field corresponding to their maximal yields observed in the experiments, which, as assumed, corresponded to the average equilibrated charge of Ra ions [32]. Monte Carlo (MC) simulations were used for the estimates of the ED transmission efficiency. In later experiments carried out to check feasibility of this approach the presence of an additional non-equilibrated component was revealed for Fr and Ra ERs produced in the reactions with ^{18}O and ^{12}C [33, 34], respectively. Absolute transmission efficiencies as a function of the electric field strength were determined for some ERs in the experiments. They are shown for $^{214,215}\text{Ra}$ [33] together with the results of MC simulations updated to reproduce the measurements varying the Ra-ion equilibrated and non-equilibrated charge parameters [34] in Fig. 3a. The next point concerning the data analysis is the Gaussian approximation to the angular distributions of ERs detected at a forward angle [31] in the experiments [29]. While this approximation reproduces the data in the measured angular range [29], TRIM simulations [34, 35] predict a nearly exponential drop in the ER differential cross sections to the right of their maxima (see Fig. 3c). Such dependencies in the angular distributions are confirmed by the new measurements [36] and should be taken into account in the updated analysis of the data [29].

Acknowledgements

This work was partially supported by the Russian Foundation for Basic Research through Grant No. 13-02-12052.

References

- [1] S. Hofmann and G. Münzenberg, *Rev. Mod. Phys.* **72** (2000) 733.
- [2] Yu.Ts. Oganessian and V.K. Utyonkov, *Rep. Prog. Phys.* **78** (2015) 036301.
- [3] W.J. Swiatecki, *Phys. Scr.* **24** (1981) 113.
- [4] R.S. Naik *et al.* *Phys. Rev. C* **76** (2007) 054604.
- [5] B.B. Back, *Phys. Rev. C* **31** (1985) 2104.
- [6] G.N. Knyazheva *et al.* *Phys. Rev. C* **75** (2007) 064602.
- [7] A.M. Stefanini *et al.* *Eur. Phys. J. A* **23** (2005) 473.
- [8] W. Reisdorf *Z. Phys. A* **300** (1981) 277; W. Reisdorf and M. Schädel *Z. Phys. A* **343** (1992) 47.
- [9] R.N. Sagaidak, *EPJ Web of Conferences* **21** (2012) 06001.
- [10] A.K. Nasirov *et al.* *Phys. Rev. C* **79** (2009) 024606.
- [11] A.C. Berriman *et al.* *Nature* **413** (2001) 144; D.J. Hinde *et al.* *J. Nucl. Radiat. Sci.* **3** (2002) 31.
- [12] K.T.R. Davies and A.J. Sierk, *Phys. Rev. C* **31** (1985) 915.
- [13] U.L. Businaro and S. Gallone, *Nuovo Cim.* **1** (1955) 629; *ibid.* 1277.
- [14] G. Royer and B. Remaud, *Nucl. Phys. A* **444** (1985) 477.
- [15] R. Moustabchir and G. Royer, *Nucl. Phys. A* **683** (2001) 266.
- [16] W.D. Myers and W.J. Swiatecki, Table of Nuclear Masses According to the 1994 Thomas-Fermi Model, Preprint LBL-36803 (1994).
- [17] S. Cohen, F. Plasil, and W.J. Swiatecki, *Ann. Phys. (NY)* **82** (1974) 557.
- [18] M. Wang *et al.* *Chinese Phys. C* **36** (2012) 1603.
- [19] W. D. Myers and W. J. Swiatecki, *Ark. Fys.* **36** (1967) 343.
- [20] M. Dahlinger *et al.* *Nucl. Phys. A* **376** (1982) 94.
- [21] A.J. Sierk, *Phys. Rev. C* **33** (1986) 2039.
- [22] W.D. Myers and W.J. Świątecki, *Phys. Rev. C* **60** (1999) 014606.
- [23] F.A. Ivanyuk and K. Pomorski, *Phys. Rev. C* **79** (2009) 054327.
- [24] T. Belgya *et al.* Handbook for calculations of nuclear reaction data, RIPL-2, IAEA-TECDOC-1506 Vienna (2006); <http://www-nds.iaea.org/RIPL-2/>.
- [25] P. Möller, J.R. Nix, W.D. Myers, and W.J. Swiatecki, *At. Data Nucl. Data Tables* **59** (1995) 185.
- [26] R.N. Sagaidak and A.N. Andreyev, *Phys. Rev. C* **79** (2009) 054613.

- [27] M. Cavinato *et al.* *Phys. Rev. C* **52** (1995) 2577; R. Joosten *et al.*, *Phys. Rev. Lett.* **84** (2000) 5066.
- [28] R. Sagaidak, *J. Phys.: Conf. Series* **580** (2015) 012039.
- [29] R.N. Sagaidak *et al.* *Phys. Rev. C* **68** (2003) 014603.
- [30] T. Nomura *et al.* *Nucl. Phys. A* **217** (1973) 253; S. Santra *et al.* *Phys. Rev. C* **64** (2001) 024602.
- [31] S. Beghini *et al.* *Nucl. Instrum. Methods Phys. Res. A* **239** (1985) 585.
- [32] R.N. Sagaidak and A.V. Yeremin, *Nucl. Instrum. Methods Phys. Res. B* **93** (1994) 103.
- [33] R.N. Sagaidak *et al.* LNL Annual Report 2004, INFN-LNL(REP) 204/2005 (2005) p. 37.
- [34] R.N. Sagaidak, V.K. Utyonkov, and F. Scarlassara, *Nucl. Instrum. Methods Phys. Res. A* **700** (2013) 111.
- [35] J.F. Ziegler, SRIM/TRIM code, <http://www.srim.org>.
- [36] R.N. Sagaidak *et al.* LNL Annual Report 2014, INFN-LNL Report 241 (2015) pp. 58, 60.

NUMEN Project : challenges in the investigation of double charge-exchange nuclear reactions, towards neutrino-less double beta decay

C. Agodi¹, F. Cappuzzello^{1,3}, F. Balestra^{4,5}, R. Bijker⁶, D. Bonanno², D. Bongiovanni², V. Branchina^{2,3}, L. Calabretta¹, A. Calanna¹, D. Calvo⁴, , D. Carbone¹, M. Cavallaro¹, M. Colonna¹, N. Deshmukh¹, S. Ferrero^{4,5}, A. Foti^{2,3}, P. Finocchiaro¹, G. Girauda^{4,5}, V. Greco^{1,3}, F. Iazzi^{4,5}, R. Introzzi^{4,5}, A. Lavagno^{4,5}, D. Lo Presti^{2,3}, F. Longhitano², A. Muoio¹, L. Pandola¹, D. Rifuggiato¹, M.V. Ruslan⁶, G. Santagati¹, E. Santopinto⁶, L. Scaltrito^{4,5}, S. Tudisco¹, V. Zagatto¹

¹ INFN - Laboratori Nazionali del Sud, Catania, Italy

² INFN - Sezione di Catania, Catania, Italy

³ Dipartimento di Fisica e Astronomia, Università di Catania, Catania, Italy

⁴ INFN - Sezione di Torino, Torino, Italy

⁵ Politecnico di Torino, Italy

⁶ INFN - Sezione di Genova, Genova, Italy

P.R.Gomes, R. Linares, J.Lubian, N.H. Medina, J.R.B. Oliveira, M.R.D. Rodrigues, T. Borello-Lewin, D.R. Mendes Junior, P. N. de Faria

Instituto de Física, Universidade Federal Fluminense, Niterói, RJ, Brazil
Instituto de Física, Universidade de São Paulo, São Paulo, SP, Brazil

X. Aslanoglou, A. Pakou, O. Sgouros, V. Soukeras

Department of Physics and HINP, The University of Ioannina, Ioannina, Greece

Abstract

An innovative technique to access the nuclear matrix elements entering the expression of the life time of the double beta decay by relevant cross sections measurements of double charge exchange reactions is proposed. A key aspect of the project is the use of the MAGNEX large acceptance magnetic spectrometer, for the detection of the ejectiles, and of the LNS K800 Superconducting Cyclotron (CS), for the acceleration of the required high resolution and low emittance heavy-ion beams, already in operation at INFN Laboratory Nazionali del Sud in Catania (Italy).

1 Introduction

Neutrinoless double beta decay, $0\nu\beta\beta$, is at the present time strongly pursued both experimentally and theoretically [1]. Its observation will determine whether the neutrino is a Dirac or Majorana particle and will provide a measurement of the average neutrino mass, which is one of the most fundamental problems in physics. An innovative technique to access the Nuclear Matrix Elements (NME) entering the expression of the life time of the neutrinoless double beta decay by relevant cross sections of double charge exchange reactions is proposed. The basic point is the coincidence of the initial and final state wave-functions in the two classes of processes and the similarity of the transition operators, which in both cases present a superposition of Fermi, Gamow-Teller and rank-two tensor components with a relevant implicit momentum transfer. First pioneering experimental results obtained at the INFN-LNS laboratory for the $^{40}\text{Ca}(^{18}\text{O},^{18}\text{Ne})^{40}\text{Ar}$ reaction at 270 MeV, give encouraging indication on the capability of the proposed technique to access relevant quantitative information.

First experimental results, obtained at the INFN-LNS laboratory in Catania, for the $^{40}\text{Ca}(^{18}\text{O}, ^{18}\text{Ne})^{40}\text{Ar}$ reaction at 270 MeV, in a wide range of transferred momenta, give encouraging indication on the capability to access quantitative information towards the determination of the Nuclear Matrix Elements for $0\nu\beta\beta$ decay [2]. On the basis of the above mentioned ground-breaking achievement, we propose an ambitious project, NUMEN, with the aim to go deep insight in the HI-DCE studies on nuclei of interest in $0\nu\beta\beta$ decay, looking forward at the $0\nu\beta\beta$ NME determination [3].

There are a number of important similarities among DCE and $0\nu\beta\beta$ decay processes, despite they are mediated by different interactions, also the description of NMEs extracted from DCE and $0\nu\beta\beta$ presents the same degree of complexity, with the advantage for DCE to be “accessible” in laboratory. However a simple relation between DCE cross sections and $\beta\beta$ -decay half-lives is not trivial and needs to be explored.

2 The Project

The availability of the MAGNEX spectrometer [4] for high resolution measurements of very suppressed reaction channels was essential for the first pilot experiment. Moreover the measurement of DCE high resolution energy spectra and accurate cross sections at very forward angles are key points to identify the transitions of interest [5]. The concurrent measurement of the other relevant reaction channels allows to isolate the direct DCE mechanism from the competing transfer processes. These are at least of 4th-order and can be effectively minimized by the choice of the proper projectile-target system and incident energy [6].

However with the present set-up it is difficult to suitably extend this research to the “hot” cases, where $\beta\beta$ decay studies are and will be concentrated.



Fig.1: A view of MAGNEX spectrometer at Laboratori Nazionali del Sud in Catania.

The present limit of low beam current we have experienced both for the CS accelerator and for the MAGNEX focal plane detector must be sensibly overcome. For a systematic study of the many “hot” cases of $\beta\beta$ decays an upgraded set-up, able to work with two orders of magnitude more current than the present, is thus necessary. This goal can be achieved by a substantial change in the technologies used in the beam extraction and in the detection of the ejectiles. For the accelerator the use of a stripper induced extraction is an adequate choice.



Fig.2: A view of K800 Superconducting Cyclotron at Laboratori Nazionali del Sud in Catania.

For the spectrometer the main foreseen upgrades are:

1. The substitution of the present Focal Plane Detector (FPD) [7] gas tracker with a GEM tracker system;
2. The substitution of the wall of silicon pad stopping detectors with a wall of telescopes based on SiC-CsI detectors;
3. The enhancement of the maximum magnetic rigidity;
4. The introduction of an array of detectors for measuring the coincident γ -rays.

In this framework we propose four phases in the NUMEN project, looking forward to do, in the same time, both the experimental and the up-grade activity, as indicated in the following Phases of the project.

2.1 Phase 1: the experiment feasibility

The pilot experiment : $^{40}\text{Ca}(^{18}\text{O}, ^{18}\text{Ne})^{40}\text{Ar}$ reaction at 270 MeV, with the first experimental data on heavy- ion double charge-exchange reactions in a wide range of transferred momenta, was already done. The results demonstrate the technique feasibility.

2.2 Phase 2: toward “hot” cases optimizing experimental conditions and getting first results

The necessary work for the upgrading of both the accelerator and MAGNEX will be carried out still preserving the access to the present facility. Due to the relevant technological challenges connected, in which test, with and without beam will be crucial, the Phase2 is foreseen to have a duration of a 3-4 years. In the meanwhile, experiments with integrated charge of tens of mC (about one order of magnitude more than that collected in the pilot experiment) will be performed. These will require several weeks (4-8 depending on the case) data taking for each reaction, since thin targets (a few 1018 atoms/cm2) are mandatory in order to achieve enough energy and angular resolution in the energy spectra and angular distributions. The attention will be focused on a few favorable cases, like for example $^{116}\text{Sn}(^{18}\text{O}, ^{18}\text{Ne})^{116}\text{Cd}$ reaction at 15 and 30 MeV/u and the $^{116}\text{Cd}(^{20}\text{Ne}, ^{20}\text{O})^{116}\text{Sn}$ reaction at 15 and 25 MeV/u, with the goal to achieve conclusive results for them.

2.3 Phase 3: the facility upgrade

Once all the building block for the upgrade of the accelerator and spectrometer facility will be ready at the LNS a Phase3, connected to the disassembling of the old set-up and re-assembling of the new will start. An estimate of about 18-24 months is considered.

2.4 Phase 4: the experimental campaign

The Phase 4 will consist of a series of experimental campaigns at high beam intensities (some pμA) and long experimental runs in order to reach in each experiment integrated charge of hundreds of mC up to C, for the experiments in coincidences, spanning all the variety of candidate isotopes for $0\nu\beta\beta$ decay, like: ^{48}Ca , ^{82}Se , ^{96}Zr , ^{100}Mo , ^{110}Pd , ^{124}Sn , ^{128}Te , ^{130}Te , ^{136}Xe , ^{148}Nd , ^{150}Nd , ^{154}Sm , ^{160}Gd , ^{198}Pt .

3 Perspectives

Once selected the optimal experimental condition for the different cases in the Phase2, with the upgrades, both of CS and the MAGNEX array, the Phase4 will be devoted to collect data addressed to give, with an accurate analysis, a rigorous determination of the absolute cross sections values and their uncertainties for all the system of interest, to the challenging determination of the $0\nu\beta\beta$ decay nuclear matrix elements, that is the ambitious goal of NUMEN Project.

References

- [1] Report to the Nuclear Science Advisory Committee, Neutrinoless Double Beta Decay, 2014
- [2] F. Cappuzzello, M. Cavallaro et al., "Heavy-ion double charge-exchange reactions: a tool towards $0\nu\beta\beta$ nuclear matrix elements" submitted to PRC.
- [3] C. Agodi et al., Nuclear and Particle Physics Proceedings Vol 265-266, pag.28-30
- [4] F. Cappuzzello et al., "MAGNEX: an innovative large acceptance spectrometer for nuclear reaction studies in: Magnets: Types, Uses and Safety", Nova Publisher Inc., New York, 2011, pp 1-63.
- [5] H. Matsubara, et al., Few-Body Systems 54 (2013) 1433.
- [6] D. M. Brink, Phys. Lett. B 40 (1972) 37
- [7] M. Cavallaro, et al., Eur. Phys. J. A (2012) 48: 59.

The ^{12}C Hoyle State and the Multiverse

M.B. Chadwick

Los Alamos National Laboratory, Los Alamos, NM 87544, USA

Abstract

The location of the 7.65 MeV 0^+ Hoyle State is discussed within the context of a statistical model for the excited states of carbon. It is shown that the probability of it being in an energy range needed to allow resonant nucleosynthesis is approximately 7% in this simple model, which is not so “finely tuned”. Implications of fine tuning on the possible existence of a multiverse are discussed within a Bayesian context.

1 Introduction

The nuclear structure properties of ^{12}C have been discussed by F. Nunes at the 2012 Varenna *International Conference on Nuclear Reaction Mechanisms* and in a journal article (Nguyen, 2012). This paper addresses the question of the precise location of the 0^+ state from a statistical perspective.

The creation of carbon in stars occurs through a two-step triple-alpha reaction, and is one of the cycle of nuclear reactions in which hydrogen and helium are transmuted to create heavier elements in a hot stellar environment. The first step in the reaction, where two alpha particles overcome their Coulomb repulsion to fuse and make a short-lived beryllium nucleus, is enhanced because the energy of the ^8Be ground state is close to the double-alpha threshold. In the next step an alpha-particle is captured on the beryllium-8 state, and this is also enhanced because of a spin-zero positive-parity resonance in carbon-12, the Hoyle state. The strength of the nuclear force appears to be “fine tuned” to result in this nuclear state being located just at the right energy, 7.65 MeV, with the consequence that the nucleosynthesis of the elements needed for life - carbon, nitrogen, oxygen - can occur. If the strength of the nuclear coupling force was slightly different, the states energy would no longer be resonant and there would, perhaps, be insufficient carbon in the universe for organic life to evolve.

It is not only that this reaction allows carbon to be produced in significant quantities, but that carbon itself – as part of the carbon-nitrogen-oxygen cycle – provides an essential catalytic role in converting hydrogen to helium in stars. It is intriguing, therefore, to wonder why the nuclear force has just the right value, for Hoyle used the anthropic principle to predict the existence of this state before it was found by Caltech researchers in the 1950s. Recent studies by Schlattl, Csoto, Oberhummer, and Livio on the how precise this fine tuning needs to be to create carbon in significant quantities suggests it a more complicated problem than originally thought; the fine tuning appears to be noteworthy, but not as spectacularly precise as once thought (Oberhummer, 2000; Livio, 2008). Also, Weinberg notes that when the energy of the state (7.65 MeV) is compared to the energy of the $^8\text{Be}+\alpha$ system (7.4 MeV), instead of to zero excitation energy, the fine tuning seems less impressive, “not such a close call after all” (Weinberg, 1999); and below I give an alternative estimate of the extent of fine-tuning of this state’s energy.

I present an alternative way to (very approximately) quantify one aspect of the so-called fine tuning of the location of the 7.65 MeV 0^+ Hoyle state in carbon, for its role as a gateway for the stellar nuclear reactions essential for life. The argument does not explore the sensitivity of the state’s location to the magnitude of the nuclear force, but rather takes the force as a given and instead uses a statistical

argument to consider the likelihood that a 0+ state is found at the required energy location. It will quantify the extent to which we should, or should not, be surprised to find such a state at this energy given the observed properties of carbon's excited states in general. This particular line of inquiry has merit because it is exactly this point - that some have expressed surprise that the 0+ Hoyle state is "fortuitously" located where it is - that has spawned fine tuning discussions related to nucleosynthesis (if the density of 0+ nuclear states in this energy range was very high no one would be talking of fine-tuning in this context).

2 Statistical model of carbon excited states

Nuclear excited states exhibit the following characteristics. At lower excitation energies they are widely-spaced (in their energies) and their energy locations are characteristic of the nucleus under study, depending on the nature of the nuclear force between the constituent neutrons and protons, on quantum mechanical shell effects, and on collective processes such as vibrations and rotations. With increasing excitation energy, the number of excited states increases exponentially and the density of these states becomes very high; and they can be understood more simply in terms of the statistical properties of these excited states as a function of their energy and spin. The 7.65 MeV 2nd excited state in carbon is clearly one of the characteristic lower-energy states, and in an analysis of carbon's excited states I have shown how the ensemble of such states below 12 MeV match on to statistically described states above this energy (Chadwick, 1996). But in that analysis it is evident that even below 12 MeV the statistical representation reproduces the gross features of the density of the lower-lying characteristic states, Fig. 1 and Chadwick (1996). Therefore it is illuminating to ask of this statistical description the question: what is the probability that there is a 0+ state between 7.37 MeV (the excitation energy created when ^8Be and alpha particle fuse) and 7.67 MeV (0.3 MeV higher, the upper energy of relevance in a stellar nucleosynthesis environment (Weinberg, 1999)), given the observed statistical properties of the excited states of carbon and of other nuclei.

For carbon below a few tens of MeV the constant-temperature statistical description of states (Young, 1998) can be used,

$$\rho(E) = (1/T)\exp(E-E_0)/T.$$

The parameters $T=6.209$ MeV and $E_0 = -3.040$ MeV allow both a match to the eight observed lower energy characteristic states below 12.16 MeV as well as to the higher energy systematical properties of a Fermi-gas nuclear system above 43.4 MeV, see Fig. 1. Such states typically have an approximately Gaussian-type spin distribution,

$$P(J) = [(2J+1)/2\sigma^2] \exp(-(J+0.5)^2 / 2\sigma^2),$$

and estimating the distribution from the observed states below 12 MeV gives the spin cut-off as $\sigma^2=2.1$. This statistical representation suggests the number of 0+ levels in the 0.3 MeV window between 7.37 and 7.67 MeV is then: $0.3\text{MeV} \cdot \rho(7.52) \cdot P(0) = 0.3 \text{ MeV} \cdot 0.88/\text{MeV} \cdot 0.25 = 0.07$, *i.e.* the probability of their being a 0+ state in this critical excitation-energy window is 0.07, or 7%¹.

This quantity can be interpreted as the degree of fine tuning, F , for the Hoyle state, so we find $F_{\text{Hoyle}}=0.07$. This 7% is a little lower than Weinberg's 20% estimate, but it is not so very small that the Hoyle state's location appears to involve an exquisite fine tuning: 7% is not as small as a 2-sigma probability that is often used to quantify unlikely events (which is 5%).

¹ I do not include a parity factor of 0.5 to estimate the probability of positive, rather than negative, parity states because all states in this region are positive parity.

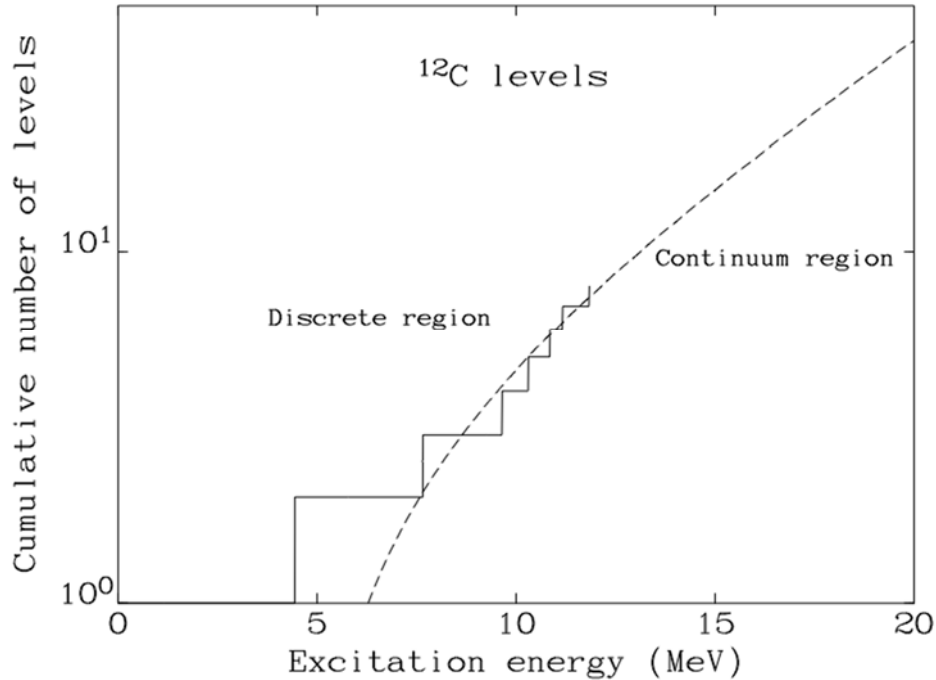


Fig. 1: Plot of the cumulative number of observed low-lying states in ^{12}C as a function of excitation energy, together with a statistical (continuum) constant-temperature model of the states (dashed line), taken from Chadwick (1996). This figure enables one to assess how a statistical model of the levels compares with the observed true values below 12 MeV. The Hoyle state is at 7.65 MeV.

It is important to understand what this argument is, and is not. Given our laws of nuclear physics, the probability of the Hoyle state being located where it is is actually unity – its location is dictated by these laws, and indeed modern *ab-initio* nuclear theory calculations such as no-core shell model (Launey, 2013), effective field theory (Epelbaum, 2011), Greens Function Monte Carlo (Lusk, 2013), and R-matrix and Faddeev approaches (Nguyen, 2012) are now providing insights into the properties of this state, why it is located where it is, and the magnitude of the triple-alpha nuclear reaction. I obtained the $F_{\text{Hoyle}}=0.07$ value from a simple idealized model. The statistical argument I outlined really just quantifies why one should not be particularly surprised to find such a state at this energy given the observed properties of carbon's excited nuclear states in general.

Having argued that the fortuitous location of this Hoyle state in carbon is not particularly fine tuned (*i.e.* $F_{\text{Hoyle}}=0.07$ is not particularly small), I note that FT evidence is much more compelling in other areas of cosmology: the magnitude of the gravitational force; the dark energy repulsion; the initial ripple inhomogeneities soon after the Big Bang; and so on (Rees, 2001). Such considerations suggest F could be very small indeed, 10^{-15} or less.

3 Bayesian insights into a Multiverse

One way to interpret such fine tuning within a naturalistic framework is that it provides evidence we live in a multiverse. In this multiverse hypothesis, physical constants and even the laws of physics vary significantly from universe to universe (Rees, 2001), being governed by deeper natural laws (in a way that we do not yet fully understand). So from a probabilistic perspective, the extraordinarily-large number of universes that embody a wide variety of physical constants combines with the small

probability of particular physical coupling constants that enable life, to result in the existence of many universes where the evolution of life is at least possible, making the existence of our particular universe less surprising. Bayes' theorem can be used to quantify the extent to which fine tuning (a small F value) supports the multiverse hypothesis, as follows.

Let $P(U)$ be the prior probability for the hypothesis of a single universe, $P(M)$ be the prior probability for the hypothesis of a heterogeneous multiverse (with a range of physical constants across the multiverse), and FT be the evidence for fine tuning. Bayes's theorem tells us the relative posterior probabilities of the two hypotheses in the light of new FT evidence:

$$P(U/FT)/P(M/FT) = P(FT/U)/P(FT/M) \cdot P(U)/P(M).$$

The first factor $P(FT/U)/P(FT/M)$ is the fine tuning parameter F, the ratio of the probability that a single universe leads to FT observations (very unlikely if by chance), to the probability that a multiverse leads to FT observations (very likely, of order unity); the second factor $P(U)/P(M)$ is of order unity since our *a priori* belief in a universe or multiverse is (arguably) equally likely. Thus the relative probability of the two hypotheses is:

$$P(U/FT)/P(M/FT) = F,$$

which is a very small number, *and we conclude it is most likely we live in a heterogeneous multiverse, not a single universe.* The degree we should conclude this depends on how finely tuned our universe is for life, *i.e.* how small F is. Even though our knowledge of particle physics and cosmology is presently inadequate to precisely determine F, the indications are that F is very small. (If on the other hand our universe was specially *designed* for life then $P(FT/U)$ is no longer small and then $P(U/FT)/P(M/FT) \sim 1$, in which case this argument cannot be used to decide between a universe or a multiverse.)

A related argument by Coleman (2013) involves an extension to an infinite world and concludes FT also favors a heterogeneous infinite multiverse by this same factor F.

References

- Chadwick, M.B. (1996). *Nucl. Sci. Eng.* **123**(1).
- Coleman, C.S. *Cosmic Fine Tuning and the Multiverse Hypothesis*, Australian Astrobiology Meeting, Sydney, June 30 - July 2, 2013 (2013), available at [arXiv.org](http://arxiv.org)
- Launey, K.D., *et al.* (2013). *Journal of Physics: Conference Series*, **436**, 012023.
- Livio, M (2008). The interconnections between cosmology and life. p.114 in *Fitness of the Cosmos for Life*.
- Lusk, E.L., Pieper, S.C., and Butler, R.M. (2010).
See <http://www.mcs.anl.gov/uploads/cels/papers/P1708.pdf>
- Nguyen, N.B., Nunes, F.M., Thompson, I.J., and Brown, E.F. *Phys. Rev. Lett.* **109** (2012) 141101
- Oberhammer, H., Csoto, A. and Schlattl, H. (2000). *Science*, **289**, 88.
- Rees, M. (2001). *Our Cosmic Habitat*. Princeton, NJ: Princeton University Press.
- Weinberg, S. (1999). *A Designer Universe?* New York Review of Books, Oct. 21.
- Young, P.G, Arthur, E.D. and Chadwick, M.B. (1998). Comprehensive Nuclear Model Calculations: Theory and Use of the GNASH Code. p.227 in *Nuclear Reaction Data and Nuclear Reactors: Physics, Design and Safety*

Measurement of $(n, xn\gamma)$ reaction cross sections in W isotopes

G. Henning^{1,2}, A. Bacquias^{1,2}, C. Dorcea³, P. Dessagne^{1,2}, J.-C. Drohé⁴, M. Kerveno^{1,2}, A. Negret³, M. Nyman⁴, A. Olacel^{3,5}, A.J.M. Plompen⁴, G. Rudolf^{1,2}, P. Scholtes^{1,2}

¹ Université de Strasbourg, IPHC, Strasbourg, France. ² CNRS, UMR7178, 67037 Strasbourg, France.

³ Horia Hulubei National Institute for Physics and Nuclear Engineering, Bucharest-Magurele, Romania.

⁴ European Commission, Joint Research Center, Institute for Reference Materials and Measurements, B-2440 Geel, Belgium. ⁵ University of Bucharest, Faculty of Physics, Bucharest-Magurele, Romania.

Abstract

Nowadays, most of nuclear reactor developments use evaluated databases for numerical simulations to optimize reactors performance and control parameters. However, the considered databases present still large uncertainties and disagreements, preventing calculations from reaching the required precision. The necessary improvement of evaluated databases entails new measurements and a better theoretical description of involved reactions. Among those, the neutron inelastic scattering (n, xn) is of great importance as it modifies the neutron spectrum, the neutron population, and produces radioactive species. In 2005, the group at IPHC started an experimental program to study these reactions. The setup and the analysis will be presented along with the first results for natural tungsten isotopes, which will be compared to the latest predictions from nuclear reaction codes. The impact of those results on reaction mechanism description will be discussed.

1. Motivation

Today most of the nuclear reactor developments are using evaluated data bases for numerical simulations. These data bases contain all necessary quantities for the simulations: total and partial cross sections, angular distributions, ... However, the considered databases still present large uncertainties and disagreements. To improve their level of precision, new measurements and theoretical developments are needed.

The (n, xn) reactions are of particular interest as they modify the neutron spectrum, the neutron population, and produce radioactive species. This type of reaction occurs purely via nuclear interaction between the incoming neutron and the nucleons, which makes them a good probe of this interaction. Moreover, the neutron inelastic scattering proceeds through three main mechanisms: direct nucleon-nucleon interaction for the highest neutron energy, compound nucleus for the slow neutrons with a long interaction time with the nucleus and pre-equilibrium reactions, for intermediate energy, in which the incoming neutron interacts with several but not all the nucleons. These three reaction regimes are described differently by the theories but overlap in reality.

To experimentally extract the total (n, xn) cross section, the study of the exclusive channels $(n, xn\gamma)$ brings very strong constrains for the comparison with theoretical predictions as such calculation requires a correct description of the reaction mechanism, the nuclear de-excitation process and the precise knowledge of the nuclear structure. The group at IPHC started a program to study $(n, xn\gamma)$ reaction on actinides in 2005 and already worked on $^{235,238}\text{U}$ and ^{232}Th [1, 2], while measurements for other elements were performed and are being analysed, including ^{nat}W .

In the following, we report on the study done on tungsten isotopes ($^{182-186}\text{W}$). Tungsten is not an active element in nuclear reactors. However, with a high melting point (3422 °C), a strong mechanical resistance (Young's modulus: 600 GPa) [3], a low thermal expansion and a high resistance to oxidation,

acids and alkaline, it is used in many alloys. The interaction of neutrons with tungsten is therefore of importance for reactor physics, in particular for fusion reactors in which tungsten is one of the most exposed material to high energy neutrons [4]. Compared to actinides, the setup of experiments using tungsten is very simple as the metal is not radioactive and does not have any toxicity.

From the structure point of view, tungsten isotopes are similar in deformation to actinides such as Uranium, as illustrated on 1. This similarity comes with the simplification, compared to actinides, that tungsten isotopes do not present a neutron-induced fission channel (the calculated liquid drop fission barrier of tungsten isotopes is around 20 MeV [5]).

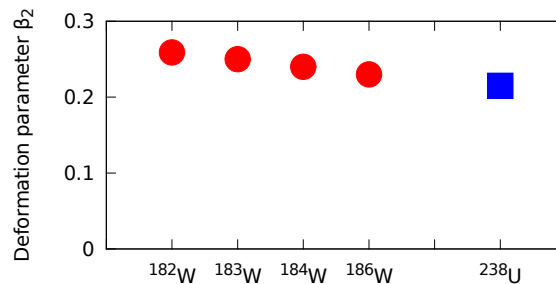


Fig. 1: Calculated ground-state deformation parameters for $^{182,183,184,186}\text{W}$ and ^{238}U [5].

As the nuclear applications do not use isotopically enriched isotopes, one has to study all the naturally abundant isotopes: ^{182}W (26.5 %), ^{183}W (14.3 %), ^{184}W (30.6 %), ^{186}W (28.4 %) [6].

Moreover, there are only a few measurements available today on these nuclides to test evaluations. Some (n, 2n) and (n, 3n) cross section data exist, and a few (n, n') level production cross sections have been measured [22, 7, 8].

2. Experimental setup: GRAPhEME@GELINA

Experimental measurements of (n, xn γ) reaction cross sections using prompt gamma spectroscopy and neutron energy determination by time of flight are performed at the neutron beam facility GELINA, at the European Commission Joint Research Center's Institute for Reference Materials and Measurements in Geel, Belgium [9, 10].

The GELINA accelerator provides a pulsed neutron white beam using electrons accelerated at 100 MeV impacting a uranium target. The accelerated particles produce Bremsstrahlung radiations in the uranium target which in turn, by photonuclear reactions, produce neutrons, with an average flux of 3.4×10^{13} neutrons/s. The neutron energy distribution ranges from subthermal to about 20 MeV, with a peak around 1-2 MeV. The flight paths, symmetrically arranged around the uranium target, lead to several experimental locations at distances of 10 to 400 m. For each flight path, a different set of moderators can be added to modify the neutron spectrum.

The GRAPhEME setup is located 30 meters away from the neutron production target and consists of a fission chamber (FC) to measure the incoming neutron flux and HPGe detectors for the detection of γ rays. The FC is a $\approx 320 \text{ cm}^3$ volume, filled with a 10 % methane- and 90 % argon-mixture at 1 atm pressure, with a ^{235}U enriched (99.5 %) UF_4 deposit. The reaction of neutrons with the ^{235}U nuclei induces fission and one of the fission fragment is detected in the gas chamber. The efficiency of the FC was determined to be $94.4 \pm 2.1 \%$ [11, 12]. An energy cut allows the differentiation between α particles and fission fragments.

After the fission chamber, planar HPGe detectors surround the sample to study. The average resolution of the detectors at 122 keV is 0.75 keV and the absolute efficiency is 0.01. The sample

and the detectors are enclosed into a lead-copper-cadmium castle to drastically reduce the background around the target.

The detectors are connected to TNT acquisition cards [13] that record in list mode the energy of the detected gamma ray (or fission fragment) and the time of the event. The time difference between the accelerator pulse and the γ -ray or fission event detection gives the energy of the neutron that induced the reaction, following $E_n = m_n c^2 \sqrt{\frac{1}{1 - \left(\frac{D}{Tc}\right)^2}}$ where m_n is the mass of the neutron, c the speed of light in vacuum, D the neutron flight path length between the production target and the sample in GRAPhEME and T is the time of flight of the neutron.

To extract cross section at a given angle θ and neutron energy E_n , one simply has to follow the intensity of a given gamma ray line detected by the HPGe detectors and make a ratio with the neutron flux determined by the fission chamber according to the following equation:

$$\frac{d\sigma}{d\Omega}(E_n, \gamma; \theta) = \frac{N_\gamma(E_n; \theta)}{\varepsilon(E_\gamma)} \frac{\sigma_{235\text{U}(n, f)}(E_n) \varepsilon_{\text{FC}}}{N_{\text{target}} N_{\text{FC}}}$$

Where $N_\gamma(E_n; \theta)$ is the number of detected γ rays for a given transition, $\varepsilon(E_\gamma)$ the efficiency of detection for this γ ray, $\sigma_{235\text{U}(n, f)}(E_n)$ the fission induced cross section of ^{235}U , ε_{FC} the detection efficiency of the fission chamber, N_{target} the number of isotope of interest in the sample and N_{FC} the number of events detected by the fission chamber.

The full angular integration is made using the Gauss quadrature method with detectors positioned at 110° and 150° [14, 15].

Measurements of $(n, xn\gamma)$ cross sections have been performed for $^{nat.182,183,184,186}\text{W}$ targets. Here only the preliminary results for the even-even isotopes studied in a ^{nat}W target are presented.

3. Results

The structure of the three isotopes $^{182,184,186}\text{W}$ is very similar, with a strong rotor-like behavior. The yrast states form a rotational band built on the 0^+ ground state. The moment of inertia $\mathcal{J}_{\text{yrast}}$ is decreasing slightly with the increase of the neutron number (N). The nuclei also present a 2^+ -based band (γ) and a 0^+ -based band (β). As N increases, the 2^+ -based band is being lowered below the 0^+ -based band. See 2 for the level schemes.

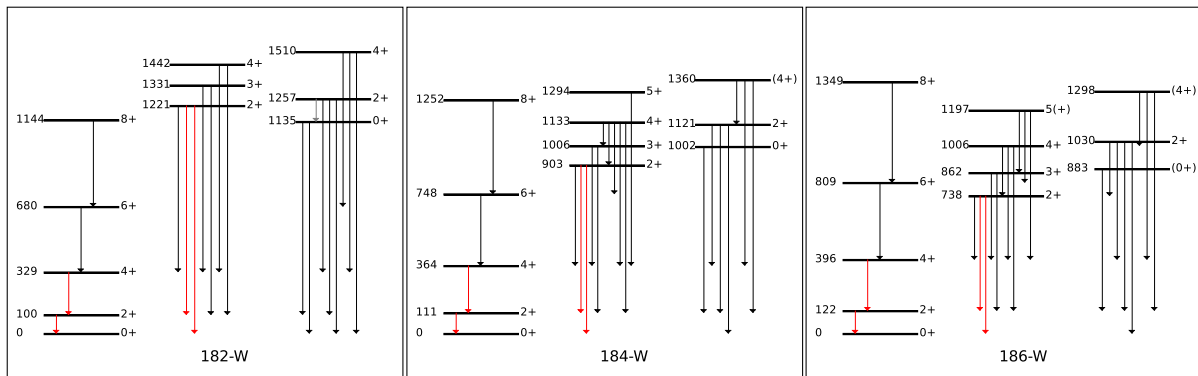


Fig. 2: Level schemes of $^{182,184,186}\text{W}$ [16, 17, 18]. The energy of levels are given in keV. The transitions in red are the ones that will be discussed here.

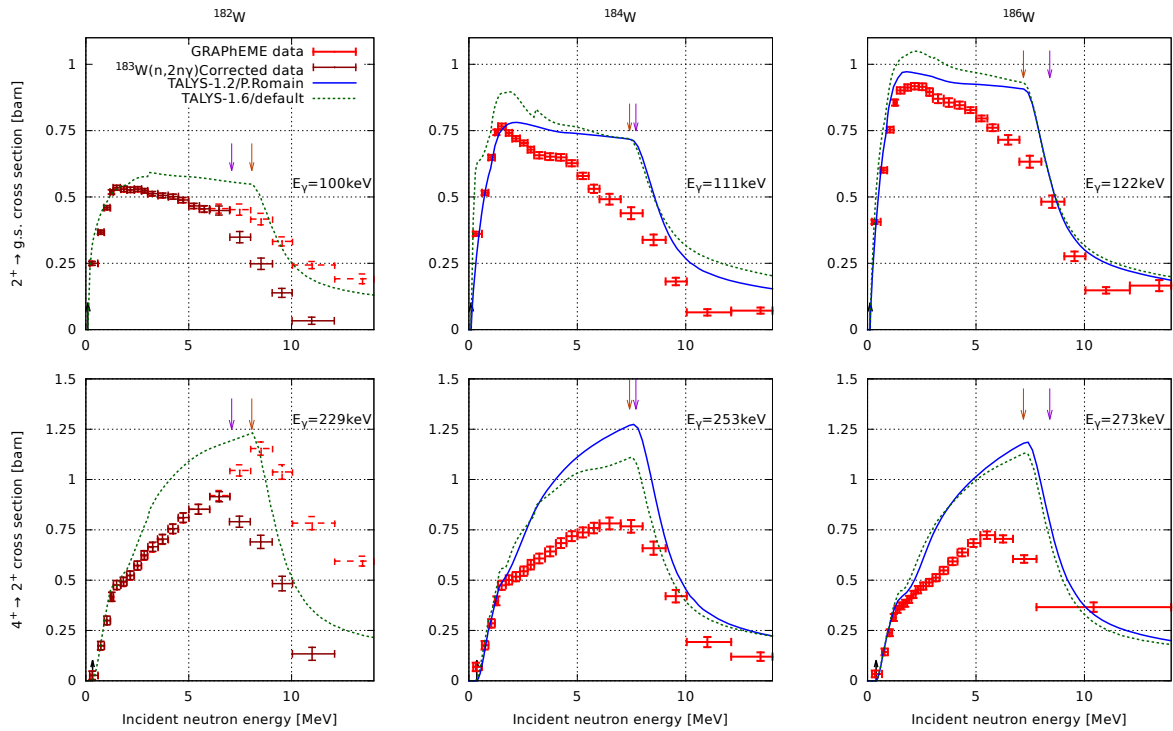


Fig. 3: $(n, n'\gamma)$ cross sections measured with GRAPHEME (red points) for the isotopes ^{182}W (left), ^{184}W (center), ^{186}W (right), for the first excited state to the ground state transition (top) and the second excited state to the first excited state (bottom). The data is compared to TALYS-1.2 calculation with optimized parameters (full blue line) and with TALYS-1.6 with default parameters (dotted green line). For references, the energy of the level from which the γ rays are decaying is marked with the black up-pointing arrow. The neutron separation energy S_n is marked with the orange down-pointing arrow, the proton separation energy S_p by the purple down-pointing arrow.

3.1 Ground state band transitions

First, we look at the transitions, in the ground state band, from the 4^+ to the 2^+ level and from the 2^+ to the *g.s.*. For $^{182}\text{W}(n, n'\gamma)$ it is necessary to correct for the contamination by $^{183}\text{W}(n, 2n)$ reactions in the natural W target. This is done by subtracting the $^{183}\text{W}(n, 2n\gamma)$ transition cross section calculated with TALYS-1.6, weighted by the isotopic ratio in natural tungsten. The profile of the cross sections (3) is very similar for the transitions along the isotopic chain. For the 2^+ to *g.s.* transition, the cross section peaks around $E_n = 1 - 2$ MeV, and starts dropping above 6 MeV. For the 4^+ to 2^+ transition, the cross section increases sharply from 0 to 500 keV, has a *softer* slope above, peaks around 6 – 8 MeV and drops just above the peak. In terms of amplitude, the maximum of the cross section for the 2^+ to *g.s.* appears to increase with larger neutron number. The 4^+ to 2^+ cross section amplitude, is slightly decreasing for increasing N. However, one should not be fooled by electron conversion. Indeed, for the W isotopes, the conversion coefficient for transitions around 100 keV is about 3, and about 0.2 for transitions around 250 keV. Correcting for conversion electrons, the 2^+ to *g.s.* transition cross sections are very similar at ≈ 2.5 barns. The 4^+ to 2^+ transition represents only about 1/3 of the 2^+ to *g.s.* transition at $E_n \approx 2 - 5$ MeV. At the highest neutron energy, most of the 2^+ to *g.s.* intensity comes from the 4^+ to 2^+ . This indicates a weak contribution from the ground state band to the 2^+ level population.

The experimental cross sections are compared to predictions by the TALYS code (shown in 3). Two TALYS calculations were performed. The first one was made in 2011 by P. Romain (CEA/DAM) with TALYS-1.2 and optimized parameters for $^{184,186}\text{W}$. The second was performed with the latest

TALYS version (1.6) with default parameters for all three isotopes. We note that TALYS-1.2 calculations using default parameters give values within 3 % of the TALYS-1.6 default results. The experimental data and the TALYS predictions match very well at low energy ($E_n < 1$ MeV) but start to differ above. In the 2^+ to *g.s.* transitions TALYS predicts a plateau from $E_n \approx 2$ MeV to ≈ 8 MeV (i.e. at the neutron separation energy) while the experimental data drops already starting at 6 MeV. In the 4^+ to 2^+ transition, TALYS overestimates the intensity of the transition from 2 to 8 MeV, by as much as a factor 2.

3.2 Interband transitions

The two transitions decaying from the 2_2^+ state (head of the γ band) are also studied. This state decays to the 2_1^+ state in the ground state band and to the ground state – it also decays to the 4_1^+ state but with a very low branching ratio) – see 4. For the ^{182}W , the transitions are contaminated by other γ lines and hard to isolate in the spectrum. In the two other isotopes ($^{184,186}\text{W}$), the transitions have very similar shapes and amplitudes, in agreement with the expectations. Electron conversion is negligible at this γ energy. Comparing to predictions by TALYS, the calculations reproduce very well the shape of the cross sections. However, the amplitude is underestimated by as much as $\approx 25\%$.

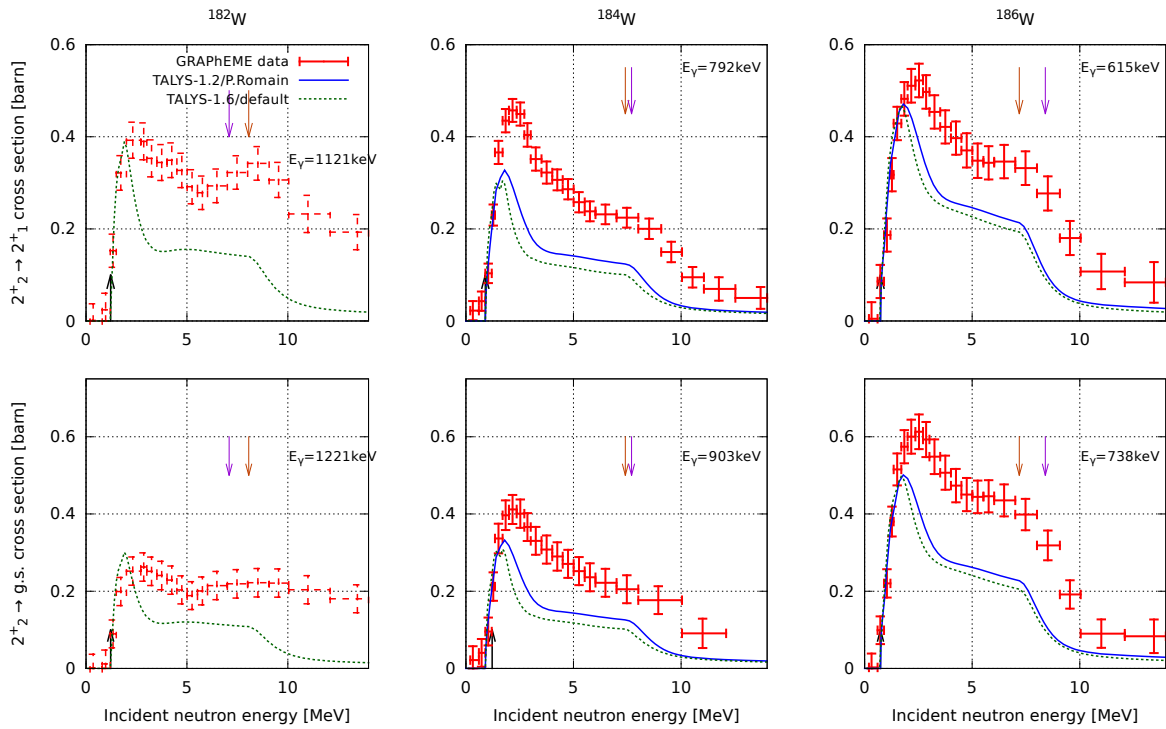


Fig. 4: Same as 3 for interband transitions decaying from the 2^+ band. Data for ^{182}W is unreliable because of γ contamination.

4. Result interpretation

Significant differences appear between the experimental results and the theoretical predictions. TALYS overestimates the ground state band intensity for the higher E_n , and underestimates the interband transitions intensity at all neutron energies.

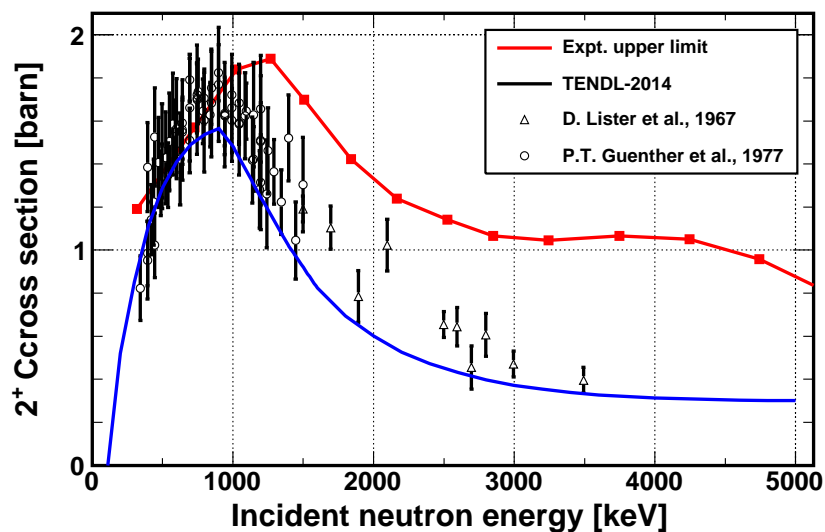


Fig. 5: Level population cross section for the first excited state (2^+) in ^{184}W . The red line is the upper limit determined from GRAPHME data. The markers are from available experimental data [22, 7, 8]. The blue line is the value in TENDL-2014 [19, 20].

A possible explanation is incorrect branching ratios in the structure information used by TALYS. To extract information that is independent of branching ratio, we tried to extract the 2^+ level population cross section from the γ cross sections. This relies on the balance formula: $\sigma_{\text{level}} = \sum_{\text{decaying transition}} \sigma_{\text{transition}} - \sum_{\text{feeding transition}} \sigma_{\text{transition}}$. With this method, it is important to correct the transition intensity extracted from γ ray intensity for the electron conversion. Although simple in principle, the extraction of the 2^+ level population cross section from gamma transition intensity is tricky. Indeed, for ^{184}W , more than 20 transitions are feeding the first excited state; many of which have a high energy, for which our setup has a low efficiency, with a highly fractionned intensity. Because of this difficulty, the level population cross section can be extracted exactly only up to 1 MeV, and only an upper limit can be determined above that energy – see 5. The comparison of the upper limit extracted from experimental data with previous data existing for the level cross section, and the TALYS prediction, show a good agreement of our data with previous experiments, but can not allow to draw further conclusions.

Another lead to explain the difference between TALYS and the experimental data is the description in the calculations of the reaction mechanism. P. Romain decomposed the total $^{186}\text{W}(n, n') \gamma_{2^+ \rightarrow \text{g.s.}}$ according to individual state contributions. The computed cross section is a good match to the experimental data from a previous analysis of the same data set presented in the current paper, with only a small renormalization. This description is very good up to 4 MeV. This is hinting that the structure information used by TALYS is good enough up to the high excitation energies. Above 5-6 MeV, the plateau predicted by TALYS, associated with scattering off continuum states continues while the experimental data is dropping. This can be explained by an incorrect description of the spin distribution from pre-equilibrium reactions, as it has been seen in U isotopes [21]. For this aspect, microscopic calculation done by M. Dupuis (CEA/DAM) could be a way to obtain correct spin distributions. In general, one can also wonder about the choice of the energy limit between continuum and discrete levels and the coupling between them.

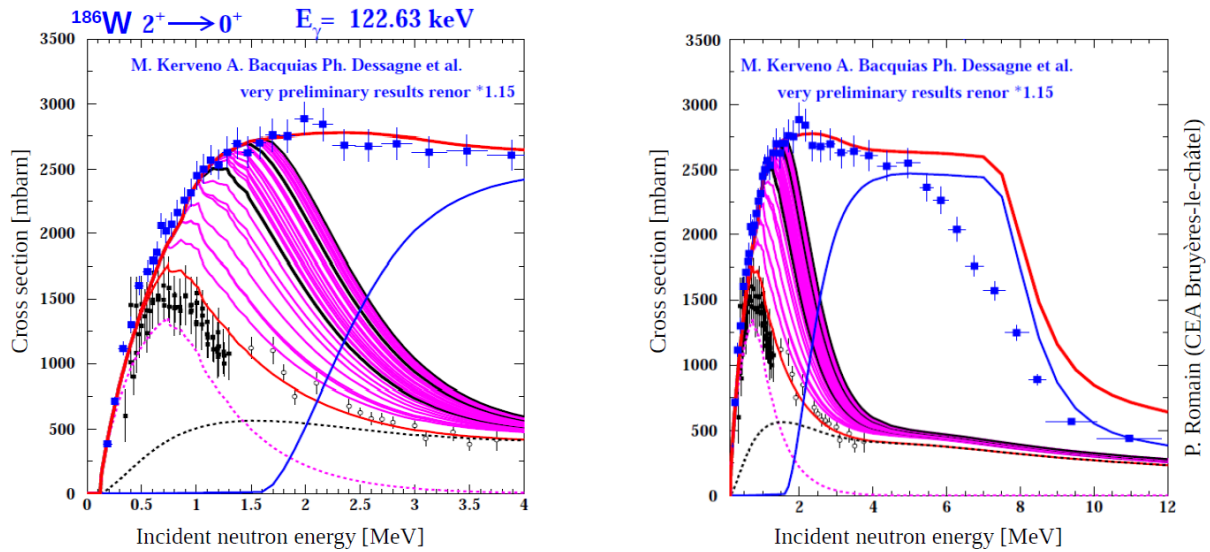


Fig. 6: Decomposition of the $^{186}\text{W}(n, n' \gamma_{2^+ \rightarrow g.s.})$ cross section according to the individual levels. The cumulative contribution of the 2^+ level is in thin red line (with the direct component in dotted black and the CN component in dotted purple). For comparison, the experimental data from [7, 8, 22] are indicated. The contribution of other levels, appropriately weighted by branching ratios are in continuous purple and black lines. The contribution of the continuum is in continuous blue. The total is the thick red line, compared to scaled data from a previous analysis (see text).

5. Conclusion and perspectives

From the preliminary results of $(n, xn\gamma)$ cross sections measured on $^{182,184,186}\text{W}$, we see that TALYS overestimates the cross section of transitions in the ground state band, while it under estimates the inter-band transitions intensity. The shape of the 2^+ to $g.s.$ transition is also not well reproduced. There is a possible effect from incomplete structure information and/or pre-equilibrium description. Looking at level production cross section would be helpful, but our data allow only the extraction of an upper limit.

Five sets of data have been recorded with GRAPHEME, using $^{nat,182,182,184,186}\text{W}$ targets. This will allow to cross-check and normalize all the cross sections. In general, 10 to 15 transitions can be studied for each isotope. A covariant analysis is being developed to reflect the correlation between measurements. All this will produce a very rich and constraining set of experimental values to compare with models.

Acknowledgments

The authors thank the team of the GELINA facility for the preparation of the neutron beam, the IRMM target laboratory for their help in the samples preparation and the technical team at IRMM and IPHC for their support. This work was funded in part by the European Commission within the Seventh Framework Programme through CHANDA, under EURATOM contract no. FP7-605203.

References

- [1] A. Kerveno *et al.*, *EPJ Web of Conferences*, 42:01005, 2013.
- [2] M. Kerveno *et al.* *Phys. Rev. C*, **87**:024609, Feb 2013.
- [3] W.M. Haynes. CRC Handbook of Chemistry and Physics. Taylor & Francis, 2012.
- [4] M.R. Gilbert *et al.* *Nuclear Fusion*, **52**(8):083019, 2012.
- [5] P. Moller *et al.* *Atomic Data and Nuclear Data Tables*, **59**(2):185 – 381, 1995.

- [6] John R. de Laeter *et al.* - Atomic weights of the elements. Review 2000 (IUPAC Technical report). 75, 2009.
- [7] D. Lister, A. B. Smith, C. Dunford. *Phys. Rev.*, **162**:1077–1087, Oct 1967.
- [8] Peter T. Guenther, Alan B. Smith, and James F. Whalen. *Phys. Rev. C*, **26**:2433–2446, Dec 1982.
- [9] D. Tronc, J.M. Salomé, and K.H. Böckhoff. *NIM A*, **228**(2–3):217 – 227, 1985.
- [10] D. Ene *et al.* *NIM A* **618**(1–3):54 – 68, 2010.
- [11] J.C. Thiry. *Measurement of (n,xn γ) Reaction Cross Sections of Interest for the Generation IV Reactors*. PhD thesis, Université de Strasbourg, 2010.
- [12] M. Mosconi *et al.* edited by E. Chiaveri (CERN, Geneva, Switzerland, 2010), September 2010.
- [13] L. Arnold *et al.* In *Proc. 14th IEEE-NPSS Conf. on Real Time, RTC'05*, pages 265–269, Washington, DC, USA, 2005.
- [14] C.R Brune. *NIM A*, **493**(1–2):106–110, 2002.
- [15] L.C. Mihailescu, L. Oláh, C. Borcea, and A.J.M. Plompen. *NIM A*, **531**(3):375–91, 2004.
- [16] Balraj Singh and Joel C. Roediger. Nuclear data sheets for a=182. *Nuclear Data Sheets*, **111**(8):2081 – 2330, 2010.
- [17] Coral M. Baglin. Nuclear data sheets for a = 184. *Nuclear Data Sheets*, **111**(2):275 – 523, 2010.
- [18] CORAL M. BAGLIN. Nuclear data sheets for a = 186. *Nuclear Data Sheets*, **99**(1):1 – 196, 2003.
- [19] A.J. Koning and D. Rochman. *Nuclear Data Sheets*, **113**(12):2841 – 2934, 2012.
- [20] A.J. Koning *et al.* TENDL-2014: TALYS-based evaluated nuclear data library, 2014.
- [21] A. Bacquias *et al.* *NEA-NSC-DOC*, 2014:13, 2014.
- [22] IAEA Nuclear Data Service Website, <http://www-nds.iaea.org/exfor/>

Determination of the important $^{30}\text{P}(p,\gamma)^{31}\text{S}$ astrophysical rapid-proton capture reaction rate

W. A. Richter^{1,2}, B. A. Brown³ and C. Wrede³

¹ iThemba LABS, Somerset West, South Africa

² Dept. of Physics, University of the Western Cape, Bellville, South Africa

³ Dept. of Physics and Astronomy and Nat. Superconducting Cyclotron Laboratory, MSU, East Lansing MI, USA

Abstract

The thermonuclear rate of the reaction $^{30}\text{P}(p,\gamma)^{31}\text{S}$ is of major importance for the interpretation of nova nucleosynthesis in the $A \geq 30$ region. Estimates based on shell-model calculations are hampered by the presence of several negative parity states in the resonance region near the proton-emission threshold. We present results of calculations in a full $(0+1)\hbar\omega$ model space which address this problem. Extensive comparisons are also made with recent experimental data for levels of ^{31}S , and it is shown that there are inconsistencies and ambiguities in the data which prevent a one-to-one correspondence with theory. The gamma-decay lifetimes and ^{30}P to ^{31}S spectroscopic factors are calculated for input into the reaction rate equations. Available experimental data is used in conjunction with the calculations to obtain a best estimate for the reaction rate.

1. Introduction

The importance of the $^{30}\text{P}(p,\gamma)^{31}\text{S}$ reaction rate for astrophysics has been extensively discussed [1]. It is, however, not well determined due to uncertainties in the properties of key resonances in the burning region. This lack of knowledge of the thermonuclear reaction rate inhibits the interpretation of observables associated with the underlying astrophysics. The uncertainties in the reaction rate stem from unmeasured quantities, ambiguities in level properties measured in different experiments, and problems with theoretical calculations stemming mainly from the presence of several negative parity states near the threshold energy.

2. Experiments to determine the reaction rate

The halflives for the target (^{30}P) and residual nucleus (^{31}S) are respectively about 2.5 minutes and 2.55 seconds. Thus direct reaction experiments are not currently feasible, so one has to resort to using beta decay, stable targets and nucleon transfer and charge exchange reactions, or alternatively inverse kinematics experiments. A brief summary of reactions used in recent major experiments follow. The dates given with each experiment refer to the date of the first publication or report, and not when the experiment was carried out.

$^{32}\text{S}(\mathbf{d},\mathbf{t})^{31}\text{S}$ (Irvine et al., 2013) This reaction was used at the Maier-Leibnitz Laboratory (MLL) in Munich to study states in ^{31}S in the energy range 6.3 - 7.1 MeV. [2].

$^{32}\text{S}(\mathbf{p},\mathbf{d})^{31}\text{S}$ (Ma et al., 2007) In a variation of the above reaction, the (p,d) reaction was utilised at the ORNL-HRIBF to study 26 states in ^{31}S , of which 17 were above the proton-emission threshold [3]. A similar experiment was done at the Yale Wright Nuclear Structure Laboratory (WNSL) by Setoodehnia et al. (2014) [4].

- $^{31}\text{P}(^3\text{He,t})^{31}\text{S}$ was employed by Wrede *et al.* (2007) [5] at the Yale-WNSL and by Parikh *et al.* [6] at the MLL, Munich (2011) in their studies of ^{31}S states. In a more extensive analysis of the first experiment [7] a total of 17 new levels, and 5 tentative new levels were determined, and 5 tentatively known levels were confirmed. The experimental information was supplemented by data from $^{32}\text{S}(d,t)^{31}\text{S}$ measurements. Parikh *et al.* [6] observed states in the energy region 6.1 - 7.1 MeV.
- $^{28}\text{Si}(\alpha,n\gamma)^{31}\text{S}$ The fusion-evaporation reaction was employed by Doherty *et al.* (2014) [8], [8] with the Gammasphere detector array at Argonne National Laboratory using the ATLAS accelerator.
- $^{12}\text{C}(^{20}\text{Ne},n\gamma)^{31}\text{S}$ (Jenkins *et al.*, 2005 [9],[10]). Excited states in ^{31}S and ^{31}P were populated in the $^{12}\text{C}(^{20}\text{Ne},n)$ and $^{12}\text{C}(^{20}\text{Ne},p)$ reactions, respectively, at a beam energy of 32 MeV, using the ATLAS accelerator at the Argonne National Laboratory. Their resulting γ decay was detected with the Gammasphere array in coincidence with ^{31}S residues at the focal plane of the Fragment Mass Analyzer.
- $^{30}\text{P}(d,n\gamma)^{31}\text{S}$ (Kankainen, 2013 [11]) This transfer reaction was studied in inverse kinematics at the NSCL, East Lansing to study key astrophysical resonances in ^{31}S . The ^{31}S ions were analyzed by the S800 spectrometer and identified by energy loss and time-of-flight measurements. γ rays from the decays of excited states in ^{31}S were detected in coincidence with the recoiling ^{31}S ions using GREINA.
- $^{31}\text{Cl}(\beta,\gamma)$ An alternative approach is to populate $l = 0$ resonances with ^{31}Cl decay. This was done in an experiment in February and March, 2014 at the NSCL, East Lansing (Bennett *et al.*) [12]. Fast beams of ^{31}Cl were produced using projectile fragmentation of a ^{36}Ar beam on ^9Be . Gammas were detected with the Yale Clovershare array of HPGe detectors.
- $^{31}\text{Cl}(\beta,p)$ and $^{31}\text{Cl}(\beta,\gamma)$ (Saastamoinen, PhD Thesis, 2011, Dept. of Physics, University of Jyväskylä.). The experiments detecting both protons and gammas from excited states in ^{31}S were carried out at Texas A&M University. In an earlier similar experiment at IGISOL (Kankainen *et al.*, 2006 [13]) ^{31}Cl nuclei were produced via $^{32}\text{S}(p,2n)$ fusion-evaporation reactions induced by a 40 MeV or 45 MeV proton beam on a ZnS target. The beta decay of ^{31}Cl was studied with a silicon detector array and a HPGe detector.

Comparisons of results from these experiments with theory are made in a later section.

3. Theoretical calculation of the reaction rate

The theory for positive parity states is based on the USDB-cd ρ n Hamiltonian as used in our previous (p, γ) rate calculations for positive parity final states in the sd -shell [14], [15], [16]. At the high excitation energies considered here, many negative parity states start to appear. We consider for the first time a microscopic model for these states. The basis consists of a complete $1\hbar\omega$ basis made from all possible excitations of one nucleon from $0p$ to $1s - 0d$ or the excitation of one nucleon from $1s - 0d$ to $0p - 1f$. The M -scheme dimension in this basis is on the order of two million and they are calculated with NuShellX in a proton-neutron basis [17]. We use the WBP Hamiltonian from [18] that was designed to reproduce the energies of $1\hbar\omega$ states for $A = 10 - 20$. WBP also contains the $sd - pf$ Hamiltonian from [19] that was designed to reproduce energies of $1\hbar\omega$ states in nuclei with $A = 35 - 43$. WBP has not before been applied to the middle of the sd shell due to the large dimensions involved. The single-particle energies for the $0p$ and $0p - 1f$ orbitals were fixed by energies of low-lying negative parity states in $A = 27$ and $A = 29$.

Table 1: Properties of levels in ^{31}S between 5.9 and 7 MeV. See text for details.

n	Experiment						Theory					
	E_{res} (keV)	E_x (keV)	$(2J)\pi$	$(2J)\pi$	$(2J)\pi$	$(2J)\pi$	$(2J)\pi k$	E_x (keV)	$(2J)\pi k$	E_x (keV)	ℓ	C^2S
	NDS 2013 [20]	NDS 2013 [20]	Wrede 2014 [1]	Doherty et al. 2012 [8]	Parikh et al. 2011 [6]	Jenkins et al. 2006 [9]	USDB-cdpn		$1h\omega$			
1		5896	3+,5+				3+6(t)	5965			0	0.018
2		5959	3+,5+	*			5+7(t)	6044			2	0.042
3		5978	(9+)				9+3(g)	5829			2	0.023
4	8	6139	(7+)	b	(3,7)+	9	3+7(t)	6141			0	0.013
5	29	6160	(5-,7+)	b	7[+]	5			5-2(t)	5825		
6	124	6255	1+	1+	[1+]	1+	1+5(g)	6259			0	0.0017
7	149	6280	3+	3+	[3+]	3+	3+8(g)	6280			0	0.00024
8	196	6327	(3)	b	3[-]	1+			3-2	6327	1	0.29
9	226	6357	(5-)	b	5[-]	3+						
10	246	6377	(9-)	(9)	(5,9) [9-]	[9-]			9-1(g)	6313	3	0.39
11	261	6392	(5+)	a,(5+)	5+						2	0.061
12	263	6394	(11+)	a,(11)	11[+]	[11+]	5+8	6402				$p3$
13	270	6401		a,c	[7(-)]		11+1(g)	6364				
14	289	6421	(1+,3+,5+)	*			7+6(t)	6298			2	0.053
15	411	6542	(3-)	b	3[-]	(7,9)			3-3	6757	1	0.037
16	451	6583	(7)	(7)	(3,5,7)[-]	7			5-3	6792	1	0.0043
17	505	6636	(9-)	(9)	(5,9)[9-]	9[-]			9-2(g)	6682	3	0.11
18	589	6720	(5)			5					2	0.081
19	618	6749	3+			3+					0	0.0045
20	665	6796		*			5+9(t)	6862				$p4$
21	702	6833	(11-)			11[-]	3+9	6965				$p5$
22	705	6836		*					11-1(g)	6833		
23	717	6848		*								
24	741	6872	(11)			11						
25	806	6937	(1+,3+,5+)			(1-5)+						
26	830	6961				1+	1+6	6995			0	0.0026
27	844	6975	1+				1+7	7028			0	0.000015
28									5-2	5825	1	0.067
29	116								1-2	6247	1	0.23
30	471								1-3	6602	1	0.068
31	252								7-3	6838	3	0.0058
32	712								9-3	6843	3	0.10
33	760								7-4	6891	3	0.18
34	765								3-4	6896	1	0.19
35	790								5-4	6921	1	0.48
36	767						9+4	6898				
37	848						7+7	6979			2	0.00092

4. Comparison between experiment and theory

Selected experimental and the theoretical results are shown in Table I and Fig. 1. The first columns 2-8 give the experimental data. Columns 3-4 are the values given in the recent Nuclear Data Sheets (NDS) compilation [20], and the 2nd column is the resonance energy based on the NDS energy. The 5th column gives the spin-parity assignments from the recent review by Wrede [1] that are based purely on the data for ^{31}S and excludes spin-parity assignments based upon assumed correspondence with mirror levels in ^{31}P , that are indicated by the spin-parity inside the square brackets in columns 6-8. The letters (a,b,c) in column 5 correspond to the footnotes given by Wrede. For (a) there is some question of whether there are two or three levels between $E_x = 6390$ keV and 6405 keV. If one assumes that the two levels seen in Ref [8] are at their reported energies, then one of the two levels reported in Refs. [5], [6] and [2] is different and there would be three levels all together. For (b) there are conflicting spin-parity assignments between Parikh et al. [6] and Doherty et al. [8]. The spin-parity of the 6139 keV state assigned by Doherty et al. [8] is based only on a possible match to a level in ^{31}P and it was changed by Irvine et al. [2]. For (c) the spin-parity is unconstrained. The * indicate levels of questionable existence. The levels at 5959 and 6848 keV that are only seen in a low resolution (p,d) experiment [3] are probably amalgams of neighboring levels. The level at 6421 keV has only been seen a ^{31}Cl beta-decay experiment [13] and not confirmed in a reaction experiment. The level at 6796 keV has only been seen in a low resolution ($^3\text{He},n$) experiment and has not been confirmed. The placement of two nearby levels at 6833 and 6836 keV was inferred from the fact that a significant proton emission

was observed at this energy that may not be expected for a level with $J = 11/2$ that would decay by $\ell=5$ [1]. Wrede has suggested that increased communication between the relevant experiment groups would facilitate some resolution of the conflicting spin-parity assignment [1], and a workshop was held to this end in 2014; the results will be published in an upcoming Focus Issue of *Eur. Phys. J. Plus*.

Columns 11-12 give the results obtained with the $1\hbar\omega$ Hamiltonian. The format in the 11th column is $(2J) - k$, where $-$ indicates negative parity and k is the number of the state for a given J . Columns 13-14 give the calculated spectroscopic factors. The labels in the last column indicate the largest contributions for positive parity p . For negative parity see the comments in section 5.

Columns 9-10 give the results obtained with the USDB-cdnp Hamiltonian. The format in the 9th column is $(2J) + k$ where $+$ indicates positive parity and k is the number of the state for a given J . All of the USD-cdnp energies given have been shifted down by 240 keV in order to align theory and experiment for the well established $3/2^+$ T=3/2 level at 6280 keV. This gives energies for other positive parity states in the region of interest within 100 keV of possible associations with experiment as shown in Table I. A similar energy shift is also found for the comparison of theory and experimental levels in ^{31}P , and is about the same with the USDA Hamiltonian. This shift indicates a possible systematic failure of the USD Hamiltonians at high energy. For future work it may be interesting to include some these levels in the determination of the empirical two-body matrix elements [21]. Since the reaction rate is exponentially sensitive to the resonance energy, the association with experimental energies levels is important. Some of the associations in Table I are rather certain (good, g) but others are very tentative (t). All unmarked and t matches need to be confirmed. Unmatched theoretical levels are given at the bottom.

The energies for the $1\hbar\omega$ states in Table I are shifted down by 354 keV in order to align theory and experiment for the well established $11/2^-$ level at 6824 keV. The theoretical levels have been associated with known experimental levels in the Table with the labels good (g) and tentative (t). This association is crucial for a precise calculations of the rates. Thus, the rates we obtain will depend upon a confirmation of the experimental and theoretical associations. The $1\hbar\omega$ states that cannot be matched with experiment are given in the bottom of the Table I. All levels up to 6.8 MeV can be tentatively matched with theory except for the experimental levels at 6160, 6420 and 6796 keV; but the latter two of these are of questionable experimental existence. There are two $1/2^-$ negative-parity states predicted at 6247 and 6602 that cannot be matched to know experimental levels. Above 6.8 MeV the two $1/2^+$ levels at 6961 and 6975 MeV have a good association with theory with the upper of these in theory being the $1/2^+$ T=3/2 level. In addition, between 6.8 and 7.0 MeV there are four unmatched experiment levels and seven theoretical levels, indicating that there are several levels in this region that have not yet been observed.

The experimental information on the states in the mirror nucleus ^{31}P in the 6-8 MeV energy range is not complete enough to help resolve the spin-parity ambiguities in the ^{31}S or to help with the associations between experiment and theory we have made in Table I.

5. Calculation of the reaction rate

Our calculated rates are shown in Fig. 1 based on the resonance energies and spectroscopic factors given in Table I. They are based on the Eqs. used in [16] with the information in Table I together with gamma-decay lifetimes for positive-parity states obtained with the USDB-cdnp Hamiltonian and the effective gamma-decay operator for M1 and E2 from [22]. (Fig. 1 and Table II of Ref. [23] did not include the contribution from the theoretical $3/2_2^-$ state that was associated with the experimental state at 6327 keV in Table I. The corrected versions are given here.) The most important negative parity states are labeled in panel (c). The spectroscopic properties of the $3/2_3^-$ and $1/2_2^-$ states are given in Table III of Ref. [23]. The spectroscopic properties of the $3/2_2^-$ state shown in panel (c) are: $\Gamma_\gamma = (0.009)$ eV, $\Gamma_p = 6.7 \times 10^{-6}$

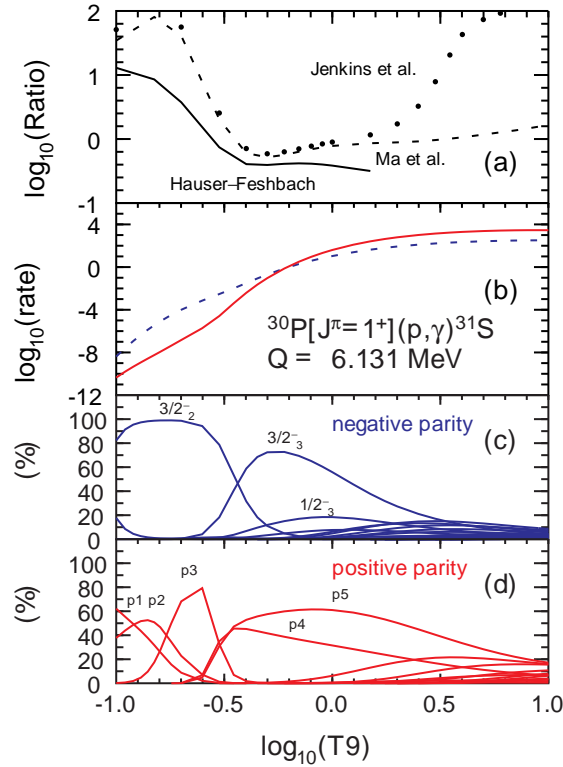


Fig. 1: The total rp reaction rate versus temperature $T9$ (GigaK) (top panel) and the contribution of each of the final states (lower panels) obtained with the data from Table I. The results are separated into the contributions from positive and negative parity states. The total rate is shown separately for the positive parity (red line) and negative parity (blue dashed line) final states. The top panel shows the present rate divided those from other models as discussed in the text.

eV, $\omega\gamma = 4.5 \times 10^{-6}$ eV and $C^2S(\ell=1)=0.29$. The rate in the region near $\log_{10}(T9) = -0.8$ is one to two orders or magnitude larger than those from previous works. This large increase demonstrates the importance of confirming the spin-parity assignments of levels in the excitation energy range of 6.1 to 6.7 MeV in ^{31}S .

The bottom parts of the figure show the contributions from individual final states. The labels for the most important positive-parity contributions in Fig. 1 are given on the right-hand side of Table I. For the hottest ONe novae on white dwarfs close to the Chandrasekhar limit the rate up to about $T9 = 0.5$ [$\log_{10}(T9)=-0.3$] is important [24]. For most of these $\Gamma_\gamma \gg \Gamma_p$ and the gamma lifetime is thus not important. The experimental associations of the $3/2^-_2$, $3/2^-_3$ and $5/2^+_8$ ($p3$) states need to be verified, and the gamma widths of the $3/2^-_2$ and $3/2^-_3$ states need to be measured. The $1/2^-_3$ state has not yet been associated with experiment. The experimental association of the $3/2^+_8$ ($p2$) state enters only because of its calculated small isospin-forbidden proton decay spectroscopic factor - this needs to be verified. Overall, the rate we obtain is still uncertain. But our results provide the essential ingredients that will need to be combined with experiment when the spin-parity and decay properties of these states in ^{31}S are verified.

The top panel of Fig. 1 shows the present rate divided by those give by the Hauser-Feshbach (HF) model [25], and the resonance state results based on the assumptions made by Jenkins et al. [9] and Ma et al. [3]. The rates for these are given in the Reaclib data base [26]. These previous rates are

based on assumptions that are much less microscopic than the present.

6. Conclusions

In summary, in view of the importance of the $^{30}\text{P}(p,\gamma)^{31}\text{S}$ reaction, we considered the major aspects leading to uncertainties in calculating the reaction rate. Because of the high excitation energies involved in the resonance region, several negative parity states appear. Calculations were done for the first time in this mass region in a full $(0+1) \hbar\omega$ model space to take their contributions into account. It turns out that the negative parity states make contributions to the reaction rate comparable to the positive parity states. The theoretical energies were correlated with available experimental energies, which required a review of ambiguities and uncertainties in the experimental data. A number of cases are suggested where improved data are required. It is evident that there are several experimental inconsistencies and ambiguities which would require further investigation to resolve.

Acknowledgments

This work is partly supported by NSF Grant PHY-140442, the Joint Institute for Nuclear Astrophysics NSF Grant PHY08-22648, and the National Research Foundation of South Africa Grant No. 76898.

References

- [1] C. Wrede, *AIP Advances in Physics* **4** (2014) 041004 and private communication.
- [2] D. Irvine *et al.*, *Phys. Rev. C* **88** (2013) 055803
- [3] Z. Ma *et al.*, *Phys. Rev. C* **76** (2007) 015803.
- [4] Private communication.
- [5] C. Wrede *et al.*, *Phys. Rev. C* **76** (2007) 052802.
- [6] A. Parikh *et al.*, *Phys. Rev. C* **83** (2011) 045806.
- [7] C. Wrede *et al.*, *Phys. Rev. C* **79**, 045803 (2009)
- [8] D. T. Doherty *et al.*, *Phys. Rev. Lett.* **108** (2012) 262502.
- [9] D. G. Jenkins *et al.*, *Phys. Rev. C* **73** (2006) 065802.
- [10] D. G. Jenkins *et al.*, *Phys. Rev. C* **72** (2005) 031303 .
- [11] A. Kankainen *et al.*, <http://meetings.aps.org/link/BAPS.2013.DNP.KD.2> (2013)
- [12] C. Wrede, M. B. Bennett *et al.*, *Physics Procedia* **66** (2015) 532
- [13] A. Kankainen *et al.*, *Eur. Phys. J. A* **27** (2006) 67.
- [14] W. A. Richter, B. A. Brown, A. Signoracci and M. Wiescher, *Phys. Rev. C* **83** (2011) 065803; *Phys. Rev. C* **84** (2011) 059802.
- [15] W. A. Richter and B. A. Brown, *Phys. Rev. C* **85** (2012) 045806.
- [16] W. A. Richter and B. A. Brown, *Phys. Rev. C* **87** (2013) 065803.
- [17] NuShellX@MSU, B. A. Brown, W. D. M. Rae, E. McDonald and M. Horoi, <http://www.nucl.msu.edu/~brown/resources/resources.html>.
- [18] E. K. Warburton and B. A. Brown, *Phys. Rev. C* **46** (1992) 923.
- [19] E. K. Warburton, J. A. Becker and B. A. Brown, *Phys. Rev. C* **41** (1990) 1147.
- [20] C. Ouellet and B. Singh, *Nuclear Data Sheets* **114** (2013) 209.
- [21] B. A. Brown and B. H. Wildenthal, *Ann. Rev. of Nucl. Part. Sci.* **38** (1988) 29.
- [22] W. A. Richter, S. Mkhize and B. A. Brown, *Phys. Rev. C* **78** (2008) 064302-1.
- [23] B. A. Brown, W. A. Richter and C. Wrede, *Phys. Rev. C* **89** (2014) 062801.
- [24] S. A. Glasner and J. W. Truran, *The Astrophysical Journal*, **692** (2009) 58 .
- [25] T. Rauscher and F. K. Thielemann, *Atomic Data and Nuclear Data Tables* **75** (2000) 1 .
- [26] The JINA Reaclib Database, H. Cyburt *et al.*, *Astrophys. J. Suppl. S.* **189**, 1 (2010) 240.

Enhanced low-energy γ -decay probability – Implications for r -process (n, γ) reaction rates

A. C. Larsen¹, M. Guttormsen¹, F. L. Bello Garrotte¹, L. A. Bernstein^{2,3}, D. L. Bleuel², A. Bracco⁴, B. A. Brown^{5,6}, F. Camera⁴, L. Crespo Campo¹, S. Frauendorf⁷, B. L. Goldblum³, S. Goriely⁸, A. Görger¹, K. Hadynska-Klek¹, T. W. Hagen¹, S. Harissopulos⁹, B. V. Kheswa¹⁰, M. Klintefjord¹, S. Leoni⁴, S. N. Liddick^{5,11}, F. Naqvi^{5,6}, G. Perdikakis^{12,5}, T. Renstrøm¹, A. M. Rogers¹³, S. J. Rose¹, E. Sahin¹, R. Schwengner¹⁴, S. Siem¹, A. Simon⁷, A. Spyrou^{5,6}, G. M. Tveten¹, A. Voinov¹⁵, M. Wiedeking¹⁰, H. Utsunomiya¹⁶

¹ Department of Physics, University of Oslo, Oslo, Norway

² Lawrence Livermore National Laboratory, Livermore, California, USA

³ University of California, Berkeley, California, USA

⁴ INFN, Sezione di Milano and Dipartimento di Fisica, University of Milano, Milano, Italy

⁵ Nat. Superconducting Cyclotron Laboratory, Michigan State University, East Lansing MI, USA

⁶ Department of Physics and Astronomy, Michigan State University, East Lansing, Michigan, USA

⁷ Department of Physics, University of Notre Dame, Notre Dame, Indiana, USA

⁸ Institut d'Astronomie et d'Astrophysique, Université Libre de Bruxelles, Brussels, Belgium

⁹ Institute of Nuclear Physics, NCSR "Demokritos", Athens, Greece

¹⁰ iThemba LABS, Somerset West, South Africa

¹¹ Department of Chemistry, Michigan State University, East Lansing, Michigan, USA

¹² Central Michigan University, Mount Pleasant, Michigan, USA

¹³ University of Massachusetts Lowell, Massachusetts, USA

¹⁴ Helmholtz-Zentrum Dresden-Rossendorf, Dresden, Germany

¹⁵ Department of Physics and Astronomy, Ohio University, Athens, Ohio, USA

¹⁶ Department of Physics, Konan University, Kobe, Japan

Abstract

An unexpected enhancement in the average, reduced γ -decay strength at very low γ -transition energies has been observed in fp -shell nuclei as well as in the Mo region. Very recently, it has been discovered in ^{138}La , which is, so far, the heaviest nucleus to display this feature. In this work, we present an experimental and theoretical overview of the low-energy enhancement. In particular, experimental evidence for the dipole nature of the enhancement, and shell-model calculations indicating strong, low-energy $M1$ transitions are shown. Possible implications of this low-energy enhancement on astrophysical (n, γ) reaction rates of relevance for r -process nucleosynthesis are discussed.

1. Introduction

One of the remaining major challenges in nuclear astrophysics today is to properly describe the nucleosynthesis for elements heavier than iron [1]. The main nucleosynthesis processes creating heavy elements were identified by Burbidge, Burbidge, Fowler and Hoyle [2] and also independently by Cameron [3]. The slow neutron-capture (s -) process and the rapid neutron-capture (r -) process are known to produce almost 100% of the observed nuclides heavier than iron. The s -process is rather well understood from a nuclear-physics point of view, as it relies on a nuclear reaction network in the vicinity of the β -stability line where the relevant reaction rates are to a large extent experimentally accessible (see Ref. [4] and Refs. therein). The r -process, on the other hand, remains elusive due to two main factors: (i) the astrophysical site(s) is(are) not yet clearly identified; popular suggestions include



Fig. 1: (Color online) The Silicon Ring SiRi [16] and the γ -detector array CACTUS [15].

the neutrino-driven wind following a core-collapse supernova, and neutron-star mergers [5, 6]; (ii) the majority of the crucial nuclear-data input required for modeling r -process abundances are not experimentally constrained, and large theoretical uncertainties in the determination of r -process reaction rates are a substantial obstacle for a meaningful comparison with observed r -process abundances. In sophisticated and more realistic scenarios for the rapid neutron capture (r -) process, (n, γ) rates may play a pivotal role [5], especially for cold r -process scenarios where an (n, γ) – (γ, n) equilibrium cannot be established. Hence, a good knowledge of nuclear γ -decay properties at high excitation energy (up to the neutron separation energy S_n) is crucial. The *nuclear level density* and the *γ -ray strength function* (γ SF) are two of the main ingredients needed to calculate radiative neutron-capture cross sections and reaction rates.

Until recent years, the γ SF was believed to decrease with decreasing transition energy, which is reflected in current recommendations and implementations of γ SF models [7, 8, 9]. However, measurements of the γ SF for highly excited iron isotopes (up to S_n) clearly demonstrate the opposite [10, 11]; for these nuclei, the γ SF for γ energies less than 4 MeV exhibits an increase as the γ -ray energy decreases. In the following, the experiments revealing the low-energy enhancement will be discussed, as well as theoretical interpretations of the phenomenon, and its potential impact on radiative neutron-capture rates for very neutron-rich nuclei.

2. Experiments, level density and γ SF data

The low-energy enhancement was first discovered in $^{56,57}\text{Fe}$ [10], where the Oslo method [12, 13, 14] was applied on particle- γ coincidence data from the ($^3\text{He}, ^3\text{He}'\gamma$) and ($^3\text{He}, \alpha\gamma$) reactions. The MC-35 Scanditronix cyclotron delivers proton, deuteron, ^3He and α beams. The current experimental setup at the Oslo Cyclotron Laboratory (OCL) consists of the γ -ray detection array CACTUS [15], which is built up of 26 collimated NaI(Tl) detectors, and the Silicon Ring (SiRi), which is a segmented $\Delta E - E$ particle-telescope array [16] measuring the charged particles emitted in the nuclear reactions (see Fig. 1). The energy of the emitted particles, taking into account the reaction kinematics and the Q -value of the reaction, gives information on the excitation energy of the residual nucleus. A brief overview of the Oslo method is given below.

The Oslo method consists of four main steps:

1. Unfold the excitation-energy tagged NaI spectra to correct for the detector response [12];
2. Obtain the distribution of primary γ rays for each excitation-energy bin by an iterative subtraction method [13];

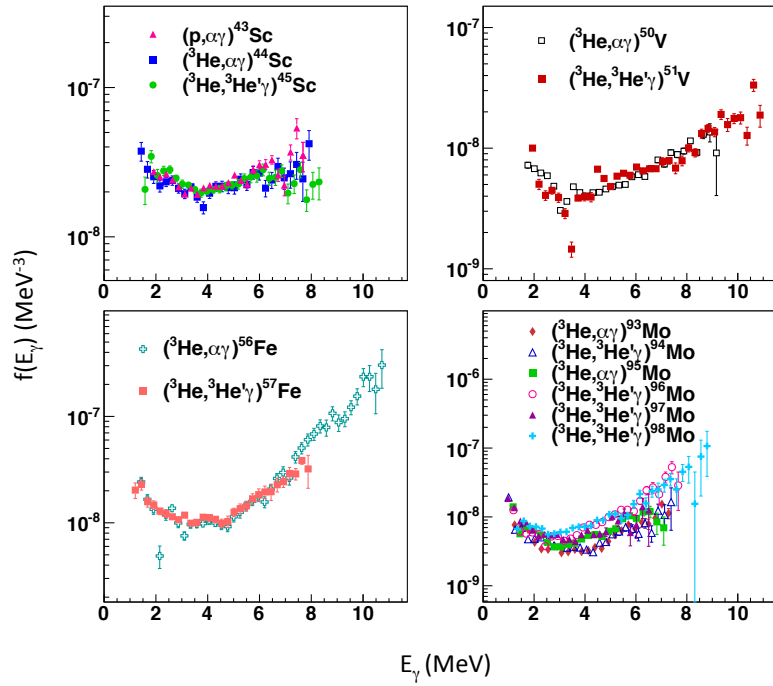


Fig. 2: (Color online) Data from OCL showing the γ SF of Sc [20, 21] (upper left), Fe [10] (lower left), V [22], and Mo isotopes [23].

3. Extract the functional form of the level density $\rho(E)$ and the γ SF $f(E_\gamma)$ from an iterative, simultaneous χ^2 fit of the landscape of primary γ rays [14];
4. Normalize the obtained level density and γ SF to known, discrete levels, neutron-resonance parameters, and/or other auxiliary data [14, 17].

Note that for step 3, no particular, initial assumptions are needed for the shape of the level density and/or the γ SF; in fact, a flat distribution is used for the first trial function. The final result does not depend on the choice of the initial trial function.

Regarding nuclear level densities, one of the perhaps most important results is that they increase linearly in a log plot (see e.g. Ref. [18] and references therein), which is interpreted as the nuclear temperature being constant and they are very well approximated by the constant-temperature expression [19]: $\rho(E) = 1/T \exp(E - E_0)/T$, where T is the nuclear temperature and E_0 is an energy shift. This implies that a first-order phase transition is taking place [18].

The low-energy enhancement has been observed in many light nuclei using the Oslo method, such as Sc [20, 21], V [22] and Mo isotopes [23] (Fig. 2). Very recently, the low-energy enhancement was found in ^{138}La [24], which is the heaviest nucleus exhibiting this feature as of today. For a full list of references and for open access to the data, see [25]. In Ref. [10], the low-energy enhancement was confirmed by examining intensities of two-step cascade spectra following neutron capture on ^{56}Fe , i.e. $^{56}\text{Fe}(n, \gamma\gamma)^{57}\text{Fe}$. Recently, the low-energy enhancement was also confirmed for the ^{95}Mo case [26], using a new technique to extract the relative γ SF from the quasicontinuum to individual low-lying levels.

As the standard Oslo method is restricted to measuring nuclei close to the valley of stability, a new method has been developed, the β -Oslo method [27], where level density and γ SF are inferred from total absorption spectra following β decay of a neutron-rich nucleus. The first case where the method was used was the β decay of ^{76}Ga into ^{76}Ge , where the γ rays emitted from ^{76}Ge were measured with

the segmented, total-absorption spectrometer SuN [28]. Now, the initial excitation energy of ^{76}Ge is given by the sum of all γ rays, while the individual segments provide the γ spectra for each excitation-energy bin. Having the excitation-energy vs. γ -ray energy matrix at hand, the Oslo method can be used to extract the level density and γSF . This technique is very promising for neutron-rich nuclei where the Q -value for β decay is close to the neutron separation energy in the daughter nucleus, and when there is no significant branch of β -delayed neutrons. New data on ^{70}Ni taken at NSCL/MSU in February 2015 represent the first case of a neutron-rich nucleus analyzed with the β -Oslo method [29].

For a long time, the low-energy enhancement was a complete puzzle, as it appeared to contradict all established models of the electric dipole strength, which was believed to be the dominant contributor to the γSF for γ -ray energies below the neutron separation energy. Speculations about its physical origin included abnormally strong rotational $E2$ transitions in the quasicontinuum, or even vibrational transitions, or simply that there were leftovers of strong $E2$ transitions from the ground-state rotational bands that were not subtracted correctly in the procedure to obtain the primary- γ distributions. Hence, gaining insight into the multipolarity of the low-energy enhancement was of utmost importance. Recent experimental work has indeed shown that the low-energy enhancement in ^{56}Fe is dominated by dipole transitions [11], as seen from angular distributions of the low-energy enhancement utilizing the angles of the NaI detectors in CACTUS. The remaining experimental challenge is to firmly establish the electromagnetic character of the low-energy enhancement, be it magnetic or electric or a mix of both, as theoretical approaches explaining this feature differ on this point. This will be discussed in the following section.

3. Theoretical descriptions of the low-energy enhancement

There has been significant progress in the theoretical understanding of the low-energy enhancement the two last years. From having no theoretical explanation, there are now three articles describing and (at least qualitatively) reproducing the experimental results. First, in Ref. [30], the authors make use of the thermal continuum quasiparticle random-phase approximation and explain the low-energy enhancement as due to $E1$ transitions from thermally excited single-quasiparticles. Moreover, the shell-model calculations presented in Refs. [31, 32] demonstrate $M1$ transitions with strong $B(M1)$ values for low transition energies, providing a steadily increasing and non-zero γSF as $E_\gamma \rightarrow 0$. The shell-model $B(M1)$ values from Ref. [32] are shown in Fig. 3; note that these are directly proportional to the $M1$ γSF and the level density at the initial excitation energy, see Eq. (1) in Ref. [32].

As the theoretical interpretations differ on the electromagnetic nature of the low-energy enhancement, it is imperative to determine experimentally whether it is magnetic or electric, or whether both contribute to the observed structure. In Ref. [10], an attempt was made to determine the electromagnetic character by calculating the $(n, \gamma\gamma)$ two-step cascade intensities within a statistical decay model, but with no success; it was found that the error bars were too large and, within the experimental uncertainties, both $E1$ and $M1$ (and even $E2$) transitions could be present.

In principle, on the theoretical side, it would be ideal to calculate both $E1$ and $M1$ transitions within the same framework and model. As of today, the shell-model calculations concern only $M1$ (and $E2$) transitions, while the QRPA approaches have been restricted to $E1$ transitions only. Hence, in the future, an experimental effort to nail down the electromagnetic character, in combination with a theoretical development to include all dipole transitions within the same framework, is highly desired to understand the mechanism behind the low-energy enhancement.

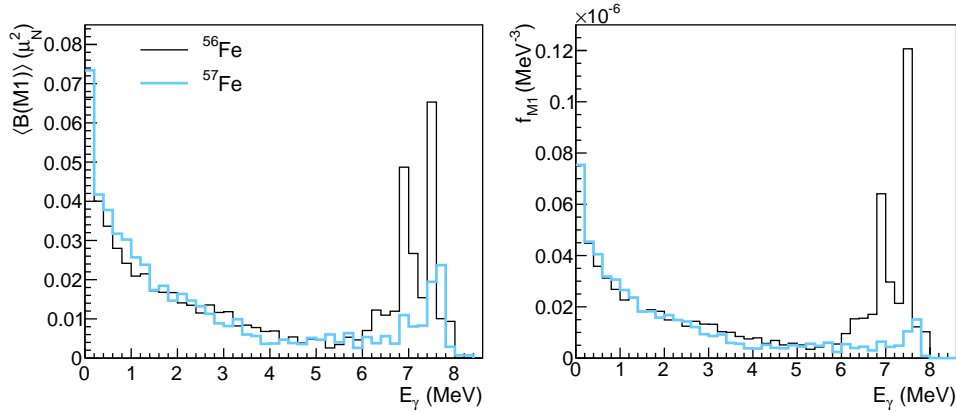


Fig. 3: Averaged $B(M1)$ values for transition-energy bins of 200 keV and excitation energies between $E \approx 6 - 8$ MeV and $\approx 5 - 8$ MeV for $^{56,57}\text{Fe}$ (left) and the corresponding γ SFs (right); from the calculations of Ref. [32]. Note that these are from positive(negative)-parity levels for ^{56}Fe (^{57}Fe) only.

4. Impact on radiative neutron-capture reaction rates

As mentioned in Sec. 1., the nuclear level density and γ SF are important input parameters for calculating astrophysical (n, γ) reaction rates. Moreover, the low-energy enhancement in the γ SF may have a non-negligible effect on these rates, as shown in e.g. Refs. [33, 34]. Here, using the nuclear-reaction code TALYS [8], and assuming that the low-energy enhancement will persist also for very neutron-rich nuclei involved during the r -process neutron irradiation, an increase in the (n, γ) rates of a factor of $\sim 10 - 100$ is found for neutron-rich Fe, Ge, Mo and Cd isotopes.

Such a significant effect on the reaction rates brings further motivation to obtain a good understanding of the low-energy enhancement, since a direct measurement of any (n, γ) rate on unstable nuclei, and even less on nuclei of r -process relevance is currently not possible, and will probably remain out of reach for many years to come. Furthermore, a large-scale r -process network calculation typically involves ≈ 5000 nuclei and ≈ 50000 reaction rates. Thus, one has to rely on theoretical estimates of these rates, which in turn call for robust and sound theoretical approaches to obtain a reasonable predictive power [5]. Hence, testing these models against experimental data, both for stable and neutron-rich nuclei, is crucial. A close interaction between nuclear experiment and theory as well as astrophysics observations and theory will hopefully bring new insight on the many remaining mysteries of the heavy-element nucleosynthesis.

5. Summary

A low-energy enhancement has been discovered in the γ SF of many nuclei. Theoretically, there are two approaches providing an explanation for the low-energy enhancement; however, they differ on the physical mechanism behind the structure and its electromagnetic character. An experimental determination of the electromagnetic character of the low-energy enhancement is necessary to resolve this discrepancy.

The low-energy enhancement, if present in very neutron-rich nuclei, may have a significant impact on astrophysical (n, γ) reaction rates relevant to the r -process. Reducing the uncertainties in the nuclear input data of large-scale r -process calculations is highly desirable, and as such, a deep understanding of the γ SF would be of great importance both for a fundamental nuclear structure perspective

as well as from a nuclear astrophysics point of view.

Acknowledgments

A. C. L. acknowledges funding from the ERC-STG-2014 under grant agreement No. 637686. M. W. acknowledges support by the National Research Foundation of South Africa under grant No. 92789. S. G. is FNRS research associate. B. A. B. acknowledges support from NSF grant No. PHY-1404442.

References

- [1] *Connecting Quarks with the Cosmos: Eleven Science Questions for the New Century*, Board on Physics and Astronomy, The National Academic Press, 2003.
- [2] E. M. Burbidge, G. R. Burbidge, W. A. Fowler, and F. Hoyle, *Rev. Mod. Phys.* **29**, 547 (1957).
- [3] A. G. W. Cameron, *Pub. Astron. Soc. Pac.* **69**, 201 (1957).
- [4] F. Käppeler, *Prog. Part. Nucl. Phys.* **43**, 419 (1999).
- [5] M. Arnould, S. Goriely and K. Takahashi, *Phys. Rep.* **450**, 97 (2007).
- [6] O. Just, A. Bauswein, R. Ardevol Pulpillo, S. Goriely, H.-T. Janka, *Month. Not. Roy. Astron. Soc.* **448**, 541 (2015).
- [7] R. Capote *et al.*, *Nucl. Data Sheets* **110**, 3107 (2009).
- [8] A. Koning, S. Hilaire, and M. C. Duijvestijn, "TALYS-1.6", *Proc. Int. Conf. on Nuclear Data for Science and Technology*, Nice, France, EDP Sciences, 2008, p. 211-214.
- [9] M. Herman *et al.*, *Nucl. Data Sheets* **108**, 2655 (2007).
- [10] A. Voinov *et al.*, *Phys. Rev. Lett.* **93**, 142504 (2004).
- [11] A. C. Larsen *et al.*, *Phys. Rev. Lett.* **111**, 242504 (2013).
- [12] M. Guttormsen *et al.*, *NIM A* **374**, 371 (1996).
- [13] M. Guttormsen, T. Ramsøy, and J. Rekstad, *NIM A* **255**, 518 (1987).
- [14] A. Schiller *et al.*, *NIM A* **447** 494 (2000).
- [15] M. Guttormsen *et al.*, *Phys. Scr.* **T 32**, 54 (1990).
- [16] M. Guttormsen *et al.*, *NIM A* **648**, 168 (2011).
- [17] A. C. Larsen *et al.*, *Phys. Rev. C* **83**, 034315 (2011).
- [18] L. G. Moretto *et al.*, in review; arXiv:1406.2642 (2015).
- [19] T. Ericson, *Nucl. Phys.* **11**, 481 (1959).
- [20] A. C. Larsen *et al.*, *Phys. Rev. C* **76**, 044303 (2007).
- [21] A. Bürger *et al.*, *Phys. Rev. C* **85**, 064328 (2012).
- [22] A. C. Larsen *et al.*, *Phys. Rev. C* **73**, 064301 (2006).
- [23] M. Guttormsen *et al.*, *Phys. Rev. C* **71**, 044307 (2005).
- [24] B.V. Kheswa *et al.*, *Phys. Lett. B* **744**, 268 (2015).
- [25] <http://www.mn.uio.no/fysikk/english/research/about/infrastructure/OCL/nuclear-physics-research/compilation/>
- [26] M. Wiedeking *et al.*, *Phys. Rev. Lett.* **108**, 162503 (2012).
- [27] A. Spyrou *et al.*, *Phys. Rev. Lett.* **113**, 232502 (2014).
- [28] A. Simon, S. Quinn, A. Spyrou *et al.*, *NIM A* **703**, 16 (2013).
- [29] S. N. Liddick *et al.*, in review (2015).
- [30] E. Litvinova and N. Belov, *Phys. Rev. C* **88**, 031302(R) (2013).
- [31] R. Schwengner, S. Frauendorf, and A. C. Larsen, *Phys. Rev. Lett.* **111**, 232504 (2013).
- [32] B. Alex Brown and A.C. Larsen, *Phys. Rev. Lett.* **113**, 252502 (2014).
- [33] A. C. Larsen and S. Goriely, *Phys. Rev. C* **82**, 014318 (2010).
- [34] T. Renstrøm *et al.*, to be submitted (2015).

Nuclear Astrophysics at n_TOF facility, CERN

G. Tagliente¹, U. Abbondanno², G. Aerts³, H. Alvarez⁴, F. Alvarez-Velarde⁵, S. Andriamonje³, J. Andrzejewski⁶, L. Audouin⁸, G. Badurek⁹, P. Baumann¹⁰, F. Bečvář¹¹, F. Belloni², E. Berthoumieux³, S. Bisterzo¹², F. Calviño¹³, M. Calviani¹⁴, D. Cano-Ott⁵, R. Capote^{15,16}, C. Carrapiço¹⁷, P. Cennini¹⁸, V. Chepel¹⁹, E. Chiaveri¹⁸, N. Colonna¹, G. Cortes¹³, A. Couture²⁰, J. Cox²⁰, M. Dahlfors¹⁸, S. David¹⁰, I. Dillman⁸, C. Domingo-Pardo²¹, W. Dridi³, I. Duran⁴, C. Eleftheriadis²², M. Embid-Segura⁵, A. Ferrari¹⁸, R. Ferreira-Marques¹⁹, K. Fujii², W. Furman²⁴, R. Gallino¹², I. Goncalves¹⁹, E. Gonzalez-Romero⁵, F. Gramegna¹⁴, C. Guerrero⁵, F. Gunsing³, B. Haas²⁵, R. Haight²⁶, M. Heil⁸, A. Herrera-Martinez¹⁸, M. Igashira²⁷, E. Jericha⁹, F. Käppeler⁸, Y. Kadi¹⁸, D. Karadimos⁷, D. Karamanis⁷, M. Kerveno¹⁰, P. Koehler²⁸, E. Kossionides²⁹, M. Krtička¹¹, H. Leeb⁹, A. Lindote¹⁹, I. Lopes¹⁹, M. Lozano¹⁶, S. Lukic¹⁰, J. Marganec⁶, S. Marrone¹, T. Martinez⁵, C. Massimi³⁰, P. Mastinu¹⁴, A. Mengoni¹⁵, P. M. Milazzo², M. Mosconi⁸, F. Neves¹⁹, H. Oberhummer⁹, J. Pancin³, C. Papachristodoulou⁷, C. Papadopoulos³¹, C. Paradela⁴, N. Patronis⁷, A. Pavlik³², P. Pavlopoulos³³, L. Perrot³, M. T. Pigni⁹, R. Plag⁸, A. Plompen³⁴, A. Plukis³, A. Poch¹³, J. Praena¹⁴, C. Pretel¹³, J. Quesada¹⁶, T. Rauscher³⁵, R. Reifarh²⁶, C. Rubbia³⁶, G. Rudolf¹⁰, P. Rullhusen³⁴, J. Salgado¹⁷, C. Santos¹⁷, L. Sarchiapone¹⁸, I. Savvidis²², C. Stephan²³, J. L. Tain²¹, L. Tassan-Got²³, L. Tavora¹⁷, R. Terlizzi¹, G. Vannini³⁰, P. Vaz¹⁷, A. Ventura³⁷, D. Villamarin⁵, M. C. Vincente⁵, V. Vlachoudis¹⁸, R. Vlastou³¹, F. Voss⁸, S. Walter⁸, H. Wendl¹⁸, M. Wiescher²⁰ and K. Wisshak⁸

¹ INFN, Bari, Italy

² INFN, Trieste, Italy

³ CEA/Irfu, Gif-sur-Yvette, France

⁴ Univ. Santiago de Compostela, Spain

⁵ CIEMAT, Madrid, Spain

⁶ Univ. Lodz, Poland

⁷ Univ. Ioannina, Greece

⁸ FZK, Institut für Kernphysik, Germany

⁹ Technische Universität Wien, Austria

¹⁰ CNRS/IN2P3 - IReS, Strasbourg, France

¹¹ Univ. Prague, Czech Republic

¹² Dip. Fisica Generale, Univ. Torino, Italy

¹³ Univ. Politecnica Catalunya, Barcelona, Spain

¹⁴ INFN, Laboratori Nazionali di Legnaro, Italy

¹⁵ IAEA, Vienna, Austria

¹⁶ Univ. Sevilla, Spain

¹⁷ ITN, Lisbon, Portugal

¹⁸ CERN, Geneva, Switzerland

¹⁹ LIP - Coimbra & Dep. Fisica Univ. Coimbra, Portugal

²⁰ Univ. Notre Dame, USA

²¹ Inst. Fisica Corpuscular, CSIC-Univ. Valencia, Spain

²² Aristotle Univ. Thessaloniki, Greece

²³ CNR S/IN2P3 - IPN, Orsay, France

²⁴ JINR, Frank Lab. Neutron Physics, Dubna, Russia

²⁵ CNRS/IN2P3 - IPN, Orsay, France

²⁶ LANL, USA

²⁷ Tokyo Inst. Technology, Japan

²⁸ ORNL, Physics Division, USA

²⁹ NCSR, Athens, Greece

³⁰ Dip. Fisica, Univ. Bologna, & INFN, Bologna, Italy

³¹ National Technical Univ. Athens, Greece

³² Inst. für Fakultät für Physik, Univ. Wien, Austria

³³ Pôle Univ. L. de Vinci, Paris, France³⁴ CEC-JRC-IRMM, Geel, Belgium³⁵ Dep. Physics and Astronomy, Univ. Basel, Switzerland³⁶ Univ. Pavia, Italy³⁷ ENEA, Bologna, Italy

The n_TOF Collaboration

Abstract

The innovative feature of the n_TOF facility at CERN, in the two experimental areas, (20 m and 200 m flight paths), allow for an accurate determination of the neutron capture cross section for radioactive samples or for isotopes with small neutron capture cross section, of interest for Nuclear Astrophysics. This contribution presents an overview on the astrophysical program carried on at the n_TOF facility, the main results and their implications.

1 Stellar nucleosynthesis

Elements heavier than Fe are dominantly produced by neutron capture reactions in stars. About half of the elemental abundances are generated in the slow neutron capture process, the s-process, in stellar environments characterized by neutron densities between $10^6 - 10^{12} \text{ cm}^{-3}$. In these sites, the nucleosynthesis path proceeds along the stability valley, since β -decays are usually faster than subsequent neutron captures on unstable species. The other half of elemental abundances is produced by the rapid neutron capture process, or r-process. This process is associated with very high neutron densities, higher than 10^{20} cm^{-3} and the reaction flow is driven towards the neutron rich side since neutron captures are faster than radioactive decays.

The s-process can be divided in two components called the *main* and the *weak* s-process. The weak component of the s-process, responsible for the a large part of the abundance of isotopes between Fe and Zr, takes place in massive stars ($M > 15 M_{\odot}$) during the He core burning and later during the C shell burning. The main s-process component essentially leads to the production of nuclides between Zr and Bi. It takes place in low mass stars ($1.5 < M < 3 M_{\odot}$) during their asymptotic giant phase.

The nuclear physics inputs for studying the s-process and calculating the s-process abundances are the stellar decay half-lives and the stellar neutron capture cross sections, that is the cross section averaged over the stellar neutron spectrum (Maxwellian Averaged Cross Section, MACS), defined as

$$\langle \sigma \rangle = \frac{2}{\sqrt{\pi}} \frac{1}{(K_B T)^2} \int_0^{\infty} \sigma(E) E \exp\left(-\frac{E}{K_B T}\right) dE \quad (1)$$

where E is the neutron energy, K_B is the Boltzmann constant and T is the temperature of the stellar site in which the capture process occurs. Since the s-process takes place during different burning stages of the stars the temperature range from 0.1 to 1 GK, corresponding to $K_B T$ values of 8 to 90 keV. To determine the MACS the excitation function needs to be known up to neutron energies of a few hundred keV.

2 The n_TOF facility

The neutron time-of-flight facility n_TOF at CERN, based on an idea by Rubbia *et al.* [1], is a pulsed white neutron source for high-accuracy neutron cross-section measurements over a wide neutron energy range. The neutrons are produced in a monolithic Pb-spallation target, where a pulsed 20 GeV/c proton

beam provided by the CERN Proton Synchrotron (PS) impinges with a maximum repetition rate of 0.8 Hz. The Pb-target is surrounded by an additional moderator layer to generate a neutron beam with energies ranging from thermal up to several GeV. At the facility, operative since 2001, the measurements take place in an experimental area placed at the end of a horizontal beam line, 200 m in length. The experimental conditions and the neutron beam characteristics of this flight path are presented in full detail in Ref. [2].

The horizontal 200 m flight path, with its record instantaneous neutron beam intensity, has allowed very important neutron capture and fission cross-sections measurements, with unprecedented accuracy and energy resolution [3-7]. It has also allowed to extend the energy range to previously unreachable values [8].

In order to extend the experimental possibilities at the n_TOF facility for cross-section measurements of very low mass sample ($< 1\text{ mg}$), reaction with small cross sections or highly radioactive samples, an additional vertical flight path of 20 m with significantly higher neutron flux was designed and constructed in 2014. The large gain in the neutron flux, of about a factor of 30 relative to the first experimental area, allows one to perform measurements with samples of correspondingly smaller mass or in a shorter time. Most importantly, the combination of the higher flux and shorter time-of-flight, a factor of 10 relative to EAR1, is particularly convenient when measuring radioactive isotopes, as it results in an increase of the signal-to-background ratio of more than two orders of magnitude for the background related to the radioactive decay of the sample. As a consequence, in EAR2 it becomes feasible to perform challenging measurements with isotopes of half-life as short as a few tens of years, offering the unique opportunity to address some open questions in Nuclear Astrophysics.

3 Experimental campaign

The n_TOF Astrophysics experimental campaign is focused on neutron magic nuclei, which act as bottle neck for the flow of s-process, nuclei with $A < 120$, branching points isotopes and isotopes of special interest, like the Os isotopes relevant for nuclear cosmochronology.

Of particular interest are the branching points, i.e. radioactive isotopes of relatively short half-life for which a competition exists between neutron capture and the β -decay. The knowledge on the associated cross sections of these isotopes is very poor, mainly due to the difficulty in obtaining enough material and to measure the cross section of sample with a high activity. For these reasons, before 2001 none of these isotopes had been measured yet, despite the fact that they could provide very important information on the thermodynamical conditions of the stellar site in which s-process occurs.

In the following the description and the most recent measurements carried out in the two experimental areas is reported.

3.1 $^{63}\text{Ni}(n,\gamma)$ measurements

The phenomenology of the s-process implies that the solar abundance distribution is composed of two parts: the main component, which mostly accounts for the mass region from Y to Bi, and the weak component, which contributes to the region from the Fe to the Sr. The main and weak component occur prevalently in low mass stars, i.e. with $1.5M_{\odot} \leq M \leq 3M_{\odot}$ and massive stars with $M \geq 15M_{\odot}$. The main difference between these two s-process scenarios is that the high neutron exposure during the main component is sufficient for establishing equilibrium in the reaction flow, resulting in the so-called local approximation, so that the emerging s-abundances are inversely proportional to the stellar cross sections. In this case, the uncertainty on the neutron cross section of an isotope affects only the abundance of that specific isotope. In contrast, the neutron exposure in massive stars is too small to achieve flow equilibrium. As a consequence, the uncertainty in the neutron capture cross section



Fig. 1: The s-process reaction path in the Ni-Cu-Zn region during He core burning (dashed lines) and the C shell burning (solid lines) [4]

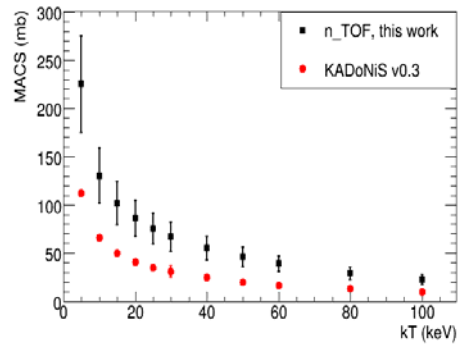


Fig. 2: Comparison between the n_TOF experimental MACS and the theoretical prediction of the KADoNIS compilation

of an isotope not only influences the abundance of that particular isotope but has a potentially strong propagation effect on the abundance of the subsequent isotopes involved in the s-process chain.

The ^{63}Ni represents the first branching point in the reaction path of the s-process as sketched in Fig.1. In the low neutron density of the weak component, during core He burning the branching is characterized by a significant production of ^{63}Cu by β -decay from ^{63}Ni . At much higher neutron density during the C shell burning the branching is closed and the ^{63}Cu is completely bypassed by the reaction flow. In this phase ^{63}Cu is only produced by the subsequent decay of the surviving ^{63}Ni abundance. The neutron capture cross section of ^{63}Ni is crucial for determining the $^{63}\text{Cu}/^{65}\text{Cu}$ ratio, which represents a sensitive constraint for stellar model calculations, because the propagation waves of these isotopes affect the entire abundance distribution of the weak s-process [9].

The measurement was performed at n_TOF with a pair of C_6D_6 liquid scintillator detectors. These detectors are optimized to exhibit a very low sensitivity to neutrons, thus minimizing the background produced by neutrons scattered by the sample. Fig. 2 shows the results obtained at n_TOF in comparison with the KADoNIS compilation [10]. The MACS ranging from $kT = 5\text{-}100$ keV exhibit total uncertainties of 20-22% and are about a factor 2 higher than the theoretical prediction. These results improved one of the main nuclear uncertainties affecting theoretical predictions for the abundances of ^{63}Cu , ^{64}Ni and ^{64}Zn .

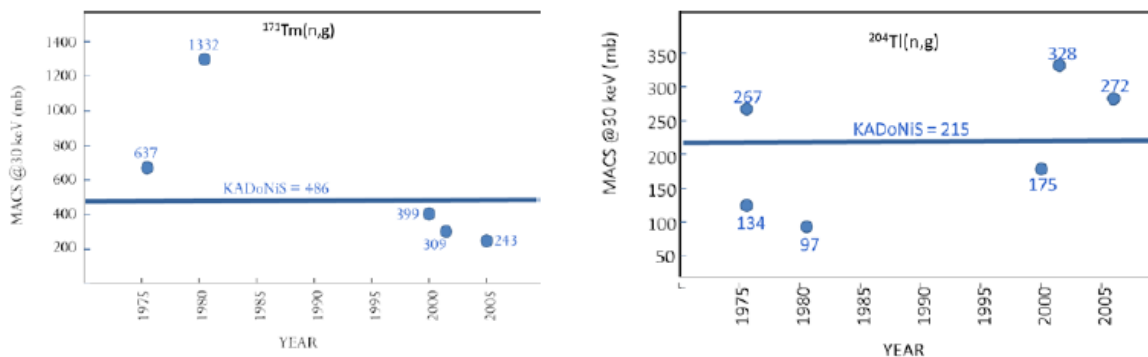


Fig. 3: Theoretical prediction of MACS values at 30 keV for ^{171}Tm and ^{204}Tl

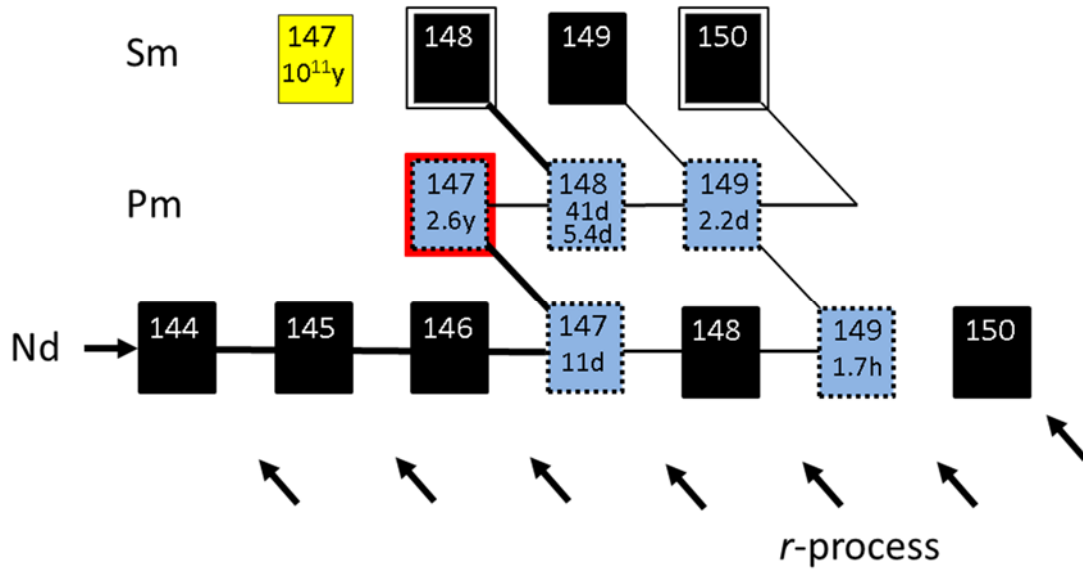


Fig. 4: The s-process flow in the mass region $A=144-150$. Branching points are indicated by dotted blue boxes.

3.2 $^{171}\text{Tm}(n,\gamma)$ and $^{204}\text{Tl}(n,\gamma)$ measurements

The isotopes ^{171}Tm and the ^{204}Tl are important s-process branching points [11]. The unstable isotope ^{171}Tm (half-life of 1.92 years) represents a branching in the s-process path that is independent of stellar temperature and therefore suited to constrain explicitly the s-process neutron density in low mass AGB stars. Being the Tm a rare earth element, the relative abundances of stable isotopes are known with high accuracy.

The isotope ^{204}Tl (half life of 3.8 years) decays in ^{204}Pb , which produces ^{205}Pb when undergoing neutron capture. The fact that both isotopes $^{204,205}\text{Pb}$ are screened from the r-process by the stable isotopes ^{204}Hg and ^{205}Tl , makes ^{204}Tl particularly interesting; indeed, its capture cross section is of crucial importance for understanding the nucleosynthesis of heavy elements in the AGB stars, but it can also be used to provide chronometric information about the time span between the last s-process nucleosynthesis events that modified the composition of the proto-solar nebula and the formation of solar system solid bodies [12].

At present the values of the neutron capture cross sections of these isotopes used to calculate the abundances in stellar model are based on theoretical predictions. Figure 2 shows the values of the MACS calculated along the years. It is clear that such large uncertainty on the cross section of these isotopes does not allow to make a reliable interpretation of the astrophysical aspect discussed above.

Apart of the natural activity of the samples, which requires a very large instantaneous neutron flux to study their neutron capture cross section, the bigger challenge is to find a sufficient amount of sample material and with enough purity.

To produce the samples of ^{171}Tm and ^{204}Tl two pellets of 5 mm diameter of ^{170}Er (isotopic purity 98,1%) and 225 mg of ^{203}Tl (isotopic purity 99,5%) have been irradiated with thermal neutron for almost two months at Institute Laue Langevin ILL (Grenoble, France) experimental nuclear reactor.

The irradiation has produced 3.6 mb and 11 mg of ^{171}Tm and ^{204}Tl , respectively. After the irradiation, the ^{204}Tl sample could be directly used for capture measurement because there was not the possibility to separate isotopically the ^{204}Tl from the initial ^{203}Tl , while it was possible, using chemical

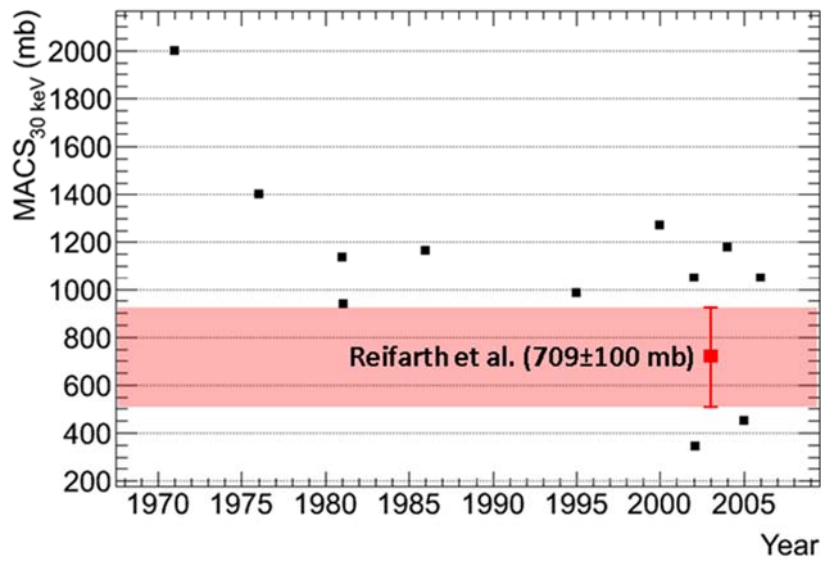


Fig. 5: Comparison between the theoretical (black) and experimental (red) MACS values at 30 keV

purification technique, to separate the ^{171}Tm from the ^{170}Er . The separation was performed at Paul Scherrer Institute PSI (Villigen, Switzerland).

The measurement had been performed in June 2015 in the EAR1 with a pair of C_6D_6 liquid scintillator detectors. The data analysis is currently in progress, but when completed it will provide for the first time experimental information on the capture cross section of these isotopes.

3.3 $^{147}\text{Pm}(n,\gamma)$ measurements

The ^{147}Pm isotope is a branching point in the mass region $A=147-148$, that is the Nd-Pm-Sm region. A detailed analysis of this branching is important for modelling the AGB star evolution and to put accurate constraints on the interplay between metallicity and initial stellar mass, mixing processes or hot bottom burning effects [13].

The s-process neutron capture flow in the mass region $A=144-150$ is reported in Fig. 3, where ^{148}Sm and ^{150}Sm are s-only isotopes because they are shielded from the r-process by Nd isotopes. The abundances ratio of $^{148,150}\text{Sm}$ are well known, being these isotopes rare-earth nuclei, which are not affected by chemical fractionation processes. Therefore this branching can provide very valuable information about the stellar conditions of this process if the capture cross sections of the branching isotopes, mainly ^{147}Pm but also ^{147}Nd , are known. Furthermore, the measurement of the ^{147}Pm capture cross section poses a direct constraint on the stellar reaction rate used in the astrophysical models, since the contribution of neutron capture cross section on thermal populated excited states for ^{147}Pm are predicted to be very small, between 0% at $kT=5$ KeV and 6% at $kT=30$ keV [14,15].

At the present there is only one measurement of the capture cross section of the ^{147}Pm in the energy region of interest for astrophysics. It is an activation measurement where 28 ng of ^{147}Pm were irradiated with a Maxwellian neutron energy distribution at $kT=25$ KeV [16]. As showed in Fig 4 the results are on average 30% smaller than most theoretical predictions.

This result allowed to estimate the range of temperatures and neutron densities in the main s-process component, but it has to be considered that the 95% of neutron exposure in TP-AGB stars

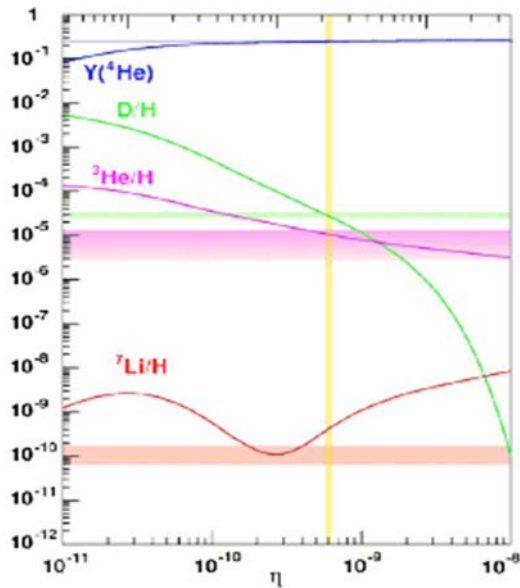


Fig. 6: The primordial light element abundances (relative to H) of D, ^3He , ^7Li , and the mass fraction of ^4He as function of the baryon-to-photon ratio η . The yellow vertical band represents the n observation from WMAP, while the colored curves and bands respectively.

“Cosmological Lithium problem” [17]. It refers to the large discrepancy between the abundances of primordial ^7Li predicted by the standard theory of Big Bang Nucleosynthesis (BBN) and the value inferred from the so-called “Spite plateau” in halo stars. The predictions of the BBN theory reproduce successfully the observations of all primordial abundances except for ^7Li , which is overestimated by more than a factor of 3.

In the standard theory of BBN, 95% of primordial ^7Li is produced by the decay of ^7Be ($t_{1/2}=53.2$ days). Several mechanisms have been put forward to explain the difference between calculations and observation. One possible explanation of the primordial ^7Li problem is related to the BBN calculations on the production and destruction of ^7Be . In particular, while the main reaction producing ^7Be , the $^3\text{He}(\alpha,\gamma)^7\text{Be}$, is relatively well known, the cross section for several reactions responsible for its destruction were still uncertain up to recently. To this end several measurements have recently been performed on charge-particle induced reaction on ^7Be . The results, however, have ruled out the possibility that reaction induced by proton, deuterium or ^3He could be responsible for the destruction of ^7Be during the BBN.

In the BBN scenario, neutron-induced reactions on ^7Be also play a role. However, despite of their importance in the BBN context, very few and uncertain experimental data are available on these reactions. In 1988 the $^7\text{Be}(n,p)$ was measured at the LANCSE neutron facility, Los Alamos. The result excluded a significant impact of this reaction on the ^7Li problem [18]. However, because of the limited energy range covered in that measurement, the estimation of the reaction rate at BBN temperature has still to rely on some assumption. Therefore a more precise measurement at temperature between 25-50 keV is needed to improve the reliability of the BBN calculations.

takes place at much lower temperatures of about $kT = 8$ keV. Therefore, measurement in this energy region was needed.

The sample was produced at ILL irradiating 97 mg of ^{146}Nd (isotopic purity 98.8%) with thermal neutrons for 56.7 days. This irradiation produced almost 300 μg of ^{147}Pm via the $^{146}\text{Nd}(n,\gamma)^{147}\text{Nd}(\beta^-)$ reaction. The Pm was separated from the dominating Nd using the exchange chromatography, precipitation and other radiochemical techniques at the PSI.

The measurement had been performed in July 2015 in EAR2. In fact, due to the small quantity and the high activity of the sample, with its extremely high flux EAR2@n_TOF is at present the only place where this very challenging time-of-flight measurement could be performed. The experimental setup consisted of four C_6D_6 liquid scintillators detectors. In this case as well the data analysis is in progress, but preliminary results indicate that it will be possible to obtain some information on this cross section as well.

3.4 $^7\text{Be}(n,\alpha)$ measurement

One of most important unresolved problems of nuclear astrophysics is the so called

The contribution of the ${}^7\text{Be}(n,\alpha)$ reaction to the destruction of the ${}^7\text{Be}$ has always been considered negligible in the BBN calculation, due to its much lower estimated cross section. However, this assumption has never been verified experimentally, so that an uncertainty of a factor 10 is typically assigned to this reaction in BBN calculation [19].

One of the main difficulties in the measurement of the ${}^7\text{Be}(n,\alpha){}^4\text{He}$ cross section is related to the availability of the ${}^7\text{Be}$ in sufficient quantity and the possibility to handle it. For the measurement at n_TOF, the sample has been prepared by the Paul Scherrer Institute (PSI), Villigen, with the ${}^7\text{Be}$ extracted from the cooling of the SINQ spallation source of PSI.

In the ${}^7\text{Be}(n,\alpha){}^4\text{He}$ reaction, two α -particles are emitted, back to back, with a relatively high energy of approximately 9 MeV. The α -particles are detected with a sandwich of two Si-detectors with a sample of $\sim 2\ \mu\text{g}$ of ${}^7\text{Bi}$ in between. The two α -particles are identified on the basis of their relatively high energy and by the coincident method. Two different Si- ${}^7\text{Be}$ -Si sandwiches were prepared at PSI, inserted in a sealed chamber and shipped to CERN. The chamber was then installed on the beam line in EAR2 in late August 2015. Soon afterwards, a 5-weeks long measurement started. Coincidences were clearly observed since the beginning. When completely analysed, this measurement will finally provide, for the first time ever, the cross section as a function of energy. In this case as well, the extremely high neutron flux in EAR2 made possible a measurement that cannot be performed at any other time-of-flight facility in the world.

3.5 Conclusion

Neutron capture cross sections of astrophysical interest have been measured at the CERN n_TOF facility. The major motivation of these measurements is to reduce the uncertainties on nuclear data to a few percent, as required to improve the stellar s-process model.

Since 2014 a second experimental area at 20 m from the spallation target, with a much higher neutron flux is available. This new experimental area now allows measurements of relatively short-lived isotopes, as the s-process branching points, or the (n, charged particle) reactions on ${}^7\text{Be}$.

References

- [1] C. Rubbia *et al.*, Tech. Rep. CERN/LHC/98-02 CERN(1998)
- [2] U. Abbondanno *et al.*, Tech. Rep. CERN/SL/2002-053 ECT(2003)
- [3] U. Abbondanno *et al.*, *Phys. Rev. Letters* **93** (2004)161103
- [4] C. Lederer *et al.*, *Phys. Rev. Letters* **110** (2013) 022501
- [5] F. Gunsing *et al.*, *Phys. Rev. C* **85** (2012)640601
- [6] C. Guerrero *et al.*, *Nuclear Data Sheets*, **119** (2014)5
- [7] M. Calviani *et al.*, *Phys. Rev. C* **85** (2012)34616
- [8] C. Paradela *et al.*, *Phys. Rev. C* **91**(2015) 24602
- [9] M. Heil *et al.*, *Phys. Rev. C* **77**(2008) 015808
- [10] I. Dilmann *et al.*, Proceeding of EFNUDAT Fast Neutrons-Scientific Workshop on Neutron Measurements, Theory & Application, Geel, Belgium, 2009 (Elesvier, Amsterdam, 2006)
- [11] F. Käppeler *et al.*, *Rev. Mod. Phys* **83**(2011)
- [12] K. Yokoi, K. Takahashi and M. Amould, *Astronomy and Astrophysics* **145**(1985) 339
- [13] F. Herwig, *Annu. Rev. Astron. Astrophys.* **43**, (2005) 435
- [14] T. Rausher, *The Astrophys. Journal Letters* **755** L10(2012)
- [15] T. Rausher, *The Astrophysical Journal Supplement* **201** (2012)26
- [16] R. Reifarh *et al.*, *The Astrophysicl Journal* **582**, (2003)1251
- [17] R.H. Cyburt *et al.*, *Phys. Rev. D* **69** (2004) 123519
- [18] P.Koehler *et al.*, *Phys. Rev. C* **37**(1988)917
- [19] P.D. Serpico *et al.*, *Jour. Cos. Astropart. Phys.***12**(2994)010

Integral cross section measurement of the $^{12}\text{C}(n,p)^{12}\text{B}$ reaction

*P. Žugec*¹⁶, *N. Colonna*², *D. Bosnar*¹, *A. Ventura*³, *A. Mengoni*⁴, *S. Altstadt*⁵, *J. Andrzejewski*⁶, *L. Audouin*⁷, *M. Barbagallo*², *V. Bécaries*⁸, *F. Bečvář*⁹, *F. Belloni*¹⁰, *E. Berthoumieux*¹¹, *J. Billowes*¹², *V. Boccone*¹³, *M. Brugger*¹³, *M. Calviani*¹³, *F. Calviño*¹⁴, *D. Cano-Ott*⁸, *C. Carrapiço*¹⁵, *F. Cerutti*¹³, *E. Chiaveri*¹³, *M. Chin*¹³, *G. Cortés*¹⁴, *M.A. Cortés-Giraldo*¹⁶, *L. Cosentino*¹⁷, *M. Diakaki*¹⁸, *C. Domingo-Pardo*¹⁹, *R. Dressler*²⁰, *I. Duran*²¹, *C. Eleftheriadis*²², *A. Ferrari*¹³, *P. Finocchiaro*¹⁷, *K. Fraival*¹¹, *S. Ganesan*²³, *A.R. García*⁸, *G. Giubrone*¹⁹, *M.B. Gómez-Hornillos*¹⁴, *I.F. Gonçalves*¹⁵, *E. González-Romero*⁸, *E. Griesmayer*²⁴, *C. Guerrero*¹³, *F. Gunsing*¹¹, *P. Gurusamy*²³, *S. Heinitz*²⁰, *D.G. Jenkins*²⁵, *E. Jericha*²⁴, *F. Käppeler*²⁶, *D. Karadimos*¹⁸, *N. Kivel*²⁰, *M. Kokkoris*¹⁸, *M. Krtička*⁹, *J. Kroll*⁹, *C. Langer*⁵, *C. Lederer*⁵, *H. Leeb*²⁴, *L.S. Leong*⁷, *S. Lo Meo*⁴, *R. Losito*¹³, *A. Manouosos*²², *J. Marganiec*⁶, *T. Martínez*⁸, *C. Massimi*²⁷, *P. Mastinu*²⁸, *M. Mastromarco*², *E. Mendoza*⁸, *P.M. Milazzo*²⁹, *F. Mingrone*²⁷, *M. Mirea*³⁰, *W. Mondalaers*¹⁰, *A. Musumarra*³¹, *C. Paradela*¹⁰, *A. Pavlik*³², *J. Perkowski*⁶, *A. Plompen*¹⁰, *J. Praena*¹⁶, *J. Quesada*¹⁶, *T. Rauscher*^{33,34}, *R. Reifarth*⁵, *A. Riego*¹⁴, *F. Roman*¹³, *C. Rubbia*¹³, *R. Sarmiento*¹⁵, *A. Saxena*²³, *P. Schillebeeckx*¹⁰, *S. Schmidt*⁵, *D. Schumann*²⁰, *G. Tagliente*², *J.L. Tain*¹⁹, *D. Tarrío*²¹, *L. Tassan-Got*⁷, *A. Tsinganis*¹³, *S. Valenta*⁹, *G. Vannini*²⁷, *V. Variale*², *P. Vaz*¹⁵, *R. Versaci*¹³, *M.J. Vermeulen*²⁵, *V. Vlachoudis*¹³, *R. Vlastou*¹⁸, *A. Wallner*^{35,32}, *T. Ware*¹², *M. Weigand*⁵, *C. Weiss*¹³, *T. Wright*¹²

¹Department of Physics, Faculty of Science, University of Zagreb, Croatia;

²Istituto Nazionale di Fisica Nucleare, Sezione di Bari, Italy;

³Istituto Nazionale di Fisica Nucleare, Sezione di Bologna, Italy;

⁴ENEA, Bologna, Italy;

⁵Johann-Wolfgang-Goethe Universität, Frankfurt, Germany;

⁶Uniwersytet Łódzki, Lodz, Poland;

⁷Centre National de la Recherche Scientifique/IN2P3 - IPN, Orsay, France;

⁸Centro de Investigaciones Energéticas Medioambientales y Tecnológicas (CIEMAT), Madrid, Spain;

⁹Charles University, Prague, Czech Republic;

¹⁰European Commission JRC, Institute for Reference Materials and Measurements, Retieseweg 111, B-2440 Geel, Belgium;

¹¹CEA/Saclay - IRFU, Gif-sur-Yvette, France;

¹²University of Manchester, Oxford Road, Manchester, UK;

¹³CERN, Geneva, Switzerland;

¹⁴Universitat Politècnica de Catalunya, Barcelona, Spain;

¹⁵C2TN-Instituto Superior Técnico, Universidade de Lisboa, Portugal;

¹⁶Universidad de Sevilla, Spain;

¹⁷INFN - Laboratori Nazionali del Sud, Catania, Italy;

¹⁸National Technical University of Athens (NTUA), Greece;

¹⁹Instituto de Física Corpuscular, CSIC-Universidad de Valencia, Spain;

²⁰Paul Scherrer Institut, 5232 Villigen PSI, Switzerland;

²¹Universidade de Santiago de Compostela, Spain;

²²Aristotle University of Thessaloniki, Thessaloniki, Greece;

²³Bhabha Atomic Research Centre (BARC), Mumbai, India;

²⁴Atominstytut der Österreichischen Universitäten, Technische Universität Wien, Austria;

²⁵University of York, Heslington, York, UK;

²⁶Karlsruhe Institute of Technology (KIT), Institut für Kernphysik, Karlsruhe, Germany;

²⁷Dipartimento di Fisica, Università di Bologna, and Sezione INFN di Bologna, Italy;

²⁸Istituto Nazionale di Fisica Nucleare, Laboratori Nazionali di Legnaro, Italy;

²⁹Istituto Nazionale di Fisica Nucleare, Sezione di Trieste, Italy;

³⁰Horia Hulubei National Institute of Physics and Nuclear Engineering - IFIN HH, Bucharest - Magurele,

Romania;

³¹Dipartimento di Fisica e Astronomia DFA, Università di Catania and INFN-Laboratori Nazionali del Sud, Catania, Italy;

³²University of Vienna, Faculty of Physics, Austria;

³³Centre for Astrophysics Research, School of Physics, Astronomy and Mathematics, University of Hertfordshire, Hatfield, United Kingdom;

³⁴Department of Physics, University of Basel, Basel, Switzerland;

³⁵Research School of Physics and Engineering, Australian National University, ACT 0200, Australia

Abstract

The integral cross section of the $^{12}\text{C}(n, p)^{12}\text{B}$ reaction was measured at the neutron time of flight facility n_TOF at CERN, from the reaction threshold at 13.6 MeV up to 10 GeV, by means of the combined activation and a time-of-flight technique. The integral result is expressed as the number of ^{12}B nuclei produced per single pulse of the neutron beam. A simple integral expression is given for calculating the number of produced ^{12}B nuclei from any given evaluated cross section and/or model prediction.

1. Introduction

Nuclear medicine, radiological protection, the design of the structural materials at neutron production facilities and the design of detectors used for fundamental nuclear physics experiments are some of the fields where data on the neutron induced $^{12}\text{C}(n, p)^{12}\text{B}$ reaction play an important role. In nuclear medicine – in particular in hadrontherapy – and in radiological protection this reaction must be taken into account when estimating the dose received by biological tissues, which is built up both by protons, as the primary reaction products, and by the highly energetic electrons from a subsequent β -decay of ^{12}B ($Q = 13.37$ MeV). At neutron production facilities where the neutron flux extends above the reaction threshold of 13.6 MeV, the emission of protons from the $^{12}\text{C}(n, p)^{12}\text{B}$ reaction leads to the production of hydrogen within the steel alloys, increasing the risk of embrittlement. In fundamental nuclear physics experiments carbon is often used both as the detector housing material and as the main chemical constituent of the active material, e.g. C_6D_6 (historically, C_6F_6 detectors) due to its extremely low neutron capture cross section providing a very low intrinsic sensitivity to scattered neutrons. However, in the presence of high energy neutrons, the $^{12}\text{C}(n, p)^{12}\text{B}$ reaction may give rise to an additional component in the neutron background and even compromise the experimental estimation of the neutron background by means of neutron irradiation of the carbon sample [1].

Despite these considerations, the experimental data on the $^{12}\text{C}(n, p)^{12}\text{B}$ reaction are very scarce and largely discrepant from each other [2, 3, 4, 5, 6, 7], as clearly shown in Fig. 1. This lack of data is also reflected in the inability of the different models to consistently predict the cross section, and thus the ^{12}B production rate of this reaction. For illustration, Fig. 1 also shows the cross sections extracted from several different models available in GEANT4 [8] – the HP (High Precision) package, Binary cascade, Bertini cascade, INCL++/ABLA model (INCL intranuclear cascade coupled to the ABLA deexcitation model) and QGS (Quark-Gluon-String) model [9]. It should be noted that HP package adopts the cross section directly from the ENDF/B-VII.1 database [10], while the other cross sections are the results of the model calculations.

The integral cross section of the $^{12}\text{C}(n, p)^{12}\text{B}$ reaction was measured at the neutron time of flight facility n_TOF at CERN, from the reaction threshold at 13.6 MeV up to 10 GeV. Although this integral value cannot be directly compared to past experimental data – all energy dependent and limited to a

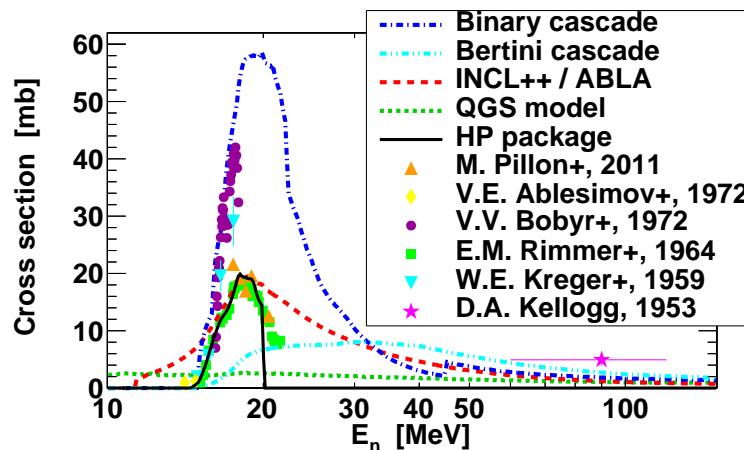


Fig. 1: Cross sections of $^{12}\text{C}(n,p)^{12}\text{B}$ reaction from different GEANT4 models, compared to the available experimental data.

reduced energy range – it may be used as a validation benchmark for different cross section evaluations and/or model calculations.

2. Experimentnal setup

At the n_TOF facility the neutron beam is produced by exposing the massive Pb spallation target to a pulsed proton beam from the CERN Proton Synchrotron. The proton beam is characterized by an energy of 20 GeV, an average of 7×10^{12} protons per pulse, 7 ns width, minimal repetition period of 1.2 s and a typical frequency of 0.4 Hz. The neutron beam (with ~ 300 neutrons produced per single proton) is moderated passing through the spallation target, through 1 cm of demineralized water from a cooling system and additional 4 cm of borated water. After moderation, the neutron flux spans an energy range from thermal (~ 10 meV) up to 10 GeV. Passing through an evacuated beam line towards the Experimental Area 1 at 185 m distance from the spallation target, charged particles are removed from the beam by a 1.5 T sweeping magnet and is shaped by two collimators. A more detailed description of the n_TOF facility may be found in Ref. [11]. We refer the reader to Ref. [12] for an in-depth description of the neutron flux measurements at n_TOF.

The integral cross section measurement of the $^{12}\text{C}(n,p)^{12}\text{B}$ reaction was performed using a natural carbon sample of 7.13 g mass, 2 cm diameter, 1 cm thickness and a chemical purity of 99.95%, which was confirmed at the Paul Scherrer Institute. The experiment relies on the detection of β -rays, with an average energy of 6.35 MeV, from the decay of ^{12}B produced by the $^{12}\text{C}(n,p)^{12}\text{B}$ reaction. Two deuterated benzene (C_6D_6) liquid scintillation detectors were used for the detection of these β -rays. One is the modified version of the Bicorn detector, while the other one (denoted as FZK) is a custom built detector from Forschungszentrum Karlsruhe, Germany. These detectors, commonly used at n_TOF for neutron capture measurements, have been optimized with the specific purpose of achieving a very low sensitivity to scattered neutrons [13]. Further details on the methodology of the experiment may be found in Refs. [14, 15].

The ^{12}B half-life of 20.2 ms is highly beneficial to the experiment, since the data acquisition window of 96 ms is sufficient to cover a significant portion of the ^{12}B exponential decay distribution. A description of a high-performance digital data acquisition system at n_TOF – based on 8-bit flash analog-to-digital converter units (FADC) with 48 MB memory buffer, operating at a typical sampling rate of 500 MHz – may be found in Ref. [16].

3. Data analysis

There are several sources of background affecting the measurement, all of which have been clearly identified. The first background component, related to the scattering of in-beam γ -rays off the ^{nat}C sample, was measured with a Pb sample and was found completely negligible. The background caused by the neutron beam crossing the experimental area was measured by irradiating the overall experimental setup without the sample in place. The ambient background, caused by the natural and induced radioactivity, was measured by turning off the neutron beam. All experimentally accessible background components were properly normalized and subtracted from the measurements with the ^{nat}C sample.

Finally, the neutron background, which is caused by neutron scattering off the sample, has been determined by means of recently developed high-precision GEANT4 simulations [1]. The simulated results have been found to be highly reliable, based on the comparison with experimental data obtained with a ^{nat}C sample. However, it was shown in Ref. [1] that the simulated neutron background which is composed mostly of the capture γ -rays, can be reliably described only by applying the Pulse Height Weighting Technique (PHWT) [17]. This procedure is commonly used in the analysis of neutron capture data obtained by detectors with a low γ -ray detection efficiency (the details on the PHWT applied at n_TOF may be found in Ref. [18]). In short, the lack of proper correlations between the simulated capture γ -rays modifies their energy distribution (relative to the experimental one), thus affecting the average detection efficiency for capture events. Applying the PHWT removes the effect of these correlations, the only condition being that the energy conservation is respected in the generation of capture γ -rays.

The PHWT is performed by assigning to each detected count a weighting factor $W(E)$, dependent on the energy E deposited in the detector. The weighting of the experimental counts $C_{\text{exp}}(t)$, expressed as a function of the decay time t , may be decomposed as:

$$W(E) \otimes C_{\text{exp}}(t) = W(E) \otimes C_{\gamma}(t) + \langle W \rangle \times C_{\beta}(t) \quad (1)$$

The application of the weighting factors is symbolically denoted by \otimes . $C_{\gamma}(t)$ is the neutron background, mostly composed of the capture γ -rays from the experimental area. $C_{\beta}(t)$ is the time distribution of detected β -rays from a decay of ^{12}B . Owing to the fact that there are no correlations between β -rays, the application of the PHWT to the corresponding spectrum $C_{\beta}(t)$ is reduced to a simple multiplication by the average weighting factor $\langle W \rangle$:

$$\langle W \rangle = \frac{\int_{200\text{keV}}^{13.37\text{MeV}} S_{\beta}(E)W(E)dE}{\int_{200\text{keV}}^{13.37\text{MeV}} S_{\beta}(E)dE} \quad (2)$$

which is directly determined by the energy spectrum $S_{\beta}(E)$ of the detected β -rays. The lower integration bound from Eq. (2) is equal to the threshold set during the data analysis. The upper bound is given by the Q -value of the ^{12}B decay. The energy spectrum $S_{\beta}(E)$, which is easily determined from simulations, allows to invert Eq. (1) and to obtain the unweighted experimental spectrum of detected β -rays:

$$C_{\beta}(t) = \frac{W(E) \otimes C_{\text{exp}}(t) - W(E) \otimes C_{\gamma}(t)}{\langle W \rangle} \quad (3)$$

The remaining spectrum corresponds to the time distribution of the ^{12}B decay:

$$C_{\beta}(t) = \frac{\varepsilon_{\beta} N_{^{12}\text{B}}}{\tau} e^{-t/\tau} \quad (4)$$

with $\tau = 29.14$ ms as the lifetime of ^{12}B and ε_{β} as the total detection efficiency of C_6D_6 detectors, de-

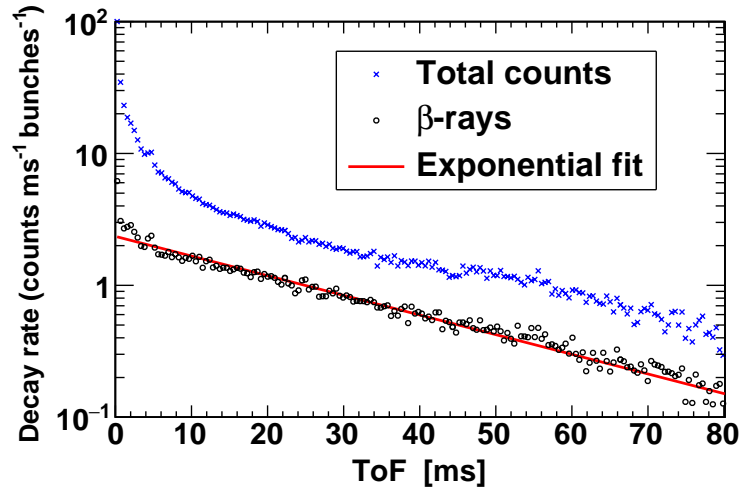


Fig. 2: Time distribution of ^{12}B decays, measured by two C_6D_6 detectors. The spectra show the total counts C from two detectors summed together, and normalized by the sum of their respective detection efficiencies ε : $(C_{\text{Bicron}} + C_{\text{FZK}})/(\varepsilon_{\text{Bicron}} + \varepsilon_{\text{FZK}})$.

terminated from the simulations (4.3% for Bicron, 6.8% for FZK). The spectra before and after the background subtraction, obtained by combining the data from both detectors, are shown in Fig. 2. The number $N_{^{12}\text{B}}$ of ^{12}B nuclei produced per single neutron bunch was found by fitting (up to 80 ms) the spectrum $C_{\beta}(t)$ to the exponential from Eq. (4), with $N_{^{12}\text{B}}$ as the only free parameter. The combination of the highly consistent results from the two detectors – $N_{^{12}\text{B}}^{(\text{Bicron})} = 68.03 \pm 0.66$ and $N_{^{12}\text{B}}^{(\text{FZK})} = 68.74 \pm 0.44$ – yields the final value of $N_{^{12}\text{B}} = 68.5 \pm 0.4_{\text{stat}} \pm 4.8_{\text{sys}}$. A systematic uncertainty of 2% was assigned to the contribution of β -rays produced outside the $^{\text{nat}}\text{C}$ sample. An additional 3% uncertainty was introduced due to the highly uncertain (n, p) , (n, d) and (n, np) reactions on ^{13}C present in natural carbon, leading to the production of both ^{12}B and ^{13}B , with the decay properties of ^{13}B being very similar to those of ^{12}B .

4. Integral cross section

The number of ^{12}B nuclei produced per neutron bunch may be brought into connection with the underlying cross section $\sigma(E_n)$ of the $^{12}\text{C}(n, p)^{12}\text{B}$ reaction:

$$N_{^{12}\text{B}} = \int_{13.6\text{MeV}}^{10\text{GeV}} \frac{1 - e^{-n\sigma_{\text{tot}}(E_n)}}{\sigma_{\text{tot}}(E_n)} \eta(E_n) \phi(E_n) \sigma(E_n) dE_n \quad (5)$$

where the lower integration limit corresponds to the reaction threshold, while the upper one corresponds to the maximal energy of the n_TOF neutron beam. The first term represents the self-shielding factor, determined by the areal density n of the $^{\text{nat}}\text{C}$ sample ($n = 0.114$ atoms/barn) and the total cross section $\sigma_{\text{tot}}(E_n)$, available from various evaluated libraries, such as ENDF/B-VII.1 [10]. Multiplied by $\sigma(E_n)$, it determines the first chance yield of the $^{12}\text{C}(n, p)^{12}\text{B}$ reaction, not taking into account the multiple scattering effect. This is accounted for separately, by the factor $\eta(E_n)$. The energy dependence of the multiple scattering factor throughout the entire energy range from the reaction threshold up to 10 GeV was obtained by simulating the neutron irradiation of the $^{\text{nat}}\text{C}$ sample, using different GEANT4 models for the ^{12}B production. It is to be noted that the elastic cross section is independent of the inelastic scattering models. Starting from widely different cross sections for the $^{12}\text{C}(n, p)^{12}\text{B}$ reaction (see

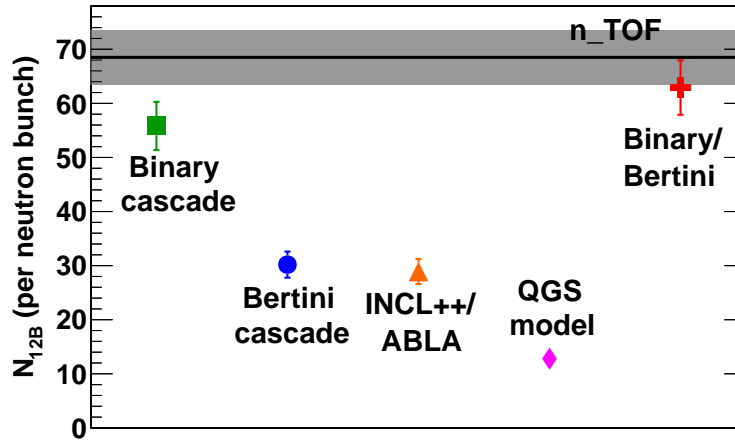


Fig. 3: Number of produced ^{12}B nuclei per single neutron pulse of the n_TOF beam, as predicted by different GEANT4 models. The values have been calculated by means of Eq. (5) and are compared to the experimental value (full line with the associated uncertainty range).

Fig. 1), all models yield very consistent multiple scattering corrections, confirming the reliability of the result. Finally, the neutron flux $\phi(E_n)$ from Eq. (5) was measured up to 1 GeV by the Parallel Plate Avalanche Counters (PPAC [19]), relying on the $^{235}\text{U}(n, f)$ reaction. Further details on the neutron flux measurements at n_TOF may be found in Ref. [12]. The neutron flux evaluation was extended above 1 GeV, based on the results from the dedicated GEANT4 simulations, normalized to the experimental data below 1 GeV. The overall energy dependent term multiplying the cross section $\sigma(E_n)$ from Eq. (5) may be treated as a unique weighting function $w(E_n)$, which was fitted to the fifth degree polynomial:

$$\log_{10} \frac{w(E_n)}{w_0} = \sum_{m=0}^5 a_m \left(\log_{10} \frac{E_n}{E_0} \right)^m \quad (6)$$

with $E_0 = 1 \text{ MeV}$ and $w_0 = 1 \text{ MeV}^{-1} \text{ mb}^{-1}$. The fit yields the following parameters: $a_0 = 12.9676$, $a_1 = -33.9199$, $a_2 = 32.3332$, $a_3 = -15.0657$, $a_4 = 3.36573$ and $a_5 = -0.291966$. The weighting function has been assigned 8% systematic uncertainty, coming from the uncertainties in each of its components – the neutron flux, self shielding and the multiple scattering factor.

With the weighting function $w(E_n)$ uniquely identified, any pointwise cross section for the $^{12}\text{C}(n, p)^{12}\text{B}$ reaction that extends over the full energy range from the reaction threshold up to 10 GeV, may be used to calculate the associated number of the ^{12}B nuclei produced per single neutron pulse of the n_TOF beam. In this way any cross section calculation or evaluation may be benchmarked against the experimental n_TOF result. This has been done for the different GEANT4 models, adopting the cross sections from Fig. 1. The results are shown in Fig. 3. Alongside results from all models extending all the way up to 10 GeV, the result from a combined Binary and Bertini cascade is also shown. The combination of Binary cascade up to 30 MeV and Bertini cascade above 30 MeV maximizes the cross section for $^{12}\text{C}(n, p)^{12}\text{B}$ reaction, yielding the integral result closest to the experimental one.

The secondary quantities such as the value analogous to the resonance integral $I_{12\text{B}}$:

$$I_{12\text{B}} = \int_{13.6\text{MeV}}^{10\text{GeV}} \frac{\sigma(E_n)}{E_n} dE_n \approx \frac{N_{12\text{B}}}{\kappa} \quad (7)$$

may also be estimated. The conversion factor κ between the number of produced ^{12}B nuclei (the true observable) and the convenient quantity $I_{12\text{B}}$ was determined to be $\kappa = 1.85 \pm 0.1 \text{ mb}^{-1}$, yielding the value $I_{12\text{B}} = 37 \pm 3 \text{ mb}$.

5. Conclusions

The integral cross section of the $^{12}\text{C}(n,p)^{12}\text{B}$ reaction was measured at the neutron time of flight facility n_TOF at CERN. A high-purity $^{\text{nat}}\text{C}$ sample was exposed to an intense, white, pulsed neutron beam, covering the energy range from below the reaction threshold at 13.6 MeV, up to 10 GeV. The measurement was performed by detecting the β -rays from the decay of the produced ^{12}B nuclei. Two liquid scintillation C_6D_6 detectors were used, which are commonly employed at n_TOF for the neutron capture measurements, due to their very low intrinsic sensitivity to the scattered neutrons. All sources of background were clearly identified – either by the dedicated measurements or simulations – and subtracted from the measurements with a high-purity $^{\text{nat}}\text{C}$ sample. The remaining time distribution of β -decays was fitted to an exponential form with the lifetime of ^{12}B , thus obtaining the number of ^{12}B nuclei produced per neutron pulse: $N_{12\text{B}} = 68.5 \pm 0.4_{\text{stat}} \pm 4.8_{\text{sys}}$. This observable was related to the cross section of the $^{12}\text{C}(n,p)^{12}\text{B}$ reaction, by means of a properly determined weighting function, which has been used to calculate the expected number of ^{12}B nuclei produced per single pulse of the n_TOF beam.

Acknowledgements

This research was funded by the European Atomic Energy Community's (Euratom) Seventh Framework Programme FP7/2007-2011 under the Project CHANDA (Grant No. 605203) and by the Croatian Science Foundation under Project No. 1680. GEANT4 simulations have been run at the Laboratory for Advanced Computing, Faculty of Science, University of Zagreb.

References

- [1] P. Žugec, N. Colonna, D. Bosnar *et al.*, Nucl. Instr. and Meth. A **760**, 57 (2014).
- [2] M. Pillon, M. Angelone, A. Krása *et al.*, Nucl. Instr. and Meth. A **640**, 185 (2011).
- [3] V. E. Ablesimov, E. K. Bonjushkin and A. P. Morosov, in *Neutron Physics Conf., Kiev 1971*, Vol.1, p.173 (1971).
- [4] W. E. Kreger and B. D. Kern, Phys. Rev. **113**, 890 (1959).
- [5] E. M. Rimmer and P. S. Fisher, Nucl. Phys. A **108**, 567 (1968).
- [6] V. V. Bobyr, G. I. Primenko, K. K. Revyuk *et al.*, Izv. Akad. Nauk SSSR, Ser. Fiz. **36**, 2621 (1972) (in Russian).
- [7] D. A. Kellogg, Phys. Rev. **90**, 224 (1953).
- [8] S. Agostinelli, J. Allison, K. Amako *et al.*, Nucl. Instr. and Meth. A **506**, 250 (2003).
- [9] GEANT4 *Physics Reference Manual*, <http://geant4.cern.ch/>.
- [10] M. B. Chadwick, M. Herman, P. Obložinský *et al.*, Nucl. Data Sheets **112**, 2887 (2011).
- [11] C. Guerrero, A. Tsinganis, E. Berthoumieux *et al.*, Eur. Phys. J. A **49**, 27 (2013).
- [12] M. Barbaggallo, C. Guerrero, A. Tsinganis *et al.*, Eur. Phys. J. A **49**, 156 (2013).
- [13] R. Plag, M. Heil, F. Käppeler *et al.*, Nucl. Instr. and Meth. A **496**, 425 (2003).
- [14] P. Žugec, N. Colonna, D. Bosnar *et al.*, Phys. Rev. C **90**, 021601(R) (2014).
- [15] P. Žugec, N. Colonna, D. Bosnar *et al.*, *Measurement of the $^{12}\text{C}(n,p)^{12}\text{B}$ integral cross section up to 10 GeV*, submitted to Physical Review C.
- [16] U. Abbondanno, G. Aerts, F. Álvarez *et al.*, Nucl. Instr. and Meth. A **538**, 692 (2005).
- [17] R. L. Macklin, and J. H. Gibbons, Phys. Rev. **159**, 1007 (1967).
- [18] U. Abbondanno, G. Aerts, H. Alvarez *et al.*, Nucl. Instr. and Meth. A **521**, 454 (2004).
- [19] C. Paradela, L. Tassan-Got, L. Audouin *et al.*, Phys. Rev. C **82**, 034601 (2010).

Nuclear interaction model developments in FLUKA

A. Fontana¹, *On behalf of the FLUKA collaboration*

¹ Istituto Nazionale di Fisica Nucleare (INFN), Sezione di Pavia, Italy

Abstract

A selection of recent improvements in the modeling of nuclear interactions with the FLUKA code is presented. At low energy the new features are related to the emission of secondary particles, to the inclusion of spin-parity effects in the evaporation stage and to the extension of the pre-equilibrium step to the Relativistic Quantum Molecular Dynamics (RQMD) model. At high energy new results from Electro-Magnetic Dissociation (EMD) and cosmogenic neutron production are shown. These results confirm and extend the use of FLUKA in different fields of interest, ranging from the LHC to medical applications.

1. Hadronic interaction modeling in FLUKA

1.1 FLUKA overview

FLUKA is a multipurpose Monte Carlo code developed by an international collaboration between INFN, CERN and other institutions ([1],[2]). The code can treat hadron-hadron, hadron-nucleus, nucleus-nucleus, neutrino, electromagnetic, and μ interactions up to 10000 TeV and is able to transport about 60 kinds of particles as well as all nuclei in complex geometries. Charged particle transport includes all relevant processes, also in magnetic fields. The code also manages interaction and transport of neutrons down to thermal energies. For these characteristics the scope of FLUKA is very broad and ranges from the LHC and cosmic rays physics at high energy to hadrontherapy and other medical applications at intermediate and low energy. In addition the code has the double capability to run either in fully analogue or biased mode, can follow the on-line evolution of induced radioactivity and dose, can be used for activation studies and is able to perform radiation damage predictions in materials, like Non Ionizing Energy Loss (NIEL) and Displacement Per Atom (DPA) calculations. Finally its very user-friendly graphical interface, provided by the code Flair [3], allows to quickly set up advanced physical calculations.

1.2 From hadron-Nucleon (hN) to Nucleus-Nucleus (AA) interactions

For hadronic interactions FLUKA provides an optimized set of microscopic models of physical processes to guarantee consistency among all the reaction steps and types (see fig. 1). For this reason predictions for complex simulation problems in FLUKA are robust, arising naturally from underlying physical models.

In this scheme the basic building block is the description of the hadron-nucleon (hN) interaction over a wide energy range. This is essential to achieve a valid description of the hadron-nucleus (hA) and nucleus-nucleus (AA) interaction, which are built on top of it in a consistent way: the detailed description of the FLUKA approach philosophy and implementation can be found in the literature ([4], [5]). Here we only recall the main points.

Hadron-nucleon inelastic reactions are described in terms of resonance production and decay up to a few GeV. At higher energies, a model based on the Dual Parton Model (DPM) takes over. In this context, secondary particle production comes from the creation of two color quark strings. Hadron-nucleus interactions can be schematically described as a sequence of different steps: a Glauber-Gribov cascade followed by a generalized intra-nuclear cascade, by pre-equilibrium emission, by evaporation,

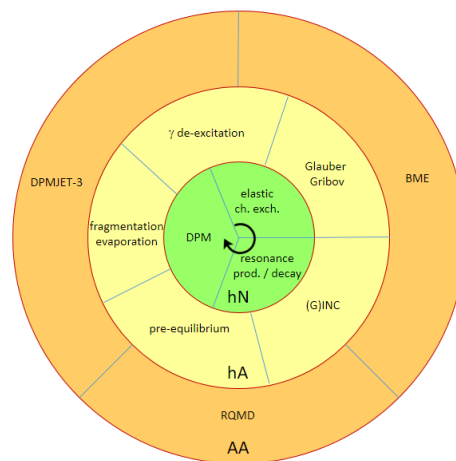


Fig. 1: Pictorial view of the approach followed by FLUKA to model hadron-nucleon (hN), hadron-nucleus (hA) and nucleus-nucleus (AA) interactions: note that the arrow indicates increasing energy in the inner and in the outer circle and increasing time in the middle circle.

fragmentation or fission and finally by γ de-excitation of the nuclear residuals. For what concerns nucleus-nucleus collisions, FLUKA is based on three complementary approaches. At low energy the Boltzmann Master Equation (BME) theory is implemented in a model developed at the University of Milan [6]. At intermediate energies the interaction among nucleons during the reaction is dynamically described, including relativistic effects, with the Relativistic Quantum Molecular Dynamics model in a modified version of RQMD-2.4 code [7], while at high energies (> 5 GeV/n) the DPM and the Glauber theory are used with the DPMJET event generator [8]. In all cases, the same equilibrium de-excitation stage applies to the produced nuclear fragments.

2. Recent improvements: low energy nuclear interactions

In this general scheme, at low energy the new features refer to the emission of α particles and deuterons from the first steps of the nucleon-induced reaction and to the inclusion of spin-parity effects in the evaporation stage. This yields a significant improvement of the β activity calculation and of the prompt γ emission. The extension of the pre-equilibrium stage to the RQMD model is also reported.

2.1 Secondary particles emission

The evidence for unsatisfactory reproduction of deuteron emission at low energy motivated the introduction in FLUKA of a direct deuteron formation mechanism at the first p-n elementary step in the cascade and in the pre-equilibrium stage in addition to the standard coalescence mechanism. This presently applies to nucleon-induced reactions on light nuclei and concerns also α particle emission. As a result, a better agreement with experimental data is found, as shown for example in Fig. 2, for angle integrated spectra of products from the interaction of 62 MeV protons on Oxygen.

In general the accurate prediction of secondary particles emission is important, not only from the theoretical point of view, but also for application cases, as for example dose monitoring in hadron-therapy treatments by the γ radiation from the annihilation of positrons emitted in radioactive decay. The pattern of activation induced as a by-product of the therapeutic irradiation is correlated to the dose delivery. Treatment verification can be achieved by comparing the activity distribution measured via Positron-Emission-Tomography [9] with a calculated one which requires an accurate description of the

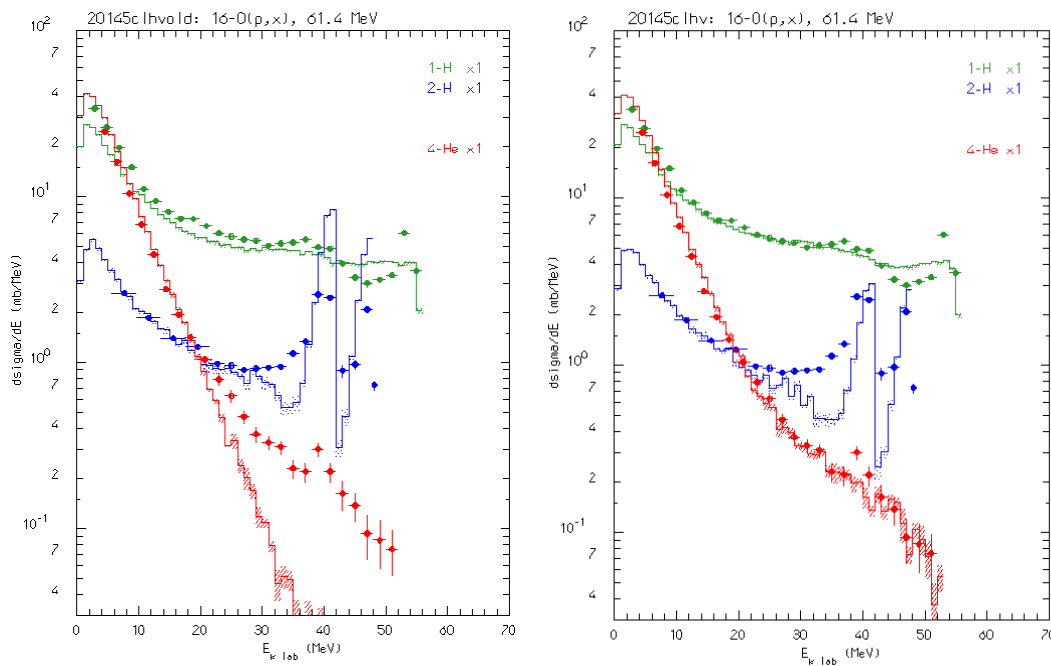


Fig. 2: Angle integrated spectra for p, d and α emission by 62 MeV protons on Oxygen. Left : Old (2011.2) FLUKA version. Right : current one (2015.0).

fragmentation reaction channels yielding β^+ -emitters. Their production cross section is in turn affected by light particle emission. In fact, the aforementioned deuteron direct production mechanism has a significant impact also on the improvement of the ^{11}C excitation function reproduction in proton on carbon reactions, as shown in fig. 3.

2.2 Spin-parity in evaporation

The prompt γ emission is also considered to monitor the dose delivery in hadron therapy although production rates are rather low ($\sim 5 \times 10^{-7}$ to 10^{-6} γ per incident ^{12}C and per millimeter). For its calculation, spin-parity effects in nuclear reactions play an important role, determining individual level population and isomer production rates. A full spin-parity dependent evaporation model (*à la* Hauser-Feshbach [10]) is still too complex to be implemented in MC codes in the energy range of interest for FLUKA applications. However, work is going on in FLUKA to keep track of the total angular momentum and parity evolution during the cascade and the pre-equilibrium stages: in this context FLUKA can now take into account spin-parity selection rules for "well defined" initial conditions (for example for photonuclear interactions) or for low energy reactions. The new implementation based on the MLO (Modified Lorentzian) model [11] includes the competition between γ emission and particle evaporation. In Fig. 4 a benchmarking concerning the ^{195}Au excitation function for the reaction $^{197}\text{Au}(\gamma, 2n)$ is shown, before and after the inclusion of these effects.

2.3 Pre-equilibrium in RQMD

The RQMD model was introduced in FLUKA several years ago as a modified version of a well known code [7]. Recently a pre-equilibrium step has been introduced after the RQMD cascade stage, applying

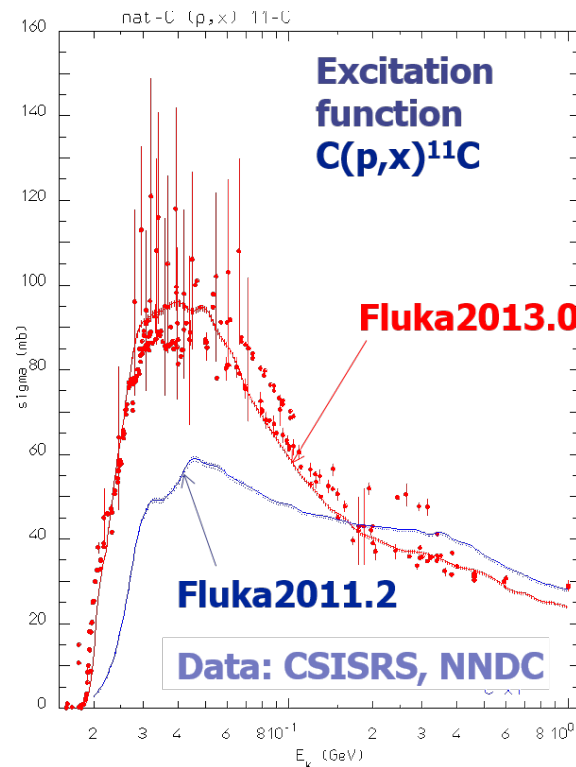


Fig. 3: Comparison between new and old FLUKA versions and experimental data for the excitation function of the reaction $C(p,X)^{11}C$

the existing PEANUT module based on the exciton model both to the target and projectile residuals. An example of the improved agreement with data is shown in Fig. 5 for ^{12}C ions on carbon at 135 MeV/n.

3. Recent improvements: high energy nuclear interactions

At high energy, we report the recent improvements on ElectroMagnetic Dissociation (EMD), with a comparison between Monte Carlo predictions and new LHC data and new results on cosmogenic neutron production.

3.1 Electromagnetic dissociation at LHC

The cross section for EMD increases with the target atomic number and the projectile energy and it is already relevant for few GeV/n ions on heavy targets (for example $\sigma_{EMD} \sim 1b$ vs $\sigma_{nucl} \sim 5b$ for 1 GeV/n Fe on Pb). Its description is therefore crucial with respect to the LHC heavy ion collision studies currently in progress. An example of results obtained for Pb-Pb collisions compared to data from ALICE is shown in fig. 6.

As recent developments, the E2 multipolarity mode, important at low energies, has been included and electronuclear interactions have been implemented.

3.2 Cosmogenic neutron production

The production of neutrons by cosmic muon interactions is an important effect in the estimation of the backgrounds in underground detectors: typically such neutrons can dominate the background and can

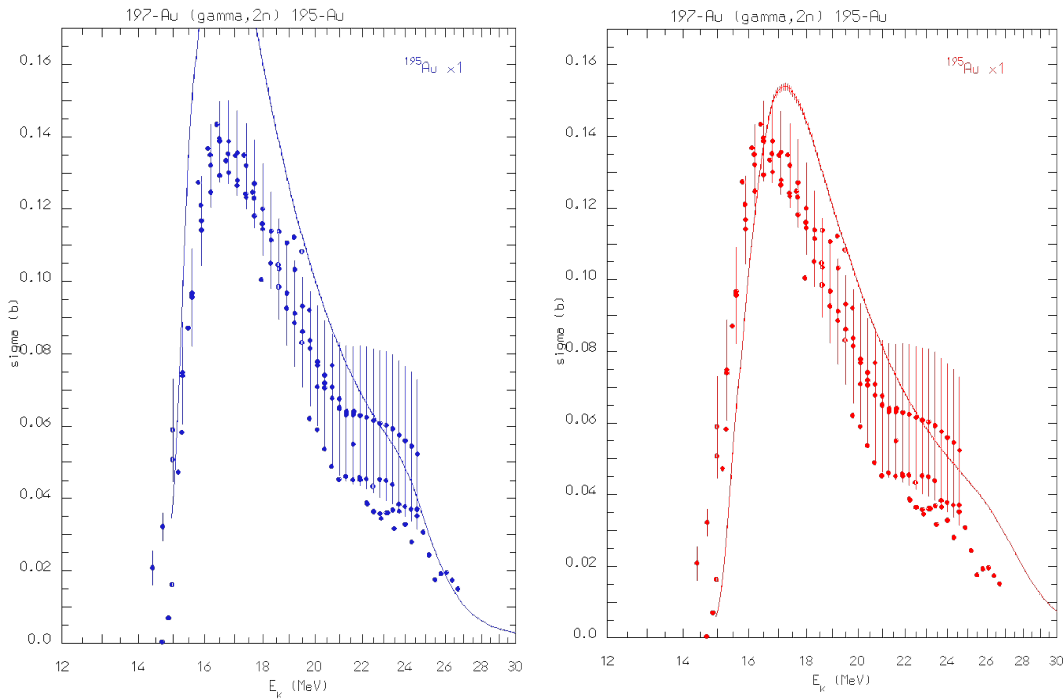


Fig. 4: Comparison between new (right panel) and old (left panel) FLUKA versions and experimental data for the excitation function of the reaction $^{197}\text{Au}(\gamma, 2n)^{195}\text{Au}$.

make the search for rare events very difficult. The production of cosmogenic neutrons in FLUKA is the result of direct muon photo-nuclear interactions, of photo-nuclear reactions by real photons generated in electromagnetic showers and in nuclear cascades within resulting hadronic showers. The photon-nucleus reactions are simulated over the entire energy range through different mechanisms: giant dipole resonance excitation at low energy, quasi-deuteron interaction, Delta resonance production and Vector Meson Dominance at high energies. Direct muon photo-nuclear reactions imply the generation of a virtual photon, whose spectrum has been now extended below the threshold for pion production on nucleon. Recently a comparison of the FLUKA predictions with new Borexino data has shown a good agreement for the yield of the residual nuclei produced (Fig. 7) [12, 13]: for example in the case of ^{11}C the updated FLUKA production yield is $767 \pm 19 \times 10^{-7} 1/\mu(\text{g}/\text{cm}^2)^{-1}$ and the experimental value is $866 \pm 115 \times 10^{-7} 1/\mu(\text{g}/\text{cm}^2)^{-1}$, while the previous FLUKA estimation was $467 \pm 23 \times 10^{-7} 1/\mu(\text{g}/\text{cm}^2)^{-1}$. The increase of the theoretical value, significantly improving its agreement with the measurement, is due both to the additional component in muon photo-nuclear reactions (given by low energy virtual photons) and to the aforementioned spin-parity effects.

4. Medical applications

FLUKA is extensively used since many years for medical applications, for example in hadrontherapy for the validation of treatment planning systems (TPS) at HIT (Heidelberg Ion-Therapy Center) [14] and CNAO (Centro Nazionale di Adroterapia Oncologica) [15]. The Flair interface to the DICOM format allows to import diagnostic images. Developments are currently in progress towards a Monte Carlo TPS [16]. In this context FLUKA has been recently used for several purposes, namely in a comparison of the lateral dose distributions experimentally obtained at CNAO [17], as a benchmark for the development

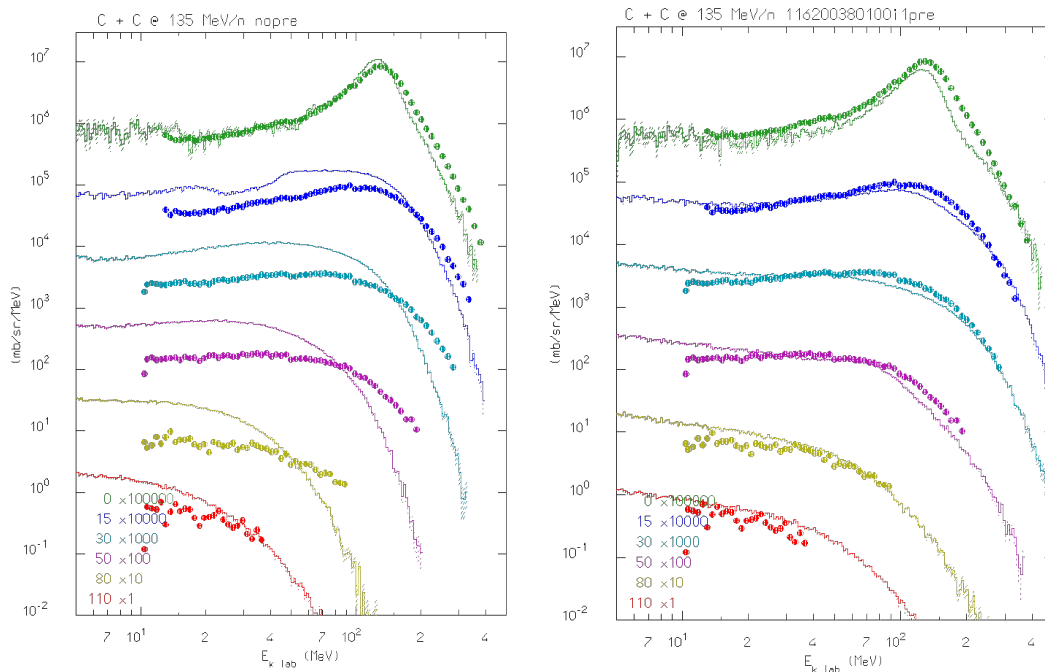


Fig. 5: Neutron double differential spectra at various angles for ^{12}C on C @ 135 MeV/n. Left: old version, right: new version. The histograms show the prediction of the RQMD model, while the symbols refer to experimental data.

of a computational model for dose calculation based on the full Molière theory [18] and in the study of the effect of the lateral penumbra in patient-like cases with proton and ^4He beams.

5. Conclusions

The well established FLUKA code provides an integrated and optimized treatment of nuclear interactions (hadron-nucleon, hadron-nucleus and nucleus-nucleus) over a wide energy range. The code is used in many different fields, both in pure and in applied physics. In this paper the more recent updates to the code with respect to nuclear interaction modeling were presented: in this scheme several improvements have been implemented at various levels (and many others are planned) and will be released with the future versions.

Acknowledgements

The author is grateful to A. Ferrari, P. Sala and A. Mairani for the very useful and constructive discussions during the preparation of this talk.

References

- [1] T.T. Böhlen *et al.*, *Nuclear Data Sheets* **120** (2014) 211
- [2] Ferrari A. *et al.*, CERN-2005-10, INFN/TC05/11, SLAC-R-773, (2005)
- [3] V. Vlachoudis, Proc. International Conference on Mathematics, Computational Methods and Reactor Physics, 2009
- [4] A. Ferrari and P.R. Sala, Proc. Workshop on Nuclear Reaction Data and Nuclear Reactor Physics, 1998
- [5] F. Ballarini *et al.*, 10th Int. Conf. on Nuclear Reaction Mechanisms, 2003

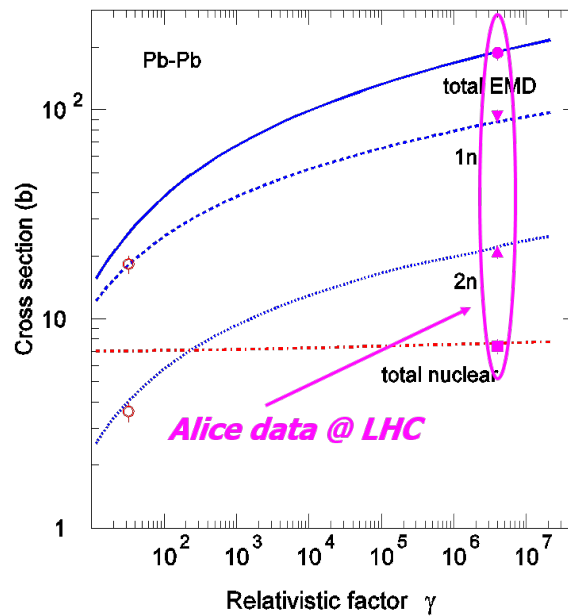


Fig. 6: Comparison between the EMD model of FLUKA and data for Pb-Pb collisions. The total EMD cross section and the EMD cross section for one and for two neutron emission respectively, are shown. The nuclear inelastic cross section is also indicated.

- [6] G. Battistoni *et al.*, *Braz. J. Phys.* **34** (2004) 897
- [7] H. Sorge *et al.*, *Nucl. Phys. A***498** (1989) 567c
- [8] S. Roesler *et al.*, SLAC-PUB-8740, 2000
- [9] V. Rosso *et al.*, 2013 JINST 8 C03021
- [10] W. Hauser and H. Feshbach, *Phys. Rev.* **87** (1952) 366
- [11] V.A. Plujko, *Nucl. Phys. A***649** (1999) 209c
- [12] A. Empl *et al.*, JCAP08(2014)064
- [13] A. Empl *et al.*, AIP Conference Proceedings 1672, 090001 (2015)
- [14] K. Parodi *et al.*, *J. of Rad. Res.* **54** (2013) i91
- [15] A. Mirandola *et al.*, *Med. Phys.* **42** (2015) 5297
- [16] A. Mairani *et al.*, *Phys. Med. Biol.* **58** (2013) 2471
- [17] A. Embriaco *et al.*, these proceedings
- [18] V.E. Bellinzona *et al.*, these proceedings

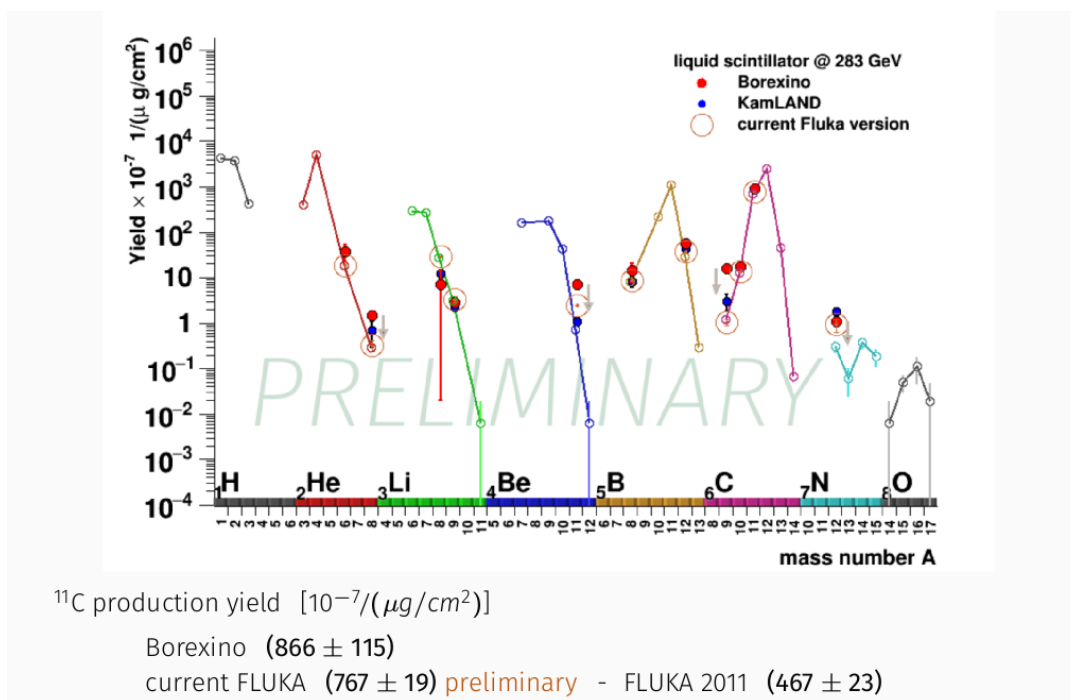


Fig. 7: Experimental muon-induced cosmogenic isotope production yields in liquid scintillator at LNGS (the indicated energy is the average of the muon spectrum). Preliminary predictions obtained with the latest version of FLUKA are shown with open symbols.

Revision of the high energy hadronic interaction models PHOJET/DPMJET-III

A. Fedynitch^{1,2} and R. Engel²

¹ CERN EN-STI-EET, CH-1211 Geneva 23, Switzerland

² Karlsruher Institut für Technologie, Institut für Kernphysik, Postfach 3640, 76021 Karlsruhe, Germany

Abstract

The high-energy hadronic interaction model DPMJET-III is responsible for simulating nuclear interactions in the particle simulation package FLUKA. On the level of individual nucleon interactions it employs PHOJET, which provides sophisticated forward physics and diffraction models. This paper summarizes some of the recent developments, in particular regarding minimum-bias physics at the LHC, which apply to DPMJET-III and PHOJET at the same time.

1. Introduction

PHOJET is a minimum-bias Monte Carlo event generator [14, 15] for hadron-hadron, photon-hadron and photon-photon interactions. The basis of the model is the two-component Dual Parton Model [9], which integrates the ideas of Regge theory [19, 20], non-perturbative and perturbative expansions of QCD within a common framework. Generally accepted arguments, such as unitarity or duality [11, 7], support the self-consistency of the model and should allow to make relatively robust extrapolations up to very high future collider or cosmic ray energies. Historically the model DTUJET-93 [6] contained an almost complete description of soft processes and a model for gluon-gluon scattering as the hard component. PHOJET superseded it in the second part of the 1990's with a complete (source code) rewrite, a new model for photon-hadron and photon-photon interactions and a full set of leading-order QCD processes, an interface to parton distribution function libraries and many more features. For fragmentation, as the last step in the generation of an event, PHOJET interfaces with PYTHIA 6.

DPMJET-III [8] is a generator for hadron-nucleus, photon-nucleus and nucleus-nucleus collisions. It uses PHOJET to generate individual hadron-hadron and photon-hadron collisions. I.e. calling DPMJET-III for a proton-proton collision is identical to calling PHOJET for the same setup. DPMJET-III provides a realization of the Glauber model for nuclear collisions, photo-nuclear interactions, intranuclear cascade models, spectator fission and fragmentation, and it includes models for low energy interactions. DPMJET-III-III is released as a public version and also as part of the FLUKA particle physics simulation package [16, 8]. The influx of LHC data motivated this revision of the models for recent and future collider developments and the astroparticle physics community.

2. Goals for the new version

At the time of writing the LHC just restarted with Run-II at 13 TeV center-of-mass energy. For the previous run at 0.9, 2.36, 7 and 8 TeV the majority of minimum-bias results is already published.

Studies on LHC upgrades or on future hadron colliders, such as Future Circular Collider (FCC) project at CERN, and astroparticle physics put strong requirements on the quality of hadronic interaction models, in particular regarding the extrapolation into unexplored energy regimes and the prediction of very forward distributions. These requirements include the simulation at ultra-high energies, strict energy and momentum conservation, models for meson-nucleon, hadron-nucleus and nucleus-nucleus interactions. Also some technical features have to be present for cascade functionality, such as the

support for multiple projectile target combinations in one run and smooth, consistent behavior of total and partial process cross-sections over the entire energy range.

DPMJET-III together with PHOJET fulfill many of these requirements, but other features are missing. The first shortcoming is PHOJET's model for the total and partial process cross sections. It tops out at several tens of TeV in center-of-mass frame, because some of the diffractive cross-sections become negative. Also, LHC data on total and elastic cross-sections constraints the extrapolation to higher energies. The second shortcoming is the lack of the possibility to handle multiple projectile-target combinations simultaneously.

3. Multi-particle modification

PHOJET supported only one projectile-target combination per initialization. Multiple calls to the initialization routines were not supported and not recommended. The most time consuming part, taking seconds on modern computers, is the calculation of the hard cross-section as a convolution of leading-order QCD matrix elements with parton densities over the entire phase-space. Therefore it is crucial to avoid repetitions of this step when switching between different projectiles. In the new version the data structures for storing cross-section tables and counters can not change significantly, due to the close relationship with DPMJET-III and FLUKA. Otherwise, significant effort would be needed to re-validate correct functionality.

The new implementation is an on-demand scheme, i.e. it inserts additional initialization steps if a different projectile is requested. The minimal modification to the data structures, keeping the user interface unchanged, is the extension of cross-section tables by one dimension, which index points to an unique projectile-target combination. A new common block contains tables and variables that keep track of the currently active particle combination. Some projectiles for which cross-sections or other details of the interaction are not known can be "mapped" to known particle combinations. For example, neutral kaon K^0 interactions are treated in the same way as K^+ interactions, substituting its quark content $u\bar{s}$ with $d\bar{s}$. The cross-sections are calculated during the first event generation call for the current projectile-target particle combination. This approach implies, that switching between the particle combinations after they have been initialized is instantaneous and that there is no need to change external interfaces.

4. New energy dependence of transverse momentum cutoff

In the old version of PHOJET the p_T^{cutoff} , defining the perturbative scale, grows with energy as a function of $\log \sqrt{s}$. This purely phenomenological parametrization is motivated by the fact, that at very high energies at tens or hundreds of TeV in center-of-mass frame, the dense partonic matter in the interaction region prevents the scattered partons from escaping without re-scattering or additional interactions. It is not clear anymore that scatterings resulting in a $p_T \sim 2.5$ GeV can be considered as perturbative processes. In fact, there is no unambiguous guidance from theory what is a sufficiently high transverse momentum and where the separation between the technical terms "soft" and "hard" lies.

The need to find a robust approach to this question stems from the energy dependence of the $2 \rightarrow 2$ QCD cross-section

$$\sigma_{\text{QCD}} = \sum_{i,j,k,l} \frac{1}{1 + \delta_{kl}} \int dx_1 dx_2 \int_{Q_{\min} \propto p_{\perp}^{\text{cutoff}}} dQ^2 f_i(x_1, Q^2) f_j(x_2, Q^2) \frac{d\sigma_{i,j \rightarrow k,l}}{dQ^2}, \quad (1)$$

where x_1, x_2 are the longitudinal momentum fractions of the incoming partons i, j , Q the virtuality or the momentum transfer of the process, $\sigma_{i,j \rightarrow k,l}$ the leading-order QCD matrix elements, and f_i, f_j the density (PDFs) of flavor i partons in the incoming particle on side 1 and j for the other particle,

respectively. This equation makes use of the factorization theorem, since the density of partons is independent of the process and since there are no correlations between side 1 and 2 (no convolution of f_i with f_j). Clearly, since there is no dependence on the impact parameter, the partons are assumed to be localized in a point-like region.

The integral in Eq. (1) returns the cross-sections for the sum over all initial and final state pairs of partons. As s grows, more phase-space is available for interactions at small x , leading at some point to $\sigma_{\text{QCD}} > \sigma_{\text{inel}}$. Since σ_{QCD} is the inclusive partonic cross-section one estimate for the average number of multiple parton interactions (MPI) by

$$\langle n_{\text{di-jet}} \rangle = \frac{\sigma_{\text{QCD}}}{\sigma_{\text{inel}}}. \quad (2)$$

This number emerges from a very simplified picture and can be considered at most as an upper limit for the case where all scatterings occur uncorrelated.

Due to the lack of guidance on the value of p_T^{cutoff} from first principles, the choice for a new parametrization fell on predictions from the phenomenological dipole-model. In their studies of small- x physics and saturation effects the authors of [18] propose that the transition between the "soft" and the "hard" regime has an energy dependence proportional to

$$Q_{\text{min}} \propto p_T^{\text{cutoff}} \sim p_{T,0} \sqrt{s}^{\lambda_{\text{eff}}}. \quad (3)$$

The new energy dependence of the cutoff in PHOJET contains more degrees of freedom but keeping the idea of the Regge motivated power-law behavior

$$p_T^{\text{cutoff}} = p_0 \left(\frac{\sqrt{s} + p_1}{p_2} \right)^\lambda. \quad (4)$$

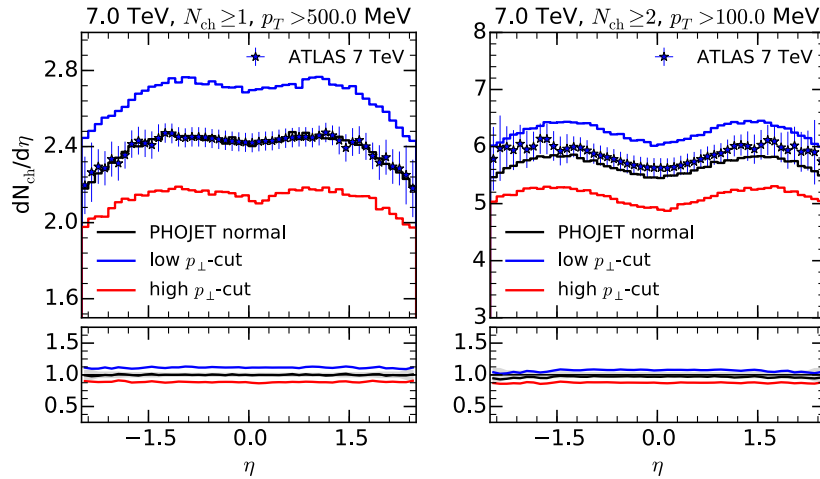


Fig. 1: Charged particle pseudo-rapidity densities at 7 TeV for two different phase-space cuts. The low, normal and high p_{\perp} -cut values are 3.5, 4.0 and 4.5 GeV, respectively. Measurement by ATLAS [1].

Figure 1 confirms the expectation, that the variation of the p_T^{cutoff} produces different scaling behaviors of the pseudo-rapidity plateau. With the higher cut on $p_T > 500$ MeV, the left plot emphasizes the role of hard interactions. In the right panels, where the lower cut on p_T permits more particles from the fragmentation of soft strings, the effect is milder.

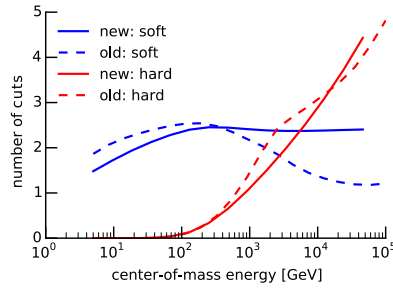


Fig. 2: Distribution of the number of soft and hard pomeron cuts with new p_T^{cutoff} model and updated cross-section fits.

Together with new cross-section fits (see next section) and the new energy behavior, PHOJET obtains a new distribution of MPI as shown in Figure 2. In addition, a more balanced choice of other parameters, in particular of those related to the triple-pomeron vertex, resulted in a smoother, feature-less behavior.

5. New parton density functions

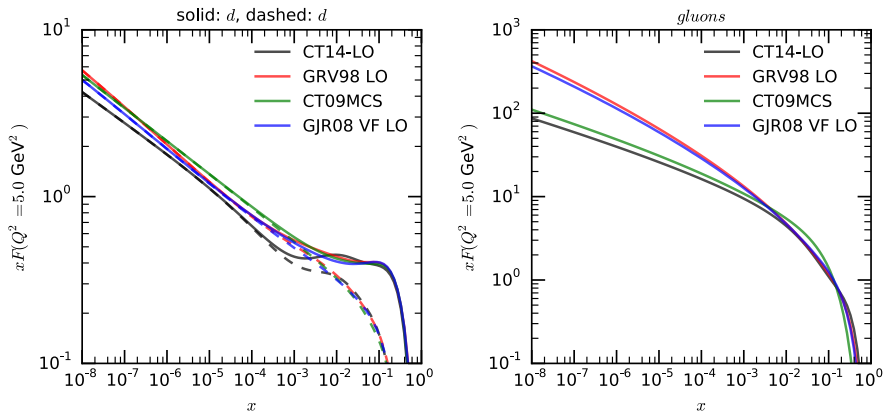


Fig. 3: Parton densities at low $Q^2 \sim \hat{p}_{T,min}^2$.

Before the start of the LHC Run-II several groups released updated sets incorporating LHC Run-I data. Minimum-bias events do not necessarily depend on the absolute choice of the PDF and many of its features can be absorbed into parameter retuning. First of all, because the absolute value of hard QCD cross-section depends on the free p_T^{cutoff} parameter and second, because details of partonic final states are smeared out by hadronization and final state radiation in later steps of event generation. Choosing a high-quality PDF is still not meaningless, since the behavior of the energy-dependent p_T^{cutoff} influences the multiplicity of minijets at cosmic-ray energies. In this sense, incorporating the latest PDF can be seen as additional guidance by data.

After the CTEQ-TEA group published the CT14 LO set, the choice fell in favor of it. The equivalent competitor NNPDF3.0, although suitable for this application, produced numerical inaccuracies using the central value, presumably due to the performance optimized integration scheme. The GJR08 dynamical PDFs [17] sets were not yet exposed to LHC data and could therefore be of smaller value. As it can be seen in Figure 3, down-quarks in CT14 gained some substructure at $x \sim 10^{-2}$ and are significantly lower compared to its predecessor CT09 and the dynamical PDFs. The CTEQ-TEA group

argues that to a large extent the measurements of the W -boson's charge asymmetry lead them to this result [13].

Another advantage of the CT sets is the smaller gluon density at very small x when compared with GJR. Although the accuracy of both results is questionable without appropriate data, fewer soft gluons are an advantage when extrapolating to high energy, since the model needs to correct less for phase-space limitations and realizable final states.

At higher virtualities Q^2 the differences vanish between the CT14 and CT09 or GJR08 and GRV98, respectively. This is due to the fact, that at higher virtualities perturbation theory fully applies and the DGLAP equations become exact.

6. New cross-section fits

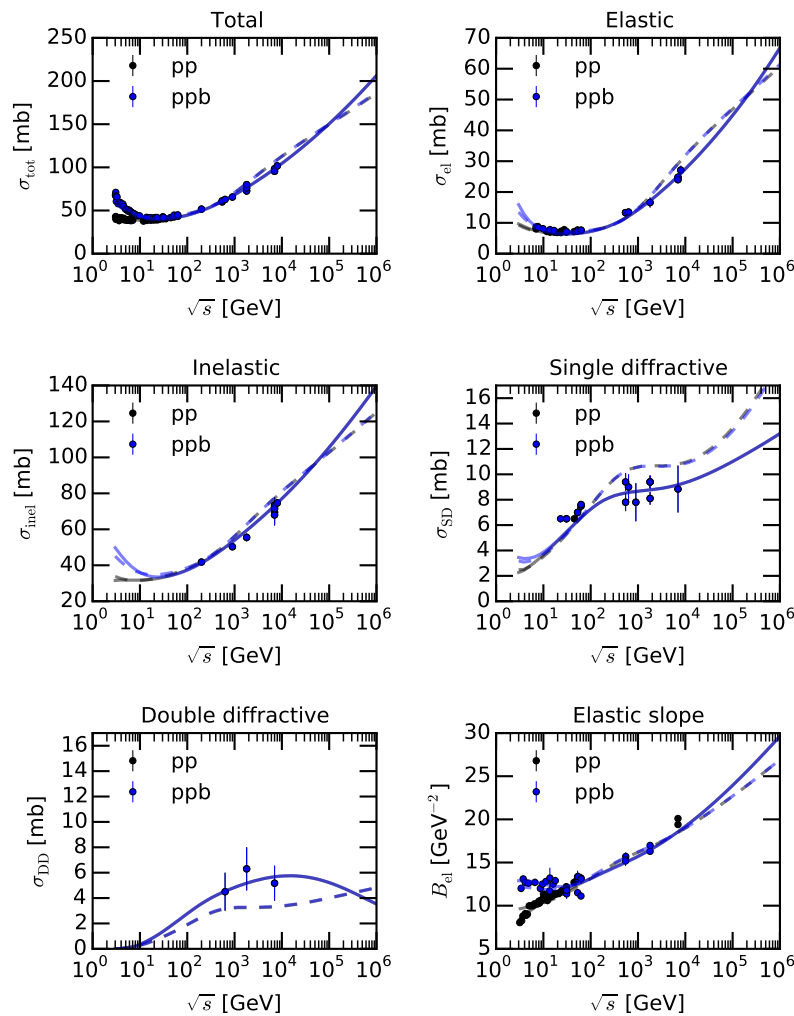


Fig. 4: Total, elastic, inelastic, diffractive cross-sections and the elastic slope. Solid lines correspond to the new model and dashed to the old DPMJET-III-III. Lower energy data are taken from a compilation published in [12]. Data points at LHC energies are from [4, 5, 10, 3, 21]

Figure 4 shows a comparison of total, elastic, inelastic and diffractive cross-sections between the

old and the new PHOJET/DPMJET-III versions. One of the more challenging requirements is the ability to extrapolate to ultra-high energies above hundreds of TeV in center-of-mass. The old version could initialize up to PeV energies only for pp interactions, but not with pion or kaon projectiles.

The fit is obtained by minimization of the model predictions to a vast set of data. The data-points at LHC significantly constrain the model. The new fit of total and elastic cross-sections in Figure 4 is smooth and compatible with Regge-type power-law behavior. The diffractive cross-sections are in line with experimental trends. Although the total, elastic and inelastic cross-sections are within experimental uncertainties, the elastic slope is too low and can not be compensated by parameter tuning.

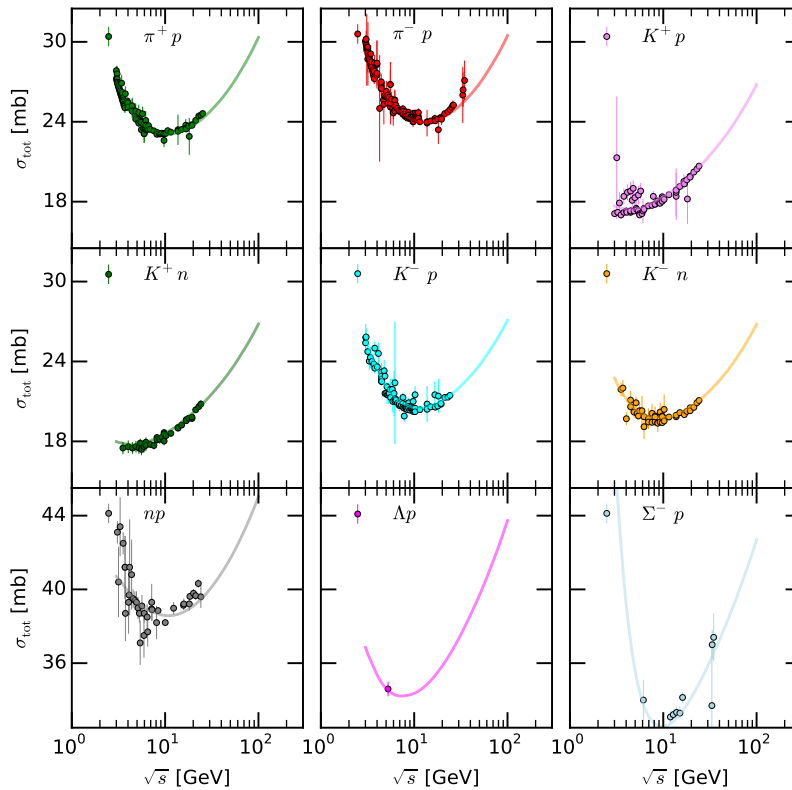


Fig. 5: Total cross-sections of supported projectile-target combinations in PHOJET. Data points are taken from a compilation published in [12].

The original version of PHOJET does not ship with parameter sets for pion-proton or kaon-proton interactions. DPMJET-III contained a work-around type of implementation, where mesons behave according to the proton parameters with the exception of a modified valence quark content. The FLUKA code does not make use this feature and instead falls back to its internal two-string model, which is insufficient to describe particle interactions at very high energies above 10 - 100 TeV in laboratory frame.

Together with the multi-particle extension, PHOJET and DPMJET-III contain new sets of parameters for p , n , \bar{p} , π^\pm , K^\pm , K^0 , Λ and Σ^- projectiles combined with p and n targets. The Figure 5 shows a compilation of the fit results. Since high-energy data are not available for most of the projectiles, the parameter sets are derived from the results of the pp and $p\bar{p}$ fits with a modified low-energy part. At low energies the highest contribution to the total cross-section comes from effective Reggeon exchanges. Fitting just the pomeron-particle coupling $g_{\mathcal{P},0}$ and the reggeon-particle coupling $g_{\mathcal{R},0}$ on the

non-proton side plus the Reggeon intercept $\alpha_{\mathbb{R}}$ turned out to be sufficient in most cases.

7. DPMJET-III vs. LHC data

For an event generator which was not maintained for more than 12 years, DPMJET-III performed very well in comparisons with LHC minimum-bias data at 0.9, 2.3 and 7 TeV. Very extensive comparisons with the majority of LHC minimum-bias data taken by all of the experiments have been performed and here only very few examples are mentioned. The investigation revealed two major problems, a low particle multiplicity in the central region and the lack of very high multiplicity events ($N_{ch} > 100$). The (technical) truncation of the MPI probability distribution was the origin of this deficit. The predictions significantly improved afterwards.

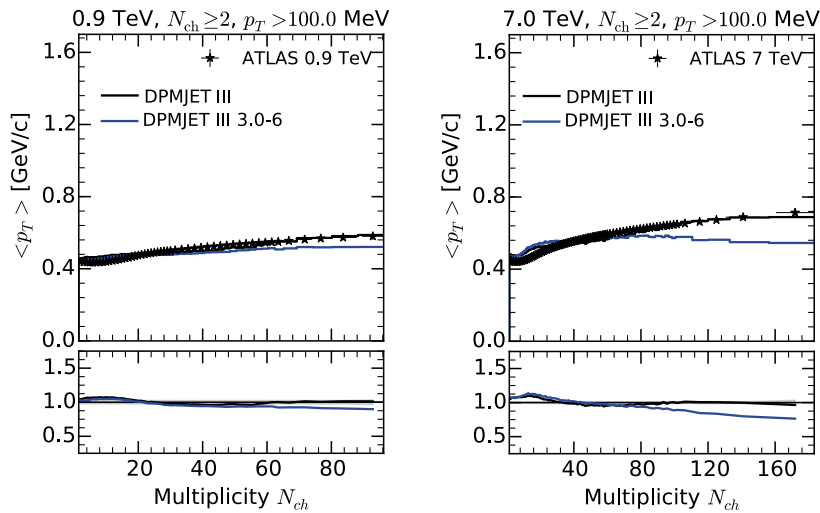


Fig. 6: (top) Average transverse momentum vs multiplicity and (bottom) charged-particle transverse momentum distributions. DPMJET-III 3.0-6 is the last public version and the other is the new version. ATLAS data [1].

At smaller multiplicities, the average p_T in Figure 6 is well described by the both models. In the old model, the lack of high multiplicity events decreases the average p_T because events with a high number of MPI are cut away.

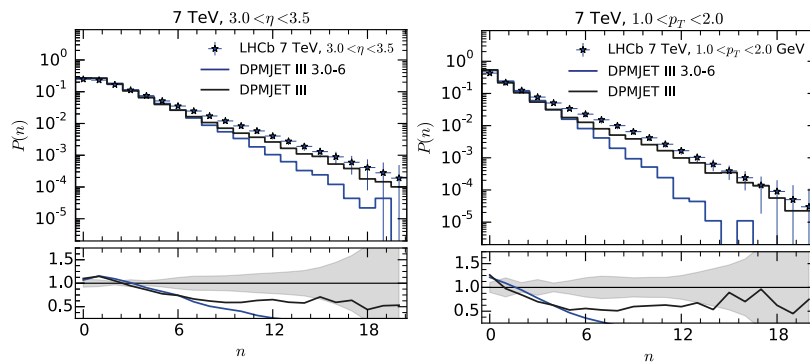


Fig. 7: Comparison with forward multiplicity distributions at LHCb [2] for a pseudo-rapidity bin and for a p_T bin.

More forward distributions, as those in Figure 7, could be improved by re-adjusting the hard cross-section, the PDFs and MPI probabilities. In terms of cascade physics, the LHCb experiment is still

rather central. The cut $p_T > 200$ MeV biases the selection towards events containing hard scatterings. Therefore, the improved central multiplicities influence positively the forward distributions as well.

In general, minimum-bias physics is quite well described, especially if one takes into account that the model works from pion threshold energies up to cosmic ray energies with a mostly energy independent parameters. There are still some tension, in particular with too frequently occurring high multiplicity events. This has already been identified as an effect of approaching the black disk limit and will be discussed in a separate paper.

8. Discussion

Due to technical issues and model features the Monte Carlo event generators PHOJET and DPMJET-III could not be recommended for calculations at very high energies beyond several tens of TeV in center-of-mass frame. Cascade and air-shower simulations for were either limited by the energy range or by the lack of the possibility to treat secondary interactions within the same run of the program. The limitation of a single projectile-target combination per program initialization has been removed by modifying the way how cross-section tables and counters are stored. The new on-demand initialization scheme stores tables for several particle combinations, switching between them in run-time without performance impact.

In light of new LHC data, the high energy behavior of the model has been reviewed. The new experimental results helped to find an unphysical, technical limitation, which was the origin of the lack of high multiplicity events. The availability of results in various phase-space cuts simplified the choice for the energy behavior of the p_T cutoff. Precise measurements of the total and elastic cross-section reduced the extrapolation ambiguity. The choice of a new standard PDF required re-tuning of many parameters when going from the GRV94 to CT14.

The model in its recent state can be used in LHC, FCC and extensive air-shower simulations and, in principle in all kinds of cascade codes. A crucial advantage of DPMJET-III, compared to EPOS for example, is the possibility to go as low as a few GeV per nucleon in the simulation of hadronic and nuclear collisions.

The updated DPMJET-III is now in an extended testing period and will become soon available as part of the FLUKA simulation package and as standalone version.

Acknowledgements

This work is partly sponsored by the Wolfgang Gentner Programme of the Federal Ministry of Education and Research (BMBF) and the Helmholtz Alliance for Astroparticle Physics (HAP), which is funded by the Initiative and Networking Fund of the Helmholtz Association.

References

- [1] G. Aad et al. *New Journal of Physics*, **13**(5) 3033, May 2011.
- [2] R. Aaij et al. *Computer Physics Communications*, **hep-ex**, 2014.
- [3] B. Abelev et al. *The European Physical Journal C*, **73** 2456, June 2013.
- [4] G. Antchev et al. *Europhys. Lett.*, **96**(2) 21002, 2011.
- [5] G. Antchev et al. *Europhys. Lett.*, **101** 21004, 2013.
- [6] P. Aurenche et al. *Computer Physics Communications*, **83**(1) 107, October 1994.
- [7] V. Barone and E. Predazzi. *High-Energy Particle Diffraction*. Springer Science & Business Media, Berlin, Heidelberg, March 2013.
- [8] T. T. Böhlen et al. *Nuclear Data Sheets*, **120**,211, June 2014.
- [9] A. Capella et al. *Phys.Rept.*, **236**, 225, 1994.
- [10] T. A. Collaboration et al. *Nature Communications*, **2**,463, September 2011.

- [11] P. D. B. Collins. *An Introduction to Regge Theory and High-Energy Physics*. Cambridge Monographs on Mathematical Physics. Cambridge Univ. Press, Cambridge, UK, 2009.
- [12] J. R. Cudell, A. Lengyel and E. Martynov. *Physical Review D*, **73**(3) 034008, February 2006.
- [13] S. Dulat et al. June 2015. 1506.07443.
- [14] R. Engel. *Zeitschrift für Physik C Particles and Fields*, volume 66(1) 203, March 1995.
- [15] R. Engel and J. Ranft. *Physical Review D*, **54**(7) 4262, October 1996.
- [16] A. Ferrari et al. *FLUKA: A multi-particle transport code (program version 2005)*. CERN, Geneva, 2005.
- [17] M. Glück et al. *Physics Letters B*, **664**(1-2) 133, June 2008.
- [18] K. Golec-Biernat and M. Wusthoff. *Physical Review D*, **59**(1) 014017, January 1999.
- [19] V. N. Gribov. *Sov. Phys. JETP*, **53** 654, 1968.
- [20] V. N. Gribov and A. A. Migdal. *Sov. J. Nucl. Phys.*, **8** 583, 1969.
- [21] V. Khachatryan et al. *Physical Review D*, **92**(1) 012003, July 2015.
- [22] S. Roesler, R. Engel and J. Ranft. *arXiv.org*, December 2000. hep-ph/0012252v1.

Revision of JAERI-QMD for analysis of peripheral nucleus-nucleus collisions

T.Ogawa, T.Sato, S.Hashimoto and K.Niita

Japan Atomic Energy Agency, Research Organization for Information Science and Technology

Abstract

The JAERI quantum molecular dynamics (JQMD) model was improved to reproduce production of projectile-like fragments in nucleus-nucleus collisions by refining the description of reaction mechanisms in peripheral collisions. In the previous version of JQMD, the formulation of the interaction between nucleons was not Lorentz-covariant therefore JQMD adopted supplementary assumptions to inhibit unrealistic phenomena. In the new version (JQMD-2.0), by adopting Lorentz-covariant formulation of nucleon-nucleon interactions, the extra assumptions were eliminated. Fragment production cross sections calculated by JQMD-2.0 combined with a statistical decay model were compared with the experimental data. The comparison shows that fragment production cross sections calculated by JQMD-2.0 are generally in good agreement with the experimental data. In particular, the agreement of the production cross sections for projectile-like fragments underestimated by JQMD are substantially improved.

1. Introduction

For prediction of radiological impact by heavy ions in space and heavy-ion accelerator facilities, nucleus-nucleus reaction models play a fundamental role. Some approaches have been developed and applied to study various nucleus-nucleus reactions. Quantum molecular dynamics [4] is one of such approaches commonly adopted in general-purpose Monte-Carlo radiation transport codes [5, 6, 7]. JAERI Quantum Molecular Dynamics (JQMD) model is used as the event generator of Particle and Heavy Ion Transport Code System (PHITS) for the dynamical part of nucleus-nucleus reaction simulation. JQMD combined with the statistical decay model GEM [8] was successfully applied to predict fragment production cross sections [9, 10, 11] and neutron production cross sections [12, 13, 14]; however, it was suggested that JQMD systematically underestimated heavy fragments [9]. Moreover, Mancusi *et al.* indicated [15] that Lorentz-covariant treatment of nucleon-nucleon interactions was necessary to reproduce peripheral collisions, in which the stability of nuclei was particularly important to distinguish true nuclear abrasion and spurious nuclear disintegration.

Generally, peripheral collisions are responsible for production of fragments with mass number close to that of target or that of projectile (hereafter referred to as near-target fragments) because in such reactions, small number of nucleons are involved and are knocked-out from the nuclei. In addition, fragment production cross sections increase with decrease in the loss of mass through fragmentation reactions. Therefore production cross sections for near-target fragments are larger than those for lighter fragments and depend on the description of peripheral collisions. Because of the large production cross sections, near-target fragments are important in radiation safety of accelerator operation and cancer therapy. Substantial portion of remanent dose is attributed to decay radiation of near-target fragments; however, there were some technical challenges in simulating near-target fragment production. For the first thing, nuclei were sometimes spuriously disintegrated even without interacting with other nuclei owing to the instability inherent to the description of nucleon-nucleon interactions. In this case, model cannot distinguish the spurious decay and peripheral collisions. Secondly, nucleon-nucleon interactions

at the nuclear surface and those in dense nuclear medium are different in a sense that Pauli-blocking is strong in the depth of nuclei and thereby interactions between nucleons are suppressed.

In this study, we revise the description of reaction mechanisms in JQMD to simulate peripheral collisions accurately. In association with the description of the interaction between nucleons, the complementary assumptions adopted in JQMD were also revised. Fragment production cross sections calculated by the revised JQMD (JQMD-2.0) were compared with experimental data of earlier studies for benchmarking.

2. Methods

JQMD-2.0 was developed as an upgrade of JQMD, whose details are provided elsewhere [7]. As pinpointed previously [15], the description of nucleon-nucleon interactions was not Lorentz-covariant in JQMD, therefore nuclei were spuriously excited or disintegrated occasionally during time evolution in the center-of-mass frame. Lorentz-covariant equation of motion adopted in JQMD-2.0 is described as follows;

$$\begin{aligned}\dot{\mathbf{r}}_i &= \frac{\mathbf{p}_i}{2p_i^0} + \sum_j^N \frac{m}{p_j^0} \frac{\partial \langle \hat{V}_j \rangle}{\partial \mathbf{p}_i}, \\ \dot{\mathbf{p}}_i &= - \sum_j^N \frac{m}{p_j^0} \frac{\partial \langle \hat{V}_j \rangle}{\partial \mathbf{r}_i}. \\ p_i^0 &= \sqrt{\mathbf{p}_i^2 + m^2 + 2m \langle \hat{V}_i \rangle},\end{aligned}\tag{1}$$

where \mathbf{r}_i is the spatial coordinate of the centroid of the i -th nucleon, \mathbf{p}_i is the momentum of the i -th nucleon, m is the rest mass of nucleons, $\langle \hat{V}_j \rangle$ is the potential of j -th particle, and N is the number of particles in the system. In both JQMD and JQMD-2.0, the potential term of the Hamiltonian V is a sum of the Skyrme-type force term, Coulomb interaction term, and symmetry term. The potential V_i is described by the following formula;

$$V_i = \frac{1}{2} \frac{A}{\rho_s} \langle \rho_i \rangle + \frac{1}{1 + \tau} \frac{B}{\rho_s^\tau} \langle \rho_i \rangle^\tau + \frac{1}{2} \sum_j \frac{c_i c_j e^2}{|\mathbf{R}_i - \mathbf{R}_j|} \operatorname{erf}\left(\frac{|\mathbf{R}_i - \mathbf{R}_j|}{\sqrt{4L}}\right) + \frac{C_s}{2\rho_s} \sum_j (1 - 2|c_i - c_j|) \rho_{ij},$$

where A is a Skyrme force parameter ($= -219.4$ MeV), ρ_s is the saturation density ($= 0.168$ fm $^{-3}$), $\langle \rho_i \rangle$ is the overlap integral of wave packets between the i -th nucleon and all the other nucleons, B is another Skyrme force parameter ($= 165.3$ MeV), τ is $4/3$, c_i is 1 for protons and 0 for neutrons, e is the elementary charge, \mathbf{R}_i denotes the position of i -th nucleon, L is the square of the width of wave packet representing nucleons ($= 2$ fm 2), C_s is the symmetry energy parameter ($= 25$ MeV), and ρ_{ij} is the overlap integral of wave functions of the i -th and j -th nucleons. The potential description of JQMD-2.0 was inherited from previous JQMD without any modifications. Using the new equation of motion, nuclei at the ground state almost always stay stable over a typical reaction period of 150 fm/c.

Moreover, the medium effects on nucleon-nucleon scattering cross sections were modified. Previously, the cross sections were calculated with the modified version of the Cugnon's formula [16, 17], which assumed that cross sections were reduced by Pauli blocking. In the new version, on the other hand, the cross sections in the free space were adopted in case the impact parameter was larger than 60% of maximum impact parameter b_{\max} . Here, b_{\max} was estimated by carrying out reaction simulation using different random number seeds with sweeping the impact parameter from zero. The impact parameter at which inelastic reaction probability reached below 20% was defined as the maximum impact

parameter.

In addition to the above-described improvements on the physical reaction mechanisms, supplementary algorithms were revised accordingly. To disregard spurious excitation in JQMD, the simulated events in which the excitation energies of target and projectile were lower than the threshold calculated using Eq. 2;

$$E_{\text{ex}} = 0.3 \times A, \quad (2)$$

where A is the mass number of the nucleus, were rejected and reaction simulation was started afresh. This formulization was reasonable in a sense that the spurious excitation energy was increased with the size of nuclei in JQMD; however, in case of $^{12}\text{C}(^{12}\text{C},x)$ reaction for example, peripheral collision events in which 4 MeV of excitation energy was given to target and projectile were accepted as true reaction events. In this case, projectile and target just pass by without abrading each other reality. Because spurious excitation was substantially suppressed in JQMD-2.0, the separation energy of proton, neutron, and alpha was adopted as the excitation energy threshold as calculated by Eq. 3;

$$E_{\text{ex}} < \min(S_n, S_p + V_p, S_\alpha + V_\alpha). \quad (3)$$

The impact parameter was sampled from zero to a threshold calculated by Eq. 4 in JQMD to cut off spurious reactions;

$$b_{\text{max}} = 1.15 \times (A_t^{1/3} + A_p^{1/3}) - 0.4(\text{fm}), \quad (4)$$

where A_t is target mass number and A_p is projectile mass number. On the other hand, impact parameter was cut off intrinsically in JQMD-2.0, which means that projectile and target stay without losing nucleons in reactions at extremely large impact parameters. In this case, reaction simulation was started afresh after newly sampling the impact parameter. It should be mentioned that impact parameter sampling algorithm in central collisions was also revised. In both JQMD and JQMD-2.0, energy conservation was occasionally violated owing to numerical integration of time evolution. If the deviation of total energy at the beginning and that at the end of reaction was small, the energy was balanced by scaling the excitation energy of the reaction residues. In case the total energy could not be balanced by the scaling of excitation energy (hereafter referred to as a non-energy-conserving event), the event was rejected and reaction simulation was started from the beginning. In JQMD, the impact parameter was newly sampled at random after the rejection; however, central collision events, in which energy balance was often violated, were considerably rejected by this scheme. As a result, the impact parameter sampling was biased. Therefore, JQMD-2.0 restarted reaction simulation with the same impact parameter in the non-energy-conserving events.

Despite the revision on the description of nucleon-nucleon interactions, nuclei were occasionally excited or disintegrated spuriously owing to their intrinsic instability. To avoid such spurious reactions, time evolution of initialized nuclei was followed for a time scale of 150 fm/c to check if spurious excitation or disintegration were observed. This check was performed if the impact parameter was larger than $(b_{\text{max}} - 4)$ fm, otherwise stability check was not performed because reaction was not sensitive to stability of the nuclei. The further details on JQMD-2.0 are provided elsewhere [18].

3. Results and Discussion

Typical fragment production cross sections calculated using PHITS-JQMD-2.0 are compared with experimental data [19] in Fig. 1. JQMD-2.0 predicts the increase in fragment yields by a factor of 4 in the range from $Z=20$ to $Z=25$ accurately owing to the reasonable treatment of peripheral collisions. On the other hand, the cross section calculated by JQMD is almost constant; therefore the yields for

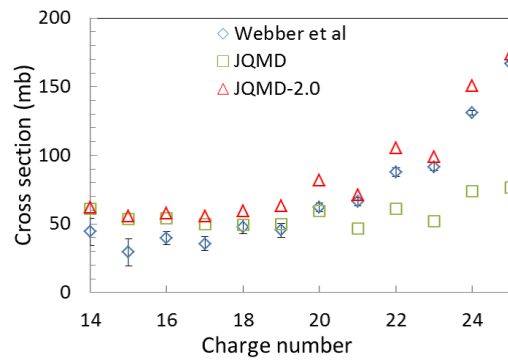


Fig. 1: Partial charge-changing cross section of 724 MeV/nucleon $^{56}\text{Fe}(^{Nat}\text{C},x)$ reaction.

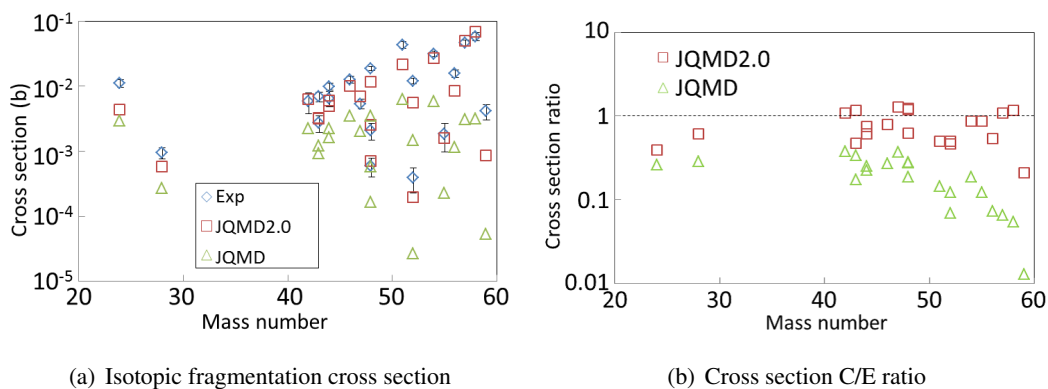


Fig. 2: Isotopic fragmentation cross section of 3650 MeV/nucleon $^{59}\text{Co}(^{12}\text{C},x)$ reaction.

fragments with large Z are systematically underestimated. It is also suggested that the odd-even effect is overestimated by both JQMD and JQMD-2.0 although the odd-even effect was considered only in the statistical decay phase.

Comparison of fragmentation cross sections in higher energy is shown in Fig. 2. Isotopic fragmentation cross sections of $^{59}\text{Co}(^{12}\text{C},x)$ reactions measured at 3650 MeV/nucleon [20] are compared with the cross sections calculated using the old JQMD and JQMD-2.0. The cross sections calculated by JQMD-2.0 agree with experimental data within a factor of 2 except those of ^{24}Na and ^{59}Fe , on the other hand, JQMD generally underestimates cross sections and the deviation systematically increases with increase in product mass above $A=40$. In this region, the production cross section tends to increase with mass by one order of magnitude at maximum but the production cross section calculated using JQMD cannot follow this trend, similar to the cross section in Fig. 1. Fig. 2 (a) shows that fragmentation cross sections vary with isotopic identity by orders of magnitude; however, JQMD-2.0 can predict production cross sections accurately regardless of the absolute magnitude of cross sections as shown in Fig. 2 (b). Because soft neutron-proton exchange mechanism is necessary to simulate $^{59}\text{Co}(^{12}\text{C},x)^{59}\text{Fe}$ reactions, the improvement of JQMD-2.0 is not effective. On the other hand, the improvement is effective for production of fragments with mass number close to that of the target (e.g., $^{59}\text{Co}(^{12}\text{C},x)^{58}\text{Co}$).

By taking advantage of JQMD-2.0, accuracy of β^+ -emitter production calculation, which is useful for dose monitoring in heavy-ion radiotherapy, can be improved. Fig. 3 shows depth profiles of ^{11}C and ^{10}C measured in a thick PMMA (Poly Methyl MethAcrylate) target irradiated with 266

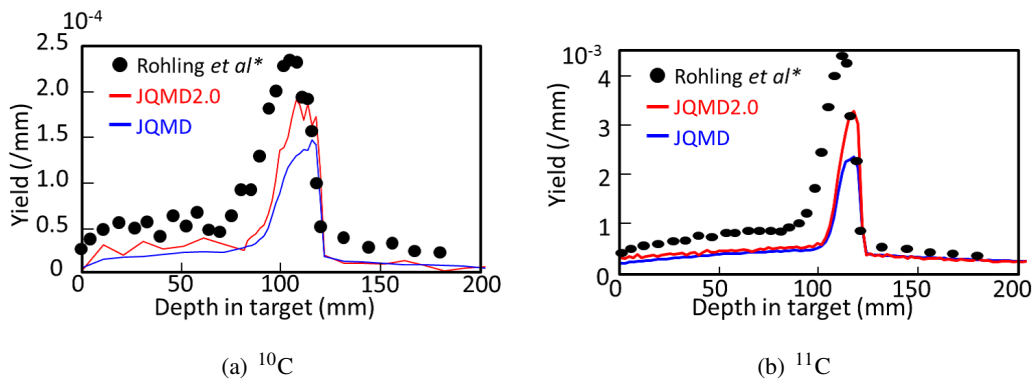


Fig. 3: Depth profile of ^{10}C and ^{11}C produced in a thick PMMA target bombarded by 266 MeV/nucleon ^{12}C ion beam.

MeV/nucleon ^{12}C ions [21]. ^{11}C and ^{10}C are produced dominantly by fragmentation of ^{12}C in PMMA induced by projectiles. Production is still underestimated by JQMD-2.0; however, production is increased by the upgrade of JQMD, which indicates that precise treatment of peripheral collisions is an important factor of this calculation. Although some portion of ^{11}C production is attributed to secondary neutrons, protons, and alphas, fragment yield near the projectile range is accumulation of projectile fragments produced along the paths and they are underestimated. This means that production of primary ion fragment is still underestimated. In contrast, the fragments along the projectile path (between the target surface and 90 mm of depth) are target fragments produced at higher energies. The underestimation of fragment yields in this region indicates that further improvements effective for high energy reactions are still necessary.

4. Conclusion

JAERI quantum molecular dynamics model was improved to accurately reproduce fragment production. Production of target-like fragments, which are generally attributed to peripheral collisions is predicted by JQMD-2.0 at higher accuracy compared to JQMD. Increase in fragmentation cross sections with increase in product mass near the target mass is well reproduced by JQMD-2.0 in the relativistic energy range. This improvement is beneficial for the applications such as dosimetry in heavy ion cancer therapy and remanent dose prediction in accelerator facilities.

Because the CPU time spent per reaction event was almost doubled by this improvement, the algorithm should be optimized in future upgrade. JQMD-2.0 has been incorporated to PHITS Ver. 2.76 and later.

References

- [1] T. Goorley *et al.* Initial MCNP6 release overview. *Nuclear Technology*, **180**(3):298–315, 2012.
- [2] A Ferrari, Paola R Sala, A Fasso, and Johannes Ranft. *FLUKA: A multi-particle transport code (program version 2005)*. CERN, Geneva, 2005.
- [3] S. Roesler, R. Engel, and J. Ranft. In *Adv. Monte Carlo for Radiation Physics, Particle Transport Simulation and Applications*, pages 1033–1038. Springer, Berlin Heidelberg, 2001.
- [4] J. Aichelin and H. Stoecker. *Physics Letters B*, **176**(1-2):14 – 19, 1986.
- [5] H. Sorge. *Phys. Rev. C*, **52**:3291–3314, Dec 1995.

- [6] T. Koi. *Proc. Joint Int. Conf. on Supercomputing in Nuclear Applications and Monte Carlo 2010 (SNA + MC2010)*, **734**(0):536 – 540, 2010.
- [7] K. Niita. *Phys. Rev. C*, **52**:2620–2635, Nov 1995.
- [8] S. Furihata. *NIM B*, **171**(3):251 – 258, 2000.
- [9] H. Yashima *et al.* *NIM B*, **226**(3):243 – 263, 2004.
- [10] L. Sihver *et al.* *Acta Astronautica*, **63**(7-10):865 – 877, 2008.
- [11] Davide Mancusi *et al.* *NIM B*, **254**(1):30 – 38, 2007.
- [12] D. Satoh *et al.* *J. Korean Phys. Soc.*, **59**:1741–1744, Aug 2011.
- [13] Y. Imahayashi *et al.* *JAEA-Conf*, 2014-002:133–138, 2014.
- [14] D. Satoh *et al.* *NIM A* **583**(2-3):507 – 515, 2007.
- [15] Davide Mancusi, Koji Niita, Tomoyuki Maruyama, and Lembit Sihver. *Phys. Rev. C*, **79**:014614, Jan 2009.
- [16] J. Cugnon, T. Mizutani, and J. Vandermeulen. *Nuclear Physics A*, **352**(3):505 – 534, 1981.
- [17] J. Cugnon. *Phys. Rev. C*, **22**:1885–1896, Nov 1980.
- [18] T. Ogawa *et al.* *Phys. Rev. C*, *et al.*:024614, Aug 2015.
- [19] W. R. Webber, J. C. Kish, and D. A. Schrier. *Phys. Rev. C*, **41**:547–565, Feb 1990.
- [20] P. Kozma, B. Tumendemberel, and D. Chultem. *Czech. J. Phys.*, **40**:29, Feb 1990.
- [21] Heide Rohling, Lembit Sihver, Marlen Priegnitz, Wolfgang Enghardt, and Fine Fiedler. *Phys. Med. Biol.*, **58**(18):6355, 2013.

Comparison of a deterministic reaction model with an INC model for the production of nucleon in nucleon induced reaction on light nuclei

H. Duarte

CEA, DAM, DIF, F-91297, Arpajon Cedex, France

Abstract

Among many reaction models, the intranuclear cascade (INC) calculates particle production in continuum and other physical quantities for nucleon induced reaction on target nuclei. Since it is based on Monte-Carlo method, the time of computation of the INC model is rather large to get reasonable statistical error on double differential cross sections of outgoing particles in continuum for reaction on very light target nuclei. We propose a deterministic approach to calculate double differential cross sections much faster than INC model does. We present some preliminary results and compare them with the results of our INC code.

1. Introduction

The intranuclear cascade (INC) model is well designed to compute the production of particles in phase-space in nucleon induced reaction on nuclei. It simulates nucleon-nucleon and other hadron-hadron collisions in nuclear medium with a classical approach where some quantum effects or at least nuclear medium effects are included.

In INC model the criterium on nucleon-nucleon collision is based on the calculation of the mean free path of moving nucleons in nuclear matter. The mean free path is derived from the NN cross sections evaluated at the center-of-mass energy of the NN pair and from the local matter density of the target nucleus.

In our INC approach (BRIC code) [1][2] each nucleon is described by its time-dependent position in space and its time-dependent energy-momentum. The first collision of the incident nucleon is determined by the distance of minimum approach between its trajectory and the position of the target nucleons of the nucleus. and defines the mean free path of the incident nucleon in the target nucleus. For heavy target nuclei, the probability of occurrence of the first collision, the collision of the incident nucleon with one nucleon of the target nucleus, is high except at high impact parameter. Indeed at high impact parameter the incident nucleon crosses the surface of the nucleus where the density of target nucleon is very low. For medium and heavy nuclei this problem of low density of target nucleon at the surface is reduced by the integration of the impact parameter of the incident nucleon which covers also the high density core of the nucleus. However it remains for very light nuclei: the probability of the first collision is rather low for very light target nuclei, and the latter appear to be mostly transparent to the incident nucleon. This last point is not convenient to calculate double differential cross sections of outgoing nucleons for very light target nuclei since a large part of the calculations is useless.

2. Description of the deterministic approach

We were interested to get a more efficient way to compute those double differential cross sections of outgoing nucleons in the continuum in reaction induced by nucleons on very light nuclei.

In the following we assume that the very light nuclei can be viewed as a dilute system of A nucleons inside a potential well and that the double differential cross section of outgoing nucleons is the incoherent sum of all contributions from single collisions that can occur between the incident

nucleon and one of the nucleons of the light target nucleus. Then the total double differential cross section for the selected type τ_{out} of outgoing nucleon is

$$\left(\frac{d^2\sigma}{dE d\Omega}\right)_{lab}^{(\tau_{out})} = \sum_i^{A_{targ}+1} \delta(\tau_i - \tau_{out}) \left(\frac{d^2\sigma^{(in-med)}}{dE_i d\Omega_i}\right)_{lab}.$$

The incident nucleon, the hit nucleon of the target have the index p (proj) and t_j (target j) before the collision, respectively, and they have the index i and $i+1$ after the collision: $N_p + N_{t_j} \rightarrow N_i + N_{i+1}$. The double differential cross section of nucleon i in the continuum is $(d^2\sigma^{(in-med)}/dE_i d\Omega_i)_{lab}$ in the laboratory frame, where $(in-med)$ means that the energy-momentum of nucleons i and $i+1$ take into account in-medium effects such as the Pauli exclusion principle.

The incident nucleon N_p has the momentum-energy (\mathbf{P}_p, E_p) of a plane wave. The nucleon N_{t_j} of the target nucleus is described by a harmonic oscillator wave function $\Phi_{n,l}(r_{t_j})$ in the fermi gas approximation: $0 < P_{t_j} < P_F(r_{t_j})$ where $P_F(r_{t_j})$ is the local Fermi momentum in the potential well of the nucleus $V_{neut/prot}(r_{t_j}) = V_\tau(r_{t_j})$. The wave functions $\Phi_{n,l}(r_{t_j})$ of the target nucleons are such that they give realistic matter density $\rho(r)$.

The total in-medium double-differential cross section in the laboratory frame of nucleon i after $N_p N_{t_j}$ collision comes from the integration on the distribution of position \mathbf{r}_{t_j} and on the distribution of momentum \mathbf{P}_{t_j} of the target nucleon:

$$\left(\frac{d^2\sigma^{(in-med)}}{dE_i d\Omega_i}\right)_{lab} = \mathcal{N} \int_0^\infty dr_{t_j} r_{t_j}^2 \Phi_{n,l}^2(r_{t_j}) \int_0^{P_F(r_{t_j})} dp_{t_j} p_{t_j}^2 \int_{\Omega_{p_{t_j}}} d\Omega_{p_{t_j}} \mathcal{P}_{Block}(i, i+1) \mathcal{J}_{cm \rightarrow lab} \frac{d\sigma}{d\Omega_{cm}}.$$

where the normalisation \mathcal{N} equals to 1 when the distribution $(\frac{d^2\sigma}{dE_i d\Omega_i})_{lab}$ (without Pauli blocking) is integrated over the energy and the angle of the outgoing nucleon i . In this expression $\frac{d\sigma}{d\Omega_{cm}}$ is the differential center-of-mass NN cross section, $\mathcal{P}_{Block}(i, i+1)$ is the Pauli blocking applied to the two nucleons i and $i+1$ after collision, and $\mathcal{J}_{cm \rightarrow lab} = \frac{(\partial E \partial \Omega)_{cm}}{(\partial E \partial \Omega)_{lab}}$ is the jacobian that transforms the derivative in the center-of-mass system $\partial E_{cm} \partial \Omega_{cm}$ into the derivative in the laboratory system $\partial E_{lab} \partial \Omega_{lab}$.

For the differential center-of-mass NN cross section $\frac{d\sigma}{d\Omega_{cm}}$, we use the parametrisation fitted on experimental data and included in our INC code BRIC [1]. The Pauli blocking is given by

$$\mathcal{P}_{Block}(i, i+1) = [1 - Heav(P_i - P_F(r_i))][1 - Heav(P_{i+1} - P_F(r_{i+1}))]$$

where $Heav$ is the Heaviside function, and the local Fermi momentum of nucleon i , $P_F(r_i)$, is derived from $e_F(r_i) = -V_{\tau_i}(r_i) - |e_{bind \tau_i}|$, with $e_{bind \tau_i}$ the binding energy of nucleon of type τ_i .

The jacobian $\mathcal{J}_{cm \rightarrow lab}$ depends on $\beta_{p_{t_j}} = \frac{\mathbf{P}_p + \mathbf{P}_{t_j}}{E_p + E_{t_j}}$. In the general case, $\beta_{p_{t_j}}$ is not along the momentum of the incident nucleon \mathbf{P}_p and the calculation of jacobian can not be done easily by analytical derivation apart for the case $P_{t_j} = 0$. We use a Monte-Carlo integration to calculate the jacobian. The Monte-Carlo method suppress the "double-value" problem that occurs when the velocity of the center-of-mass system is greater than the velocity of particles in the center-of-mass system and which gives two different kinetic energies in laboratory frame for one emission angle θ_{lab}). We also use a Monte-Carlo integration of the jacobian in order to compare directly the results of this deterministic method with the results of our BRIC code.

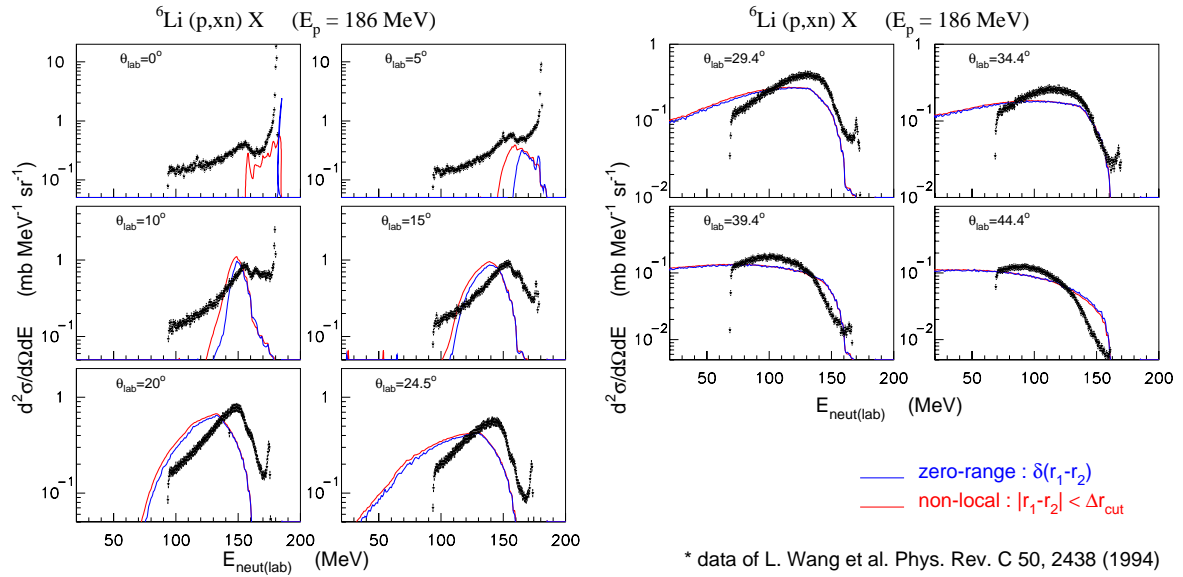


Fig. 1: Double differential cross sections of neutron production in $p + {}^6\text{Li}$ reaction at 186 MeV in the laboratory frame. The blue and red histograms are the results of the calculation with the zero-range approximation and the non-local interaction, respectively. The black symbols are the data of L. Wang *et al.* [3].

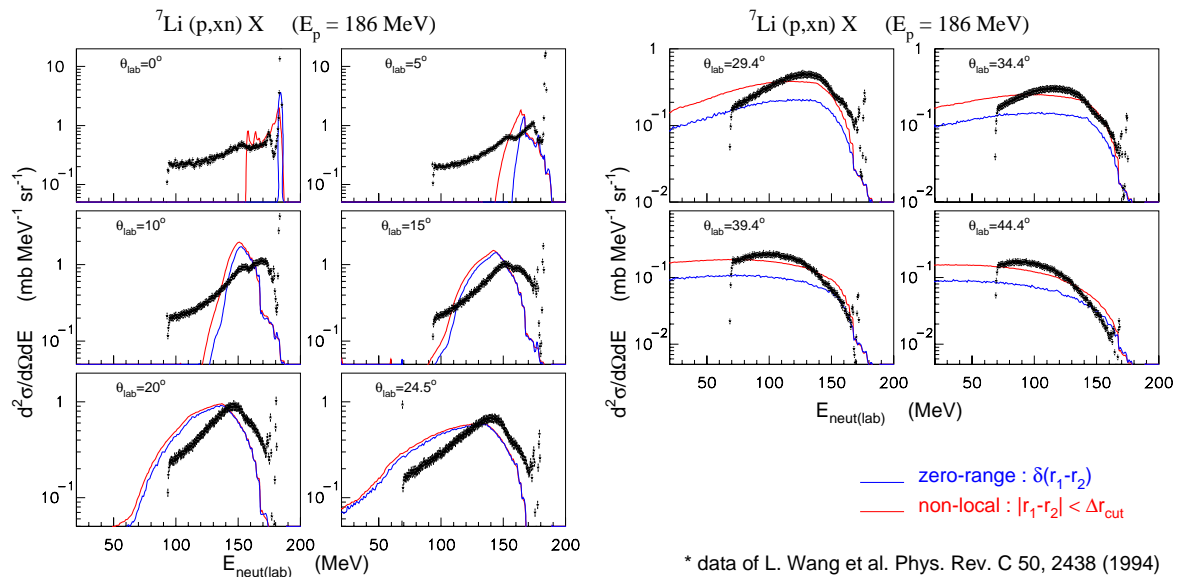


Fig. 2: Double differential cross sections of neutron production in $p + {}^7\text{Li}$ reaction at 186 MeV in the laboratory frame. The blue and red histograms are the results of the calculation with the zero-range approximation and the non-local interaction, respectively. The black symbols are the data of L. Wang *et al.* [3].

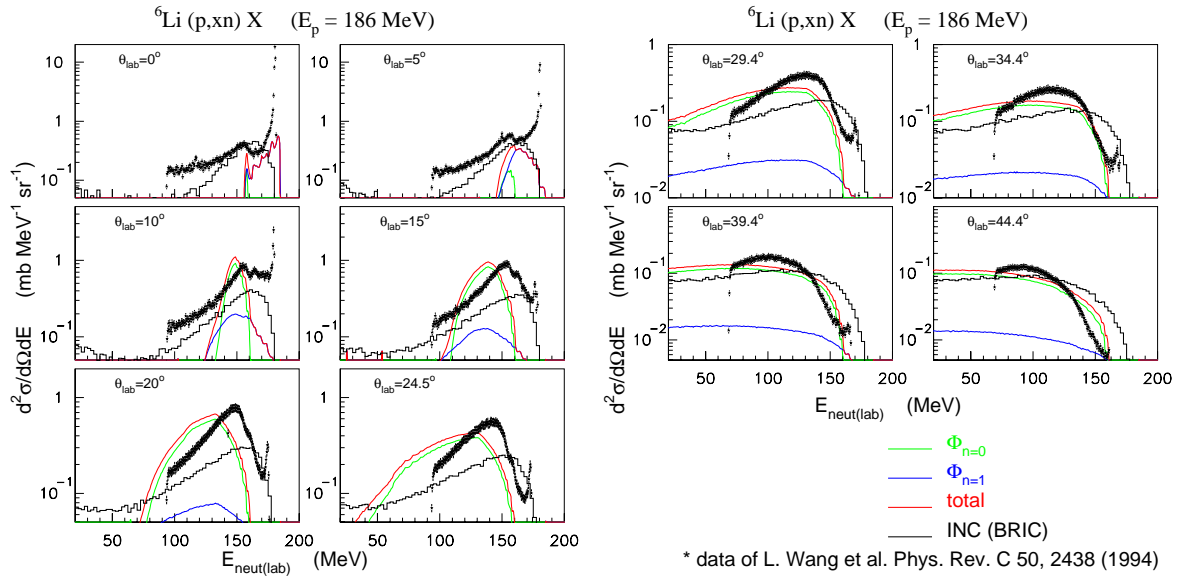


Fig. 3: Same as figure 1. The green and blue histograms are the contributions of the two levels $n = 0$ and $n = 1$ of target nucleons in ${}^6\text{Li}$, respectively. The red histograms is the sum of the two contributions. The black histograms are the results of the calculation of BRIC. The black symbols are the data of L. Wang *et al.* [3].

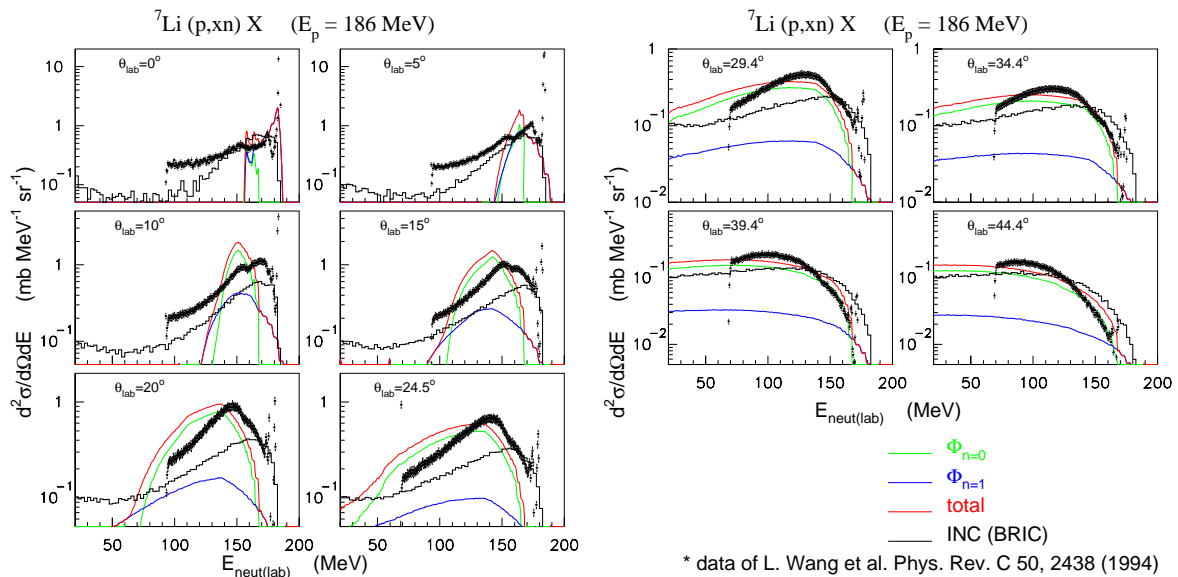


Fig. 4: Same as figure 2. The green and blue histograms are the contributions of the two levels $n = 0$ and $n = 1$ of target nucleons in ${}^7\text{Li}$, respectively. The red histograms is the sum of the two contributions. The black histograms are the results of the calculation of BRIC. The black symbols are the data of L. Wang *et al.* [3].

3. Results

In order to compare the results of this deterministic approach with those of our INC model, we have investigated two types of interactions: a zero-range approximation given by $\delta(\mathbf{r}_p - \mathbf{r}_{t_j})$;

$$\int_0^\infty dr_{t_j} r_{t_j}^2 \Phi_{n,l}^2(r_{t_j}) \int_0^{P_F(r_{t_j})} dp_{t_j} p_{t_j}^2 \int_{\Omega_{p_{t_j}}} d\Omega_{p_{t_j}},$$

and a non-local interaction $|\mathbf{r}_p - \mathbf{r}_{t_j}| < r_{p_{t_j}}^{(cut)} = \sqrt{\sigma_{p_{t_j}}(\mathbf{P}_p, \mathbf{P}_{t_j})/\pi}$

$$\int_0^\infty dr_{t_j} r_{t_j}^2 \Phi_{n,l}^2(r_{t_j}) \int_0^{P_F(r_{t_j})} dp_{t_j} p_{t_j}^2 \int_{\Omega_{p_{t_j}}} d\Omega_{p_{t_j}} \int_0^{r_{p_{t_j}}^{(cut)}} \int_{\Omega_{p_{t_j}}} d^3 r_{p_{t_j}}.$$

Indeed the collision criterium in our INC model is based on the distance of minimum approach between the trajectory of the incident nucleon and the position of the target nucleon and it corresponds to a non-local interaction.

In figures 1 and 2 we present the results of the calculation of double differential cross sections of neutron production for the reaction of proton on ${}^6\text{Li}$ and on ${}^7\text{Li}$ at 186 MeV, and compare them with the experimental data of [3]. In the two figures we present the results with the zero-range approximation (blue histograms) and with the non-local interaction (red histograms). The peak of the distribution at 0° is very sharp for the calculation with the zero-range approximation due to the local Pauli blocking, while the double differential cross section is more spread at very forward angles for the non-local calculation. This indicates that an INC model with a non-local interaction should give better results at very forward angles than an INC model with a zero-range interaction.

In figures 3 and 4 we show the results of the calculation of the same double differential cross sections of neutron production for the non-local interaction, and the contribution from the 2 shells we used in the calculation $\Phi_{0,0}$ (green histograms) and $\Phi_{1,l}$ (blue histograms). We also compare these preliminary results (red histograms) to the results of our INC code BRIC (black histograms). Our preliminary results indicate that a large part of the production at intermediate angles, between 10° and 45° , comes from the single interactions of the incident nucleon and that the density distribution of the target nucleons plays a significant role. Indeed it is the main difference between our deterministic approach and our INC code, the other ingredients (differential center-of-mass NN cross section $\frac{d\sigma}{d\Omega_{cm}}$, Pauli blocking and momentum distribution of target nucleons) are globally the same in BRIC and in the deterministic approach. Apart the very forward angles where double interaction have to be taken into account as INC does implicitly, the results are in better agreement with data on average for the deterministic model than for our BRIC model. The deterministic model is all the more powerful that it is much faster than our INC code to calculate nucleon production. A calculation needs several minutes with the deterministic approach compared to several hours for the BRIC code on one CPU to get better statistical results (bin width in energy and angle are 1 MeV and 1° compared to 2.5 MeV and 3° for INC calculation).

In one hand the second and higher-order are missing in the deterministic approach while they are implicitly included in INC calculation; on the other hand, the optimization of parameters can be done easier, for instance the energy levels of inner nucleons of target nucleus $E_{n=0,1}$, or the range of interaction $r_{p_{t_j}}^{(cut)}$. We hope then that we can test more efficiently some parameters of the deterministic approach in order to report them into our INC model.

4. Conclusions

The preliminary results of the deterministic method described in this paper are encouraging when we compare the results and the times of computation of this method and of our INC code BRIC for the nuclear reactions on light nuclei. This method allows to get the results of double differential cross sections faster than the INC model can provide since it does not need a mean free path calculation but uses directly the nucleon-nucleon cross section in nuclear medium for nucleon induced reaction on a dilute system. The calculation of $\frac{d^2\sigma}{dE d\Omega}$, $\frac{\sigma}{dE}$ and $\frac{\sigma}{d\Omega}$ are currently available for 2 type of outgoing particles (proton and neutron), and 2-particles correlations $\frac{d^3\sigma}{dE d\Omega_i d\Omega_k}$ can be obtained.

The extension to higher incident energy will require pion and resonance degree of freedom but we expect that it should be more or less straight forward as long as the reaction is on light nuclei (1st order approximation).

References

- [1] H. Duarte, Phys. Rev. C 75, 024611 (2007).
- [2] H. Duarte, "The nonelastic reaction code BRIEFF and its intranuclear cascade BRIC", in Proceedings of the International Conference on Nuclear Data for Science and Technology, April 22-27, 2007, Nice, France, ed. O.Bersillon, F.Gunsing, E.Bauge, R.Jacqmin, and S.Leray, EDP Sciences, 2008, pp 1117-1120.
- [3] L. Wang *et al*, Phys. Rev. C 50, 2438 (1994).

Nuclear reactions in the context of LHC operation

N. Shetty, F. Cerutti, A. Ferrari, A. Lechner, E. Skordis and V. Vlachoudis

CERN, Geneva, Switzerland

Abstract

Beam losses in accelerator elements of the LHC may pose a limit for machine performance or can give rise to long-term damage of equipment. In this paper, we present a selection of beam-machine interaction simulations with FLUKA, considering different sources of beam losses like collisions in the interaction regions or halo collimation. Relevant nuclear reactions, as well as atomic displacement mechanisms that lead to long-term radiation damage, are briefly reviewed. The impact on the machine is illustrated by means of a few examples, like the radiation damage induced in collimators and magnets or the risk of magnet quenches due to secondary ions emerging from lead-lead collisions.

1. Introduction

The Large Hadron Collider (LHC) [1] has a circumference of about 27 km. A chain of accelerators, as shown in 1, delivers beams of 450 GeV into the LHC. At top energy (7 TeV) and nominal beam intensities (2808 bunches with a bunch intensity of 1.15×10^{11} protons), each of the two counter-rotating LHC beams carries an energy of 362 MJ. Owing to this unprecedented stored energy, it is important to analyse the consequences of beam losses considering that already a small fraction of the energy can provoke a magnet quench if being released in the coils of one of the thousands of superconducting magnets. Besides posing a risk for quenches, beam losses can also affect the accelerator performance

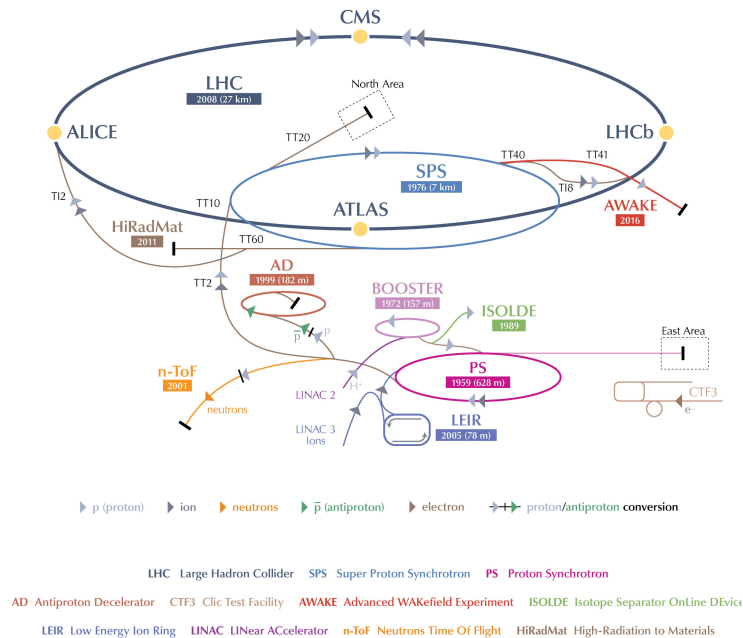


Fig. 1: CERN's accelerator complex.

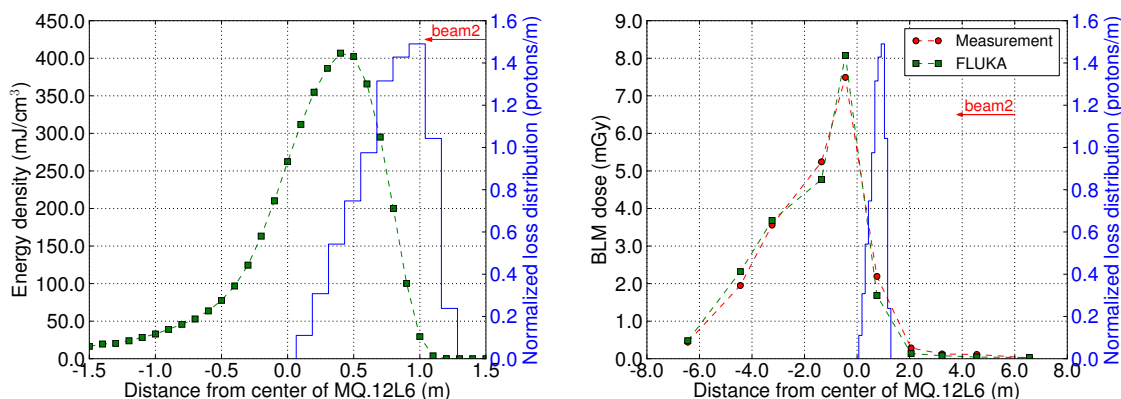


Fig. 2: Simulated peak energy density in quadrupole coils (left), as well as simulated and measured BLM dose (right), for a controlled beam loss experiment with 4 TeV proton beams in the LHC. The beam direction is from the right to the left. The blue histograms illustrate the longitudinal proton impact distribution on the magnet beam screen derived with MAD-X [2, 3].

and equipment in other ways, for example they give rise to long-term radiation damage and ageing of magnets and other components. In order to estimate the consequences of beam losses and to derive relevant quantities such as dose, fluences or displacement damage, a detailed description of hadronic and electromagnetic particle showers is required. This in turn requires adequate nuclear reaction models, which allow to predict the production of secondary particles. Monte Carlo codes like FLUKA [4, 5], embedding such models, represent a powerful tool for simulating cascades initiated by high-energy particles in accelerators. FLUKA is regularly used at CERN to study particle-matter interactions in the LHC environment, for example to analyse the energy deposition in magnets, to estimate the radiation to electronics, or to design new equipment for accelerator upgrades. This article illustrates typical beam-machine interaction calculations by means of a few examples.

2. Magnet quench tests

Magnet quenches adversely affect the machine availability as a significant amount of time is lost in recovering from a quench. In order to detect beam losses which can potentially quench a magnet or even induce damage, more than 3000 Beam Loss Monitors (BLMs) are placed around the LHC rings. The monitors are ionization chambers filled with pressurized Nitrogen gas, which record the dose deposition by secondary showers initiated by beam particles interacting with accelerator equipment. Most of these ionization chambers are mounted on cryostats hosting the superconducting magnets. If the dose measured by BLMs exceeds a predefined abort threshold, the beams are extracted onto the beam dump block. In order to define adequate abort thresholds, one requires a good knowledge of magnet quench levels, i.e. of the minimum amount of energy deposition required to provoke the transition from superconducting to normal-conducting state.

In 2013, a test campaign was carried out to probe the quench level of magnets for different time regimes and loss scenarios [2]. In one of the tests, 4 TeV protons were deliberately disposed on the aperture of a quadrupole (MQ) located in the LHC arcs. The magnet quenched when some 10^8 protons were lost within a few milliseconds. The superconducting coils of LHC magnets are separated from the beam vacuum by a mm thick stainless steel vacuum chamber, which further accommodates a mm thick beam screen for absorbing the beam-generated heat load. When impacting on the beam screen,

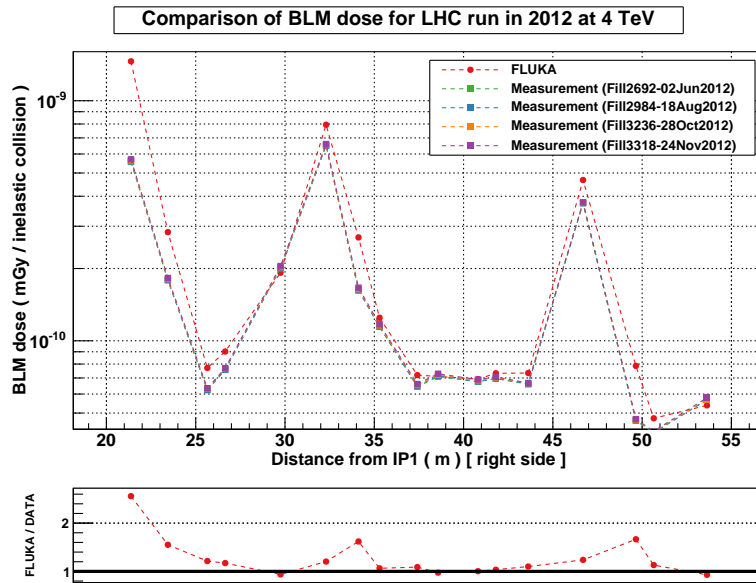


Fig. 3: Comparison of simulated and measured BLM dose due to proton-proton collision debris from the interaction point in ATLAS. The measurements were recorded during 4 TeV proton operation in 2012. All dose values are normalised per inelastic proton-proton collision. The lower panel illustrates the ratio of simulation and measurement.

protons typically have very grazing angles and hence they undergo an inelastic nuclear collision before reaching the coils. As the energy deposition inside magnets cannot be measured directly, FLUKA simulations were carried out for the above described test to estimate the energy density in the coils and to provide a correlation with BLM signals (see Fig. 2). The shower simulations were based on proton loss distributions derived with the MAD-X code (taken from Ref. [3]). As can be seen in Fig. 2, simulated and measured BLM signals generally agree better than 20%. The results further illustrate that, due to the shielding of showers in the magnet yoke, the energy density in the coils is more than one order of magnitude higher than at the location of BLMs.

3. Secondary particle production in the experiments

The LHC accommodates four experimental insertions where large-scale detectors (ATLAS, CMS, LHCb and ALICE) are installed. A fraction of secondary particles produced in the collision of LHC beams in the interaction points leaks from the experimental caverns to neighbouring accelerator regions, leading to a non-negligible power deposition in magnets. In the following subsections, we compare simulated and measured BLM signals induced by secondary particles from proton-proton and Pb-Pb collisions in the ATLAS and CMS experiments. Such comparative studies are important for understanding the complex radiation environment, but they also strengthen the confidence in the simulation model.

3.1 Proton-Proton Collisions

Fig. 3 presents a comparison of simulated and measured BLM signals induced by the debris from proton-proton collisions at a center-of-mass energy of 8 TeV in the ATLAS experiment. The BLMs shown in the figure are located along the inner triplet quadrupoles which are used to squeeze the beams at the interaction point. Measured signals were recorded during different physics fills in 2012. All signals are expressed per inelastic collision, assuming an inelastic cross section of 74.7 mb [6]. The

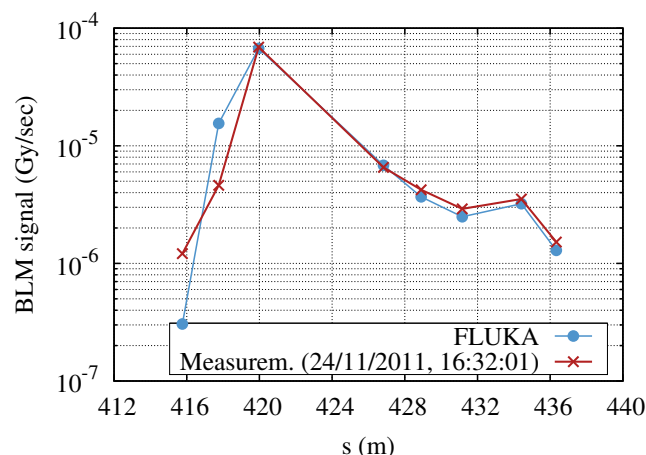
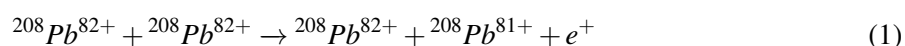


Fig. 4: Comparison of simulated and measured BLM signals due to secondary ions produced in bound-free pair production in the CMS experiment. The shower simulations were based on impact distributions derived in [7].

production of secondary particles in the interaction point was simulated using the DPMJET-III event generator [9, 8] (which has been interfaced to FLUKA), followed by FLUKA shower simulations in machine elements. The simulated signals generally agree well with the measured ones (better than 50%), with a few exceptions which are probably due to some approximations in the accelerator model used in the simulation setup.

3.2 Lead-Lead Collisions

During dedicated run periods, the LHC operates as a heavy ion collider ($^{208}\text{Pb}^{82+}$). Electromagnetic processes in ultra-peripheral Pb-Pb collisions give rise to secondary ion species, which are lost at certain locations inside the accelerator owing to their magnetic rigidity which differs from the beam rigidity [10, 11]. The process with the largest cross-section is bound-free pair production (BFPP), where one of the outgoing Pb ions is no longer fully stripped, but has a charge of 81+:



The secondary ions produced in BFPP remain inside the vacuum chamber for more than 400 m until they impact on the magnet aperture in the dispersion suppressor. Fig. 4 compares simulated and measured BLM signals due to BFPP ions from the collision point in the CMS experiment. The shower simulations were based on ion impact distributions derived in Ref. [7]. In general, simulation and measurement are found to be in good agreement, in particular downstream of the loss location.

4. Radiation damage in collimators

The LHC accommodates a multi-stage collimation system for cleaning the beam halo such that losses in superconducting magnets are reduced to acceptable values. It is estimated that about 10^{16} protons are lost in the collimation system for every $30 - 40 \text{ fb}^{-1}$ of integrated luminosity achieved in the experiments. Owing to the high radiation loads, long term radiation damage is a concern for the absorber materials of collimators and requires careful study. This applies in particular to the 60 cm long primary collimators (TCPs), made of carbon-reinforced carbon. The primary collimators represent a global aperture bottleneck and can be impacted by protons multiple times until the particles are subject to

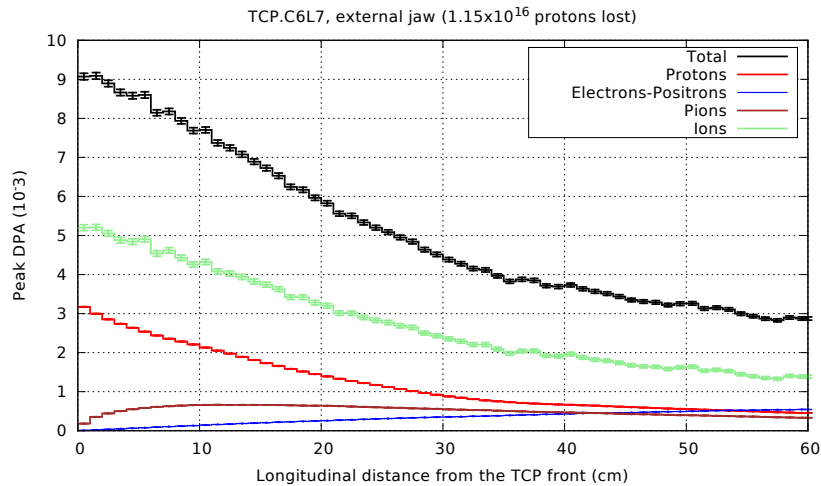


Fig. 5: Contribution to the total peak DPA of the different particle families. A damage threshold of 35 eV was assumed for the material of the collimator which is a carbon-carbon composite.

an inelastic collision or have large enough amplitudes to be intercepted in the downstream collimator hierarchy.

A useful quantity to measure long term radiation damage in non organic materials is Displacements Per Atom (DPA). DPA is related to the total number of defects (Frenkel pairs of interstitial and vacancies) generated in a material after irradiation, which could affect some macroscopic properties of the material (e.g. electrical resistivity). Displacement damage in collimators can be induced directly by primary protons but also indirectly by charged particles, neutrons or ions produced in hadronic cascades, as well as by particles produced in electromagnetic cascades. As most protons typically impact close to the collimator edge (some μm impact parameter), the induced damage is mainly concentrated within a superficial layer on the collimator surface, but steeply drops inside the bulk material. Figure 5 shows the simulated peak DPA, for 7 TeV protons, over the length of the most impacted jaw of the horizontal TCP along with the individual contribution of the different particle families. The maximum damage of about 9×10^{-3} DPA is observed at the beginning of the collimator dropping to 4×10^{-3} DPA by the end the longitudinal length. The peak observed at the start is in a surface layer of a few μm and can be mainly attributed to recoils produced in elastic encounters of primary protons.

5. Conclusion

In this paper, the importance of nuclear reaction modelling for high-energy accelerator applications has been highlighted by means typical beam-machine interaction calculations carried out at CERN. The shown examples demonstrate the capabilities of Monte Carlo codes like FLUKA for predicting relevant quantities related to complex radiation environments like at the LHC.

Acknowledgements

We would like to thank V. Chetvertkova for providing the proton loss distribution for the quench test, M. Schaumann for providing the ion loss distribution in the dispersion suppressor, and the CERN Collimation Team for providing input for the DPA simulations. The results presented in this paper make use of the software repositories maintained by the FLUKA team at CERN. Therefore we would like to acknowledge and thank all the involved people for their contributions.

References

- [1] O. S. Brüning, P. Collier *et al.* CERN, Geneva, 2004, <https://cds.cern.ch/record/782076>.
- [2] B. Auchmann *et al.*, *Phys. Rev. ST Accel. Beams* **18**, 061002 (2015).
- [3] V. Chetvertkova *et al.*, Proc. Workshop on Beam-Induced Quenches, CERN, 2014.
- [4] T. T. Bohlen *et al.*, *Nuclear Data Sheets* **120**, 211-214 (2014).
- [5] A. Ferrari, P. R. Sala, A. Fassò and J. Ranft, CERN-2005-10 (2005), INFN/TC_05/11, SLAC-R-773.
- [6] G. Antchev *et al.*, *Phys. Rev. Lett.* **111**, 012001 - Published 3 July 2013.
- [7] M. Schaumann, “*Heavy-ion performance of the LHC and future colliders*”, PhD-Thesis, RWTH Aachen, 2015.
- [8] S. Roesler, R. Engel and J. Ranft. *arXiv.org*, December 2000. hep-ph/0012252v1.
- [9] A. Fedynitch, R. Engel *these proceedings*, 2015
- [10] H. Meier, Z. Halabuka, K. Hencken, D. Trautmann, and G. Baur *Phys. Rev. A* **63**, 032713 (2001).
- [11] R. Bruce, D. Bocian, S. Gilardoni, J.M. Jowett, *Phys. Rev. ST Accel. Beams* **12**, 071002 (2009).

The new generation ISOL facility SPES at LNL

G. La Rana, on behalf of the SPES collaboration
Università di Napoli Federico II and INFN Napoli

Abstract

Angular distribution for the inelastic scattering of 28 MeV ${}^6\text{Li}$ on ${}^{76}\text{Ge}$ was measured using the São Paulo Pelletron-Enge-Spectrograph facility. The Coulomb-nuclear interference (CNI) analysis was applied to the first quadrupole state transition. The value of $C_2 = \delta_2^C / \delta_2^N$, the ratio of charge to isoscalar deformation lengths, and of δ_2^N were extracted through the comparison of experimental and DWBA-DOMP predicted cross sections. The ratio of reduced charge to isoscalar transition probabilities, $B(E2)$ to $B(IS2)$ respectively, is related to the square of the parameter C_2 and was thus obtained due to the advantage of scale uncertainty cancellation with a relative accuracy of less than 4%. The value of $C_2 = 1.101(20)$ obtained indicates a slight predominance of the protons relative to the neutrons in the transition for ${}^{76}\text{Ge}$. In this context the present result composed with previous results of CNI measurements obtained in ${}^{70,72,74}\text{Ge}$ suggests for ${}^{74}\text{Ge}$ a strong ground state configuration mixing.

1 Introduction

The characteristics of excited states 2_1^+ are widely used as indicators of nuclear structure, particularly the electric reduced transition probability $B(E2)$ is used as a measure of the collective characteristic of these transitions. The $B(E2)$ is in principle sensitive, if polarization effects may be disregarded, only to the contribution of the charge and to quantify the contributions of neutrons is also an important ingredient to characterize the collective behaviour. The Ge ($Z=32$) isotopic chain, in the transitional mass region around $A=70$, is particularly well suited to study the role of the neutrons. In fact, the evolution of $B(E2)$ values indicate around $N=40$ a transition and furthermore the nucleus ${}^{72}\text{Ge}$ presents a 0^+ first state, possible consequence of the correspondent subshell closure [1,2]. In this context it to be stressed that direct access to reduced isoscalar transition probability $B(IS2)$ is also required. Particularly suitable to reach this aim are inelastic scattering measurements of isoscalar interacting projectiles in an incident energy that enhance coulomb-nuclear interference (CNI). These measurements allow simultaneous extractions of $B(IS2)$ and the ratio between electric and isoscalar reduced transition probabilities $B(E2)/B(IS2)$ [3-5]. The values of $C_2 = \delta_2^C / \delta_2^N$, the ratio of charge to isoscalar deformation lengths, and of $(\delta_2^N)^2$ are extracted through the comparison of experimental and DWBA-DOMP predicted angular distributions. The ratio of reduced charge to isoscalar transition probabilities, $B(E2)$ to $B(IS2)$ respectively, are related to the square of the parameter C_2 and were thus obtained with the advantage of scale uncertainties cancellation. This paper refers to the CNI study of 28 MeV ${}^6\text{Li}$ inelastic scattering on ${}^{76}\text{Ge}$ recently measured using the São Paulo Pelletron-Enge-Spectrograph facility in comparison with the results of the previous work on ${}^{70,72,74}\text{Ge}$ [5]. The C_2 values obtained for ${}^{70,72}\text{Ge}$ are slightly higher than 1.0, indicating a homogeneous excitation with a small predominant contribution of protons in the transition to the first quadrupole state 2_1^+ . On the other hand an abrupt change with $C_2 = 0.775(8)$ was obtained for ${}^{74}\text{Ge}$.

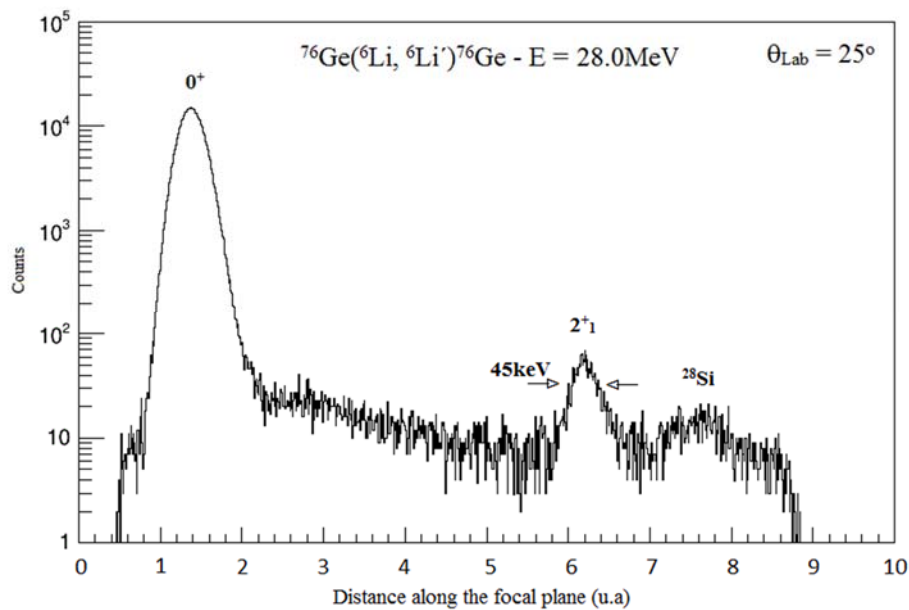


Fig. 1: Position spectrum at the scattering angles $\theta_{\text{Lab}} = 25^\circ$.

2 Experimental setup

Inelastic scattering of ${}^6\text{Li}$ on ${}^{76}\text{Ge}$ data were obtained using the Pelletron-Spectrograph-Magnet-Enge facility. A solid-state position sensitive detector (PSD) of $500\ \mu\text{m}$ thickness, area $47 \times 8\ \text{mm}^2$ was positioned on the focal plane. The ${}^6\text{Li}$ is the lightest isoscalar projectile appropriate for CNI measurements in the region around $A=70$, at bombarding energies suitable for stable operation of the São Paulo Pelletron accelerator. The 28.0 MeV energy ${}^6\text{Li}$ beam was focused after passing defining slits of $1.0 \times 2.0\ \text{mm}^2$ on an enriched self-supported target of ${}^{76}\text{Ge}$ with $510.5 \cdot 10^{15}\ \text{atoms/cm}^2$ thickness. An entrance solid angle of 0.65 msr was used, the emerging ions of the reaction admitted and momentum analysed by the field of the spectrograph were detected in the PSD. Twenty-six spectra were measured at carefully chosen scattering angles in a range of $10^\circ \leq \theta_{\text{Lab}} \leq 55^\circ$, in order to characterize CNI in the angular distribution corresponding to the first quadrupole excitation. Relative normalization of the data for the various scattering angles was obtained through the total charges collected by the Faraday cup. The absolute normalization was obtained from the target thickness and the solid angle values. The scale uncertainty was estimated to be around 20%.

The digital pulse processing (DPP) acquisition system used in the measurement was composed by the board PCI-6133 from National Instrument, setting 2.5 MS/s as the maximum rate sample of analogic inputs for the digitalization. The analysis of the pulse shape and the use of electronic noise filters provide an important resolution improvement. Figure 1 shows the position spectrum along the focal plane at the scattering angle $\theta_{\text{Lab}} = 25^\circ$. The three peaks observed on figure are associated with the elastic scattering, the inelastic scattering to the 2_1^+ state and the elastic scattering on silicon contaminant. The energy resolution achieved was about 45 keV.

3 Data analysis and Results

The distorted wave Born approximation (DWBA) prediction using the deformed optical potential model (DOMP) approach with global optical parameters was applied.

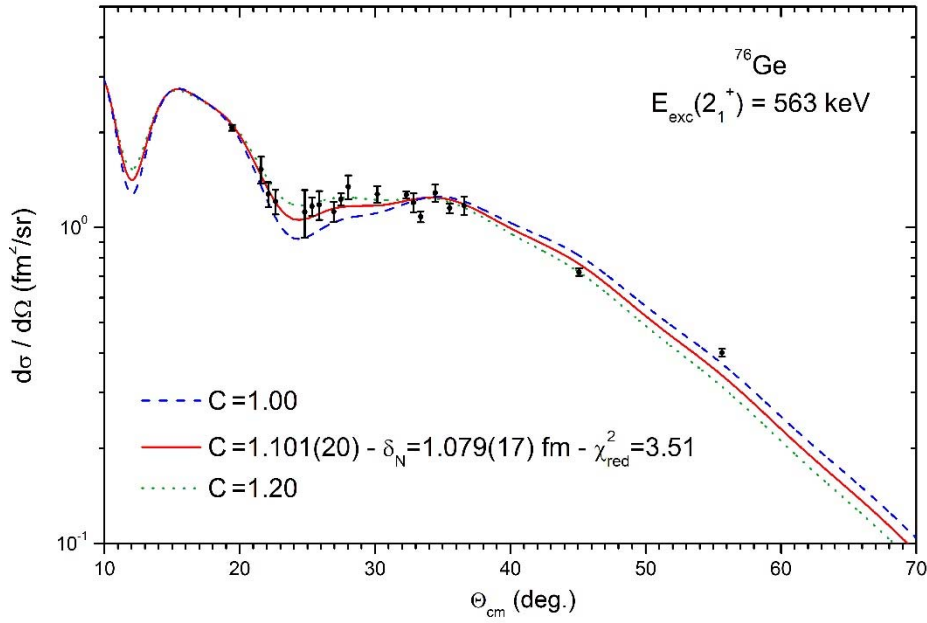


Fig. 1: Experimental angular distribution in comparison with DWBA-DOMP predictions.

The value of the ratio between charge (δ_2^C) and mass (δ_2^N) deformation lengths C_2 was obtained from the angular distribution shape. The square of mass deformation length, $(\delta_2^N)^2$, is also extracted, as a scale factor. The procedure applied for the χ^2 minimization was the iterative method of Gauss [6], extracting the correlated parameters δ_2^N and C_2 .

Figure 2 illustrates the results obtained in the fit from the experimental angular distribution of $^{76}\text{Ge}(^6\text{Li}, ^6\text{Li})^{76}\text{Ge}$ to the first quadrupole excited state in comparison with the DWBA-DOMP prediction. The error bars shown represent only the relative uncertainties. These ones are composed by the statistical uncertainties and the contribution from the background and contaminant subtraction. The prediction was calculated using the global optical model parameters of Cook [7] and considering the reduced Coulomb radius $r_C = 1.22$ fm (red curve). The results for the two correlated parameters in the data analysis are $C_2 = 1.101(20)$ and $\delta_2^N = 1.079(17)$ fm. In order to illustrate the sensibility of the method and that the experimental angular distribution does not admit a fit that could result in a C_2 value much smaller than one, as obtained for the neighbor ^{74}Ge [5], two predictions corresponding to $C_2 = 1.00$ (interrupted blue curve) and $C_2 = 1.20$ (dotted green curve) are also shown.

The C_2 value extracted is slightly higher than 1.0, indicating a homogeneous excitation with a slight predominant contribution of protons in the first quadrupole excited state 2_1^+ of ^{76}Ge . Due to the uncertainty scale cancellation, the experimental ratio $B(E2)/B(IS2)$ e^2 , proportional to the square of C_2 , was obtained with a relative accuracy of less than 4%.

The present CNI study composed with the results of the previous work [5], using the same technique, indicates that although the protons relative to the neutrons reveal a small predominant contribution in $^{70,72,76}\text{Ge}$ to the first quadrupole excitation, the neutron role is strongly enhanced in ^{74}Ge . In fact a C_2 abrupt change is shown comparing the ^{74}Ge value with those observed for neighbor isotopes $^{72,76}\text{Ge}$.

Discontinuities of some experimental indicators in even-A germanium chain from ^{70}Ge to ^{76}Ge were associated with shape transition or shape coexistence and described in the literature by a two-state coexistence model of some kind [8,9]. The investigation by means of large-scale shell model calculation

suggested that a rapid increase in the number of $g_{9/2}$ protons and neutrons could explain the structure change near $N=40$ [2], associated with the strong neutron-proton interaction. The basic idea of the two-state model is the existence of different configurations which may coexist and mix in different proportions to form the physical states observed. The experimental results obtained by Coulomb excitation and two neutron transfer measurements [10-13] indicate that the ground state configuration transition should occur between ^{72}Ge and ^{74}Ge . The analyses of the $L=0$ transfers in both (t,p) and (p,t) reactions, had shown transition strengths indicating similar nature between the ground states of ^{74}Ge and ^{76}Ge . On the other hand, the CNI results reveal a C_2 value strongly depressed in the first quadrupole excitation for ^{74}Ge , in comparison with the almost homogeneous excitation in ^{76}Ge . It is to be noted that the inelastic scattering, even if there is configuration mixing in the ground state, would excite only the configuration that connects the ground and the 2_1^+ states of each isotope which are rather pure [8,14]. In this context, the ^{74}Ge C_2 value suggests a strong ground state configuration mixing involving not only the neutron degree of freedom, but also probably other configurations. One possibility could be an alpha plus ^{70}Zn ($Z=30$, $N=40$) isomeric state configuration involving a subshell closure.

Acknowledgements

This work was partially supported by the Brazilian Agencies CNEN and FAPESP.

References

- [1] G. Gurdal et al., *Phys. Rev. C* **88** (2013) 014301.
- [2] M. Hasegawa et al., *Nucl. Phys. A* **789** (2007) 46.
- [3] G. M. Ukita et al., *Phys. Rev. C* **64** (2001) 014316.
- [4] J. L. M. Duarte et al., *Phys. Rev. C* **56** (1997) 1855.
- [5] M. D. L. Barbosa et al., *Phys. Rev. C* **71** (2005) 024303.
- [6] W. H. Press, B. P. Flannery, S. A. Teukolsky, and W. T. Vetterling, *Numerical Recipes* Cambridge, New York (1990).
- [7] J. Cook, *Nucl. Phys. A* **388** (1982) 153.
- [8] H. T. Fortune and M. Carchidi, *Phys. Rev. C* **36** (1987) 2584.
- [9] M. Carchidi et al., *Phys. Rev. C* **30** (1984) 1293.
- [10] R. Lecomte, M. Irshad, S. Landsberger, G. Kajrys, P. Paradis, S. Monaro, *Phys. Rev. C* **22** (1980) 2420.
- [11] R. Lecomte, G. Kajrys, S. Landsberger, P. Paradis, S. Monaro, *Phys. Rev. C* **25** (1982) 2812.
- [12] F. Guilbault et al., *Phys. Rev. C* **16** (1977) 1840.
- [13] A. C. Rester, J. B. Ball, R. L. Auble, *Nucl. Phys. A* **346** (1980) 371.
- [14] M. Sugarawa et al., *Eur. Phys. J. A* **16** (2003) 409.

Nuclear data measurements at the upgraded neutron time-of-flight facility n_TOF at CERN

F. Gunsing^{1,2}, O. Aberle¹, J. Andrzejewski³, L. Audouin⁴, V. Bécaries⁵, M. Bacak⁶, J. Balibrea-Correa⁵, M. Barbagallo⁷, S. Barros⁸, F. Bečvář⁹, C. Beinrucker¹⁰, F. Belloni², E. Berthoumieux², J. Billowes¹¹, D. Bosnar¹², M. Brugger¹, M. Caamaño¹³, F. Calviño¹⁴, M. Calviani¹, D. Cano-Ott⁵, R. Cardella¹, D. M. Castelluccio^{15,16}, F. Cerutti¹, Y. Chen⁴, E. Chiaveri¹, N. Colonna⁷, M. A. Cortés-Giraldo¹⁷, G. Cortés¹⁴, L. Cosentino¹⁸, L. Damone⁷, K. Deo¹⁹, M. Diakaki², C. Domingo-Pardo²⁰, R. Dressler²¹, E. Dupont², I. Durán¹³, B. Fernández-Domínguez¹³, A. Ferrari¹, P. Ferreira⁸, P. Finocchiaro¹⁸, R. J. W. Frost¹¹, V. Furman²², S. Ganesan¹⁹, A. Gawlik³, I. Gheorghe²³, T. Glodariu²³, I. F. Gonçalves⁸, E. González⁵, A. Goverdovski²⁴, E. Griesmayer⁶, C. Guerrero¹⁷, K. Göbel¹⁰, H. Harada²⁵, T. Heftrich¹⁰, S. Heinitz²¹, A. Hernández-Prieto^{1,14}, J. Heyse²⁶, G. Jenkins²⁷, E. Jericha⁶, F. Käppeler²⁸, Y. Kadi¹, T. Katabuchi²⁹, P. Kavargin⁶, V. Ketlerov²⁴, V. Khryachkov²⁴, A. Kimura²⁵, N. Kivel²¹, M. Kokkoris³⁰, M. Krtička⁹, E. Leal-Cidoncha¹³, C. Lederer^{31,10}, H. Leeb⁶, J. Lerendegui¹⁷, M. Licata^{16,32}, S. Lo Meo^{15,16}, R. Losito¹, D. Macina¹, J. Marganiec³, T. Martínez⁵, C. Massimi^{16,32}, P. Mastinu³³, M. Mastroianni⁷, F. Matteucci³⁴, E. A. Mauger²¹, E. Mendoza⁵, A. Mengoni¹⁵, P. M. Milazzo³⁴, F. Mingrone¹⁶, M. Mirea²³, S. Montesano¹, A. Musumarra¹⁸, R. Nolte³⁵, A. Oprea²³, F. R. Palomo Pinto¹⁷, C. Paradela¹³, N. Patronis³⁶, A. Pavlik³⁷, J. Perkowski³, J. I. Porras^{1,38}, J. Praena¹⁷, J. M. Quesada¹⁷, T. Rauscher^{39,40}, R. Reifarth¹⁰, A. Riego-Perez¹⁴, M. Robles¹³, C. Rubbia¹, J. A. Ryan¹¹, M. Sabaté-Gilarte^{1,17}, A. Saxena¹⁹, P. Schillebeeckx²⁶, S. Schmidt¹⁰, D. Schumann²¹, P. Sedyshev²², A. G. Smith¹¹, A. Stamatopoulos³⁰, S. V. Suryanarayana¹⁹, G. Tagliente⁷, J. L. Tain²⁰, A. Tarifeño-Saldivia²⁰, L. Tassan-Got⁴, A. Tsinganis³⁰, S. Valenta⁹, G. Vannini^{16,32}, V. Variale⁷, P. Vaz⁸, A. Ventura¹⁶, V. Vlachoudis¹, R. Vlastou³⁰, A. Wallner⁴¹, S. Warren¹¹, M. Weigand¹⁰, C. Weiss^{1,6}, C. Wolf⁴⁰, P. J. Woods³¹, T. Wright¹¹, P. Žugec^{12,1}
The n_TOF Collaboration

Abstract

Applications of nuclear data like neutron-induced reaction cross sections are related to research fields as stellar nucleosynthesis, the study of nuclear level densities and strength functions, and also play a key role in the safety and criticality assessment of existing and future nuclear reactors, in areas concerning radiation dosimetry, medical applications, transmutation of nuclear waste, accelerator-driven systems and fuel cycle investigations. The evaluations in nuclear data libraries are based both on experimental data and theoretical models. CERN's neutron time-of-flight facility n_TOF has produced a considerable amount of experimental data since it has become fully operational with the start of its scientific measurement programme in 2002. While for a long period a single measurement station (EAR1) located at 185 m from the neutron production target was available, the construction of a second beam line at 20 m (EAR2) in 2014 has substantially increased the measurement capabilities of the facility. An outline of the experimental nuclear data activities at CERN's neutron time-of-flight facility n_TOF will be presented.

1. Introduction

Nuclear data is a generic notion comprising the physical properties related to nuclear structure and nuclear reactions. Evaluated nuclear reaction data are intended to be complete and to contain all reactions and all energy regions, even where experimental data are missing, insufficient or inconsistent with other experimental data sets. A nuclear data evaluation is a complicated process resulting from a careful

analysis of available existing, sometimes inconsistent experimental data sets combined with optimum theoretical models describing experimental data and providing data for gaps in experimental information. The outcome of this process is a single recommended dataset, the evaluation. Both theoretical models and experimental data are the fundamental ingredients in evaluated data.

Nuclear data in general, and neutron-induced reactions in particular, are important for a number of research fields. They play a key role in the safety and criticality assessment of nuclear technology, not only for existing power reactors but also for medical applications [1], radiation dosimetry, the transmutation of nuclear waste, accelerator-driven systems, future reactor systems as in Generation IV, and the thorium-based nuclear fuel cycle [2, 3, 4]. Other applications of nuclear data are related to research fields as the study of nuclear level densities [5, 6] and stellar nucleosynthesis [7, 8, 9].

The nuclear data of nuclear reactions needed for such calculations are usually based on evaluated nuclear data libraries, like JEFF [10], ENDF [11], JENDL [12], CENDL, BROND and several others. Contributions to nuclear data come from a variety of experimental facilities, including the pulsed white neutron source n_TOF at CERN, which has been recently upgraded with a second beam line.

2. The neutron time-of-flight facility n_TOF at CERN

The neutron time-of-flight facility n_TOF was constructed after an idea proposed by Rubbia *et al.*[45] and has become fully operational with the start of the scientific measurement programme in May 2002. The facility is based on the 6 ns wide, 20 GeV/c pulsed proton beam from CERN's Proton Synchrotron (PS) with typically 7×10^{12} protons per pulse, impinging on a lead spallation target, yielding about 300 neutrons per incident proton. A layer of water around the spallation target moderates the initially fast neutrons down to a white spectrum of neutrons covering the full range between meV and GeV neutron energy. The minimal time between two proton pulses is a multiple of 1.2 s, related to the operation cycle of the PS. This allows to cover the neutron energy range down to subthermal energies without overlap of slow neutrons from previous cycles.

During phase-I when the first spallation target was used from 2001 up to 2004, the water coolant also served as the moderator. The spallation target was a block of lead of dimensions $80 \times 80 \times 60 \text{ cm}^3$. During phase-II, after the installation in 2008 of an upgraded cylindrical lead spallation target 60 cm in length and 40 cm in diameter, the target was enclosed with a separate cooling circuit resulting in a 1 cm water layer in the beam direction, followed by an exchangeable moderator with a thickness of 4 cm. Normal water has been used as a moderator, as well as water with a saturated ^{10}B -solution in order to reduce the number of 2.23 MeV gamma rays from hydrogen capture, which otherwise forms an important contribution to the background due to in-beam gamma rays. The ^{10}B -loaded moderator affects the energy distribution of the neutron flux only noticeably below 1 eV. The kinetic energy of the neutrons is determined by time-of-flight which, combined with the known flight distance, gives the neutron velocity.

A first neutron beam is collimated and guided through a vacuum neutron tube over a distance of approximately 185 m to an experimental area (EAR1) where samples can be mounted in the beam and neutron induced reactions can be studied. A more detailed description of the neutron source and EAR1 can be found in Ref. [46] and references therein.

A second neutron beam line and experimental area (EAR2), sketched in Fig. 1 has been constructed and is operational since 2014. This flight path is vertical and about 20 m long, viewing the top part of the spallation target. In this case the cooling water circuit acts as a moderator. Due to the about 10 times shorter flight length, a much higher neutron flux of about a factor 25 is available, as shown in Fig. 2. The about 10 times shorter flight path implies also in about 10 times shorter flight times,

Table 1: The measurements performed at n_TOF during phase-I from 2001-2004.

nucleus	reaction	detector	ref.	nucleus	reaction	detector	ref.
²⁴ Mg	(n,γ)	C ₆ D ₆	[13]	²³² Th	(n,γ)	C ₆ D ₆	[30, 31]
²⁶ Mg	(n,γ)	C ₆ D ₆	[13]	²³³ U	(n,γ)	TAC	
⁹⁰ Zr	(n,γ)	C ₆ D ₆	[14]	²³⁴ U	(n,γ)	TAC	
⁹¹ Zr	(n,γ)	C ₆ D ₆	[15]	²³⁷ Np	(n,γ)	TAC	[32]
⁹² Zr	(n,γ)	C ₆ D ₆	[16]	²⁴⁰ Pu	(n,γ)	TAC	
⁹⁴ Zr	(n,γ)	C ₆ D ₆	[17]	²⁴³ Am	(n,γ)	TAC	[33]
⁹⁶ Zr	(n,γ)	C ₆ D ₆	[18]	²³³ U	(n,f)	FIC	[34, 35]
¹²⁹ La	(n,γ)	C ₆ D ₆	[19]	²³⁴ U	(n,f)	FIC	[36]
¹⁵¹ Sm	(n,γ)	C ₆ D ₆	[20, 21, 22]	²³⁶ U	(n,f)	FIC	[37]
¹⁸⁶ Os	(n,γ)	C ₆ D ₆	[23, 24]	²⁴¹ Am	(n,f)	FIC	[38]
¹⁸⁷ Os	(n,γ)	C ₆ D ₆	[23, 24]	²⁴³ Am	(n,f)	FIC	[39]
¹⁸⁸ Os	(n,γ)	C ₆ D ₆	[23, 24]	²⁴⁵ Cm	(n,f)	FIC	[40]
²⁰⁴ Pb	(n,γ)	C ₆ D ₆	[25]	²³⁴ U	(n,f)	PPAC	[41, 42]
²⁰⁶ Pb	(n,γ)	C ₆ D ₆	[26, 27]	²³⁷ Np	(n,f)	PPAC	[41]
²⁰⁷ Pb	(n,γ)	C ₆ D ₆	[28]	²⁰⁹ Bi	(n,f)	PPAC	[43]
²⁰⁸ Pb	(n,γ)	C ₆ D ₆		^{nat} Pb	(n,f)	PPAC	[43]
²⁰⁹ Bi	(n,γ)	C ₆ D ₆	[29]	²³² Th	(n,f) ang.	PPAC	[44]

resulting in an additional factor 10 gain in the signal to noise ratio due to radioactivity. More details on EAR2 can be found in Refs. [47, 48].

2.1 Nuclear data measurements during phase-I (2001-2004)

During the first phase from 2001 to 2004 capture and fission data for a number of isotopes have been taken. Capture measurements with C₆D₆ liquid scintillator detectors concerned ^{24,25,26}Mg, ⁵⁶Fe, the stable isotopes ^{90,91,92,94,96}Zr and the radioactive one ⁹³Zr, as well as the nuclei ¹³⁹La, ¹⁵¹Sm, ^{186,187,188}Os, ¹⁹⁷Au, ^{204,206,207,208}Pb, ²⁰⁹Bi, and ²³²Th. A 4π calorimeter consisting of 40 BaF₂ crystals has been used for neutron capture measurements of ¹⁹⁷Au, ²³³U, ²³⁴U, and ²³⁷Np, ²⁴⁰Pu, and ²⁴³Am. Fission cross sections were measured with the FIC-0 fission detector containing the actinides ²³²Th, ²³⁴U, ²³⁵U, ²³⁶U, ²³⁸U, and ²³⁷Np. A similar detector, FIC-1, which was ISO-2919 compliant, was used to measure neutron-induced fission cross sections of the actinides ²³³U, ²³⁵U, ²³⁸U ²⁴¹Am, ²⁴³Am, and ²⁴⁵Cm. Fission detectors based on Parallel Plate Avalanche Counters (PPACs) were developed and used in measurements of the fission cross sections of ^{nat}Pb, ²⁰⁹Bi, ²³²Th, ²³⁷Np, ²³³U, ²³⁴U, ²³⁵U and ²³⁸U. A list of measured isotopes and reactions together with the final or most relevant publication is given in table 1.

2.2 Nuclear data measurements during phase-II (2009-2012)

During phase-II from 2009-2012 mostly capture measurements were performed. The (n,γ) reaction on the light nucleus ²⁵Mg was investigated, as well as on several enriched iron and nickel isotopes (⁵⁴Fe, ⁵⁶Fe, ⁵⁷Fe, ⁵⁸Ni, ⁶²Ni, ⁶³Ni), and on the stable ⁹²Zr and radioactive ⁹³Zr. Capture reactions on the actinides ²³⁶U, ²³⁸U and ²⁴¹Am were performed, for the latter two with two different capture detector systems: C₆D₆ scintillators using the total energy method, and the TAC, the BaF₂ scintillator array using the total absorption method. The TAC was also used in combination with a MicroMegas detector in a first attempt to measure the ²³⁵U(n,γ) reaction using a veto on the ²³⁵U(n,f) reaction.

Table 2: The measurements performed at n_TOF during phase-II from 2009-2012.

nucleus	reaction	detector	ref.	nucleus	reaction	detector	ref.
³³ S	(n,α)	MGAS		⁹³ Zr	(n,γ)	C ₆ D ₆	[56]
⁵⁹ Ni	(n,α)	CVD	[49]	¹⁹⁷ Au	(n,γ)	C ₆ D ₆ /TAC	[57, 58]
²⁵ Mg	(n,γ)	C ₆ D ₆	[50]	²³⁵ U	(n,γ)/(n,f)	TAC/MGAS	[59]
⁵⁴ Fe	(n,γ)	C ₆ D ₆	[51]	²³⁶ U	(n,γ)	C ₆ D ₆	[60]
⁵⁶ Fe	(n,γ)	C ₆ D ₆		²³⁸ U	(n,γ)	C ₆ D ₆	[61]
⁵⁷ Fe	(n,γ)	C ₆ D ₆	[51]	²³⁸ U	(n,γ)	TAC	[62]
⁵⁸ Ni	(n,γ)	C ₆ D ₆	[52]	²⁴¹ Am	(n,γ)	C ₆ D ₆	[63]
⁶² Ni	(n,γ)	C ₆ D ₆	[53]	²⁴¹ Am	(n,γ)	TAC	[64]
⁶³ Ni	(n,γ)	C ₆ D ₆	[54]	²⁴² Pu	(n,f)	MGAS	[65]
⁸⁷ Sr	(n,γ) spin	TAC	[55]	¹² C	(n,p) activ.	C ₆ D ₆	[66, 67]
⁹² Zr	(n,γ)	C ₆ D ₆					

In addition to these measurements several other techniques have been tested at this facility. An experiment aiming at resonance spin assignments was performed on a ⁸⁷Sr sample. A first test measurement with a MicroMegas detector was done to perform a fission measurement on ²⁴⁰Pu and ²⁴²Pu. The results on ²⁴⁰Pu(n,f) were not conclusive due to the high radioactivity of this nucleus, degrading the detector over time. This measurement was repeated in 2014 in the new EAR2, where the flux is much higher, allowing to collect enough statistics in only a few weeks of measurement time. Another reaction that was investigated was the ³³S(n,α) reaction with a MicroMegas detector. Also this measurement was repeated later in EAR2 in 2015 to take advantage of the higher flux. A CVD diamond detector was used to measure the ⁵⁹Ni(n,α) cross section. Finally the ¹²C(n,p)¹²B reaction was exploited by in-beam activation [67]. A list of the phase-II measurements and their references are given in table 2.

2.3 Nuclear data measurements during phase-III (from 2014)

During the long planned shutdown of CERN's accelerator complex from the end of 2012 to mid 2014, the construction of n_TOF's new second beam line and experimental area EAR2 [68] was performed and delivered by July 2014. The design was based on extensive Monte Carlo simulations with FLUKA [48] in order to optimize the beam line and collimation for a high neutron flux together with a minimized background. An impression of the EAR2 is shown in fig. 1. In order to remove charged particles from the beam, a permanent 0.25 T magnet had to be installed since unlike the beamline for EAR1, there was no room for an electromagnet. Since then, the facility has been taking data in both the experimental area EAR1 (185 m horizontal flight path), and in the new EAR2 (20 m vertical flight path), using the neutron beams simultaneously produced by the same cylindrical lead spallation target as used in Phase-II.

For the operation of Phase-III, a new data acquisition system was developed, based on 175 MSample digitizers with 1 ns of time-, and 12 bit amplitude resolution. In addition to the higher-amplitude resolution, which was 8 bits with the previously used digitizers, a larger on-board memory allows now to expand the exploitable time-of-flight range down to thermal neutron energies.

A set of in-house designed C₆D₆-based gamma-ray detectors and newly designed neutron flux detectors based on silicon detectors and MicroMegas detectors [69] were used in beam. An XY-MircoMegas detector with dedicated electronics was developed to measure the neutron beam profile.

The measurement programme in EAR2 started with a first part of commissioning by measuring the elementary quantities as flux and background and focussing on the feasibility of fission measurements. The energy dependence of the number of neutrons incident on the sample, approximatively re-

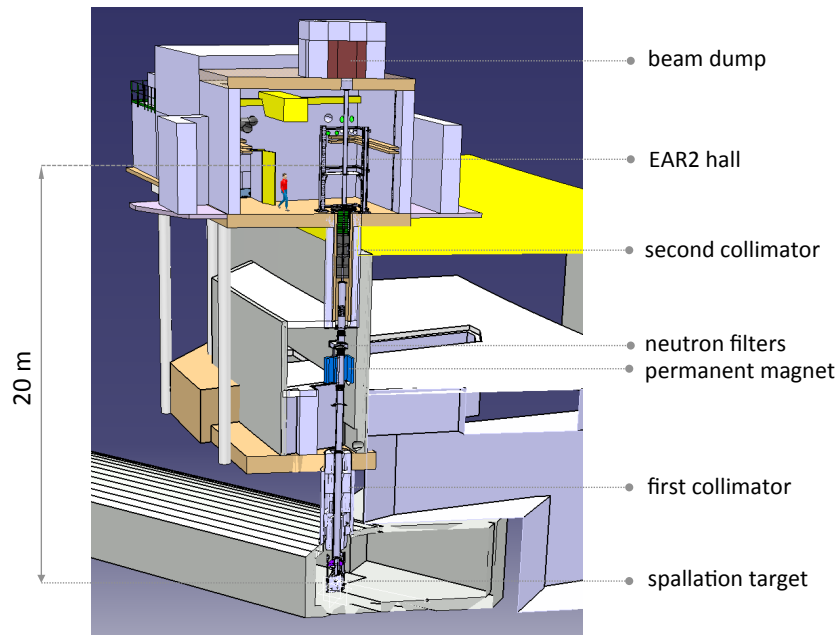


Fig. 1: Impression of n_TOF EAR2 from the spallation target up to the experimental hall.

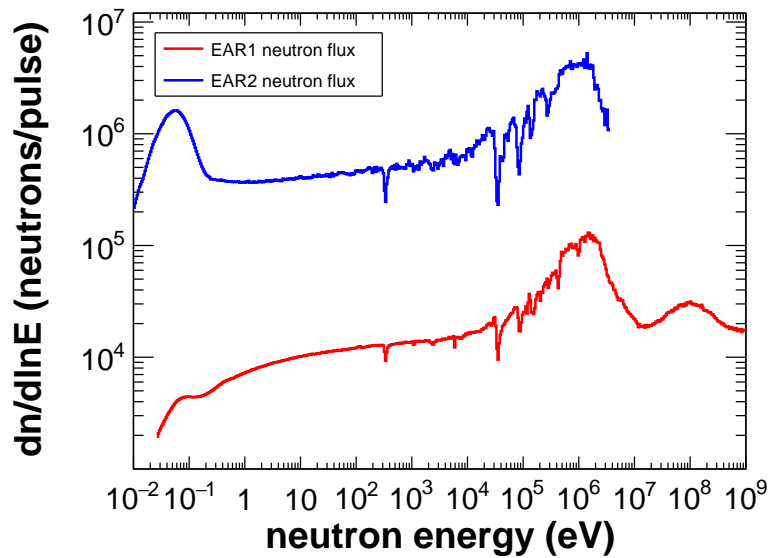


Fig. 2: The number of neutrons per equidistant logarithmic energy bin ($dn/d\ln E$) per 7×12 protons on target, as seen at the sample position at nominal distances of 185 m (EAR1) and 20 m (EAR2). The shown fluxes are the preliminary results of several measurements and simulations.

ferred to as the neutron flux, was measured both with an in-beam neutron-to-charged-particle converter foil, monitored by off-beam silicon detectors, and foils combined with in-beam MicroMegas detectors. The neutron converters consisted of isotopes with well known reactions as ${}^6\text{Li}(n,\alpha)$, ${}^{10}\text{B}(n,\alpha)$ and ${}^{235}\text{U}(n,f)$ in order to cover the energy dependence over a broad energy range. In fig. 2 the measured

Table 3: The nuclear data measurements performed at n_TOF during phase-III in 2014 and 2015 for both EAR1 and EAR2.

nucleus	reaction	detector	EAR	ref.
^{70}Ge	(n, γ)	C ₆ D ₆	EAR1	
^{73}Ge	(n, γ)	C ₆ D ₆	EAR1	
^{74}Ge	(n, γ)	C ₆ D ₆	EAR1	
^{76}Ge	(n, γ)	C ₆ D ₆	EAR1	
^{171}Tm	(n, γ)	C ₆ D ₆	EAR1, EAR2	
^{204}Tl	(n, γ)	C ₆ D ₆	EAR1	
^{242}Pu	(n, γ)	C ₆ D ₆	EAR1	
^{237}Np	(n,f)	PPAC	EAR1	
^{33}S	(n, α)	MGAS	EAR2	
^7Be	(n, α)	MGAS	EAR2	
^{240}Pu	(n,f)	MGAS	EAR2	[70]
^{147}Pm	(n, γ)	C ₆ D ₆	EAR2	
^{235}U	(n,f)FF	STEFF	EAR2	

neutron fluxes in EAR1 and EAR2 are shown. The thermal peak is strongly suppressed for EAR1 due to the addition of ^{10}B in the separate moderator. The thermal flux in EAR2 is not affected because in this direction only the cooling water acts as a moderator.

After the first part of commissioning, the very first physics measurement in EAR2 concerned the $^{240}\text{Pu}(n,f)$ reaction with MicroMegas detectors [70]. In 2015, the commissioning of EAR2 continued, exploring the possibilities of (n, γ) measurements, for applications in nuclear astrophysics [71] and nuclear technology, as well as neutron-induced charged particle reactions like the $^7\text{Be}(n,\alpha)$ and upcoming $^7\text{Be}(n,p)$ experiments. A list of measurements during 2014 and 2015 and their references are given in table 3.

Conclusion

The key features of the n_TOF facility with its two beam lines and experimental areas EAR1 and EAR2 are a large energy range, high neutron-energy resolution, and a high instantaneous neutron flux. EAR2 with its about 25 times higher flux than in EAR1, combined with an additional reduction by a factor 10 of the background due to radioactivity, significantly enhances the possible measurements on unstable targets at n_TOF. The preparation and characterization of such targets suitable for neutron cross-section measurements is an increasingly complicated task, feasible only in highly specialized laboratories.

References

- [1] S. M. Qaim. *Radiochimica Acta*, **101**(8):473–480, 2013.
- [2] G. Aliberti, G. Palmiotti, M. Salvatores, et al. *Nuclear Science and Engineering*, **146**(1):13–50, 2004.
- [3] A. Nuttin, D. Heuer, A. Billebaud, et al. *Progress In Nuclear Energy*, **46**(1):77–99, 2005.
- [4] A. Nuttin, P. Guillemin, A. Bidaud, et al. *Annals of Nuclear Energy*, **40**(1):171–189, 2012.
- [5] T. von Egidy and D. Bucurescu. *Phys. Rev. C*, **73**(4):049901, 2006.
- [6] H. A. Weidenmuller and G. E. Mitchell. *Rev. Mod. Phys.*, **81**(2):539–589, 2009.
- [7] S. E. Woosley, A. Heger, T. Rauscher, et al. *Nucl. Phys. A*, **718**:3C–12C, 2003.
- [8] F. Käppeler, R. Gallino, S. Bisterzo, et al. *Rev. Mod. Phys.*, **83**(1):157–193, 2011.
- [9] T. Rauscher. *Aip Advances*, **4**(4):041012, 2014.
- [10] A. J. Koning, E. Bauge, C. J. Dean, et al. *J. Korean Phys. Soc.*, **59**(2):1057–1062, 2011.

- [11] M. B. Chadwick, M. Herman, P. Oblozinsky, et al. *Nucl. Data Sheets*, **112**(12):2887–2996, 2011.
- [12] K. Shibata. *J. Nucl. Sci. Tech.*, **50**(5):449–469, 2013.
- [13] C. Massimi, P. Koehler, S. Bisterzo, et al. *Phys. Rev. C*, **85**(4):044615, 2012.
- [14] G. Tagliente, K. Fujii, P. M. Milazzo, et al. *Phys. Rev. C*, **77**(3):035802, 2008.
- [15] G. Tagliente, P. M. Milazzo, K. Fujii, et al. *Phys. Rev. C*, **78**(4):045804, 2008.
- [16] G. Tagliente, P. M. Milazzo, K. Fujii, et al. *Phys. Rev. C*, **81**(5):055801, 2010.
- [17] G. Tagliente, P. M. Milazzo, K. Fujii, et al. *Phys. Rev. C*, **84**(1):015801, 2011.
- [18] G. Tagliente, P. M. Milazzo, K. Fujii, et al. *Phys. Rev. C*, **84**(5):055802, 2011.
- [19] R. Terlizzi, U. Abbondanno, G. Aerts, et al. *Phys. Rev. C*, **75**(3):035807, 2007.
- [20] U. Abbondanno, G. Aerts, F. Alvarez-Velarde, et al. *Phys. Rev. Lett.*, **93**(16):161103, 2004.
- [21] S. Marrone, U. Abbondanno, G. Aerts, et al. *Nucl. Phys. A*, **758**:533C–536C, 2005.
- [22] S. Marrone, U. Abbondanno, G. Aerts, et al. *Phys. Rev. C*, **73**(3):034604, 2006.
- [23] K. Fujii, M. Mosconi, A. Mengoni, et al. *Phys. Rev. C*, **82**(1):015804, 2010.
- [24] M. Mosconi, K. Fujii, A. Mengoni, et al. *Phys. Rev. C*, **82**(1):015802, 2010.
- [25] C. Domingo-Pardo, U. Abbondanno, G. Aerts, et al. *Phys. Rev. C*, **75**(1):015806, 2007.
- [26] C. Domingo-Pardo, U. Abbondanno, G. Aerts, et al. *Phys. Rev. C*, **76**(4):045805, 2007.
- [27] C. Domingo-Pardo, U. Abbondanno, G. Aerts, et al. *J. Phys. G*, **35**(1):014020, 2008.
- [28] C. Domingo-Pardo, U. Abbondanno, G. Aerts, et al. *Phys. Rev. C*, **74**(5):055802, 2006.
- [29] C. Domingo-Pardo, U. Abbondanno, G. Aerts, et al. *Phys. Rev. C*, **74**(2):025807, 2006.
- [30] G. Aerts, U. Abbondanno, H. Alvarez, et al. *Phys. Rev. C*, **73**(5):054610, 2006.
- [31] F. Gunsing, E. Berthoumieux, G. Aerts, et al. *Phys. Rev. C*, **86**(1):019902, 2012.
- [32] C. Guerrero, D. Cano-Ott, E. Mendoza, et al. *Phys. Rev. C*, **85**(4):044616, 2012.
- [33] E. Mendoza, D. Cano-Ott, C. Guerrero, et al. *Phys. Rev. C*, **90**(3):034608, 2014.
- [34] M. Calviani, J. Praena, U. Abbondanno, et al. *Phys. Rev. C*, **80**(4):044604, 2009.
- [35] F. Belloni, M. Calviani, N. Colonna, et al. *Eur. Phys. J. A*, **47**(1):2, 2011.
- [36] D. Karadimos, R. Vlastou, K. Ioannidis, et al. *Phys. Rev. C*, **89**(4):044606, 2014.
- [37] R. Sarmiento, M. Calviani, J. Praena, et al. *Phys. Rev. C*, **84**(4):044618, 2011.
- [38] F. Belloni, M. Calviani, N. Colonna, et al. *Eur. Phys. J. A*, **49**(1):2, 2013.
- [39] F. Belloni, M. Calviani, N. Colonna, et al. *Eur. Phys. J. A*, **47**(12):160, 2011.
- [40] M. Calviani, M. H. Meaze, N. Colonna, et al. *Phys. Rev. C*, **85**(3):034616, 2012.
- [41] C. Paradela, L. Tassan-Got, L. Audouin, et al. *Phys. Rev. C*, **82**(3):034601, 2010.
- [42] E. Leal-Cidoncha, I. Duràn, C. Paradela, et al. *Nucl. Data Sheets*, **119**(0):42 – 44, 2014.
- [43] D. Tarrio, L. Tassan-Got, L. Audouin, et al. *Phys. Rev. C*, **83**(4):044620, 2011.
- [44] D. Tarrio, L. S. Leong, L. Audouin, et al. *Nucl. Instr. Meth. A*, **743**:79–85, 2014.
- [45] C. Rubbia et al. "a high resolution spallation driven facility at the CERN-PS to measure neutron cross sections in the interval from 1 eV to 250 MeV". Technical report, 1998.
- [46] C. Guerrero, A. Tsinganis, E. Berthoumieux, et al. *Eur. Phys. J. A*, **49**(2):27, 2013.
- [47] C. Weiss, , et al. The new vertical neutron beam line at the {CERN} n_TOF facility design and outlook on the performance. *Nucl. Instr. Meth. A*, **799**:90 – 98, 2015.
- [48] S. Barros, I. Bergström, V. Vlachoudis, C. Weiss, and n_TOF collaboration. Optimization of n_TOF-EAR2 using FLUKA. *Journal of Instrumentation*, **10**(09):P09003, 2015.
- [49] C. Weiss, C. Guerrero, E. Griesmayer, et al. *Nucl. Data Sheets*, **120**(0):208 – 210, 2014.
- [50] C. Massimi, P. Koehler, F. Mingrone, et al. *Nucl. Data Sheets*, **119**(0):110 – 112, 2014.
- [51] G. Giubrone, C. Domingo-Pardo, J.L. Taín, et al. *Nucl. Data Sheets*, **119**(0):117 – 120, 2014.
- [52] P. Žugec, M. Barbagallo, N. Colonna, et al. *Phys. Rev. C*, **89**(1):014605, 2014.
- [53] C. Lederer, C. Massimi, E. Berthoumieux, et al. *Phys. Rev. C*, **89**(2):025810, 2014.
- [54] C. Lederer, C. Massimi, S. Altstadt, et al. *Phys. Rev. Lett.*, **110**(2):022501, 2013.
- [55] F. Gunsing, K. Fraval, M. Mathelie, et al. *Nucl. Data Sheets*, **119**(0):132 – 136, 2014.
- [56] G. Tagliente, P. M. Milazzo, K. Fujii, et al. *Phys. Rev. C*, **87**(1):014622, 2013.
- [57] C. Massimi, C. Domingo-Pardo, G. Vannini, et al. *Phys. Rev. C*, **81**(4):044616, 2010.
- [58] C. Lederer, N. Colonna, C. Domingo-Pardo, et al. *Phys. Rev. C*, **83**(3):034608, 2011.
- [59] J. Balibrea, E. Mendoza, D. Cano-Ott, et al. *Nucl. Data Sheets*, **119**(0):10 – 13, 2014.
- [60] M. Barbagallo, N. Colonna, M.J. Vermeulen, et al. *Nucl. Data Sheets*, **119**(0):45 – 47, 2014.
- [61] F. Mingrone, C. Massimi, S. Altstadt, et al. *Nucl. Data Sheets*, **119**(0):18 – 21, 2014.

- [62] T. Wright, C. Guerrero, J. Billowes, et al. *Nucl. Data Sheets*, **119**(0):26 – 30, 2014.
- [63] K. Fraval, F. Gunsing, S. Altstadt, et al. *Phys. Rev. C*, **89**(4):044609, 2014.
- [64] E. Mendoza, D. Cano-Ott, C. Guerrero, et al. *Nucl. Data Sheets*, **119**(0):65 – 68, 2014.
- [65] A. Tsinganis, E. Berthoumieux, C. Guerrero, et al. *Nucl. Data Sheets*, **119**(0):58 – 60, 2014.
- [66] P. Žugec, N. Colonna, D. Bosnar, et al. *Phys. Rev. C*, **90**(2):021601, 2014.
- [67] P. Žugec et al. *These proceedings*, 2015.
- [68] E. Chiaveri et al. "Proposal for n_TOF experimental area 2". Technical report, 2011.
- [69] F. Belloni, et al. "Micromegas for neutron detection and imaging". *Mod. Phys. Lett. A*, **28**, 13 (2013) 1340023
- [70] A. Tsinganis et al. *These proceedings*, 2015.
- [71] G. Tagliente et al. *These proceedings*, 2015.

Present Status and Future Plans of J-PARC Hadron Experimental Facility

Kazuhiro Tanaka¹

Institute of Particle and Nuclear Studies (IPNS) and Particle and Nuclear Physics Division, J-PARC Centre, High Energy Accelerator Research Organization (KEK), Tsukuba-shi, Japan

Abstract

Recovery of J-PARC Hadron Experimental Facility from the radioactive material leakage incident occurred on May 23, 2013 is reported. Recovery took long time. However its essential part was completed by the beginning of Japanese Fiscal Year 2015. Then we could start the beam operation of Hadron Experimental Facility from April 9, 2015. Experiments with slow extraction beam started on April 24, 2015. The beam intensity delivered to Hadron Experimental Facility reached approximately 32kW by the end of June, 2015. Recent activities on particle and nuclear physics in the Hadron Experimental Facility are described also.

1 Introduction to J-PARC

J-PARC (Japan Proton Accelerator Research Complex) is the brand-new and the most advanced accelerator facility in Japan. J-PARC consists of three accelerators, i.e. 400MeV Linac, 3 GeV Rapid Cycle Synchrotron (RCS) and 50 GeV Main Ring (MR). The most important characteristic of J-PARC is its high design beam power, which is 1MW for RCS and 0.75MW for MR. RCS provides its intense proton beam to neutron spallation source (n) and pulsed muon source (μ) prepared in Materials and Life Science Facility (MLF). Some fraction of the beam extracted from RCS is injected to MR and accelerated up to 30 GeV. Two extractions from MR were prepared. One is the fast extraction for Neutrino Beam Facility (ν) for long baseline oscillation experiment, T2K, and the other is the slow extraction for counter experiments in Hadron Experimental Facility (Hd). Four experimental facilities (n , μ , ν , and Hd) could provide their characteristic beams for experimental users. Even after the big earthquake occurred in March 11, 2011, we could resume user beam operation after 10 months beam off period for the recovery.

Unfortunately, we had the other incident on May 23, 2013, i.e. the leakage of radioactive materials at the Hadron Experimental Facility (Hd) of MR [1]. After the incident, J-PARC was experienced the long shut down again in order to improve its safety performance for future stable and safe operation. As results of the improvements, MLF of RCS resumed its operation in February 2014 and ν of MR re-started its neutrino beam aiming to SuperKAMIOKANDE for T2K experiment in May 2014. The renovation programs of Hd took much more long time. However those have been completed by the end of March 2015.

On April 9 in 2015 at 23:11 pm (JST), we had the first slow extraction beam from MR to Hd after the radiation leak incident. It took almost 2 years for the recovery of Hd. Immediately after the first beam, we made a lot of tests of safety performances of beam related things of Hd, i.e. interlocks, human interfaces including various displays, and many and many things. Tuning of slow extraction itself was, of course, intensively done! Inspection of the radiation safety authority was made on April 17 with actual beam condition and we received the new operation license of Hd as a radiation facility on April 20. On April 24, we could re-start the beam operation of Hd for experimental users.

¹ kazuhiro.tanaka@kek.jp

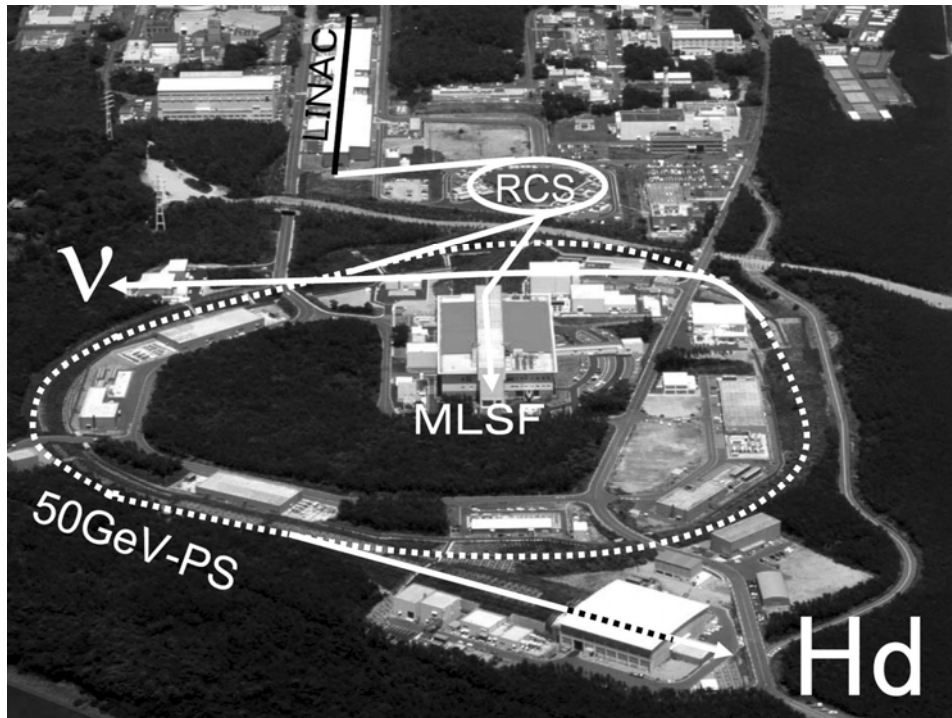


Fig. 1: J-PARC site at Tokai campus of JAEA. “Hd” means the Hadron Experimental Facility for the fixed target experiments with slow extraction. “v” indicates the Neutrino Experimental Facility with fast extraction. “MLSF” indicates the Material and Life Science Research Facility where the spallation neutron and pulsed muon sources are operated by using intense 3 GeV proton beam provided from Rapid Cycle Synchrotron (RCS).

2 Hadron Hall Incident

At present it became clear that the radioactive material leakage incident, occurred on May 23, 2013, developed through the following five stages.

- 1) Due to the malfunction of electromagnets which control the slow extraction of MR, more than 100 times intense and sharply pulsed proton beam was transported to the secondary particle production target, which was made of gold, placed in the Hadron Experimental hall (Hd-hall) of Hadron Experimental Facility (Hd).
- 2) The gold target was instantaneously heated up to a very high temperature and was partially damaged, causing vaporization of gold and dispersion of radioactive material accumulated in the gold target itself.
- 3) The radioactive material leaked into the beam line tunnel which housed the primary proton beam line, because the target container was not very tightly sealed hermetically.
- 4) The radioactive material leaked into the Hd-hall since the airtightness of the beam line tunnel was not perfectly sufficient. Workers in the Hd-hall were, then, exposed to the radiation.
- 5) Due to operation of exhaust ventilation fans in the Hd-hall, the radioactive material was released into the environment outside of the radiation controlled area of the Hd-hall and J-PARC.

Thirty-four out of 102 people who entered the Hd-hall during the incident, was internally exposed to radiation. The maximum amount of their radiation doses was found to be 1.7 mSv through a whole-body counter measurement. Fortunately medical examination confirmed the absence of any adverse effects due to the radiation exposure. The total amount of radioactive material released into the Hd-hall was estimated to be approximately 20 billion (2×10^{10}) Bq. The radiation dose of the site

boundary at the location closest to the Hd-hall was estimated below $0.29\mu\text{Sv}$.

Based on the analysis of this incident through the development described above, we established the recovery plan of Hd-hall against the recurrence of similar incidents. The frameworks for the recovery plan are as follows;

- 1) preventive measures against the malfunction of electromagnets of slow extraction,
- 2) ensuring of airtightness of the target container and the beam line tunnel,
- 3) management of exhaust ventilation of Hd-hall,
- 4) reinforcement of monitoring radioactivity in and near the Hd-hall.

It is very important to decrease a frequency of a malfunction of the magnet power supply system of MR. However, we know that it is impossible to completely eliminate a malfunction through any examination of various preventive measures. Essentials of the preventive measures against the radioactive material leakage are reinforcement of airtightness of the target container and the beam line tunnel. The exhaustion of the air through filters from a stack after checking concentration of radioactive material is also important. In this meaning, it is found that the frameworks 2~4 are essentials of the Hd-hall renovation.

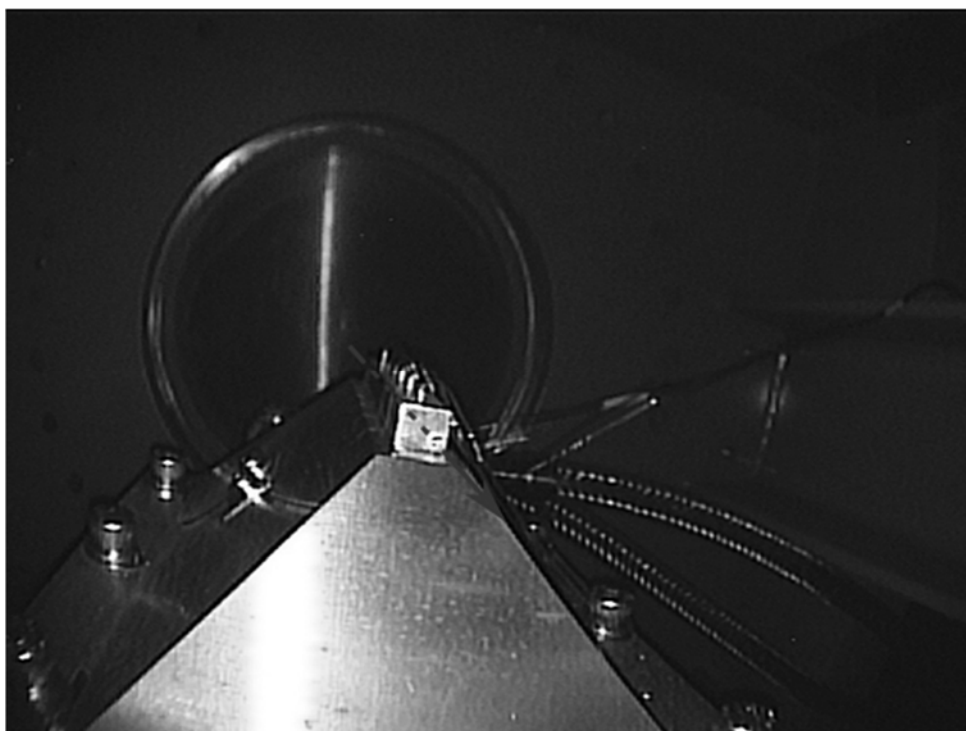


Fig. 2: Photograph of damaged gold target observed from the downstream: a 1mm in diameter hole was seen at the downstream end. Arrow in the Photograph is the direction of the beam.

On December 12 and 13 in 2013, we could observe the gold target at the Hd-hall by a fiberscope for the first time after the radioactive material leak incident. During the observation, we verified:

- 1) a hole of 1 mm in diameter at a downstream end of the gold target,
- 2) gold-colored nubs, which probably are traces of dripped out melting gold from slits of a gold rod of the target,
- 3) probably droplets of melted gold on the copper base block and

4) traces of sprayed out melting gold on a beryllium vacuum window placed at the beam-downstream of the target.

These observations nicely match with our expectations and simulation results, i.e. the development of the incident. Consequently, we consider that, at the injection, temperature of the gold target partially exceeded melting and further vaporizing points, and melted gold was pushed outward due to a rapid volume expansion resulted from vaporization of the melted gold.

3 Hadron Hall Renovation

The new production target, i.e. indirectly water cooled gold target, was designed and manufactured with more efficient water cooling paths. The target can be used up to 50kW with 2 s slow extraction time. The target was placed newly prepared hermetically sealed target container which was filled with He gas. He gas was circulated by the He gas pump which was placed almost 50 m away from the target container. Radioactivity contained in the He gas was monitored by a Ge detector placed near the pump. Then we can detect the target failure by measuring unexpectedly enormous amount of radioactive fragments produced from the target, i.e. gold nuclei. The temperature of the target is always monitored by thermocouples and the measurement timing is increased to every 100 ms. Then heating up and cooling down trends of the target temperature can be recorded in detail and are compared with the FEM analysis expectation.

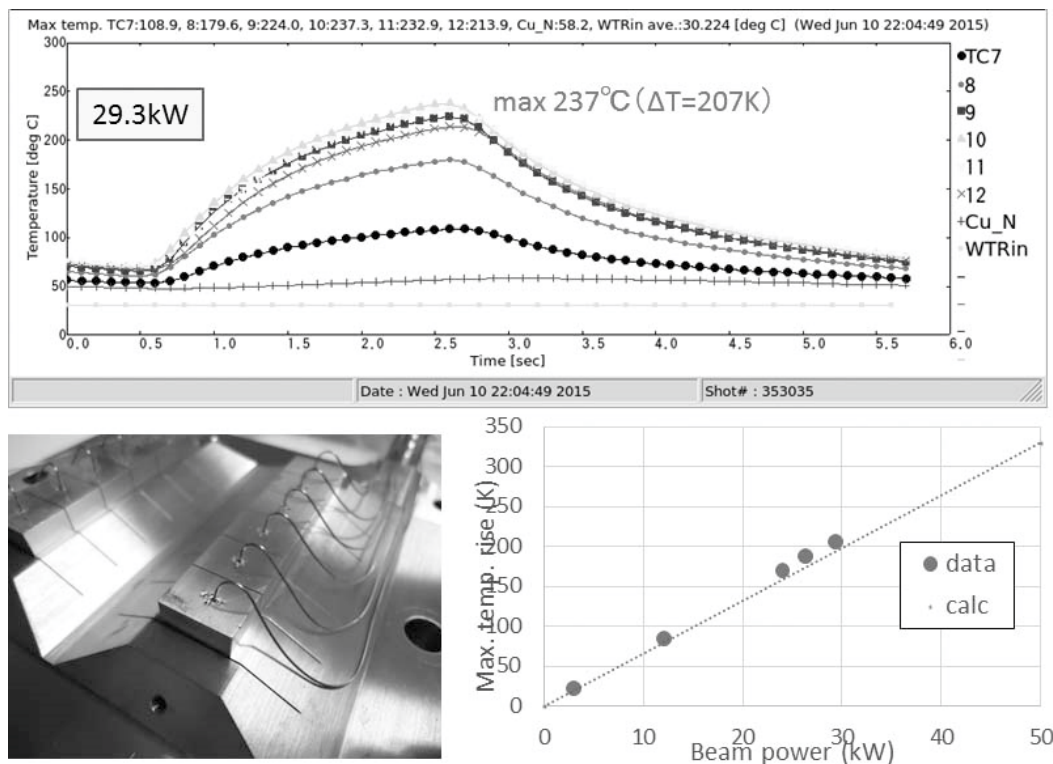


Fig. 3: Temperature change of gold target measured at every 100 ms (Up). Target was divided to 6 segments as shown in down-left photo. The temperature of each segment was measured independently. Measured results were compared with calculated results obtained from FEM analysis (Down-right) and agreed well.

The beam line tunnel for the primary proton beam is air-tightly sealed by double layers of air-tight film, which is usually used for the manufacturing of balloons. Leakage through the double seal layers was measured by He leak detector and was found to be sufficiently small. Two types of new exhaust air ventilation system were introduced to the Hd-hall. One is the air exhaust volume of 10000

m^3/h system and the other is $74000 \text{ m}^3/\text{h}$ system. Both systems can exhaust the air inside the Hd-hall through filters. The $10000 \text{ m}^3/\text{h}$ air exhaust system is sufficient for usual radiation control inside the Hd-hall. However $74000 \text{ m}^3/\text{h}$ air exhaust system is necessary for keeping the clean circumstance in the Hd-hall. This large scale $74000 \text{ m}^3/\text{h}$ system can exchange the whole air inside the Hd-hall by fresh air within 1 hour in the case of needs.

The interlock system on radiation and radiation related matters of Hadron Experimental Facility were completely renewed and strengthened. Fast target temperature monitor and target gas radiation monitor described above are typical examples. In addition, sharing system of safety information was very much strengthened. Experimental team members inside the Hd-hall are automatically included in the beam operation team and can share the radiation interlock signals. Experimental team members have to receive a set of safety training classes before the beam usage. Emergency drills were made including users under the assumption of several abnormal and/or serious situations. After these renovations in both software and hardware sides, we could re-start the beam operation of the Hadron Experimental Facility.

Please see the photo (Fig. 4), which was taken on April 28, 2015, a few days after the re-start of user beam operation. People seen in the photo are from the beam operation team of Hadron experimental Facility including related support groups and hadron experimental teams including students and professors from Universities.

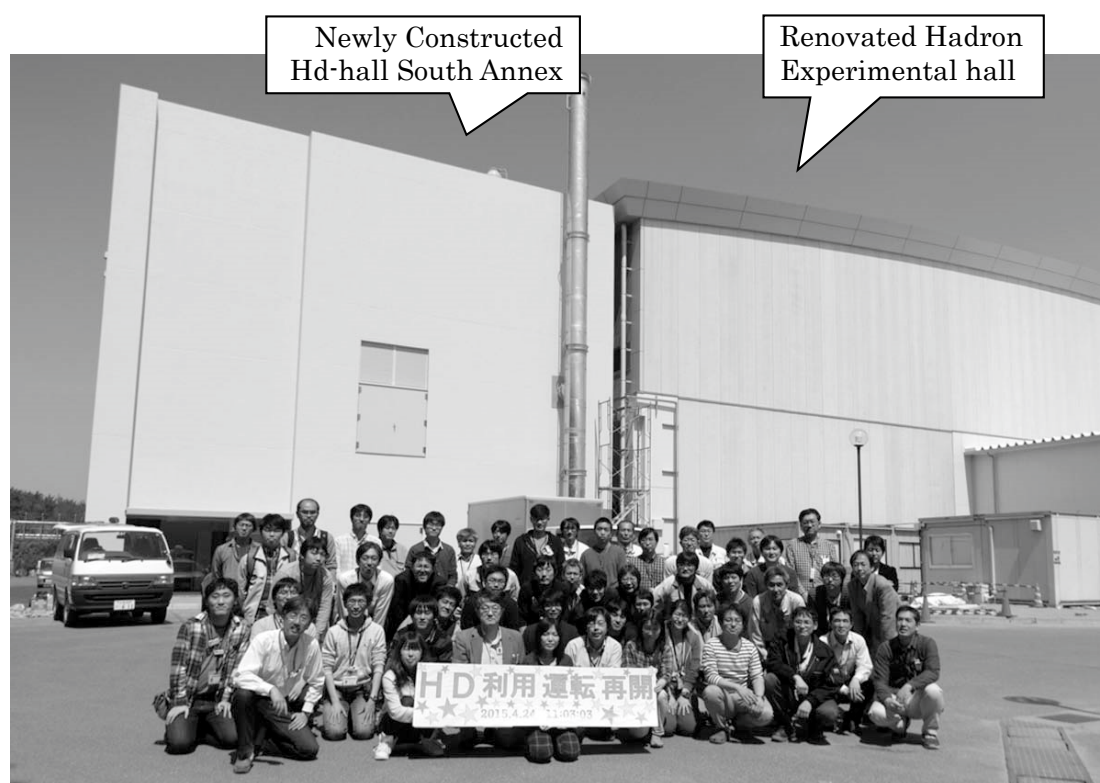


Fig. 4: Photograph taken just few days after the re-start of user operation of Hadron Experimental Facility (Hd). People seen in the photo are from the beam operation team of Hd and related groups, hadron experimental teams including students and professors from Universities. Buildings behind are Hadron Experimental hall (right) and newly constructed South Annex of Hadron Experimental hall for COMET experiment as well as the beam operation Headquarter (left).

4 Physics Results from Hadron Hall

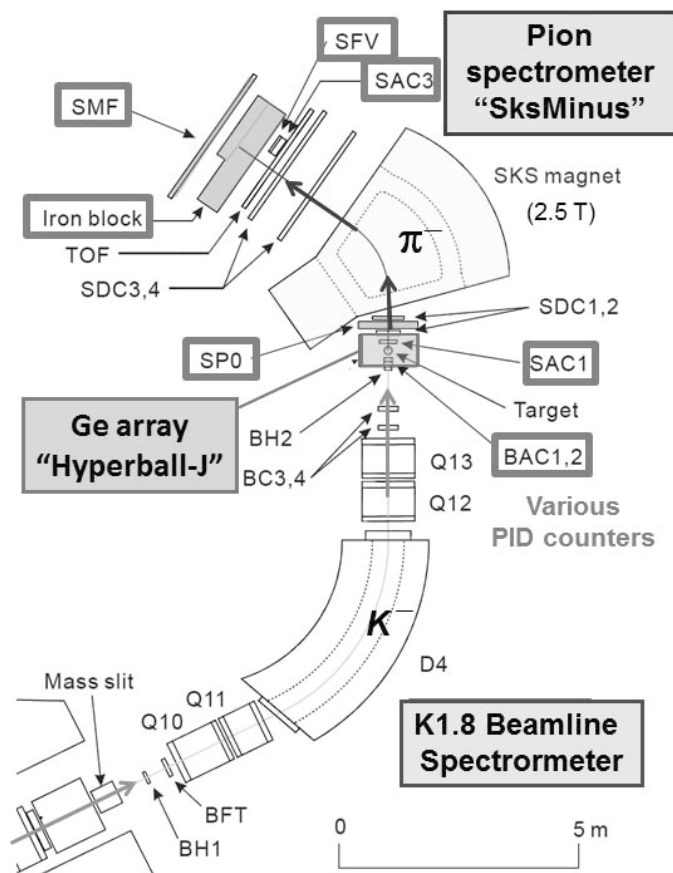


Fig. 5: Experimental setup of hypernuclear γ -ray measurements prepared by Tamura and his colleagues. The data were taken in the April-June beam time in 2015 at Hadron Experimental hall. ${}^4\text{He}(K^-, \pi^-){}^4_\Lambda\text{He}$ reaction was tagged by combining SKS (SksMinus position) and K1.8 Beam line Spectrometer. Hypernuclear γ -rays were measured by “Hyperball-J” Ge detector array surrounding the He target placed at the entrance of SKS

Even during the beam off period, new physics results were appeared from analysis of experimental data taken before the incident. Evidences of the existence of K^-pp bound state [2], existence of Ξ^- -hypernuclei [3], and negative results of Θ^+ -production in hadronic (π, K) reactions [4] and neutron rich light hypernuclei [5] were the main interesting results appeared in these two years.

Some very new experimental data were become available in April-June beam time in 2015. One of the most surprising results is obtained from the measurements of γ -rays from ${}^4_\Lambda\text{He}$ hypernuclei. Tamura and his collaborators prepared versatile Germanium detector array, named “Hyperball-J”. Using this Hyperball-J, γ -rays from ${}^4_\Lambda\text{He}$ produced in ${}^4\text{He}(K^-, \pi^-){}^4_\Lambda\text{He}$ reactions were measured. Observed γ -ray from the first excited 1^+ to 0^+ (spin flip γ -ray of Λ particle in ${}^3\text{He}$ core) transition was 1.406 MeV and was completely different from known γ -ray energy of 1.09 MeV of 1^+ to 0^+ transition of ${}^4_\Lambda\text{H}$ (spin flip γ -ray of Λ particle in ${}^3\text{H}$ core). If the nuclear forces between Λ, p, n particles are essentially the same without charge effect, the energy of these two γ -rays must be the same. Such large difference between ${}^4_\Lambda\text{He}$ and ${}^4_\Lambda\text{H}$ clearly indicates the existence of the charge symmetry breaking (CSB) in generalized nuclear force including strange baryons. Some theoretical model suggests the ΛN - ΣN coupling is responsible for CSB. Details of the results will be published soon [6].

5 Hadron Hall Extension

We have just re-started the operation of Hadron Experimental Facility. However many users require more and more beam time for experiments. At present, we have only one production target in the Hadron Experimental hall and only three secondary beam lines (two charged and one neutral kaon beams). Such small number of beam outlets is NOT sufficient for strong requests of experimental users. High momentum beam line which will introduce charged particles up to 31 GeV/c to experimental area for the direct use of primary protons and high momentum secondary unseparated particles is now under construction. COMET branch, i.e. low energy primary proton beam line up to 9 GeV/c, is prepared for μ -e conversion experiment, COMET, at the middle point of the high

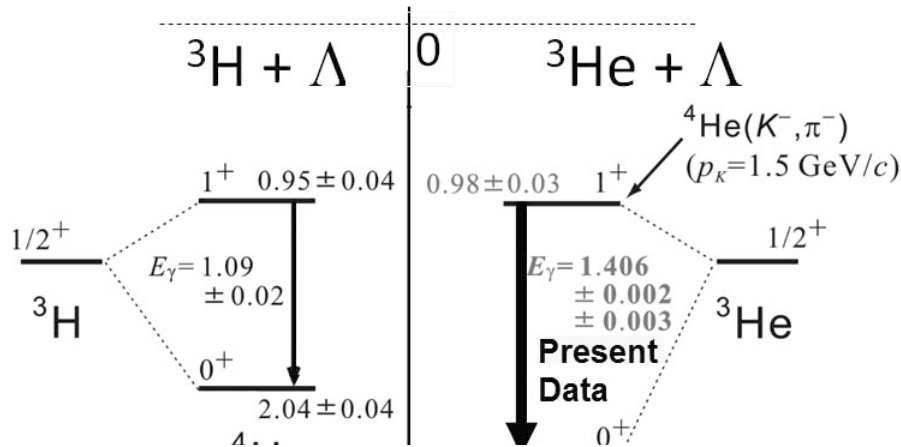


Fig. 6: Existence of CSB confirmed by γ -ray data obtained in the April-June beam time in 2015 by Tamura and his collaborators. Comparing the γ -ray energy of the spin flip of Λ in ${}^3\text{He}$ core (right, Present Data) with the same case γ -ray energy of ${}^3\text{H}$ core (left, Bedjidian et al.), large difference between two cases was found [6]

momentum beam line. New experimental area is under preparation in newly constructed South Annex of Hadron hall. However these two new beam lines can not cover the very wide range of experimental requests of users.

Then we are now trying to extend the area of Hadron Experimental hall three times. Two new target stations will be constructed and four new secondary beam lines will be connected to these two targets. Very forward angle neutral kaon beam line, high momentum separated kaon/antiproton beam line, very high resolution dispersion matching beam line and very low energy separated kaon beam line are now under consideration. Once the extension completed, the Hadron Experimental Facility of J-PARC will be a real MECCA of nuclear and particle physics using kaons and the other rare hadrons.

Acknowledgements

The author wish to thank members of Primary Proton Beam Channel Group of J-PARC Hadron Experimental Facility, and other colleagues of J-PARC, for their co-operation throughout the renovation and recovery works of the Hadron Experimental Facility.

References

- [1] <http://j-parc.jp/en/topics/HDAccident20130531.pdf>
- [2] Y. Ichilawa *et al.*, PTEP 2015 (2015) **2**, 021D01
- [3] K. Nakazawa *et al.*, PTEP (2015) 033D02.
- [4] M. Moritsu *et al.*, Phys. Rev. **C90**, 035205(2014).
- [5] H. Sugimura *et al.*, Phys. Lett. **B729** (2014) 39-44.
- [6] T.O. Yamamoto *et al.*, arXiv:1508.00376 [nucl-ex]

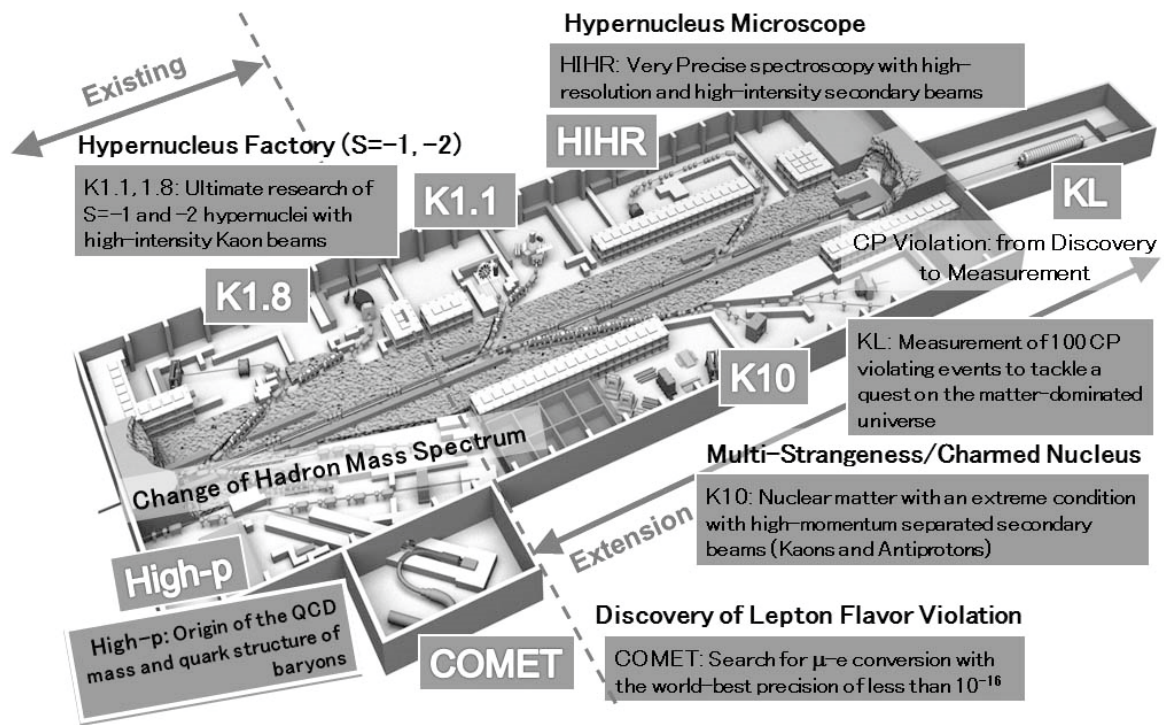


Fig. 7: Drawing of the extension of Hadron Experimental hall. Two new target stations are constructed and four new secondary beam lines are connected to these two targets. Very forward angle neutral kaon beam line, KL, high momentum separated kaon/antiproton beam line, K10, very high resolution dispersion matching beam line, HIHR, and very low energy separated kaon beam line, K1.1, are now under consideration. High-p beam line with COMET branch is now under construction at present Hadron Experimental hall.

On the parametrization of lateral dose profiles in proton radiation therapy

A. Embriaco

University of Pavia & INFN, Pavia, Italy

Abstract

Hadrontherapy requires a good knowledge of the physical interactions of the particles when they cross the biological tissue: one of the aspects that determine the characterization of the beam is the study of the lateral profile. We study different parametrizations for the lateral dose profile of protons beam in water considering different energies at different depth. We compare six functions: we start from the well known Gaussian and Double Gaussian parametrizations and also analyse more recent parametrization obtained with Triple Gaussian and Double Gaussian Lorentz-Cauchy functions. Finally we propose alternative parametrizations based on the Gauss-Rutherford and Gauss-Levy functions. The goal is to improve the performances of the actual treatment planning used in proton beam therapy by suggesting alternative approaches to the Gaussian description typically employed.

1. Introduction

The propagation of a proton beam in water can be decomposed in a longitudinal and transverse profile. The longitudinal profile is well known as Bragg Peak, while laterally we have a beam spread.

The accurate study of lateral beam profile is important to delimit the dose to the cancer volume, saving as much as possible the surrounding healthy tissue.

The form of lateral beam profile comes from the combination of two processes: the Multiple Coulomb scattering and nuclear interactions. The multiple Coulomb scattering is described by Molière's theory [1] and takes into account only electromagnetic interaction. In addition on the tails of lateral profile, we have the effect of nuclear interactions, that produce nuclear fragmentation. The nuclear contribution for protons is between 5% to 15% and cannot be neglected [2].

Therefore, the shape of lateral beam profile is not Gaussian. Actually, the Treatment Planning System (TPS) parametrize the lateral profile with Gaussian or Double Gaussian.

2. Parametrizations

2.1 Gaussian

First of all, we try to fit the lateral dose profile with a single Gaussian, but the agreement is present in only first 2 decades of the deposited energy distribution. This parametrization does not take into account the tails of distribution.

$$f(y) = N \frac{1}{\sqrt{2\pi}\sigma} \exp \left[-\frac{y^2}{2\sigma^2} \right] \quad (1)$$

This function, being centered at a zero mean value, has only 2 free parameters, the standard deviation σ and the normalization factor N .

2.2 Double Gaussian

An improvement of the previous model adds a second broader Gaussian to better describe the tails of dose distribution as proposed by R. Fruhwirth and M. Regler [3] and applied already in clinical

environment.

$$f(y) = N \left\{ (1 - W) \frac{1}{\sqrt{2\pi}\sigma_1} \exp \left[-\frac{y^2}{2\sigma_1^2} \right] + W \frac{1}{\sqrt{2\pi}\sigma_2} \exp \left[-\frac{y^2}{2\sigma_2^2} \right] \right\} \quad (2)$$

The idea behind this parametrization is to describe the core with a narrow Gaussian of width σ_1 whereas with the large Gaussian of width σ_2 the tails of lateral dose profile. This parametrization has 4 free parameters.

2.3 Triple Gaussian

Following this approach, we upgraded the previous model adding a further Gaussian of width σ_3 . This parametrization is better than double Gaussian but the number of free parameter increase to 6.

$$f(y) = N \left\{ (1 - W_1 - W_2) \frac{1}{\sqrt{2\pi}\sigma_1} \exp \left[-\frac{y^2}{2\sigma_1^2} \right] + W_1 \frac{1}{\sqrt{2\pi}\sigma_2} \exp \left[-\frac{y^2}{2\sigma_2^2} \right] + W_2 \frac{1}{\sqrt{2\pi}\sigma_3} \exp \left[-\frac{y^2}{2\sigma_3^2} \right] \right\} \quad (3)$$

From the Gaussian approach, we select the triple Gaussian as a possible good parametrization and discard the single Gaussian.

2.4 Gauss-Rutherford

Taking into account that multiple scattering occurs at small angle and single scattering at wide angle, we considered a new model consists of a Gaussian core to describe the multiple scattering effect and a Rutherford-like hyperbole to represent single scattering.

$$f(y) = N \left\{ (1 - W) \frac{1}{\sqrt{2\pi}\sigma} \exp \left[-\frac{y^2}{2\sigma^2} \right] + W \frac{2b^{3/2}}{\pi} \frac{1}{(y^2 + b)^2} \right\} \quad (4)$$

This function depends only on 4 free parameters, the width σ of the Gaussian core, a relative weight W and a normalization factor N . The parameter b mathematically represents the horizontal shift of the hyperbolic function and physically allows to depict a smooth transition between small and wide angle distributions. Typically b gives information on the lateral position where the distribution loses its Gaussian profile and corresponds to about 1/600 of the peak value [4].

This parametrization, whose application to a TPS is innovative to our knowledge, is inspired by the Rutherford scattering experiment and seems physically well justified.

2.5 Gauss-Levy

An alternative parametrization with a similar behavior on the tails is given by adding to the Gaussian core a Levy function.

$$f(y) = N \left\{ (1 - W) \frac{1}{\sqrt{2\pi}\sigma} \exp \left[-\frac{y^2}{2\sigma^2} \right] + W \frac{1}{\mathcal{L}} \frac{\exp \left[-\frac{y+c}{2} \right]}{(y+c)^{3/2}} \right\} \quad (5)$$

where the Levy function normalization integral \mathcal{I} does not exist in analytic form and must be computed numerically and stored in a look-up table:

$$\mathcal{I} = \int_{-\infty}^{\infty} \frac{\exp\left[-\frac{y+c}{2}\right]}{(y+c)^{3/2}} dy$$

This function depends only on 4 free parameters as above: in addition to σ , W and N we introduce the parameter c as a scale parameter that describes the dispersion of the tails in analogy with σ in the core. Also this function is original when applied to TPS, although less accurate than the Gauss-Rutherford.

2.6 Double Gaussian and Lorentz Cauchy

Finally, we also analysed a recent parametrization proposed by Soukup et al. [5] and by Li et al. [6], where a second Gaussian function with a large standard deviation and a modified Cauchy-Lorentz distribution function are added to the Gaussian profile of the core.

These functions are used to describe the long-range scatters caused by nuclear interaction and large-angle Coulomb scattering that are not accounted for using the primary Gaussian components, but requires 6 parameters.

$$f(y) = N \left\{ (1 - W_1 - W_2) \frac{1}{\sqrt{2\pi}\sigma_1} \exp\left[-\frac{y^2}{2\sigma_1^2}\right] + W_1 \frac{1}{\sqrt{2\pi}\sigma_2} \exp\left[-\frac{y^2}{2\sigma_2^2}\right] + W_2 \frac{1}{\mathcal{I}} \frac{1 - A \exp\left[-\frac{y^2}{2b^2\sigma_2^2}\right]}{\pi b \left(\frac{y^2}{b^2} + 1\right)} \right\} \tag{6}$$

where:

$$A = \frac{2\sigma_2^2}{2\sigma_2^2 + 1}$$

$$\mathcal{I} = \int_{-\infty}^{\infty} \frac{1 - A \exp\left[-\frac{x^2}{2b^2\sigma_2^2}\right]}{\pi b \left(\frac{x^2}{b^2} + 1\right)} dx$$

Obviously other parametrizations are possible and are currently being proposed (up to 25 free parameters [7]), but for the purpose of this study we decided to limit the number of parameters in view of a possible use in a future customizable TPS.

3. Simulations & Data

The functions reported in the previous sections were compared with experimental data measured at CNAO and with Monte Carlo simulations obtained with FLUKA. We have implemented a C++ program based on ROOT and MINUIT to fit lateral dose distribution obtains by FLUKA simulation with six different functions.

The simulation setup implemented in FLUKA is very simple. The geometry consists in a parallelepiped of water that represents the water phantom, into a parallelepiped of air. The position of isocenter and the geometry reflects the CNAO facilities (Fig. 1). The Physic setting used is HADRONTHE and the source is the CNAO phase space. A phase space distribution is a file containing the parameters for a large set of particles: in particular the energy, the position and the directional cosine. In these simulation, we have scored the energy deposition in water in a mesh of this dimension:

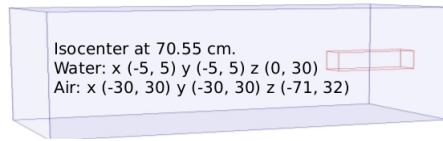


Fig. 1: The geometry implemented in FLUKA simulation.

- 1bin in x: (-0.1, 0.1)cm
- 400 bins in y: (-5, 5)cm
- 2000 bins in z: (0, 20)cm

We have made 10 run to 10^7 particles each and we consider the Fluka errors.

This simulation are compared with CNAO data. The measurements are the transversal dose profile of the proton pencil beam and were acquired using a cylindrical PinPoint ionization chamber in a remotely-controlled 3D motorized water phantom.

4. Results

Results of the best fits for the simulated beam profiles are shown in Fig.2-3 for two energies at different depth in water.

The grey line represents 0.1% of the central axis dose, assumed as the lowest level of clinical relevance.

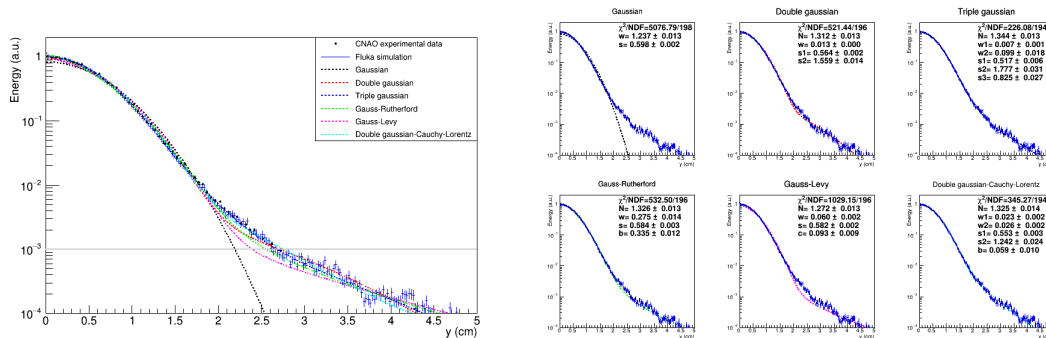


Fig. 2: Left: Lateral half-profile of deposited energy for the CNAO beamline measured and simulated from a phase space beam of 117.75 MeV protons in 2.5 cm water depth. Data are normalized to the central axis. Right: different parametrizations fitted to the same simulated data.

The constant N is an additional normalization that varies with energy and depth and in a TPS, where the lateral and longitudinal profiles are factorized, it is typically described by the Depth Dose Deposition (DDD) profile. The values of N are used as a cross-check of the goodness of fit: for each E and z , N is similar among all six functions and this indicates that the overall profile is normalized correctly.

4.1 Accuracy

For the accuracy, we have analysed the trend of the reduced χ^2 as a function of the depth z for six different measurements as well seen in Fig.4. The χ^2 has acceptable values for each function apart for the single Gaussian (reported in the inset because of the different scale) at all depths analysed. The fit quality depends on the water depth and all function show an acceptable value: clearly the triple

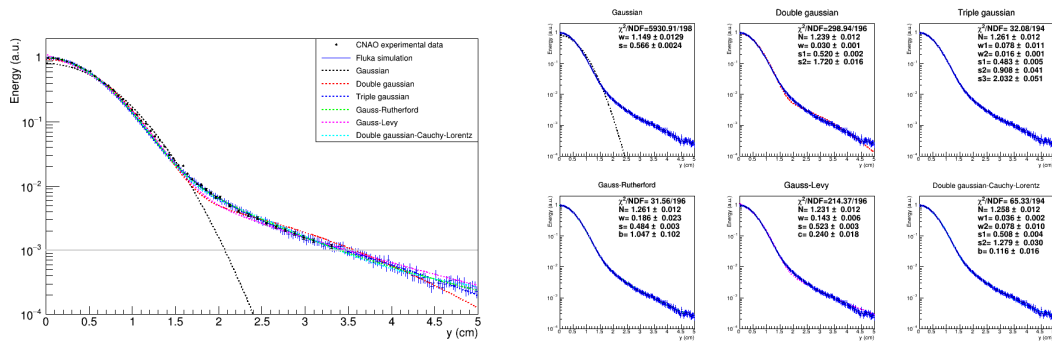


Fig. 3: As in Fig.2 for a phase space beam of 154.25 MeV protons in 10 cm water depth.

Gaussian and the double Gaussian Cauchy- Lorentz give better results, but the double Gaussian and the Gauss-Rutherford are both comparable.

In general, all functions show a worse description of the true profile in correspondence of the Bragg

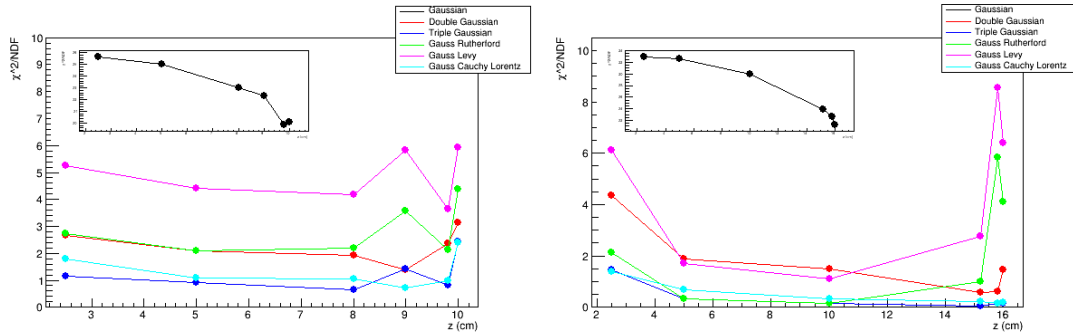


Fig. 4: Trend of reduced χ^2 as a function of water thickness for energy 117.75 MeV (left) and 154.25 MeV (right) beam energies.

peak depth, where inelastic processes, that are not easy to parametrize by simple functions with few parameters, dominate.

Qualitatively the six functions can be classified in 3 groups: the Gaussian and Gauss-Levy functions that show an average value greater than 3 (bad fit), the double Gaussian and Gauss-Rutherford function that are on average between 2 and 3 (good fit) and the triple Gaussian and the double Gaussian Cauchy-Lorentz that are close to one (best fit).

Moreover, we have performed a Kolmogorov-Smirnov test between the FLUKA distribution and the six functions to assess the goodness of fit: all the functions pass the test but have different maximum distances that we report in Tab.1 and that we use as a criterion to evaluate the accuracy of the parametrization.

The use of the maximum distance D in this test is complementary to the use of the standard p-value. In case of binned data D is a parameter which, although not having a universal statistical meaning, allows to estimate the different fits quality in a relative manner. In addition this method is suggested as an alternative to the χ^2 method for histograms with low statistics [8].

Looking at the values of D the Gauss-Rutherford parametrization shows an accuracy comparable or better than the one of the double Gaussian, making it an interesting option.

Table 1: Maximum distance D of Kolmogorov-Smirnov test for two depths at energies 117.75 MeV and 154.25 MeV.

Function	$E = 117.75$ MeV		$E = 154.25$ MeV	
	2.5 cm	8 cm	10 cm	15.2 cm
Gaussian	0.0471	0.0517	0.0493	0.0512
Double Gauss	0.0247	0.0229	0.0216	0.0155
Triple Gauss	0.0025	0.0013	0.0029	0.0009
Gauss-Rutherford	0.0168	0.0178	0.0024	0.0119
Gauss-Levy	0.0216	0.0216	0.0142	0.0149
Double Gauss Lorentz Cauchy	0.0111	0.0073	0.0047	0.0051

Table 2: Computational time relative to double Gaussian τ for energies 117.75 MeV and 154.25 MeV.

Function	number of parameters	τ	
		117.75 MeV	154.25 MeV
Gaussian	2	0.74	0.76
Double Gaussian	4	1.00	1.00
Triple Gaussian	6	1.19	1.16
Gauss-Rutherford	4	1.11	1.10
Gauss-Levy	4	0.87	0.91
Double Gauss-Lorentz Cauchy	6	1.76	1.73

4.2 Time Calculation

With this program we have also estimated the calculation time τ for all the functions relative to the double Gaussian function which is available in the commercial TPS used at CNAO. The results on the computation time for all functions are shown in Tab.2.

Most of the computation time in a TPS is determined by the dose calculation in a longitudinal profile and not by the lateral parametrization. Therefore the impact of these times is not crucial and we report them for completeness as a possible optimization to shorten the calculation without a loss of accuracy.

5. Conclusions

In this study we have analysed different parametrizations currently available to describe the lateral dose profile in proton therapy. In addition to functions already published, we propose in particular a new parametrization: Gauss-Rutherford.

The Gauss-Rutherford function is a good compromise to evaluate the lateral energy deposition of real beam shapes: indeed, with only 4 free parameters, it ensures a good accuracy, but also a fast calculation time. Moreover, this parametrization is firmly justified by a physical explanation.

This study was recently published in *Physica Medica* [9].

References

- [1] G.Molière, *Z. Naturforsch.* 3a (1948) 78
- [2] W.Ulmer et al.(2012) *Journal of Nucl. And Part. Phys.*,2:42-56
- [3] R.Fruhwith and M.Regler, *Nuclear Instruments and Methods in Physics Research*, 369 (2000)
- [4] Jackson JD, *Classical Electrodynamics*. John Wiley and Sons; 1975
- [5] M.Soukup et al, *Phys. Med. Biol.* 50 (2005) 5089-5104
- [6] Y.Li et al, *Phys. Med. Biol.* 57 (2012) 983-997
- [7] B.Gottschalk et al.(2014) *ArXiv:1409.1938v1* [physics.med-ph]
- [8] R. Brun, F. Rademakers, *Nucl Instr Meth A* (1997) 389:81-6.
- [9] V.E.Bellinzona, M. Ciocca, A. Embriaco, A. Fontana, A. Mairani, M. Mori, K. Parodi, *Phys. Med.* 31 (2015), 484-492

An analytical solution to lateral dose prediction in Hadrontherapy

E. V. Bellinzona^{1,2,3}, *M. Ciocca*⁴, *A. Embriaco*^{1,2}, *A. Ferrari*⁵, *A. Fontana*², *A. Mairani*^{4,6}, *K. Parodi*^{3,6}, *A. Rotondi*^{1,2}, *P. Sala*⁷, *T. Tessonier*⁶, *et al.*

¹Dipartimento di Fisica, Università degli Studi di Pavia, 27100 Pavia, Italy

²Istituto Nazionale di Fisica Nucleare (INFN), Sezione di Pavia, 27100 Pavia, Italy

³ Department of Medical Physics, Ludwig Maximilians University, Munich, Germany

⁴ Centro Nazionale di Adroterapia Oncologica (CNAO), 27100 Pavia, Italy

⁵ European Organization for Nuclear Research CERN, CH-1211, Geneva 23, Switzerland

⁶Heidelberg Ion Beam Therapy Center (HIT), Heidelberg, Germany

⁷ Istituto Nazionale di Fisica Nucleare (INFN), Sezione di Milano, 20133 Milano, Italy

Abstract

A flexible model for the calculation of the lateral deflection of a proton pencil beam in hadrontherapy is presented. The model is based on the full Molière theory for Coulomb multiple scattering, that is reliable for any depth and for every kind of media and mixture, since energy loss effects by primary process are fully taken into account. The use of the original equations of the theory, without any free parameter, allows the exact description of the electromagnetic interaction with a full accuracy and a fast computing time. The contribution of the nuclear interactions are also fully taken into account with a fit, with only two free parameters, on the prediction of the FLUKA Monte Carlo (MC) code. The model gives results with the same accuracy of the MC code with a much shorter computing time, and is also in good agreement with some experimental data from Heidelberg Ion-Beam Therapy Center (HIT).

1. Introduction

Challenging issues in treatment planning for hadrontherapy are the accurate calculation of dose distribution, the reduction in the memory space required to store the dose kernel of individual pencil beams and shortening of computation time for dose optimization and calculation.

The best accuracy in this kind of calculations can be obtained by MC methods, but at the expense of a long computing time. Alternatively, models can be used that calculate the total dose as the sum of the dose delivered by an ensemble of pencil beams corresponding to the structure of the real beam delivered by the accelerator.

In this framework, lateral dose distribution prediction is a topic of great interest because, currently, only a double Gaussian parametrization [1], [2] is used as approximation; other parametrizations are also available [3],[4], [5]. As alternative we propose a flexible model for the calculation of the lateral deflection of a pencil proton beam. This model is composed by two contributions: the electromagnetic and the nuclear part [6]. The electromagnetic interaction uses the original equations of the complete Molière theory [7], [8] removing the need for any free parameter, at the expense of a reasonable increase in the computing time, with respect to simpler cases. In addition to the traditional angular distribution, the linear lateral displacement is also provided.

To take into account the nuclear interactions, the model relies only on two parameters that are determined as a function of energy and depth by best fits to FLUKA MC simulations.

The model agrees very well with the MC code predictions and with experimental data for protons in water, which were acquired at the Heidelberg Ion Beam Therapy Center (HIT) at clinically relevant energies and depths.

2. Model structure

This section summarizes the two parts of the model; it results in a standalone C++ code that can be used in the context of treatment planning for hadrontherapy. The model has been developed for a proton pencil beam in water but it can be easily extended to more realistic cases to reproduce mathematically the lateral beam scan in a given region.

2.1 Electromagnetic core

Molière theory

The Molière theory is mathematically based on the standard transport equation, with the Bessel transforms and the small angle approximation i.e. $\sin(\theta) \approx \theta$.

Physically, the theory only accounts for electromagnetic interactions and assumes the Rutherford form for the single scattering cross section:

$$\rho \sigma(\theta) = 2\chi_c^2 \frac{1}{(\theta^2 + \chi_\alpha^2)^2}, \quad (1)$$

where ρ is the number of atoms/cm², the integration over ϕ is performed and χ_c , χ_α are the two crucial parameters of the model. The first one is connected to the rms scattering angle:

$$\chi_c^2 = 0.1569 \cdot 10^{-6} Z^2 z^2 \frac{x}{A} \frac{1}{p^2 \beta^2}, \quad (2)$$

where z is the Atomic number of the incident particle, Z and A the atomic and the mass number of the target, x is the thickness of the target (g/cm²), p is the momentum in GeV/c and $\beta = v/c$.

The second one is the parameter connected to the electron screening of the Coulomb potential:

$$\chi_\alpha^2 = \mu^2 \chi_0^2 \quad (3)$$

$$\mu^2 = \left(1.13 + 3.76 \frac{z^2 Z^2}{137^2 \beta^2} \right) \quad (4)$$

$$\chi_0^2 = \left(\frac{\hbar}{p} \frac{Z^{1/3}}{0.468 \cdot 10^{-8} (cm)} \right)^2. \quad (5)$$

When $\mu = 0$ equation (1) is the Rutherford cross section of a point charge.

The total number of multiple scattering events, from equation (1), is given by:

$$\rho \int_0^\infty \sigma(\sigma) d\theta = \int_0^\infty 2\chi_c^2 \frac{\theta}{(\theta^2 + \chi_\alpha^2)^2} d\theta = \frac{\chi_c^2}{\chi_\alpha^2} \equiv \Omega_0 \quad (6)$$

The standard form for the Molière distribution is given by [9] and the projected angle θ_x (that has the same trend of θ_y) follows the distribution described in [9]. In the small angle approximation, using simple geometry consideration, the connection between the mean square of the projected angle in the transverse plane and the spatial angle is obtained:

$$\langle \theta^2 \rangle = 2 \langle \theta_x^2 \rangle. \quad (7)$$

Therefore, the connection between the rms of the space and projected angles is:

$$\theta_{xR} = \frac{\theta_R}{\sqrt{2}} = \frac{\chi_c \sqrt{B}}{\sqrt{2}} \tag{8}$$

where B is the solution of the equation:

$$B - \ln B = b \tag{9}$$

$$b = \ln \frac{\chi_c^2}{\chi_\alpha^2} - 0.154432 = \ln \Omega_0 - 0.154432 \tag{10}$$

Compound extension

This theory is valid for any kind of compounds and mixture, modifying the calculation of χ_c and χ_α ; in this case the basic formulae must be substituted by a proper summation over the constituents.

$$Z_M = \sum_i n_i Z_i, \quad A_M = \sum_i n_i A_i. \tag{11}$$

with Z_i, A_i respectively the atomic number and atomic weights of the molecule or mixture of n_i constituents.

Equation (2) for the calculation of χ_c must be modified as:

$$\chi_c^2 = \sum_i \chi_{ci}^2 = \chi_w^2 \frac{x}{p^2 \beta^2}, \tag{12}$$

where χ_w^2 represents the energy loss independent part.

The generalization of χ_α to a molecule is more complicated. Since the logarithm of the Bessel transform of the cross section, that gives the effective number of events, depends on $\chi_c^2 \ln \chi_\alpha^2$, the equation is [9],[10]:

$$\ln \chi_\alpha^2 = \frac{1}{\chi_c^2} \sum_i \chi_{ci}^2 \ln \chi_{\alpha i}^2 \tag{13}$$

where χ_c^2 and χ_{ci}^2 are defined in equation (12), whereas $\chi_{\alpha i}^2$ are calculated from equations (3-5) with the substitution $Z = Z_i, i = H, O, Z_H = 1, Z_O = 8$ for water.

To complete the theory for the water molecule, one has to take into account the fact that the incident particle is scattered by atomic electrons as well as by the screened Coulomb field of the nucleus [10], which requires to modify equation (13) as follows:

$$\ln \chi_\alpha^2 = \frac{1}{\chi_c^2} \sum_i \chi_{ci}^2 \left(\ln \chi_{\alpha i}^2 - \frac{D_i}{Z_i} \right), \tag{14}$$

where D_i is the Fano correction [11].

Energy loss

Since in realistic hadrontherapy cases the paths of protons in water is very long, the basic equations have to be modified to take into account the energy loss process. Considering that the parameters χ_c and χ_α depend on p, β , the energy loss problem can be solved if one finds the dependence of these quantities on the water thickness x traversed. If we indicate as $p(x)$ and $\beta(x)$ the current values at the

depth x in the target, from equation (12) we have:

$$\chi_c^2 = \chi_w^2 \int_0^x \frac{1}{p(t)^2 \beta(t)^2} dt . \quad (15)$$

where the integral depends on the Range R ; we calculate R with an analytic formulation that we have verified to be accurate for water to a more than 0.5%.

The calculation of χ_α is more complicated and cannot be obtained in closed form; so $\ln \chi_\alpha^2$ is evaluated with the Simpson numerical integration rule because of the smooth behaviour of the integrand. In water, integration steps of 0.5 cm are enough to provide good accuracy.

The lateral displacement

Including the energy loss effects, the general formula for passing from angular to spatial displacements can be derived.

The rms y_M of the transverse displacement on a measuring plane at x due to a layer dt at the depth t is given by $(x-t)\theta_{xR}$, where the angle is given by equation (8), that presents a logarithmic dependence on χ_c , which contains the thickness x (see equations (2, 9)). The physical meaning is that two successive layers act in a dependent manner, since the second layer receives trajectories deflected by the first one. For this reason one usually combines in quadrature the χ_c^2 contributions and multiplies the result for an average value of B . Therefore, the lateral displacement can be written:

$$y_M = \frac{\chi_w \sqrt{B}}{\sqrt{2} p \beta} \left[\int_0^x \frac{(D-t)^2}{\left(1 - \frac{t}{R}\right)^k} dt \right]^{1/2} \quad (16)$$

where x is the layer thickness, $D \geq x$ the detector plane distance and t the depth from the beginning of layer x .

The rms from this equation corresponds to the projection on the measuring plane of the rms θ_{xR} from equation (8) of the Gaussian core of the angular distribution. Therefore, the factor

$$\delta = \frac{y_M}{\theta_{xR}} = \frac{y_M \sqrt{2}}{\chi_c \sqrt{B}} \quad (17)$$

represents the scale factor that allows the passage from the angular to the spatial distribution observed after the passage of a thickness x . The change of variable therefore is

$$\delta = \frac{y}{\theta_x} \rightarrow \theta_x = \frac{y}{\delta} , \quad (18)$$

giving the formula [6]

$$f_M(y) = \frac{1}{\pi \chi_c \delta} \int_0^\Gamma \cos\left(\frac{y\eta}{\chi_c \delta}\right) \exp\left[-\frac{\eta^2}{4} \left(b - \ln \frac{\eta^2}{4}\right)\right] \eta d\eta . \quad (19)$$

Monte Carlo validation

Until this point the Molière basic formulae have been applied to obtain a complete analytical model without free parameters. The results can be directly compared with the same distributions predicted by some MC codes of current use (FLUKA 2011.2c and MCNP6) with all nuclear effects switched off.

FLUKA [12],[13] uses a special transport algorithm, based on Molière's theory of multiple Coulomb

scattering improved by Bethe [14]. MCNP6 instead is based on the full Goudsmit-Saunderson model of multiple scattering as described in [15].

The comparisons have shown that the prediction of our model are fully in agreement with those of FLUKA and in good agreement with MCNP6 [6].

2.2 Nuclear effects

In order to obtain a complete prediction of deposited energy, nuclear interactions have to be taken into account in the proper way, i.e. accounting for the primary protons fluence decrease.

Therefore an additional term is added to describe the interaction of non-primary particles that affects the tails to the distribution; this is particularly relevant when big thicknesses are involved, such as in the case of hadrontherapy (it can be estimated as about 1% per cm of depth). However at therapeutic energies ($E < 300$ MeV), a minor contribution arises also from nuclear reactions that result in the production of secondary particles and heavy recoils.

Tails parametrization

The influence of the secondary reaction products on the lateral energy deposition is evaluated a modified Cauchy-Lorentz distribution [4], [16]:

$$t(y) = \frac{1 - A \exp\left[-\frac{y^2}{2b^2\sigma^2}\right]}{\pi b \left(\frac{y^2}{b^2} + 1\right)} \tag{20}$$

where the three free parameters are the amplitude A , the Half Width Half Maximum (HWHM) b and the variance σ^2 .

Weight factor

At a certain water thickness x , the percentage W_p of protons with incident kinetic energy E_k and range R that have not experienced nuclear interactions, as a function of the traversed thickness, is given by [17]:

$$W_p = \frac{1}{2} \left[1 - \left(\frac{E_k - E_{th}}{m} \right)^f \frac{x}{R} \right] \left[1 + \operatorname{erf} \left(\frac{R - x}{\tau} \right) \right], \tag{21}$$

where erf is the error function, $f = 1.032$, m is the proton mass in MeV, $E_{th} = 7$ MeV is the ^{16}O threshold energy for the (p, p') reaction.

The parameter τ takes into account the range variation due to the straggling along the beam path and can be parametrized as [18]

$$\tau = 0.0179651452 R^t \quad \text{where } t = \begin{cases} 0.9352 & \text{if } R \geq 1 \text{ cm} \\ 1.1763 & \text{if } R < 1 \text{ cm} \end{cases} \tag{22}$$

2.3 Complete model

Combining the nuclear tail parametrization with the electromagnetic core, taking into account the weight factor, the total normalized final distribution for the lateral displacement, can be formulated

as:

$$f(y) = W_p f_M(y) + (1 - W_p) \frac{t(y)}{\int_{-\infty}^{+\infty} t(y) dy}, \quad (23)$$

where $f_M(y)$ is the distribution of equation (19) and W_p is the weight from equation (21). Both $f_M(y)$ and $t(y)$ are normalized to unit area.

The free parameters A , b and σ^2 , have been determined by fitting the complete FLUKA MC lateral displacement distributions, and they are parametrised with Chebyshev polynomials.

During the fit procedure we found that good results were obtained with the variance fixed at the value $\sigma^2 = 1$.

3. Results

The prediction of the complete model has been tested on a real case, comparing the theoretical calculation with both FLUKA simulation with all interactions switched on, and experimental data acquired at the HIT Heidelberg Ion Beam Therapy Center [19].

The comparison is shown in figure 1: we have found that in any case FLUKA predictions agree very well with the model results, and also the agreement with the measurement data is good.

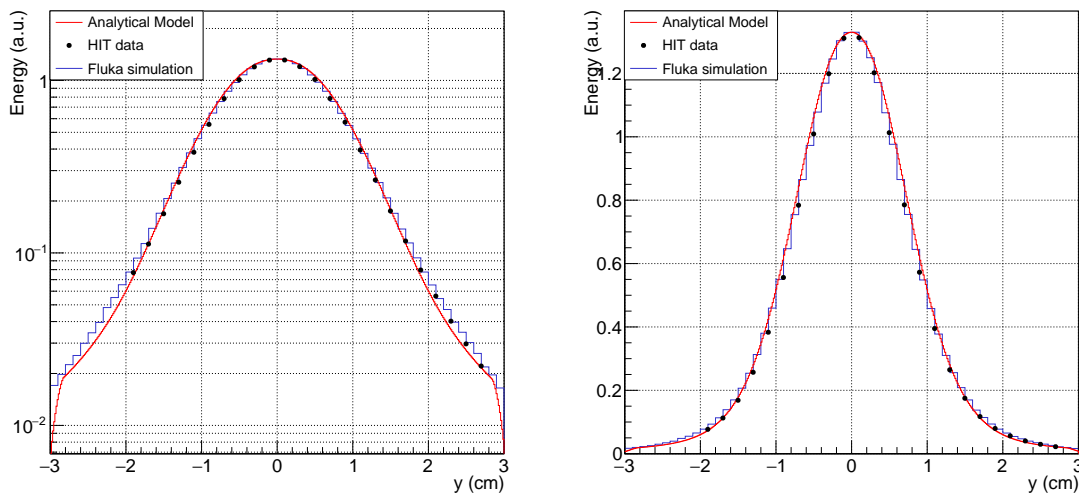


Fig. 1: Comparison between analytical model, FLUKA simulation and experimental data for $E=157.43$ MeV in water at a thickness $z=11.55$ cm in logarithmic (left) and linear (right) scales. The curves are normalized to the maximum of the FLUKA histogram, obtained by fitting the highest dose channels with a smooth curve. In the normalization zone the error of the data points is 2%.

4. Conclusion

A pencil beam model based on Molière theory has been presented, able to reproduce the same lateral energy displacement, as the one predicted by Monte Carlo codes, with the advantage of a much smaller computing time.

The model is fully analytic for the electromagnetic interaction and uses only two parameters to include the nuclear effects in the tail of the lateral displacement.

In perspective, this model can be implemented in research TPS and also extended to other materials, geometries and beam particles of interest in hadrontherapy.

Acknowledgements

We thank Jürgen Debus from HIT and the University Hospital Heidelberg, for granting permission on the usage of HIT data for the comparison.

References

- [1] Frühwirth R., Regler M., *Nucl. Instr. Meth. Phys. Res.* **369** (2000)
- [2] Parodi K., Mairani A., Sommerer F., *J. Radiat. Res.* **54** Suppl 1:i91-6, (2013)
- [3] Bellinzona V. E. *et al.*, *Physica Medica* doi: 10.1016/j.ejmp.2015.05.004 (2015)
- [4] Soukup M. *et al.*, *Phys. Med. Biol.* **50**, 5089-5104 (2005)
- [5] Pedroni E. *et al.*, *Phys. Med and Biol.* **50** 541-61(2005)
- [6] Bellinzona E. V. *et al.*, A model for the accurate computation of the lateral scattering of protons in water, (*under review*)
- [7] Molière G., Mehrfach und Vielfachstreuung, *Z. Naturforsch.* **3a** 78-97 (1948)
- [8] Bethe H. A., *Phys.Rev.***89**, 1256, (1953)
- [9] Scott W.T., *Rev. Mod. Phys.* **35** 231-312 (1963)
- [10] Gottschalk B. *et al.*, *Nucl. Instr. Meth. Phys. Res.* **B74** 467-490 (1993)
- [11] Fano U., *Phys.Rev.* **93** 117-20 (1954)
- [12] Bohlen T.T. *et al.*, *Nuclear Data Sheets* **120**, 211-214, (2014)
- [13] Ferrari A. *et al.*, CERN-2005-10, INFN/TC05/11, SLAC-R-773, (2005)
- [14] Ferrari A. *et al.*, *Nucl. Instr. Meth. Phys. Res.* **B71** 412 (1992)
- [15] Goorley J. T. *et al.*, LA-UR-13-22934 (2013)
- [16] Li Y. *et al.*, *Phys. Med. Biol.* **57** 983-97 (2012)
- [17] Ulmer W, *Rad. Phys. and Chem.* **76** 1089-107 (2007)
- [18] Ulmer W. and Schaffner B., *Rad. Phys. and Chem.* **80** 378-89 (2011)
- [19] Schwaab J. *et al.*, *Phys. Med. Biol.* **56** 7813-27 (2011)

Measurements of secondary particles emitted by ^{12}C , ^4He and ^{16}O ion beams in view of innovative dose profiling technique in Particle Therapy

A. Rucinski^{b,d}, G. Battistoni^g, F. Collamati^{a,b}, E. De Lucia^c, R. Faccini^{a,b}, M. Marafini^{a,b}, I. Mattei^g, S. Muraro^g, R. Paramatti^b, V. Patera^{b,d,e}, D. Pinci^b, A. Russomando^{a,b,f}, A. Sarti^{c,d,e}, A. Sciubba^{b,d,e}, E. Solfaroli Camillocci^a, M. Toppi^c, G. Traini^{a,b}, C. Voena^{a,b}

^a Dipartimento di Fisica, La Sapienza Università di Roma, Roma, Italy ^b INFN Sezione di Roma, Roma, Italy ^c Laboratori Nazionali di Frascati dell'INFN, Frascati, Italy ^d Dipartimento di Scienze di Base e Applicate per Ingegneria, La Sapienza Università di Roma, Roma, Italy ^e Museo Storico della Fisica e Centro Studi e Ricerche "E. Fermi", Roma, Italy ^f Center for Life Nano Science@Sapienza, Istituto Italiano di Tecnologia, Roma, Italy ^g INFN Sezione di Milano, Milano, Italy

Abstract

Hadrontherapy is a technique that uses accelerated charged ions for cancer treatment. The high irradiation precision and conformity achievable during hadrontherapy treatments allows for local tumor control and sparing of the surrounding healthy tissues. Such a high spatial selectiveness requires the development of new dose monitoring techniques.

It has been proved that the beam emits secondary particles in the path to the tumor, namely γ from β^+ emitters, prompt γ from nuclear de-excitation and charged particles, that can be used to monitor Bragg Peak (BP) position and the related dose release.

In this contribution preliminary results obtained in the study on the neutral and charged secondary particles produced by ^{12}C , ^4He and ^{16}O ion beams of therapeutical energy impinging on PMMA phantoms will be presented. The data acquisition have been performed at GSI (Darmstadt, Germany) and HIT (Heidelberg, Germany) facilities. A correlation between the secondary generation regions and BP position will be shown and the design of a monitoring device exploiting all the secondary information will be outlined.

1. Introduction

Currently about 50 radiotherapy centers using proton and/or carbon ion beams for treatment of solid tumors are in operation around the world and several others are under construction or in the planning phase [1]. The benefit from application of ion pencil beams for radiotherapy is related to (i) their favorable, inversed in comparison with photons dose deposition profile (Bragg Peak - BP), (ii) reduced scattering due to the application of active scanning technique for beam delivery and (iii) increased in comparison to photons Radiobiological Effectiveness (RBE) resulting from high Linear Energy Transfer (LET) of those beams [2]. Recent research discussions consider the use of Helium and Oxygen beams for radiotherapy and few synchrotron based hospital centers offer those ions for research, mainly for the radio-biological studies [3]. Helium beams are considered as a compromise between the high LET of Carbon ions and low LET in plateau region of Protons, which could be an optimal solution for the treatment of radio-resistant tumors of pediatric patients [4]. The increased LET characteristic of Oxygen beams, exceeding the LET of Proton, Helium and Carbon beams, is expected to improve efficiency of radio-resistant tumor treatments.

Independently of the ion beam used for treatment, major drawbacks of scanned pencil beam delivery (typical longitudinal profile up to teens of millimeters) in comparison with a passive, broad beam approach, are related to the high sensitivity of this technique to the patient mis-positioning and anatomy

variations. For this reason, one of the crucial research aspects of hadrontherapy is a development of on-line monitoring techniques allowing real time control of the beam range and dose released per raster point. The presence of such techniques in clinical routine would potentially allow for a reduction of the treatment planning margins and/or application of unconventional irradiation fields, which normally cannot be used due to the proximity of critical organs at risk located after the distal fall-off of the BP [5]. So far, the most established monitoring technique for ion therapy is based on the detection of the back-to-back photons produced by the annihilation of positrons coming from β^+ emitters generated by the beam interaction with the patient, typically using Positron Emission Tomography (PET). However, the obtained information is indirect, and the signal level is lower in comparison with PET signals known from clinical diagnostics, which indicates a need for investigation on other methods [6]. Recent developments focus on the detection of particles produced by the beam interaction in the target, in particular charged particles, originating from the projectile and target fragmentation and prompt photons from nucleus de-excitation [7, 8].

The measurements presented here were performed with PMMA target and confirm substantial photon and charged secondary production from ^{12}C , ^4He and ^{16}O beams at 90° and 60° with respect to the primary beam direction. This information is required to calibrate and operate the multimodal dose profile monitor which is currently assembled in our group and will be installed in the Centro Nazionale per l'Adroterapia Oncologica (CNAO) in Pavia, Italy. The monitor system will be composed of a two PET heads module, for online monitoring of the β^+ emitters production, and of a range monitor detector able to detect, track and measure energy of both secondary charged particles and prompt gammas (Fig. 1 right).

2. Experimental setup

The test beam was performed in the experimental cave of Heidelberg Ion Beam Therapy Center (HIT) and the obtained results were compared with the previously published results of the experiments performed with Carbon beams at 80 MeV/u in Catania, IT [9, 10] and 220 MeV/u in Darmstadt, DE [7, 8]. At HIT several millions of collisions of Helium (102, 125 and 145 MeV/u), Carbon (120, 160, 180, 220 MeV/u) and Oxygen (210, 260, 300 MeV/u) beams with PMMA targets were registered and secondary production was measured at large angles with respect to the primary beam direction (90° and 60°). Those angular configurations are considered as optimal for dose monitoring as the spatial resolution in the fragment emission point improves with the emission angle, even if the emission statistics worsens and multiple scattering of particles inside the target increases at the large angles with respect to the primary beam direction [7].

The target box with a $4.8 \times 4.8 \text{ cm}^2$ face orthogonal to the beam line was positioned at the beam isocenter $\sim 1 \text{ m}$ away from the beam nozzle. The primary beam rate impinging the PMMA target was measured with a 0.2 cm thin plastic scintillator (Start Counter, SC) read out by two opposite Hamamatsu H10580 photomultiplier tubes. The angular distribution of the secondary particles produced in the target were studied by three isocentrically positioned detectors mounted on a movable support: (i) 0.1 cm-thick plastic scintillator (LTS), (ii) 21 cm-long drift chamber (DC) and (iii) an array of four LYSO $1.5 \times 1.5 \times 12 \text{ cm}^3$ crystals [9, 10, 12]. The primary energy of the beam and PMMA target length (7.65, 10.0, 12.65 cm) were selected in such a way, that the BP position was in-line with the center of LTS, DC and LYSO detectors. For ^{12}C beam PMMA target at one length (10 cm) was used. The DC [11], consisting of six alternated horizontal and six vertical wire layers, was used for three dimensional reconstruction of the charged secondaries tracks [7]. The readout and performances of the DC as well as the tracking algorithm and DC calibration have been reported elsewhere [10]. The sketch of the experimental setup is shown in Fig. 1 (left).

Time and charge information from all described above detectors have been used to select prompt

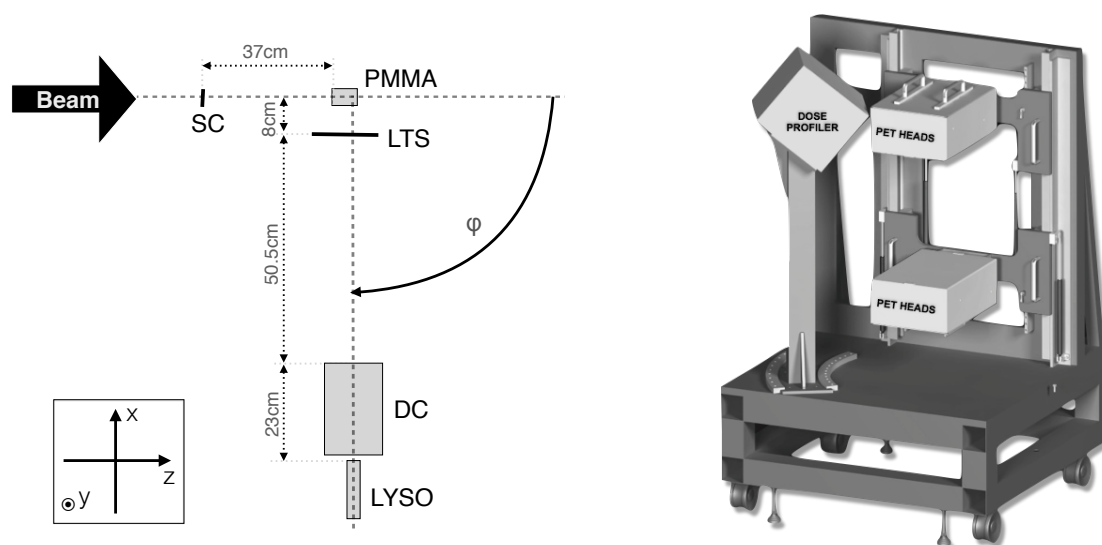


Fig. 1: **LEFT:** Experimental setup at HIT. Beam - primary beam, SC - start counter, PMMA - target, LTS - plastic scintillator, DC - drift chamber, LYSO - matrix of four LYSO crystals, φ - angular configuration of movable support with LTS, DC and LYSO detectors (90° and 60° with respect to the primary beam). The coordinate system is plotted in the box on the bottom left side of the figure. BP was expected within the PMMA target at the intersection of the dashed lines for ^{12}C at 220 MeV/u, ^4He and ^{16}O beams. **RIGHT:** A sketch of the multi-modal in-beam dose monitor able to detect at the same time, back-to-back gammas from β^+ annihilation (PET HEADS, not covered in this contribution), charged secondary particles emerging from the patient and prompt gammas with energies higher than 1 MeV (DOSE PROFILER).

gamma and charged secondaries. The lateral profile of the primary beams (FWHM) was ~ 1 cm. The trigger was performed by requiring SC and LYSO coincidence within 100 ns. The maximal beam rate was of few MHz whereas the maximal trigger rate was ~ 10 kHz.

3. Preliminary results

3.1 Charged secondaries

The charged secondary particles were selected by exploiting the DC information together with the energy released in the LYSO detector. In addition the kinetic energy of the particle was estimated from Time of Flight (TOF) calculated as the time difference between LTS and LYSO signals. Figure 2 (left) shows the number of DC cells (N_{hit}) fired by charged secondary particles produced in the 90° setup configuration by the 220 MeV/u Carbon beam. Most of the events cross all the DC planes, which appears as a peak for $N_{hit}=12$. The charged particles tracks were reconstructed requiring at least eight cells fired in the DC.

The particle identification was performed by selecting the events on the plot of charge released in LYSO as a function of TOF of the particle. A non negligible production of charged fragments at large angles is observed for all beam types. The emission shape reconstructed from the tracked particles can be correlated to the beam entrance window and the Bragg Peak position as it was already discussed elsewhere [7]. In Fig. 2 (right) the reconstructed emission positions of the charged fragments projected along the beam direction (longitudinal profile; y-z plane) for the Carbon beams of all the exploited energies is shown for 90° setup configuration.

The reconstructed emission position projected perpendicularly to the beam direction (lateral pro-

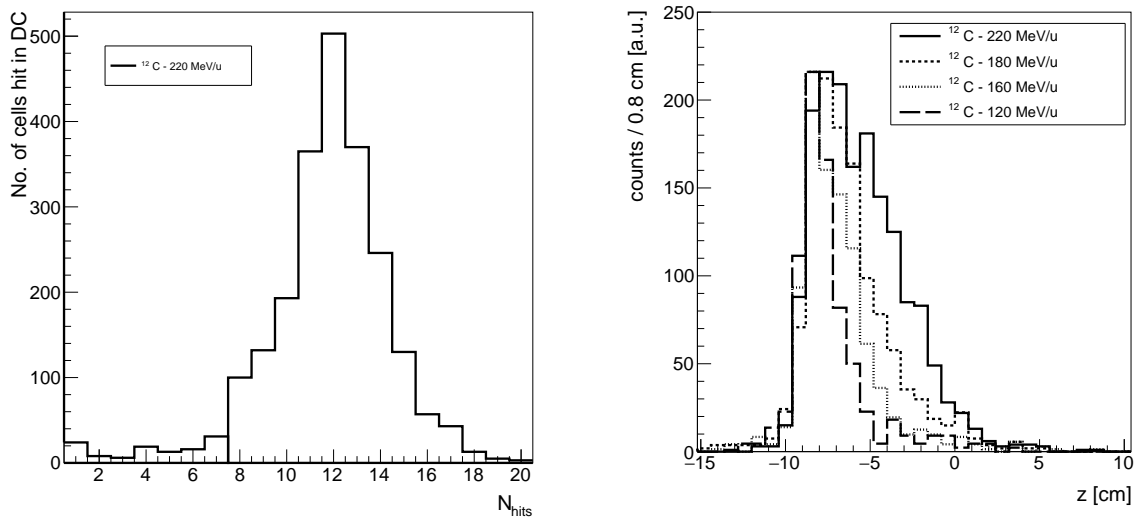


Fig. 2: **LEFT:** Distribution of the number of cells hit in the DC (N_{hit}) for secondary charged particles emitted from the interactions of ^{12}C beams with the PMMA target. The peak at $N_{hit}=12$ is an indication of a charged particle that went through all the DC planes. **RIGHT:** Emission profiles of secondaries produced by Carbon beam at different energies. The PMMA target (10 cm long) ranged from $z=-9$ cm (beam entrance window) to $z=+1$ cm with BP position for ^{12}C at 120 MeV, 160 MeV, 180 MeV, and 220 MeV approximately at $z=-6$ cm, $z=-4$ cm, $z=-3$ cm, and $z=0$ cm, respectively.

file; x-y plane) is a convolution of the transverse profile of the primary beam (spot size), multiple scattering (MS) of the fragments in the PMMA target and DC tracking resolution, which has been studied in detail elsewhere [7]. The lateral profile can be used to evaluate the MS of the fragments inside the target knowing the remaining two contributions a priori.

3.2 Prompt- γ

Prompt- γ events were selected requiring less than three fired DC cells. The bi-dimensional distribution of energy deposited in the LYSO crystal for these events as a function of their TOF was used to select the prompt photons. An example of such a distribution for ^{12}C beam at 220 MeV/u is shown on Fig. 3 (left).

The prompt photon signal corrected by the slewing effect induced by the front-end electronics fixed voltage threshold is a vertical band at 0 ns. The LYSO intrinsic noise is visible as the horizontal low energy band, while the diffused cloud is mainly due to neutrons at ToF values greater than of prompt photons. The number of prompt photons has been extracted from an unbinned maximum likelihood fit to the time pull distribution for each energy bin and energy spectra of the prompt gamma emitted from all the beams were obtained.

In Fig. 3 (right) the energy spectrum for the prompt- γ emitted in the interaction of the ^{12}C beam with the PMMA target at 90° is shown. The observed spectra are given by the sum of the raw spectra corresponding to the nuclear de-excitation of both projectile and target fragments produced in the interaction of the ion beam with the PMMA target. While in Helium and Carbon beam interactions the target de-excitation is dominant, in the study of Oxygen spectral characteristics a non negligible contribution from projectile fragmentation was observed. Helium and Carbon energy spectra are in good agreement with the experimental results obtained with 80 MeV/u Carbon beam [9] and with 220 MeV/u Carbon beam [8].

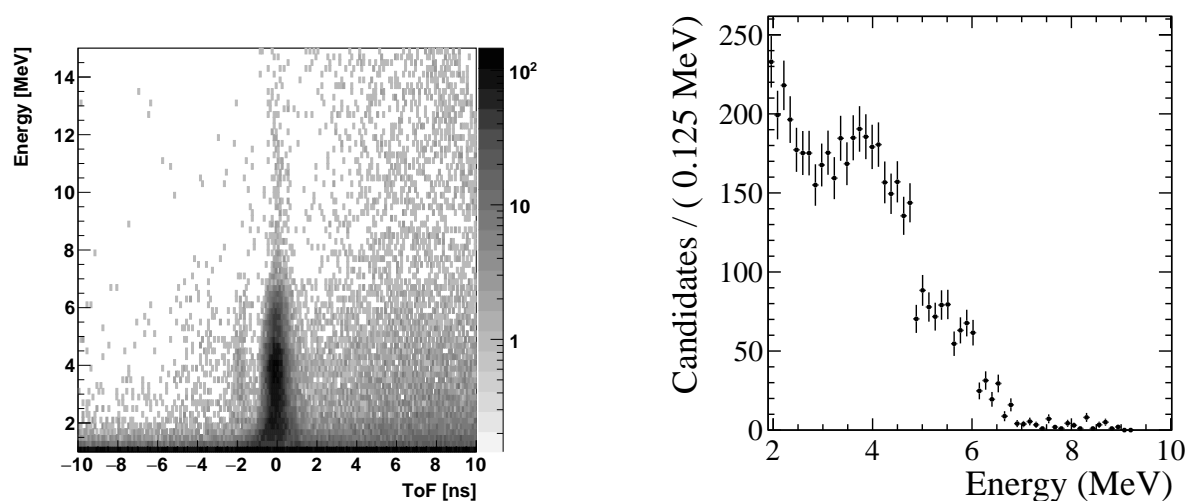


Fig. 3: **LEFT** Energy deposited in the LYSO crystal as a function of TOF. Vertical band at 0 ns corresponds to prompt- γ events. **RIGHT:** Energy spectrum of prompt- γ for ^{12}C beam at 220 MeV.

4. Dose Profiler - charged secondary on-line monitor

The non negligible production of charged secondary particles emitted by all the investigated primary beam interaction with a PMMA target allows to exploit the correlation of charged secondary protons emission profile with position of the primary beam for monitoring of the dose release in ion beam therapy.

For this purpose a tracking device, "Dose Profiler" (Fig. 1 right), made out of a scintillating fibers system, coupled to a calorimeter and realized by means of LYSO crystals matrix for measurement of particles energy was designed and is currently under construction. The materials of the detector were selected minimizing the charged particles multiple scattering in the detector. The Dose Profiler dedicated to track protons generated by the primary beam inside the patient consists of six planes of squared ($0.5 \times 0.5 \text{ mm}^2$) scintillating fibers (2 orthogonal layers in each plane) connected to silicon photo multipliers (SiPM) and read out by Basic32 front-end boards. The secondary proton detection and tracking efficiency is expected to be above 90%.

Depending on the position of the tumor in the patient, before reaching the detector the particles have to travel few centimeters inside the patient losing their energy. In order to reduce the impact of multiple scattering, the device design maximize the geometrical acceptance in order to improve statistics collected for a given dose to the patient.

5. Conclusions

During the test beam at HIT several millions of collisions of ^{12}C , ^4He and ^{16}O beams with a PMMA target were collected exploring the range of energies that is of interest for particle therapy. The experiment confirms an evidence of a non negligible secondary charged and prompt- γ production at 60° and 90° with respect to the primary beam, supporting the concept of on-line dose monitoring with those secondaries in ion beam therapy. The correlation of charged fragments emission profile with the position of Bragg Peak is possible with Helium, Carbon and Oxygen beams at all investigated energies. The development of a prototype monitoring system "Dose Profiler" dedicated for tracking of charged secondary particles on-line with a purpose of emission profile reconstruction is on the advanced stage. First tests, calibration and installation of the device in the treatment room of Centro Nazionale di Adroterapia

Oncologica (CNAO) is foreseen in 2016.

References

- [1] M. Jermann, *Int J Particle Ther.*, available at the URL <http://www.theijpt.org/doi/pdf/10.14338/IJPT-15-00013>.
- [2] J. S. Loeffler, M. Durante, *Nat Rev Clin Oncol*, <http://dx.doi.org/10.1038/nrclinonc.2013.79>.
- [3] C. Kurz *et al.*, *Phys. Med. Biol.*, <http://iopscience.iop.org/article/10.1088/0031-9155/57/15/5017>.
- [4] H. Fuchs *et al.* *Radiotherapy and Oncology*, [http://dx.doi.org/10.1016/S0167-8140\(15\)30498-9](http://dx.doi.org/10.1016/S0167-8140(15)30498-9).
- [5] A.C. Knopf and A. Lomax *Phys. Med. Biol.*, <http://iopscience.iop.org/article/10.1088/0031-9155/58/15/R131/pdf>.
- [6] K Parodi *et al.*, *IJROBP*, <http://dx.doi.org/10.1016/j.ijrobp.2008.02.033>.
- [7] L. Piersanti *et al.* *Phys. Med. Biol.*, available at the URL <http://iopscience.iop.org/article/10.1088/0031-9155/59/7/1857/pdf>.
- [8] I Mattei *et al.* *Accepted for publication in JINST*
- [9] C Agodi *et al.* <http://iopscience.iop.org/article/10.1088/1748-0221/7/03/P03001/pdf>.
- [10] C Agodi *et al.* <http://iopscience.iop.org/article/10.1088/0031-9155/57/18/5667/pdf>.
- [11] Z Abou-Haidar *et al.*, <http://iopscience.iop.org/article/10.1088/1748-0221/7/02/P02006/pdf>.
- [12] C. Agodi *et al.*, *Nucl. Instrum. Methods Phys. Res. B*, <http://arxiv.org/pdf/1202.1676v2.pdf>.

Modelling the induction of cell death and chromosome damage by therapeutic protons

M.P. Carante ^{1,2} and F. Ballarini ^{1,2,*}

¹ University of Pavia, Physics Department, Pavia, Italy

² INFN, Sezione di Pavia, Pavia, Italy

Abstract

A two-parameter biophysical model called BIANCA (Biophysical ANalysis of Cell death and chromosome Aberrations), which assumes a pivotal role for DNA cluster damage and for “lethal” chromosome aberrations, was applied to calculate cell death and chromosome aberrations for normal and radio-resistant cells along a 62-MeV eye melanoma proton beam. The yield of DNA “Cluster Lesions” and the probability for a chromosome fragment of not being rejoined with any partner were adjustable parameters. In line with other works, the beam effectiveness at inducing both biological endpoints was found to increase with increasing depth, and high levels of damage were found also beyond the dose fall-off, due to the higher biological effectiveness of low-energy protons. This implies that assuming a constant RBE along the whole SOBP, as is currently done in clinical practice, may be sub-optimal, also implying a possible underestimation of normal tissue damage. Furthermore, the calculations suggested that for higher fractional doses, like those delivered in hypo-fractionation regimes, the relative increase in effectiveness along the SOBP may be less pronounced than for lower fractional doses.

1 Introduction

Worldwide, the number of new cases of cancer is expected to increase from 14 million in 2012 to about 22 million over the next two decades [1]. In Europe, cancer is a leading cause of morbidity and mortality, where 3.45 million new cancer cases and 1.75 million deaths from cancer have been estimated for 2012 [2]. About half of the patients diagnosed with cancer undergo radiotherapy. While the most frequently adopted treatment modalities use high energy (~MeV) photon or electron beams, alternative modalities are becoming increasingly important. One example is provided by treatments using proton or carbon ion beams. While the main advantage of carbon ions is a higher biological effectiveness, which makes them particularly suitable to treat those tumours that are resistant to conventional radiotherapy, the rationale of using protons mainly relies on the ability of these particles to reduce the dose to normal tissues, thanks to the dose localization in the (Spread-Out) Bragg peak, or SOBP [3]. In addition to different types of tumors, it is worth mentioning that protons can also be used to treat some non-cancer diseases, such as arteriovenous malformations [4]. According to the Particle Therapy Co-operative Group [5], 49 proton therapy centers were operating and 32 were under construction in June 2015.

Protons are usually considered low-LET radiation, and a constant Relative Biological Effectiveness (RBE) of 1.1 is generally applied in clinics. However, both *in vitro* and *in vivo* studies

* Corresponding author (francesca.ballarini@unipv.it)

indicate that proton effectiveness tends to increase with decreasing energy, that is increasing LET [6]. This implies an increase of effectiveness with depth along the SOBP, as well as an extension of the biologically effective range. Furthermore, the RBE depends not only on the particle energy, but also on many other factors including dose, dose-rate, cell type and biological endpoint. For instance, both *in vitro* and *in vivo* data show a significant RBE increase for lower fractional doses [7], especially for cells and tissues with low α/β ratio. It should also be considered that, although the main endpoint of interest for tumor cells is cell death, other endpoints (e.g. mutations, non-lethal chromosome aberrations...) might be relevant for normal tissues.

Although clinical results do not indicate that the use of a constant RBE is incorrect, one should also consider that no trials specifically targeted RBE variations. Moreover, tighter treatment margins may increase the importance of taking into account such variations [6]. Applying a constant RBE of 1.1 may lead to an underestimation of the damage to normal tissues, especially for treatments involving organs at risk just beyond the tumor, such as the retina for eye tumors. On the other side, the currently available RBE data might be insufficient to support a change in clinical practice [6]. Incorporating variations in biological effectiveness without directly considering the RBE may be an alternative strategy: for instance, it has been suggested that LET distributions in the patient can be used to guide treatment plan optimization [8].

In this framework, a biophysical model of chromosome aberrations [9-11] and cell death [12-15] developed at the University of Pavia and INFN-Pavia, Italy, was applied to AG01522 normal cells and V79 radio-resistant cells exposed at different depth positions along a 62-MeV proton beam used to treat ocular melanoma at INFN-LNS in Catania, Italy [16]. The model, which is called BIANCA (BIophysical ANalysis of Cell death and chromosome Aberrations), assumes that DNA cluster damage can lead to chromosome aberrations and that some aberration types lead to cell death. The fact that the model does not require the use of (experimental) RBE values, which can be a source of uncertainties, represents a potential advantage of this approach. Moreover, the capability of calculating the induction of different types of chromosome aberrations, some of which are related to the risk to normal tissues [17], may be of help for estimating normal tissue damage.

2 The model

The model is based on the following assumptions: 1) radiation induces DNA “Cluster Lesions” (CLs), and each CL produces two independent chromosome fragments; 2) two chromosome fragments can be rejoined only if their *initial* distance is smaller than a threshold distance d , leading to chromosome aberrations in case of rejoining with an incorrect partner; 3) dicentrics, rings and large deletions lead to clonogenic cell death, i.e. the loss of the cell ability to give rise to a colony. Since the characterization of the ‘critical’ DNA damage(s) that can lead to chromosome aberrations and cell death is still an open question in radiobiology, the Cluster Lesions mentioned above were not defined *a priori*, and the mean number of CLs per Gy and per cell was considered as an adjustable parameter. A previous work [15], in which CL yields for different radiation qualities have been compared with yields of DNA fragments of different sizes, has suggested that clusters of DNA double-strand breaks (DSBs) at the kilo-base-pair scale (which corresponds to geometrical distances in the order of some tens nanometres in the chromatin fibre), possibly in addition to other levels of clustering, may play a relevant role.

Assumption 2) reflects the fact that chromosome fragment rejoining is distance-dependent. In particular, a recent work has suggested the existence in the cell nucleus of “repair centres”, where DSBs should migrate after travelling 1-2 μm [18]. While in previous works (e.g., [15]) the threshold distance d has been considered as an adjustable parameter, in the present work d was set equal to the mean distance between two adjacent chromosome territories (which resulted to be 3.0 μm for AG cells and 3.6 μm for V79 cells, see below), basing on the idea that repair mainly takes place in small

channels separating adjacent chromosome domains [19]. According to this approach, d is fixed *a priori* and depends on the specific features of the considered cell nucleus (i.e., nucleus shape and dimensions and number of chromosomes). This allowed reproducing experimental yields of chromosome aberrations not only for the so-called “lethal aberrations” (i.e. dicentrics plus rings plus deletions), but also for each single aberration category including deletions, which previously were underestimated. While in previous works a chromosome fragment having at least one potential partner for rejoining (that is, at least another fragment within the threshold distance d) has been assumed to undergo rejoining with 100% probability, in the present work a more realistic scenario was considered where a fragment has a certain probability f of remaining un-rejoined, even if one or more potential “partners” are available within d . f was considered as a cell-line-specific parameter, to be adjusted *a posteriori* by comparison with experimental dose-response curves.

Assumption 3) derives from the relationship between chromosome aberrations and cell death shown by many works available in the literature. In particular, for AG1522 normal human fibroblasts exposed to X-rays, Cornforth and Bedford [20] found a one-to-one relationship between the mean number per cell of lethal aberrations and $-\ln S$, where S is the fraction of surviving cells. According to another work, an analogous relationship may hold for V79 cells as well [21].

Like in previous works, cell nuclei were modelled as cylinders, with elliptical base for AG cells (major axis: 20 μm ; minor axis: 10 μm), and circular base for V79 cells (radius: 6 μm). The nucleus thickness was 4 μm for AG cells, 6 μm for V79 cells. A discussion on these choices can be found elsewhere [15]. Each interphase chromosome territory (i.e., the intranuclear region occupied by a chromosome during most of the cell cycle) was represented as the union of adjacent cubic voxels of 0.2 μm side, to obtain chromosome territories with volume proportional to their DNA content. More details on the construction of chromosome territories can be found in [13]. Within the cell nucleus volume, the various CLs were distributed uniformly for X-rays, and along segments parallel to the cylinder axis for (low-energy) protons. A detailed description of this part of the simulation can be found elsewhere [13,14].

The subsequent simulation steps consisted of: identification of the chromosome and the chromosome-arm that was hit by each CL; rejoining of chromosome fragments within the threshold distance d ; scoring of dicentrics, rings and large deletions, where “large” means larger than 3 Mbp [20]; calculation of the corresponding surviving fraction. The repetition for different cells (i.e., different runs of the code) provided statistically-significant yields of chromosome aberrations and cell

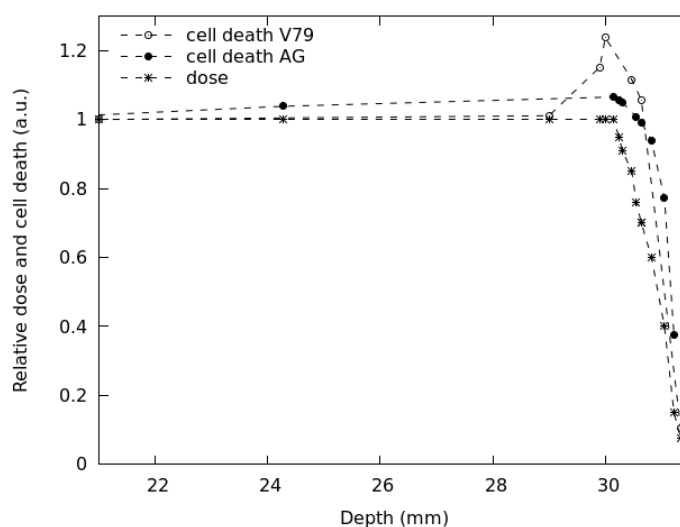


Fig. 1: Relative dose (asterisks) and relative fraction of inactivated cells for AG01522 (full circles) and V79 (empty circles) cells at different depth positions. The lines are simply guides for the eye.

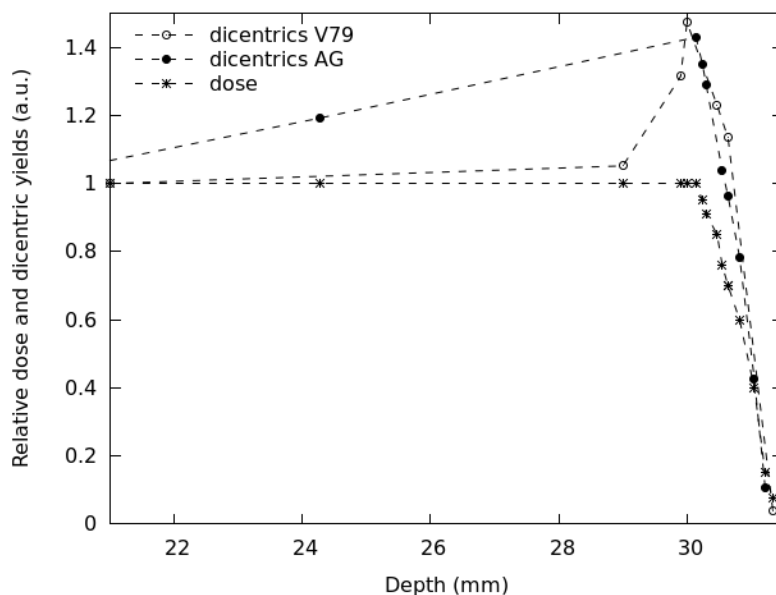


Fig. 2: Relative dose (asterisks) and relative dicentric yields for AG01522 (full circles) and V79 (empty circles) cells at different depth positions. The lines are simply guides for the eye.

death after a given dose, and the repetition for different doses provided simulated dose-response curves directly comparable with experimental data.

3 Calculation of cell death and chromosome aberrations for a eye-melanoma proton beam

Following the reproduction of cell survival curves in previous works [13-15], in the present work the model was applied to investigate the depth- and dose-dependence of the Catania beam effectiveness, both in terms of cell death and in terms of chromosome aberrations. For different depths of the proton SOBP dose profile reported in [16], figure 1 reports calculated relative fractions of inactivated cells assuming a dose of 2 Gy in the plateau region, together with the relative dose. “Relative” means that the various quantities were normalized with respect to the proximal position. With respect to the experimental work considered for comparison, the simulations allowed predicting AG01522 cell death also for additional positions, with particular attention on the dose fall-off region that can be critical for normal tissue damage. Furthermore, the model allowed predicting cell death also for V79 cells, which have not been investigated in the experiments.

Consistent with the experimental data reported in [16] and with other works available in the literature (e.g., [7]), the beam effectiveness was found to increase with depth along the plateau, and high levels of cell death were found also beyond the dose fall-off. For instance at ~31 mm, where the physical dose was about 40% of the proximal dose, the fraction of AG01522 inactivated cells was almost 80% with respect to the proximal position. This can be explained taking into account that, as protons slow down, their LET increases, leading to a higher biological effectiveness. Interestingly, the increase in biological effectiveness was different for the two considered cell types: while AG01522 cells tended to show a continuous increase along the whole plateau, for V79 cells the effectiveness remained basically flat for most of the plateau, but increased sharply in the distal region. This kind of behavior for V79 cells is consistent with the characteristics of this cell line – and, more generally, cells

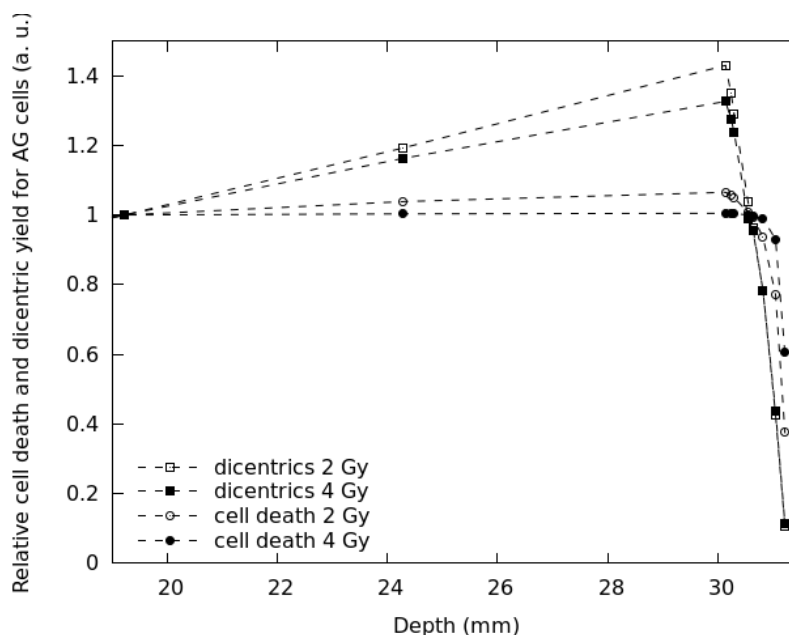


Fig. 3: Relative fraction of inactivated cells (circles) and relative dicentric yields (squares) for AG01522 cells, assuming a plateau dose of 2 Gy (empty symbols) or 4 Gy (full symbols). The lines are simply guides for the eye.

with a low α/β ratio -, which is rather radio-resistant at low LET but tends to become particularly sensitive to LET variations when the LET increases.

Figure 2 reports predicted relative yields of chromosome aberrations for different depth positions along the same dose profile, again assuming a dose of 2 Gy in the plateau region; the relative dose already shown in figure 1 is reported as well. Among the various chromosome aberration types, the attention was focused on dicentrics, since dicentric yields are considered as representative of the yields of reciprocal translocations, which can be related to cell conversion to malignancy [17] and thus can help evaluating the damage to normal tissues.

Like for cell death, also for chromosome aberrations the beam effectiveness increased with depth along the plateau, and high aberration yields were found also beyond the dose fall-off. Moreover, AG01522 cells showed a continuous increase in the yields of dicentrics along the whole plateau, whereas for V79 cells the dicentric yield remained flat along most of the plateau, and showed a sharp increase in the distal region. For both cell types, the increase in chromosome aberrations with depth was more pronounced than the increase in cell killing: dicentrics in the distal region were higher by a factor ~ 1.5 with respect to the proximal region for both cell types, whereas cell death increased by a factor that was less than 1.3 for V79 cells, and less than 1.1 for AG01522 cells. This is consistent with many experimental observations, and is a typical example of how the beam effectiveness can depend on the considered biological endpoint.

Predictions of cell death and chromosome aberrations were also performed assuming different plateau doses, which can be interesting for hyper- or hypo-fractionation regimes. Figures 3 and 4 report the relative fraction of inactivated cells and the relative mean number of dicentrics per cell for AG01522 and V79 cells, respectively, calculated assuming a plateau dose of 4 Gy (full symbols). For comparison, the corresponding results for 2 Gy (empty symbols) are also shown. For both endpoints and both cell lines, increasing the physical dose from 2 to 4 Gy in the plateau reduced the increase in biological effectiveness along the plateau itself. This is consistent with the well known dose-dependence of RBE, which tends to become lower at higher doses and *vice-versa*. However, for V79

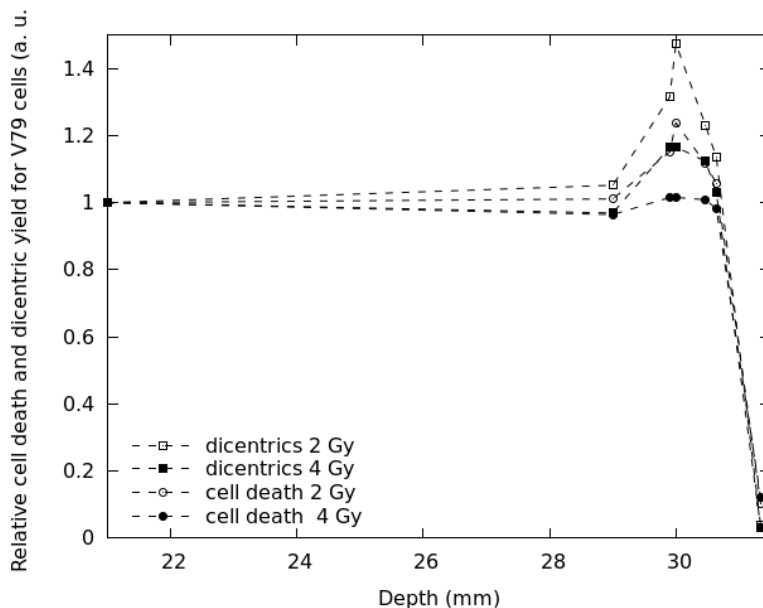


Fig. 4: Relative fraction of inactivated cells (circles) and relative dicentric yields (squares) for V79 cells, assuming a plateau dose of 2 Gy (empty symbols) or 4 Gy (full symbols). The lines are simply guides for the eye.

cells this effect was more pronounced than for AG01522 cells. This can be explained taking into account that V79 photon survival curves are characterized by a lower α/β ratio and thus a more pronounced “shoulder”, which implies a higher variation of effectiveness with dose. Concerning the fall-off region, a peculiar behavior, inverse with respect to the plateau region, was found for cell death in AG01522 cells, for which the increase in effectiveness at inducing cell death was more pronounced at the higher doses with respect to the lower doses. This issue, which is under investigation, might be related to the small shoulder that characterizes AG01522 photon survival curves.

4 Conclusions

A two-parameter biophysical model called BIANCA, which assumes a pivotal role for DNA cluster damage and for “lethal” chromosome aberrations, was applied to calculate cell death and chromosome aberrations for normal and radio-resistant cells along a 62-MeV eye melanoma proton beam. In line with other works, the beam effectiveness at inducing both biological endpoints was found to increase with increasing depth and high levels of damage were found also beyond the dose fall-off, due to the higher biological effectiveness of low-energy protons. This implies that assuming a constant RBE along the whole SOBP, as is currently done in clinical practice, may be sub-optimal, also implying a possible underestimation of normal tissue damage. Furthermore, the calculations suggested that for higher fractional doses, like those delivered in hypo-fractionation regimes, the increase in effectiveness may be less pronounced. More generally, considering the uncertainties that affect the currently available RBE data, this work may be regarded as a starting basis for future characterizations of therapeutic hadron beams without making use of RBE. Of course, before becoming of practical use, the model/code needs to be further refined (e.g., extending it to other cell lines) and “coupled” to a radiation transport code and/or a Treatment Planning System.

Acknowledgements

The authors wish to thank K. Prise and G. Schettino for useful discussions.

References

- [1] B. W. Stewart and C. P. Wild (Eds.), World Cancer Report, World Health Organization, Lyon (2014).
- [2] J. Ferlay *et al.*, *Eur. J. Cancer* **49** (2013) 1374.
- [3] M. Durante and J.S. Loeffler, *Nat. Rev. Clin. Oncol.* **7** (2010) 37.
- [4] C. Bert *et al.*, *Med. Phys.* **39** (2012) 1716.
- [5] <http://www.ptcog.ch/>
- [6] H. Paganetti and P. van Luijk, *Semin. Radiat. Oncol.* **23** (2013) 77.
- [7] B.G. Wouters *et al.*, *Radiat. Res.* **146** (1996) 159.
- [8] C. Grassberger and H. Paganetti, *Phys. Med. Biol.* **56** (2011) 6677.
- [9] A. Ottolenghi *et al.*, *Adv. Space Res.* **27** (2001) 369.
- [10] F. Ballarini and A. Ottolenghi, *Radiat. Environ. Biophys.* **43** (2004) 165.
- [11] F. Ballarini *et al.*, *New J. Phys.* **10** (2008), 075008, <http://www.njp.org>
- [12] F. Ballarini, *J. Nucleic Acids* (2010), doi:10.4061/2010/350608
- [13] F. Ballarini *et al.*, *Radiat. Res.* **180** (2013) 307.
- [14] F. Ballarini *et al.*, *Radiat. Environ. Biophys.* **53** (2014) 525.
- [15] M.P. Carante *et al.*, *Radiat. Environ. Biophys.* **54** (2015) 305.
- [16] P. Chaudhary *et al.*, *Int. J. Radiat. Oncol. Biol. Phys.* **90** (2014) 27.
- [17] T. Rabbits, *Nature* **372** (1994) 143.
- [18] T. Neumaier *et al.*, *PNAS* **109** (2012) 443.
- [19] J.M. Bridger *et al.*, *J. Cell Sci.* **111** (1998) 1241.
- [20] M. Cornforth and J. Bedford, *Radiat. Res.* **111** (1987) 385.
- [21] A.V. Carrano, *Mutat. Res.* **17** (1973) 341.

GDR in Radiotherapy Treatment Fields with 18 MV Accelerators

R. Martín-Landrove¹, J. Dávila¹, H. R. Vega-Carrillo², M. T. Barrera³, A.J. Kreiner⁴, F. Pino³, H. Barros³, E. D. Greaves³ and L. Sajo-Bohus^{3}*

¹Universidad Central de Venezuela and Física Médica C. A., Caracas, Venezuela

²Universidad Autónoma de Zacatecas, Unidad Académica de Estudios Nucleares, C. Ciprés 10, Fracc. La Peñuela, 98068 Zacatecas, Zac. México

³Universidad Simón Bolívar, Nuclear Physics Laboratory, Sartenejas, Caracas, Venezuela

⁴Departamento de Física, CNEA, Buenos Aires, Argentina. Escuela de Ciencia y Tecnología, Universidad Nacional de San Martín, San Martín, Argentina y CONICET, Argentina.

* Visiting Professor at the University of Padova, Italia

Abstract

Giant dipole photo-nuclear reactions generated during Linac radiotherapy are of concern due to the undesirable neutron dose delivered to patients. Nuclear track methodology provides an estimation of gradients of photo-neutrons fields in radiotherapy treatments for 18 MV linear accelerators and it revealed an unexpected behaviour around isocenter. Enhancement effects are observed on absorbed dose due to both scattered photo-neutrons and (γ,n) reactions. Thermal neutrons can give a dose boost if the tumour is loaded with ^{10}B and a new BNCT approach combined with the standard photon field is proposed.

1 Introduction

Energetic gamma rays or bremsstrahlung photons interacting with highly deformed nuclei produce photo-neutrons mainly related to high-frequency collective excitation. Photo-neutrons energy window is defined by reaction mechanisms and for a given energy window, nucleons and mostly neutrons, break free during photo-nuclear and electro-nuclear reactions. Photons impinging on heavy targets such as tungsten, lead and iron produce photo-neutrons with a well-established spectrum and in that sense, Liu et al. [1] reported giant-dipole-resonance photo-neutrons (GRN) produced by a clinical medical accelerators (Varian Clinac 2100C/2300C). Photo-neutron contributions produce an additional gamma-radiation dose delivered to the patients during radiation treatment. It is expected that the neutron dose is not negligible and it should be in principle determined for every single radiotherapy facility working with clinical linear accelerators working at operating potentials above 10 MV. A proper estimation of the in-field contribution to the absorbed gamma dose, which is the dominant one, requires an adequate knowledge of the neutron spectrum. Simulations by Monte Carlo methods provide information on expected photo-neutron production, neutron spectrum and diffusion in materials under realistic geometries related to patient, accelerator material and accessories. For practical reasons the choice for passive detectors with two energy windows in the thermal and epithermal energy range for the neutron spectrum was made. Further refinements were accomplished by Monte Carlo simulation in order to confirm the measurements made by nuclear track methodology (NTM) using polyallyl diglycol carbonate (PADC), which are passive detectors type CR-39TM.

2 Photo-neutron production during radiotherapy with high energy linear accelerators

The photo-nuclear interaction between bremsstrahlung radiation and heavy nuclei leads to the breaking of neutron-nucleus bound system and releasing a photo-neutron. Within the tungsten target photons

produce photo-neutron reactions in the accelerator target, shielding, collimators and equipment materials. Some metals with threshold energies in the MeV region like Al (13.06), Fe (7.65), Au (8.06), Pb (8.09), W (6.19) are involved [2]. Also, neutrons are produced by virtual photon reactions that take place in the tungsten target and their frequency depends mainly on the structural materials of linear accelerator heads. Kase et al. [3] reports that 35% of production takes place at the primary collimator. Furthermore, photo-neutrons could reach the surrounding matter inducing neutron activation. Consequently some radioisotopes will decay, through prompt and delayed gamma-rays. Thus, in principle, the patient and staff may receive an undesirable dose [4] increasing the lifetime probability risk for oncogenesis; photo-neutron energies between 5.6 and 18 MeV may induce significant dose equivalents to critical organs [5].

3 Simulation of neutron production and transport

Several studies have been reported with the aim of determining the neutron spectra in the treatment halls with linear accelerators. Neutron spectra are measured with a Bonner sphere spectrometer with a passive neutron detector, or the dose is obtained through the linear energy transfer spectrum of recoils in CR-39TM plastic nuclear track detectors. Some work also includes the Monte Carlo calculation of neutron spectra and the dose [8]. A review on photoneutron characteristics in radiation therapy with high-energy photon beams are given elsewhere [9-11,1]. Our study is oriented to determine the photo-neutron gradient around the isocenter for a medical linear accelerator operating at 18 MV. A model of the accelerator head and vault was used with the MCNP5 code [12]. The program runs a large number of histories for every particle and so significant computing time is necessary to obtain good statistics. Several methods exist to overcome this drawback and one of them is offered by the code called the F5 tally [13]. Following the F5 tally, neutron spectra and room dose equivalent were calculated in several points inside the accelerator vault. Also, calculations at different locations on the treatment couch were carried out. The amount of histories was large enough to have uncertainties less than 3% on the location point for every detector. To handle the photo-neutron source term during the simulation we follow Tossi et al. [14] approach which takes into account the contribution due to evaporation and neutrons produced by the knock on reaction mechanism. The source term was allocated on the target and the accelerator head was modelled as a spherical shell made of W, Fe and Pb. The isocenter was located on the treatment couch which was modelled as made out of carbon fiber.

4 Nuclear track-etching methodology for photo-neutron detector

The CR-39TM is particularly useful for charged particle detection in the linear energy transfer (LET) range above the threshold value of ~ 10 keV. Photo-neutrons can be detected through latent tracks induced in PADC by proton and heavier nuclei recoils or charged reaction products. The method is characterized by short irradiation times of around 40 s at 600MU/min. To deploy detectors with a proper positioning and to prepare the irradiation configuration takes a few minutes. This is an important advantage over other techniques based on active systems, which require a whole day of activity. Exposed detectors to photo-neutrons and scattered neutrons at the photon-beam isocenter, provide useful information on the existing neutron field for patients undergoing, for instance, prostate treatment. In this case, using the Intensity-Modulated Radiation Therapy (IMRT) as an advanced radiotherapy modality has the main advantage of smaller expected side effects as compared with conventional radiotherapy. On the other hand, it has also been shown that collimators made out of W, Fe and Al, increase photo-neutron production rate so that an additional dose is expected. The NTM to be considered combines CR-39TM with converters and neutron fields are determined indirectly by charged fragments from a $^{10}\text{B}(n,\alpha)$ reaction. The high LET products (He^{++} and $^7\text{Li}^+$) leave their kinetic energy in the PADC where a large number of atoms ionize, and before electronic recombination takes place; the resulting electronic avalanche extends ionization to about 1000 nm far away from the impinging direction. To produce latent

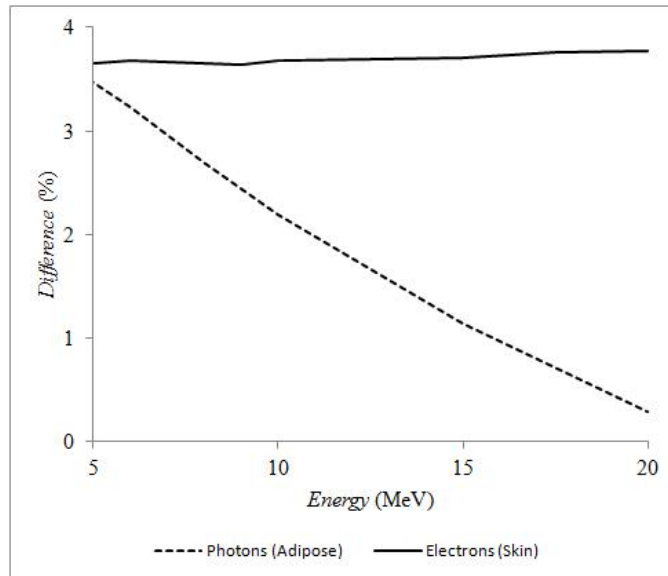


Fig. 1. Difference in the 5-20 MeV range of: (a) Photon mass attenuation coefficients (dotted line) for CR-39TM and adipose tissue. (b) Electron mass stopping power (solid line) for CR-39TM and skin.

tracks related to thermal and fast neutrons, the detector surface is covered with highly enriched ¹⁰B boric acid with or without a 0.8 mm thick cadmium cover. The resultant size and shape of the damaged volume depends on the absorbed ion energy, mass and momentum and it is visible in CR-39TM after chemical etching (6N, NaOH, 70°C) under light transmission microscope (10 x 40). Tracks of the order of micrometers are visible and their diameters are measured and collected in histogram bars.

5 Expected photo-neutron dose during radiotherapy

An important feature for a radiation detector is that it should produce a minimal distortion of the observed radiation fields. In that sense CR-39TM is quite adequate when used for dosimetry purposes in radiotherapy. Minimal distortion can be assured if its radiation transport properties are not very different from those of surrounding tissues and in that sense CR-39TM can be considered equivalent to skin and/or adipose tissue. Measurements show that, for photons, the difference of total mass attenuation coefficients for adipose tissue and CR-39TM was under 3.5 % in the 5-20 MeV range and it falls quickly in the high energy range. In the case of electrons the difference of mass stopping powers for skin and CR-39TM was under 4 % and it is nearly constant in the same energy range. In principle these results indicate that the detector can be placed on the patient's skin for external in vivo dosimetry. When neutron transport is considered, the hydrogen atom density is the relevant quantity to be compared for CR-39TM, adipose tissue and skin. It turns out that these densities have very similar values. In Fig. 1 we report the difference Photon mass attenuation coefficients and Electron mass stopping power in the 5-20 MeV range for CR-39TM - adipose tissue and CR-39TM - skin respectively. For the absorbed dose evaluation a good knowledge of neutron fluence as a function of the energy is required as input information. In principle such evaluation is beyond the scope of this work because our experimental array provides a measurement of integrated neutron fluxes for three energy windows. Nevertheless, the neutron fluxes calculated from simulation of neutron production and transport in the presence of a water

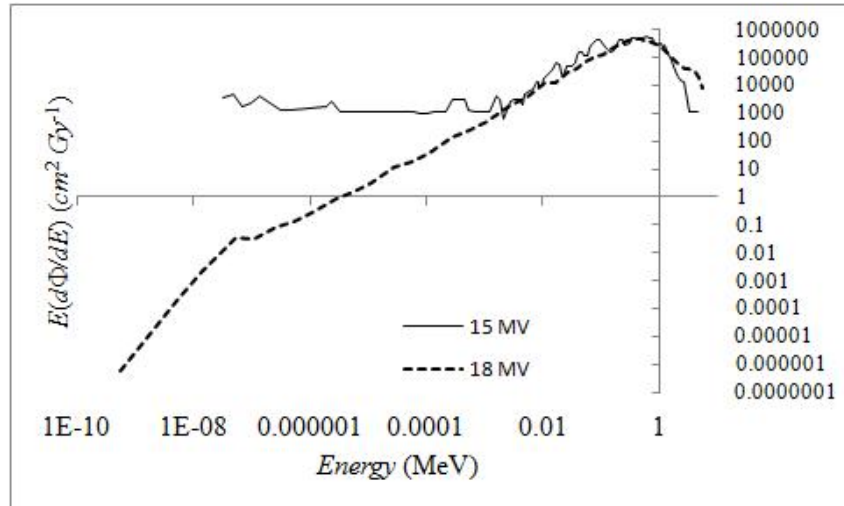


Fig.2. Comparison of simulations where neutron fluence is a function of letargy for two experiments with photon beams ($10 \times 10 \text{ cm}^2$ field): (a) CR-39TM detector irradiation at isocenter (dotted line). (b) Water tank phantom irradiation at isocenter (solid line). This comparison is still relevant in spite of accelerator operational voltage difference because the delivered dose should be the same in compliance to medical standards. The remarkable features are an important suppression of fluence in the thermal neutron energy range for CR-39TM and a nearly perfect overlap in the fast neutron energy range.

tank phantom [15] compared with those related to nuclear-track detectors alone allow the evaluation of the role of thermal neutrons coming from the patient for the absorbed dose build-up. In Fig. 2 a comparison is made for such simulations and it can be seen that for the same dose delivery at isocenter (which is achieved in both cases to comply with medical standards, regardless the particular features of each accelerator) there is a remarkable difference in the thermal neutron energy range and a nearly perfect overlap in the fast neutron energy range. The bigger contribution of thermal neutrons is due to the presence of the patient or the water tank phantom in this case. The probability distributions of non-elastic interactions are depicted in Fig. 3 and in all of them the main contribution is related to the thermal neutron energy range. The absorbed dose break-down per delivered Gy at isocenter is shown in Table I for breast tissue. The dominant contributions correspond to (n, γ) and (n, p) reactions and if we take 0.5 MeV as the top energy for thermal neutrons, they deliver 86.1% and 56.6% of the absorbed dose for each channel, which implies that for the in-field case most of the absorbed dose is induced by the patient. Clearly the presence of a patient is paramount for thermal neutron production and it should be related to the fact that the patient's body has very high hydrogen content. The lifetime probability risk for oncogenesis is shown in Table II [16-17]. In terms of a risk/benefit basis it does not pose a significant risk although it is advisable to avoid this kind of treatments in children.

6 Experimental Details and Results

The experimental set-up used in our measurements consists of a passive detector with different assembled configurations i.e. bare, lined with and without Cd-filter. The Linac was operated at a nominal voltage of 18 MV for a time of 39.6 s, for a total dose of 400 MU and a dose rate of 600 MU/min (MU, monitor unit, corresponds to 1cGy in a field of $10 \times 10 \text{ cm}^2$ in the Dmax point at 3.2cm depth in water). Detectors were placed at different locations on the treatment couch and the origin of the reference system corresponds to the isocenter. Fig. 4 shows comparison between simulated and measured data.

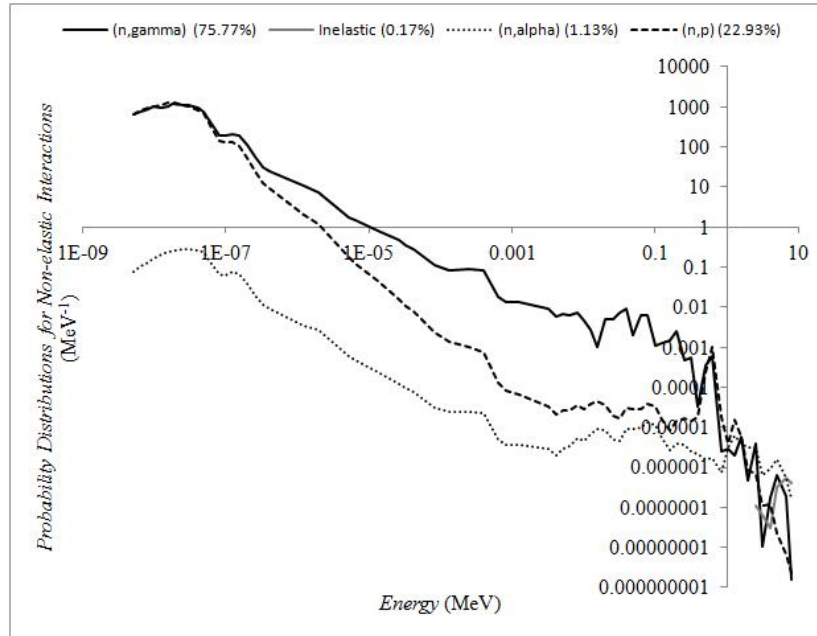


Fig.3. Non-elastic interaction probability distribution for the relevant nuclear reactions. The contribution from the thermal neutron energy range is going to play a leading role in dose build-up.

Table I: Absorbed dose break-down (mGy) per delivered Gy at isocenter

Total	γ from (n,γ)	β^a	γ after β^a	(n,α)	(n,p) Inelastic	(n,p) Elastic
0.357	0.225	0.012	0.004	0.022	0.003	0.091

^a Accumulated dose 50 years after irradiation.

Table II: Lifetime probability risk for oncogenesis (% , 30 Gy treatment) by age^a

Source	5 years	20 years	40 years	60 years	80 years
ICRP 60	0.150	0.086	0.032	0.021	0.005
BEIR V	0.150	0.123	0.064	0.054	0.021

^a For breast tissue (ICRU-44)

7 Discussion

As a first result it was found that detectors without neutron converter show tracks of small area due to recoils; these are mainly protons produced by (n, p) reactions due to thermal or fast neutrons. The track distribution is shown at the top in Fig.6, around channel 5 it shows a maximum and then it decreases as a nearly exponential curve to negligible values as get closer to the channel where heavy ions are expected to be recorded. Few large tracks above channel 25 are shown but these are due to heavy nuclei recoils (PADC oxygen and carbon). We do not expect to observe tracks related to cosmic ray particles due to the short exposure time of the PADC-NTD. The proton track spectrum is subtracted from the histograms of those that are related to PADC-covered with a ^{10}B -converter and a Cd-filter. The resulting histogram is free from tracks related to proton recoils and it shows a peak produced by alpha-tracks as a product of the photo-neutron reaction $^{10}\text{B}(n,\alpha)$. The amount of alpha tracks from PADC lined by Cd is less than those without a Cd-filter. This result is explained by the $^{10}\text{B}(n,\alpha)$ reaction cross section (~ 3838 b) for

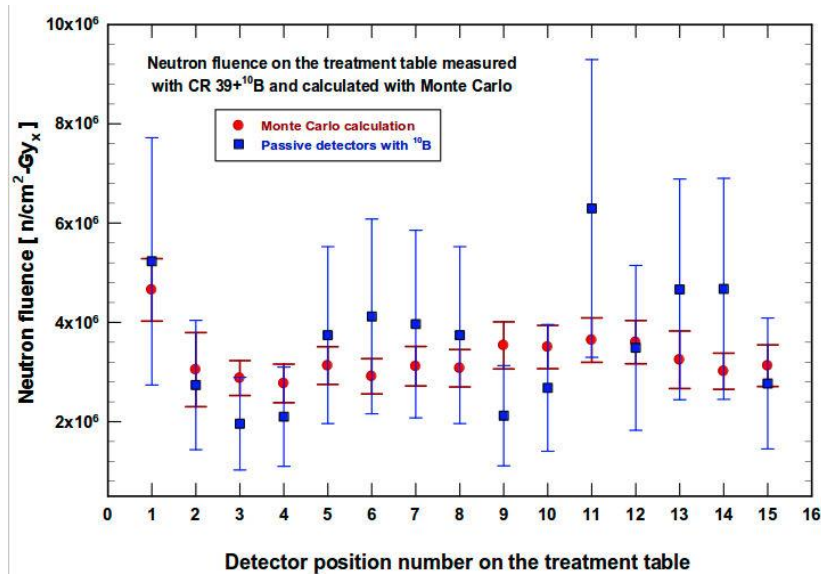


Fig. 4. Neutron fluence on the treatment couch measured with ¹⁰B+CR-39 and simulated with Monte Carlo. Passive detectors results are shown by squares.

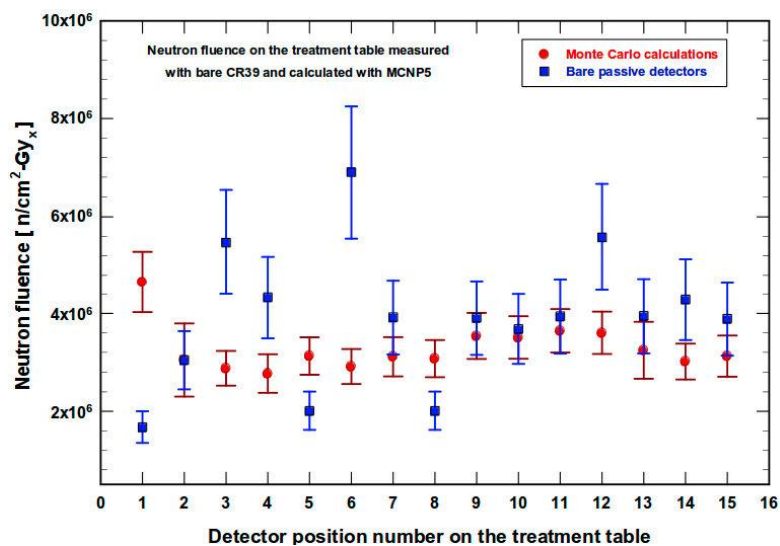


Fig.5. Neutron fluence on the treatment table measured with bare CR-39TM (only proton tracks) and determined by Montecarlo simulation.

thermal neutrons but still has high value in the neutron resonance energy region (assured by the Cd-filtering property).

Therefore, the spectral difference is related to alpha-tracks from photo-neutrons with energy above the thermal region. Similar procedure to determine spectral differences are applied to the whole set of detectors positioned around the treatment couch. The results provide data to draw a photo-neutron field map indicating the intensity gradient of thermal and fast neutron region.

This result is important when a dosimetric evaluation should be performed for a shielding geometry assessment. Three other results were obtained, the first is the simulation to determine the neutron fluence around the treatment couch. The next is the agreement between the PADC detector track

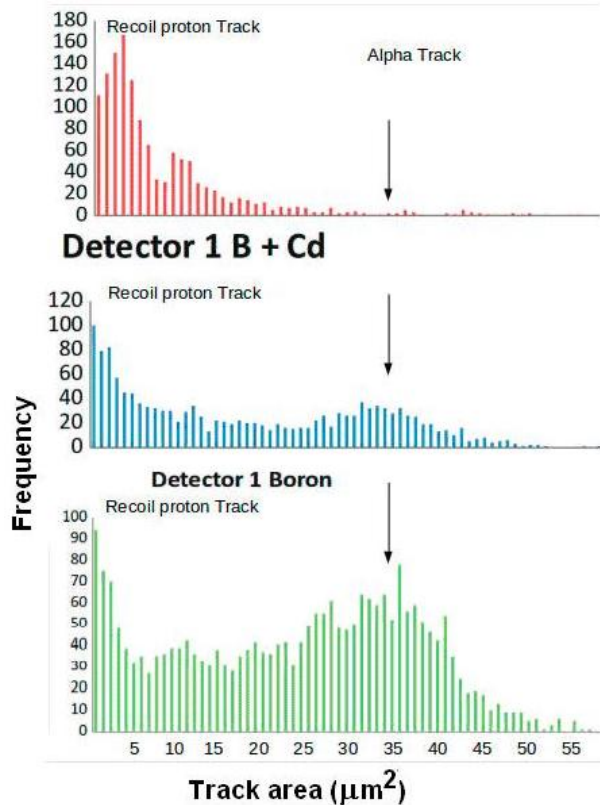


Fig.6. Track distributions. Frequency as function of the channel (track area in μm^2) is shown to illustrate how the thermal and epithermal components for photo-neutron field spectra can be discriminated.

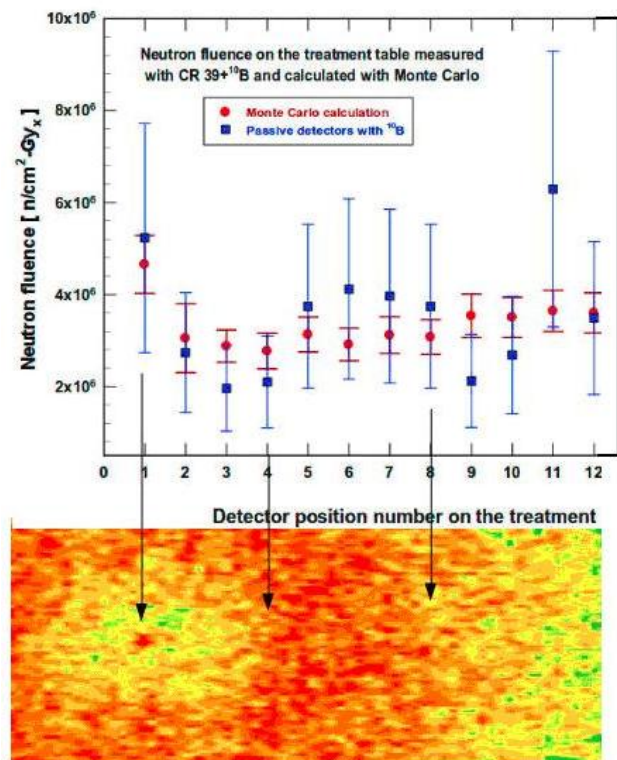


Fig.7. Comparison of results given by simulations and measurements. Areas delimited by arrows are related to photo-neutron fluence; It is highest at the isocenter (red spot at No. 1) then decreases (yellow area between the first two arrows) and then increases again with distance. After the third arrow it diminishes slowly.

density with the one predicted by Monte Carlo, as it is shown in Fig. 4. The latter is related to an effect not reported so far which can be determined comparing expected neutron fluence with track density at the same spot. The outcome (see Fig. 7) is that as we depart from the isocenter on the treatment couch the neutron fluence decreases sharply first and then it slowly increases to maintain a steady value. This has not been reported so far in the literature and it could be an important result that needs to be studied in detail in order to have a better control of neutron dose.

8 Conclusions

The experiments were carried out at a radiotherapy facility with a Varian Clinac 2300 accelerator and the goal was to determine the photo-neutron fluence and its gradient. The track distributions are due to proton recoils and alphas particles produced by photo-neutrons. The NTM was used advantageously by the combination of CR-39TM with neutron converters and cadmium filters to determine the photo-neutron field in a radiotherapy hall and it leads to similar results already obtained by other authors with different approaches. Monte Carlo simulations give some hint on the expected neutron dose gradient during treatments. As a byproduct, enhanced effect on the absorbed dose due to both scattered neutrons and by (γ, n) reactions, could be considered as a relevant processes to improve tumor treatment. The possibility exists for thermal neutrons to give a dose boost if the tumor is previously loaded with ^{10}B . We observed the existence at the isocenter of a non uniform photo-neutron dose rate. The calculated photo-neutron fluence has a value comparable with current BNCT practice. Hence the two effects overlap and could be used for therapy with the combination of standard phototherapy and boron photo-

neutron capture therapy (BNCT) as a new approach in glioblastoma multiforme treatment. This is a new possibility not yet discussed in the literature. A deconvolution technique, for thermal and fast neutron discrimination and gradient determination has not been reported in literature as well and it could be considered a new procedure in neutron spectrometry by NTM.

Acknowledgements

The authors are grateful to Erik Salcedo (M.Sc.) for his skillful help during Linac operation and detector exposure, as well as to the GURVE Radiotherapy Center at La Trinidad Medical Institute in Caracas for providing the experimental facility.

References

- [1] Liu J. C. *et al.* (1975) SLAC-PUB-7404 .
- [2] NCRP. (1984). NCRP report No. 79. Bethesda, MD. 19-21.
- [3] Kase K.R *et al.*, *Medical Accelerator. Health Phys.* **74**(1) (1998) 38-47.
- [4] Vega-Carrillo H.R. *et al.* (2015). <http://dx.doi.org/10.1016/j.apradiso.2015.05.004>
- [5] NCRP No. 116, (1993) Accessed June 2014, www.ncrponline.org/Publications.
- [6] Yeh, J. J., and I. Lindau. "Atomic data and nuclear data tables." *Academic Press* 32 (1985) 1-155.
- [7] Harvey R. R *et al.*, *Phys. Rev.* **136**, (1964) B126.
- [8] Fujibuchi T. *et al.*, *Nucl. Instrum. Meth. Phys. Res. B* **349** (2015) 239-235.
- [9] Vega-Carrillo H.R *et al.*, *J. Radioanal. Nucl. Chem.*, **283** 261-265.
- [10] Esposito A., Bedogni R., Lembo L., Morelli M., *Radiat. Meas.* **43** (2008) 1038-1043.
- [11] Kralik M., Turek K., Vondracek V. *Radiat. Prot. Dosim.* **132** (2008) 13-17.
- [12] X-5 Monte Carlo Team. Los Alamos, NM. LANL report CP-03-0245
- [13] F5 tally, Accessed June 2015, http://www.nucleonica.com/wiki/index.php?title=F5_tally
- [14] Tossi G. *et al.*, *Med. Phys.* **18** (1991) 54-60.
- [15] Patil *et al.* *Nucl. Instr. Meth. Phys. Res. B* 269(2011)3261-3265.
- [16] ICRP 60, Pergamon Press, Oxford, England, 1991.
- [17] BEIR V, Health effects of exposure to low levels of ionizing radiation, National Academy Press, Washington, DC, 1990.
- [18] Mameli A. *et al.*, *Nucl. Instr. Meth. Phys. Res. B* **266** (2008) 3656–3660
- [19] Castillo, R., J. Dávila, and L. Sajo Bohus. X Latin American Symp. on Nucl. Physics and Applications (2013)

Nuclear Matrix Elements for the $\beta\beta$ Decay of ^{76}Ge

B.A. Brown¹, D.L. Fang², and M. Horoi³

¹ Department of Physics and Astronomy and National Superconducting Cyclotron Laboratory Michigan State University, East Lansing, Michigan 48824-1321, USA

² College of Physics, Jilin University, Changchun 130012, China

³ Department of Physics, Central Michigan University, Mount Pleasant, Michigan 48859, USA

Abstract

The nuclear matrix elements for two-neutrino double-beta ($2\nu\beta\beta$) and zero-neutrino double-beta ($0\nu\beta\beta$) decay of ^{76}Ge are evaluated in terms of the configuration interaction (CI), quasiparticle random phase approximation (QRPA) and interacting boson model (IBM) methods. We show that the decomposition of the matrix elements in terms of intermediate states in ^{74}Ge is dominated by ground state of this nucleus. We consider corrections to the CI results that arise from configurations admixtures involving orbitals outside of the CI configuration space by using results from QRPA, many-body-perturbation theory, and the connections to related observables. The CI two-neutrino matrix element is reduced due to the inclusion of spin-orbit partners, and to many-body correlations connected with Gamow-Teller beta decay. The CI zero-neutrino matrix element for the heavy neutrino is enhanced due to particle-particle correlations that are connected with the odd-even oscillations in the nuclear masses. The CI zero-neutrino matrix element for the light neutrino contains both types of correlations that approximately cancel each other.

Many properties of the active neutrinos are measured, but it is not yet established whether they are Dirac or Majorana type particles and their absolute masses are not known. Left-right symmetric extensions to the standard model provide an explanation for the non-zero masses of the left-handed light neutrinos and also predict the existence of right-handed heavy neutrinos [1]. Neutrinoless double-beta ($0\nu\beta\beta$) decay of nuclei provides unique information and constraints on these neutrino properties [2], [3], [4], [5], [6]. The $\beta\beta$ decay process and the associated nuclear matrix elements (NME) have been investigated by using several approaches including the quasiparticle random phase approximation (QRPA), [7], [8] the configuration interaction (CI) model, the interacting boson model (IBM), the generator coordinate method [9], and the projected Hartree-Fock Bogoliubov model [10].

Assuming contributions from the light left-handed (ν) neutrino-exchange mechanism and the heavy right-handed (N) neutrino-exchange mechanism, the decay rate of a neutrinoless double-beta decay process can be written as [4], [11]

$$\left[T_{1/2}^{0\nu}\right]^{-1} = G^{0\nu} \left(|M^{0\nu}|^2 |\eta_\nu|^2 + |M^{0N}|^2 |\eta_N|^2 \right), \quad (1)$$

where $G^{0\nu}$ is the phase space factor [12], [13], M are the nuclear matrix elements (NME), and η are combinations of the neutrino masses [11], [4].

Since the experimental decay rate is proportional to the square of the calculated nuclear matrix elements, it is important to calculate these matrix elements with good accuracy to be able to determine the absolute scale of neutrino masses. However, the theoretical methods used give results that differ from one another by factors of up to 2-3. It is important to understand the nuclear structure aspects of these matrix elements and why the models give differing results.

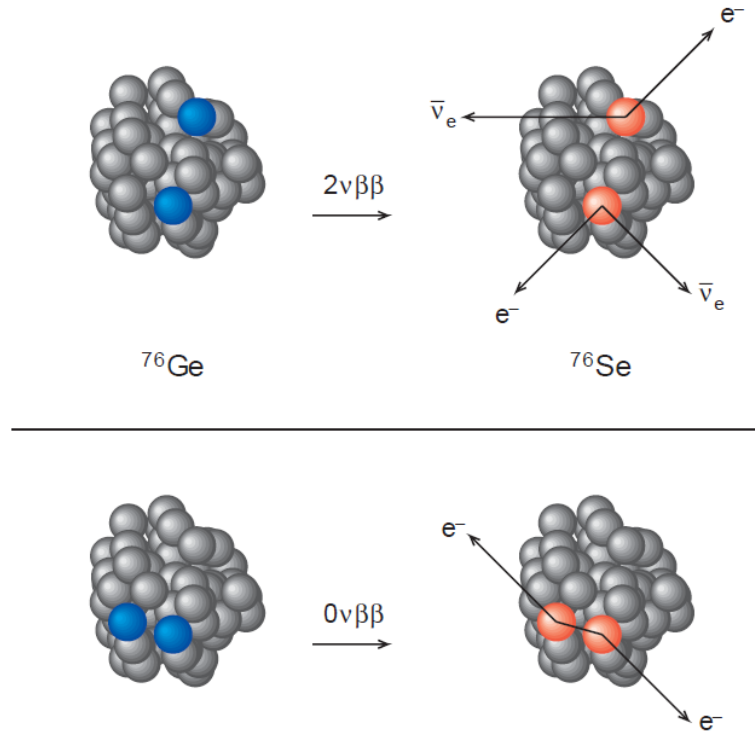


Fig. 1: The $\beta\beta$ decay of ^{76}Ge . The top part shows the conversion of two neutrons (blue on the left) into two protons (red on the right) in $2\nu\beta\beta$ decay. The bottom part shows the $0\nu\beta\beta$ decay where a virtual neutrino is exchanged.

In this talk we discuss the NME for the $\beta\beta$ decay of ^{76}Ge obtained with the CI, QRPA and IBM-2 methods. We will show that all of these methods have deficiencies. Some of the deficiencies can be addressed with many-body perturbation theory (MBPT) approaches, and connections to other observables.

The nuclear matrix elements can be presented as a sum of Gamow-Teller (M_{GT}), Fermi (M_F), and Tensor (M_T) matrix elements (see, for example, Refs. [14], [15]),

$$M = M_{GT} - \left(\frac{g_V}{g_A} \right)^2 M_F + M_T, \quad (2)$$

where g_V and g_A are the vector and axial constants, correspondingly. We use $g_V = 1$ and $g_A = 1.27$. The M_α are matrix elements of scalar two-body potentials. The Gamow-Teller has the form $V_{GT}(r, A, \mu) \sigma_1 \cdot \sigma_2 \tau_1^- \tau_2^-$ and the Fermi has the form $V_F(r, A, \mu) \tau_1^- \tau_2^-$, where τ^- are the isospin lowering operators. The neutrino potentials depend on the relative distance between the two decaying nucleons, r , the mass number A , and the closure energy μ [16]. The radial forms are given explicitly in [14]. For the heavy-neutrino exchange, the potential does not depend on μ . For the light neutrino matrix element the closure approximation is good to within 10% [17].

The operators for M_{GT} are given to a good approximation by $f(r) \sigma_1 \cdot \sigma_2 \tau_1^- \tau_2^-$, where $f(r)^{2\nu} = 1$ (in closure), $f(r)^{0\nu} = a/r$ and $f(r)^{0N} = b \delta(r)$ where the constants a and b depend on A , μ and the SRC. The results discussed below follow from the expansions of the many-body matrix elements for these three operators in terms of the particle-hole (ph) in ^{76}As or particle-particle (pp) intermediate states in ^{74}Ge [18]. The expansion over pp states ($J_m = J_{pp}$) in ^{74}Ge is shown in Fig. 1. The left-hand column

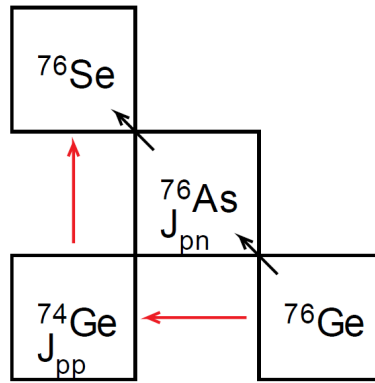


Fig. 2: Nuclei involved in the calculations for the double-beta decay of ^{76}Ge .

shows the light-neutrino results (ν) for the sum of the GT, F and T contributions. The middle column shows the light-neutrino results for GT contribution only. The right-hand column shows the heavy-neutrino results (N) for the sum of the GT, F and T contribution. The bottom row shows the running sums for 0^+ intermediate states. The middle row shows the running sums for 0^+ and 2^+ intermediate states. The top row shows the running sums for all intermediate states. The red dots are the exact results for the sum over all intermediate states. This shows that the $J_{pp}=0^+$ contribution is completely dominated by a path through the ground state of ^{74}Ge . There is some cancellation from higher J_{pp} values mainly coming from 2^+ that is spread over intermediate states up to about 6 MeV.

The expansion of the NME over intermediate J values obtained from the QRPA calculations is shown in Fig. 2. This figure shows the different types of correlations for the three operators. The 2ν decay is completely determined by the 1^+ states of the ph channel and its expansion over pp is complicated. The heavy neutrino is dominated by the 0^+ states of the pp channel and its expansion over ph states is complicated. The light neutrino NME is some where between these and but looks simplest in the pp channel.

The 2ν tensor NME is zero and the Fermi NME is zero since isospin is conserved. For 0ν and $0N$ the Fermi and tensor parts are both relatively small, and we define a correction factor for these given by $R_{GT} = M/M_{GT}$, where M contains all three terms of Eq. 2. The CI calculations give $R_{GT}^{0\nu} = 1.10(3)$. Larger values of 1.23 for QRPA [19] and 1.33 for IBM-2 [20] were obtained with the older calculations. But more recently, it was found that the 2ν Fermi matrix element was not zero because isospin was being treated incorrectly in QRPA [21] and IBM-2 [22]. After this was corrected the new $M_F^{2\nu}$ values are now zero in all methods. The new results for $R_{GT}^{0\nu}$ are 1.10 [21] and 1.19 [8] for QRPA, and 1.04 [22] for IBM-2. Taking these results into account we adopt a correction factor from the tensor plus Fermi contributions of $R_{GT}^{0\nu} = 1.12(7)$. The ratio for the heavy neutrino is 1.20 for CI, 1.26 for QRPA [8] and 1.00 for IBM-2 [22]. The adopted correction factor is $R_{GT}^{0N} = 1.13(13)$.

In the following we first focus on results for M_{GT} . At the end, the total matrix element M will be obtained from M_{GT} via a product of correction factors R given by $M = [M_{GT}(\text{CI})][R_V][R_S][R_{GT}]$. R_{GT} is defined above. We start with the use of short-range correlations (SRC) [15] based on the CD-Bonn potential [23]. At the end we will give a value and error for the correction to this, R_S , based on a range of assumptions about the SRC. R_V represents the correction coming from a “vertical” expansion of the CI model space that includes the effect of orbitals below and above those in $jj44$. R_V is the main focus of attention of this talk. The orbitals, model spaces and expansion methods are shown in Fig. 3.

The model space for CI and IBM-2 is $jj44$ that consists of the four valence orbitals $0f_{5/2}$, $1p_{3/2}$,

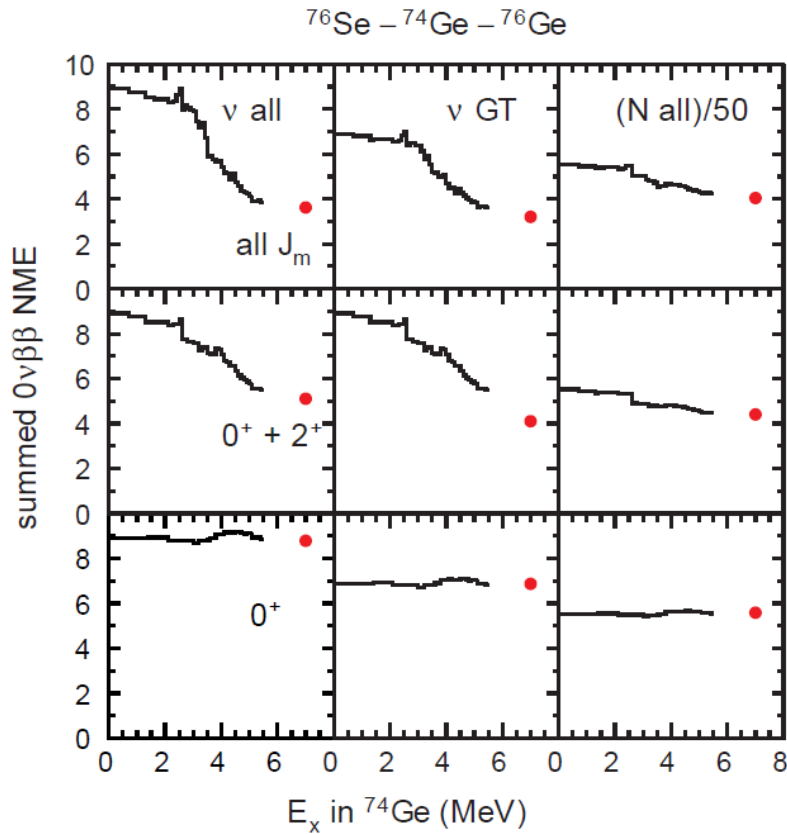


Fig. 3: Expansion of the NME over intermediate states ^{74}Ge .

$1p_{1/2}$ and $0g_{9/2}$ for protons and neutrons. The model space for QRPA are the 21 orbitals with oscillator quanta $N \leq 5$ where $N = 2n + \ell$ for protons and neutrons. The QRPA results are also given when the evaluation of the NME are restricted to $jj44$ and to fp ($jj44$ plus $0f_{7/2}$ and $0g_{7/2}$). In addition to our own CI calculations with the JUN45 [24] and $jj4bnp$ [25] Hamiltonians, we will show results from the $gcn28:50$ Hamiltonian [26] for 2ν [27], 0ν [28] and $0N$ [29].

The method and parameters used for the QRPA calculations [30] are similar to those used in [21]. For the particle-particle channel in order to restore the isospin symmetry, we follow the formalism introduced in [31], [21], by separately fitting the $T = 0$ and $T = 1$ parts of the interaction. For the $T = 1$ part, $g_{pp}^{T=1} = 0.985$ is taken to give $M_F^{2\nu} = 0$. For the $T = 0$ particle-particle channel, two parameter sets were used: (a) $g_{pp}^{T=0} = 0.673$ reproduces the experimental value for $M_{GT}^{2\nu}$, and (b) $g_{pp}^{T=0} = 0.643$ gives a value for $M_{GT}^{2\nu}$ that is a factor of $(1/0.75)^2$ larger than experiment, anticipating that there may be MBPT corrections beyond QRPA that could reduce the strength to low-lying states.

Results for the $2\nu\beta\beta$ NME are shown in Fig. 4. This NME is completely determined by $J_{ph}^\pi = 1^+$ intermediate states in ^{76}As . In CI the summation over intermediate including the energy denominator (Eq. 2 in [27]) is obtained with the strength-function method [32]. The IBM-2 result is not shown because it uses an approximation for the NME based on the closure result for the operator $\sigma_1 \cdot \sigma_2 \tau_1^- \tau_2^-$ together with average closure energies from other methods (Eq. 16 in Ref. [22]). Experiment is reduced by a factor of about $R_V^{2\nu} = 0.45$ compared to CI. $R_V^{2\nu} = M^{2\nu}/M^{2\nu}(\text{CI})$ denotes the correction beyond the $jj44$ model space, due to a “vertical” expansion that includes correlations from orbitals below and above the $jj44$ model space. The QRPA results for $jj44$ and pf show that part of this reduction

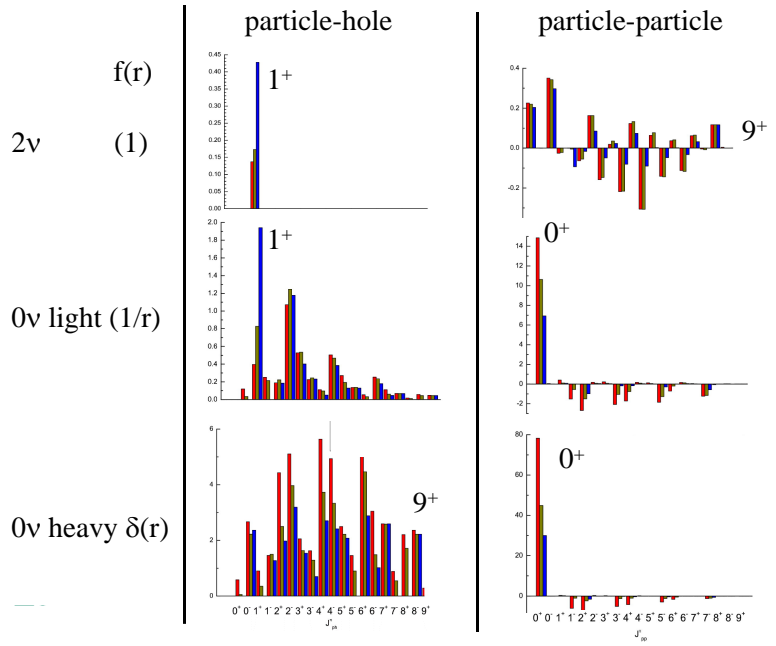


Fig. 4: The NME obtained in the QRPA calculations expressed in terms of their contributions from the J_{ph} states in ^{76}As on the left-hand side and the J_{pp} states in ^{74}Ge on the right-hand side. The color code is blue for the results obtained in $jj44$, black for the results obtained in fpg and red for the results obtained in the 21-orbit model spaces.

is due to the missing spin-orbit partners in the $jj44$ model space. The particle-hole correlations are dominated by a strong repulsive interaction in the 1^+ channel. Relative to the non-interacting single-particle distribution, Gamow-Teller strength is reduced in low-lying states and shifted into the giant Gamow-Teller resonance. As shown by the QRPA results for $jj44$ and fpg , both spin-orbit partners are important for the reduction. A similar behavior was observed for CI in the case of ^{136}Xe [33].

Beyond QRPA, it is known that two-particle two-hole (2p-2h) admixtures into the model space wavefunctions are important for Gamow-Teller beta decay. The experimental Gamow-Teller strength is observed to be reduced by a factor of $R'_V = 0.5 - 0.6$ relative to the CI calculations in the sd [35] and pf [36] model spaces. Also the strength extracted from charge-exchange reactions for the total Gamow-Teller strength up to about 25 MeV in excitation energy is reduced by this factor relative to QRPA [37] and the $3(N - Z)$ Ikeda sum rule [38]. Arima et al. [39] and Towner [40] have explained this reduction using MBPT in terms of 2p-2h admixtures into the model-space wavefunctions. Earlier calculations claimed that the reduction in GT strength was due to Δ excitations [41] in the nucleus. However, calculations with a realistic $N\Delta\pi$ interaction vertex have shown that the influence of Δ (and other mesonic-exchange currents) is small [39], [40]. These results are compared to the empirical sd results in Fig. 13 of [35]. In order to conserve the Ikeda sum rule, the reduction in low-lying B(GT) strength is associated with a spreading of strength to high excitation energy [42] that gets removed from the 2ν NME due to the energy denominator in the summation over intermediate states. In summary, relative to CI in the $jj44$ model space, reductions due to a spin-orbit complete model space, together with 2p-2h admixtures are required for the $2\nu\beta\beta$ NME. The observed factor of $R_V = 0.45$ is consistent with expectations.

The results for 0ν (heavy neutrino) are shown in Fig. 5. In addition to our own QRPA results, we show the QRPA result from [8]. The J_{pp} intermediate states are dominated by the 0^+ ground state

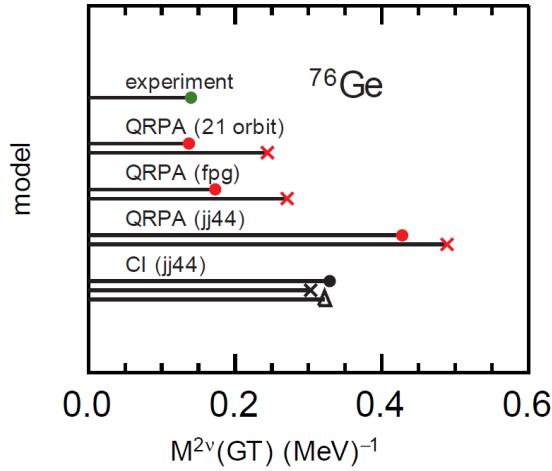


Fig. 6: Nuclear matrix elements for $2\nu\beta\beta$ decay of ^{76}Ge . The top point in green is the experimental value [34]. The QRPA results are shown for $g_{pp}^{T=0} = 0.673$ (red dots) and $g_{pp}^{T=0} = 0.643$ (red crosses). The CI results are shown for the JUN45 (dot), jj44bpn (cross) and gcn28:50 (triangle) Hamiltonians.

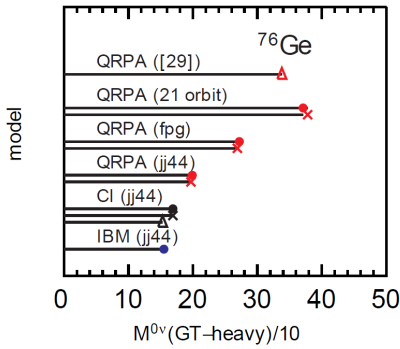


Fig. 7: The $0N$ NME for heavy neutrino decay of ^{76}Ge . See caption to Fig. 4. The QRPA point with the triangle is from Ref. [8].

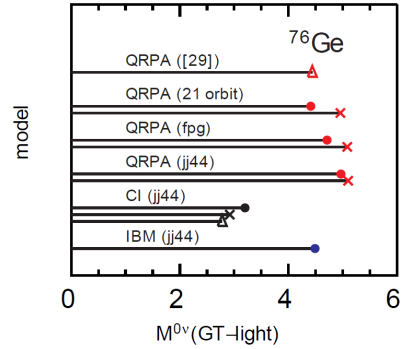


Fig. 8: The 0ν NME for the light-neutrino decay of ^{76}Ge . See captions to Figs. 2 and 3.

The results shown above are based on the CD-Bonn SRC. This is the weakest of several SRC that have been used [15]. The strongest is the AV18 SRC, and the UCOM [47] SRC is about half way between. For our final result we use the average of CD-Bonn and AV18 with an error that encompasses both. The result is that the $0N$ NME are multiplied by $R_S^{0N} = 0.80(20)$ and the 0ν NME are multiplied by $R_S^{0\nu} = 0.97(3)$, where R_S is the SRC correction relative to the CD-Bonn starting point.

Finally, we combine all of the factors discussed above in the form $M = [M_{GT}(CI)][R_V][R_S][R_{GT}]$. Based on the experimental value [34] for 2ν the NME is,

$$M^{2\nu} = 0.140(5) = [0.31(3)][0.45][1][1]. \quad (3)$$

The second term is the empirical correction for R_V due to mixing beyond the $jj44$ model space. The error in the CI NME reflects the spread obtained with the three different Hamiltonians used (Fig. 4). For $0N$,

$$M^{0N} = [155(10)][1.65(25)][0.80(20)][1.13(13)] = 232(80), \quad (4)$$

where the CI value is from Fig. 5. The error for $0N$ is dominated by the SRC correction. Finally For 0ν ,

$$M^{0\nu} = [3.0(3)][1.2(2)][0.97(3)][1.12(7)] = 3.9(8), \quad (5)$$

where the CI value is from Fig. 6. The error for 0ν is dominated by an estimated uncertainty of 20% in the correction beyond $jj44$. Comparison to previous values must take into account the isospin correction for QRPA and IBM discussed above, and the choice of SRC (in our R_S factor). The range is from 2.8 for CI [28] to 4.7 for IBM-2 [22] and 5.3 for QRPA [8]. Our result is in between these, but it is not an average since we have made comments on the deficiencies of all of these models. Using Eq. 1 with the experimental limit of the half-life ($T_{1/2}^{0\nu} > 3 \times 10^{25}$ yr [48]), and the phase space factor from [12], we obtain $|\eta_V| m_e c^2 < 0.3$ eV.

Sometimes the 2ν correction factor (0.45 in this case) is expressed in terms of an effective g_A value ($g'_A = 0.85$ in this case). Since the factor $(g_A)^4$ appears inside the phase-space factor of Eq. 1, one might think that the decay rate for 0ν and $0N$ could be reduced by a factor of $(g'_A/1.27)^4 = 0.20$ [22], [49]. However, this g'_A is only for a specific operator associated with a specific observable ($2\nu\beta\beta$ decay) relative to a specific model (CI in $jj44$ in this case). The operators involved in 0ν and $0N$ beta decay are different (short ranged), and corrections beyond CI cannot be expressed in terms of an overall change in g_A . It is better to express the renormalizations in terms of factors such as R_V that are operator and model space dependent.

The model-space truncation contributions to R_{pp} should be understood. The error for the R_{GT} correction could be reduced if reasons for the variations within the models is understood. The error for the R_V correction could be reduced if the MBPT results such as those in [46] should be expanded to include the renormalization of the separate effects in the ph and pp channels in order to compare to the results found previously relative to the $jj44$ model space. This includes the reduction in Gamow-Teller beta decay strength [39], [40], and the enhancements of the pairing strength seen in the D values. The basic division between CI and its MBPT corrections from all other orbitals can be checked by no-core and ab-initio CI in lighter nuclei where they are tractable. Other methods such as in-medium SRG [50] and coupled cluster [51] can be used in place of MBPT, and at this level the division between short-range renormalization, R_S , and long-range renormalization, R_V , might be merged. The CI results for the $A = 76$ region can be further checked against spectroscopic observables (occupations number are in good agreement with CI [28]) including two-nucleon transfer. Future calculations should be presented in terms of changes relative to various contributions we have discussed, and evaluations for other cases of interest [52] should be made.

We acknowledge correspondence from Jose Barea, Scott Bogner, Mark Caprio, Javier Menendez, Alfredo Poves and Fedor Simkovic. Support from the NUCLEI SciDAC Collaboration under U.S. Department of Energy Grant No. DE-SC0008529 is acknowledged. MH and BAB also acknowledge U.S. NSF Grant No. PHY-1404442.

References

- [1] J. C. Pati and A. Salam, Phys. Rev. D **10**, 275 (1974); R. N. Mohapatra and J. C. Pati, Phys. Rev. D **11**, 2558 (1975); W.-Y. Keung and G. Senjanovic, Phys. Rev. Lett. **50**, 1427 (1983).
- [2] M. Doi et al., Prog. Theor. Phys. **66**, 1739 (1981); **69**, 602 (1983).
- [3] W. C. Haxton and G. J. Stephenson, Prog. Part. Nucl. Phys. **12**, 409 (1984).
- [4] J. D. Vergados, H. Ejiri, and F. Simkovic, Rep. Prog. Phys. **75**, 106301 (2012).
- [5] F.T. Avignone, S.R. Elliott, and J. Engel, Rev. Mod. Phys. **80**, 481 (2008).
- [6] T. Tomoda, Rep. Prog. Phys. **54**, 53 (1991).
- [7] A. Faessler, M. Gonzalez, S. Kovalenko, and Fedor Simkovic, Phys. Rev. D **90**, 096010 (2014).

- [8] J. Hyvarinen and J. Suhonen, Phys. Rev. **91**, 024613 (2015).
- [9] T.R. Rodriguez and G. Martinez-Pinedo, Phys. Rev. Lett. **105**, 252503 (2010).
- [10] P.K. Rath, R. Chandra, K. Chaturvedi, P.K. Raina, and J.G. Hirsch, Phys. Rev. C **82**, 064310 (2010).
- [11] M. Horoi, Phys. Rev. C **87**, 014320 (2013).
- [12] J. Kotila and F. Iachello, Phys. Rev. C **85**, 034316 (2012).
- [13] S. Stoica and M. Mirea, Phys. Rev. C **88**, 037303 (2013).
- [14] R. A. Senkov and M. Horoi, Phys. Rev. C **88**, 064312 (2013).
- [15] M. Horoi and S. Stoica, Phys. Rev. C **81**, 024321 (2010).
- [16] R. A. Senkov, M. Horoi and B. A. Brown, Phys. Rev. C **89**, 054304 (2014).
- [17] R. A. Senkov and M. Horoi, Phys. Rev. C **90**, 051301(R) (2014).
- [18] B. A. Brown, M. Horoi and R. A. Sen'kov, Phys. Rev. Lett. **113**, 262501 (2014).
- [19] M. S. Yousef, V. Rodin, A. Faessler and F. Simkovic, Phys. Rev. C **79**, 014314 (2009).
- [20] J. Barea and F. Iachello, Phys. Rev. C **79**, 044301 (2009).
- [21] F. Simkovic, V. Rodin, A. Faessler and P. Vogel, Phys. Rev. C **87**, 045501 (2013).
- [22] J. Barea, J. Kotila and F. Iachello, Phys. Rev. C **91**, 034304 (2015).
- [23] R. Machleidt, Phys. Rev. C **63**, 024001 (2001).
- [24] M. Honma, T. Otsuka, T. Mizusaki, and M. Hjorth-Jensen, Phys. Rev. C **80**, 064323 (2009).
- [25] B. Cheal et al., Phys. Rev. Lett. **104**, 252502 (2010).
- [26] A. Gniady, E. Caurier, and F. Nowacki (unpublished).
- [27] E. Caurier, F. Nowacki and A. Poves, Phys. Lett. B **711**, 62 (2012).
- [28] J. Menendez, A. Poves, E. Caurier and F. Nowacki, Phys. Rev. C **80**, 048501 (2009), and A. Poves, private communication.
- [29] M. Blennow, E. Fernandez-Martinez, J. Lopez-Pavon, and J. Menendez, JHEP07, 096 (2010); and J. Menendez, private communication.
- [30] The single-particle energies are taken from a Woods-Saxon potential with Coulomb corrections. All of the residual interactions for QRPA are obtained from solutions of Bruckner G-matrix based on the CD-Bonn one-boson exchange nucleon-nucleon potential. We solve the BCS equations with the CD-Bonn pairing interactions adjusted to give the experimental five-point mass pairing gap. The renormalization factors are $g_{pair}^p = 0.858$ and $g_{pair}^n = 0.978$ for ^{76}Ge , and $g_{pair}^p = 0.894$ and $g_{pair}^n = 1.008$ for ^{76}Se . For the renormalization of the QRPA residual interactions, we use $g_{ph} = 1.0$ for the particle-hole channel.
- [31] V. Rodin and A. Faessler, Phys. Rev. C **84**, 014322 (2011).
- [32] M. Horoi, AIP Conf. Proc. **1304**, 106 (2010).
- [33] M. Horoi and B. A. Brown, Phys. Rev. Lett. **110**, 222502 (2013).
- [34] A. S. Barabash, Phys. Rev. C **81**, 035501 (2010).
- [35] B. A. Brown and B. H. Wildenthal, Annu. Rev. Nucl. Part. Sci. **38**, 29 (1988).
- [36] G. Martinez-Pinedo, A. Poves, E. Caurier, and A. P. Zuker, Phys. Rev. C **53**, R2602 (1996).
- [37] E. Litvinova, B. A. Brown, D. L. Fang, T. Marketin and R. G. T. Zegers, Phys. Lett B **730**, 307 (2014).
- [38] B. D. Anderson, T. C. Chittrakarn, A. R. Baldwin, C. Lebo, R. Madey, J. W. Watson, B. A. Brown and C. C. Foster, Phys. Rev. C **31**, 1161 (1985), and references therein.
- [39] A. Arima, K. Shimizu, W. Bentz, and H. Hyuga, Adv. Nucl. Phys. **18**, 1 (1987).
- [40] I. S. Towner, Phys. Rep. **155**, 263 (1987).
- [41] M. Rho, Nucl. Phys. A **231**, 493 (1974).
- [42] G. F. Bertsch and I. Hamamoto, Phys. Rev. C **26**, 1323 (1982); G. F. Bertsch and H. Esbensen, Rep. Prog. Phys. **50**, 607 (1987).
- [43] B. A. Brown, Phys. Rev. Lett. **111**, 162502 (2013).

- [44] B. A. Brown; Journal of Physics: Conference Series **445**, 012010 (2013).
- [45] E. Caurier, J. Menendez, F. Nowacki, and A. Poves, Phys. Rev. Lett. **100**, 052503 (2008).
- [46] J. D. Holt and J. Engel, Phys. Rev. C **87**, 064315 (2013).
- [47] R. Roth, H. Hergert, P. Papakonstantinou, T. Neff and H. Feldmeier, Phys. Rev. C **72**, 034002 (2005).
- [48] M. Agostini, et al., Phys. Rev. Lett. **111**, 122503 (2013).
- [49] J. Menendez, D. Gazit and A. Schwenk, Phys. Rev. Lett. **107**, 062501 (2011).
- [50] S. K. Bogner, H. Hergert, J. D. Holt, A. Schwenk, S. Binder, A. Calci, J. Langhammer, and R. Roth, Phys. Rev. Lett. **113**, 142501 (2014).
- [51] G. R. Jansen, J. Engel, G. Hagen, P. Navratil, and A. Signoracci, Phys. Rev. Lett. **113**, 142502 (2014).
- [52] http://science.energy.gov/~media/np/nsac/pdf/docs/2014/NLDBD_Report_2014_Final.pdf